COASTS UNDER CHANGING CLIMATE: OBSERVATIONS AND MODELING

EDITED BY: Rafael Almar, Marta Marcos, Goneri Le Cozannet and Roshanka Ranasinghe

PUBLISHED IN: Frontiers in Marine Science

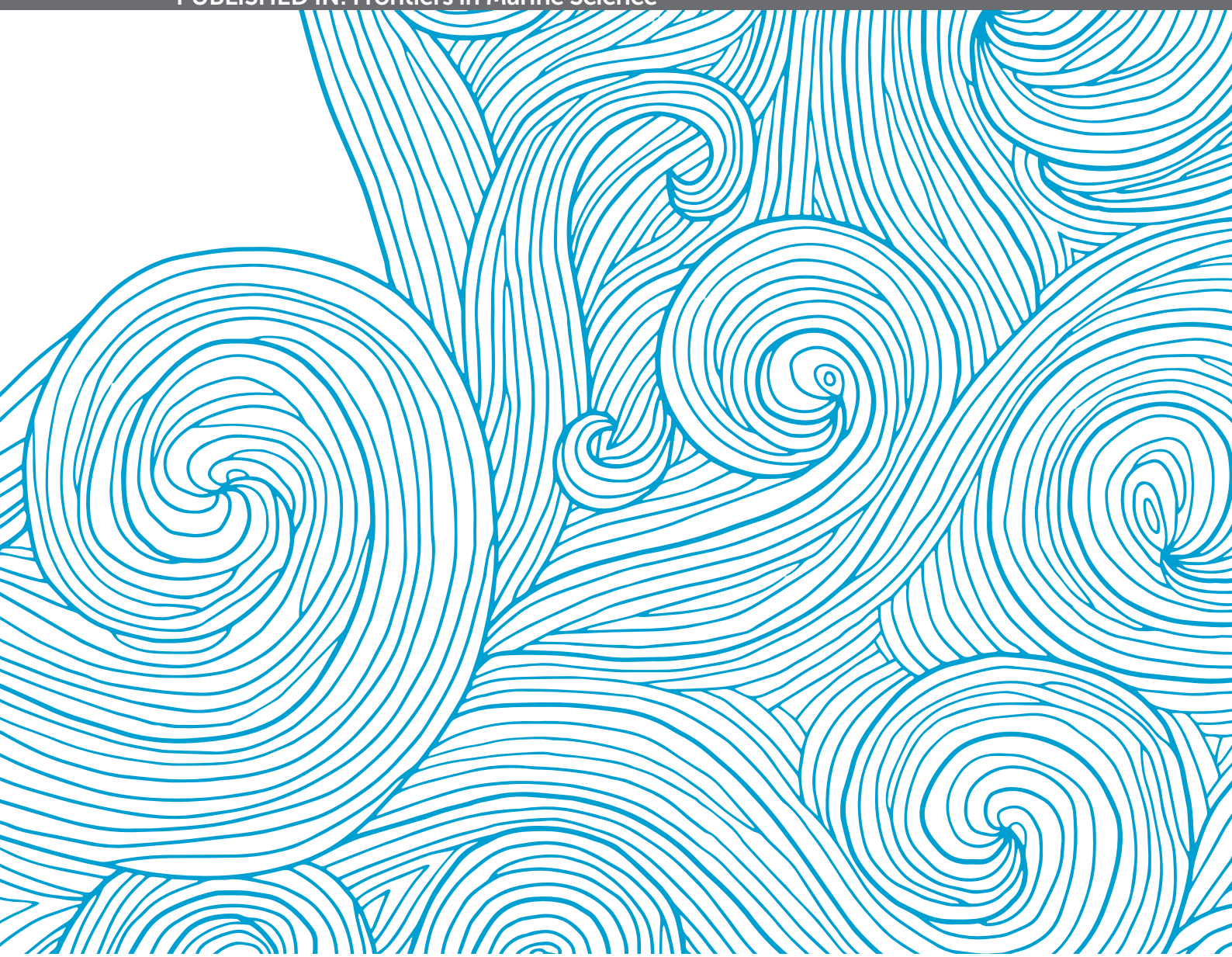

frontiers Research Topics

frontiers

ISSN 1664-8714
ISBN 978-2-88971-926-6
DOI 10.3389/978-2-88971-926-6

About Frontiers

Frontiers is more than just an open-access publisher of scholarly articles: it is a pioneering approach to the world of academia, radically improving the way scholarly research is managed. The grand vision of Frontiers is a world where all people have an equal opportunity to seek, share and generate knowledge. Frontiers provides immediate and permanent online open access to all its publications, but this alone is not enough to realize our grand goals.

Frontiers Journal Series

The Frontiers Journal Series is a multi-tier and interdisciplinary set of open-access, online journals, promising a paradigm shift from the current review, selection and dissemination processes in academic publishing. All Frontiers journals are driven by researchers for researchers; therefore, they constitute a service to the scholarly community. At the same time, the Frontiers Journal Series operates on a revolutionary invention, the tiered publishing system, initially addressing specific communities of scholars, and gradually climbing up to broader public understanding, thus serving the interests of the lay society, too.

Dedication to Quality

Each Frontiers article is a landmark of the highest quality, thanks to genuinely collaborative interactions between authors and review editors, who include some of the world's best academicians. Research must be certified by peers before entering a stream of knowledge that may eventually reach the public - and shape society; therefore, Frontiers only applies the most rigorous and unbiased reviews.
Frontiers revolutionizes research publishing by freely delivering the most outstanding research, evaluated with no bias from both the academic and social point of view. By applying the most advanced information technologies, Frontiers is catapulting scholarly publishing into a new generation.

What are Frontiers Research Topics?

Frontiers Research Topics are very popular trademarks of the Frontiers Journals Series: they are collections of at least ten articles, all centered on a particular subject. With their unique mix of varied contributions from Original Research to Review Articles, Frontiers Research Topics unify the most influential researchers, the latest key findings and historical advances in a hot research area! Find out more on how to host your own Frontiers Research Topic or contribute to one as an author by contacting the Frontiers Editorial Office: frontiersin.org/about/contact

COASTS UNDER CHANGING CLIMATE: OBSERVATIONS AND MODELING

Topic Editors:
Rafael Almar, Institut de Recherche Pour le Développement (IRD), France
Marta Marcos, University of the Balearic Islands, Spain
Goneri Le Cozannet, Bureau de Recherches Géologiques et Minières, France
Roshanka Ranasinghe, IHE Delft Institute for Water Education, Netherlands

Citation: Almar, R., Marcos, M., Le Cozannet, G., Ranasinghe, R., eds. (2021). Coasts Under Changing Climate: Observations and Modeling. Lausanne: Frontiers Media SA. doi: 10.3389/978-2-88971-926-6

Table of Contents

frontiers in Marine Science

EDITORIAL
published: 01 November 2021
doi: 10.3389/fmars.2021.785608

Editorial: Coasts Under Changing Climate: Observations and Modeling

Rafael Almar[1]*, *Marta Marcos*[2], *Gonéri Le Cozannet*[3] and *Roshanka Ranasinghe*[4]

[1] LEGOS/IRD, Toulouse, France, [2] Department of Physics, University of the Balearic Islands, Palma de Mallorca, Spain, [3] Bureau de Recherches Géologiques et Minières, Orléans, France, [4] International Institute for Infrastructural Hydraulic and Environmental Engineering (IHE Delft) Institute for Water Education, Delft, Netherlands

Keywords: numerical modeling, earth satellite observations, artificial intelligence, data-driven models, forecast, remote sensing-GIS

Editorial on the Research Topic

Coasts Under Changing Climate: Observations and Modeling

As sea-level rises due to climate change, providing salient information to support coastal risk management and adaptation is becoming a critical issue for numerous coastal communities and economic activities. The way this information is produced is now evolving rapidly as new observation and modeling capabilities are becoming available. This includes numerous multi-scale, multi-platform, terrestrial, airborne, and spatial remote sensing data, which can be combined with numerical modeling tools to improve our capabilities to reproduce past coastal evolutions and disasters, as well as to anticipate the future (e.g., Copernicus satellite and climate services). This Research Topic presents new research supporting coastal engineering and risk management, land use planning, integrated coastal zone management and coastal adaptation. It includes studies using and combining observations (e.g., *in-situ*, aerial, remote sensing) and models to understand and anticipate future coastal risks. Observation and modeling are key to facilitate the design and implementing prevention solutions that mitigate coastal risks. Among the articles published in this Research Topic, most deal with deterministic or probabilistic modeling with observations used for model validation and initialization. Six articles address coastal flooding, three address coastal erosion and one article focuses on ecosystem damage, while two articles concern coastal policy and management.

Flooding is often a result of the compound processes acting at multiple space scales, such as wind, waves, and surges, and their impacts on coastal zones is generally most accurate at local scales, where the flooding dynamics can be best represented. The contribution in this Research Topic, Höffken et al. investigates the influence of the duration and intensity of storm surge events on flood extent and water depths in coastal zones, and assesses the associated flood exposure for the case of the municipality of Eckernförde, Germany. Another local study by Orejarena-Rondón et al. presents an analysis on the coastal flooding impacts of the combined effect of extreme waves and sea level extremes in Bocagrande, Cartagena (Colombia). Both studies also evaluate the impacts of projected mean sea-level rise, further demonstrating the. Trošelj et al. quantify the impact of two extreme storm surge events in October 2006 on the Ibaraki Coast (Japan) in terms of sea surface elevation, water velocities and hydrographic imprints, using a fine (2 km) resolution dynamical downscaling.

Other studies in this Research Topic build upon the recent progresses obtained in broad scale or global flood modeling by the coastal scientific community. Tadesse et al. explore the potential of data-driven models to simulate storm surges based on atmospheric fields and indices at global scale. They find that at ∼70% of tide gages, mean sea-level pressure is the most important predictor to model daily maximum surge. Instead of using a statistical approach, Muis et al. present a novel CMIP6 global dataset of extreme sea levels, the Coastal Dataset for the Evaluation of Climate Impact

OPEN ACCESS

Edited and reviewed by:
Charitha Bandula Pattiaratchi, University of Western Australia, Australia

***Correspondence:**
Rafael Almar
rafael.almar@ird.fr

Specialty section:
This article was submitted to Coastal Ocean Processes, a section of the journal Frontiers in Marine Science

Received: *29 September 2021*
Accepted: *12 October 2021*
Published: *01 November 2021*

Citation:
Almar R, Marcos M, Le Cozannet G and Ranasinghe R (2021) Editorial: Coasts Under Changing Climate: Observations and Modeling. Front. Mar. Sci. 8:785608. doi: 10.3389/fmars.2021.785608

(CoDEC), generated with a hydrodynamic model, which can be used to accurately map the impact of climate change on coastal regions around the world.

Understanding the long-term (50–100 year) evolution of coasts perturbed by human activities in a changing climate is of great importance for coastal zone planners and managers. Roelvink et al. present a new free-form coastline model, ShorelineS, that is able to simulate long term, local scale shoreline change based on relatively simple principles of alongshore transport gradient driven changes as a result of coastline curvature, including under highly obliquely incident waves. The model can reproduce complex behavior such as a splitting and merging of coastlines, and longshore transport disturbance by hard structures. Also describing possible evolution of coastal systems, the contribution by Bamunawala et al. focuses on the development and piloting of an innovative reduced complexity model G-SMIC that can probabilistically simulate climate-change driven evolution of inlet-interrupted coasts at 50–100 year time scales, while taking into account the contributions from catchment-estuary-coastal systems in a holistic manner. G-SMIC also quantifies the input-driven uncertainties associated with the evolution of Catchment-Estuary-Coastal systems over the twenty-first century.

A global increase in coastal hypoxia has emerged over the past decades due largely to a considerable rise in anthropogenically-derived nutrient loading. Zhou et al. investigate the physical and biogeochemical processes that create high-biomass phytoplankton production and hypoxia off the Changjiang (Yangtze River) Estuary in the East China Sea. Extensive *in situ* datasets are linked with a coupled Regional Ocean Modeling Systems (ROMS) and the Carbon, Silicate, and Nitrogen Ecosystem (CoSiNE) model to investigate the temporal decoupling of phytoplankton production and hypoxia. Such studies ultimately support better forecasts and projections of coastal hypoxia.

Finally, some of these multiple vulnerabilities are integrated in the perspective of management and policies. Terorotua et al. emphasize their major role in the co-design of tailored coastal climate services based on a case study of French Polynesia. In their contribution, the authors assess climate change perceptions by public authorities and identify their needs with regard to climate-related science. To enable a better anticipation of future risks due to sea level rise, Dayan et al. provide global to regional High-End Scenarios exploring an unlikely, but not impossible, scenario of rapid melting of ice-sheets from now to 2,200, supported by expert elicitation. While Dayan et al. remind that high-end scenarios can be relevant for risk-averse stakeholders concerned with e.g., critical infrastructure, the paper by Terorotua et al. delivers empirical evidence that the governance able to address the challenge still needs to be built up in many regions. Building this adaptation governance and capacity is part of today's coastal adaptation challenge that comes in addition to mitigating climate change and curbing marine and coastal biodiversity losses.

The coastal system can be regarded as co-evolving socio-economic and ecological systems experiencing substantial environmental pressures owing to the mechanisms of change exerted by human activities against a background of natural and climatic changes (Dada et al., 2021). Planning for the future use of the goods and services available from coastal ecosystems will therefore continue to be influenced or disturbed by unpredictable events. One way to account for the large volume of model projections and observations is their integration into increasingly complex holistic approaches and dissemination to the widest possible audience through simplified indices (Koroglu et al., 2019) available to coastal communities, which will maximize their use in sustainable coastal development and management. Papers in this Research Topic adds evidence for this sustainability challenge being increasingly considered in coastal science and operational coastal zones management.

AUTHOR CONTRIBUTIONS

RA, MM, GL, and RR contributed to the ideas development and writing. All authors contributed to the article and approved the submitted version.

REFERENCES

Dada, O., Almar, R., Morand, P., and Ménard, F. (2021). Towards West African coastal social-ecosystems sustainability: interdisciplinary approaches. *Ocean Coastal Manage.* 211:105746. doi: 10.1016/j.ocecoaman.2021.105746

Koroglu, A., Ranasinghe, R., Jiménez, J. A., and Dastgheib, A. (2019). Comparison of coastal vulnerability index applications for Barcelona Province. *Ocean Coastal Manage.* 178:104799. doi: 10.1016/j.ocecoaman.2019.05.001

Conflict of Interest: The authors declare that the research was conducted in the absence of any commercial or financial relationships that could be construed as a potential conflict of interest.

frontiers in Marine Science

ORIGINAL RESEARCH
published: 01 October 2019
doi: 10.3389/fmars.2019.00614

Coastal Impacts Driven by Sea-Level Rise in Cartagena de Indias

*Andrés F. Orejarena-Rondón[1], Juan M. Sayol[2], Marta Marcos[3,4], Luis Otero[1], Juan C. Restrepo[1], Ismael Hernández-Carrasco[3] and Alejandro Orfila[3]**

[1] Departamento de Física y Geociencias, Universidad del Norte, Barranquilla, Colombia, [2] Department of Hydraulic Engineering, Delft University of Technology, Delft, Netherlands, [3] Instituto Mediterráneo de Estudios Avanzados, IMEDEA (CSIC-UIB), Esporles, Spain, [4] Department of Physics, University of the Balearic Islands, Palma, Spain

This work analyzes the coastal impacts of the combined effect of extreme waves and sea level extremes, including surges and projected mean sea level rise in Bocagrande, Cartagena (Colombia). Extreme waves are assessed from a wave reanalysis that are propagated from deep waters to the beach considering the hydrodynamic processes and taking into account the interaction between waves and the coastal elevation within the study area. First, we consider present sea level, storm surges and waves affecting the area. Next, we analyze the effect of sea level rise according to a moderate (RCP4.5) climate change scenario for the 21st century (years 2025, 2050, 2075, and 2100). The most pessimistic scenario (year 2100) yields a percentage of flooded area of 97.2%, thus revealing the major threat that represents sea level rise for coastal areas in the Caribbean Sea.

Keywords: sea level rise, coastal flooding, RCP4.5, Cartagena de Indias, run-up

OPEN ACCESS

Edited by:
Isabel Iglesias, University of Porto, Portugal

Reviewed by:
Alexandre Nicolae Lerma, Bureau de Recherches Géologiques et Minières, France
Simone Simeone, Italian National Research Council (CNR), Italy

****Correspondence:***
Alejandro Orfila
aorfila@imedea.uib-csic.es

Specialty section:
This article was submitted to Coastal Ocean Processes, a section of the journal Frontiers in Marine Science

Received: *23 June 2019*
Accepted: *18 September 2019*
Published: *01 October 2019*

Citation:
Orejarena-Rondón AF, Sayol JM, Marcos M, Otero L, Restrepo JC, Hernández-Carrasco I and Orfila A (2019) Coastal Impacts Driven by Sea-Level Rise in Cartagena de Indias. Front. Mar. Sci. 6:614. doi: 10.3389/fmars.2019.00614

INTRODUCTION

Low crested coasts and beaches are among the most vulnerable ecosystems on the Earth since the mean sea-level rise (SLR), land subsidence, and variations in the frequency and/or strength of marine extreme events have the potential to substantially affect their present morphology, uses, landscapes, and functions (Nicholls and Cazenave, 2010). The availability of these physical drivers at regional and even local spatial scales is crucial to quantify the most probable retreat of coastlines, which is essential to implement appropriate mitigation measures as well as for the development of adaptation plans (Hunt and Watkiss, 2011; Willis and Church, 2012; Lyu et al., 2014; Melet et al., 2018). This kind of information is being increasingly demanded by stakeholders and social actors in order to take the best possible decisions for present and future urban development (Hunt and Watkiss, 2011). Previous works have estimated the impact of SLR on coastal inundation at global scale (e.g., Nicholls et al., 2011; Hinkel et al., 2013; Passeri et al., 2015; Vitousek et al., 2017), and also at regional and local scales. Some examples are found in the United States (Limber et al., 2018), Portugal (Bon de Sousa et al., 2018), Spain (Enríquez et al., 2017, 2019) or in the Netherlands (Verschuur, 2018) Previous results suggest that the retreat rates of coastlines could increase with respect to the present values, notably when the most pessimistic scenarios of greenhouse gases emissions are considered (e.g., Vermeer and Rahmstorf, 2009; Nicholls and Cazenave, 2010; Alexander et al., 2012).

The total water level on the coast is the result of the combined effect of mean sea-level (SL) (with the addition of seasonal and inter-annual effects), low-level atmospheric pressures (surges), surface wind fields, tidal dynamics, wave breaking (set-up and run-up) and the topo-bathymetric heights (Nicholls et al., 2014; Guimarães et al., 2015). Mean sea-level variations result from changes in different contributors such as glaciers, ice sheets mass loss, land water storage or the ocean

thermal expansion (Gregory et al., 2013). Tide-gauge based observations corrected by vertical land motions and changes in the geoid show a trend in the global mean SLR of 1.1 ± 0.3 mm y^{-1} before 1990 for the 20th century, and of 3.1 ± 1.4 mm y^{-1} from 1993 to 2012 (Dangendorf et al., 2017). According to the last report from the Intergovernmental Panel on Climate Change (IPCC), the global mean sea-level will continue to rise during the 21st century and beyond (Church et al., 2013), but the total amount will depend on the greenhouse-gas concentrations, with a projected global mean SLR for the high-end scenario close to 2 m in the 2100 (Church et al., 2013; Le Bars et al., 2017). Moreover, projections at regional scales can differ substantially from those for the global mean SLR (Slangen et al., 2014), stressing the importance of performing studies that incorporate, where possible, the local SL contributions. The mean SLR increases the exposure of coastal zones to extreme marine events, causing the submersion of low-lying coasts, with obvious socioeconomic implications affecting human activities, coastal defense, development, growth and ecosystems (Nicholls and Cazenave, 2010; Jackson and Jevrejeva, 2016).

As it has been shown in the North Atlantic, the effects of extreme marine events on the coast also may increase due to changes in the storm wave climate (e.g., Masselink et al., 2016). Based on altimetric data from recent decades Young et al. (2011) found an increment of wind speed and, to a lesser degree, of wave height on a global scale, although, these changes are difficult to predict on a regional scale since storm tracks may shift in the near future (Bengtsson et al., 2006). On a local scale, these changes have been documented by other authors in the north and northeast Atlantic Ocean and in the northeast and northwest Pacific Ocean, where the increase of wave height is associated with the upsurge in the intensity of the storms (e.g., Ruggiero et al., 2010; Masselink et al., 2016; Castelle et al., 2018). Potential changes in wind-waves have also been evaluated taking into account the last IPCC projections (Hemer et al., 2013; Casas-Prat et al., 2018). Apart from wave heights, projections also indicate some variations in the mean wave peak period and in the mean wave direction, which could have an enormous effect on sandy coasts since the beach planform depends on the energy flux direction (Vousdoukas et al., 2018).

Some studies determined the wave run-up on beaches during normal and extreme conditions without considering the role of the SLR (e.g., Callaghan et al., 2009; Dietrich et al., 2011; Peláez-Zapata et al., 2012; Andrade et al., 2013; Fleming et al., 2013) and, only since recently, the combined effect of SLR and extreme events under greenhouse scenarios has been assessed

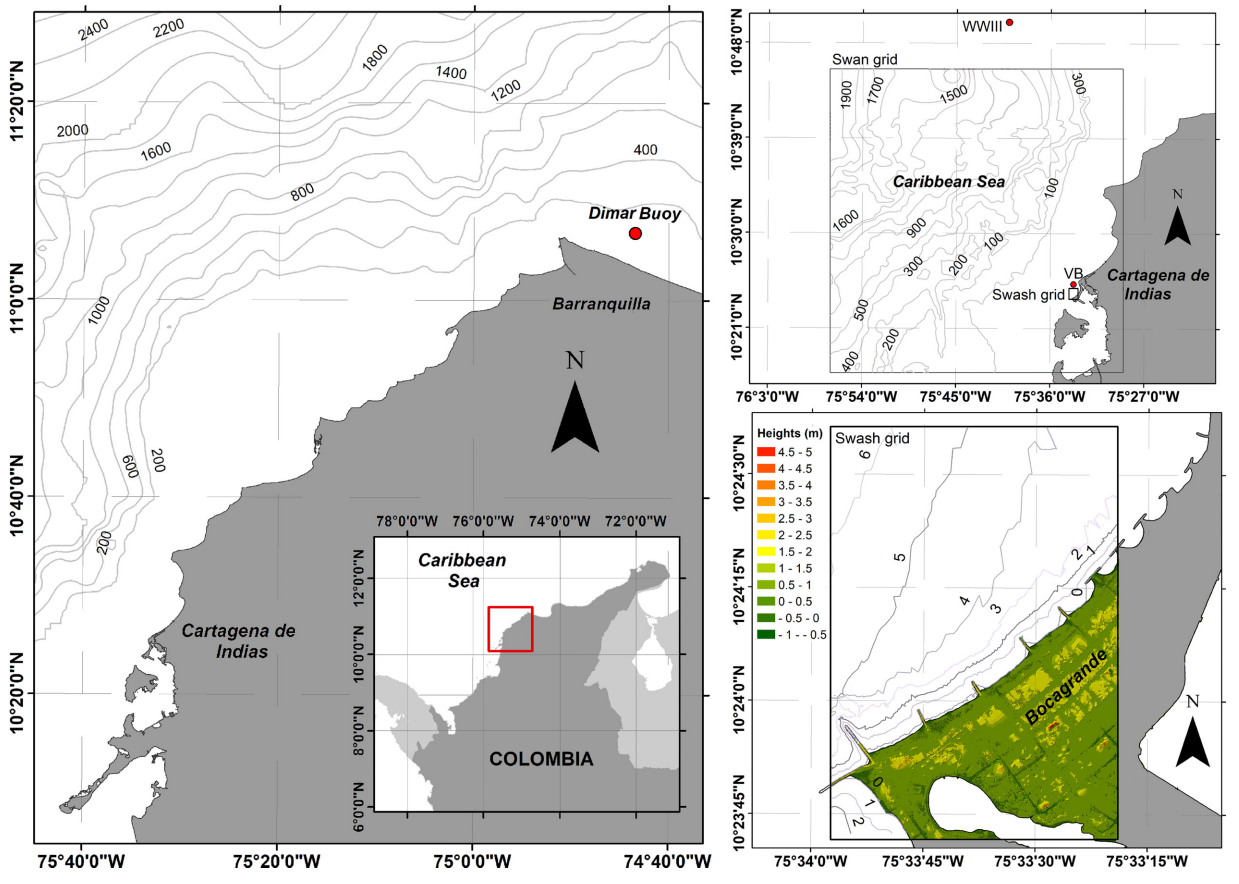

FIGURE 1 | Study area representation. Indicates the location of the computational domain of SWAN and SWASH models in the **right panel**. The red dot in the **left panel** indicates the NOAA buoy used for the SWAN model validation. The bottom **right panel** shows the elevation of the dry area.

(e.g., Masselink et al., 2016; Mentaschi et al., 2017; Melet et al., 2018; Sayol and Marcos, 2018).

Here, we evaluate to local scale the flood hazard in Bocagrande sand spit (Cartagena de Indias, Colombia) including all variables affecting the set-up and the run-up (i.e., the mean SL, tides, storm surges and waves) over the topography of the area. Taking into account all these variables is crucial to determine where and which mitigation actions have to be considered in front the impact of SLR. In order to account for future changes in the wave set-up, we will consider a moderate IPCC scenario corresponding to the Representative Concentration Pathway of 4.5 W/m^2, hereinafter RCP 4.5 (Moss et al., 2010).

AREA OF STUDY

Cartagena de Indias is located in the northwestern South America within the Colombian Caribbean basin (**Figure 1**). It is a densely populated area and one of the most visited touristic destinations in the Caribbean region (Asociación Colombiana de Agencias de Viajes y Turismo [ANATO], 2018). Its beaches are mainly located in Bocagrande area (**Figure 1**, bottom-right panel). They conform a set of dissipative beaches controlled by groins spaced every 250 m approximately. These beaches, totally anthropized and without dunes are around 2.5 km length and between 30 and 70 m wide. The area is mainly exposed to offshore waves from the NE (**Figure 2**). The astronomical tide in the region is of mixed type primarily diurnal with a range of 0.40–0.60 m (Nicolae-Lerma et al., 2008; Restrepo et al., 2017) and the atmospheric-induced surges can exceed 0.2 m during strong storms (Andrade et al., 2013). The mean SL for the period 1908–2009 in the Caribbean Sea shows a rise of 5.3 mm y^{-1}, about 4 times larger than the global mean SLR during the same period, whit around 5.6 mm y^{-1} in Cartagena for the period between 1950 and 2009 (Torres and Tsimplis, 2012). Moreover, local subsidence measured in the Cartagena region between 2000 and 2008 yielded a rate of 1.4 mm/year (Seemüller et al., 2009; Molares, 2011) thus contributing to exacerbate the mean SLR.

The regional climate is modulated by the location of the Intertropical Convergence Zone (ITCZ) as well as by the American Monsoon System, presenting two marked climatic seasons; the dry (or windy) season from December to April and the wet season from August to November (Poveda et al., 2002). During the dry season, the NE trade winds dominate the area due to the location of the ITCZ at the latitude 0–5°N. During the wet season the trade winds from the south reach the Colombian basin due to the migration of ITCZ toward latitude 10–12°N producing intense rain (Andrade, 1993). The rest of the year, from May to June (the transition season) is characterized by the weakening of the trade winds. Wave climate is modulated by these seasons presenting a bimodal distribution; during the dry season the significant wave height (H_s) present larger values and smaller in October (Osorio et al., 2009; Thomas et al., 2011; Andrade et al., 2013). Cold fronts during the dry season are considered the major cause of extreme waves in the central sector of the Caribbean littoral of Colombia (Otero et al., 2016), affecting periodically the Bocagrande area with energetic northwestern waves. From June to November, the passage of hurricanes near the Colombian Caribbean Sea can be accompanied also by the occurrence of extreme events (e.g., as those caused by hurricanes Joan in 1988 and Lenny in 1999), which have the potential to severely affect the continental Caribbean (Ortiz et al., 2015).

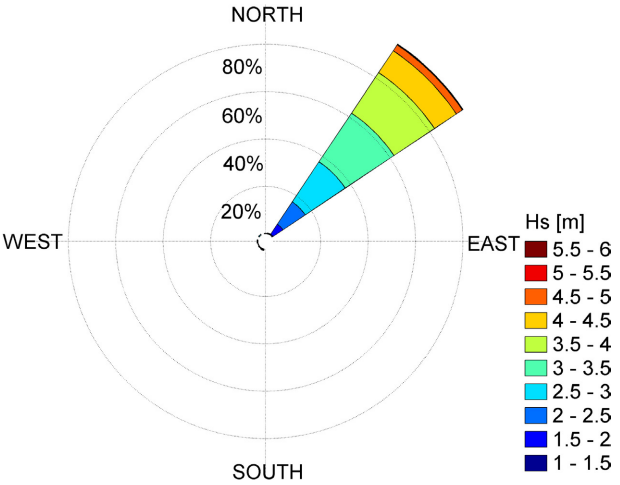

FIGURE 2 | Wave rose from the NOAA wave hindcast (WaveWatch III). 38 years (1979-2016) of 3-hourly significant wave height (H_S) and wave direction (D_p) from the closest grid point to Cartagena de Indias are used.

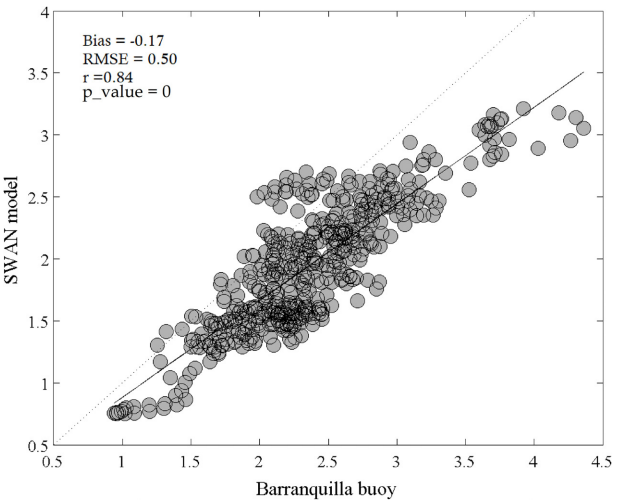

FIGURE 3 | Dispersion diagram where the WWIII data propagated with SWAN model are correlated with the wave data of the buoy 41194 available in the National Data Buoy Center of the NOAA.

DATA AND METHODS

The mean wave set-up in present day conditions is obtained from a tide-gauge located in Cartagena de Indias (current mean SL), while future conditions under the RCP 4.5 scenario are derived from a global model mean ensemble (Church et al., 2013).

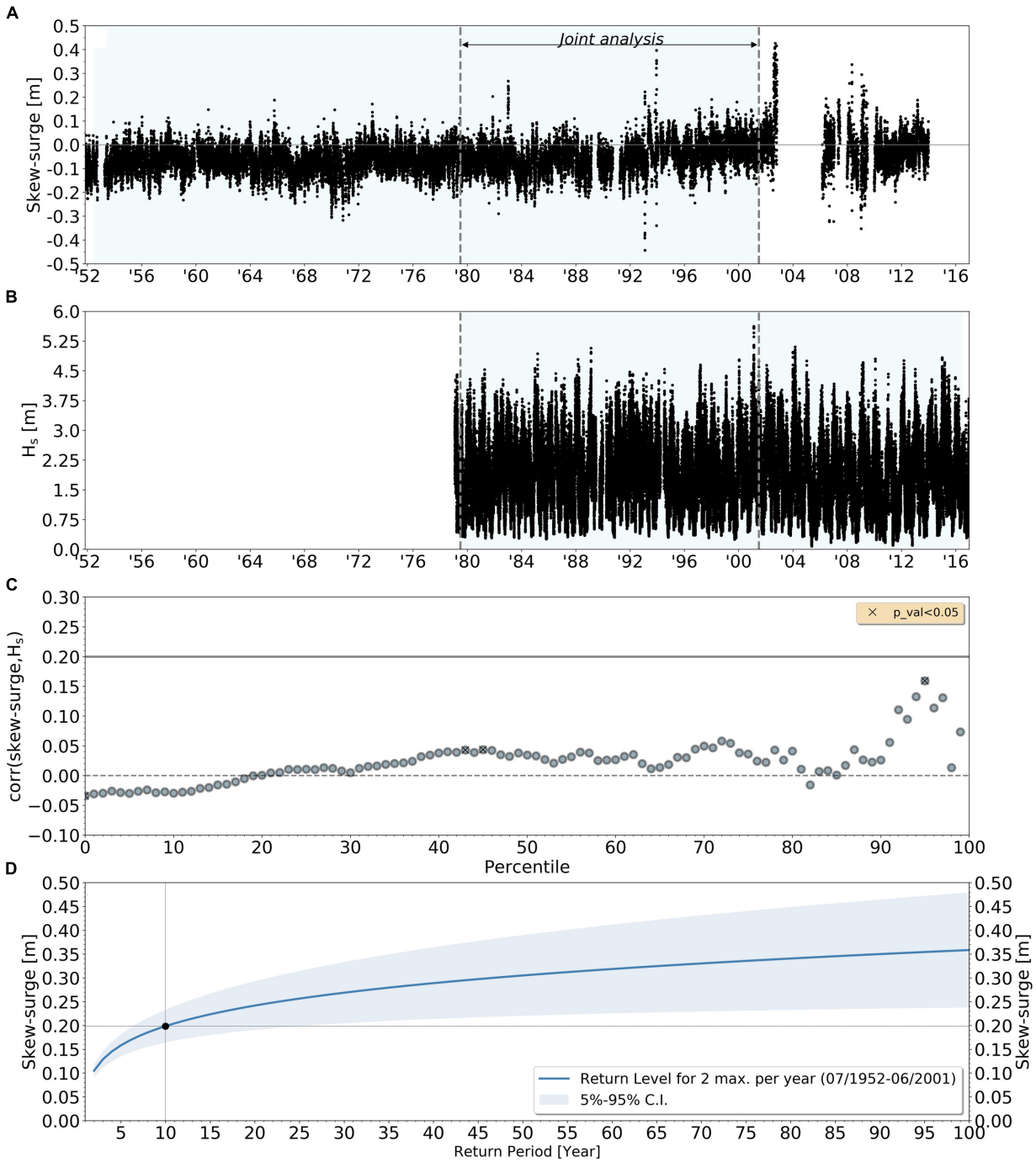

FIGURE 4 | Timeseries of skew-surge derived from the Cartagena tide-gauges **(A)**; timeseries of significant wave height (*Hs*) from the WWIII reanalysis at the closest grid point with respect to Cartagena **(B)**; Kendal correlation between skew-surge and *Hs* **(C)** for the period indicated as joint analysis in the top panel (the black cross remarks significant correlation at 95%, see legend). The blue shading depicts the timeseries used to estimate the extreme events in the independent assessment; return level for skew-surge using 2 max. per year **(D)**. The blue shading reflects the 5–95% range of uncertainty.

Other contributions to the wave set-up such as astronomical tides and sporadic extreme surges induced by storms are also computed from the above tide-gauge. We consider that waves propagate over the mean wave set-up, which is the result of adding to the mean sea level the astronomical tides and extreme surges obtained from a nearby tide-gauge located in Cartagena de Indias. Extreme deep water-wave conditions from WaveWatch III (WWIII) are propagated to the coast combing SWAN and SWASH (a non-linear shallow water solver) models to finally obtain the run-up.

Sea Level Observations and Projection

Hourly time series of sea level from tide-gauges located at Cartagena were obtained from http://gesla.org/ (Woodworth et al., 2017). Since tide-gauges records cover different periods (11/1951-4/1993 and 5/1993-12/2013), time series were homogenized, detrended and unified to have a unique long record. Astronomical tides were estimated with the UTide MATLAB software (Codiga, 2011). The analysis of the sea level data confirmed that the amplitude of astronomical tides in the region is around 0.2 m (microtidal). In order to reduce timing errors and non-linear effects we analyzed skew-surges over the sea level time series, which are defined as the difference between the maximum SL and the maximum predicted tidal level over one tidal cycle (Mawdsley et al., 2015). Projections of SLR according to the RCP 4.5 scenario for the Cartagena de Indias area were downloaded from the Integrated Climate Data Center (IDC) of the University of Hamburg[1]. This global database include different geophysical sources that drive long term changes in the relative sea surface height (SSH), such as, ice components, ocean-related components (derived from CMIP5 models), land water storage and glacial isostatic adjustment. From the above data a set of mean wave set-up is constructed by adding to the projected RCP 4.5 sea level scenarios for years 2025, 2050, 2075 and 2100, the spring astronomical tides and extreme storm surge for a return period of 10 years derived from the skew-surges time series (further details on this are provided in section "Selection of Extreme Events of Skew-Surges and Waves").

Wave Data

Extreme wave climate was obtained by performing a statistical analysis of the NOAA hindcast over a period of 38 years[2]. This hindcast is based on the WWIII model forced by the Global Forecast System (GFS) analysis winds for the period of 1979–2016 with a 3-hourly temporal resolution. Here we use the closest model grid point to Bocagrande beaches, located around 15 km off the coast of Cartagena (see **Figure 1**, top-right panel).

[1]http://icdc.cen.uni-hamburg.de/1/daten/ocean/ar5-slr.html

[2]ftp://polar.ncep.noaa.gov/pub/history/waves/multi_1/

TABLE 1 | Wave regime analysis in deep waters – basic statistical parameters.

DIR	Prob (%)	H_s 50%	H_s 90%	H_s 99%	H_s 12
N	0.54	0.95	2.01	2.76	3.21
NNE	1.93	1.12	2.16	2.96	4.02
NE	92.89	1.89	3.03	3.92	4.50
ENE	1.42	0.55	0.85	1.23	2.09
ESE	0.01	0.73	1.23	1.26	1.26
SSW	0.64	0.91	1.48	2.13	2.92
SW	0.74	0.86	1.66	2.45	2.85
WSW	0.25	0.84	1.70	2.37	2.55
W	0.14	1.10	1.81	2.09	2.10
WNW	0.18	0.64	1.21	1.94	1.95
NW	0.40	0.97	2.22	2.77	2.95
NNW	0.72	1.00	2.02	2.98	3.07

Modeling Set-Up

Based on the statistical analysis of the NOAA hindcast referred above, two energetic sea states were selected in deep waters that were characterized by their H_s, D_p (peak direction) and T_p (peak period). These sea states were propagated using the SWAN model in stationary mode to obtain the corresponding wave conditions at shallow waters. These dispersive waves are transformed up to the beach using SWASH model in non-stationary mode. Present SL as well as those given by the moderate RCP4.5 scenario are analyzed in order to obtain the respective target inundations.

The SWAN model solves the equation of action balance for the propagation of the wave spectrum, allowing realistic estimations of wave parameters in oceanic and coastal zones (Booij et al., 1999). To assess the performance of SWAN in the area, the model is first validated in a non-stationary simulation using the Japanese 55-year wind Reanalysis, JRA-55 (Kobayashi et al., 2015). Sea states from a model grid point at the same position of the NOAA buoy # 41194 belonging to the Dirección General Maritima (DIMAR) were used for the validation of the simulated waves. This buoy is 126 km NW off Bocagrande at 11.161°N, 74.681°W (see location in **Figure 1**, left panel). Wave growth by wind was set as exponential following the formulation of Komen et al. (1984), and the deep water non-linear interaction by using the Webb-Resio-Tracy method. The relevant processes of interest: wave braking, energy dissipation by whitecapping and bottom friction were took into account for the simulation. The time step was set as 30 min and results stored every 3 h. The bias and root mean square error (RMSE) between the buoy and the SWAN model grid point time series are close to zero whereas the correlation coefficient is 0.84 showing a good fit between modeled and observed data. This relationship is statistically significant at a confidence level of 95% according to a two-tailed t-Student distribution (p-value $<10^{-5}$) (**Figure 3**).

The SWAN domain had a resolution of 100 × 100 m^2 (471 × 481 grid points) with bottom left UTM coordinates at 1136524.46N, 395970.14E (**Figure 1** Swan grid in the right panel). Bathymetry was obtained from the nautical charts COL 042, COL 261, COL 263, COL 615 from the Colombian Hydrographic Institute, with scale ranges of between 1:15000 and 1:250000.

Regarding SWASH, the model solves the non-linear shallow water equations including the non-hydrostatic pressure being suitable for wave propagations up to beaches (Zijlema et al., 2011). SWASH was executed on a fine mesh with a spatial resolution of 3 × 3 m^2 (341 × 551 grid points) and with bottom left UTM coordinates at 836992N, 1641707E. For this domain the bathymetry was obtained from using a single-beam ODOM Hydrotrac 2 echo-sounder merged with a high-resolution LIDAR topography for the emerged part of the domain (**Figure 1** Swash grid in the bottom-right panel). All vertical heights in the Digital Terrain Model (DTM) were referenced to the mean low water spring (MLWS) and the horizontal coordinates were referenced to UTM 18N. According to Smit et al. (2014), to accurately resolve waves in a phase-resolving model the mesh resolution has to be at least 10 times smaller than the shortest wavelength to be resolved i.e., $L/\Delta x = O(10)$ [similarly this applies to the time step i.e., $T/\Delta t = O(10)$], thus satisfying this criteria with

TABLE 2 | Propagation cases for determining run up in Bocagrande beaches.

Case		Deep water			Shallow water			Sea level (m)		SLR (m)
		DIR	H_s (m)	T_p (s)	DIR	H_s (m)	T_p (s)	Tide	Surge	
Present	A1	NE	3.0	12	NNW	1.5	12	0.20	0.0	0.0
	A2							0.20	0.20	0.0
	A3		4.5	11		2.3	11	0.20	0.0	0.0
	A4							0.20	0.20	0.0
	B1	NW	2.2	10	WNW	2.3	10	0.20	0.0	0.0
	B2							0.20	0.20	0.0
	B3		3.0	14		3.2	14	0.20	0.0	0.0
	B4							0.20	0.20	0.0
2025	C1	NE	4.5	11	NNW	2.3	11	0.20	0.20	0.11
2050	C2									0.24
2075	C3									0.38
2100	C4									0.52

Deep waters information concerns to the sea states extracted of the WaveWatch III virtual buoy at 700 meters deep. Shallow waters information corresponds to the sea states taken in the virtual buoy at 5 m deep, as a result of propagation of the sea states determined in deep waters.

the implemented resolution. The simulation length for each case was 30 min and the simulation time step Δt was set to 0.1 s. Results were stored every 5 s and the minimum and maximum Courant number were kept between 0.1 and 0.7. The Manning friction coefficient was set as 0.04 $m^{-1/3}s$ and the horizontal viscosity Prandtl mixing length hypothesis L_{mix} = 2 m (Conde-Frias et al., 2017).

Video Imagery

Video monitoring systems developed after the apparition of digital cameras, have shown to be a powerful and low-cost tool to monitor the coast in a wide range of studies, such as, coastal variability (Nieto et al., 2010; Simarro et al., 2015), intertidal bathymetry (Aarninkhof et al., 2003) or evolution of beach systems (Ojeda and Guillén, 2008). Since video systems have the advantage of providing continuous monitoring of coastal areas they are also a valuable tool to validate numerical models (Salmon et al., 2007; Andrade et al., 2013; Morales-Márquez et al., 2018; Osorio et al., 2019). In this work, we have used video images from the HORUS monitoring system[3] at Bocagrande, to validate the run-up provided by SWASH model. The images passed through a scale rectification process and merged with digital orthophotography for visualization purposes.

SELECTION OF EXTREME EVENTS OF SKEW-SURGES AND WAVES

In this section we evaluate if the extremes of skew-surges and waves are significantly correlated. Our purpose is to estimate return level probabilities of both types of extremes. Based on this result we use the most suitable theoretical framework to estimate the magnitude of the skew-surge and waves that will be employed in section "Results" to model the coastal run-up.

[3]http://www.horusvideo.com

Selection of Independent Events of Surges and Significant Wave Height (H_s)

To study the correlation between time series of skew-surges (section "Sea Level Observations and Projection") and H_s (section "Wave Data"), we selected the maximum of skew-surges and H_s as follows; For each maximum value of skew-surge the associated maximum value of H_s within an interval of $\pm$ 6 h is selected, thus having a set of pairs of both variables. To be sure that the selected skew-surges corresponded to different events, they had to span at least 3 days between them (see Torres and Tsimplis, 2014 for further details). Since the location of the ITCZ has a large influence on the waves in the Caribbean Sea there are only two seasons to be analyzed; the dry season from December to April and from July to August and the wet season from April to May and from August to November. The common time range between skew-surges and waves extends from July 1979 to June 2001, accounting for a total of 21 years (see **Figures 4A,B**).

Correlation Between Skew-Surges and H_s

If a peak of skew-surge is correlated with a high wave, the probability of having a hazardous total water level will increase (the return period will decrease) respect to the case where both events are independent. In the former case, if the probability is computed independently, the actual risk would be underestimated. To avoid this, first we will assess the correlation between extremes of skew-surges and waves. Then, correlation is assessed with the Kendall rank correlation. Previous studies in the US coast and globally have suggested that an indicative value of 0.2 may be already significant enough (Wahl and Chambers, 2014) to require the computation of the joint probability using a multivariate approach such as the Copula functions (e.g., Sayol and Marcos, 2018; Enríquez et al., 2019; Marcos et al., 2019). Correlations for those independent events are shown in **Figure 4C** for all percentiles being in all cases very low with

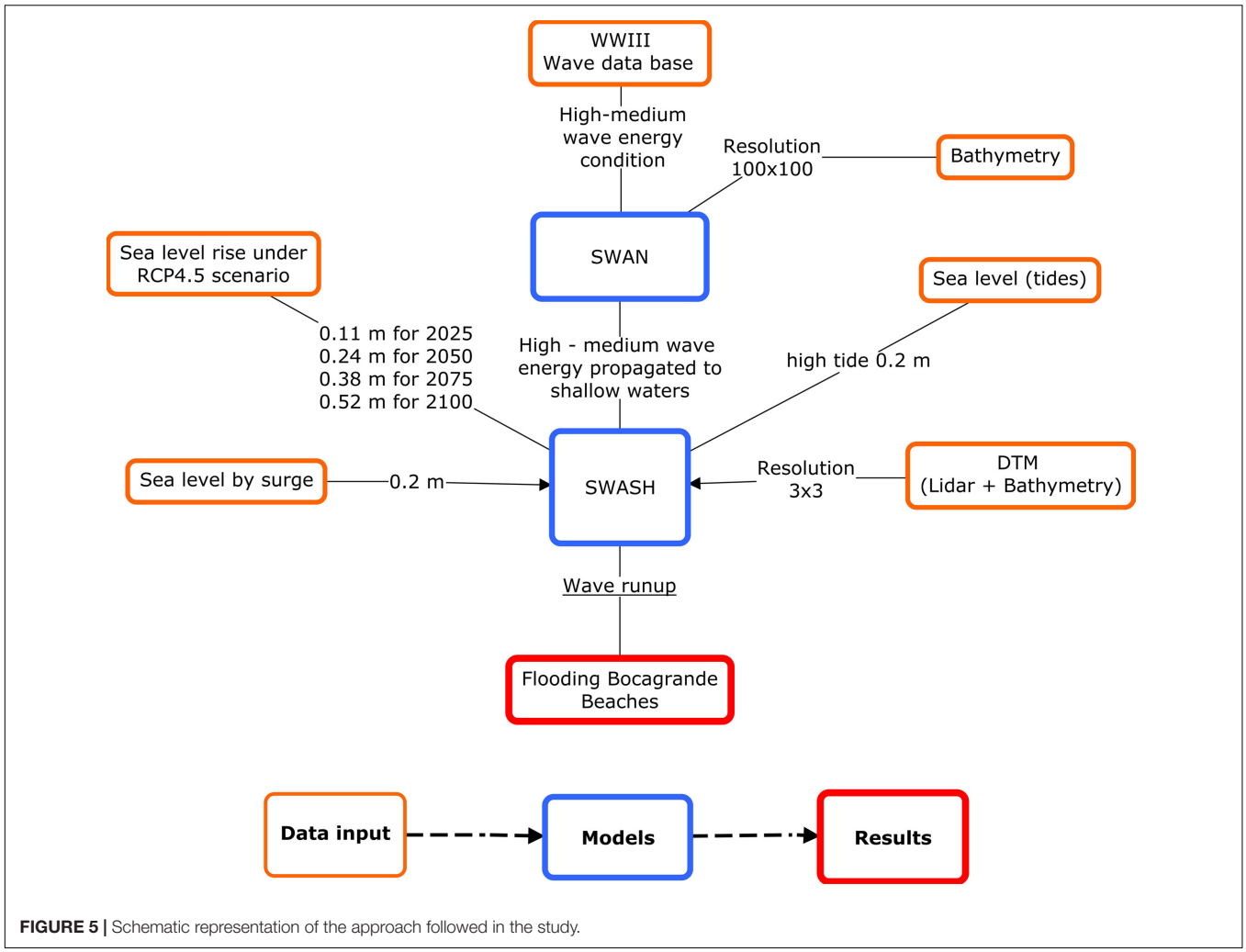

FIGURE 5 | Schematic representation of the approach followed in the study.

the maximum correlation of 0.175 corresponding to the 95-percentile. The cross over the circles indicate the correlations that are significant at the 95% level according to a series of permutation distributions (Gibbons and Chakraborti, 2011). In the light of these results, it is reasonable to assume that the extremes of skew-surges and H_s are uncorrelated and hence we compute their extremes independently.

Selection of Extreme Skew-Surges

The largest available time series for skew-surges (from July 1952 to June 2001) is used to compute the return levels using the block maxima approach. For each defined year (from July to June) we seek for the highest N independent events of skew-surges (they must be separated at least 3 days) collecting a set of N × M maxima, where M is the number of years. In order to estimate the return levels associated to a given probability, the extremes are fitted separately using the Generalized Extreme Value-GEV distribution (Tsimplis, 1995; Marcos et al., 2009). After checking the return levels for the range $N = 1$ to $N = 5$ we did not find a significant difference among them and thus we computed the return level with blocks of $N = 2$. As a reference we choose a return period of 10 years, which is at the same time extreme and statistically probable. The resulting return level for skew-surges found under this assumption is 0.2 m (**Figure 4D**).

Selection of Extreme Waves

Time series of deep-water H_s, T_p, and D_p (section "Wave Data") are here used to characterize wave conditions (**Figure 2**). Based on this almost 93% of waves come from the NE, 2% from the NNE, 1.5% from ENE and the remaining from other directions (see **Table 1**). After considering the direction with the highest probability of occurrence and the joint probability analysis of H_s and T_p, two cases representing extreme events were chosen for the NE direction: the significant wave height that exceeded 12 h per year (H_{s12}, cases A1–A2 in **Table 2**) which corresponds to H_s = 4.5 m and T_p = 11 s; and (ii) the significant wave height with a 10% probability of exceedance (H_{s90}, cases A3-A4 in **Table 2**) corresponding to H_s = 3.0 m and a T_p = 12 s. As the passage of cold fronts is the cause of some of the highest waves in the central of the Colombian Caribbean Sea (Otero et al., 2016), we also study (although they have a lower probability of occurrence) the extreme waves from the NW direction. For

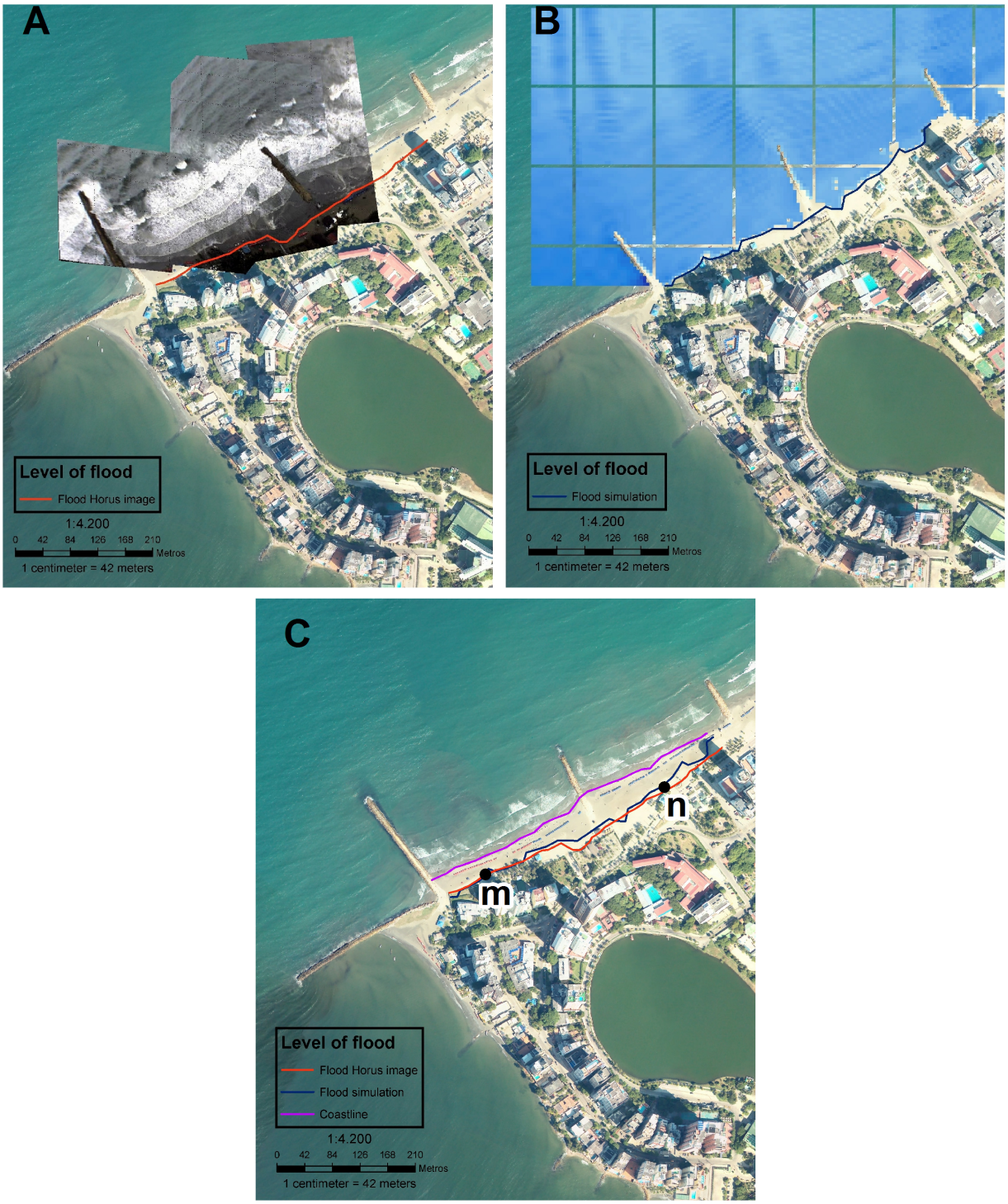

FIGURE 6 | Run-up in Bocagrande beach during the passage of a cold front in November 8th, 2010: **(A)** As recorded by HORUS camera system (red line), **(B)** simulated with SWASH (blue line), and **(C)** comparison between simulated and recorded run up. The magenta line represents the coastline.

this case, considering the joint probability analysis of H_s and T_p, corresponds to H_s = 3.0 m and T_p = 14 s (H_{s12}, cases B1–B2 in **Table 2**) and to H_s = 2.2 m and T_p = 10 s (H_{s90}, cases B3–B4 in **Table 2**).

RESULTS

Extreme waves at deep waters have been propagated toward the coast following the workflow outlined in **Figure 5**. Two type of

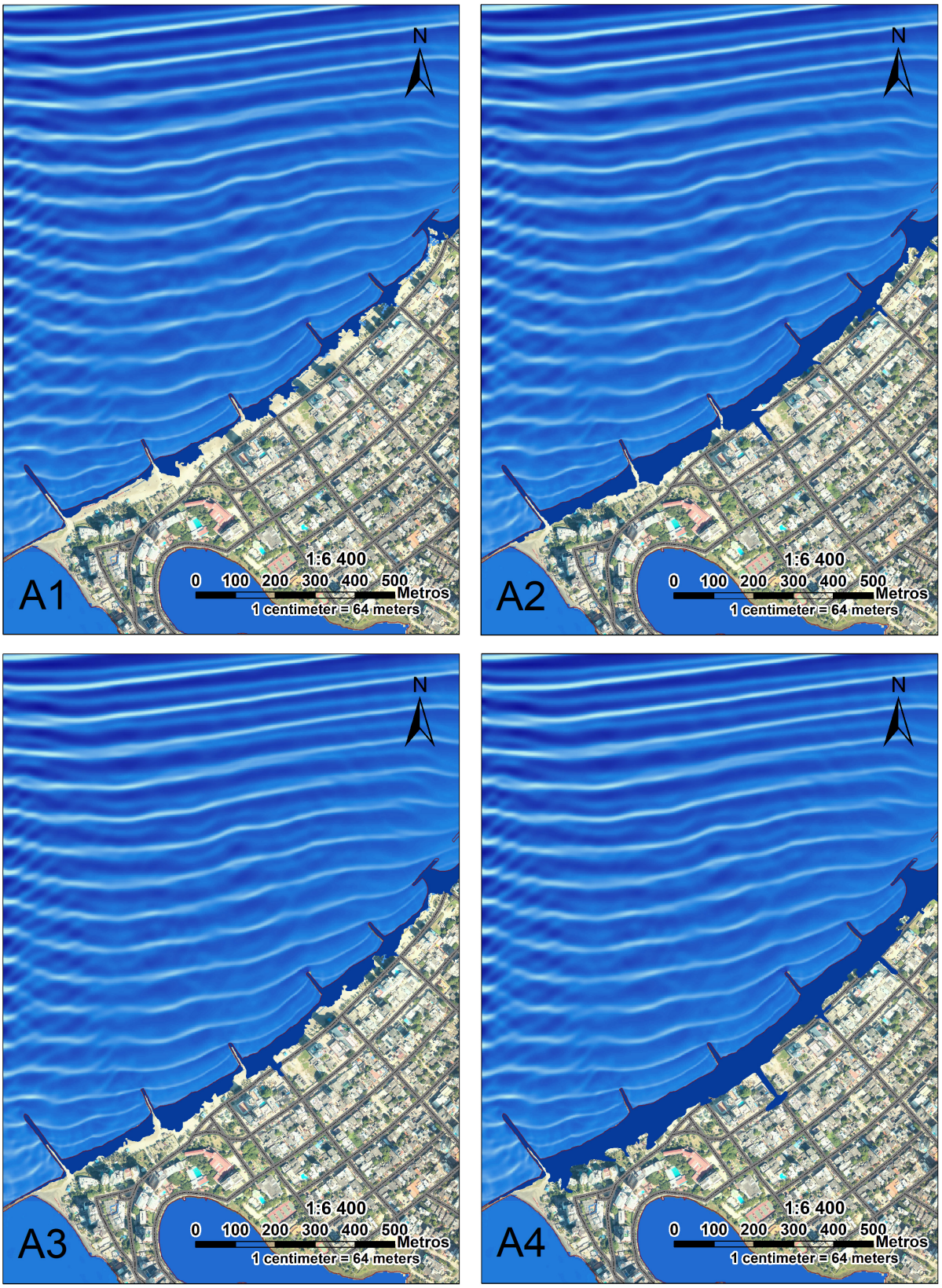

FIGURE 7 | Flooded area generated by cases under present-day conditions and NE coming waves (**A1–A4**, **Table 3**).

extreme wave conditions have been identified to be the most probable in terms of H_{s12} and H_{s90} corresponding to incoming waves from the NE and those resulting from the passage of cold fronts (NW). The remainder of this section describes the validation process followed for the models used to simulate waves in deep and coastal ocean areas. Moreover, coastal flood maps for Bocagrande and surrounding beaches under present-day conditions and for the RCP4.5 sea level projection for the set of time horizons are presented and discussed.

Model Validation

Run-up validation was performed using the images obtained with HORUS video monitoring. As an example, **Figure 6** shows the HORUS image corresponding to November 8th of 2010, coinciding with the passage of a cold front in the Colombian Caribbean. Wave conditions for this event were H_s = 2.3 m and T_p = 9 s from the NE direction. All comparisons were done using ArcGis 10.1, in which the maximum run-up from both data sets were plotted on the coast. **Figure 6A** shows the maximum run-up manually detected over the georeferenced image (red line) while **Figure 6B** shows the maximum run-up given by the numerical model (blue line). Along the m-n transect, the longitudinal distance from the coastline to the maximum run-up obtained by the numerical model and the HORUS image was 61 and 72 m, respectively (**Figure 6C**). The difference in the elevation between the simulation and the image run-up was 0.3 m, with a higher run-up measured at the image. In other areas of the transect, the differences were lower, in both the horizontal (<3 m) as in the vertical (<0.2 m) (**Figure 6C**). As seen in **Figure 6C**, the run-up from the modeling and from the observations are in very good agreement and thus we used the model approach as a proxy for the projections.

Modeled Coastal Inundation

Based on the analysis of the deep water wave conditions and taking into account the statistical independence of the wave climate and storm surges, we have analyzed 12 cases for the deep water mean direction (NE) as well as for the front cold passages (NW) (**Table 2**). Eight cases correspond to present-day conditions (SLR = 0, A1 to B4) and four additional cases under the projected SLR for years 2025, 2050, 2075, 2100 under the RCP 4.5 (C1–C4, **Table 2**). The flooded areas obtained for all case studies are presented and discussed below.

Flooding Under Present-Day Conditions

Present day conditions correspond to the combination of the deep water wave analysis outlined in section "Selection of Extreme Waves" with the inclusion (or not) the extreme skew-surge (section "Selection of Extreme Skew-Surges") (**Table 2**). Note that for all cases-studies astronomical spring tides of 0.2 m are assumed. The corresponding flooded areas for deep water waves from the NE (A1–A4) and from the NW (B1–B4) are shown in **Figures 7**, **8** and are summarized in **Table 3** (A1–A4 and B1–B4, respectively). The most severe flooding for the present state is given for those cases that account for the combined effect of waves and skew-surges, regardless of the wave direction. This is shown in **Figures 7A2,A4**, **8B2,B4**). H_{s90} for case A2, which corresponds to NE waves (case A2 in **Table 2**) correspond to wave conditions of H_s = 1.5 m and T_p = 12 s over a skew-surge of 0.2 m yields a flooded area of approximately 0.062 km^2 (A2, **Table 3**), whilst the H_{s12} conditions for NE waves (case A3 in **Table 2**) correspond to wave conditions of H_s = 2.3 m and T_p = 11 s without skew-surge and results in a flooded area of 0.048 km^2. The worst scenario for the NE waves in terms of flooded area is given under the case A4 (the most extreme waves and skew-surge) resulting in a flooded area of 0.087 km^2. In summary, the flooded area for the A1, A2, A3, and A4 cases comprise 9.8, 20.4, 15.7, and 28.4% of the surveyed area, respectively (**Figure 7** and **Table 3**).

For the NW direction (cold front passage), which corresponds to cases B1–B4 in **Table 2**, the flooded area is smaller compared with NE cases despite that the significant wave height in shallow waters is larger (**Figure 8**). The H_{90} wave conditions (case B1) correspond to H_s = 2.3 m and T_p = 10 s with no skew-surge, results in a flooded area of approximately 0.014 km^2. Same wave conditions over a sea level with an extreme skew-surge (case B2) yields a flooded area of approximately 0.052 km^2. The H_{12} conditions correspond to H_s = 3.2 m and T_p = 10 s (cases B3 and B4 without and with skew-surge, respectively) yield flooded areas of approximately 0.030 and 0.068 km^2, respectively. For all cases (B1–B4 in **Table 3**) the flooded area comprises the 4.5, 17.0, 9.6, and 22.3% of the total surveyed area, respectively (**Figure 8**).

Flooding Under Projected SLR

For the future global warming scenario, we assume the worst present flooding situation given by the case A4 that corresponds to the H_{12} from the NE direction (**Table 3**). Here we consider for all cases a skew-surge of 0.2 m, a high astronomical tide (0.2 m) and the regional SLR from RCP 4.5 for years 2025 (0.11 m), 2050 (0.24 m), 2075 (0.38 m) and 2100 (0.52 m) (**Table 2**). We note that the SLR scenario here considered is one of the most conservative. The corresponding flooded area is displayed in **Table 3** comprising the 38.7, 53.9, 73.7, and 97.2% of the surveyed area, respectively (**Figure 9**). It indicates that for the short term simulation (C1, year 2025) the flooded area will increase around 10% with respect to the present-day situation. For the remainder

TABLE 3 | Flooded area generated by run up cases – from NE (A1–A4) in present state, for cold fronts from NW (B1–B4) and for worst case for NE with RCP4.5 scenarios.

Case	Year	Flood area (km^2)	% Flood area
A1	Present state	0.030	9.9%
A2		0.062	20.4%
A3		0.048	15.7%
A4		0.087	28.4%
B1	Present state	0.014	4.5%
B2		0.052	17.0%
B3		0.029	9.6%
B4		0.068	22.3%
C1	2025	0.118	38.7%
C2	2050	0.165	53.9%
C3	2075	0.225	73.7%
C4	2100	0.297	97.2%

FIGURE 8 | Flooded area generated by cases under present-day conditions and NW coming waves (**B1–B4**, **Table 3**).

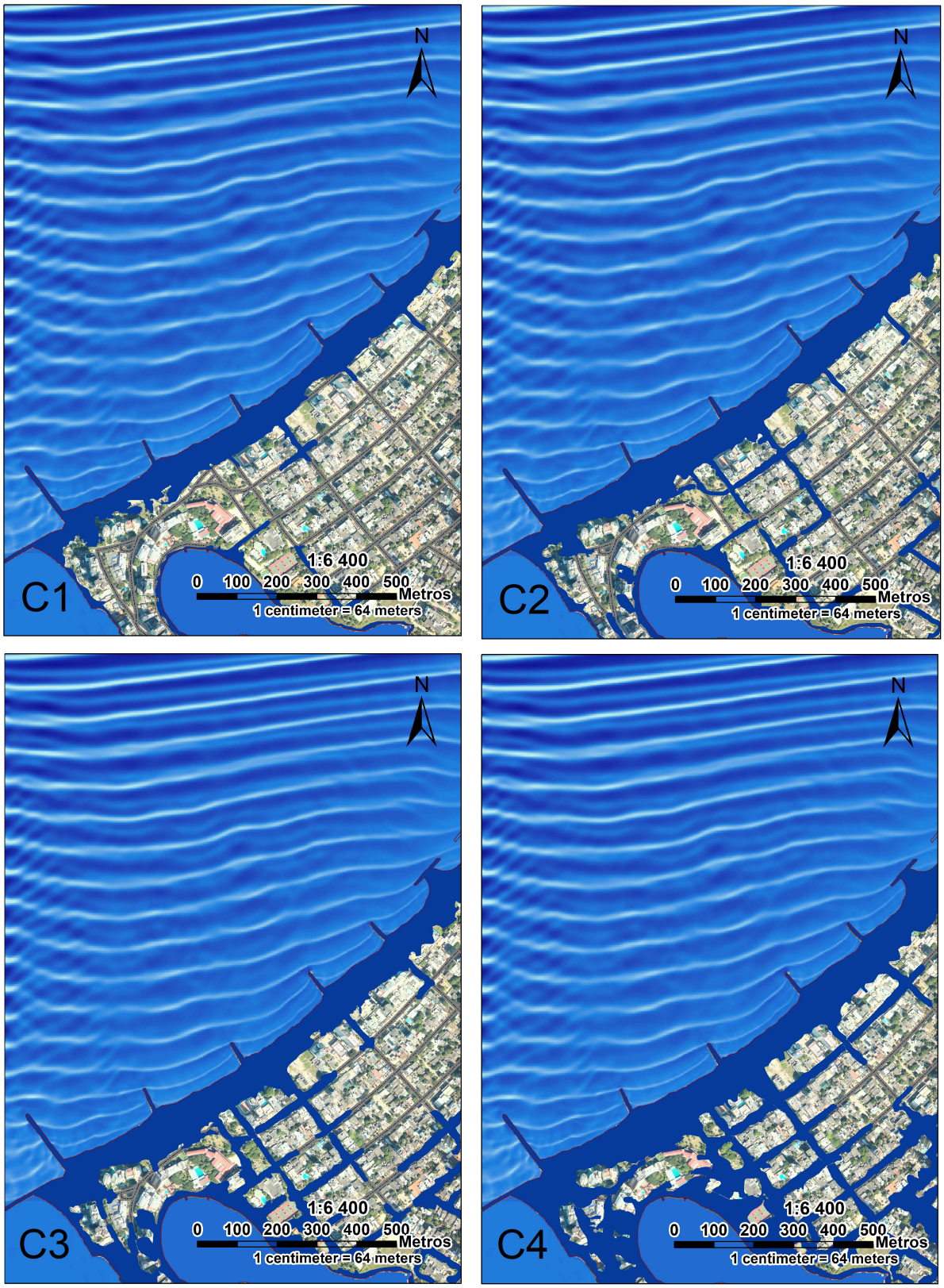

FIGURE 9 | Flooded area after the most energetic wave event coming from the NE, considering the projected SLR under the RCP 4.5 W/m^2 pathway for years **(C1)** 2025, **(C2)** 2050, **(C3)** 2075, and **(C4)** 2100. Also see **C1–C4** cases in **Table 3**.

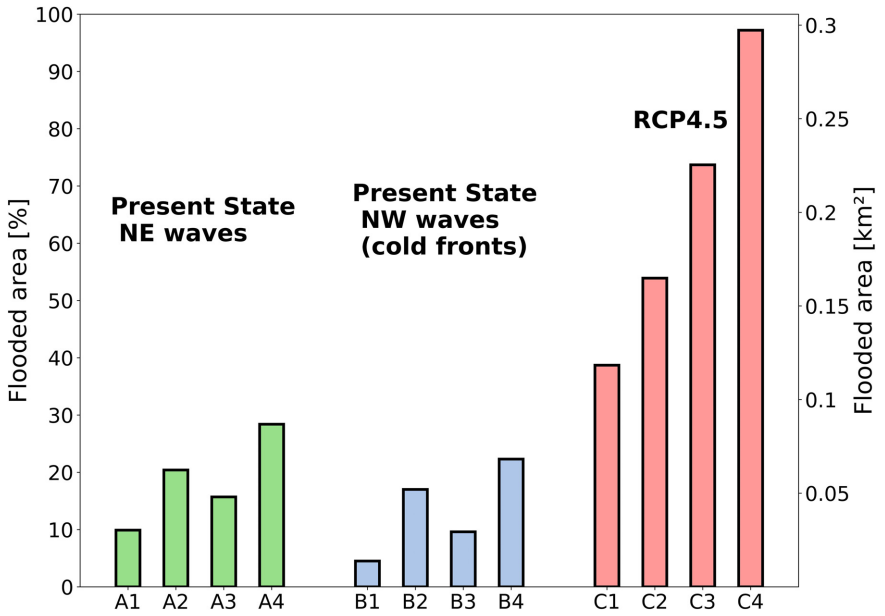

FIGURE 10 | Summary of flooded area results (left *y*-axis in percentage; right *y*-axis in total surface in km^2) for NE and NW coming waves under present-day conditions (**A1–A4,B1–B4,** respectively), and under SLR considering the projected sea level under the RCP 4.5 W/m^2 pathway **(C1–C4)**. See wave set-up and properties used in the simulations in **Table 2**.

years (2050, 2075, and 2100), flooded areas increase 25, 45, and 70% with respect to the present-day A4 case.

DISCUSSION AND CONCLUSION

In this work we study the coastal impacts of the combined effect of extreme waves and sea level extremes in Cartagena (Colombia). A summary of the flooded area for the present day conditions and for the projected RCP4.5 scenario is presented in **Figure 10**. Sea level has been rising since 1870, mainly due to the global warming that melts of land ice and causing ocean expansion (Church and White, 2006). One of the immediate consequences of SLR is land submergence and a higher risk of coastal flooding (Nicholls and Cazenave, 2010). However, the degree of affectation of the coastal areas depends on the regional and local features (profile slope, topographic heights, sediment type, wave conditions, tide conditions, meteorological conditions, etc.). Therefore, to take the most appropriate mitigation and adaptation measures, it is necessary to perform local studies accounting for all physical variables to determine the impact of SLR over the coastal zones. Sayol and Marcos (2018), estimated the impact of local sea level rise, extreme surge and waves in the Ebro Delta (Spain) under the climate change scenarios RCP4.5 and RCP8.5. The results show that for the year 2050 under the RCP 4.5 and RCP 8.5 sea level rise will flood a 65% of the Delta in both cases. While for the year 2099 under the RCP 4.5 and RCP 8.5 SLR projections the values of the flooded area will be 85 and 90%, respectively. Wang et al. (2018) assessed the effects of sea level rise, land subsidence, bathymetric changes and typhoon tracks on storm flooding in the coastal areas of Shanghai. Their results show that for the year 2025, the combined effect of these variables will flood 1053 Km^2 in the study area. While to year 2050 the combined effect of these variables would increase the flood area to 4026 km^2. Enríquez et al. (2017) assessed the changes in the shoreline due to sea level rise and waves in two micro-tidal beaches in Majorca island (Calla Millor and Playa de Palma). Their results show that beaches would suffer a coastal retreat between 7 and 49 m under RCP4.5 and RCP 8.5 sea level rise projections, respectively, which is equivalent to half of the present-day aerial beach surface. This last study, present lesser affectation over above mentioned studies because de beach profile has a steeper slope.

Flooding in Bocagrande beaches is also related with their low topographic elevation as well as with the discontinuous elevations of the berm with values below the actual sea level in some areas. This fact, together with the coupled to the specific response of the Caribbean Sea under the future scenarios (fast thermos-steric response) makes it a highly risky spot for the SLR. Moreover, the poor correlation between extremes of skew-surges and waves supports the major relevance of swell waves in the generation of flooding in this part of the Caribbean region. Therefore, in order to assess the effect of the projected mean SLR under the RCP 4.5 scenario combined with the tides, high energy waves, surges and topo-bathymetric heights at the Bocagrande beaches we use the coupled models SWAN-SWASH.

Since non-stationary numerical simulations are computationally extremely demanding, we have evaluated the risk of flooding for a set of specific events. In this regard, after a statistical assessment of historical extreme skew-surge and wave conditions, the most representative case-studies have been selected. Besides we have considered the potential effects of SLR in Bocagrande beaches for the most hazardous present-day considered scenario (A4), in an attempt to optimize

the computational time. Despite this limitation and in contrast to other methodologies previously used to assessed coastal inundation in Cartagena beaches and its surrounding areas (Nicolae-Lerma et al., 2008; Andrade et al., 2013; Nicolae-Lerma et al., 2013) the coupling of SWAN-SWASH models has allowed us to determine the extreme wave run-up over the Bocagrande beaches in two dimensions, with a good agreement when tested against measured wave data and video images. With this methodology we have taken into account the mean SL, high astronomical tides, and extreme skew-surges and waves, as well as the projected mean SLR under the RCP 4.5 scenario and the actual structural elements (groins, breakwaters, dams, etc.) that interact with the wave field. Therefore, this approach can be used to search for specific solutions (either soft and/or hard engineering approaches) to mitigate the effects of the SLR in the studied area. Indeed, a good representation of waves (H_s and direction) is mandatory to adequately study coastal flooding. These processes can only be taken into account with the use of numerical models. From the above results, although the shallow water significant wave height is larger for the cold-front configuration (NW direction at deep waters, B1–B4 in **Table 2**), the inundation resulting from the NE extreme waves is higher due to waves refraction and location of the coast line. Because the coastline of the study area is parallel to waves from NNW direction (see **Figure 1**, bottom-right panel), NE waves have a direct impact on the beaches. On the other hand, incoming waves from the NW direction (WNW direction in shallow waters), had impact directly over the groins, thus not affecting beaches.

The combined effect of astronomical tides and extreme skew-surge contribute to coastal inundation only between 25 and 45% of the projected SLR under RCP 4.5 (for year 2025 and 2100, respectively). Therefore, SLR appears to be the most dominant factor in this study area. We note that in this work it has been analyzed a conservative climate change scenario, hence even a higher importance of SLR can be expected for more pessimistic projections. This result is inferred from **Figure 9** (cases C1–C4), where the inundated area increases dramatically as we move closer to the end of the 21st century. The main reason is the low topographic elevation, which in some cases are directly below the mean sea level.

Finally, we want to remark that among the factors that may influence the flooding in Bocagrande beaches, we have not considered the geodynamic processes, the changes in the beach profile as the sea level rises, the change in beach planform in response to a potential variation in the mean wave energy flux and eventual changes in the wave dynamics related to variations in the atmospheric patterns as a consequence of climate change. These limitations imply that; (i) for the year 2100 the total flooded area could be higher than the one provided in this study. According to the analysis of Andrade-Amaya et al. (2017) from a geodetic station located in Cartagena de Indias, this zone present subsidence processes with values between -1.78 ± 0.4 and -1.88 ± 0.44 mm/year. (ii) The response of the beach profile to sea level rise and wave dynamics also could have an influence on the value of the flooded area provided for each of the scenarios if there were a constant sediment flux and if the beach front would not be totally urbanized. Considering the latter, to limit the number of variables used in this work, we have assumed that the beach profile remains inalterable under the proposed scenarios which, as a first approach, is a reasonably assumption since changes in beach profile are below 20 cm under the worst SLR scenarios (Enríquez et al., 2017). (iii) Flood processes generated by the run – up under wave energetic conditions over Bocagrande beaches could result in an underestimation of the percentage of flooded area obtained in this study, especially for the year 2100 SLR scenario. According to Mentaschi et al. (2017) and Casas-Prat et al. (2018) wave energy conditions will probably change globally in response to a shift in the wind regimes because of the undergoing global warming.

DATA AVAILABILITY STATEMENT

The datasets generated for this study are available on request to the corresponding author.

AUTHOR CONTRIBUTIONS

This work was part of AO-R's Ph.D. thesis. AO-R wrote the manuscript and performed the simulations. AO and JR were the supervisors and contributed to conceiving the topic and the development of the argument, interpretation of the results, and writing. JS, MM, LO, and IH-C contributed to the interpretation of the results and writing.

FUNDING

This work was supported by COLCIENCIAS (Departamento Administrativo de Ciencia, Tecnología e Innovación) through of convocatoria 727 and from the Spanish Government MICINN/FEDER through projects MUSA (CTM2015-66225-C2-2-P) and MOCCA (RTI2018-093941-B-C31). The authors acknowledge the financial support from the Spanish Government MICINN/FEDER through projects MUSA (CTM2015-66225-C2-2-P) and MOCCA (RTI2018-093941-B-C31). AO-R is supported by a grant from Colombian COLCIENCIAS (Convocatoria 727). JS thanks the financial support by the Netherlands Scientific Research Foundation (NWO) through the VIDI grant number 864.13.011 awarded to C. A. Katsman. IH-C acknowledges the Vicenç Mut contract funded by the Government of the Balearic Island. This work was partially performed while AO was a visiting scientist at the Earth, Environmental and Planetary Sciences Department at Brown University through a Ministerio de Ciencia, Innovación y Universidades fellowship (PRX18/00218).

REFERENCES

Aarninkhof, S. G. J., Turner, I. L., Dronkers, T. D. T., Caljouw, M., and Nipiusc, L. (2003). A video-based technique for mapping intertidal beach bathymetry. *Coast. Eng.* 49, 275–289. doi: 10.1016/S0378-3839(03)00064-4

Alexander, K. S., Ryan, A., and Measham, T. G. (2012). Managed retreat of coastal communities: understanding responses to projected sea level rise. *J. Environ. Plan. Man.* 55, 409–433. doi: 10.1080/09640568.2011.604193

Andrade, C. A. (1993). Análisis de la velocidad del viento en el mar Caribe. *Bol. Cient. Cioh.* 13, 33–43. doi: 10.26640/01200542.13.33_43

Andrade, C. A., Thomas, Y. F., Lerma, A. N., Durand, P., and Anselme, B. (2013). Coastal flooding hazard related to swell events in cartagena de indias. *Colombia. J. Coastal Res.* 29, 1126–1136. doi: 10.2112/JCOASTRES-D-12-00028.1

Andrade-Amaya, C. A., Ferrero-Ronquillo, A. J., León-Rincón, H., Mora-Páez, H., and Carvajal-Perico, H. (2017). Sobre cambios en la línea de costa entre 1735 y 2011y la subsidencia en la Bahía de Cartagena de Indias, Colombia. *Rev. Acad. Colomb. Cienc. Ex. Fis. Nat.* 41, 94–106. doi: 10.18257/raccefyn.360

Asociación Colombiana de Agencias de Viajes y Turismo [ANATO] (2018). *Compendio de estadísticas turísticas de ANATO*. https://www.anato.org/es/investigaciones?qt-investigaciones=1#qt-investigaciones (accessed September 24, 2019).

Bengtsson, L., Hodges, K. I., and Roeckner, E. (2006). Storm tracks and climate change. *J. Clim.* 19, 3518–3543. doi: 10.1175/JCLI3815.1

Bon de Sousa, L., Loureiro, C., and Ferreira, O. (2018). Morphological and economic impacts of rising sea levels on cliff-backed platform beaches in southern Portugal. *Appl. Geogr.* 99, 31–43. doi: 10.1016/j.apgeog.2018.07.023

Booij, N., Ris, R. C., and Holthuijsen, L. H. (1999). A third-generation wave model for coastal regions 1. Model description and validation. *J. Geophys. Res. Oceans.* 104, 7649–7666. doi: 10.1029/98JC02622

Callaghan, D. P., Roshanka, R., and Andrew, S. (2009). Quantifying the storm erosion hazard for coastal planning. *Coast. Eng.* 56, 90–93. doi: 10.1016/j.coastaleng.2008.10.003

Casas-Prat, M., Wanga, X. L., and Swartb, N. (2018). CMIP5-based global wave climate projections including the entire Arctic Ocean. *Ocean Mod.* 123, 66–85. doi: 10.1016/j.ocemod.2017.12.003

Castelle, B., Dodet, G., Masselink, G., and Scott, T. (2018). Increased winter-mean wave height, variability, and periodicity in the northeast Atlantic over 1949–2017. *Geophys. Res. Lett.* 45, 3586–3596. doi: 10.1002/2017GL076884

Church, J. A., Clark, P. U., Cazenave, A., Gregory, J. M., Jevrejeva, S., Levermann, A., et al. (2013). "Sea level change in: Climate change 2013: the physical science basis," in *Contribution of Working Group I to the fifth Assessment report of the Intergovernmental Panel on Climate Change*, eds T. F. Stocker, D. Qin, G. K. Plattner, M. Tignor, S. K. Allen, and J. Boschung (Cambridge: Cambridge University Press).

Church, J. A., and White, N. J. (2006). A 20th century acceleration in global sea-level rise. *Geophy. Res. Lett.* 33:L01602. doi: 10.1029/2005GL024826

Codiga, D. L. (2011). *Unified Tidal Analysis and Prediction Using the UTide Matlab Functions. Technical Report 2011-01*. Narragansett, RI: University of Rhode Island, 5.

Conde-Frias, M., Otero, L., Restrepo, J. C., Ortiz, J. C., Ruiz, J., and Osorio, A. F. (2017). Swash oscillations in a microtidal dissipative beach. *J. of Coast. Res.* 33, 1408–1422. doi: 10.2112/JCOASTRES-D-16-00147.1

Dangendorf, S., Marcos, M., Wöppelmann, G., Conrad, C. P., Frederikse, T., and Riva, R. (2017). Reassessment of 20th century global mean sea level rise. *Proc. Natl. Acad. Sci. U.S.A.* 114, 5946–5951. doi: 10.1073/pnas.1616007114

Dietrich, J., Tanaka, S., Westerink, J., Dawson, C., Luettich, R. A. Jr., Zijlema, M., et al. (2011). Performance of the unstructured mesh, SWAN+ADCIRC model in computing hurricane waves and surge. *J. Sci. Comput.* 52, 468–497. doi: 10.1007/s10915-011-9555-6

Enríquez, A. R., Marcos, M., Álvarez-Ellacuría, A., Orfila, A., and Gomis, D. (2017). Changes in beach shoreline due to sea level rise and waves under climate change scenarios: application to the Balearic Islands (western Mediterranean). *Nat. Hazards Earth Syst. Sci.* 17, 1075–1089. doi: 10.5194/nhess-17-1075-2017

Enríquez, A. R., Marcos, M., Falqués, A., and Roelvink, D. (2019).). Assessing beach and dune erosion and vulnerability under sea level rise: a case study in the mediterranean sea. *Front. Mar. Sci.* 6:4. doi: 10.3389/fmars.2019.00004

Fleming, R. J. V., Luettich, R., and Fleming, J. G. (2013). Comparative hydrodynamics during events along a barrier island: explanation for overwash. *Estuar. Coasts.* 36, 334–346. doi: 10.1007/s12237-012-9578-8

Gibbons, J. D., and Chakraborti, S. (2011). "Nonparametric Statistical Inference," in *International Encyclopedia of Statistical Science*, ed. M. Lovric (Berlin: Springer).

Gregory, J. M., White, N. J., Church, J. A., Bierkens, M. F. P., Box, J. E., van der Broeke, M. R., et al. (2013). Twentieth-century global-mean sea level rise: is the whole greater than the sum of the parts? *J. Clim.* 26, 4476–4499. doi: 10.1175/JCLI-D-12-00319.1

Guimarães, P. V., Farina, L., Toldo, E. Jr., Diaz-Hernandez, G., and Akhmatskaya, E. (2015). Numerical simulation of extreme wave runup during storm events in tramandaí beach. Rio Grande do Sul Brazil. *Coast. Eng.* 95, 171–180. doi: 10.1016/j.coastaleng.2014.10.008

Hemer, M. A., Fan, Y., Mori, N., Semedo, A., and Wang, X. L. (2013). Projected changes in wave climate from a multi-model ensemble. *Nat. Clim. Change.* 3:471. doi: 10.1038/nclimate1791

Hinkel, J., Lincke, D., Vafeidis, A. T., Perrette, M., Nicholls, R. J., Tol, R. S. J., et al. (2013). Coastal flood damage and adaptation costs under 21st century sea-level rise. *PNAS* 111, 3292–3297. doi: 10.1073/pnas.1222469111

Hunt, A., and Watkiss, P. (2011). Climate change impacts and adaptation in cities: a review of the literature. *Clim. Change.* 104, 13–49. doi: 10.1007/s10584-010-9975-6

Jackson, L. P., and Jevrejeva, S. (2016). A probabilistic approach to 21st century regional sea-level projections using RCP and high-end scenarios. *Glob. Planet. Change.* 146, 179–189. doi: 10.1016/j.gloplacha.2016.10.006

Kobayashi, S., Ota, Y., Harada, Y., Ebita, A., Moriya, M., Onoda, H., et al. (2015). The JRA-55 reanalysis: general specifications and basic characteristics. *J. Meteo. Society of Japan.* 93, 5–48. doi: 10.2151/jmsj.2015-001

Komen, G. J., Hasselmann, K., and Hasselmann, K. (1984). On the existence of a fully developed wind-sea spectrum. *J. Phys. Oceanogr.* 14, 1271–1285. doi: 10.1175/1520-0485(1984)014<1271:oteoaf>2.0.co;2

Le Bars, D., Drijfout, S., and de Vries, H. A. (2017). High-end sea level rise probabilistic projection including rapid Antarctic ice sheet mass loss. *Environ. Res. Lett.* 12, 1–10. doi: 10.1088/1748-9326/aa6512

Limber, P. W., Barnard, P. L., Vitousek, S., and Erikson, L. H. (2018). A model ensemble for projecting multidecadal coastal cliff retreat during the 21st century. *J. Geophys. Res. Earth Surf.* 123, 1566–1589. doi: 10.1029/2017JF004401

Lyu, K., Church, J. A., Slangen, A. B. A., and Hu, J. (2014). Time of emergence for regional sea-level change. *Nat. Clim. Change.* 4, 1006–1010. doi: 10.1038/NCLIMATE2397

Marcos, M., Rohmer, J., Vousdoukas, M. I., Mentaschi, L., Le Cozannet, G., and Amores, A. (2019). Increased extreme coastal water levels due to the combined action of storm surges and wind waves. *Geophys. Res. Lett* 46, 4356–4364. doi: 10.1029/2019GL082599

Marcos, M., Tsimplis, M. N., and Shaw, A. G. P. (2009). Sea level extremes in southern Europe. *J. Geophys. Res.* 114:C01007. doi: 10.1029/2008JC004912

Masselink, G., Castelle, B., Scott, T., Dodet, G., Suanez, S., Jackson, D., et al. (2016). Extreme wave activity during 2013/2014 winter and morphological impacts along the Atlantic coast of Europe. *Geophys. Res. Lett.* 43, 2135–2143. doi: 10.1002/2015GL067492

Mawdsley, R. J., Haigh, I. D., and Wells, N. C. (2015). Global secular changes in different tidal high water, low water and range levels. *Earth Fut.* 3, 66–81. doi: 10.1002/2014EF000282

Melet, A., Meyssignac, B., Rafael Almar, R., and Le Cozannet, G. (2018). Under-estimated wave contribution to coastal sea-level rise. *Nat. Clim. Change.* 8, 234–239. doi: 10.1038/s41558-018-0088-y

Mentaschi, L., Vousdoukas, M. I., Voukouvalas, E., Dosio, A., and Feyen, L. (2017). Global changes of extreme coastal wave energy fluxes triggered by intensified teleconnection patterns. *Geophys. Res. Lett.* 44, 2416–2426. doi: 10.1002/2016GL072488

Molares, R. (2011). *The INFLUENCE of the Dique Channel Discharge on the Seawater of Cartagena Bay—Colombia*. dissertation/master's thesis, Universitat Politecnica de Catalunya, Barcelona.

Morales-Márquez, V., Orfila, A., Simarro, G., Gómez-Pujol, L., Álvarez-Ellacuría, A., Conti, D., et al. (2018). Numerical and remote techniques for operational beach management under storm group forcing. *Nat. Hazards Earth. Syst. Sci.* 18, 3211–3223. doi: 10.5194/nhess-2018-173

Moss, R. H., Edmonds, J. A., Hibbard, K. A., Manning, M. R., Rose, S. K., van Vuuren, D. P., et al. (2010). The next generation of scenarios for climate change research and assessment. *Nat* 463, 747–756. doi: 10.1038/nature 08823

Nicholls, R. J., and Cazenave, A. (2010). Sea-level rise and its impact on coastal zones. *Science* 328, 1517–1520. doi: 10.1126/science.1185782

Nicholls, R. J., Hanson, S. E., Lowe, J. A., Warrick, R. A., Lu, X., and Long, A. J. (2014). Sea-level scenarios for evaluating coastal impacts. *WIREs Clim. Change* 5, 129–150. doi: 10.1002/wcc.253

Nicholls, R. J., Marinova, N., Lowe, J. A., Brown, S., Vellinga, P., Gusmão, D., et al. (2011). Sea-level rise and its possible impacts given a 'beyond 4°C world' in the twenty-first century. *Philos. Trans. R. Soc. A Math. Phys. Eng. Sci.* 369, 161–181. doi: 10.1098/rsta.2010.0291

Nicolae-Lerma, A., Thomas, Y.-F., Durand, P., Anselme, B., and Andrade, C. A. (2013). Modélisation de submersions marines et leur validation par observation vidéo à Carthagène des Indes, Colombie Coastal floods modeling and video observation validation in Cartagena de Indias, colombia. *Géomorphol. Relief Processus Environ.* 4, 481–498. doi: 10.4000/geomorphologie. 10417

Nicolae-Lerma, A., Thomas, Y.-F., Durand, P., Torres, R. R., and Andrade, C. A. (2008). Variabilidad del nivel del mar desde 1950 hasta el 2000 y riesgos asociados a episodios de Mar de leva en las Penı̀nsulas de bocagrande y castillogrande. Cartagena de Indias, colombia. *Bol. Cient. Cioh* 26, 71–84.

Nieto, M. A., Garau, B., Balle, S., Simarro, G., Zarruk, G. A., Ortiz, A., et al. (2010). An open source, low cost video-based coastal monitoring system. *Earth Surf. Process. Landforms.* 35, 1712–1719. doi: 10.1002/esp.2025

Ojeda, E., and Guillén, J. (2008). Shoreline dynamics and beach rotation of artificial embayed beaches. *Mar. Geol.* 253, 51–62. doi: 10.1016/j.margeo.2008.03.010

Ortiz, J. C., Plazas, J. M., and Lizano, O. (2015). Evaluation of extreme waves associated with cyclonic activity on san andrés island in the caribbean sea since 1900. *J. Coast. Res.* 31, 557–568. doi: 10.2112/JCOASTRES-D-14-00072.1

Osorio, A. F., Mesa, J., Bernal, G., and Montoya, R. (2009). Reconstrucción de cuarenta años de datos de oleaje en el mar Caribe colombiano empleando el modelo WWIII^{TM} y diferentes fuentes de datos. *Bol. Cient. Cioh* 27, 37–56. doi: 10.26640/01200542.27.37_56

Osorio, A. F., Montoya-Vargas, S., Cartagena, C. A., Espinosa, J., Orfila, A., and Winter, C. (2019). Virtual BUOY: a video-based approach for measuring near-shore wave peak period. *Comput. Geosci.* 133:104302. doi: 10.1016/j.cageo.2019.07.006

Otero, L. J., Ortiz-Royero, J. C., Ruiz-Merchan, J. K., Higgins, A. E., and Henriquez, S. A. (2016). Storms or cold fronts what is really responsible for the extreme waves regime in the colombian caribbean coastal region? *Nat. Hazards Earth Syst. Sci.* 16, 1–11. doi: 10.5194/nhess-16-391-2016

Passeri, D. L., Hagen, S. C., Medeiros, S. C., Bilskie, M. V., Alizad, K., and Wang, D. (2015). The dynamic effects of sea level rise on low gradient coastal landscapes: a review. *Earth's Future.* 3, 159–181. doi: 10.1002/2015EF000298

Peláez-Zapata, D. S., Osorio, A. F., Alvarez-Silva, O. A., Osorio-Cano, J. D., and Payán, L. (2012). "Estimación de la Cota de Inundación Como Herramienta Para la Conservación de las Tortugas Marinas en el Pacífico Colombiano," in *XXV Congreso Latinoamericano de Hidráulica San José*, (Costa Rica), 9–12. doi: 10.13140/2.1.5035.8402

Poveda, G., Velez, J. I., Mesa, O. J., Hoyos, C. D., Mejía, J. F., Barco, O. J., et al. (2002). Influencia de fenómenos macro climáticos sobre el ciclo anual de la hidrología colombiana: cuantificación lineal, no lineal y percentiles probabilísticos. *Meteorol. Colomb* 6, 121–130

Restrepo, J. C., Escobar, J., Otero, L., Franco, D., Pierini, J., and Correa, I. (2017). Factors influencing the distribution and characteristics of surface sediment in the bay of cartagena. *Colombia. J. Coast. Res.* 33, 135–148. doi: 10.2112/JCOASTRES-D-15-00185.1

Ruggiero, P., Komar, P. D., and Allan, J. C. (2010). Increasing wave heights and extreme value projections: the wave climate of the U.S. Pacific Northwest. *Estuar. Coast. Shelf Sci* 183, 221–234.

Salmon, S. A., Bryan, K. R., and Coco, G. (2007). "The use of video systems to measure run-up on beaches," in *Proceedings of the 9th International Coastal Symposium*, ed. J. Coast (Gold Coast), 211–215.

Sayol, J. M., and Marcos, M. (2018). Assessing flood risk under sea level rise and extreme sea levels scenarios. application to the Ebro Delta (Spain). *J. Geophys. Res. Oceans* 123, 794–811. doi: 10.1002/2017JC013355

Seemüller, W., Seitz, M., Sánchez, L., and Drewes, H. (2009). *The Position and Velocity solution SIR09P01 of the IGS Regional Network Associate Analysis Centre for SIRGAS (IGS RNAAC SIR). DGFIReport 85*. Berlin; Springer.

Simarro, G., Bryan, K. R., Guedes, R. M. C., Sancho, A., Guillen, J., and Coco, G. (2015). On the use of variance images for runup and shoreline detection. *Coast. Eng.* 99, 136–147. doi: 10.1016/j.coastaleng.2015.03.002

Slangen, A. B. A., Carson, M., Katsman, C. A., van de Wal, R. S. W., Köhl, A., Vermeersen, L. L., et al. (2014). Projecting twenty-first century regional sea-level changes. *Clim. Change* 124, 317–332. doi: 10.1007/s10584-014-1080-9

Smit, P., Janssen, T., Holthuijsen, L., and Smith, J. (2014). Nonhydrostatic modelling of surf zone wave dynamics. *Coast. Eng.* 83, 36–48. doi: 10.1016/j.coastaleng.2013.09.005

Thomas, Y.-F., Nicolae Lerma, A., Durand, P., Posada, B., Garcia Valencia, C., and Andrade Amaya, C. A. (2011). Altura significativa del oleaje en la cuenca colombiana del caribe, datos de altimetría radar Bol. *Cient. Cioh.* 29, 27–45. doi: 10.26640/01200542.29.27_45

Torres, R. R., and Tsimplis, M. N. (2012). Seasonal sea level cycle in the caribbean sea. *J. Geophys. Res.* 117, C07011. doi: 10.1029/2012JC008159

Torres, R. R., and Tsimplis, M. N. (2014). Sea level extremes in the Caribbean Sea. *J. Geophys. Res. Oceans.* 119, 4714–4731. doi: 10.1002/2014JC009929

Tsimplis, M. N. (1995). The response of sea level to atmospheric forcing in the mediterranean. *J Coast. Res.* 11, 1309–1321.

Vermeer, M., and Rahmstorf, S. (2009). Global sea level linked to global temperature. *PNAS* 106, 21527–21532. doi: 10.1073/pnas.0907765106

Verschuur, J. (2018). *Implications of uncertain Antarctic ice sheet dynamics for managing future coastal erosion: A probabilistic approach for a data-scarce environment in the Caribbean*. dissertation/master's thesis, Delft University of Technology, Koninkrijk der Nederlanden.

Vitousek, S., Barnard, P. L., Fletcher, C. H., Frazer, N., Erikson, L., and Storlazzi, C. D. (2017). Doubling of coastal flooding frequency within decades due to sea-level rise. *Sci. Rep.* 7:1399. doi: 10.1038/s41598-017-01362-7

Vousdoukas, M. I., Mentaschi, L., Voukouvalas, E., Verlaan, M., Jevrejeva, S., Jackson, L. P., et al. (2018). Global probabilistic projections of extreme sea levels show intensification of coastal flood hazard. *Nat. Commun.* 9:2360. doi: 10.1038/s41467-018-04692-w

Wahl, T., and Chambers, D. P. (2014). Evidence for multidecadal variability in US extreme sea level records. *J. Geophys. Res. Oceans.* 120, 1527–1544. doi: 10.1002/2014JC010443

Wang, J., Yi, S., Li, M. Y., Wang, L., and Song, C. C. (2018). Effects of sea level rise, land subsidence, bathymetric change and typhoon tracks on storm flooding in the coastal areas of Shanghai. *Sci Total Environ* 621, 228–234. doi: 10.1016/j.scitotenv.2017.11.224

Willis, J. K., and Church, J. A. (2012). Regional Sea-Level Projection. *Science* 336, 550–551. doi: 10.1126/science.1220366

Woodworth, P. L., Hunter, J. R., Marcos, M., Caldwell, P., Menendez, M., and Haigh, I. (2017). Towards a global higher-frequency sea level dataset. *Geosci. Data J.* 3, 50–59. doi: 10.1002/gdj3.42

Young, I. R., Zieger, S., and Babanin, A. V. (2011). Global trends in wind speed and wave height. *Science* 332, 451–455. doi: 10.1126/science.1197219

Zijlema, M., Stelling, G., and Smit, P. (2011). SWASH: an operational public domain code for simulating wave fields and rapidly varied flows in coastal waters. *Coast. Eng.* 58, 992–1012. doi: 10.1016/j.coastaleng.2011.05.015 doi: 10.1016/j.coastaleng.2011.05.015

Conflict of Interest: The authors declare that the research was conducted in the absence of any commercial or financial relationships that could be construed as a potential conflict of interest.

frontiers in Marine Science

ORIGINAL RESEARCH
published: 21 February 2020
doi: 10.3389/fmars.2020.00098

Effects of the Temporal Variability of Storm Surges on Coastal Flooding

Jorid Höffken[1], Athanasios T. Vafeidis[1], Leigh R. MacPherson[2] and Sönke Dangendorf[2,3]*

[1] Institute of Geography, Christian-Albrecht University of Kiel, Kiel, Germany, [2] Research Institute for Water and Environment, University of Siegen, Siegen, Germany, [3] Department for Ocean, Earth and Atmospheric Sciences, Old Dominion University, Norfolk, VA, United States

Assessments of flood exposure and risk are usually conducted for individual events with a specific peak water level and hydrograph, without considering variations in the temporal evolution (duration and intensity) of storm surges. Here we investigate the influence of temporal variability of storm surge events on flood characteristics in coastal zones, namely flood extent and inundation depth, and assess the associated flood exposure in terms of affected properties for the case of the municipality of Eckernförde, Germany. We use a nested hydrodynamic model to simulate five physically plausible, stochastically simulated storm surge events, with peak water levels corresponding to a univariate return period of 200 years and varying intensities. In a second step, the events are also combined with high-end sea-level rise projections corresponding to the RCP 8.5 scenario to analyze if the influence of temporal variability changes with rising sea-levels. Results show differences exceeding 5% in flood extent when comparing storm surges with the highest and lowest intensities. The number of properties exposed differs by approximately 20%. Differences in mean and maximum inundation depths are approximately 5%, both with and without sea-level rise. However, deviations in flood extent increase by more than 20%, depending on the sea-level rise projection, whereas differences in the number of exposed properties decrease. Our findings indicate that the temporal variability of storm surges can have considerable influence on flood extent and exposure in the study area. Taking into account that flood extent increases with rising sea-levels, we recommend that uncertainty related to the temporal variability of storm surges is represented in future flood risk assessments to ensure efficient planning and to provide a more comprehensive assessment of exposed infrastructure and assets.

Keywords: storm surge, temporal variability, coastal flooding, extreme sea levels, Eckernförde Bay

OPEN ACCESS

Edited by:
Rafael Almar, Institut de Recherche pour le Développement (IRD), France

Reviewed by:
Rory Benedict O'Hara Murray, Marine Scotland Science, United Kingdom
Alejandro Orfila, Spanish National Research Council, Spain

****Correspondence:***
Jorid Höffken
jorid.hoeffken@web.de

Specialty section:
This article was submitted to Coastal Ocean Processes, a section of the journal Frontiers in Marine Science

Received: *27 October 2019*
Accepted: *06 February 2020*
Published: *21 February 2020*

Citation:
Höffken J, Vafeidis AT, MacPherson LR and Dangendorf S (2020) Effects of the Temporal Variability of Storm Surges on Coastal Flooding. Front. Mar. Sci. 7:98. doi: 10.3389/fmars.2020.00098

INTRODUCTION

Coastal flooding due to extreme water levels constitutes a major hazard for coastal systems and low-lying areas (Vousdoukas et al., 2018). Such flooding events are likely to become more frequent under sea-level rise on global and local scales, which contributes to an expected increase in the intensity and probability of extreme water levels over the next decades (Church et al., 2013; Arns et al., 2017; Wahl et al., 2017; IPCC, 2019). Furthermore, coastal zones are heavily populated areas which attract many people and are therefore characterized by higher rates of population growth

and urbanization in comparison to landlocked regions (Wong et al., 2014; Neumann et al., 2015). This results in an increased exposure of people and assets to coastal flooding. Managing coastal flood risk is a crucial aspect of adapting to these challenging developments, and is becoming increasingly important for coastal communities (Wadey et al., 2015; Vousdoukas et al., 2016). To obtain sustainable adaptation solutions, coastal management strategies must take climate change, socio-economic development and urbanization into account.

Analyzing coastal flood risk requires quantifying damages associated with specific return water levels (Stewart and Melchers, 1997). This is commonly done by means of inundation modeling. However, a number of uncertainties arise during this process, and it is important that they are quantified and communicated to policy-makers (Teng et al., 2017). First, uncertainties arise as a result of the methods used to model inundation, the specific model used and the model parameters (Wahl et al., 2017). A number of different model types and methods are available for use in flood risk assessments, depending on factors such as scale, investigation focus, application purpose, data availability, computing capacity, location characteristics, and others. 2D-hydrodynamic models, which simulate water propagation according to certain physical properties, have gained much attention in recent years (Néelz and Pender, 2013). These models are able to simulate water velocity, flood extent and inundation depth with high accuracy, which is an important requirement for flood risk assessment and management. However, due to their high data and computational requirements, they are mostly applied at local scales. For large-scale applications simplified conceptual models can be used, which calculate inundation based on simplified hydraulic concepts (Teng et al., 2017). These approaches, such as the bathtub method or simple hydrodynamic models, are less accurate than 2D-hydrodynamic models but require far less resources for computation. A comparison of different types of models that are applicable on a large scale can be found in Vousdoukas et al. (2016).

A second source of uncertainty is the estimation of return water levels, which is affected by the length of available water level records. These records are often limited to a few decades and may not contain events of exceptional magnitude. Consequently, return water levels can be significantly underestimated (Dangendorf et al., 2016). In addition, flood risk analyses typically only consider the peak water level of extreme events, and do not consider the effect of other storm surge parameters, such as duration or variability (Wahl et al., 2017). In particular, the temporal variability of extreme sea level events can result in large uncertainties in the estimation of flood impact (Quinn et al., 2014; Santamaria-Aguilar et al., 2017). Despite the ability of hydrodynamic models to account for water propagation and inundation during a complete storm surge curve, temporal variability typically is disregarded in flood risk analyses (Gallien et al., 2014). Such models are commonly forced by water level time-series of past extreme events, or an upscaling of such events to specific return water levels (Santamaria-Aguilar et al., 2017). Therefore, the modeled inundation is only representative for a specific event. Care must be taken as disregarding uncertainties arising from estimates of extreme water levels, storm surge variability and model application can lead to inadequate coastal risk management (Quinn et al., 2014; Santamaria-Aguilar et al., 2017). Therefore, a variety of possible extreme water levels with temporal developments typical for the investigated area are required to account for the range of uncertainties and to produce a more accurate risk assessment. One approach to generate a sufficient number of extreme water level events is outlined in Wahl et al. (2011), who developed a method to stochastically simulate large numbers of extreme water level curves at two locations in the North Sea, Cuxhaven and Hörnum, based on observed events. This approach is further developed by MacPherson et al. (2019) and applied along the micro-tidal German Baltic Sea coast, generating artificial events at 45 tide gauge stations. The model contains three methodological main steps; identification of extreme events within water level records, parameterization of each identified event, and the generation of artificial events using Monte-Carlo Simulations.

This study assesses the influence of the temporal variability of storm surges on flood characteristics in coastal zones for the case of the city of Eckernförde. For this analysis, five statistically simulated storm surge events generated by MacPherson et al. (2019) are simulated using the hydrodynamic model Delft3D (Deltares, 2018). To analyze variations in flood extent and inundation depth due to temporal variability, each event has the same peak water level corresponding to a univariate return period of 200 years but with varying durations and intensities, which we chose artificially to the specified return period. Intensity is hereby defined as the area between the water level curve and a pre-defined threshold, in this case, mean sea-level. Additionally, we consider one sea-level rise projection to examine the effect of higher mean water levels on deviations in both flood characteristics and exposure due to storm surge temporal variability. The paper is structured as follows: the characteristics of the study area as well as the model and the data used for the analysis are described in section "Study Area and Data"; the applied model setup and the generation of the simulated scenarios are outlined in section "Materials and Methods". The results of the study are presented in section "Results" and discussed in section "Discussion". Last, the most important findings are provided as concluding statements in section "Conclusion".

STUDY AREA AND DATA

Study Area

Eckernförde Bay is located in the south-west Baltic Sea in Kiel Bay and has a length of approximately 16 km (**Figure 1**). The shallow, elongated bay was formed during the last glacial period (Hofstede, 2008). Its topography is mostly characterized by a gradual coast and low-lying coastal areas with elevation below 10 m referenced to the vertical datum DHHN92 and a maximum elevation of approximately 50 m in the hinterland. The south-eastern coastline of the bay consists of cliffs. The tidal range in the Baltic Sea is small (less than 10 cm) and major variations in water levels are mostly defined by large scale atmospheric

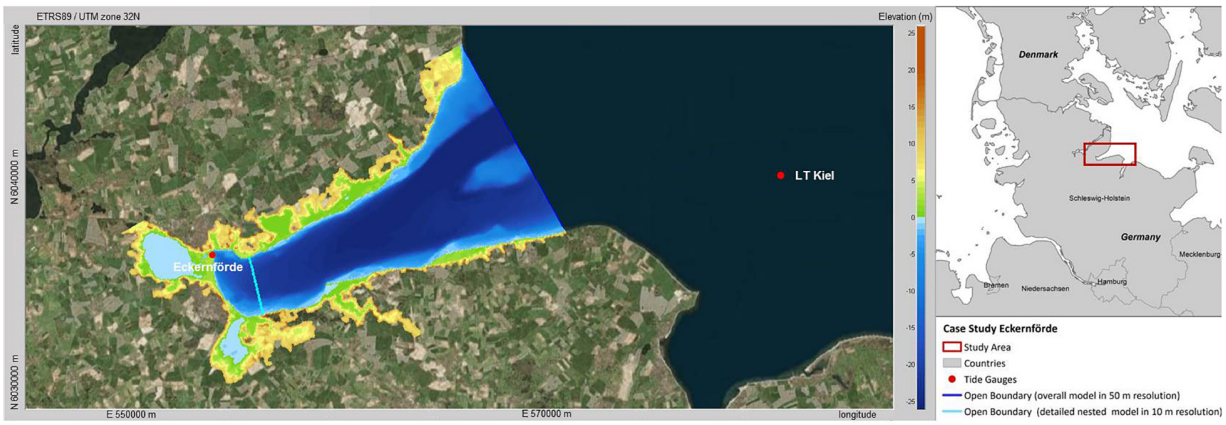

FIGURE 1 | Location of the study area Eckernförde Bay and computational domain of the nested model setup in Delft3D including the tide gauges and the open boundaries of the coarser and the nested model. Bathymetry is displayed in shades of blue and land surface is displayed in green to red colors. The coastal boundary runs along NHN.

pressure and wind (Gräwe and Burchard, 2012). Extreme water levels are mainly influenced by strong north-easterly winds, but seiches acting over the entire Baltic Sea may contribute several decimeters as well (Jensen and Müller-Navarra, 2008). The municipality of Eckernförde has experienced several extreme flood events in the past. The highest event recorded reached 3.15 m above mean sea-level during the 1872 storm surge (WSA Lübeck, 2017), approximately 1 m higher than all following events. The storm surge resulted in 271 fatalities and represents the beginning of systematic planning of flood defenses and protection measures at the Baltic Sea coast in Schleswig-Holstein (Hofstede, 2008).

The city of Eckernförde has a population of 22,031 inhabitants (status 30.09.2017, City of Eckernförde) and is situated at the western tip of Eckernförde bay in Schleswig-Holstein, the northernmost federal state of Germany. As a Baltic Seaside resort, it is a popular tourist location in the region. Although there is a certain level of coastal defense measures, such as dikes along the federal road or bulkheads, and the area is protected against moderate storm surges, parts of the city are vulnerable to low-frequency, high-magnitude events (PROKOM GmbH, 2017). This is especially true for the city center where economic activities and population are concentrated and elevation is low (large areas beneath 5 m elevation). Martinez and Bray (2011) analyzed the awareness of political decision-makers regarding climate change and possible adaptation in the German Baltic Sea region. Although there is certain recognition of climate change and sea-level rise, knowledge is lacking on how to use the information for appropriate adaptation responses.

Flood risk assessments in Schleswig-Holstein are conducted by simulating flood events using site-specific water levels. As safety standards for coastal protection measures, the federal state uses water levels with a 200-year return period and adds 0.5 m to account for sea-level rise (Ministerium für Energiewende, Landwirtschaft, Umwelt und ländliche Räume des Landes Schleswig-Holstein, 2012). However, the temporal evolution of storm surge events, namely differences in storm surge intensity and duration, are not considered and methods to account for this aspect are not described. On behalf of the city administration of Eckernförde, a master plan to develop an integrated coastal zone management program was published in 2017 (PROKOM GmbH). This plan includes strategies for protecting the coast of the Eckernförde Bay against future floods, and suggests flood protection walls as the main strategy of protection.

Data

Data preparation and processing for the hydrodynamic simulation was performed in ArcGIS (10.3.1), Delft Dashboard, R-Studio (1.1.423), and Matlab (R2016b). The following datasets are used as a basis for the model setup and further analysis (**Table 1**).

Water level data were used for model boundary forcing and for the calibration and validation of the model setup. We use data measured at two tide gauges (TG) located in the area of Eckernförde Bay, TG Eckernförde which is located in the harbor of Eckernförde, and TG LT Kiel, located approximately ten kilometers to the east (**Figure 1**). Water level time series for both tide gauges was provided by "Wasserstraßen- und Schifffahrtsamt Lübeck" (WSA Lübeck) department of "Wasserstraßen- und Schifffahrtsverwaltung des Bundes" (WSV). The hourly records cover a time period of 27 years from the 1st November 1990 until the 31st October 2017. Furthermore, the Digital Landscape Model (DLM) is used to structure the study area according to different land uses and land covers. We prepared a bottom roughness map with spatially varying Manning's roughness coefficients as the landscape characteristics of the floodplain are important for the water propagation.

For the final simulations we use five events of the artificial events stochastically generated by MacPherson et al. (2019) which are based on the LT Kiel and Eckernförde tide gauge records. Here, extreme events are identified within the tide-gauge records and characterized according to a number of specific parameters, such as peak water level, event duration, storm surge shape, etc. By modeling parameter dependencies using a Gaussian copula,

TABLE 1 | Summary of data.

Data	Data characteristics	Source
Digital elevation model (DEM)	5 m resolution	Landesamt für Vermessung und Geoinformation Schleswig-Holstein, 2018
Bathymetry	50 m resolution	Geoseaportal (Bundesamt für Seeschifffahrt und Hydrographie, 2005)
Water level time series (Eckernförde / LT Kiel tide gauges)	hourly frequency	Wasserstraßen- und Schifffahrtsverwaltung des Bundes
Digital landscape model (DLM)	1:50 000 scale	ATKIS (Landesamt für Vermessung und Geoinformation Schleswig-Holstein, 2018)
Infrastructure	1:1.000 scale	ALKIS (Landesamt für Vermessung und Geoinformation Schleswig-Holstein, 2018)

a large number of artificial events may be generated through Monte-Carlo Simulations, each as a time series of water levels referred to as hydrographs. From the tide gauge record of LT Kiel, no event corresponding to a return period of 200 years is present. However, using the stochastic model developed by MacPherson et al. (2019), several such events are generated. We selected five events for our study, with peak water levels corresponding to a 200 year return period and a range of intensities.

MATERIALS AND METHODS

Hydrodynamic Model

Hydrodynamic models are a common tool used in simulating detailed flood dynamics. In this study, we use Delft3D-FLOW, a module of the Delft3D computational program created to simulate processes related to flow, sediment transport, waves, water quality, etc. for coastal, river and estuarine areas (Deltares, 2014). The FLOW module is a complex, multi-dimensional hydrodynamic model which can be used for 3D-simulations or 2D-simulations (depth averaged) where flow and transport phenomena are solved using the unsteady shallow water equation. In this analysis, we use a 2D-model to calculate flow on a Cartesian rectilinear grid.

Model Setup, Calibration and Validation

A rectilinear model grid of Eckernförde Bay (approx. 119.63 km^2) was constructed with a resolution of 50 m (**Figure 1**). This model is forced with water levels at the open boundary using data from the tide gauge LT Kiel. For a more accurate representation of inundation in the city of Eckernförde, we constructed a second nested model grid of the western bay area (approx. 20 km^2) with a resolution of 10 m. This nested model is forced with parameters extracted from the coarser model. Running one high resolution model over the whole domain is not feasible due to computational restrictions. Modeled water levels are recorded in 3 min intervals at select locations, most importantly at the location of the tide gauge Eckernförde (see blue lines in **Figure 2**) which is used for model calibration. Simulations run for periods of 34–100 h depending on the simulated event. Computational time steps are defined based on the CFL number. This results in a time step (at which stability is still given) of 18 s for the overall model and 1.8 s for the detailed model. The focus of this study is the area covered by the nested model, where the city of Eckernförde is located. Therefore, the output of the coarse model is not further analyzed, and is used only for boundary forcing of the high-resolution nested model.

We calibrate the model using two observed storm surge events which occurred in November 1995 and January 2017. To determine the performance of the model, modeled water levels at TG Eckernförde were compared to observations using root mean square error (RMSE) and model skill (Willmott, 1984). The calibrated model performs well with a RMSE of 0.117 m and 0.061 m, and model skill of 0.988 and 0.998 for the 1995 and 2017 events, respectively. Here, a model skill of 1 would suggest perfect correlation and 0 no correlation. The model slightly underestimates the peak water level by 10 cm, most likely due to the lack of atmospheric forcing (**Figures 2A,B**). Atmospheric forcing is not considered as the final simulations will be based on artificial water levels, where no observed/simulated atmospheric data exists. Overall, the model simulates water levels with high accuracy and we therefore consider the setup of the model to be suitable for the study area.

Validation of flood extent and depth is challenging due to a lack of observations. There exists no record or exact documentation of these parameters, for example via pictures (on social media) or remote sensing. Nevertheless, a comparison of several newspaper articles on the January 2017 event allows for the calculation of flood extent. Here, the storm surge reached a maximum water level of 1.625 m above NHN (WSA Lübeck). This led to a filling of the harbor basin at the end of the bay and to minimal overtopping. Based on newspaper articles, there were two critical points at both sides of the harbor where the quay wall was overtopped. However, personnel responsible for the emergency action protected buildings with sandbags so that damages were avoided and buildings were not affected (Kühl, 2017; Rohde, 2017; Technisches Hilfswerk Ortsverband Eckernförde, 2017). We compare modeled flood extent with that estimated using the descriptions and photos in the newspaper articles as a method to validate the model. Here, we see basic agreement between the exposed buildings named in the articles (e.g., "Hotel/Restaurant Siegfried-Werft" and "Yachtsport-Geschäft Nielsen") and those buildings which intersect the modeled flood extent (**Figure 3**).

Land Use Classification and Manning's Roughness Coefficients

The propagation of water in the model is highly influenced by the characteristics of the Digital Elevation Model (DEM) and the roughness of the surface. Surface roughness, induced for example by the presence of vegetation, causes flow resistance and leads to reduced current velocities (Mignot et al., 2006).

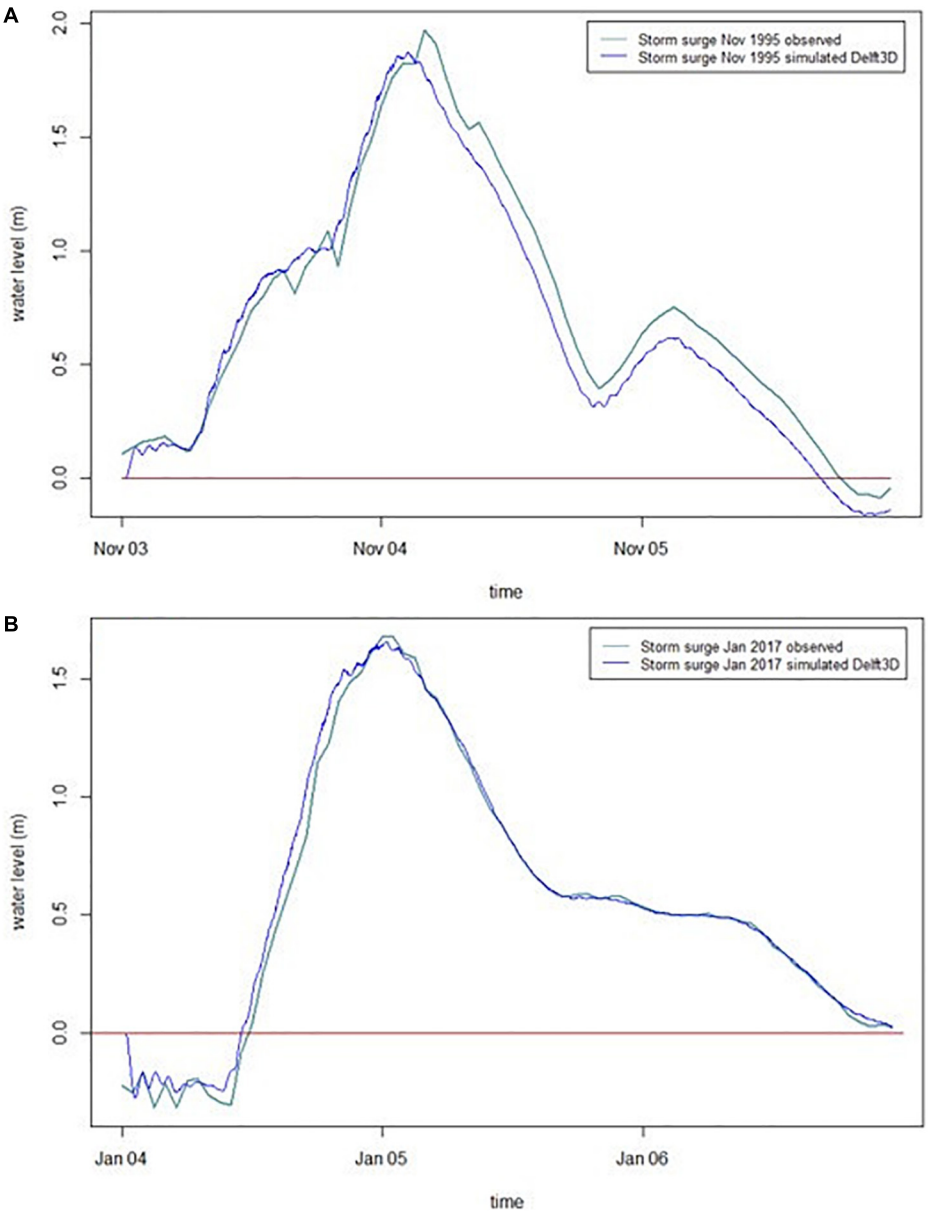

FIGURE 2 | Comparison of observed and simulated water levels November 1995 **(A)** and January 2017 **(B)** at the tide gauge Eckernförde.

A common approach in estimating the bottom friction within flood simulations is the attribution of specific coefficients to land use types and land cover. One of the most widely used coefficients for flow computation is the Manning's roughness coefficient (Garzon and Ferreira, 2016). Therefore, a map with spatially varying Manning's roughness coefficients according to land use classes is included in the simulation. Common Manning values are obtained from published literature (Fisher and Dawson, 2003; Phillips and Tadayon, 2006; Hossain et al., 2009; Oregon Department of Transportation, 2014; Garzon and Ferreira, 2016). We performed five model runs in order to investigate the sensitivity of the model to changes in the roughness parameter using the five parameterizations described in the following paragraph (**Table 2**).

The land use classification in this analysis is based on ATKIS data categories, which are grouped into classes (**Table 2**). The second column shows a mean value of the Manning coefficients found in the reviewed literature for every land use class. Since the range of the recommended values for some classes (forest, urban, wetland) is large, additional simulations with the lowest and highest value (**Table 2** column 3 and 4) for these classes are performed. Some studies also use a uniform value representative for the whole study area or only differentiate between land and water areas (Quinn et al., 2014; Garzon and Ferreira, 2016).

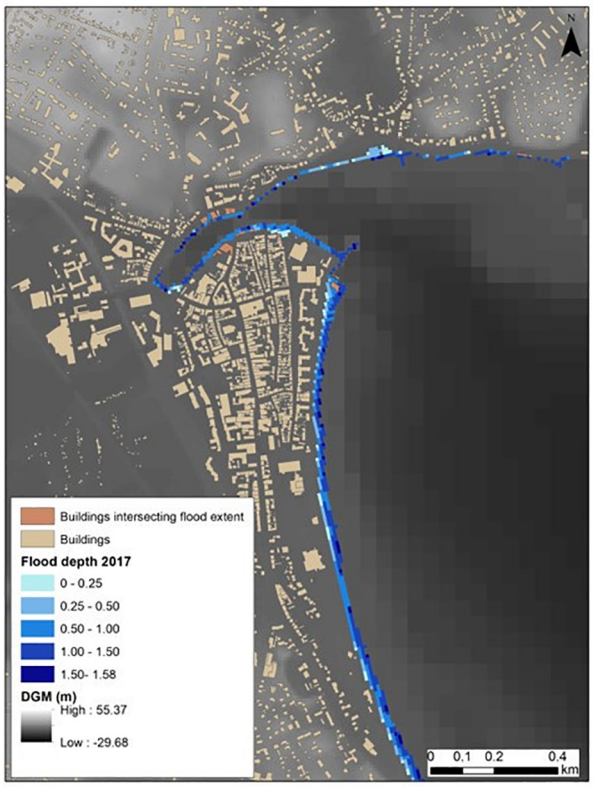

FIGURE 3 | Simulated flood extent for the January 2017 storm surge.

Therefore, two additional setups are tested. The first setup consist of a uniform roughness value (0.025) for the entire model domain, while the second uses a uniform value (0.035) for all land surface areas combined with a separate value (0.025) for water surfaces.

Model Simulations

To test the effect of temporal variability on flood extent, the model is forced using water levels from extreme sea-level hydrographs generated stochastically. The temporal variability of the storm surge is described by the storm surge intensity. Five hydrographs of the stochastically simulated events from MacPherson et al. (2019) at the tide gauge LT Kiel are used as boundary conditions in the hydrodynamic simulations (**Figure 4**). Each storm surge event reaches a peak water level which is equally probable (return period of 200 years: 1.98 m), but with varying durations and intensities (see **Table 3** and **Figure 4**). Waves are not considered in this study as we focus on the effect of storm-surge temporal variability on inundation.

We also consider a number of simulations where future sea level rise is accounted for by manually adjusting the heights of the artificial hydrographs. However, there is high uncertainty regarding the development and dimension of future sea-level rise (Vermeersen et al., 2018). Hinkel et al. (2014) employed a median global mean sea-level rise of 74 cm for RCP 8.5 (Representative Concentration Pathway) for the end of the 21st century. In their analysis, the highest projected global mean sea-level rise, comparing different models linked to different emission scenarios, is 123 cm. Grinsted et al. (2015) calculated even higher values for regional projections of 21st century sea-level rise in northern Europe under RCP 8.5, which is in particular linked to the different handling of uncertainties surrounding the future ice-mass contributions. Based on the estimates of Hinkel et al. (2014) related to the 95% quantile (upper bound) of global mean sea-level rise under RCP 8.5 we used an artificial value of 1 m, which lies at the upper end of the IPCC's AR5 projections (Church et al., 2013).

RESULTS

Simulation of Hydrographs

This section presents the simulation results of the five hydrographs with peak water levels corresponding to a 200-year return period. Moreover, the results of the simulations combined with 1 m sea-level rise are provided. The results and output of Delft3D are post-processed in ArcGIS. The grid in Delft3D is not oriented in a north-south direction but in the direction of inflow into the bay. Since bathymetry and topography are resampled to fit the depth point of the grid, there is a slight shift in the data visible in the output. The width of the bay is about one pixel longer, so the results are adjusted to the DEM by identifying additional pixels which are classified as water (below zero) in Delft3D but are above zero in the DEM. Inundation depth for these pixels is calculated via interpolation with the Inverse Distance Weighted (IDW) method. The pixels cover an area of approximately five hectares along the coastline.

TABLE 2 | Manning's roughness coefficients for land use classes.

Class	Varying	High	Low	Uniform	Land/Water
Agriculture	0.035	0.035	0.035	0.025	0.035
Forest	0.125	0.250	0.080	0.025	0.035
Urban	0.080	0.400	0.050	0.025	0.035
Wetland	0.075	0.100	0.035	0.025	0.035
Water	0.025	0.025	0.025	0.025	0.025
Green urban areas	0.030	0.030	0.030	0.025	0.035
Fallow	0.025	0.025	0.025	0.025	0.035
Traffic	0.015	0.015	0.015	0.025	0.035

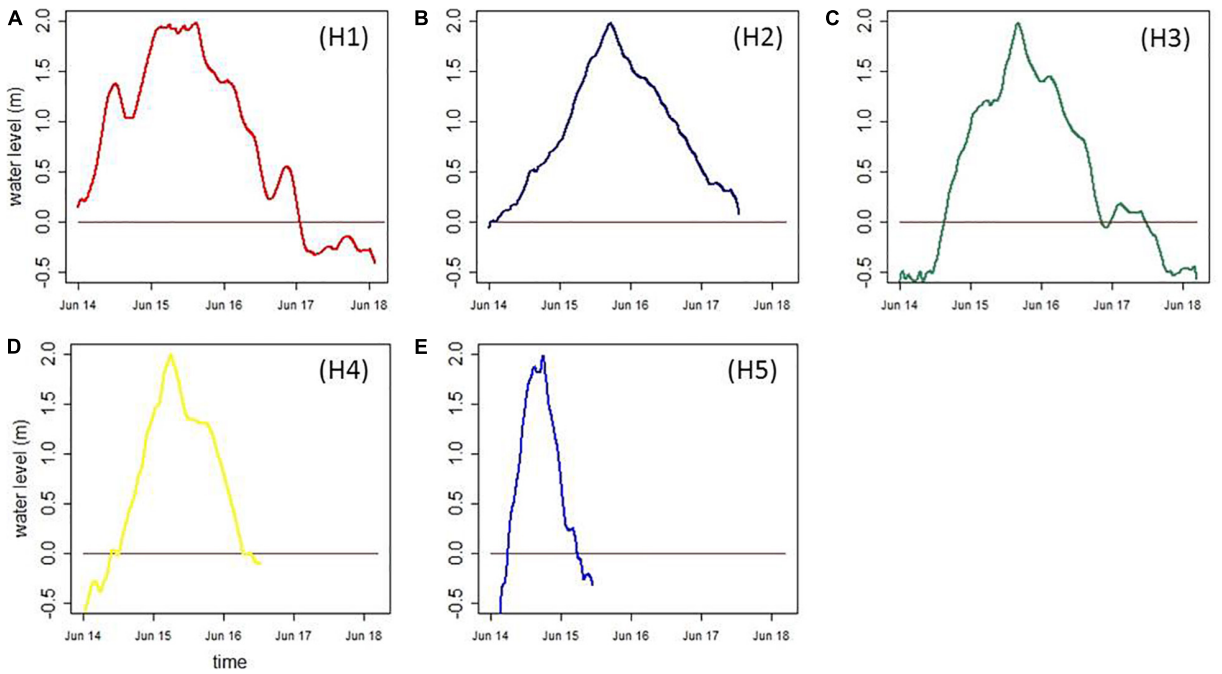

FIGURE 4 | Five selected hydrographs [H1 **(A)**, H2 **(B)**, H3 **(C)**, H4 **(D)**, and H5 **(E)**] of the simulated storm surge events by MacPherson et al. (2019) for the tide gauge LT Kiel.

TABLE 3 | Results for all five hydrographs with water levels corresponding to a 200-year return period and in combination with 1 m sea-level rise.

Hydrograph	Duration o. NHN [h]	Intensity [cm*min/1000]	Flood extent [ha]	Deviation [%]	Buildings	Mean flood depth [m]	Example depth [m]
H1	73	505.112	21.38	–	60	1.006	0.214
H2	72	457.670	20.95	2.01	54	1.043	0.223
H3	53	359.468	21.25	0.61	56	1.034	0.243
H4	41	275.278	21.35	0.14	59	1.009	0.206
H5	23	152.689	20.10	5.99	49	1.003	0.147
+1 m sea-level rise							
H1	97	1055.829	156.23	–	1192	0.960	1.149
H2	84	967.573	138.76	11.18	1156	0.906	1.139
H3	100	882.863	134.54	13.88	1161	0.939	1.160
H4	60	619.728	135.56	13.23	1168	0.925	1.154
H5	31	333.648	122.10	21.85	1048	0.923	1.109

Flood duration indicates the time in hours during which the water level is higher than "normal height zero" (NHN). Differences in flood extent are presented as a percentage change from the first hydrograph.

Table 3 (upper part) shows the results for the flood extent of the five simulated hydrographs. The intensity of modeled storm surges decreases from H1 to H5 by approximately 70%. However, despite this large change in intensity, variations in flood extent between hydrographs is small (0.14–5.99%). The number of exposed properties decreases from 60 to 54 when comparing H1 and H2. There is a significantly larger but still small change when comparing H1 and H5, with a reduction in flood extent of approximately 6% and 49 properties exposed. When comparing flood depth at a select point (see **Figure 5**), which experiences flooding in all simulations, the largest variances in flood depth are noticeable in H5, which is 6–9 cm lower compared to the other hydrographs (**Table 3** upper part). Overall flood depths during the five simulations are very similar with similar mean values. The maximum difference between mean values is small (4 cm), which is true for all inundation depths over the whole range of simulated values (**Figure 6**).

The effect of storm surge temporal variability on flood impact is significantly larger when sea-level rise is considered (see **Table 3** lower part). Firstly, there exists a large difference in flood extent between H1 and the other hydrographs, decreasing by 11% to H2 and 22% to H5. Differences in flood extent between H2, H3, and H4 are small, with a maximum difference of approximately four hectares. However, flood extent during H5 is approximately 10% less (13.5 hectares). These values are significantly higher than those during simulations under present sea levels, which

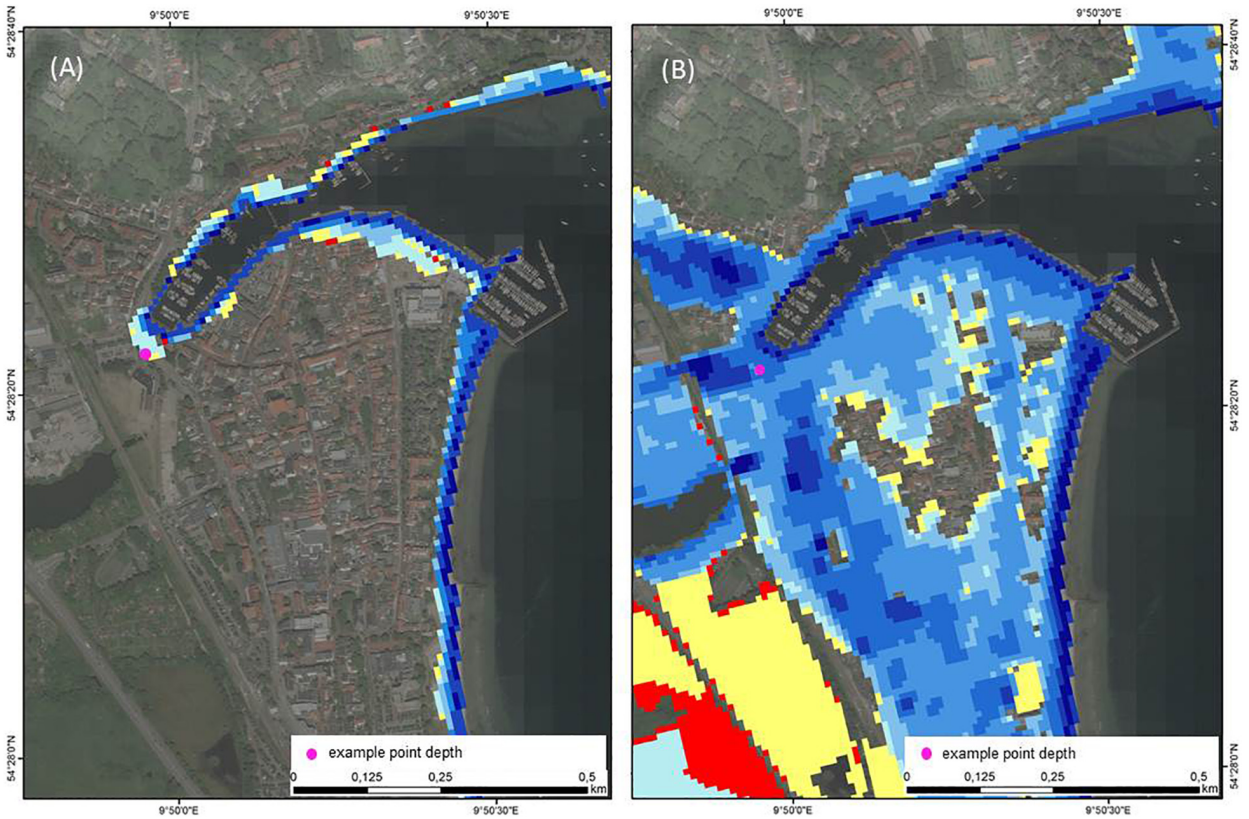

FIGURE 5 | Flood extent simulated with Delft3D for hydrographs with water levels corresponding to a 200-year return period **(A)** and in combination with 1 m sea-level rise **(B)** in the city center of Eckernförde.

show differences in flood extent of no more than 1.3 hectares. The number of affected properties when considering sea level rise ranges from 1,192 in H1 to 1,048 in H5. Overall, changes in inundation depth (mean and at the example point) are slightly smaller during simulations with sea-level rise. In contrast, the variances in extent are significantly larger.

Figure 7A illustrates the results for visual comparison. As the differences are hardly visible at the presented scale only three of five hydrographs are selected. Differences in extent are especially visible at the western end of the bay in the harbor area, where the majority of the buildings inside the flooded area are located. As a consequence, the change in the number of buildings exposed (ca. 18% decrease between H1 and H5) is larger than the change in flood extent. This is shown in more detail in **Figure 5**, which shows a close-up view of the city center of Eckernförde. **Figure 7B** visualizes the results for the same hydrographs but with sea level rise included in the simulations. Flood waters during H4 and H1 extend west of the city center (**Figure 7B**: yellow colored), where land use classification show mostly green urban areas (allotment gardens) and wetlands. Flooding which occurs only during H1 (**Figure 7B**: red colored) is mostly located around the Windebyer Noor, an inland lake west of Eckernförde. Flood extent also increases in areas inside the city center when comparing to H5. Overall, for the simulations including sea-level rise, deviations in the number of buildings flooded are smaller than the deviations in extent, as variations in extent mostly cover areas which are not classified as urban and thus have a lower density of buildings.

A large increase in flood extent due to sea-level rise can be seen in **Figures 5**, **7**. Whereas flood extent for a storm surge with a 200-year return period is 21.38 ha (H1), and limited to areas along the coastline, inundation extends further into the city center and surrounding areas when 1 m of sea-level rise is added. Here, water levels reach a peak of 2.985 m. In comparison to simulations with no sea level rise, flood extent increases by more than 500% (H5) to 630% (H1), resulting in a maximum area of inundation of 156.23 ha. The number of affected properties increases by a far greater rate from 60 to 1192 (H1). The southern part of the model domain is less affected by these changes. Most of the flooding appears in central parts of the model domain, around and south of the narrowing end of the bay (city center), which include mostly urban areas with a high density of buildings. Furthermore, the inundation reaches into two depressions at the northern side of the bay. Large areas in these parts experience inundation depths over 1 m.

Sensitivity to Manning's Roughness Coefficients

Estimates of flood characteristics are not highly sensitive to changes in the model's roughness coefficients. Changes account

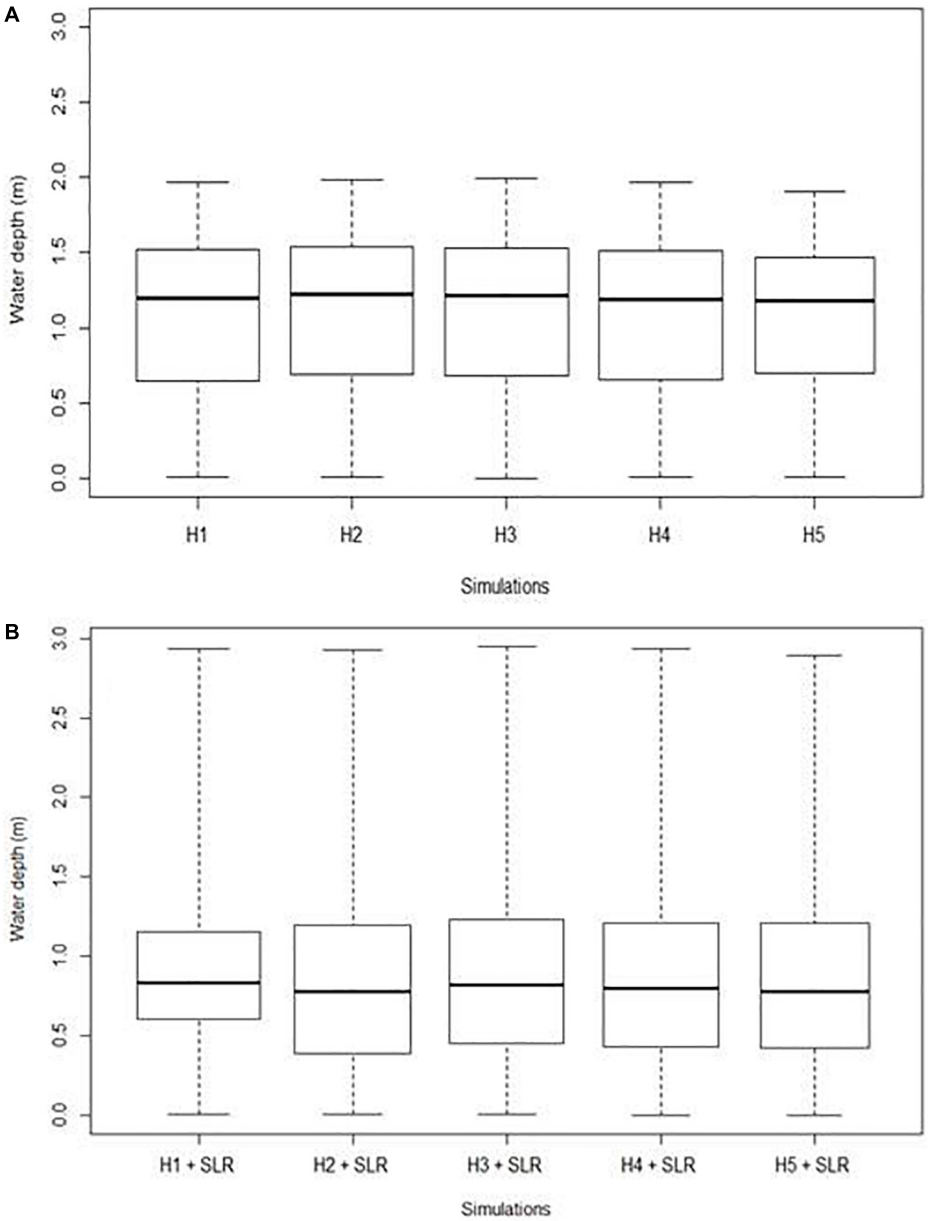

FIGURE 6 | Flood depth for all hydrographs with water levels corresponding to a 200-year return period **(A)** and combined with 1 m sea-level rise **(B)** – The box shows values between the upper (75%) and lower (25%) quartiles. The black line inside the box indicates the median. The whiskers extent to the maximum and minimum.

for approximately 3% difference in flood extent (calculated by number of pixels) (see **Table 4**) and around 2.75% in mean inundation depth. The total range of inundation depth differs by less than 1 cm. The largest differences occur when either the highest or lowest Manning roughness coefficients are used (**Table 4**). Modification of roughness coefficients based on the three land use classes (forest, urban, and wetland) results in a larger flood extent and smaller mean inundation depth for low roughness values and smaller extent and larger mean depth for high values. If mean values are selected, the use of varying roughness values dependent on land use produces similar results in terms of flood extent and depth to the two-part classification, where coefficients were determined for only land surfaces and water surfaces (see **Table 4**). Hence, the medium varying roughness coefficients are used for further model setups.

DISCUSSION

Model Performance and Limitations

We have set up a model of Eckernförde bay capable of simulating extreme water levels, including inundation due to extreme events.

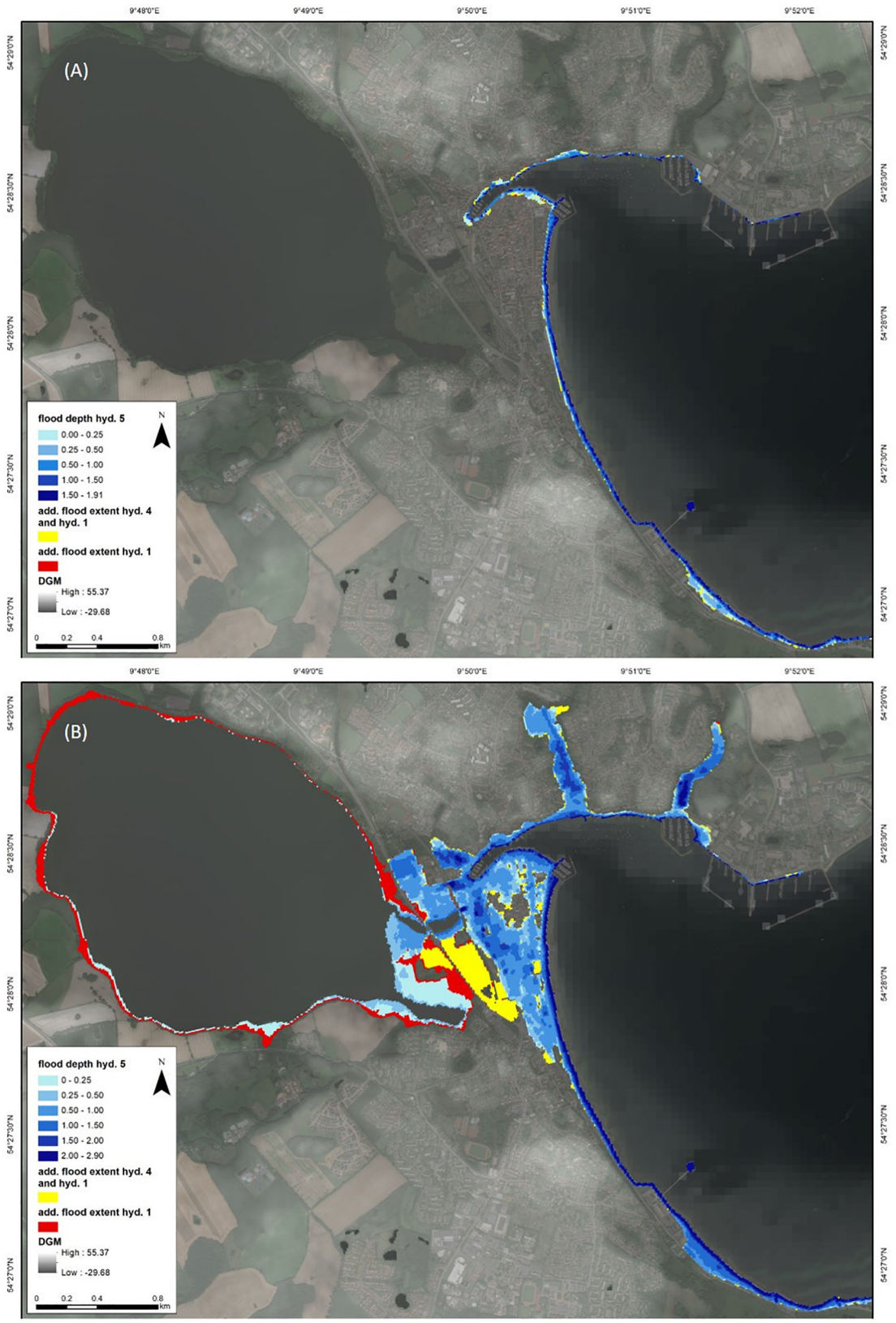

FIGURE 7 | Flood extent simulated with Delft3D for hydrographs with water levels corresponding to a 200-year return period **(A)** and in combination with 1 m sea-level rise **(B)**. The areas visualized in blue represent the flood extent of H5. The yellow colored pixels indicate the additional extent flooded in the simulation of H4 and H1. The red pixels display the extent only flooded in the case of H1.

TABLE 4 | Flood extent in case of changes in roughness coefficients.

Roughness	Flood extent [ha]
Varying	21.25
High	20.98
Low	21.62
Land/Water	21.25
Uniform	21.13

The model was validated at the Eckernförde tide gauge for two storm surge events which occurred in November of 1995 and January of 2017. RMSE and model skill for the two events indicate that the model performs well in the study area. The use of a nested model setup is a valuable tool to utilize datasets of two tide gauges with a certain distance for calibration and validation, while still obtaining detailed results for the areas of interest. The validation of the model is based on the comparison of observed and modeled water levels. Flood extent was validated using newspaper articles, which provide a qualitative evaluation of the model results. A more extensive validation of modeled flood extent and depth is not possible due to a lack of inundation data, which is a common problem when modeling inundation (Vousdoukas et al., 2018). One option to validate inundation depth is to use social media footage (e.g., photos and reports) with place and time signatures taken during a storm surge event. In such a case, inundation depth could be determined using reference objects, and used to validate points in the model domain. There are few photos of the storm surge event of 2017 available, as water overtopping the quay wall was controlled. For previous events, no visual documentation was found. Therefore, this validation procedure was not possible.

The model is not sensitive to variations in surface roughness coefficients in the study area. Mean varying Manning values found in literature reviews as well as values bisecting the area in water and land surfaces present good options. The latter might be recommendable for study areas where land use information is not available or only available at coarse resolutions. Since the model is applied on a local scale, distances are relatively small. If distances increase the sensitivity toward variations in surface roughness coefficients are expected to be larger.

The available water level records of both tide gauges are limited to a period of 27 years, which has an influence on the estimation of return water levels. Arns et al. (2013) show that 30 years of data are sufficient to estimate water levels with long return periods (>100 years). In our case, we estimate water levels with a return period of 200 years, which corresponds with the design heights of coastal protection in the region (LKN, 2013). Although this is the best estimate based on the available data, the above mentioned limitations should be carefully considered when using this value. When considering the documentation of single extreme events by WSA Lübeck (2017), which extends beyond the period of the tide gauges, three flood events over the last 150 years are equal to or greater than our estimated 200-year return water level. Therefore, we can assume that we are underestimating a 200-year water level due to these historical events. The inclusion of such historical events into the extreme value analysis is therefore important, especially when the results influence policy on flood protection. Furthermore, the magnitude of the calculated values is highly dependent on the method used. For example, in 2012 the "Ministerium für Energiewende, Landwirtschaft, Umwelt und ländliche Räume des Landes Schleswig-Holstein" (MELUR) published a value of 2.11 m for a flood with a 200-year return period in Eckernförde, whereas a value of 3.00 m was released by PROKOM GmbH (2017). This underlines the uncertainties of extreme water level estimates, which have to be outlined to avoid misinterpretation of flood characteristics based on the modeling of these extreme values.

Flood Characteristics of Temporally Variable Hydrographs

Our simulations show that variations in flood characteristics are affected by the temporal evolution of storm surge water levels. While changes in inundation depth are comparatively small for all modeled hydrographs, changes to flood extent between the different modeled hydrographs are substantial. Further, changes in flood extent are considerably larger when sea-level rise is considered. This leads to the conclusion that the temporal variability of storm surges is an important parameter to consider when conducting flood risk analyses, especially when future sea-levels are considered.

There are significant differences between H5 (shortest duration and lowest intensity: **Figure 4E**) and the other hydrographs with regard to both flood extent and maximum inundation depth. The change in flood extent between H1 and H5 is approximately twice as large as the difference between H1 and the other three hydrographs. Inundation depth is at least three to 9 cm lower during H5 than during all other hydrographs. This decrease is also apparent in simulations where sea-level rise is considered, which suggests a threshold of duration in which flood impact does not change substantially. If the duration of the storm surge is shorter than 40 h (such as for H5) flood extent and inundation depth is noticeably smaller. This is likely caused by declining water levels before maximum inundation depth occurs. Further research is needed to determine whether such assumptions can be validated by additional simulations and whether a possible threshold in duration can be identified.

In general, there are large differences in the flood characteristics of all five hydrographs due to the length of time at which maximum water levels are sustained. This is particularly noticeable during H1 in combination with sea-level rise. **Figure 4** outlines the temporal evolution of water levels during each simulation. In H1, the water level curve is characterized by a plateau (**Figure 4A**), where water levels remain at the peak level for several hours. In contrast, the other hydrographs show only one clear peak (**Figures 4B–E**). This leads to a considerable increase in flood extent, especially when sea level rise is considered. Here, water levels do not decline immediately after the peak is reached, allowing for water to propagate further inland. In the case of the municipality of Eckernförde, mostly the lakeside and marshlands experience inundation.

Exposure to Floods and Sea-Level Rise

There is a high range of uncertainty regarding the occurrence and the development of extreme events such as storm surges and sea-level rise. In our study we investigate the consequences of two plausible scenarios in order to display the exposure of the municipality of Eckernförde to future storm surges and calculated the number of buildings intersecting the flooded area to provide insights regarding exposed infrastructure and assets. To accurately quantify potential damages, an impact assessment could be conducted by applying depth-damage functions for assets exposed to certain inundation depths (Büchele et al., 2006). Additionally, other types of infrastructure such as roads have to be regarded.

Flood exposure in Eckernförde is relatively small for the storm surges with a 200-year return period. The exposed areas (20.10–21.38 ha) are located mainly along the coastline, affecting a maximum number of 60 buildings, leading to economic damages. Since the embankment of the harbor area and also parts of the northern shore are 1.80 m (above NHN) or lower, storm surges below 2 m are capable of flooding parts of the city (PROKOM GmbH, 2017). Although events with a 200-year return period might not seem very likely to occur in the near term, the probability that events of such magnitude will be exceeded increases with regard to global sea-level rise over the century (Wahl et al., 2017).

Hydrographs simulated with 1 m sea-level rise represent examples of high-end extreme events. In their sea-level rise projections for northern Europe under RCP 8.5., Grinsted et al. (2015) highlight the development of the Antarctic ice sheet as the main source of uncertainty, which accounts for 81% of the variance in relative sea-levels. Including the risk and potential rate of Antarctic ice sheet collapse, they consider an increase in water levels of 1.70 m to be a possible high-end scenario for the western Baltic Sea in the 21st century. Such events are rare by definition, however, they are not unrealistic as higher water levels have already been observed at this location in the past. In 1872, a storm surge of 3.15 m caused immense damages and resulted in a large loss of life. Therefore, it is important that such scenarios are considered in flood risk assessment (Hinkel et al., 2015).

Our results show large parts of the city are exposed to water levels with a return period of 200 years. Exposure of the urban center of Eckernförde is especially high where the historic city center is located and the concentration of population and assets is high. Up to 1192 properties could be affected under a future sea-level rise of 1 m. Inundation depth in the city center mostly exceeds 0.5 m with large concentrations of more than 1 m depth in the western part and around the harbor. Apart from severe damages to buildings and assets, flooding can lead to traffic and transport disruption as streets become impassable. The southern and northern parts of the study area experience only little to moderate increases in flood extent. Since flooding related damages are high, people expectedly will adapt to coastal flooding and sea-level rise. In this investigation, the exposure in the municipality is calculated with the current protection level. Enhanced adaptation measures and protection schemes, in turn, should substantially reduce damages of extreme events over the next decades (Hinkel et al., 2014). This should be taken into consideration.

CONCLUSION

This study quantifies uncertainties in flood extent and inundation depth due to storm surge temporal variability using an inundation model in the study area Eckernförde Bay. We compared five artificial storm surge events with equal peak water levels corresponding to a return period of 200 years and varying durations and intensities, under present day and future high-end sea level rise scenarios.

Based on this analysis we conclude that under current sea levels, the effect of storm surge temporal variability is relatively small, however, this is not the case when we consider sea-level rise. Whereas differences in storm surge intensity are large (approximately 70% between H1 and H5), changes in flood extent and depth are small under present day sea levels (<10%). Such changes are significantly larger under a sea-level rise scenario of 1 m (up to 21.85%). Therefore, in consideration of projected sea-level rise until 2100, temporal variations in storm surges should be particularly reflected in future coastal flood risk assessment and management. The analysis of flood exposure shows that there is a considerable increase in flood extent when a 1 m sea-level rise scenario is combined with the scenario of a storm surge with a return period of 200 years. The specific propagation of water depends on the temporal evolution of the storm surge. This is noticeable within the urban center and further west, in the green urban areas and marshlands between the urban center and Windebyer Noor. This research can be used for further analysis, for instance, it can underpin the calculation of damages due to flooding as well as estimations on how the range of possible damages are affected by the temporal variability of extreme water level events. As the urban center of Eckernförde is not well protected against storm surges, there is a need for action to reduce potential impacts by adaptation or protection measures. These measures should not only focus on the prevention of flooding, but also on how mitigation, preparedness and response may reduce damages.

DATA AVAILABILITY STATEMENT

The datasets generated for this study are available on request to the corresponding author.

AUTHOR CONTRIBUTIONS

JH, AV, and SD designed the research. JH set up the model and collected the data, with contributions from LM. JH, AV, and LM analyzed the results. JH wrote the manuscript with contributions from AV, LM, and SD. All authors read and approved the final manuscript.

REFERENCES

Arns, A., Dangendorf, S., Jensen, J., Talke, S., Bender, J., and Pattiaratchi, C. (2017). Sea-level rise induced amplification of coastal protection design heights. *Nat. Sci. Rep.* 7:40171. doi: 10.1038/srep40171

Arns, A., Wahl, T., Haigh, D., Jensen, J., and Pattiaratchi, C. (2013). Estimating extreme water level probabilities: a comparison of the direct methods and recommendations for best practise. *Coast. Eng.* 81, 51–66. doi: 10.1016/j.coastaleng.2013.07.003

Büchele, B., Kreibich, H., Kron, A., Thieken, A., Ihringer, J., Oberle, P., et al. (2006). Flood-risk mapping: contribution towards an enhanced assesssment of extreme events and associated risks. *Nat. Hazards Earth Syst. Sci.* 6, 485–503. doi: 10.5194/nhess-6-485-2006

Bundesamt für Seeschifffahrt und Hydrographie (2005). *Sturmflutem in der südlichen Ostsee. Berichte Des Bundesamtes Für Seeschifffahrt Und Hydrographie, 39*. Rostock: Bundesamt für Seeschifffahrt und Hydrographie.

Church, J. A., Clark, P. U., Cazenave, A., Gregory, J. M., Jevrejeva, S., Levermann, A., et al. (eds) (2013). "Sea level change," in *Climate Change 2013: The Physical Science Basis. Contribution Of Working Group I to the Fifth Assessment Report of the Intergovernmental Panel on Climate Change*, eds T. F. D. Stocker, G.-K. Qin, M. Plattner, S. K. Tignor, J. Allen, A. Boschung, et al. (Cambridge: Cambridge University Press), 1137–1216.

Dangendorf, S., Arns, A., Pinto, J. G., Ludwig, P., and Jensen, J. (2016). The exceptional influence of storm 'Xaver' on design water levels in the German Bight. *Environ. Res. Lett.* 11:54001.

Deltares (2014). *Delft3D-FLOW User Manual: Simulation of Multi-Dimensional Hydrodynamic Flows and Transport Phenomena, Including Sediments*. Delft: Deltares.

Deltares (2018). *Release Notes Delft3D Version 4.00.02*. Delft: Deltares.

Fisher, K., and Dawson, H. (2003). *Reducing Uncertainty in River Flood Conveyance: Roughness Review*. Lincoln: DEFRA.

Gallien, T. W., Sanders, B. F., and Flick, R. E. (2014). Urban coastal flood prediction: integrating wave overtopping, flood defenses and drainage. *Coast. Eng.* 91, 18–28. doi: 10.1016/j.coastaleng.2014.04.007

Garzon, J., and Ferreira, C. (2016). Storm surge modeling in large estuaries: sensitivity analyses to parameters and physical processes in the Chesapeake Bay. *J. Mar. Sci. Eng.* 4, 1–32.

Gräwe, U., and Burchard, H. (2012). Storm surges in the Western Baltic Sea: the present and a possible future. *Clim. Dyn.* 39, 165–183. doi: 10.1007/s00382-011-1185-z

Grinsted, A., Jevrejeva, S., Riva, R. E., and Dahl-Jensen, D. (2015). Sea level rise projections for northern Europe under RCP8.5. *Clim. Res.* 64, 15–23. doi: 10.3354/cr01309

Hinkel, J., Jaeger, C., Nicholls, R. J., Lowe, J., Renn, O., and Peijun, S. (2015). Sea-level rise scenarios and coastal risk management. *Nat. Clim. Chang.* 5, 188–190. doi: 10.1038/nclimate2505

Hinkel, J., Lincke, D., Vafeidis, A. T., Perrette, M., Nicholls, R. J., Tol, R. S., et al. (2014). Coastal flood damage and adaptation costs under 21st century sea-level rise. *Proc. Natl. Acad. Sci. U.S.A.* 111, 3292–3297. doi: 10.1073/pnas.1222469111

Hofstede, J. (2008). Coastal flood defence and coastal protection along the baltic sea coast of Schleswig-Holstein. *Die Küste* 74, 169–178.

Hossain, A., Jia, Y., and Chao, X. (2009). *Estimation of Manning's Roughness Coefficient Distribution for Hydrodynamic Model Using Remotely Sensed Land Cover Features*. Fairfax, VA: IEEE.

IPCC (2019). "Summary for policymakers," in *IPCC Special Report on the Ocean and Cryosphere in a Changing Climate*, eds H.-O. Pörtner, D. Roberts, V. Masson-Delmotte, P. Zhai, M. Tignor, E. Poloczanska, et al. (Geneva: IPCC).

Jensen, J., and Müller-Navarra, S. (2008). Storm surges on the German coast. *Die Küste* 74, 92–124.

Kühl, G. (2017). *Hochwasser Hält Eckernförde in Atem*. Flensburg: Eckernförder Zeitung.

Landesamt für Vermessung und Geoinformation Schleswig-Holstein, (2018). *Produktkatalog*. Kiel: Landesamt für Vermessung und Geoinformation Schleswig-Holstein.

LKN (2013). *Generalplan Küstenshutz des Landes Schleswig-Holstein, Fortschreibung 2012*. Kabelhorst: Landesbetrieb für Küstenschutz, Nationalpark und Meeresschutz Schleswig Holstein.

MacPherson, L., Arns, A., Dangendorf, S., Vafeidis, A., and Jensen, J. (2019). A stochastic storm surge model for the German Baltic Sea coast. *J. Geophys. Res. Oceans* 124, 2054–2071.

Martinez, G., and Bray, D. (2011). *Befagung politischer Entcheidungsträger zur Wahrnehmung des Klimawandels und zur Anpassung an den Klimawandel an der deutschen Ostseeküste*. Berlin: Ecologic Institut.

Mignot, E., Paquier, A., and Haider, S. (2006). Modeling floods in a dense urban area using 2D shallow water equations. *J. Hydrol.* 327, 186–199. doi: 10.1016/j.jhydrol.2005.11.026

Ministerium für Energiewende, Landwirtschaft, Umwelt und ländliche Räume des Landes Schleswig-Holstein (2012). *Generalplan Küstenschutz des Landes Schleswig-Holstein: Fortschreibung 2012*. Kiel: Ministerium für Energiewende, Landwirtschaft, Umwelt und ländliche Räume des Landes Schleswig-Holstein.

Néelz, S., and Pender, G. (2013). *Benchmarking the Latest Generation of 2D Hydraulic Modelling Packages*. Bristol: Environment Agency.

Neumann, B., Vafeidis, A. T., Zimmermann, J., and Nicholls, R. J. (2015). Future coastal population growth and exposure to sea-level rise and coastal flooding - a global assessment. *PLoS One* 10:e0118571. doi: 10.1371/journal.pone.0118571

Oregon Department of Transportation (2014). *ODOT Hydraulics Manual Appendix*. Salem, OR: Oregon Department of Transportation.

Phillips, J., and Tadayon, S. (2006). *Selection of Manning's Roughness Coefficient for Natural and Constructed Vegetated and Non-Vegetated Channels, and Vegetation Maintenance Plan Guidelines for Vegetated Channels in Central Arizona*. Virginia: U.S. Geological Survey.

PROKOM GmbH (2017). *Masterplan Eckernförder Bucht*. Lübeck: PROKOM GmbH.

Quinn, N., Lewis, M., Wadey, M., and Haigh, D. (2014). Assessing the temporal variability in extreme storm-tide time series for coastal flood risk assessment. *J. Geophys. Res. Oceans* 119, 4983–4998. doi: 10.1002/2014jc010197

Rohde, C. (2017). *Sturmflut: Geringe Schäden in Eckernförde*. Available at: http://www.kn-online.de/Lokales/Eckernfoerde/Sturmflut-in-Eckernfoerde-Keine-groesseren-Schaeden-durch-Hochwasser (accessed September 22, 2019).

Santamaria-Aguilar, S., Arns, A., and Vafeidis, A. T. (2017). Sea-level rise impacts on the temporal and spatial variabil-ity of extreme water levels: a case study for St. Peter-Ording, Germany. *J. Geophys. Res. Oceans* 122, 2742–2759. doi: 10.1002/2016jc012579

Stewart, M. G., and Melchers, R. E. (1997). *Probabilistic Risk Assessment of Engineering Systems*. Netherlands: Springer.

Technisches Hilfswerk Ortsverband Eckernförde (2017). *Sturmtief Axel - Unkalkulierbare Wassermassen schwappen in Eckernförder Altstadt!*. Available at: https://ov-eckernfoerde.thw.de/aktuelles/aktuelle-meldungen/artikel/sturmtief-axel-unkalkulierbare-wassermassen-schwappen-in-eckernfoerder-altstadt/ (accessed September 22, 2019).

Teng, J., Jakeman, A. J., Vaze, J., Croke, B., Dutta, D., and Kim, S. (2017). Flood inundation modelling: a review of methods, recent advances and uncertainty analysis. *Environ. Model. Softw.* 90, 201–216. doi: 10.1016/j.envsoft.2017.01.006

Vermeersen, B., Slangen, A., Gerkema, T., Baart, F., Cohen, K., Dangendorf, S., et al. (2018). Sea-level change in the Dutch Wadden Sea, Netherlands. *J. Geosci.* 97, 79–127. doi: 10.1007/s11027-015-9640-5

Vousdoukas, M. I., Mentaschi, L., Voukouvalas, E., Verlaan, M., Jevrejeva, S., Jackson, L. P., et al. (2018). Global probabilistic projections of extreme sea levels show intensification of coastal flood hazard. *Nat. Commun.* 9, 1–12. doi: 10.1038/s41467-018-04692-w

Vousdoukas, M. I., Voukouvalas, E., Mentaschi, L., Dottori, F., Giardino, A., Bouziotas, D., et al. (2016). Developments in large-scale coastal flood hazard mapping. *Nat. Hazards Earth Syst. Sci.* 16, 1841–1853. doi: 10.5194/nhess-16-1841-2016

Wadey, M. P., Cope, S. N., Nicholls, R. J., McHugh, K., Grewcock, G., and Mason, T. (2015). Coastal flood analysis and visualisation for a small town. *Ocean Coast. Manag.* 116, 237–247. doi: 10.1016/j.ocecoaman.2015.07.028

Wahl, T., Haigh, I. D., Nicholls, R. J., Arns, A., Dangendorf, S., Hinkel, J., et al. (2017). Understanding extreme sea levels for broad-scale coastal

impact and adaptation analysis. *Nat. Commun.* 8:16075. doi: 10.1038/ncomms16075

Wahl, T., Mudersbach, C., and Jensen, J. (2011). Assessing the hydrodynamic boundary conditions for risk analyses in coastal areas: a stochastic storm surge model. *Nat. Hazards Earth Syst. Sci.* 11, 2925–2939. doi: 10.5194/nhess-11-2925-2011

Willmott, C. J. (1984). "On the evaluation of model performance in physical geography," in *Spatial Statistics and Models. Theory and Decision Library*, Vol. 40, eds G. L. Gaile and C. J. Willmott (Berlin: Springer), 443–460.

Wong, P. P., Losada, I. J., Gattuso, J.-P., Hinkel, J., Khattabi, A., McInnes, K. L., et al. (2014). *Coastal Systems and Low-Lying Areas. Climate Change 2014: Impacts, Adaptation, and Vulnerability. Part a: Global and Sectoral Aspects. Contribution of Working Group II to the Fifth Assessment Report of the Intergovernmental Panel on Climate Change*. Cambridge: Cambridge University Press.

WSA Lübeck (2017). *Historische Wasserstände - Pegel Eckernförde*. Available at: https://www.wsv.de/wsa-hl/wasserstrassen/gewaesserkunde/historisch/pdf/Eckernfoerde.pdf (accessed September 22, 2019).

Conflict of Interest: The authors declare that the research was conducted in the absence of any commercial or financial relationships that could be construed as a potential conflict of interest.

frontiers in Marine Science

ORIGINAL RESEARCH
published: 18 March 2020
doi: 10.3389/fmars.2020.00160

Assessing Perception of Climate Change by Representatives of Public Authorities and Designing Coastal Climate Services: Lessons Learnt From French Polynesia

Heitea Terorotua[1,2], Virginie K. E. Duvat[2], Aurélie Maspataud[3] and Jehane Ouriqua[1]*

[1] Créocéan, La Rochelle, France, [2] UMR LIENSs 7266, La Rochelle University-CNRS, La Rochelle, France, [3] BRGM, French Geological Survey, Coastal Risks and Climate Change Unit, Orléans, France

Institutional actors have a crucial role in adaptation to climate change, especially for highly vulnerable territories such as small tropical islands. Here, we emphasize their major role in the co-design of tailored coastal climate services (CCS) based on a case study of French Polynesia. In this perspective, we assessed climate change perceptions by public authorities and identified their needs with regard to climate-related science. This assessment included an analysis of the decision-making context, semi-structured interviews with practitioners representing 23 administrative divisions directly or indirectly involved in climate change issues, and a workshop dedicated to discussing needs in terms of CCS. Generally, respondents did not identify climate change as a major current issue in French Polynesia; they showed more concern for economic growth, pollution, land tenure, and land use planning. However, interviewees were concerned about future impacts of sea-level rise (SLR) and ocean warming and acidification, mentioning in particular their detrimental impacts on marine ecosystems, shoreline position, economy (especially agriculture and the blue economy), and freshwater resources. The interviewed practitioners showed particular interest in SLR projections for future decades up to a century, and for knowledge on expected impacts to critical infrastructure, coastal systems, and natural resources. Practitioners' needs made it possible to co-define four CCS to be developed: (1) the design of sea-level-rise-compatible critical infrastructures (airports and ports); (2) adapting to the risk of destabilization of beaches and reef islands; (3) professional training on climate change impacts and adaptation, including an analysis of potentially emerging new jobs in the SLR context; and (4) the development of participatory approaches for observing climate change impacts. While the co-development of these CCS will require a multi-year engagement of stakeholders concerned with climate change adaptation, our results already shed light on specific needs for salient CCS in highly vulnerable tropical island territories.

Keywords: adaptation to climate change, climate change perception, climate governance, coastal climate services, French Polynesia

OPEN ACCESS

Edited by:
Rafael Almar,
Institut de Recherche Pour le Développement (IRD), France

Reviewed by:
Alejandro Orfila,
Spanish National Research Council, Spain
Matthew John Eliot,
Seashore Engineering, Australia

****Correspondence:***
Heitea Terorotua
terorotua@creocean.fr

Specialty section:
This article was submitted to Coastal Ocean Processes, a section of the journal Frontiers in Marine Science

Received: *18 November 2019*
Accepted: *02 March 2020*
Published: *18 March 2020*

Citation:
Terorotua H, Duvat VKE, Maspataud A and Ouriqua J (2020) Assessing Perception of Climate Change by Representatives of Public Authorities and Designing Coastal Climate Services: Lessons Learnt From French Polynesia. Front. Mar. Sci. 7:160. doi: 10.3389/fmars.2020.00160

INTRODUCTION

Small tropical islands are recognized as being at the forefront of climate change (CC) impacts, although they are not the principal emitters of greenhouse gases (Sinivasan, 2010). Because of their biophysical characteristics (limited terrestrial surface area, high exposure to storm-related events, important role of the reef ecosystem as a sedimentary source and as a wave buffer; Duvat et al., 2016), they are highly exposed to SLR and to the intensification of storm waves that increase the risk of coastal erosion, marine flooding, and salinization of soils and aquifers, in addition to ocean heating and acidification which carries a high risk to the decline of ecosystems (Gattuso et al., 2015; Perry et al., 2018; Scandurra et al., 2018). And even more so because future impacts of climate change will be greater than current impacts (Nicholls and Cazenave, 2010; Church et al., 2013; Oppenheimer et al., 2019). Socioeconomic characteristics of small tropical islands, notably the Small Island Developing States, also contribute to their vulnerability (Duvat et al., 2017; Scandurra et al., 2018): the high density and rapid population increase of some islands, the scale of economic activities and subsistence depending on the climate and environment (Kuruppu and Willie, 2015; Pondorfer, 2019), the limited nature of terrestrial natural resources, in addition to human, technical, and financial capacities that are limited compared to those of continental countries (Nunn, 2009). Moreover, the fact that these are States or territories with recent political constitutions (recently formed) and a history of colonization, of which some remain contested (e.g., land tenure), contributes to their vulnerability. For these different reasons, the small tropical islands are among the most exposed and the most vulnerable to the impacts of climate change (Nurse et al., 2014).

Small tropical islands' high vulnerability to climate change impacts make it urgent to implement a process of adaptation to climate change (Kelman and West, 2009; Barnett and O'Neill, 2011) and especially policies of adaptation to climate change. These policies must be specific to each territory because the vulnerability of each small tropical island is itself specific, due to its physical, social, political, cultural, and other factors (Tompkins et al., 2010; Nunn et al., 2014). The goal of climate change adaptation policies is to maintain the viability of these territories (Keener, 2013) which, in the case of atolls, in a context of SLR, is threatened by increasing frequency of marine flooding (Beetham et al., 2017; Storlazzi et al., 2018). These adaptation policies must be carried out by public authorities. In our paper, we identify institutional actor as an individual involved in decision-making and the implementation of public policies, and therefore include decision-makers and practitioners. Their decisions are, like those of individuals, influenced by several factors. Although we do not study institutional actors as individuals, we acknowledge they carry 'personal baggage' that affects perceptions of climate change. Therefore, decisions may be influenced by personal factors related to gender, age, values, beliefs, experience, training, social rank, ethnicity, and personality, as well as wider factors such as social environment, media influence, and economic system (Montreux and Barnett, 2009; Deressa et al., 2011; Goeldner-Gianella et al., 2019). The more they consider climate change as distant, whether spatial or temporal, the less they feel concerned by its impacts and the less they accept and support policies of adaptation to climate change. Generally speaking, the knowledge of an individual about a given issue affects perceptions and actions with respect to this issue (Singh et al., 2017). According to the authors, individuals are conscious that climate change will have major consequences in their territory in the future, but they generally think they will not be affected in the short term. Secondly, decisions made by institutional actors are affected by the perceptions, necessarily subjective (Beyerl et al., 2018), that they have of the problems and questions they deal with on a daily basis within the framework of their work. In third and fourth places, the decisions they make are affected, on one hand, by the perception they have of the situation of their territory, and on the other by their perception of climate change and its impacts on this territory (Frondel et al., 2017). As a result, the institutional actor's knowledge and understanding of climate change, while acting as an individual and going about assigned tasks, will affect their perception of climate risk and, as a result, the manner in which tasks are understood and fulfilled within the domain of climate change adaptation.

With regard to these elements, it is important that these institutional actors have access to scientific knowledge to understand climate change and its impacts and thus to be in a position to plan and implement measures to better adapt to climate change (Lata and Nunn, 2012). Even so, there remains a gap between data produced by various areas of science and the needs of institutional actors (Hewitt et al., 2012). For small tropical islands, this can be illustrated by the few scientific studies related to risks connected to SLR and cyclone impacts (Willis and Church, 2012; Brown et al., 2013) or by scientific data formats unsuited to the needs of institutional actors (Brasseur and Gallardo, 2016). For the establishment of effective projects for adaptation to climate change (e.g., laws and regulations, field actions) it is necessary for institutional actors to understand the specific current and future impacts of climate change on their territory, which in turn necessitates adequate and technically accessible scientific information (Webber, 2017). It is the goal of climate services to reduce the gap between science and action (Vaughan et al., 2016). More concretely, it is a question of providing to users, including institutional actors, scientific information related to past, present and future climates that may be pertinent and suitable for their needs, and thus useful, and directly usable for the goal of aiding their decision-making (World Meteorological Organization [WMO], 2011; Le Cozannet et al., 2017; Damm et al., 2019). The users formulate the crucial needs for scientific knowledge to implement their projects and/or decision-making, needs that are satisfied by the scientific community, which supplies pertinent climate data and formulates answers to problems raised by the actors.

According to Ishaya and Abaje (2008), most studies on climate change perception have been conducted in developed countries in the northern hemisphere. Moreover, Lee et al. (2015) highlight that "current research on public perceptions of climate change has been dominated by studies in Australia, the United States and Europe." Thus, our study contributes to enriching our knowledge of climate change perception among institutional actors of an

island territory in the southern hemisphere, and more precisely the Pacific. This article presents the results of a methodological protocol that was used in French Polynesia to co-construct coastal climate services (CCS) with institutional actors. This protocol, which includes an analysis of the governance context of this territory, semi-structured interviews with practitioners, and a workshop, was set up for the purpose of defining CCS that support the adaptation of this territory to SLR. This approach is part of a multi-disciplinary and iterative approach to develop CCS based on principles of co-conception and co-development (Gibbons et al., 1994; Lang et al., 2012), including their societal, economic, scientific, and educational dimensions (Chambwera et al., 2014). The goal of this article is to respond to the following question: "How to co-develop CCS for adaptation to SLR with institutional actors of a given territory."

We present the territorial context and methods used, then the results of the perception study that was developed with institutional actors, and the identified CCS.

CONTEXT OF STUDY

Study Area

French Polynesia is a French overseas territory located in the South Pacific between 10 and 30°S latitude and between 133 and 155°W longitude. It comprises five archipelagos, the Marquesas Islands, the Tuamotu Islands, the Gambier Islands, the Society Islands, and the Austral Islands (**Figure 1**). The most recent census (2017) counted 281,674 inhabitants, 87.7% of which live in the Society archipelago (Institut de la Statistique de la Polynésie française [ISPF], 2017). In 2017, the GDP of French Polynesia increased to 5,04 billion € an increase compared to the preceding year (4,91 billion €). The service sector occupies a major position in the economy, with a rate of 8 out of 10 salaried people (Institut d'Emission d'Outre-Mer [IEOM], 2018) with more than 52,000 salaried people representing 82% of salaried persons, compared to 15% in the manufacturing sector and 3% for the primary (agriculture, fishing) sector (Institut d'Emission d'Outre-Mer [IEOM], 2018). Tourism (17% of the GDP; Institut d'Emission d'Outre-Mer [IEOM], 2018), pearl farming (63% of export revenue in 2018), fishing (11.5% of export revenue in 2018) and agriculture are the principal economic resources of this overseas territory (Institut d'Emission d'Outre-Mer [IEOM], 2018).

French Polynesia has held autonomous status since 2004, defined by Article 74 of the Constitution (Organic Law No. 2004-192 of 27 February 2004, concerning the autonomy statute of French Polynesia) which establishes governance shared by the Country, represented by the institutions of French Polynesia, and the French State, represented on site by the High Commission, directed by the High Commissioner. The High Commissioner oversees the coherence of activities conducted by locally present services of the French State. His principal mission is to ensure that laws are respected and to exercise oversight of the legality of the proceedings of the community. Nationality, civic, civil and electoral rights, justice, foreign policy, defense, entry and visitation period of foreigners, safety, public order, treasury, police, surveillance of maritime fishing, rules relative to administration, audiovisual communication, higher education or research fall within the jurisdiction of the authorities of the French State. French Polynesia has four institutions: President of the government, the government, Assembly (which votes on laws) and the Economic, Social, and Cultural Council. The services of the Country are distributed between the President and the ministries that make up local government. The 2004 organic law mentions that all jurisdictions not attributed to the State (article 14 of the 2004 organic law) and to the municipalities revert to the Country. Thus, in this overseas community, the institutional and decisional landscape is composed of State services and Country services (**Figure 2**).

State services are overseen by the High Commissioner and those of the Country are under the supervision of members of local government, namely the President and his ministers.

Materials and Methods

The methodological protocol that was developed includes three principal and complementary stages: an analysis of governance done for the purpose of identifying institutional actors involved in the subject of climate change; the administration of semi-structured interviews with these actors; and the organization of participatory workshops seeking to identify CCS to develop for adaptation to SLR.

Identification of Concerned Institutional Actors

As discussed previously, French Polynesia has an autonomy statute that permits the transfer of numerous jurisdictions from the State to the Territory (**Table 1**). These jurisdictions can be distributed among the services of various ministries and are described in various official (bills) and informational (e.g., annual report of the Overseas Issuing Institute, documentation of the Statistical Institute of French Polynesia, scientific article) documents, which were consulted.

The distribution of jurisdictions between State and Territory, illustrated in **Table 2** for the two domains of development and construction, on one hand, and the environment and biodiversity on the other, shows complex governance (**Table 2**). For example, the Department of Public Engineering (DPE), which is a service of the State, can be asked to provide engineering for the Territory, although the Territory has a dedicated service, the Department of Construction (DC). Another example that illustrates governance complexity is the organization of activities to undertake during and after an exceptional event such as a tropical cyclone. Protection of property and persons remains within the jurisdiction of the State. The High Commissioner must activate the ORSEC plan (emergency organization) with the participation of State services (army, police) and the mayors involved (municipal police and firemen). The armed forces of French Polynesia, in liaison with the High Commission, ensure among others, emergency missions to populations. Even so, the DC, a service of the Territory, also has as its mission "the assistance to populations threatened or affected by events calling for the emergency delivery of persons, material, supplies, provisions, and commodities of all types useful for the preservation or the re-establishment of normal living

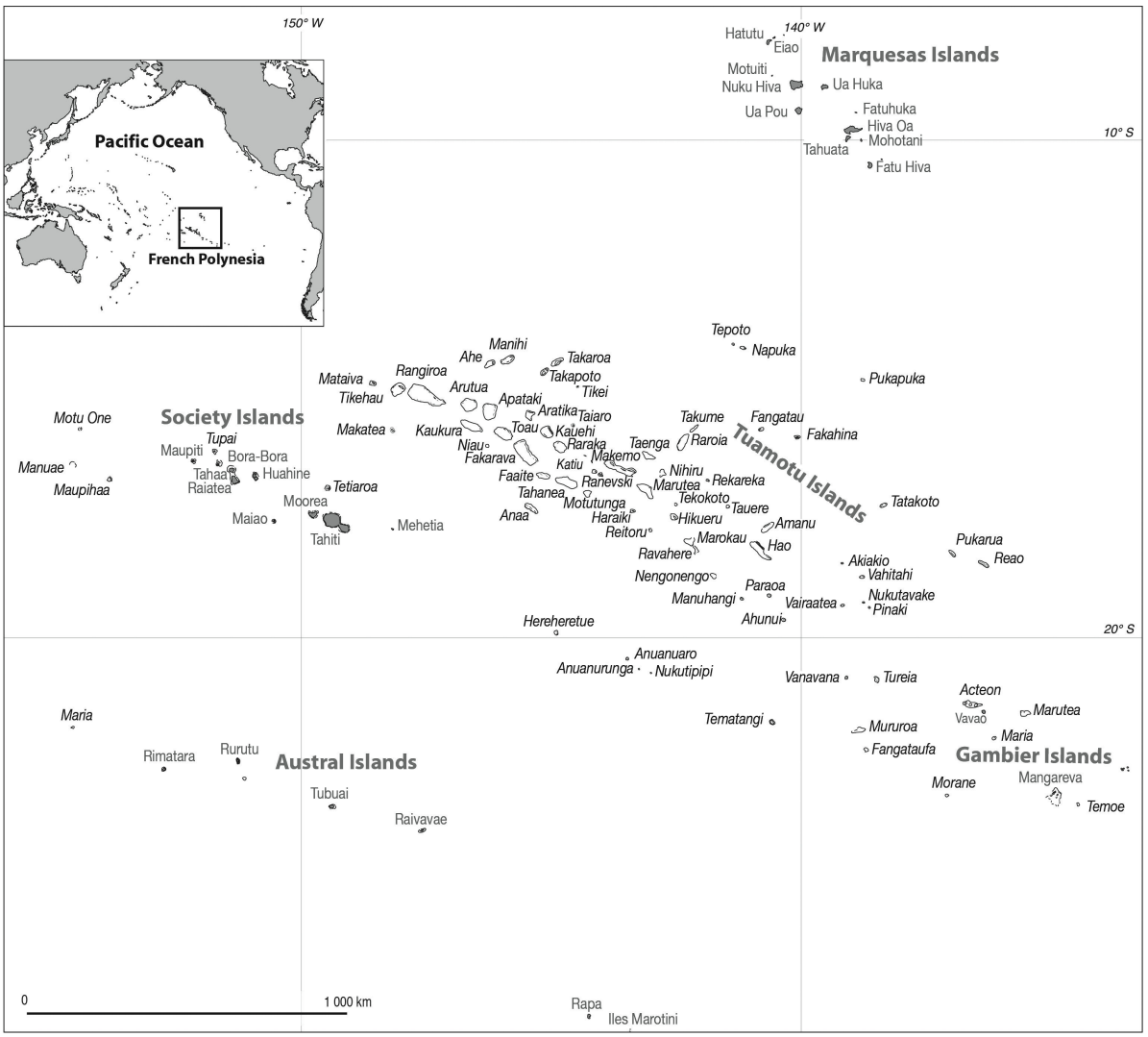

FIGURE 1 | Map of French Polynesia.

conditions." Thus, although protection of the population is the responsibility of the State, the Territory can provide support to populations through the DC.

In this context of complex governance, it is not easy to determine if a service has jurisdiction and/or missions related to climate change. In fact, the term "climate change" is rarely used in the description of the jurisdictions of the services and divisions of the Territory and the State. In this study, a service was considered to be involved with climate change if its jurisdictions and assignments consider, at a minimum, one of the following four criteria:

1. The service is dedicated to a climate-dependent activity;
2. The service is dedicated to an issue that could be impacted by climate change;
3. The service includes emergency services in the event of a natural disaster;
4. The service is in charge of studies or research related to climate or environment (physical or biological).

Perception of Climate Change by Institutional Actors in French Polynesia

Based on preliminary identification of climate change services in French Polynesia, semi-structured interviews were conducted with their representatives, following an interview guide whose rubrics and questions are presented in **Table 3**. The two objectives of these interviews were to determine the institutional actors' perception of climate change and their needs in terms of scientific knowledge. This interview guide addresses five principal themes, approached through eleven open questions. The five themes that were raised, ordered from general to particular, are the following:

1. Climate change in French Polynesia.
2. SLR in French Polynesia.

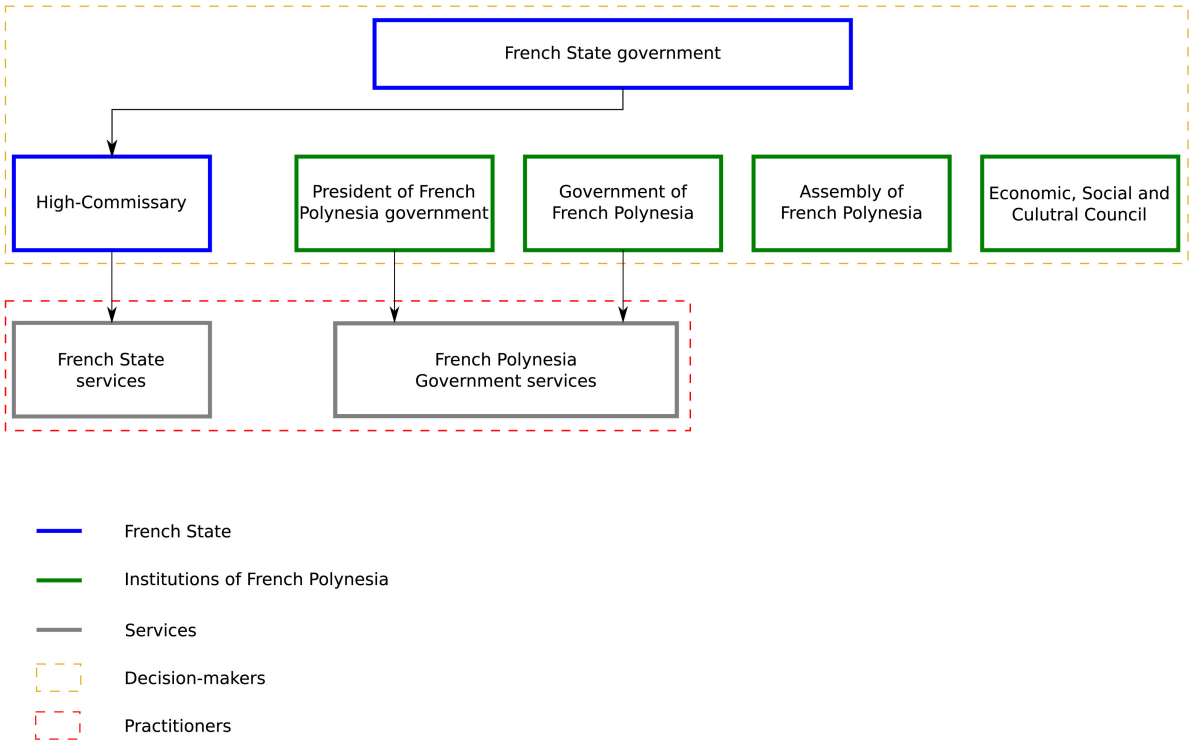

FIGURE 2 | Organizational chart of French Polynesia governance.

3. Actions and projects implemented and in the process of implementation to adapt to climate change, and the barriers to carrying out these projects in French Polynesia.

TABLE 1 | Documents used to identify services involved in climate change in French Polynesia.

Source	Information
Organic Law No. 2004-192 of 27 February 2004	Autonomy Statute of French Polynesia – Distribution of jurisdictions between the State, the Territory and the municipalities of French Polynesia – Institutions of French Polynesia – Role and activities of the State and the High Commissioner of the Republic in French Polynesia
Official Journal of French Polynesia http://lexpol.cloud.PF/	– Components of the Territory – Description of ministries and their actions – Description of ministerial services
Official site of the High Commission of the Republic in French Polynesia http://www.polynesie-francaise.pref.gouv.fr/	– Description of State services – Description of the services of the High Commission
Moyrand A, 2013. Introduction to the study of political and administrative institutions of French Polynesia	– Institutions of French Polynesia and distribution of power among them – Powers of the State in French Polynesia

4. Needs for scientific understanding on climate change and SLR.
5. Involvement at regional level in adaptation to climate change

To provide consistency, a single interviewer conducted all interviews. The interviewer strove to maintain the order and designation of the questions in all interviews. The interviews were recorded, with the agreement of participants. This process allowed the interviewer to listen well and favored a fluid exchange. In the treatment phase, the fact that interviews were recorded made it possible to do a faithful re-transcription of the responses given and build a list of responses. This list enabled quantitative (rate of response occurrence, after regrouping) and qualitative (re-transcription of speech) analysis of the climate change perception of the institutional actors involved. The choice of this methodology was inspired by previously conducted environmental change perception studies and was based on the meetings with various types of participants, such as residents, managers or community leaders (Beyerl et al., 2018; Lemahieu et al., 2018; Martin et al., 2018; Stancioff et al., 2018; Wetende et al., 2018; Cuthbertson et al., 2019).

Workshop Organization

Following the interviews conducted with the institutional actors, a workshop was held in Tahiti on March 22-23, 2018, to define CCS to be developed. The workshop pulled together the identified institutional actors, representatives of environmental protection associations, representatives of research institutes based in French Polynesia, and project scientists. The workshop included scientific presentations, a round table, and focus groups.

TABLE 2 | Examples of jurisdiction sharing between State and Territory.

Domain	Entity	Service	Principal jurisdiction
Development and construction	State	Department of Public Engineering	– Engineering services for the State, French Polynesia, or public establishments – Technical assistance to municipalities and administrative divisions of the State
	Territory	Department of Construction	– Monitoring, management, conservation, maintenance of terrestrial, fluvial, and maritime public domain of the territory and related engineering works.
Environment and biodiversity	State	French Agency for Biodiversity	– Support for the implementation of public policies in the domains of knowledge, preservation, management, and restoration of biodiversity of terrestrial, aquatic, and marine environments – Technical support for the Government of French Polynesia related to the creation and management of protected marine areas
	Territory	Department of the Environment	– Implementation of the policy of prevention, reduction, or suppression of pollution and nuisances related to economic and human activities – Monitoring, preservation, and protection of habitats of fauna and flora – Conservation and development of natural protected spaces

TABLE 3 | Questions asked and objectives of the semi-structured interview guide.

Theme	Question asked	Objectives
1	In your opinion, what are the three major issues facing French Polynesia now + in 2050 + in 2100?	Find out if climate change is identified as a major issue in French Polynesia, and at which timescales
	In your opinion, which climate change effects will significantly affect French Polynesia?	Find out if sea-level rise is a current concern
	In your opinion, what climate change impacts do you expect in French Polynesia in the future?	Find out what climate change impacts (including sea level rise) are of concern for actors
2	In your opinion, is sea-level rise already an issue in French Polynesia? If it isn't, will it become a major issue in the future? In 2050, 2070, 2100? What are the main problems that SLR may cause in French Polynesia? In your opinion, what might be solutions to employ against sea-level rise?	Determine their perception of SLR
	According to you, what territories/islands/areas are the most threatened in French Polynesia?	Find out about their perception of the highly-threatened areas
3	Does your service lead/participate in adaptation to climate change actions? Which ones?	Take stock of adaptation to climate change actions, including the consideration of sea-level rise and scientific research in these actions
	Do you face difficulties carrying out adaptation to climate change action in which you are involved? If yes, what kind of problem?	Identify barriers to adaptation to climate change, and determine if the lack of knowledge/access to knowledge is a barrier
4	Do you have needs in regard to climate change, especially sea-level rise?	Identify actors' needs in scientific data on sea-level rise impacts
5	Are you involved in regional adaptation to climate change programs/actions?	Identify regional adaptation to climate change programs in which French Polynesia is involved

This workshop with institutional actors made it possible to better identify the need for scientific information and to co-define climate services to develop to respond to their needs for adapting to sea-level rise (Maspataud et al., 2018).

RESULTS

Identification of Services Related to Climate Change

A meeting proposal was sent to the heads of services identified as being involved in the area of climate change (**Figures 3**, **4**). In all, representatives of six State services and seventeen Territory services were contacted and interviewed. In some cases, the chief of service was represented by a third person or accompanied by colleagues. In the results presented below, the response is counted for each service, rather than the number of persons contributing.

Representation of Climate Change by Institutional Actors in French Polynesia

Major Problems Perceived by Institutional Actors

Problems that the interviewed institutional actors considered major are, first of all, lack of economic growth and pollution,

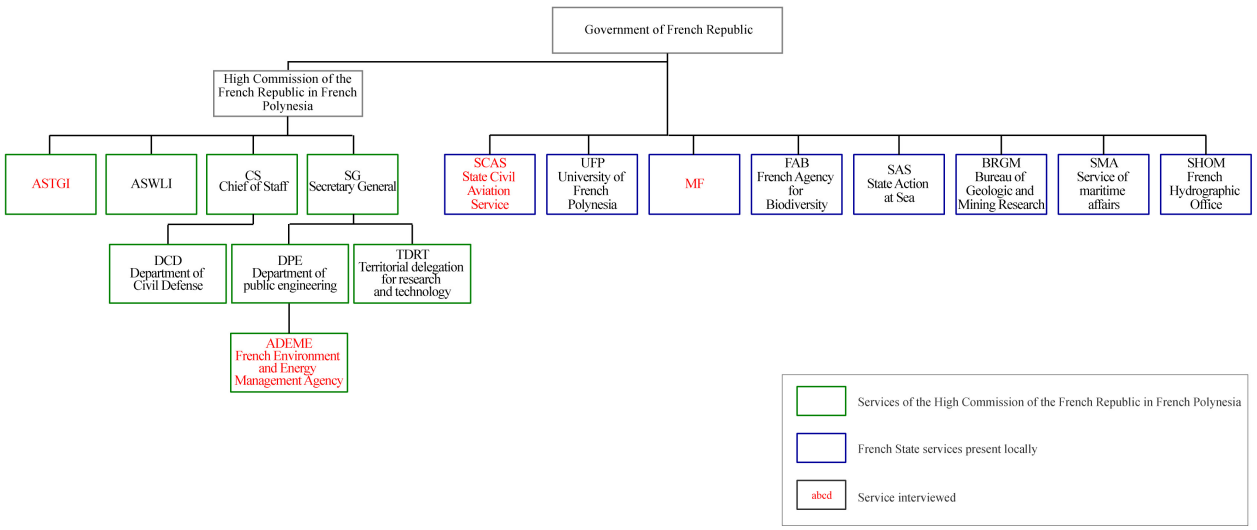

FIGURE 3 | Services of the State in French Polynesia identified as involved in the issue of climate change in 2018 and encountered through semi-structured interviews. ASTGI, Administrative subdivision of the Tuamotu and Gambier Islands; ASWLI, Administrative subdivisions of the Windward and Leeward Islands; MF, Meteo France - French National Meteorological Service.

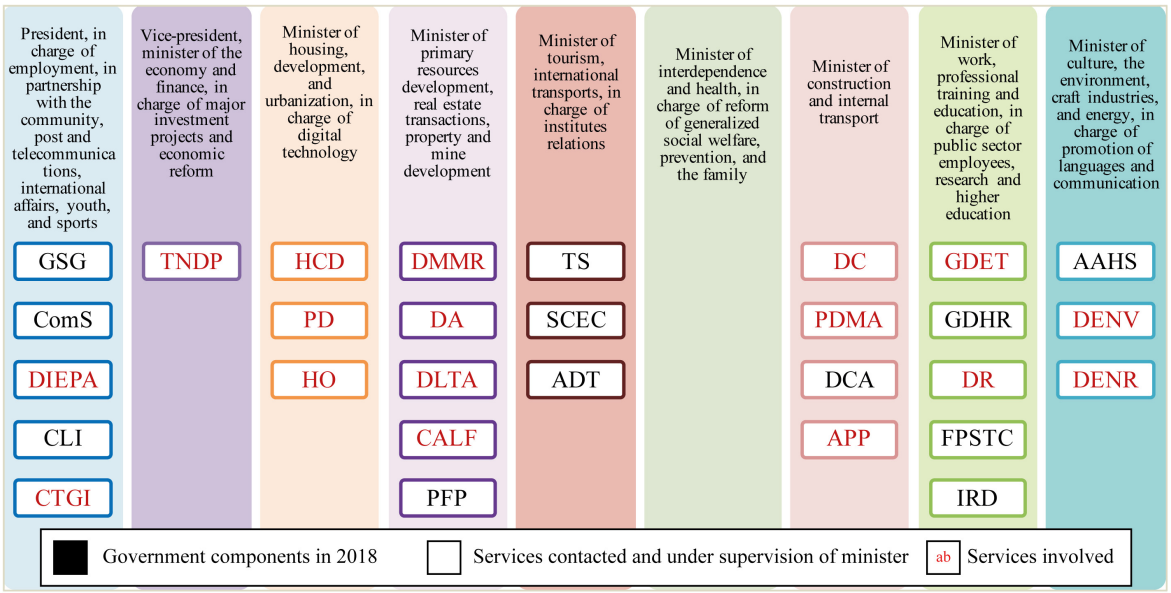

FIGURE 4 | Services of the government of French Polynesia identified as involved in the subject/thematic of climate change in 2018 and encountered through semi-structured interviews. GSG, General Secretariat of Government; ComS, Communication service; DIEPA, Delegation to International, European and Pacific Affairs; CLI, Circumscription of the Leeward Islands; CTGI, Circumscription of the Tuamotu-Gambier Islands; TNPD, Tahiti Nui Planning and Development; HCD, Habitat and City Delegation; PD, Planning Department; HO, Housing Office; DMMR, Department of marine and mining resources; DA, Department of agriculture; DLTA, Department of Land tenure Affairs; CALF, Chamber of agriculture and lagoon fisheries; PFP, Papeete fishing port; TS, Tourism Service; SCEC, General Secretariat of the Social and Cultural Economic Council; ADT, Aéroport de Tahiti; DC, Department of Construction; PDMA, Polynesian Department of Maritime Affairs; DCA, Department of Civil Aviation; APP, Autonomous Port of Papeete; GDET, General Department of education and teaching; GDHR, General Department of human resources; DR, Department of Research; FPSTC, French Polynesia Sea Trade Center; IRD, Institute for Research and Development; AAHS, Archive and Audiovisual Heritage Service; DENV, Department of the Environment; DENR, Department of Energy.

with 7 responses out of 23 (**Figure 5**). The results show that their primary concerns are environmental and socio-cultural, and related to development and management of the territory. Among environmental concerns, pollution was regularly cited. Freshwater resources are also among the concerns of some interviewees, who referred to the atolls of Tuamotu Archipelago. Finally, although less cited, dependence on fossil fuel was identified as a current problem

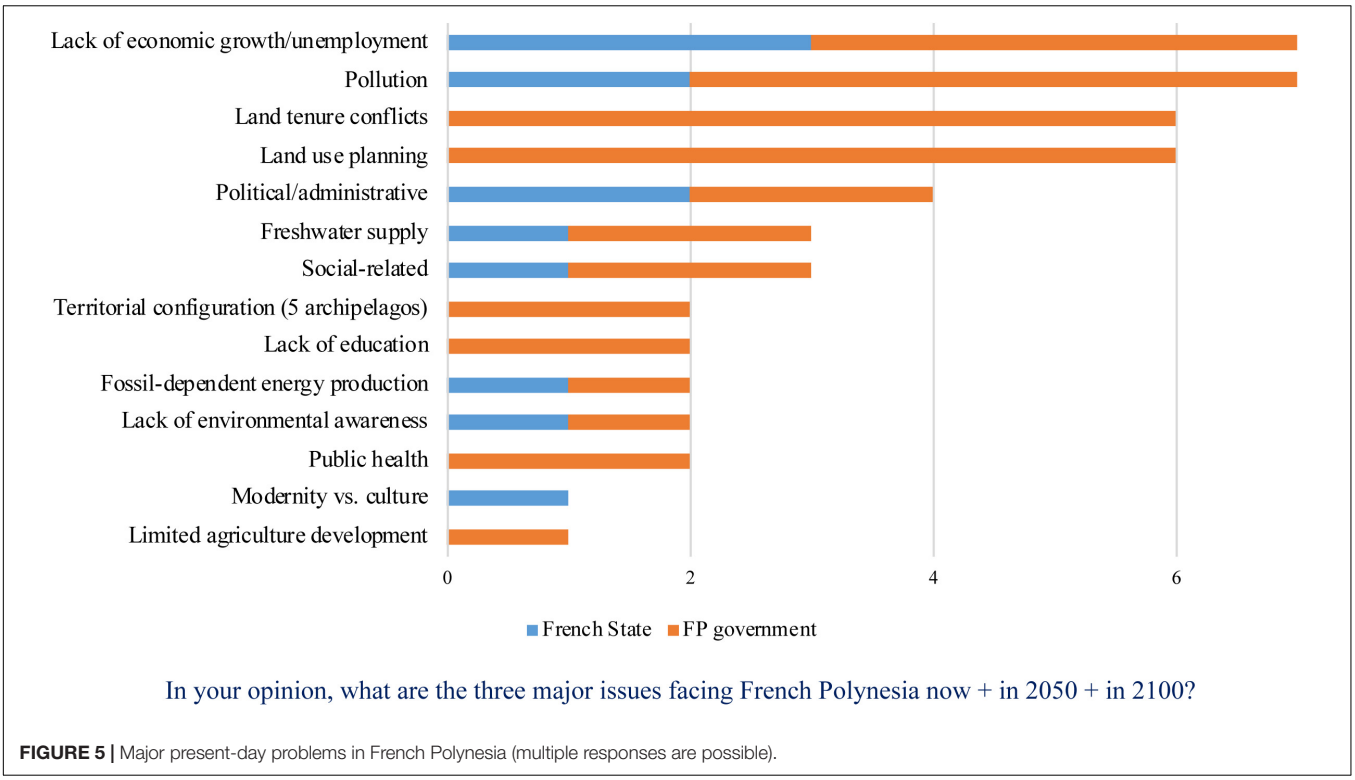

FIGURE 5 | Major present-day problems in French Polynesia (multiple responses are possible).

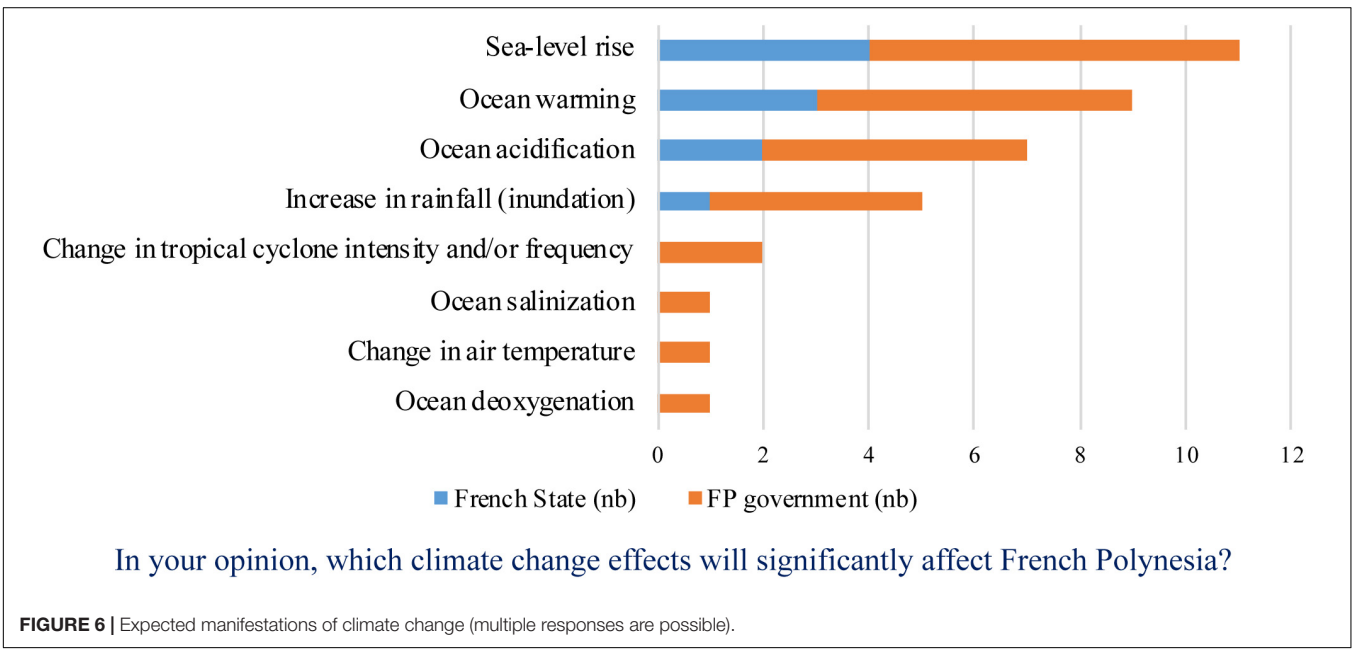

FIGURE 6 | Expected manifestations of climate change (multiple responses are possible).

in French Polynesia. Socio-cultural concerns are diverse; they include in particular property disputes, then to a lesser degree, social conflicts, crime, public health problems, lack of education, and even lack of sensitivity to the environment. Finally, regarding problems related to territorial development, the interviewees often referred to difficulties due to the configuration of the territory (i.e., vast and made of scattered islands). We highlight that the interviewees responded to this question only for the present case, and not for the other timelines.

In sum, the interviewees mentioned numerous problems of a diverse nature that did not refer to climate change. They acknowledged having more important concerns than climate change in the short term, as the GDET interviewee mentioned, "*Before tackling climate change, we should tackle practical problems (waste/pollution).*" For the time being climate change

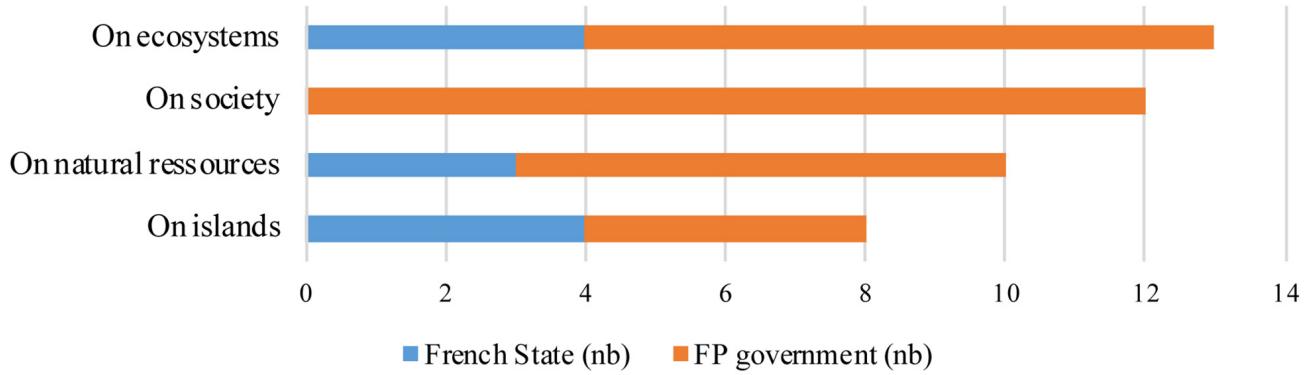

FIGURE 7 | Principal feared impacts of climate change (multiple responses are possible).

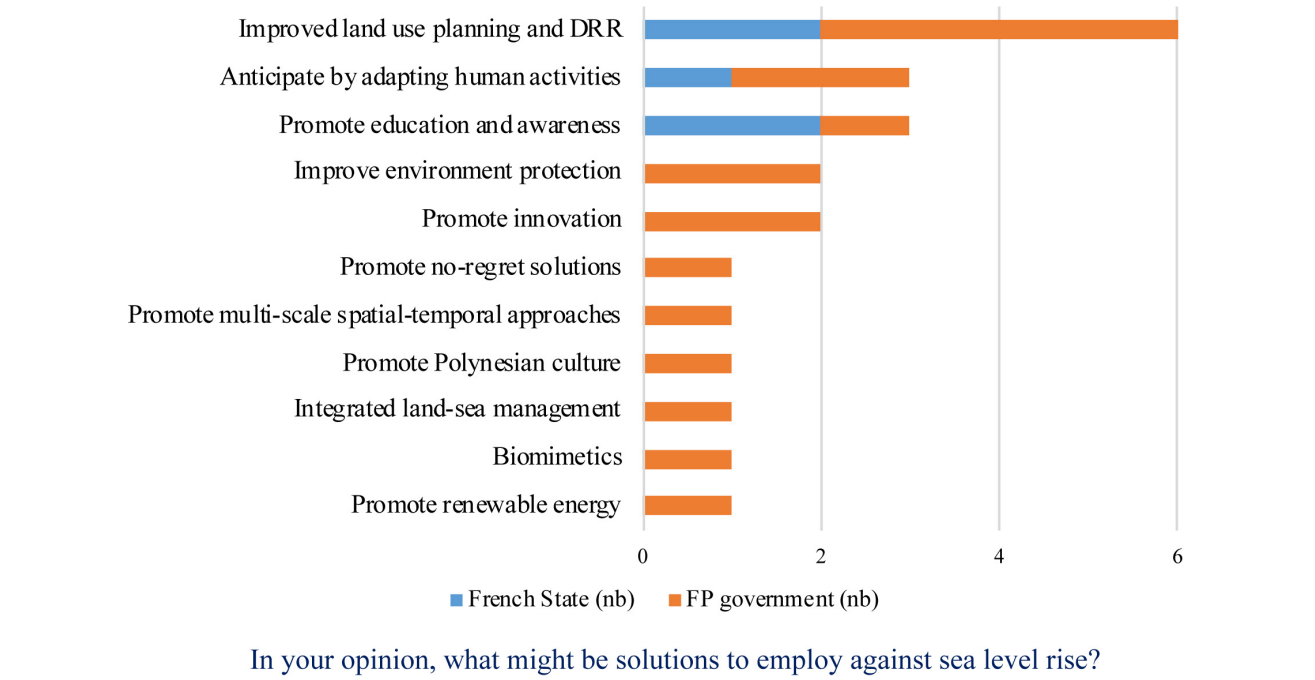

FIGURE 8 | Solutions proposed to adapt to sea-level rise. DRR, disaster risk reduction (multiple responses are possible).

does not concern the majority of the actors interviewed. Some explain it by the absence of visible measurable and restrictive impacts to the territory, as one PDMA interviewee stated: "*Climate change is not a preoccupation at the moment (. . .). We will become concerned when the first migrants appear*"; and a PD representative "*when there are manifestations (of climate change), there will be reaction.*" Conversely, other actors, such as the one interviewed at DLTA, indicated observing environmental changes but without knowing if these changes were attributable to climate change: "*Because of our way of life we don't have a very heavy impact on the land but we are among the populations that observe changes in our environment. Is it because of climate change? Because of sea-level rise? I don't know the reasons, but we observe the fact that there is a change in our environment.*" We gather from these conversations that climate change is known among the interviewees, who are also conscious that this global phenomenon will intensify in the coming years and that French Polynesia thus risks suffering more of its effects. Thus, the DLTA interviewee recognized that "(*climate change is) a problem that touches the Pacific, the island States*". The PDMA representative stated that "*climate change is not a concern for the moment. [. . .] But in the future, it will become more of a problem.*"

Expected Manifestations of Climate Change

Although the interviewees did not identify climate change as a major problem, we asked them their point of view on the type of climate change manifestations that might have an important effect on their territory (**Figure 6**). Sea-level rise (9 responses out of 23), warming (9 out of 23) and ocean acidification (7 out of 23) were the most cited manifestations. Even if rising sea level was the most often mentioned manifestation, some actors, like one of the DMMR interviewees, think that the increased ocean temperature will have a greater effect than rising sea level in French Polynesia: "*The [important] parameter is temperature. If sea level rises faster than temperature, great; if temperature rises faster than sea level, that is not good.*" As this actor explained to us, some coral species are capable of growing as sea level rises, if environmental parameters (especially sea temperature, depth, turbidity) are favorable. This capability may decrease if oceanic temperature increases rapidly. In French Polynesia above 30°C, coral bleach and can die (Salvat, pers. comm).

Furthermore, five services cited flooding, referring to the heavy rain in 2017 that caused flooding on the coast of Tahiti. The interviewees remembered bridges that gave way under the pressure of high water, flooding of Tahiti's only international airport, numerous homes destroyed, and evacuees to be housed rapidly or even a young fireman who died while responding to the event. Some interviewees also mentioned tropical cyclones, and the perspective of their intensification and possible increased frequency and their effects. Overall, actors' responses show that the most anticipated manifestations of climate change are related to changes affecting the ocean. Finally, 7 of the services interviewed gave no response to this question.

Representations of Climate Change Impacts

The principal impacts expected from climate change are, in first place, impacts to ecosystems, with 13 responses (**Figure 7**). This category includes environmental degradation generally, and of the marine ecosystem in particular, with the degradation of coral reefs (6 responses out of 13) shown by bleaching and the decline of giant clams. The interviewees stressed the loss of ecosystem services provided by coral reefs. In second place, with 12 responses, are impacts to Polynesian society. Among them, impacts to economic activities were cited 8 times. Agriculture, particularly copra production, and the blue economy (giant clam production, fishing, and pearl farming) were the principal sectors cited. Furthermore, 4 services referred to climate change impacts on safety and public health, territorial management, internal migration and on the built environment, mentioning more precisely the risk of destruction of infrastructure. In third place, impacts to natural resources were listed in 10 responses. Interviewees are worried about maintenance of freshwater resources on atolls. Impacts to marine resources were also mentioned, particularly increased competition between species due to environmental changes resulting from climate change. Eight services out of 23 mentioned climate change impacts to the islands themselves (particularly coastal erosion) and increased areas at risk because of increased natural risk, particularly coastal erosion. Among the services interrogated, 10 did not respond to this question.

Detailed answers include: For impacts on ecosystems, "detrimental impacts on the reef ecosystem" (6/13), "detrimental impacts on marine ecosystems" (4/13), and "detrimental impacts on the natural environment" (3/13); For impacts on human society, "detrimental impacts on agriculture" (4/12), "detrimental impacts on the blue economy" (4/12), "improved territorial development" (1/12), "decreased island accessibility (unusable airstrips)" (1/12), "destruction of human constructions" (1/12) and "detrimental impacts on health and security" (1/12); For impacts on natural resources, "decreased freshwater supply" (4/10), "increased species competition" (3/10), "detrimental impacts on marine resources" (2/10), and "change in vegetation cycle" (1/10); For impacts on islands, "shoreline retreat/island erosion" (5/8), "increased natural risks" (2/8), and "marine flooding" (1/8).

Representations of Rising Sea Level, Its Impact, and Responses to Implement

Nine services out of 23 do not consider SLR a present-day problem in French Polynesia, versus 7 services who hold the opposite position. The opinions are thus split. Some actors are not worried by SLR, for example, the PD representative, who told us that "*as long as it doesn't have any concrete manifestation, I will question rising sea level*" or they compared French Polynesia to other territories more exposed to SLR "*there is time to spare*." Other participants consider SLR a present-day problem, as is the case of the CTGI [Circumscription of the Tuamotu and Gambier Islands] which manages atolls of French Polynesia and is thus very sensitive to this question: "*It's already a problem. There have been worries among mayors (of the Tuamotu) who say that they are going to be climate refugees [. . .] they see that sea water is warming more and more.*" These results are not surprising, since we have seen, on the one hand, that climate change is not considered a major present-day problem (**Figure 5**) and on the other hand, that SLR is a climate change manifestation that may greatly affect this territory in the years to come (**Figure 6**): "*Rising sea level is not a problem today, (but) certainly [will be] in the future*" (PDMA).

Other than these responses, the interviewees had difficulty determining a date at which SLR will become a serious problem, and therefore remained vague on this subject. Regarding the places most threatened by SLR, most of them cited atoll islands (19 respondents) and low-lying coastal areas on high islands (10 respondents).

Although the participants were not able to express precisely the impacts of SLR, with the exception of the risk of flooding, some of them did, however, propose solutions to meet them (**Figure 8**). All considered that to develop the territory more sustainably, development planning, management of natural risks, and technical adaptation of buildings in particular constitute a solution to adapt to sea-level rise. The HCD representative stated: "*This climate change dimension does not involve just protecting ourselves, it calls us to better develop the territory, better define urbanization policies. Climate change must be considered in territorial development.*" Other participants shared this point of view, such as the DPE representative who said, concerning SLR,

that it would be necessary "*to plan and anticipate so as to not to be subjected to it.*"

According to other participants (3 respondents) it is necessary to reduce local human disturbances. In fact, if these were discussed and thought about sustainably and if they integrated SLR, SLR might have less impact. In addition, three services suggested improving education and raising the awareness of private and public stakeholders and of residents to climate change and SLR because "*Protection is not innate. It has to be taught. When you know, you can protect*" (GDET). In addition, improving environmental protection was proposed as a solution because, as a representative of CTGI said: "*Man must work with nature, integrate nature into his environment and not work against it*." Promoting innovation in French Polynesia also played a part in actors' suggestions: "*Finding solutions by innovating (. . .) and why not a floating island in the lagoon, and the population stays on its island, the resources are always there*" (CTGI). Moreover, actors had other ideas for reacting to SLR, such as promoting no-regret actions, biomimetics, renewable energy, or advancing Polynesian culture, as an DENR actor indicated: "*refocusing on our fenua (country) would lead to better resilience.*"

Finally, on the notion of temporality, not all participants agree. Some, like the DPE representative, highlighted the importance of encouraging the adoption of a global vision in time and space, "*there is not a single reflection, there are many reflections at several different time scales*," whereas others, such as PDMA were nevertheless of the opinion that "*we must act at our scale and reflect over the long term.*" Finally, 13 services did not want to talk about solutions to implement to confront SLR.

Activities for Adaptation to Climate Change

Although climate change is not perceived as a major problem at the present for the institutional actors, they are aware of projects and actions for adapting to climate change. Solutions most often mentioned (5 services out of 23) are the Risk Prevention Plan (PPR) and the RESCCUE project (Restoration of eco-systemic services and adaption to climate change). The first is a statutory tool of the Territory that seeks to manage land use with regard to natural risks present in French Polynesia. The second is a regional project managed in French Polynesia by a service of the State, the French Agency for Biodiversity; it seeks to reinforce the resilience of the territories studied (New Caledonia and French Polynesia), that is, [the resilience] of their ecosystems and their populations with respect to climate change. Three services cited cyclone shelters and SAGE (Action plan for general development of French Polynesia). The actors in question referred to cyclone shelters on the distant islands of Tahiti, in particular the Tuamotu atolls. Not all inhabited atolls are provided with shelters. SAGE is a territorial project that seeks to define trends for territorial planning and development for the next two decades. Finally, to a lesser extent, other actions and projects were cited, such as the Management Plan for Maritime Space (PGEM) of Moorea, the energy climate plan, the strategic climate plan, and educational marine zones. Three services did not respond to this question.

Barriers to Projects of Adaptation to Climate Change

Interviewed actors identified problems of governance as the number one barrier to adaptation to climate change (**Figure 9**). This includes political problems, especially the regular changes of government that cause (1) a rupture in the continuity of decisions, as a TNPD representative pointed out: "*Each time the government changes, planning changes*"; (2) corruption of individuals leading the Territory, and (3) the lack of will dedicated to the topic of climate change. A DC representative told us that "*There is no political will to go in this direction. It will be done at the last minute, when it has become urgent. It is not an easy political approach, and we are not on this approach.*" According to 7 services, the second perceived barrier to climate change adaption projects is complexity of laws and regulations, in addition to administrative sluggishness, mentioned by 4 services. The third-ranking barrier to adaptation to climate change is lack of financing. Other barriers cited are distance and isolation of the islands, the land tenure system of Polynesia, problems of social acceptability (social and cultural) of projects that could modify the habits of the population. For example, a representative of DLTA explained to us that "*there have been periods when the public domain has entered the private domain. It then becomes the property of individuals through definitive concessions. The coast is no longer public; it is private. It's a major mental barrier (to action)*" because any public coastal project in favor of adaptation to climate change would necessarily involve changes, for example, by *de facto* reintegrating the coastal zone into the public domain. But the inhabitants concerned refuse to renounce their privileges. In addition, according to an actor from the DENR, even if "*Polynesians have a large capacity for adaptation (creative and inventive), they don't plan for the long term*" and thus imagine that a project could reap benefits over the long term. Six services did not respond to this question.

Need for Scientific Information

Most interviewees (15 services out of 23) said they are interested in scientific data related to climate, as long as it is easily accessible, standardized, and up to date (**Figure 10**). The actors indicated that information is not lacking, because "*there is (generally) too much information*" said a DC representative. On the other hand, what is necessary, according to an actor of CTGI, is "*to standardize the information so that we are all talking about the same thing. And not 'each talking according to his version,' [because] you don't know what he's talking about, when you are talking about the same thing."*

In addition, 14 services showed an interest in sea level projections on a regional scale, for the territory or by archipelago, over the next decades. These projections will assist actors in their projects, and a DPE representative mentioned, "*We must build in terms of sea level projections.*"

The institutional actors also expressed interest in natural resource studies for the purpose of using and/or preserving these resources. The actors (5 services out of 23) also expressed the need to use information about the risks of SLR on infrastructure

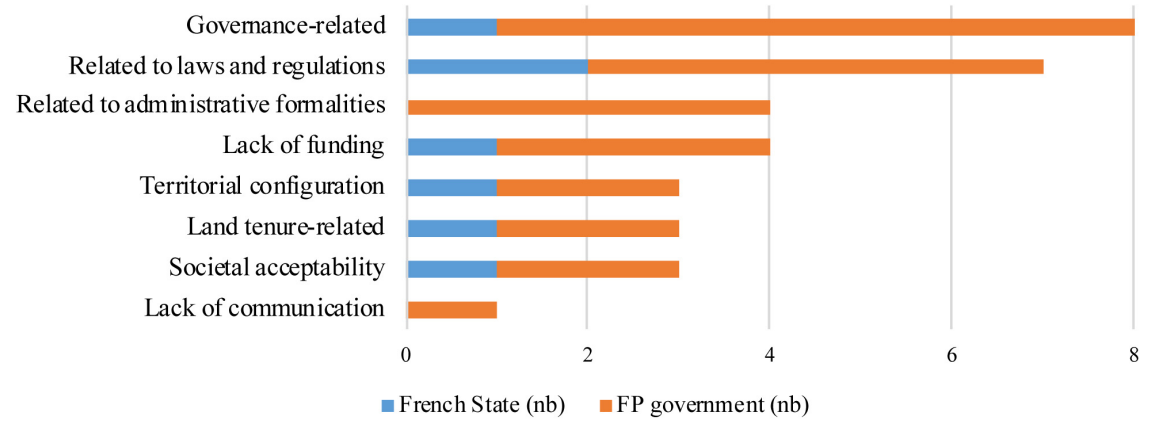

FIGURE 9 | Barriers to projects of adaptation to climate change in French Polynesia (multiple responses are possible).

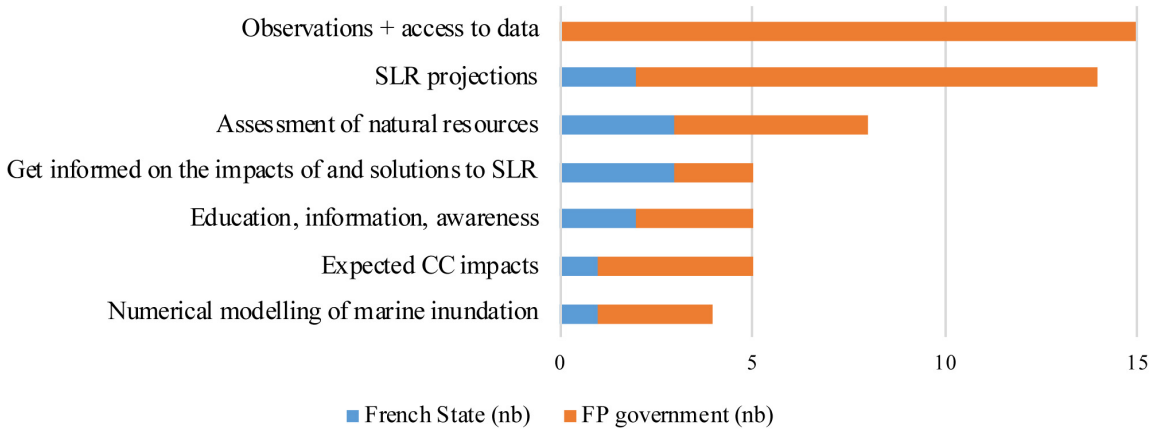

FIGURE 10 | Need for scientific information (multiple responses are possible).

and coastal construction, and for adaptations required to address these risks. Actors such as those of the CTGI are conscious that "*we are not going to limit erosion by building protection walls; that will in fact make our coasts more fragile. But for now, what is a good solution*?" Finally, the need for public awareness of climate change and its impacts in French Polynesia and modeling of marine submersion were mentioned by 4 services during interviews.

Determination of Coastal Climate Services to Develop for the Benefit of Actors

A workshop with representatives of the identified services (**Figures 3**, **4**) included a discussion of the results obtained during the semi-structured interviews.

These exchanges made it possible to highlight subjects of concern regarding climate change and SLR among institutional actors in French Polynesia. They are: taking note of successful concrete actions, co-construct action proposals, determine the necessary conditions to guarantee the success of climate services for coastal adaptation, identify key partners to mobilize to set up case studies. An assessment of actions and policies carried out or anticipated to integrate climate change effects has been set up. Finally, topics reflected and discussed among local actors included the need for climate services with thoughts on trajectories of adaptation to global change.

The proposals formulated in this workshop were formalized across the 4 CCS: the design of SLR-compatible critical infrastructures (airports and ports); adapting to the risk of destabilization of beaches and reef islands; professional training on climate change impacts and adaptation, including the analysis

of potentially emerging new jobs in the SLR context; and the development of participatory approaches for the observation of climate change impacts.

DISCUSSION

Climate Change and Sea-Level Rise Are Not Perceived as Present-Day Problems by Institutional Actors in French Polynesia

Generally, the institutional actors interviewed feel that at this point they are protected from climate change impacts and as a result, do not consider climate change as a present-day problem. According to the literature, this result is the same throughout the Pacific territories. For example, in New Zealand, Archie et al. (2018) noticed weak engagement of the central government in policies of adaptation to and attenuation of climate change. However, and this agrees with results of our interviews (section Major Problems Perceived by Institutional Actors), Archie et al. (2018) think that the level of concern will increase over time, as climate change impacts are felt, and that this will be favorable for the implementation of actions that promote adaptation to climate change. The situation is different in Kiribati, where decision-makers are already concerned by climate change, particularly SLR (Mallin, 2018), and have already implemented policies of adaptation to climate change (e.g., Kiribati Joint Implementation Plan for Disaster Risk Management and Climate Change 2014–2023). In French Polynesia, the low level of concern among institutional actors with respect to climate change is not related to the absence of knowledge of the phenomenon and/or its impacts (**Figures 6**, **7**).

This view of climate change is understandable if the present-day impacts of climate change are put in perspective with problems of planning and development that confront the institutional actors of French Polynesia. First of all, the morphological characteristics of islands (mountainous or low-lying) often limit territorial planning and in particular the construction of homes and infrastructure. Add to this property disputes, which are a societal problem of cultural origin. In fact, numerous plots of land are held jointly by several families who share a common ancestor. Sometimes land parcels were not claimed at the time the cadaster was done and they entered into the public domain. Today family groups claim plots on the basis of some proof. This is a general problem in French Polynesia, which pits families against each other and sometimes, private individuals against public entities (Bambridge, 2009; Charpy, 2016; Stahl, 2018).

Another example is related to the complexity of exchanges and relationships between the five archipelagos that make up French Polynesia. It must be kept in mind that French Polynesia is a territory as large as Europe. Some islands do not have aircraft landing strips, and can only be reached by boat. This isolation can cause social problems. For example, primary education is offered on each inhabited island, but middle and high school students of many islands must often leave their homes to continue their studies on another island. As an example, in 2018 there were ten public and private high schools (general and technological, professional, and multi-purpose education) in French Polynesia. The latter are all located in the Society archipelago, including eight in Tahiti[1]. In other words, only three islands have high schools, which requires high school students to travel to one of these islands to pursue their studies. It requires organization to transport these students. For example, for the 2017–2018 school year, the total amount for air transport of secondary education students (middle and high school together) exceeded 3 million €. In terms of health, the distance to some islands also poses problems, particularly for health evacuations. For example, pregnant women are highly encouraged to give birth in Tahiti (in 2004, more than 80% of births took place in Tahiti). According to the health minister, in 2018 there were more than 36,000 health evacuations within French Polynesia (separate from international health evacuations) which cost almost 16.7 million €.

The Climate Change Perception Study Helps Identify the Need for Scientific Information Related to Climate

Interviews on climate change perception of institutional actors in French Polynesia showed that they did not consider climate change to be a present-day problem, particularly because they have not yet observed impacts (section Major Problems Perceived by Institutional Actors). This is essential information, which makes it possible to identify a need for scientific information, particularly on the present-day and expected impacts of climate change in French Polynesia and to identify the CCS that will make it possible to anticipate these impacts. Smith and Mayer (2018) point out that a person who perceives climate change as a threat is more inclined to take measures to adapt to it. In addition, the semi-structured interviews and the workshop showed that institutional actors in French Polynesia were interested in knowing more about climate change impacts and requested data and localized measurements. This finding shows that there exists within French Polynesian institutions a climate favorable to changing climate change awareness toward actions seeking to remediate its impacts.

Stancioff et al. (2018) found that sometimes climate change is not perceived as a concern by societies of the Small Island Developing States and make the point that effective measures against climate change can be adopted only by considering the point of view of these societies. To "extrapolate" this to our case study, we can surmise that for effective climate change adaptation actions and projects to be implemented in French Polynesia, the perceptions of actors must be considered, since climate change is not currently one of their principal concerns. Starting from this state of affairs is crucial for planning useful climate services. Our study of climate change perception, which establishes this *status quo*, thus constitutes an important stage in the process of implementation of pertinent actions in favor of adaptation to climate change.

[1] www.presidence.pf

This finding highlights the necessity of raising awareness among institutional actors in French Polynesia not only with respect to climate change and its current impacts, but also to the role that humans play in "increasing the vulnerability" of the coastal zone. Considering the implications of modalities of current planning and development in the territory with the exacerbation of future climate change impacts will help the institutional actors of French Polynesia make a connection between the problems that concern them and climate change impacts. There is probably a trigger within this process to stimulate adaptation to climate change policies. Therefore, climate service training for actors on climate change impacts may play a role. More globally, it is the role of the researcher to transmit to institutional actors the scientific knowledge that may be useful to them. For example, the study of Cuthbertson et al. (2019) on the perception of catastrophic risk in Oceania shows a gap between risk perception and real measured risk. To improve risk management, Cuthbertson et al. (2019) recommend a focus on bottom-up and educational approaches, which can be done with a strong political will and good governance practices. The CCS co-developed in French Polynesia and presented in this article incorporate such an approach.

Limitations of the Method

Interviews were generally recorded, with the agreement of interviewees. This may have been a barrier to liberty of expression of the interviewee, who represented a public service and was thus required to be consistent with the principal ideas and values communicated by the State and/or the Territory. The method used thus encouraged a politically-correct attitude.

Although we identified them as belonging to services involved in climate change, the institutional actors interrogated do not necessarily work with this subject. This explains not only why some did not respond to certain of our questions but also the results obtained with respect to their perception of climate change in French Polynesia. In addition, each service being dedicated to a specific sector (e.g., agriculture) their representatives responded to questions with a "filter," in other words, with a specific point of view when they responded to general questions that were directed at them. For example, and logically, SLR is not a problem for agricultural fields in high islands such as Tahiti. In fact, this land is often in mountains or in a valley. This service is more interested in changes in precipitation. This explains the nature of the responses supplied by actors to the questions asked, and more globally the actor's underestimation of certain impacts of climate change; each of the actors interrogated not being affected by the suite of climate change impacts because of the limited domain of his activities.

LIFE SCIENCES RESEARCH INTEGRITY

Our study is based on results obtained thanks to semi-structured interviews and workshop organized with publics actors. Thus, an ethical review process was not required for our study which does not involve human subjects under no circumstances for medical research. Also, we reminded them that is a scientific study realized in the frame of INSeaPTION research project. All participants were over 16 and their anonymity is respected since no personal information allowing the identification of the interviewees is revealed.

DATA AVAILABILITY STATEMENT

The datasets generated for this study are available on request to the corresponding author.

AUTHOR CONTRIBUTIONS

Every author of this article has contributed to its development. All contributed to data collection in the field. Interviews were conducted by HT. Results were then presented to the institutional actors of French Polynesia during a workshop led by AM in March 2018. The results were discussed during this session by VD and JO. This workshop led to the identification of four CCS.

FUNDING

This study was supported by the INSeaPTION project, which is part of ERA4CS, an ERA-NET initiated by JPI Climate, and funded by BMBF (DE), MINECO (ES), NOW (NL), and ANR (FR), with co-funding by the European Union (Grant No. 690462).

ACKNOWLEDGMENTS

We are grateful to the Government of French Polynesia and to the French State services for fruitful collaboration.

REFERENCES

Archie, K., Chapman, R., and Flood, S. (2018). Climate change response in New Zealand communities: local scale adaptation and mitigation planning. *Environ. Dev.* 28, 19–31. doi: 10.1016/j.envdev.2018.09.003

Bambridge, T. (2009). "Le foncier en Polynésie Française-Comment réconcilier pratiques, légalité et légitimité," in *Proceedings of the Colloque Tahiti*, Vol. 8, Tahiti.

Barnett, J., and O'Neill, S. J. (2011). Islands, resettlement and adaptation. *Nat. Clim. Change* 2:8. doi: 10.1038/nclimate1334

Beetham, E., Kench, P. S., and Popinet, S. (2017). Future reef growth can mitigate physical impacts of sea-level rise on atoll islands. *Earth's Future* 5, 1002–1014. doi: 10.1002/2017ef000589

Beyerl, K., Mieg, H. A., and Weber, E. (2018). Comparing perceived effects of climate-related environmental change and adaptation strategies for the Pacific small island states of Tuvalu, Samoa, and Tonga. *Island Stud. J.* 13:e53. doi: 10.24043/isj.53

Brasseur, G. P., and Gallardo, L. (2016). Climate services: lessons learned and future prospects. *Earth's Future* 4, 79–89. doi: 10.1002/2015EF000338

Brown, J. N., Gupta, A. S., Brown, J. R., Muir, L. C., Risbey, J. S., Whetton, P., et al. (2013). Implications of CMIP3 model biases and uncertainties for climate projections in the western tropical Pacific. *Clim. Change* 119, 147–161. doi: 10.1007/s10584-012-0603-5

Chambwera, M., Heal, G., Dubeux, C., Hallegatte, S., Leclerc, L., Markandya, A., et al. (2014). "Chapter 17 - Economics of adaptation," in *Climate Change 2014: Impacts, Adaptation, and Vulnerability. Part A: Global and Sectoral Aspects. Contribution of Working Group II to the Fifth Assessment Report of the IPCC*. eds C. B. Field, V. R. Barros, D. J. Dokken, K. J. Mach, M. D. Mastrandrea, T. E. Bilir, et al. (Chatterjee, Cambridge: Cambridge University Press), 945–977.

Charpy, J. (2016). *Le foncier en Polynésie françcaise. Sciences de l'ingénieur [physics]. dumas*- 01685785. Santarém: ESGT.

Church, J. A., Clark, P. U., Cazenave, A., Gregory, J. M., Jevrejeva, S., Levermann, A., et al. (2013). "Sea level change," in *Climate Change 2013: the Physical Science Basis. Contribution of Working Group I to the Fifth Assessment Report of the Intergovernmental Panel on Climate Change*, ed. T. F. Stocker, (Cambridge: Cambridge University Press).

Cuthbertson, J., Rodriguez-Llanes, J. M., Robertson, A., and Archer, F. (2019). Current and emerging disaster risks perceptions in oceania: key stakeholders recommendations for disaster management and resilience building. *Int. J. Environ. Res. Public Health* 16:460. doi: 10.3390/ijerph16030460

Damm, A., Köberl, J., Stegmaier, P., Alonso, E. J., and Harjanne, A. (2019). The market for climate services in the tourism sector–An analysis of Austrian stakeholders' perceptions. *Clim. Serv.* 100094. doi: 10.1016/j.cliser.2019.02.001

Deressa, T. T., Hassan, R. M., and Ringler, C. (2011). Perception of and adaptation to climate change by farmers in the Nile basin of Ethiopia. *J. Agric. Sci.* 149, 23–31. doi: 10.1017/S0021859610000687

Duvat, V., Magnan, A., and Gattuso, J. P. (2016). *Les Petites îles, l'océan et le climat*. Prais: OCÉAN-CLIMAT, 2.

Duvat, V. K. E., Magnan, A. K., Wise, R. M., Hay, J. E., Fazey, I., Hinkel, J., et al. (2017). Trajectories of exposure and vulnerability of small islands to climate change. *Wiley Interdiscipl. Rev.* 8:e478. doi: 10.1002/wcc.478

Frondel, M., Simora, M., and Sommer, S. (2017). Risk perception of climate change: empirical evidence for Germany. *Ecol. Econ.* 137, 173–183. doi: 10.1016/j.ecolecon.2017.02.019

Gattuso, J. P., Magnan, A., Billé, R., Cheung, W. W., Howes, E. L., Joos, F., et al. (2015). Contrasting futures for ocean and society from different anthropogenic CO2 emissions scenarios. *Science* 349:aac4722. doi: 10.1126/science.aac4722

Gibbons, M., Limoges, C., Nowotny, H., Schwartzman, S., Scott, P., and Trow, M. (1994). *The New Production of Knowledge: The Dynamics of Science and Research in Contemporary Societies*. London: Sage Publications.

Goeldner-Gianella, L., Grancher, D., Magnan, A. K., de Belizal, E., and Duvat, V. K. (2019). The perception of climate-related coastal risks and environmental changes on the Rangiroa and Tikehau atolls, French Polynesia: the role of sensitive and intellectual drivers. *Ocean Coast. Manag.* 172, 14–29. doi: 10.1016/j.ocecoaman.2019.01.018

Hewitt, C., Mason, S., and Walland, D. (2012). The global framework for climate services. *Nature Climate Change* 2, 831. doi: 10.1038/nclimate1745

Institut de la Statistique de la Polynésie française [ISPF] (2017). *Conférence de presse du 13 novembre 2017*. Available online at: http://www.ispf.pf/docs/default-source/rp2017/cpo_rp2017.pdf?sfvrsn=2

Institut d'Emission d'Outre-Mer [IEOM] (2018). *Rapport Annuel 2018 - Polynésie française*. https://www.ieom.fr/polynesie-francaise/publications/rapports-annuels/rapports-d-activite/article/rapport-annuel-2018-de-l-ieom-polynesie-francaise

Ishaya, S., and Abaje, I. B. (2008). Indigenous people's perception on climate change and adaptation strategies in Jema'a local government area of Kaduna State. Nigeria. *J. Geogr. Region. Plan.* 1:138.

Keener, V. (2013). *Climate Change and Pacific Islands: Indicators and Impacts: Report for the 2012 Pacific Islands Regional Climate Assessment*. Washington, DC: Island press.

Kelman, I., and West, J. J. (2009). Climate change and small island developing states: a critical review. *Ecol. Environ. Anthropol.* 5, 1–16.

Kuruppu, N., and Willie, R. (2015). Barriers to reducing climate enhanced disaster risks in Least Developed Country-Small Islands through anticipatory adaptation. *Weather Clim. Extrem.* 7, 72–83. doi: 10.1016/j.wace.2014.06.001

Lang, D. J., Wiek, A., Bergmann, M., Stauffacher, M., Martens, P., Moll, P., et al. (2012). Transdisciplinary research in sustainability science: practice, principles, and challenges. *Sustain. Sci.* 7, 25–43. doi: 10.1007/s11625-011-0149-x

Lata, S., and Nunn, P. (2012). Misperceptions of climate-change risk as barriers to climate-change adaptation: a case study from the Rewa Delta. Fiji. *Clim. Change* 110, 169–186. doi: 10.1007/s10584-011-0062-4

Le Cozannet, G., Nicholls, R. J., Hinkel, J., Sweet, W. V., McInnes, K. L., Van de Wal, R. S., et al. (2017). Sea level change and coastal climate services: the way forward. *J. Mar. Sci. Eng.* 5:49. doi: 10.3390/jmse5040049

Lee, T., Markowitz, E., Howe, P., Ko, C.-Y., and Leiserowitz, A. A. (2015). Predictors of public climate change awareness and risk perception around the world. *Nat. Clim. Change* 5, 1014–1020. doi: 10.1038/nclimate2728

Lemahieu, A., Scott, L., Malherbe, W. S., Mahatante, P. T., Randrianarimanana, J. V., and Aswani, S. (2018). Local perceptions of environmental changes in fishing communities of southwest Madagascar. *Ocean Coast. Manag.* 163, 209–221. doi: 10.1016/j.ocecoaman.2018.06.012

Mallin, M. A. F. (2018). From sea-level rise to seabed grabbing: the political economy of climate change in Kiribati. *Mar. Policy* 97, 244–252. doi: 10.1016/j.marpol.2018.04.021

Martin, P. C. M., Nunn, P., Leon, J., and Tindale, N. (2018). Responding to multiple climate-linked stressors in a remote island context: the example of Yadua Island. *Clim. Risk Manag.* 21, 7–25. doi: 10.1016/j.crm.2018.04.003

Maspataud, A., Le Cozannet, G., Duvat, V., Terorotua, H., Ouriqua, J., and Walker, P. (2018). *INSeaPTION, Workshop Utilisateurs en Polyneisie Francçaise, 22-23 Mars 2018*. Papeete Tahiti:INSeaPTION.

Montreux, C., and Barnett, J. (2009). Climate change, migration and adaptation in Funafuti, Tuvalu. *Glob. Environ. Change* 19, 105–112. doi: 10.1016/j.gloenvcha.2008.09.006

Nicholls, R. J., and Cazenave, A. (2010). Sea-level rise and its impact on coastal zones. *Science* 328, 1517–1520. doi: 10.1126/science.1185782

Nunn, P. D. (2009). Responding to the challenges of climate change in the Pacific Islands: management and technological imperatives. *Clim. Res.* 40, 211–231. doi: 10.3354/cr00806

Nunn, P. D., Aalbersberg, W., Lata, S., and Gwilliam, M. (2014). Beyond the core: community governance for climate-change adaptation in peripheral parts of Pacific Island Countries. *Reg. Environ. Change* 14, 221–235. doi: 10.1007/s10113-013-0486-7

Nurse, L. A., McLean, R. F., Agard, J., Briguglio, L. P., Duvat-Magnan, V., Pelesikoti, N., et al. (2014). "Small islands," in *Climate change 2014: Impacts, Adaptation and Vulnerability. Part B: Regional Aspects. Contribution of Working Group II to the Fifth Assessment Report of the Intergovernmental Panel on Climate Change*, eds V. R. Barros, C. B. Field, D. J. Dokken, M. D. Mastrandrea, K. J. Mach, T. E. Bili, et al. (Cambridge: Cambridge University Press), 1613–1655.

Oppenheimer, M., Glavovic, B., Hinkel, J., van de Wal, R., Magnan, A. K., Abd-Elgawad, A., et al. (2019). "Chapter 4: sea level rise and implications for low lying islands, coasts and communities," in *IPCC Special Report on the Ocean and Cryosphere in a Changing Climate*, eds H. O. Pörtner, D. Roberts, V. Masson-Delmotte, P. Zhai, Y. Tignor, E. Poloczanska, et al. [in press].

Perry, C. T., Alvarez-Filip, L., Graham, N. A., Mumby, P. J., Wilson, S. K., Kench, P. S., et al. (2018). Loss of coral reef growth capacity to track future increases in sea level. *Nature* 558, 396. doi: 10.1038/s41586-018-0194-z

Pondorfer, A. (2019). The perception of climate change: comparative evidence from the small-island societies of Bougainville and Palawan. *Environ. Dev.* 30, 21–34. doi: 10.1016/j.envdev.2019.04.002

Scandurra, G., Romano, A. A., Ronghi, M., and Carfora, A. (2018). On the vulnerability of small island developing states: a dynamic analysis. *Ecol. Indicat.* 84, 382–392. doi: 10.1016/j.ecolind.2017.09.016

Singh, A. S., Zwickle, A., Bruskotter, J. T., and Wilson, R. (2017). The perceived psychological distance of climate change impacts and its influence on support for adaptation policy. *Environ. Sci. Policy* 73, 93–99. doi: 10.1016/j.envsci.2017.04.011

Sinivasan, U. T. (2010). Economics of climate change: risk and responsibility by world region. *Clim. Policy* 10, 298–316. doi: 10.3763/cpol.2009.0652

Smith, E. K., and Mayer, A. (2018). A social trap for the climate? Collective action, trust and climate change risk perception in 35 countries. *Glob. Environ. Change* 49, 140–153. doi: 10.1016/j.gloenvcha.2018.02.014

Stahl, L. (2018). Les défis présents et à venir des plans de prévention des risques naturels polynésiens. *Études caribéennes* 41. doi: 10.4000/etudescaribeennes.13106

Stancioff, C., Stojanov, R., Kelman, I., Nìmec, D., Landa, J., Tichy, R., et al. (2018). Local perceptions of climate change impacts in St. Kitts (Caribbean Sea) and Malé, Maldives (Indian Ocean). *Atmosphere* 9:459. doi: 10.3390/atmos9120459

Storlazzi, C. D., Gingerich, S. B., van Dongeren, A., Cheriton, O. M., Swarzenski, P. W., Quataert, E., et al. (2018). Most atolls will be uninhabitable by the mid-21st century because of sea-level rise exacerbating wave-driven flooding. *Sci. Adv.* 4:eaa9741. doi: 10.1126/sciadv.aap9741

Tompkins, E. L., Adger, W. N., Boyd, E., Nicholson-Cole, S., Weatherhead, K., and Arnell, N. (2010). Observed adaptation to climate change: UK evidence of transition to a well-adapting society. *Glob. Environ. Change* 20, 627–635. doi: 10.1016/j.gloenvcha.2010.05.001

Vaughan, C., Buja, L., Kruczkiewicz, A., and Goddard, L. (2016). Identifying research priorities to advance climate services. *Clim. Serv.* 4, 65–74. doi: 10.1016/j.cliser.2016.11.004

Webber, S. (2017). Circulating climate services: commercializing science for climate change adaptation in Pacific Islands. *Geoforum* 85, 82–91. doi: 10.1016/j.geoforum.2017.07.009

Wetende, E., Olago, D., and Ogara, W. (2018). Perceptions of climate change variability and adaptation strategies on smallholder dairy farming systems: insights from Siaya Sub-County of Western Kenya. *Environ. Dev.* 27, 14–25. doi: 10.1016/j.envdev.2018.08.001

Willis, J. K., and Church, J. A. (2012). Regional sea-level projection. *Science* 336, 550–551. doi: 10.1126/science.1220366

World Meteorological Organization [WMO] (2011). *Climate Knowledge for Action: A Global Framework for Climate Services — Empowering the Most Vulnerable. Report No. 1065*. Geneva: World Meteorological Organization.

Conflict of Interest: HT and JO were employed by company Créocéan.

The remaining authors declare that the research was conducted in the absence of any commercial or financial relationships that could be construed as a potential conflict of interest.

frontiers in Marine Science

ORIGINAL RESEARCH
published: 24 April 2020
doi: 10.3389/fmars.2020.00260

Data-Driven Modeling of Global Storm Surges

M. Tadesse[1], T. Wahl[1] and A. Cid[2]*

[1] Civil, Environmental, and Construction Engineering and National Center for Integrated Coastal Research, University of Central Florida, Orlando, FL, United States, [2] Geomatic and Ocean Engineering Group, Departamento de Ciencias y Técnicas del Agua y del Medio Ambiente, Universidad de Cantabria, Santander, Spain

In many areas, storm surges caused by tropical or extratropical cyclones are the main contributors to critical extreme sea level events. Storm surges can be simulated using numerical models that are based on the underlying physical processes, or by using data-driven models that quantify the relationship between the predictand (storm surge) and relevant predictors (wind speed, mean sea-level pressure, etc.). This study explores the potential of data-driven models to simulate storm surges globally. A multitude of predictors (obtained from remote sensing and climate reanalysis) along with predictands (from tide gage observations and storm surge reanalysis) are utilized to train and validate data-driven models to simulate daily maximum surge for the global coastline. Data-driven models simulate daily maximum surge better in extratropical and sub-tropical regions [average correlation and root-mean-square error (RMSE) of 0.79 and 7.5 cm, respectively], than in the tropics (average correlation and RMSE of 0.45 and 5.3 cm, respectively). For extreme events, the average correlation decreases to 0.54 (0.33) and RMSE increases to 14.5 (13.1) cm for extratropical (tropical) regions. Models forced with remotely sensed predictors showed a slightly better performance (average correlation of 0.69) than models forced with predictors obtained from reanalysis products (average correlation of 0.68). Results also highlight a significant improvement (i.e., average correlation increases from 0.54 to 0.68; RMSE reduces from 11 to 7 cm) over the Global Tide and Surge Reanalysis (GTSR), derived from the only global hydrodynamic model. For approximately 70% of tide gages, mean sea-level pressure is the most important predictor to model daily maximum surge. Our results highlight the added value of data-driven models in the context of simulating storm surges at the global scale, in addition to existing hydrodynamic numerical models.

Keywords: data-driven modeling, machine learning, Random Forest, storm surge, Global Tide and Surge Reanalysis, atmospheric reanalysis, remote-sensing, ERA-Interim

OPEN ACCESS

Edited by:
Goneri Le Cozannet, Bureau de Recherches Géologiques et Minières, France

Reviewed by:
Sanne Muis, Vrije Universiteit Amsterdam, Netherlands
Erwin Lambert, Utrecht University, Netherlands

****Correspondence:***
M. Tadesse
michaelg.tadesse@knights.ucf.edu

Specialty section:
This article was submitted to Coastal Ocean Processes, a section of the journal Frontiers in Marine Science

Received: *16 November 2019*
Accepted: *31 March 2020*
Published: *24 April 2020*

Citation:
Tadesse M, Wahl T and Cid A (2020) Data-Driven Modeling of Global Storm Surges. Front. Mar. Sci. 7:260. doi: 10.3389/fmars.2020.00260

INTRODUCTION

Storm surge is a rise in the coastal water level due to low atmospheric pressure and strong winds (Muis et al., 2016), which could be induced by tropical or extratropical cyclones (Salmun and Molod, 2015), but also modulated by the coastal bathymetry (Pore, 1964). The greatest destruction from tropical cyclones stems from storm surge driven coastal flooding (McInnes et al., 2003) and half of the fatalities owed to Atlantic tropical cyclones are caused by storm surge (Rappaport, 2013).

Many recent examples have demonstrated the vulnerability of coastal populations across the globe to such extreme events, including Hurricanes Katrina in 2005 and Sandy in 2012 in the United States, Cyclone Nargis in 2008 in Myanmar, or the 1970 Bhola Cyclone, which alone caused 300,000 fatalities along the coasts of Pakistan and India (Karim and Mimura, 2008). Storm surges caused by extratropical storms can also lead to high impacts, such as the 1993 storm of the century that affected much of the eastern United States (Thompson et al., 2013), Cyclone Xynthia in 2010 in France (Chadenas et al., 2014), and the North Sea flood in 2013 in northern Europe (Dangendorf et al., 2016).

There are two commonly used and distinct approaches to modeling storm surges, viz. dynamic numerical methods and data-driven methods. Harris (1962) expounded on the difference between the two approaches; the former integrates the governing shallow water equations explaining the underlying physical processes that induce storm surges, whereas the latter quantifies the relationship between predictors (the number of which can vary) and predictands using statistical methods and/or machine learning. Numerical models require high quality bathymetric and topographic data to simulate storm surges, and are computationally expensive. Data-driven approaches, on the other hand, do not divulge the fundamental physical processes involved in storm surge genesis and propagation, but they offer a simple and fast way to simulate storm surges by making efficient use of the data. However, these models rely on availability of historical data of predictors and predictands to identify the relationships between them.

Many studies have been conducted at various spatial scales and with different techniques to model storm surges. For example, Haigh et al. (2014) presented a combined statistical-numerical modeling approach (i.e., statistically simulated tropical cyclones and numerically simulated surges) toward estimating the present-day extreme water level probabilities for the whole coastline of Australia. Due to coarse temporal (6 hourly) and spatial (2.5°) resolution of the model, extreme surge events were underestimated. Muis et al. (2016) presented the first global reanalysis of storm surges, termed Global Tide and Surge Reanalysis (GTSR), based on hydrodynamic modeling, using the Delft3D Flexible Mesh Suite with D-Flow. They reported an root-mean-squared error (RMSE) of less than 0.45 m for 90% of the stations for the 1 in 10-year water level. However, extreme sea levels are highly underestimated in the tropics. Vousdoukas et al. (2016) used a similar model and studied the effect of climate change on extreme storm surge levels along the European coastline by forcing the hydrodynamic model with wind and pressure fields from climate models. For the validation period, they reported RMSE below 0.1 m for most of the Mediterranean, the Atlantic coast, and the Norwegian Sea. Montblanc et al. (2019) demonstrated the implementation and validation of the pan-European storm surge forecasting system (EU-SSF) based on an unstructured hydrodynamic storm surge and tidal model. An average RMSE of below 0.1 m was reported, whereas extreme surge events (>99th percentile) were simulated with lower than 0.25 m RMSE.

In the realm of statistical modeling, Salmun (2009) applied multiple regression analysis to model the maximum storm surge for a given storm at The Battery tide gage, New York. Using statistical-empirical wind-surge formulations, Dangendorf et al. (2014) modeled the relationship between surge, wind, and sea level pressure (SLP) at the German North Sea coast and reported a correlation of 0.91 and RMSE of 13.9 cm for the daily surges at the Cuxhaven tide gage. Wahl and Chambers (2016) implemented simple and multiple linear regression models to investigate the relationship between multidecadal extreme sea level variation and large-scale climate variability along the United States coastline. Cid et al. (2017) applied multiple linear regression to provide a global storm surge database (covering the period from 1871 to 2010) relating mean SLP and gradients from ERA-Interim reanalysis, and using the Twentieth Century Reanalysis (20CR) (Compo et al., 2011) to construct the database. They reported a correlation >0.65 for the majority of the modeling domain, which includes the open ocean. Based on a similar methodology, Cid et al. (2018) reconstructed daily maximum storm surges for the Southeast Asia region from 1866 to 2012. They found correlation of 0.7 or higher for 50% of the tide gages in the region. However, lower model accuracy was found in semi-enclosed areas and around small islands. In addition to statistical methods, models that are based on machine learning are becoming popular due to their low computational cost and efficiency in linking predictor and predictand data. This makes them possible candidates for simulating global storm surges, since significantly more computational time would be required to do the same analysis using dynamical numerical methods. For example, Bezuglov et al. (2016) used artificial neural network (ANN) models to predict storm surges along the North Carolina coastline with a maximum mean squared error (MSE) of 0.0175 m^2 and a minimum correlation coefficient of 0.83. French et al. (2017) combined ANNs with a 2D hydrodynamic model to predict flood extent and damage potential at the Port of Immingham, United Kingdom. The study showed that model performance with ANNs (correlation of 0.94, RMSE of 0.06 m) had higher model accuracy compared to the national numerical tide-surge model (correlation of 0.82, RMSE of 0.09 m).

Here, we explore data-driven modeling approaches (a combination of statistical and machine learning techniques) to simulate global storm surges, using various predictor data sets. Such models can be used to develop long storm surge reanalyses (when validated against long tide gage records) and future projections based on individual climate models, or different model ensembles, something computationally very expensive to implement with numerical storm surge models. Our first objective is to train and validate two data-driven models (statistical and machine learning based) in order to simulate daily maximum storm surge at quasi-global scale. This is achieved by using remotely sensed meteorological and oceanographic variables (as predictors) with observed storm surges (as predictand) from a large number of tide gages distributed along the global coastline. Our second objective is to investigate the difference in performance of the data-driven models when using predictors from remotely sensed or climate reanalysis products. Our third and last objective is to compare and contrast simulation results from the data-driven models with GTSR, derived with a state-of-the-art hydrodynamic global storm

surge model. To allow for a direct comparison, the data-driven models are trained, at this stage, with the same climate reanalysis used for the hydrodynamic modeling.

DATA

Predictors

The data for this study come from several sources. Oceanographic and meteorological predictors used for the first objective are obtained from remotely sensed satellite products, where available. **Table 1** outlines the different data and their respective temporal and spatial resolutions. 10 m wind speed from 1987 onward is acquired from the Cross-Calibrated Multi-Platform (CCMP) wind vector analysis product with a spatial resolution of 0.25 × 0.25 degrees and a temporal resolution of 6 h (Atlas et al., 2011). Daily global sea surface temperature (SST) from 1998 onward with a 0.25 × 0.25 degree spatial resolution is obtained from the microwave optimally interpolated SST product. Daily global precipitation from 1996 to 2015 with a 1 × 1 degree spatial resolution is acquired from the Global Precipitation Climatology Product (GPCP) (Huffman and Adler, 2001). SLP from 1871 to 2014 with 6 hourly temporal and 1 × 1 degree spatial resolution is obtained from the 20CRV2c (Poli et al., 2016). This predictor is obtained from a climate reanalysis since there is no global remote sensing product available for SLP. Furthermore, Cid et al. (2017) showed that the minimum SLP values during storms are more noticeable in 20CR than in ERA-Interim. For the second and third objective, 10 m wind speed and SLP data with a spatial resolution of 0.75 × 0.75 degrees and 6 hourly temporal resolution from the ERA-Interim reanalysis (Dee et al., 2011) are used as predictors.

Predictands

Daily maximum surge is used as the predictand and derived from two different data sets. Observed sea level data for individual tide gages is obtained from the Global Extreme Sea Level Analysis (GESLA-2) database (Woodworth et al., 2017) and used to extract the daily maximum surge values (see section "Methodology"). The spatial distribution of the tide gages and available years of data during the 1979–2014 period are shown in **Figure 1**. In addition to *in situ* data, daily maximum surge values for the global coastline are obtained from GTSR (Muis et al., 2016). The data set (covering the period 1979–2014) is a near-coast global reanalysis of storm surges. It is obtained by forcing a hydrodynamic model, the Global Tide and Surge Model (GTSM) based on the Delft3D modeling suite, with wind speed and atmospheric pressure from the ERA-Interim reanalysis. Model outputs are provided in 16,395 locations along the global coastline. In order to compare the performance of the data-driven models with the hydrodynamic model, the closest GTSR grid points (out of the 16,395 locations) for each tide gage are identified and daily maximum surge values at those specific grid points are extracted. These values are then compared with daily maximum surge derived from the data-driven models and observed daily maximum surge.

METHODOLOGY

Harmonic Analysis

Hourly sea level time series from the tide gages are de-trended by removing the annual mean sea level (**Figure 2**). Following this, the T_Tide Matlab package (Pawlowicz et al., 2002) is used to perform a classical harmonic analysis with 67 tidal constituents on a year-by-year basis. Predicted astronomical tides are subtracted from the de-trended sea level time series to separate non-tidal residuals. The UTide (Unified Tidal Analysis and Prediction Functions) (Codiga, 2011) package has also been tested with negligible differences in the results. Non-tidal residuals, considered in this study as storm surges, are used as predictands when developing and implementing the statistical and machine learning techniques outlined below. In some instances erroneous spikes were detected (and removed) from the storm surge time series, resulting from phase shifts between the predicted tide and observed water levels (see also section "Directions for Future Research"). The effects of waves are not included in the analysis.

Predictor Selection

After identifying the daily maximum surge values for each tide gage, we localize meteorological and oceanographic predictors around each tide gage. Predictors within a 10 × 10 degree grid around the tide gages are considered for the analysis. In order to reduce the complexity of the models and the multicollinearity of predictor features, principal component analysis (PCA) is implemented (as in Cid et al., 2017, 2018). PCA is a multivariate analysis technique that reduces the dimensionality of a data set comprised of interrelated variables, while preserving the largest possible fraction of variability (Jolliffe, 2002). PCA transforms the original data to a new set of variables commonly known as principal components (PCs), which are uncorrelated and are sorted by how much of the variance in the original dataset is explained by each PC. Data from every grid point within the 10 × 10 degrees region around each tide gage are considered as predictors. Hence, the total number of predictors can get as high as 5,000. In order to reduce the large dimension, the PCs that explain 90% of the variance in the original data are selected for further analysis. This reduces the number of predictors to about 300–500. We also tested using all PCs that explain 95% of the variance. This did not improve the model performance, but adds more predictors and hence (unnecessary) model complexity.

Model Fitting

The first technique we test is based on multiple linear regression and we follow a stepwise procedure where we iteratively add or remove PCs of the respective predictors, only retaining those that provide significant information ($p < 0.05$). This reduces the complexity of the model while giving the best result possible. The daily maximum surge at a specific tide gage is then computed with the following equation:

$$\text{Surge}\,(t, d) = a + \sum_{i=1}^{N}\sum_{j=1}^{M} b_{ij} \times PC_{ij}(t,\ d)$$

TABLE 1 | Description of implemented data-driven models.

Model type	Model ID	Predictors	Source	Spatial scale	Temporal scale	Number of predictors	Simulation period	Time-lagged
Linear regression	LR-RS[1]	Wind speed (U, U^2, U^3, V, V^2, V^3)[2]	CCMP[3]	0.25° × 0.25°	Daily maximum	~50	1998–2014	X
		Mean sea level pressure (SLP)	20CRV2c[4]	2° × 2°	Daily minimum			
		Sea surface temperature (SST)	MW OI[5]	0.25° × 0.25°	Daily maximum			
		Precipitation (GPCP)	GPCP[6]	1° × 1°	Daily accumulated			
	LR-RS-lag	Wind speed (U, U^2, U^3, V, V^2, V^3)	CCMP	0.25° × 0.25°	6 hourly	~300		✓
		Mean sea level pressure (SLP)	20CRV2c	2° × 2°				✓
		Sea surface temperature (SST)	MW OI	0.25° × 0.25°	Daily maximum			X
		Precipitation (GPCP)	GPCP	1° × 1°	Daily accumulated			X
Random Forest	RF-RS-lag[7]	Wind speed (U, U^2, U^3, V, V^2, V^3)	CCMP	0.25° × 0.25°	6 hourly	~300		✓
		Mean sea level pressure (SLP)	20CRV2c	2° × 2°				✓
		Sea surface temperature (SST)	MW OI	0.25° × 0.25°	Daily maximum			X
		Precipitation (GPCP)	GPCP	1° × 1°	Daily accumulated			X
Linear regression	LR-AR[8]	Wind speed (U, U^2, U^3, V, V^2, V^3)	ERA-Interim	0.75° × 0.75°	Daily maximum	~50	1979–2014	X
		Mean sea level pressure (SLP)			Daily minimum			
	LR-AR-lag	Wind speed (U, U^2, U^3, V, V^2, V^3)			6 hourly	~300		✓
		Mean sea level pressure (SLP)						
Random Forest	RF-AR-lag[9]	Wind speed (U, U^2, U^3, V, V^2, V^3)						
		Mean sea level pressure (SLP)						

[1] *Linear regression model with remotely sensed predictors.*
[2] *Zonal (U) and meridional (V) wind speed; linear, quadratic, and cubic terms.*
[3] *Cross-Calibrated Multi-Platform gridded surface vector winds.*
[4] *Twentieth century reanalysis version 2c.*
[5] *Microwave optimally interpolated sea surface temperature product.*
[6] *Global Precipitation Climatology Project.*
[7] *Random Forest model with remotely sensed predictors.*
[8] *Linear regression model with atmospheric reanalysis predictors.*
[9] *Random Forest model with atmospheric reanalysis predictors.*

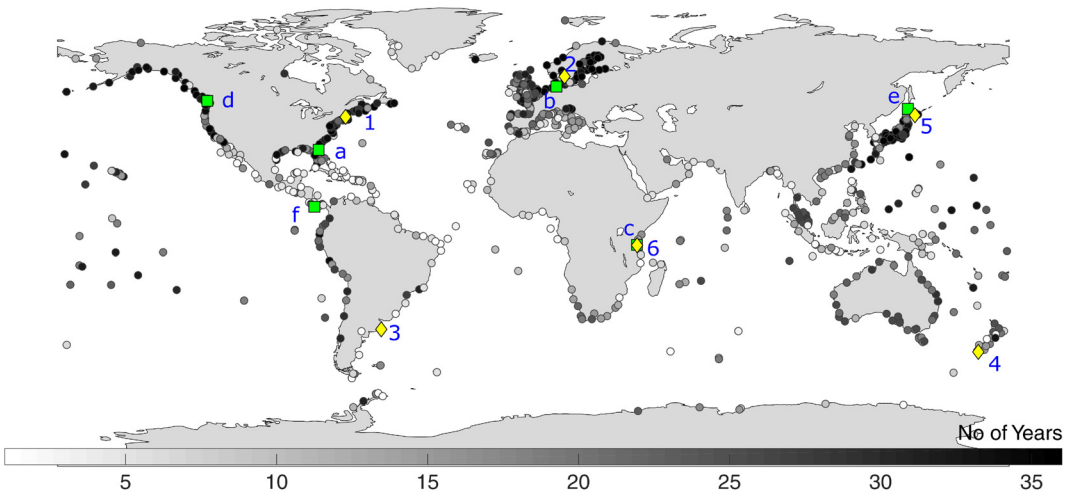

FIGURE 1 | Number of years available for analysis during the 1979–2014 period. Green squares and yellow diamonds represent two sets of tide gages used in section "Results" to assess model performance in more detail: (a) St. Augustine, (b) Cuxhaven, (c, 6) Zanzibar (d) Victoria Harbor, (e) Wakkanai (f), Puerto Armuelles, (1) Boston, (2) Goteborg-Torshamnen, (3) Mar del Plata, (4) Bluff Harbor, and (5) Kushiro.

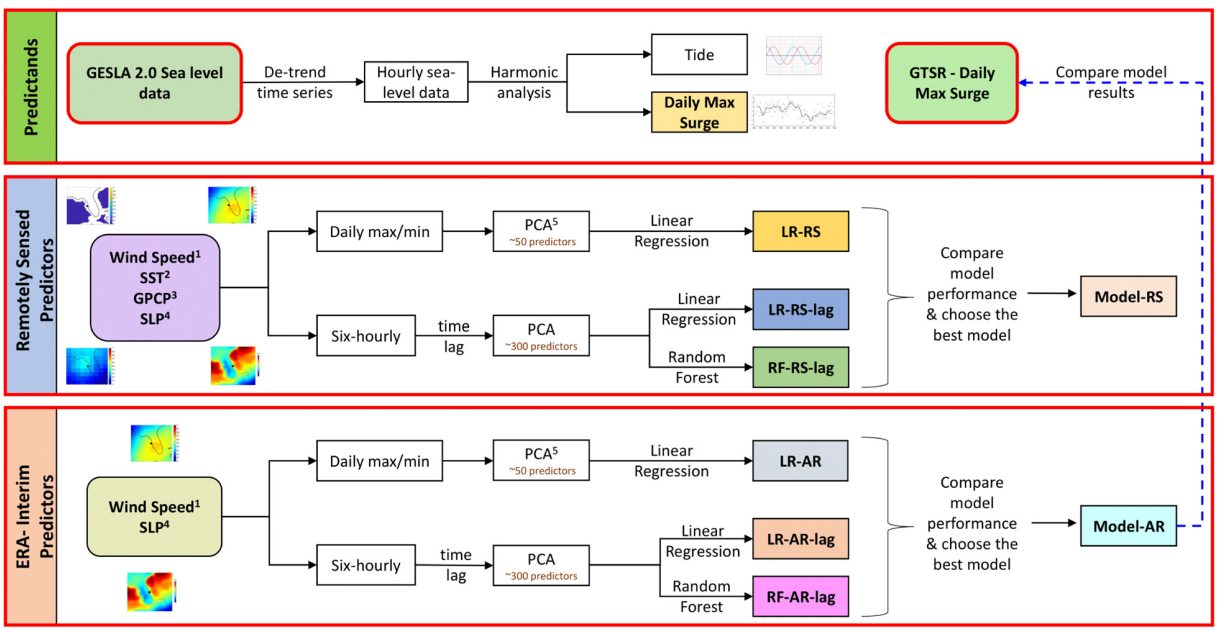

FIGURE 2 | Framework outlining the applied methodology to develop data driven storm surge models using different predictor data sets, and comparison with numerical model output. Key: wind speed1, zonal and meridional wind speed; SST2, sea surface temperature; GPCP3, Global Precipitation Climatology Project; SLP4, mean sea-level pressure; PCA5, principal component analysis.

where Surge (t, d) is the maximum surge on day d at the t-th tide gage, PC_{ij} (t, d) represents the j-th PC of the i-th predictor on day d, whereas N and M represent the total number of predictors and their corresponding number of PCs, respectively. a and b_{ij} are coefficients obtained from the regression model.

The second technique we implement and test is based on Random Forest, a supervised machine learning algorithm which incorporates the concepts of classification and regression trees, and bagging (where the model is trained using bootstrap samples of original predictor data) with some additional degree of randomization (see for example, Tyralis et al., 2019 for a detailed review of Random Forests). This study requires the implementation of Random Forest regression. The prediction of each trained regression tree is then averaged to provide a single value (here, the value of daily maximum surge at a tide gage location). Random Forests are (1) capable of capturing the non-linear dependencies between predictors

and predictands, (2) fast and easy to use, (3) not prone to overfitting, and (4) suitable for high dimensional data (Tyralis et al., 2019). A sensitivity analysis is carried out to select the optimal number of regression trees for our analysis, based on the out-of-bag error, where the MSE for samples outside the bootstrapping set is quantified and minimized. For each tide gage, the out-of-bag error is computed for several numbers of bagged trees (1–200). This error is then normalized in order to compare results across tide gages (**Figure 3**). Considering the out-of-bag error behavior and the increased computational expense with an increased number of trees, we chose 50 as the optimal number for our analysis; beyond that the reduction in error is small, while the computational expense increases.

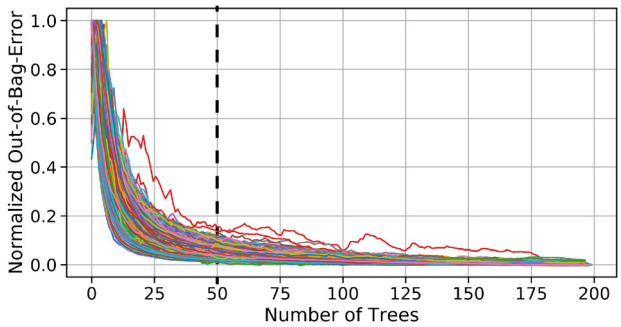

FIGURE 3 | Sensitivity analysis to find the optimal number of decision trees: the relationship between the number of decision trees and the standardized out-of-bag-error. Each line represents the decrement of the standardized-out-of-bag-error of a tide gage with increase in the number of trees.

Model Configuration

Six different model configurations (see **Table 1**) are set up by varying the inputs (predictor types, either remotely sensed or atmospheric reanalysis) and their temporal resolution (daily and 6 hourly). Model IDs starting with LR represent model configurations that use linear regression to fit the model, whereas model IDs starting with RF represent model configurations that use Random Forest. Models trained with remotely sensed predictors have the suffix "RS" attached to the model ID. For instance, LR-RS is the model ID that represents models that use linear regression trained with remotely sensed predictors. On the other hand, the suffix "AR" is used to represent models trained with atmospheric reanalysis, particularly ERA-Interim reanalysis. For instance, RF-AR represents the Random Forest model trained with atmospheric reanalysis. We trained models with atmospheric reanalysis datasets for two reasons: the first one is to investigate the influence of the two types of predictors (from remote sensing and from reanalysis), on model accuracy. The second one is to compare the performance of the data-driven models with model outputs from GTSR, which is based on a hydrodynamic model and also uses ERA-Interim as forcing. As remotely sensed mean sea-level pressure is not available, models trained with remotely sensed predictors use mean sea-level pressure from 20CR. The period in which all the remotely sensed predictors overlap, and hence models are developed and tested, ranges from 1998 to 2014. Models trained with atmospheric reanalysis have a simulation period from 1979 to 2014.

In order to investigate the delay effects of predictors on daily maximum surge, predictors are lagged as far back as 30 h from the time the daily maximum surge occurred (i.e., predictors between the time of surge occurrence and

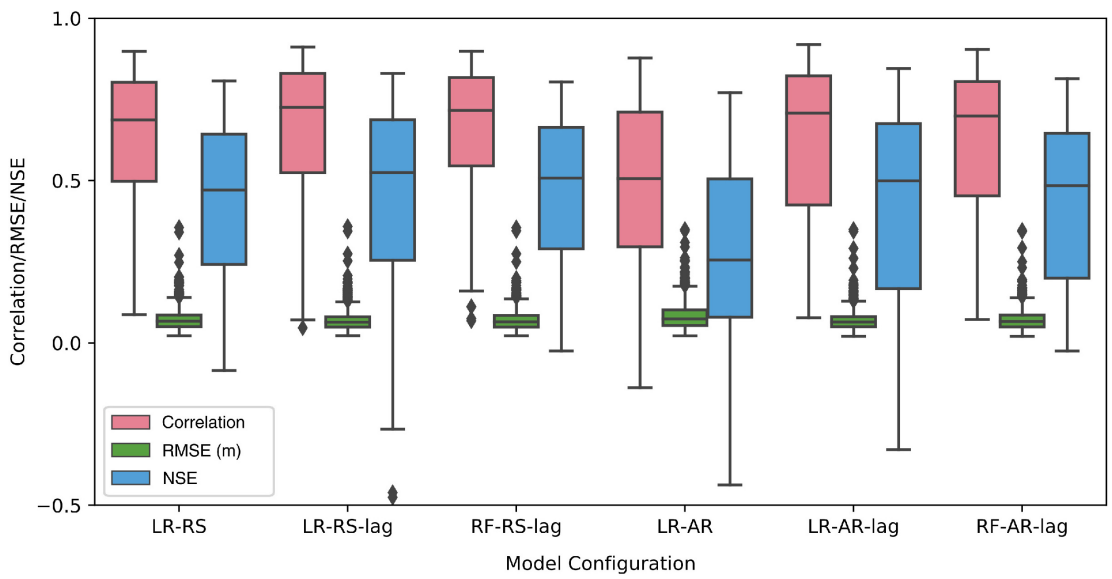

FIGURE 4 | Validation of the six model configurations (LR-RS, LR-RS-lag, RF-RS-lag, LR-AR, LR-AR-lag, and RF-AR-lag) in terms of correlation coefficient, RMSE, and NSE.

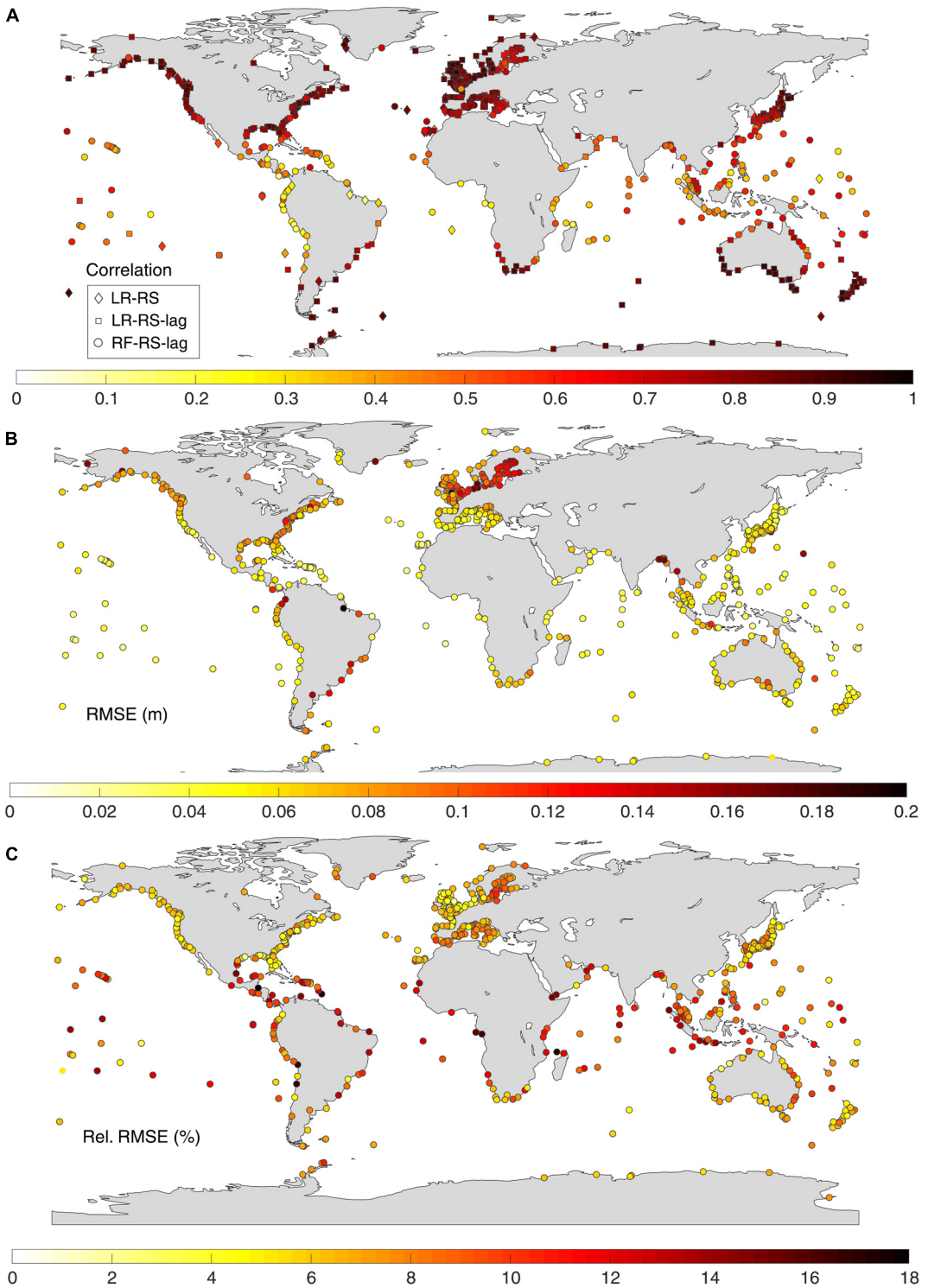

FIGURE 5 | Validation of Model RS in terms of **(A)** Pearson's correlation coefficient – diamonds, rectangles, and squares represent the three model configurations (LR-RS, LR-RS-lag, and RF-RS-lag) that make up Model-RS; **(B)** RMSE in m; and **(C)** relative RMSE in %.

30 h before are all used in the regression models). For instance, LR-AR-lag represents the linear regression model that was trained with atmospheric reanalysis predictors that are lagged up to 30 h. Similarly, RF-RS-lag represents the Random Forest model trained with remotely sensed predictors that are lagged up to 30 h. Model IDs without the suffix

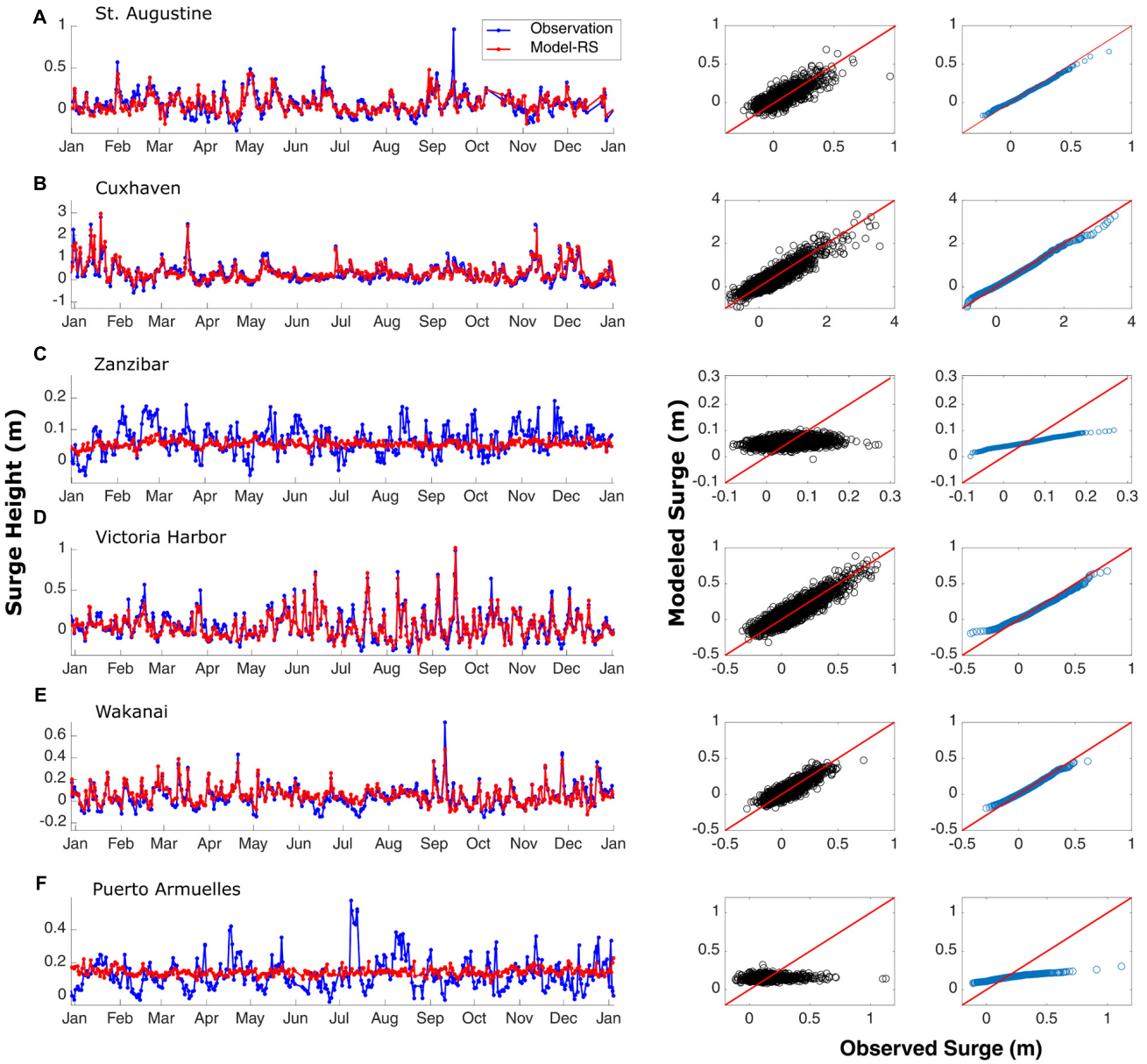

FIGURE 6 | Daily maximum surge time series comparison **(left)**, scatter plots **(middle)**, and quantile-quantile plots **(right)** for observed and modeled (Model-RS) daily maximum surge for six tide gage locations (marked in green in **Figure 1**).

"lag" represent models that are trained with predictors of daily temporal resolution. Hence, for each predictor type (remotely sensed and atmospheric reanalysis), there are three model configurations (see **Table 1**). Each of these three model configurations is evaluated by different performance metrics (see section "Model Validation") and the model configuration that gives the highest performance metrics is chosen as the best model configuration for a given tide gage. For ease of interpretation, the collection of the best model configurations under the remotely sensed category is named as Model-RS. Similarly, the collection of the best model configurations under the atmospheric reanalysis category is named Model-AR.

Model Validation

Based on the data availability, we consider 732 tide gages for calibration/validation of Model-RS (using predictor information from remote sensing) and 840 tide gages for Model-AR (using predictor information from ERA-Interim). The models are validated using k-fold cross-validation. We follow Kohavi (1995) in selecting k = 10-folds. The validation process starts by randomly dividing the data set into k approximately equal groups,

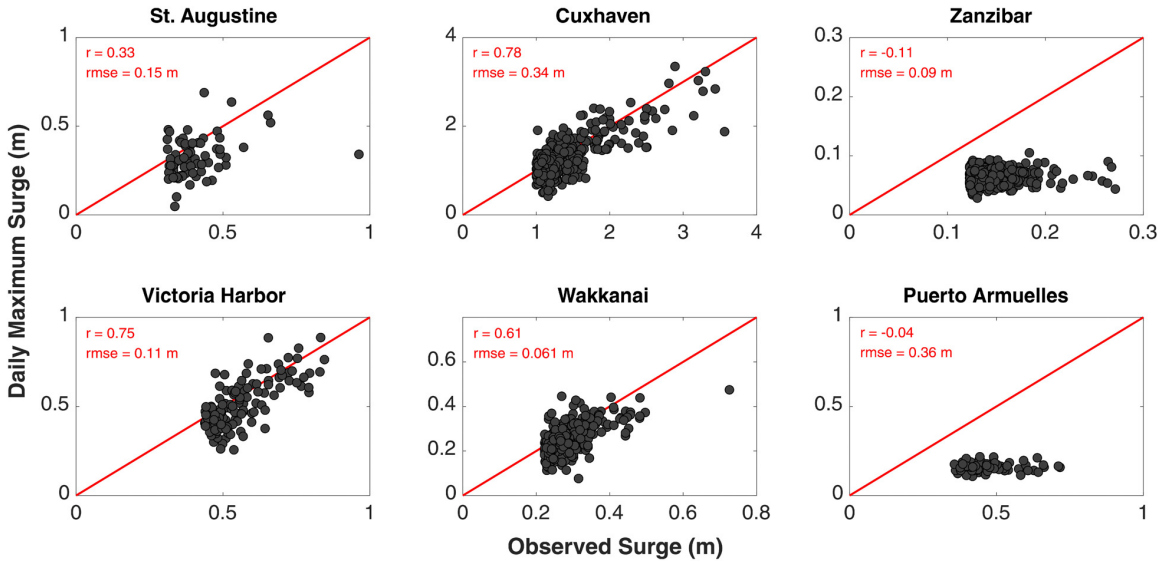

FIGURE 7 | Validation of Model-RS performance for extreme events (surge values above the 95th percentile threshold).

or folds. The model parameters are then estimated from using $k-1$ groups while the remaining group is used to test the model performance. Finally, the full time series can be reconstructed once all groups have been used for testing. We use the observed and reconstructed time series to compute three commonly used error statistics: Pearson's correlation coefficient, Nash-Sutcliffe efficiency (NSE), and RMSE. One shortcoming inherent to the Pearson's correlation coefficient (r) is that it only measures the strength of the relationship between the compared datasets, i.e., it does not indicate how similar the magnitudes of the compared time series are RMSE. On the other hand, quantifies the bias between the compared time series, but it is not a dimensionless metric. As a result, the modified Mielke index was proposed by Duveiller et al. (2016) as a combination of r and RMSE. We also derived this index (ranging from 0 for no agreement to 1 for perfect agreement) in addition to the three other metrics outlined above (results for the modified Mielke index are shown in the **Supplementary Material**).

We also test the sensitivity of the model results to the availability of tide gage data, by shortening the available tide gage records (until only one year of data is left for training and testing) and performing the same validation as outlined above.

RESULTS

Model-RS – Models Forced With Remotely Sensed Predictors

This model category consists of three configurations, viz. LR-RS, LR-RS-lag, and RF-RS-lag (see **Table 1**). All three are trained and validated for 732 tide gages and results are compared with corresponding observed daily maximum surge values. For any given tide gage, the model configuration that gives the best error statistics in terms of Pearson's correlation, RMSE, and NSE is selected for that specific tide gage (note that in all cases at least two of the error statistics pointed to the same best model configuration). In addition, the model was validated by the modified Mielke index and the results (very similar to the Pearson's correlation coefficient) are shown in **Supplementary Figure 1**. On average, across all tide gages, we find that models LR-RS-lag and RF-RS-lag perform better than LR-RS (**Figure 4**; the same results but for tropical and extra-tropical regions separately are shown in **Supplementary Figure 2**); they are also selected at many more sites than LR-RS (**Figure 5**). LR-RS, which is forced with predictors of daily temporal resolution, gives the best eror statistics (highest correlation coefficient, highest NSE, and lowest RMSE) for only 12% of the tide gages (shown by diamonds in **Figure 5A**). The average correlation coefficient and RMSE are 0.64 and 7.8 cm, respectively. LR-RS-lag, which is forced with lagged predictors with 6 hourly temporal resolution, gives the best error statistics for most of the tide gages, 58% in total. The average correlation coefficient is 0.78 and average RMSE is 7.3 cm. This model configuration is effective mostly in subtropical/extratropical regions (shown by squares in **Figure 5A**; see also **Supplementary Figure 8** for model performance across different latitude bands). RF-RS-lag gives the best error statistics for tide gages around the tropical region (the remainder 30% of sites, shown by circles in **Figure 5A**) with an average correlation coefficient of 0.5 and average RMSE of 5.7 cm. Higher correlation coefficients (as high as 0.9) are found in extratropical regions (30–60° north and south of the equator), whereas the tropical and sub-tropical regions (0–30° north and south of the equator) show lower correlation, especially along the west and north coasts of South America. The average correlation coefficient in the extratropical regions is 0.79, whereas in the tropical regions it drops to 0.45. The average RMSE in the extratropical regions is 7.5 cm, and 5.3 cm in tropical regions. These results match the ones that are reported by Cid et al.

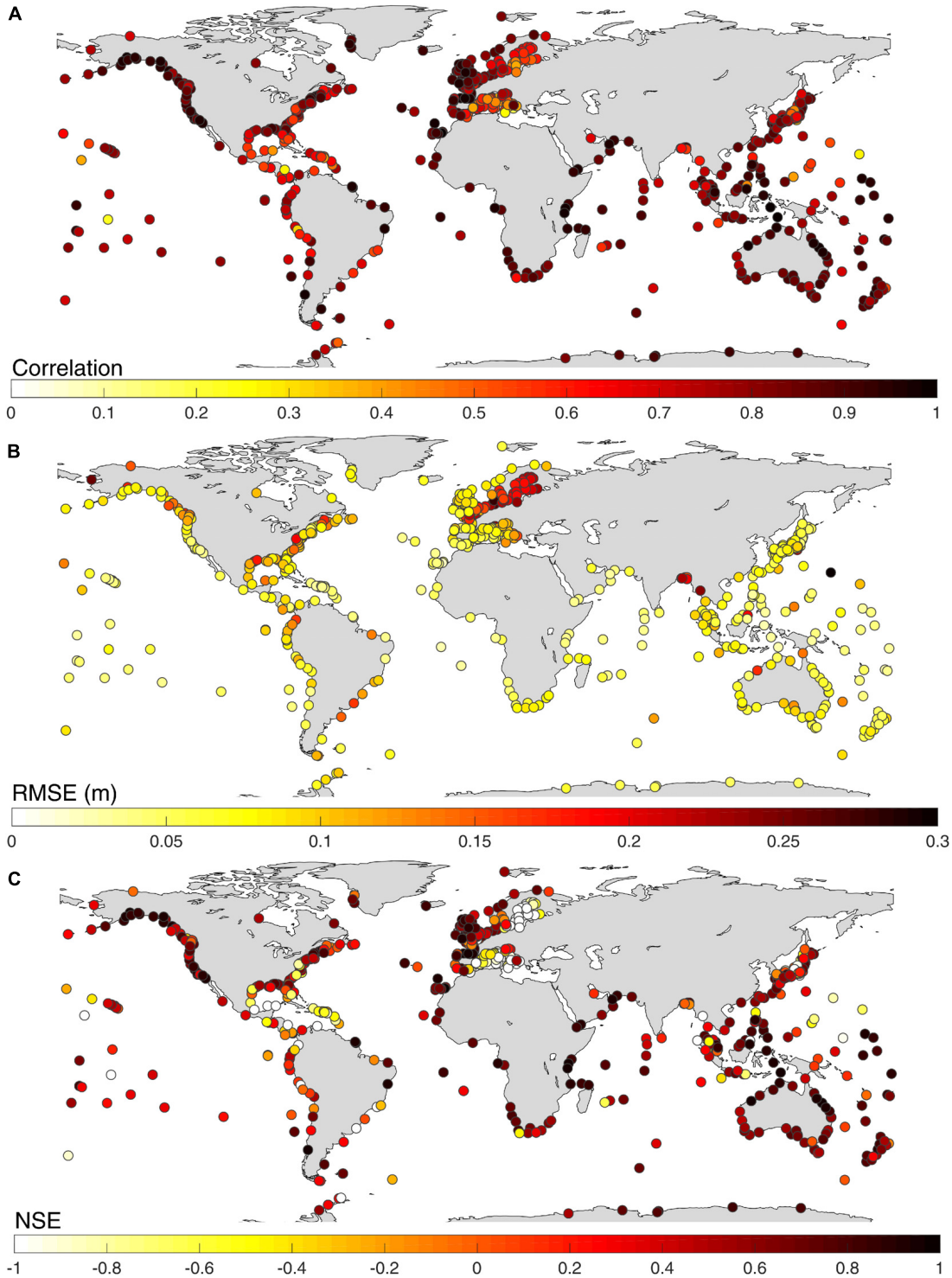

FIGURE 8 | Validation of Model-RS for total still water levels above the 95th percentile threshold: **(A)** Pearson's correlation coefficient; **(B)** RMSE in m; and **(C)** NSE.

(2017), where average correlation in the extratropical and tropical regions are in the order of 0.8 and 0.5, respectively. In addition, **Figure 5C** displays the relative RMSE, which is the ratio of RMSE to the maximum surge variability at each tide gage (difference between highest and smallest daily maximum surge). In tropical regions, the relative RMSE is higher (up to 18%) compared to the extratropical regions. This value is also comparable with the one reported by Cid et al. (2017), which is 20%.

Model accuracy of LR-RS is lower than that of LR-RS-lag and RF-RS-lag as it is relating daily min/max values of predictors with daily maximum surge. However, the daily maximum surge on a given day may also be affected by oceanographic and atmospheric conditions from previous days. The lower model accuracy for the tropical regions could be due to several reasons. First, historical time series analysis of the predictors shows that the variance of the most important predictors, wind speed and SLP, in tropical/sub-tropical regions are very low compared to extratropical regions (**Supplementary Figure 3**). Second, for some tide gages in the tropics (e.g., Santana, Brazil), river discharge may affect the tide gage measurements, adding additional non-tidal residuals that cannot be explained by the local predictors (the same mechanism would have a smaller effect in higher latitudes, where storm surges are relatively higher); rainfall may serve as a proxy to capture some of the discharge, but not when it is remotely driven (e.g., rainfall further upstream, or discharge from snow melt). Third, the predictors that explain tropical cyclone induced surges (for instance at the Bay of Bengal) are not captured well due to low temporal and spatial resolution.

Additional validation of Model-RS is shown in **Figure 6**. Six tide gages (marked as green squares in **Figure 1**), are chosen from different climatic regions to assess model performance for a specific year (2007) by comparing observed and simulated daily maximum surge time series (**Figure 6**, left), scatter plots (**Figure 6**, middle), and quantile–quantile plots (**Figure 6**, right). For tide gages in sub-tropical and extratropical regions (St. Augustine, Cuxhaven, Victoria Harbor, and Wakkanai), the daily maximum surge is relatively well reproduced with minimum and maximum correlation of 0.79 and 0.91, respectively; in some cases lowest surges are overestimated and highest surges are slightly underestimated. However, for tide gages in tropical regions (Zanzibar and Puerto Armuelles), the daily maximum surge is strongly underestimated.

Figure 7 displays the performance of Model-RS in capturing extreme surge events. Observed surge values above the 95th percentile threshold of the daily maximum surge are selected for the same tide gages shown in **Figure 6**, and compared to corresponding surges derived from Model-RS. Again, model performance increases from low to high latitudes. Extreme surge events are better reproduced at Cuxhaven (r = 0.78), Victoria Harbor (r = 0.75), and Wakkanai (r = 0.61), compared to Zanzibar (r = −0.11) and Puerto Armuelles (r = −0.04) in the tropics, where the model strongly underestimates the extreme surge events (all modeled surge values are below the 1:1 reference line). Validation of Model-RS for extreme surges globally (**Supplementary Figure 7**) leads to an average correlation of 0.54 and an average RMSE of 14.5 cm in extratropical regions, whereas in the tropics the average correlation is 0.32 and average RMSE is 13.1 cm.

Finally, extreme total still water levels (here, defined as events above the 95th percentile threshold) are calculated by superimposing the corresponding daily maximum surge and tide values for each tide gage. The observed and modeled total still water levels have very strong agreement at the vast majority of the tide gages [**Figures 8** and **Supplementary Figure 8** (right)]; the average correlation coefficient is 0.74 and average RMSE is 9.4 cm. This overall improvement is to be expected, as the tidal component is the same in both the observed and modeled datasets. Tide gages in the Gulf of Mexico, the Mediterranean Sea, and the Baltic Sea have slightly lower correlation. The total still water level (at the time of daily maximum surge) at these locations is dominated by the surge while tidal contributions are small, or even negligible. Surges at these locations are, however, also simulated with relatively lower accuracy compared to other locations (**Figure 5C**), which in turn propagates to the total still water level results presented here.

The relative importance of predictors in Model-RS is also investigated. Since two model fitting techniques are used (linear regression and Random Forest), the predictor importance is assessed for both methods separately. For the linear regression method, important predictors would have relatively higher regression coefficients. The level of importance of all predictors across all tide gages according to the linear regression and Random Forest models are shown in **Figure 9**. For the Random Forest method (pertaining to RF-RS-lag), the values of each predictor are randomly reordered (permuted) and the change in the accuracy of Model-RS is measured in terms of MSE. A predictor that, when randomly reordered, affects the accuracy of RF-RS-lag significantly is considered an important predictor. Therefore, predictors in **Figure 9** are ranked based on how much they can modify results of Model-RS. For linear regression, it is found that mean sea-level pressure is the most important predictor for 77% of the tide gages, followed by daily accumulated precipitation (16%), and meridional wind speed (3%). Whereas the Random Forest analysis shows that mean sea-level pressure is the most important predictor for about 65% of the tide gages, followed by meridional wind speed (12%), and SST (10%). Overall, both models (linear regression and Random Forest) point to mean sea-level pressure and its time-lagged components as the most important predictors to model daily maximum surge at the majority of the tide gages.

Model-AR – Models Forced With Predictors From ERA-Interim Reanalysis

Under this category, three model configurations (LR-AR, LR-AR-lag, and RF-AR-lag) are forced with wind speed and SLP from the ERA-Interim reanalysis. This is done for two main purposes: (1) to investigate the added value (if any) of using remotely sensed predictors, (as in Model-RS) as compared to atmospheric reanalysis data, and (2) to compare the performance of the data-driven model with GTSR. Model configurations under this category, LR-AR, LR-AR-lag, and RF-AR-lag give the best error statistics for 4, 62, and 34% of the tide gages, respectively. Average correlation coefficients for the three model configurations are 0.39, 0.77, and 0.46, whereas average RMSE values are 7.7, 7.6, and 5.6 cm, respectively. As in the case of Model-RS, LR-AR-lag gives the best results for tide gages in the sub-tropical/extratropical regions. **Figure 10** displays the validation of Model-AR in terms of Pearson's correlation coefficient, RMSE, and relative RMSE. Further validation results pertaining to Model-AR are

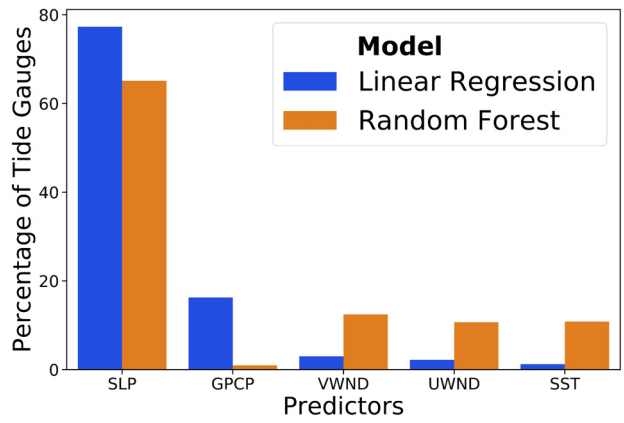

FIGURE 9 | Percentage of the number of tide gages where individual predictors are deemed most relevant (see text for more details) for Model-RS for stepwise regression and Random Forest; VWND and UWND are zonal and meridional wind speeds.

shown in **Supplementary Figures 4–6**. Similar to Model-RS, the daily maximum surge from these model configurations shows strong agreement with observed daily maximum surge in the sub-tropical/extratropical regions, where the average correlation coefficient is 0.75. This value drops to 0.42 in the tropical regions for the same reasons explained in section "Model-RS – Models Forced With Remotely Sensed Predictors". Average RMSE is 7.8 and 5.5 cm in the sub-tropical/extratropical and tropical regions, respectively. The highest relative RMSE is found in the tropics (reaching up to 18% of the daily maximum surge variability). LR-RS performs better in all three performance statistics compared to LR-AR (see **Figure 4**). In addition, LR-RS-lag and RF-RS-lag are also performing slightly better than LR-AR-lag and RF-AR-lag. When choosing the best model configuration for Model-RS and Model-AR the mean correlation coefficients are 0.68 and 0.65, respectively, whereas the mean RMSE values are 6.9 and 7 cm. It has to be noted that the spatial resolution of the wind speed used for Model-RS is three times higher than that of the reanalysis wind speed (see **Table 1**). However, the spatial resolution of the SLP in Model-RS (coming from 20CRV2c, as no remote sensing product is available) is approximately three times coarser than the one used for Model-AR.

We also used this model setup to test the sensitivity of model accuracy with respect to data availability and found that as little as 5 years of data is required to achieve good model accuracy and further increase in data availability does not improve model accuracy (see **Supplementary Figure 9**).

Comparison With GTSR

As described in section "Data", the GTSR grid points closest to the tide gages are identified and the daily maximum surge time series at these grid points are extracted for the 1979–2014 period. The surge values from GTSR are then compared with observed values (for the overlapping periods) and are validated using Pearson's correlation coefficient and RMSE. Average correlation and RMSE are 0.54 and 11.2 cm, respectively. For sub-tropical/extratropical regions, average correlation and RMSE are 0.65 and 11 cm, whereas for tropical regions average correlation and RMSE are 0.28 and 13 cm, respectively. The direct comparison of performance between Model-AR and GTSR (both forced with ERA Interim reanalysis data) is shown in **Figure 11**.

Figure 11A displays the spatial differences in correlation between GTSR and Model-AR, i.e., comparing correlation coefficients for Model-AR vs observations and correlation coefficients for GTSR vs observations. The Fisher's Z transformation method is used to assess significance of the difference between the two correlation coefficients. For a large percentage (92%) of the tide gages, there is a significant difference between the two correlation coefficients (Model-AR and GTSR have no significant difference in correlation for tide gages marked by blue stars in **Figure 11A**). and for 88% of these tide gages Model-AR has higher correlation coefficients than GTSR. Similarly, the RMSE for both models vs observations is computed and is found to be lower for Model-AR at all tide gages (**Figure 11B**).

Figure 12 illustrates a comparison of daily maximum surge time series and scatter plots from Model-AR, GTSR, and observations. Model results for six tide gages, which are also shown in Muis et al. (2016) and marked as yellow diamonds in **Figure 1**, are chosen for illustration. Both Model-AR and GTSR reproduce the observed surges well in locations such as Goteborg and Kushiro. However, Model-AR simulates the surge events better than GTSR at Mar del Plata (GTSR underestimates), Bluff Harbor (GTSR overestimates), and at many other tide gages not shown here. However, both models fail to simulate the daily maximum surge at Zanzibar, owing to very little variance of predictors that cannot explain the variation in the predictand. In order to test the performance of the two models for extreme events, observed surge values above the 95th percentile threshold are compared with their corresponding Model-AR and GTSR values in **Figure 13**, including scatter plots (left) and quantile–quantile plots (right). Differences in model performance for extreme events are most evident for Boston and Mar del Plata, where GTSR underestimates the surge values, and at Bluff Harbor, where GTSR overestimates the extreme surge values. Both models perform poorly for Zanzibar.

Concerning extreme storm surges, Model-AR has an average correlation of 0.51 and 0.29 in extratropical and tropical regions, respectively. For GTSR correlation is lower, 0.44 and 0.20. Model-AR has an average RMSE of 15 and 13 cm in extratropical and tropical regions. For GTSR RMSE is higher, 23 and 19 cm. Model results are also validated for specific extreme events. Three tropical/extratropical events (Superstorm Sandy, Cyclone Xaver, and Hurricane Katrina) are selected to test the performance of the three models: Model-RS, Model-AR, and GTSR. Three tide gages are chosen for each event as shown in **Figure 14**. Model-RS and Model-AR show similar results for all cases, whereas

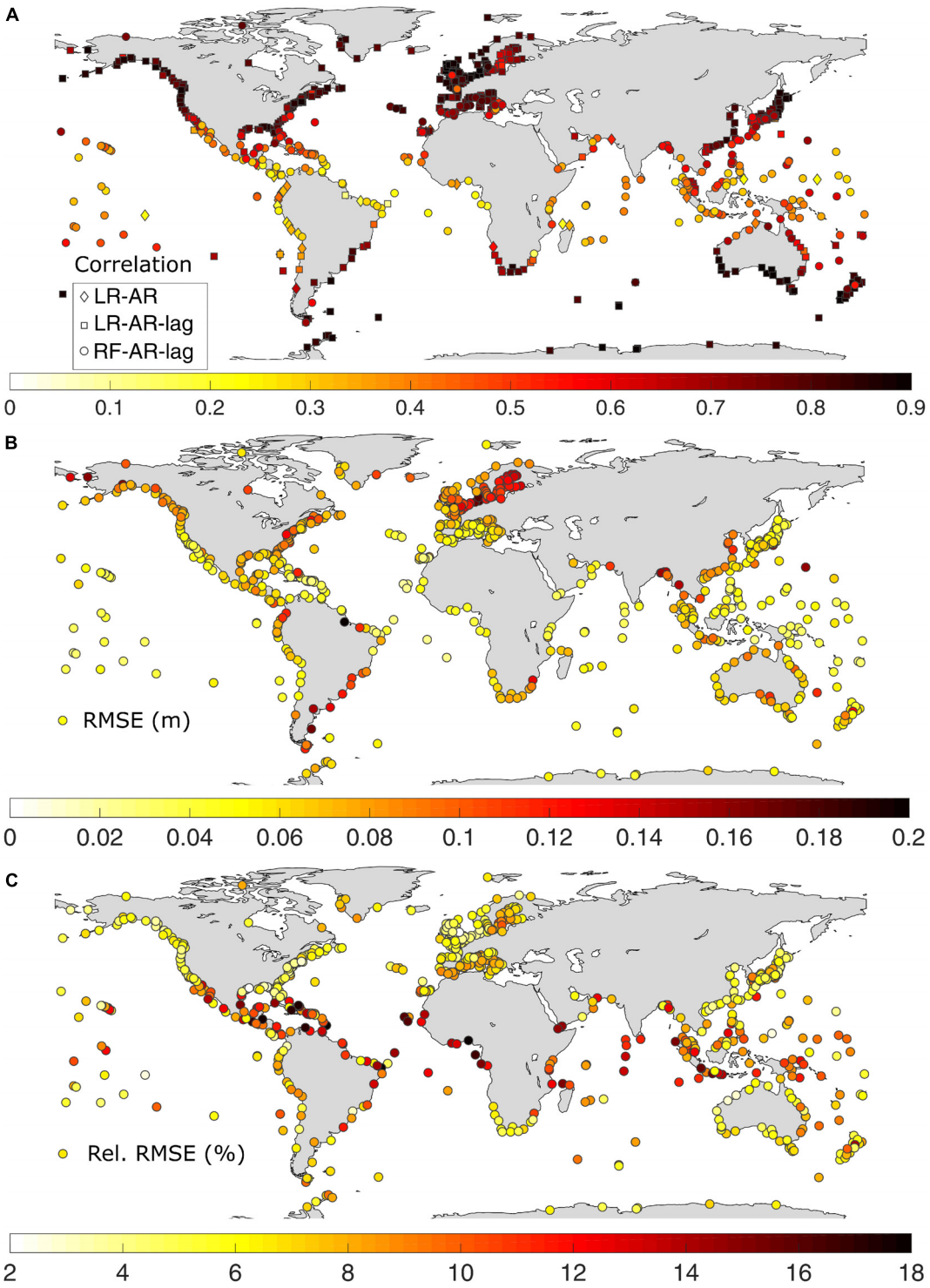

FIGURE 10 | Validation of modeled (Model-AR) daily maximum surge in terms of **(A)** Pearson's correlation coefficient – diamonds, rectangles, and squares represent the three sub-models (LR-AR, LR-AR-lag, and RF-AR-lag) that make up Model-AR; **(B)** RMSE in m; and **(C)** relative RMSE in %.

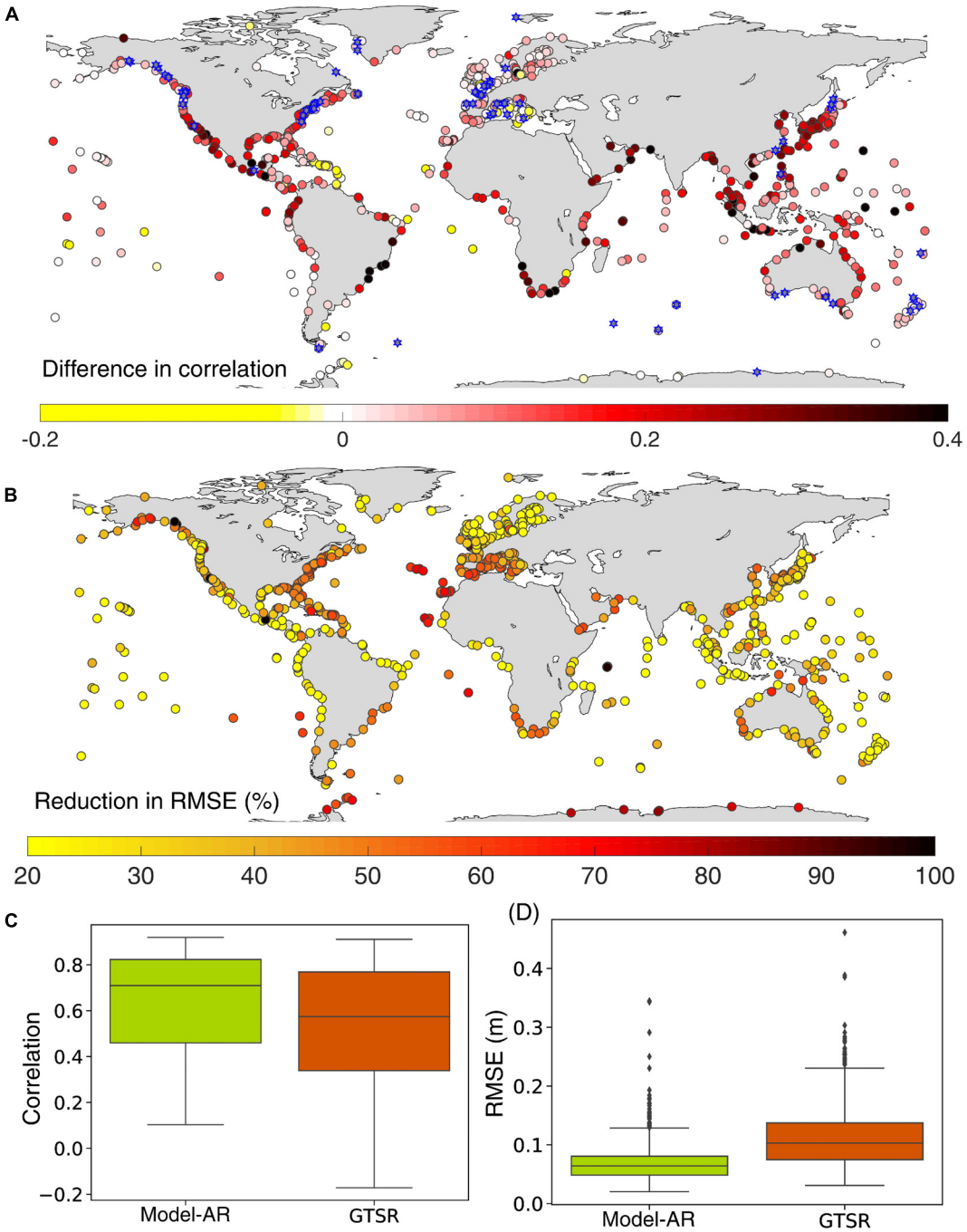

FIGURE 11 | Comparison of Model-AR with GTSR. **(A)** Difference in Pearson's correlation coefficients of Model-AR and GTSR with observations. Red colors indicate that Model-AR has higher correlation than GTSR, whereas blue stars denote tide gages where the difference in correlation is insignificant. **(B)** Reduction of RMSE in Model-AR compared to GTSR expressed in percent. Boxplot comparison of correlation **(C)** and RMSE **(D)** for Model-AR and GTSR.

GTSR often underestimates the peak surge, e.g., at Bridgeport during Superstorm Sandy, or for Hurricane Katrina at all three tide gages. The surge values during Cyclone Xaver are well captured by all models, except for a slight overestimation by Model-RS and GTSR.

DIRECTIONS FOR FUTURE RESEARCH

Although the data-driven models show better performance than the numerical model, a number of expansions (discussed below) could further improve the predictive skill.

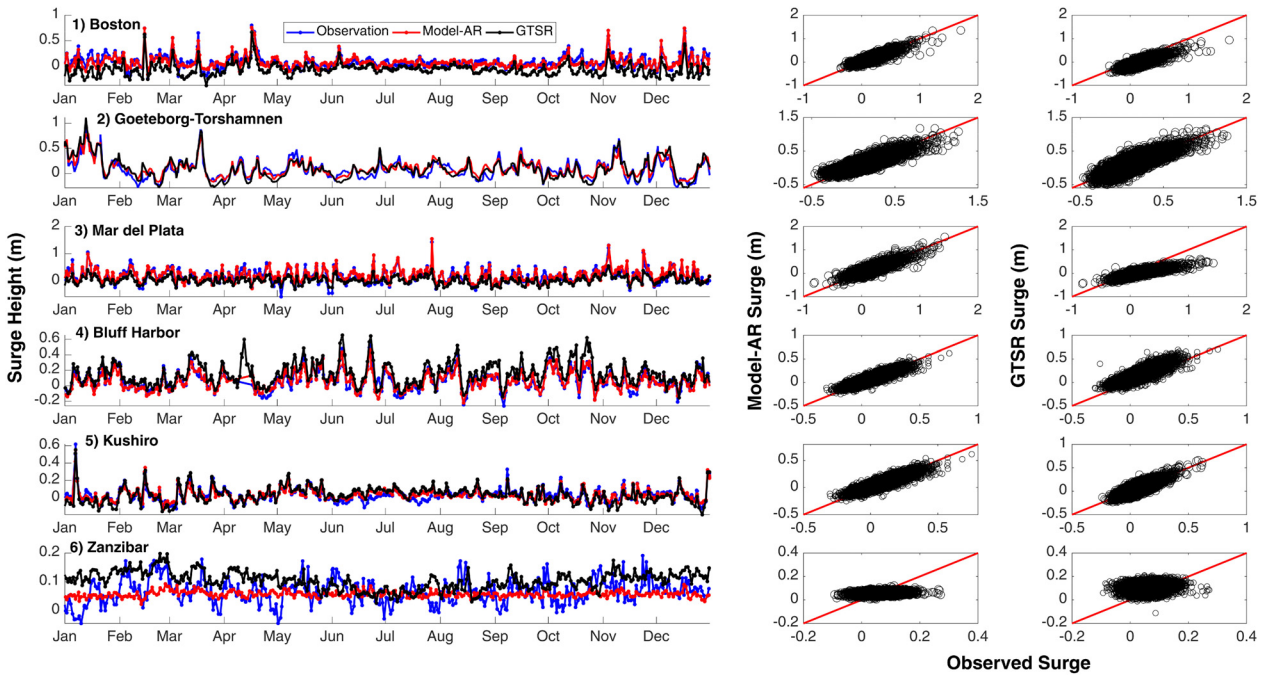

FIGURE 12 | Daily maximum surge time series comparison between observations, Model-AR, and GTSR (left); scatter plots for Model-AR and observed surge values (middle) and scatter plots for GTSR and observed surge values (right) for tide gages marked in yellow in **Figure 1**.

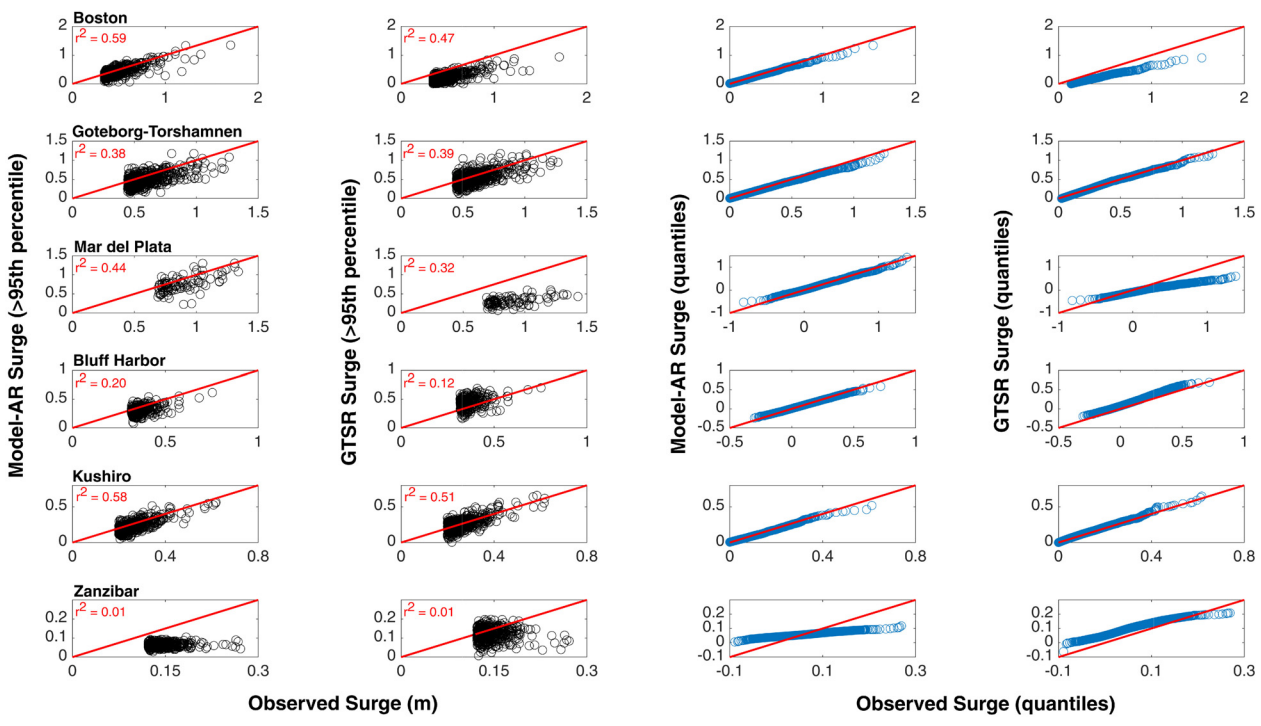

FIGURE 13 | Performance of Model-AR and GTSR (see *y*-axis labels) for extreme surge events (surge values higher than 95th percentile of observed daily maximum surge) shown as scatterplots (left) and q–q plots (right).

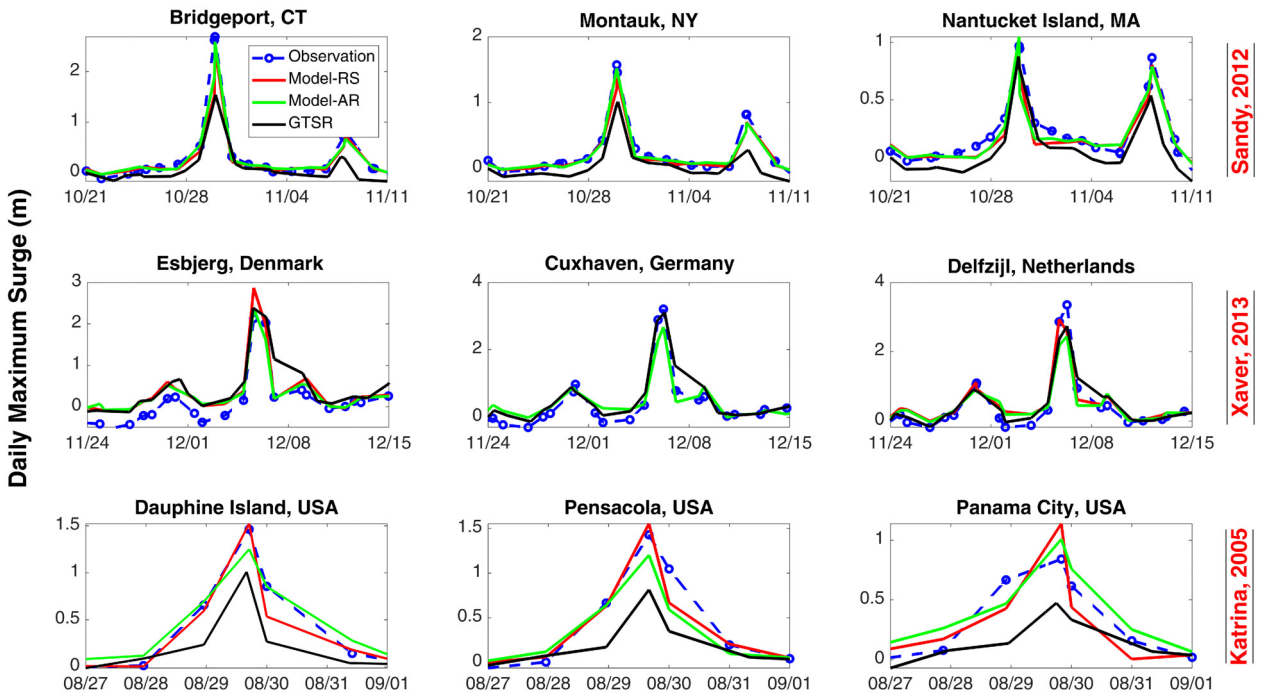

FIGURE 14 | Validation of Model-RS, Model-AR, and GTSR for individual storm events: Superstorm Sandy (top), Cyclone Xaver (middle), and Hurricane Katrina (bottom).

The effects of wave set-up have not been incorporated in this study. However, Tait (1972) has shown that in tropical and sub-tropical islands, wave set-up can add more than 20% of the incident wave height to the "tide + surge" estimation of the sea level. Incorporating this effect (e.g., with simple approximations as in Vousdoukas et al., 2018) using data from models akin to the one used by Perez et al. (2017) and Camus et al. (2017) could potentially improve the model performance, especially in the tropics, where model accuracy of the data-driven models (but also GTSR) is poor.

Model accuracy would also likely increase when predictors with higher spatial and/or temporal resolution are used. Bloemendaal et al. (2019) showed that a horizontal resolution of 0.225° is adequate to simulate tropical cyclone induced storm surges. New reanalysis products such as ECMWF re-analysis Version 5 (ERA-5) (Hersbach et al., 2019) or The Modern-Era Retrospective-analysis for Research and Applications, Version 2 (MERRA-2) (Bosilovich et al., 2016) have recently become available and could be used to improve storm surge modeling in the tropics. Furthermore, the comparison between Models-RS and Model-AR would be more complete with the availability of remotely sensed global SLP data. We show that SLP is the most important predictor for modeling storm surges at many tide gage locations, and hence further analysis would allow for a better understanding of the value of remotely sensed and reanalysis predictors for data-driven (but also hydrodynamic) storm surge modeling.

In several recent studies authors opted to use skew surge, which is the absolute difference between the maximum observed sea level and the predicted tidal high water within a tidal cycle (Williams et al., 2016), as an alternative measure to non-tidal residuals (e.g., Haigh et al., 2015; Marcos and Woodworth, 2017). This has the advantage of reducing the amount of errors in the storm surge proxy when there are small phase shifts in the observations or tidal predictions; those can lead to artificial high peaks in non-tidal residuals, whereas skew surges are less affected by such errors. Skew surges are also largely independent of the phase of the tide, at least in regions where semi-diurnal tides dominate. Santamaria-Aguilar and Vafeidis (2018) showed that in mixed tidal regimes there is still dependence between extreme skew surge events and tides. A significant shortcoming of the skew surge concept consists in the loss of the hydrograph information, which is essential for inundation and risk assessments. Here, we use non-tidal residual data instead of skew surge for the global analysis, as this allows direct comparison with the results presented in earlier studies, such as GTSR. We tested using skew surge at selected sites and found very similar results compared to using non-tidal residuals in terms of model performance.

Another area of improvement would be to include tide-surge interaction in either the modeling of surges (or skew surges) or when combining the surge data with tidal data to obtain total still water levels. We use the same approach as Muis et al. (2016), which ignores tide-surge interaction, but allows a direct comparison of the results. Capturing tide-surge interaction in numerical model studies requires running coupled tide-surge simulations (Pugh and Woodworth, 2014), which increases the computational cost significantly.

The methodology presented here can be implemented operationally to provide daily maximum surge forecasts at tide gages around the globe. The data-driven models could be forced with forecast wind speed and SLP as well as other relevant predictors. Tidal predictions can be superimposed to the predicted surges in order to compute the forecast total still water level. In order to include uncertainty stemming from predictors (captured through ensemble forecasting systems), the modeling paradigm could shift from deterministic (implemented in this study) to probabilistic. Such a tool could possibly provide useful information for decision-makers, or inform other modeling efforts, in particular in regions where no dedicated storm surge forecasting systems are in place. Finally, surge values derived from GTSR can also be used as predictand (instead of surge values derived from tide gage observations) to train and validate data-driven models with full global coverage, including ungaged locations.

CONCLUSION

In this study, we explored the applicability of data-driven models to simulate global storm surges. Our first objective was to train and validate data-driven models (based on multiple regression and Random Forest) at tide gage locations across the globe for the purpose of simulating daily maximum surge; models were trained and validated at more than 800 tide gages. The predictand, daily maximum surge, is simulated well in sub-tropical and extratropical regions with average correlation coefficients of 0.79 and 0.75 for Model-RS and Model-AR, and average RMSE of 7.5 and 7.8 cm, respectively. In the tropics, model accuracy drops, mainly due to the little variance of local predictors in the region and the coarse temporal and spatial resolution of predictors. We find that sea-level pressure is the most important predictor for simulating daily maximum surges at most tide gage locations.

Our second objective was to compare performance of the data-driven models when (1) remotely sensed predictors and (2) reanalysis predictors are used. Model-RS, which is trained with remotely sensed predictors, outperforms Model-AR (trained with ERA-Interim reanalysis) overall (albeit slightly), even when coarser SLP data is used as predictor. Hence, remote sensing data from satellite missions is a valuable resource for the storm surge modeling community, especially when focusing on broad spatial (up to global) scales. However, further analysis is required to detect the differences between remotely sensed and reanalysis predictors as some predictors were not available for this study for a comprehensive comparison.

Our third and last objective was to compare the performance of the data-driven models to the GTSR, based on a hydrodynamic numerical model. We find that for the vast majority of the tide gages (88%), data driven Model-AR leads to significantly higher correlation coefficients and lower RMSE. When focusing only on extreme surges (above the 95th percentile) average correlation in the data driven models of 0.54 and 0.33 for extra-tropical and tropical regions is also higher than found from GTSR (i.e., 0.44 and 0.20 in the same regions). Furthermore, when comparing model performance for specific storm surge events, Model-AR captures the peak surge events equally well, or better, than GTSR. Extreme total still water levels for the global coastlines are also simulated by superimposing modeled daily maximum surges on corresponding tides, leading to average correlation of 0.74 and average RMSE of 9.4 cm. Thus, we conclude that data-driven models provide a powerful and computationally cheap complementary way to simulate storm surges (in particular over long time periods and at large spatial scales) in addition to process-based but computationally expensive numerical models.

DATA AVAILABILITY STATEMENT

Data sets used in the analysis are publicly available from various sources and described in detail in the text.

AUTHOR CONTRIBUTIONS

MT carried out the analysis and interpretation of the data for the work and wrote the manuscript. TW provided continuous supervision, revisiting the work critically for important intellectual content, and approved for the publication of the content. CA given intellectual support on designing the methodology implemented in the work.

FUNDING

MT and TW were funded by the National Aeronautics and Space Administration (NASA) under the New (Early Career) Investigator Program in Earth Science (grant number: 80NSSC18K0743). Support for the Twentieth Century Reanalysis Project version 2c dataset is provided by the United States Department of Energy, Office of Science Biological and Environmental Research (BER), and by the National Oceanic and Atmospheric Administration Climate Program Office.

ACKNOWLEDGMENTS

We thank Dr. Sanne Muis for making the GTSR model results available.

SUPPLEMENTARY MATERIAL

The Supplementary Material for this article can be found online at: https://www.frontiersin.org/articles/10.3389/fmars.2020.00260/full#supplementary-material

REFERENCES

Atlas, R., Hoffman, R. N., and Ardizzone, J. (2011). A cross-calibrated multiplatform ocean surface wind velocity product for meteorological and oceanographic applications. *Bull. Am. Meteorol. Soc.* 92, 157–174. doi: 10.1175/2010bams2946.1

Bezuglov, A., Blanton, B., and Santiago, R. (2016). Multi-output artificial neural network for storm surge prediction in North Carolina. *biorvix*. [Preprint]. Available online at: https://arxiv.org/abs/1609.07378 (accessed July 21 2019).

Bloemendaal, N., Muis, S., Haarsma, R. J., Verlaan, M., Irazoqui Apecechea, M., de Moel, H., et al. (2019). Global modeling of tropical cyclone storm surges using high-resolution forecasts. *Clim. Dyn.* 52, 5031–5044. doi: 10.1007/s00382-018-4430-x

Bosilovich, M. G., Lucchesi, R., and Suarez, M. (2016). *MERRA-2: File Specification. GMAO Office Note No. 9, Version 1.1*.

Camus, P., Losada, I. J., Izaguirre, C., Espejo, A., Menendez, M., and Perez, J. (2017). Statistical wave climate projections for coastal impact assessments. *Earths Future* 5, 918–933. doi: 10.1002/eft2.234

Chadenas, C., Creach, A., and Mercier, D. (2014). The impact of storm Xynthia in 2010 on coastal flood prevention policy in France. *J. Coast. Conserv.* 18, 529–538. doi: 10.1007/s11852-013-0299-3

Cid, A., Camus, P., Castanedo, S., Méndez, F. J., and Medina, R. (2017). Global reconstructed daily surge levels from the 20th Century Reanalysis (1871–2010). *Glob. Planet. Chang.* 148, 9–21. doi: 10.1016/j.gloplacha.2016.11.006

Cid, A., Wahl, T., Chambers, D. P., and Muis, S. (2018). Storm surge reconstruction and return water level estimation in Southeast Asia for the 20th Century. *J. Geophys. Res. Oceans* 123, 437–451. doi: 10.1002/2017JC013143

Codiga, D. L. (2011). *Unified Tidal Analysis and Prediction Using the UTide Matlab Functions*. Technical Report 2011-01. Narragansett, RI: University of Rhode Island.

Compo, G. P., Whitaker, J. S., Sardeshmukh, P. D., Matsui, N., Allan, R. J., Yin, X., et al. (2011). The twentieth century reanalysis project. *Q. J. R. Meteorol. Soc.* 137, 1–28. doi: 10.1002/qj.776

Dangendorf, S., Arns, A., Pinto, J. G., Ludwig, P., and Jensen, J. (2016). The exceptional influence of storm ' Xaver' on design water levels in the German bight. *Environ. Res. Lett.* 11.

Dangendorf, S., Müller-Navarra, S., Jensen, J., Schenk, F., Wahl, T., and Weisse, R. (2014). North sea storminess from a novel storm surge record since AD 1843. *J. Clim.* 27, 3582–3595. doi: 10.1175/JCLI-D-13-00427.1

Dee, D. P., Uppala, S. M., Simmons, A. J., Berrisford, P., Poli, P., Kobayashi, S., et al. (2011). The ERA-Interim reanalysis: configuration and performance of the data assimilation system. *Q. J. R. Meteorol. Soc.* 137, 553–597. doi: 10.1002/qj.828

Duveiller, G., Fasbender, D., and Meroni, M. (2016). Revisiting the concept of a symmetric index of agreement for continuous datasets. *Sci. Rep.* 6, 1–14. doi: 10.1038/srep19401

French, J., Mawdsley, R., Fujiyama, T., and Achuthan, K. (2017). Combining machine learning with computational hydrodynamics for prediction of tidal surge inundation at estuarine ports. *Proc. IUTAM* 25, 28–35. doi: 10.1016/j.piutam.2017.09.005

Haigh, I. D., Macpherson, L. R., Mason, M. S., Crompton, R. P., and George, S. (2014). Estimating present day extreme water level exceedance probabilities around the coastline of Australia: tropical cyclone-induced storm surges. *Clim. Dyn.* 42, 139–157. doi: 10.1007/s00382-012-1653-0

Haigh, I. D., Wadey, M. P., Gallop, S. L., Loehr, H., Nicholls, R. J., Horsburgh, K., et al. (2015). A user-friendly database of coastal fl ooding in the United Kingdom from 1915–2014. *Sci. Data* 2:150021. doi: 10.1038/sdata.2015.21

Harris, D. L. (1962). The equivalence between certain statistical prediction methods and linearized dynamical methods. *Month. Weather Rev.* 90, 331–340. doi: 10.1175/1520-0493(1962)090<0331:tebcsp>2.0.co;2

Hersbach, H., Bell, B., Berrisford, P., Horányi, A., Muñoz, J., Nicolas, J., et al. (2019). Global reanalysis: goodbye Global reanalysis: goodbye ERA-Interim, hello, (159). *ECMWF Newslett.* 147:7.

Huffman, G. J., and Adler, R. F. (2001). Global precipitation at one-degree daily resolution from multisatellite observations. *J. Hydrometeorol.* 2, 36–50. doi: 10.1175/1525-7541(2001)002<0036:gpaodd>2.0.co;2

Jolliffe, I. T. (2002). *Principal Component Analysis. Second Edition. Springer Series in Statistics*. Cham: Springer.

Karim, M. F., and Mimura, N. (2008). Impacts of climate change and sea-level rise on cyclonic storm surge floods in Bangladesh. *Glob. Environ. Change* 18, 490–500. doi: 10.1016/j.gloenvcha.2008.05.002

Kohavi, R. (1995). "A study of cross-validation and bootstrap for accuracy estimation and model selection," in *Proceedings of the Fourteenth International Joint Conference on Artificial Intelligence*, Montreal.

Marcos, M., and Woodworth, P. L. (2017). Spatiotemporal changes in extreme sea levels along the coasts of the North Atlantic and the Gulf of Mexic. *J. Geophys. Res. Oceans* 122, 7031–7048. doi: 10.1002/2017JC013065

McInnes, K. L., Walsh, K. J. E., Hubbert, G. D., and Beer, T. (2003). Impact of sea-level rise and storm surges in a coastal community. *Natural Hazards* 30, 187–207. doi: 10.1023/A:1026118417752

Montblanc, T. F., Vousdoukas, M. I, Breyiannis, G., Feyen, L., Salamon, P., Ciavola, P., et al. (2019). Towards robust pan-European storm surge forecasting. *Ocean Model.* 133, 129–144. doi: 10.1016/j.ocemod.2018.12.001

Muis, S., Verlaan, M., Winsemius, H. C., Aerts, J. C. J. H., and Ward, P. J. (2016). A global reanalysis of storm surges and extreme sea levels. *Nat. Commun.* 7, 1–11. doi: 10.1038/ncomms11969

Pawlowicz, R., Beardsley, B., and Lentz, S. (2002). Classical tidal harmonic analysis including error estimates in MATLAB using TDE. *Comput. Geosci.* 28, 929–937. doi: 10.1016/S0098-3004(02)00013-4

Perez, J., Menendez, M., and Losada, I. J. (2017). GOW2: a global wave hindcast for coastal applications. *Coast. Eng.* 124, 1–11. doi: 10.1016/j.coastaleng.2017.03.005

Poli, P., Hersbach, H., and Dee, D. P. (2016). *ERA-20C: An Atmospheric Reanalysis of the Twentieth Century*. Reading: European Centre for Medium-Range Weather Forecasts, 4083–4097.

Pore, N. A. (1964). The relation of wind and pressure to extratropical storm surges at atlantic City. *J. Appl. Meteorol.* 3, 155–163. doi: 10.1175/1520-0450(1964)003<0155:TROWAP>2.0.CO;2

Pugh, D., and Woodworth, P. (2014). *Sea-Level Science: Understanding Tides, Surges, Tsunamis, and Mean Sea-Level Changes (Second)*. Cambridge, MA: Cambridge University Press.

Rappaport, E. N. (2013). Fatalities in the United States from Atlantic tropical cyclones: new data and interpretation. *Bull. Am. Meteorol. Soc.* 95, 341–346. doi: 10.1175/bams-d-12-00074.1

Salmun, H. (2009). East Coast Cool-weather Storms in the New York Metropolitan Region. *J. Appl. Meteorol. Climatol.* 48, 2320–2330. doi: 10.1175/2009jamc2183.1

Salmun, H., and Molod, A. (2015). The use of a statistical model of storm surge as a bias correction for dynamical surge models and its applicability along the U.S. East Coast. *J. Mar. Sci. Eng.* 3, 73–86. doi: 10.3390/jmse3010073

Santamaria-Aguilar, S., and Vafeidis, A. T. (2018). Are extreme skew surges independent of high water levels in a mixed semidiurnal tidal regime? *J. Geophys. Res. Oceans* 124, 8877–8886. doi: 10.1029/2018JC014282

Tait, R. J. (1972). Wave set-up on coral reefs. *J. Geophys. Res. Oceans* 77:12. doi: 10.1029/JC077i012p02207

Thompson, P. R., Mitchum, G. T., Vonesch, C., and Li, J. (2013). Variability of winter storminess in the Eastern United States during the Twentieth Century from tide gauges. *J. Clim.* 26, 9713–9726. doi: 10.1175/JCLI-D-12-00561.1

Tyralis, H., Papacharalampous, G., and Langousis, A. (2019). A brief review of random forests for water scientists and practitioners and their recent history in water resources. *Water* 11:910. doi: 10.3390/w11050910

Vousdoukas, M. I., Mentaschi, L., Voukouvalas, E., Verlaan, M., Jevrejeva, S., Jackson, L. P., et al. (2018). Global probabilistic projections of extreme sea levels show intensi fi cation of coastal flood hazard. *Nat. Commun.* 9:2360. doi: 10.1038/s41467-018-04692-w

Vousdoukas, M. I., Voukouvalas, E., Annunziato, A., Giardino, A., and Feyen, L. (2016). Projections of extreme storm surge levels along Europe. *Clim. Dyn.* 47, 3171–3190. doi: 10.1007/s00382-016-3019-5

Wahl, T., and Chambers, D. P. (2016). Climate controls multidecadal variabilityin U.S extreme sea level records. *J. Geophys. Res. Oceans* 121, 1274–1290. doi: 10.1002/2015JC011057

Williams, J., Horsburgh, K. J., Williams, J. A., and Proctor, R. N. F. (2016). Tide and skew surge independence: new insights for flood risk. *Geophys. Res. Lett.* 43, 6410–6417. doi: 10.1002/2016GL069522

Woodworth, P. L., Hunter, J., and Marcos, M. (2017). Towards a global higher-frequency sea level dataset. *Geosci. Data J.* 3, 50–59. doi: 10.1002/gdj3.42

Conflict of Interest: The authors declare that the research was conducted in the absence of any commercial or financial relationships that could be construed as a potential conflict of interest.

frontiers in Marine Science

ORIGINAL RESEARCH
published: 29 April 2020
doi: 10.3389/fmars.2020.00263

A High-Resolution Global Dataset of Extreme Sea Levels, Tides, and Storm Surges, Including Future Projections

Sanne Muis[1,2], Maialen Irazoqui Apecechea[1], Job Dullaart[2], Joao de Lima Rego[1], Kristine Skovgaard Madsen[3], Jian Su[3], Kun Yan[1] and Martin Verlaan[1,4]*

[1] Deltares, Delft, Netherlands, [2] Institute for Environmental Studies (IVM), Vrije Universiteit Amsterdam, Amsterdam, Netherlands, [3] Danish Meteorological Institute, Copenhagen, Denmark, [4] Delft University of Technology, Delft, Netherlands

The world's coastal areas are increasingly at risk of coastal flooding due to sea-level rise (SLR). We present a novel global dataset of extreme sea levels, the Coastal Dataset for the Evaluation of Climate Impact (CoDEC), which can be used to accurately map the impact of climate change on coastal regions around the world. The third generation Global Tide and Surge Model (GTSM), with a coastal resolution of 2.5 km (1.25 km in Europe), was used to simulate extreme sea levels for the ERA5 climate reanalysis from 1979 to 2017, as well as for future climate scenarios from 2040 to 2100. The validation against observed sea levels demonstrated a good performance, and the annual maxima had a mean bias (MB) of -0.04 m, which is 50% lower than the MB of the previous GTSR dataset. By the end of the century (2071–2100), it is projected that the 1 in 10-year water levels will have increased 0.34 m on average for RCP4.5, while some locations may experience increases of up to 0.5 m. The change in return levels is largely driven by SLR, although at some locations changes in storms surges and interaction with tides amplify the impact of SLR with changes up to 0.2 m. By presenting an application of the CoDEC dataset to the city of Copenhagen, we demonstrate how climate impact indicators derived from simulation can contribute to an understanding of climate impact on a local scale. Moreover, the CoDEC output locations are designed to be used as boundary conditions for regional models, and we envisage that they will be used for dynamic downscaling.

Keywords: climate change, global model, extreme sea levels, sea-level rise, coastal flooding

OPEN ACCESS

Edited by:
Roshanka Ranasinghe, IHE Delft Institute for Water Education, Netherlands

Reviewed by:
Michalis Vousdoukas, European Commission, Joint Research Centre (JRC), Italy
Kathleen Lynne McInnes, CSIRO Oceans and Atmosphere (O&A), Australia

****Correspondence:***
Sanne Muis
sanne.muis@deltares.nl;
sanne.muis@vu.nl

Specialty section:
This article was submitted to Coastal Ocean Processes, a section of the journal Frontiers in Marine Science

Received: *18 November 2019*
Accepted: *01 April 2020*
Published: *29 April 2020*

Citation:
Muis S, Irazoqui Apecechea M, Dullaart J, de Lima Rego J, Madsen KS, Su J, Yan K and Verlaan M (2020) A High-Resolution Global Dataset of Extreme Sea Levels, Tides, and Storm Surges, Including Future Projections. Front. Mar. Sci. 7:263. doi: 10.3389/fmars.2020.00263

INTRODUCTION

The world's coastal areas are increasingly at risk of coastal flooding due to sea-level rise (SLR). By 2100, global mean sea-levels are projected to be 30–60 cm higher than today, even with a sharp reduction of greenhouse gas emissions (Church et al., 2013; Oppenheimer et al., 2019). In regions with little sea level variability, even an SLR of 10 cm could double the flooding frequency (Vitousek et al., 2017). Without mitigation and adaptation, the expected economic annual losses due to flooding may come close to 10% of the global gross domestic product (Hinkel et al., 2014). Raising flood defenses is therefore critical in densely populated and economically important coastal areas, and is cost effective for 13% of the global coastline (Lincke and Hinkel, 2018). The stabilization of global temperatures to 1.5°C, as agreed upon in the Paris Agreement, will lead to a strong reduction of the economic impact of SLR (Nicholls et al., 2018).

Accurate high-resolution projections of extreme sea levels and coastal flooding can support decision makers in identifying which regions will face the strongest increases in flood risk, and in prioritizing mitigation and adaptation efforts (Ward et al., 2015). Recent years have seen rapid progress in the application of hydrodynamic models for large-scale risk assessments (Wahl, 2017; Bouwer, 2018). With its spatially varying grid resolution, the Global Tide and Surge Model (GTSM) has sufficient resolution in coastal areas at relatively low computational costs (Verlaan et al., 2015), and as such has been leading in global hydrodynamic modeling. In recent years, GTSMv2.0 has been used to simulate extreme sea levels worldwide, with applications in operational forecasting (Verlaan et al., 2015), multi-decadal hindcasting (Muis et al., 2016), and projecting changes for future climate scenarios (Vousdoukas et al., 2018b).

The performance of the global simulations of extreme sea levels is controlled by the accuracy of the meteorological forcing, as well as by the hydrodynamic model. The previous generation of global climate models and climate reanalysis datasets typically had a resolution higher than 0.75° (approximately 79 km). While data with such a resolution performs reasonably for extra-tropical storms (Dullaart et al., 2019), it strongly underestimates the intensity of tropical cyclones (Schenkel and Hart, 2012) and associated storm surges (Bloemendaal et al., 2017; Muis et al., 2019). In 2019, the European Centre for Medium-Range Weather Forecasts (ECWMF) released the ERA5 climate reanalysis dataset. With a resolution of 0.25° (approximately 31 km), ERA5 is much better at representing the strong intensities of tropical cyclones (Belmonte Rivas and Stoffelen, 2019). Moreover, GTSMv2.0's accuracy for global tidal modeling was insufficient, and previous large-scale studies used separate models to simulate tides, surges, and changes in mean sea level (MSL; Hinkel et al., 2014; Muis et al., 2016; Vitousek et al., 2017; Vousdoukas et al., 2017, 2018a; Brown et al., 2018; Jevrejeva et al., 2018). The individual sea level components were linearly superimposed, which means non-linear interaction effects are ignored. Tide-surge interaction is important in shallow seas with a large tidal range (Horsburgh and Wilson, 2007; de Lima Rego and Li, 2010; Mawdsley et al., 2015), and tides can significantly change in response to SLR (Pickering et al., 2012, 2017; Wilmes et al., 2017). It has been shown that climate change and SLR could lead to changes in non-linear interactions (Arns et al., 2017). The next generation Global Tide and Surge Model Version 3.0 (GTSMv3.0) was recently developed. Comparison against observations indicates that GTSMv3.0 has a tidal performance comparable to other global tidal models (Stammer et al., 2014). Hence, GTSMv3.0 can now be used to dynamically simulate tides, storm surges, and changes in MSL, including interaction effects. Moreover, GTSMv3.0 has an unprecedented high resolution along the coast, with a grid size of 2.5 km globally (and 1.25 km in Europe). This is expected to further increase the model's accuracy, especially in areas with a complex geometry.

We use these developments in order to present a novel global dataset of extreme sea levels, namely, the Coastal Dataset for the Evaluation of Climate Impact (CoDEC). The CoDEC dataset consists of extreme sea levels (MSL, tides, and storm surges), and covers both the historical climate for the period 1979–2017 and future climates for different scenarios for the period 2040–2100. In this paper, we evaluate the performance of the dataset for the historical periods and analyze the changes in extreme sea levels for the future climate scenarios. Finally, we discuss how the CoDEC dataset can enhance the understanding of climate impact on the local scale.

DATA AND METHODS

Global Tide and Surge Model Version 3.0

The GTSMv3.0 is a depth-averaged hydrodynamic model with global coverage that dynamically simulates tides and storm surges. GTSMv3.0 uses the unstructured Delft3D Flexible Mesh software (Kernkamp et al., 2011) and, as such, employs an efficient distribution of resolution. The model has no open boundaries, and tides are induced by including tide generating forces using a set of 60 frequencies. Surges are caused by gradients in the surface pressure of the atmosphere and the transfer of momentum from the wind to the water. We use the relation of Charnock (1955), with a drag coefficient of 0.0041, to estimate the wind stress at the ocean surface. A combination of different datasets is used for the bathymetry: EMODnet at 250 m resolution in Europe (Consortium EMODnet Bathymetry, 2018) and General Bathymetric Chart of the Ocean with a 30 arc seconds resolution for the rest of the globe (GEBCO, 2014). The bathymetry under the permanent ice shelves in Antarctica is represented by Bedmap2 (Fretwell et al., 2013).

In comparison to GTSMv2.0, which was used in previous studies (Muis et al., 2016; Vousdoukas et al., 2018b; Bloemendaal et al., 2019), the resolution of GTSMv3.0 is increased from 5 km along the coast (50 km in the deep ocean) to 2.5 km along the coast (25 km in the deep ocean). The coastal resolution was further increased to 1.25 km for Europe. The improved resolution increased the total number of grid cells from 2.0 to 5.0 million. In addition to the improved resolution, the model performance for tides was improved by the implementation of additional physical processes. This included the implementation of self-attraction and loading, and the improved parameterization of internal tides (Irazoqui Apecechea et al., 2017). To enable the dissipation of barotropic energy through the generation of internal tides, the grid resolution is further refined in areas in deep ocean that have a steep topography.

Simulations, Scenarios, and Forcing Data

Climate Reanalysis and Future Climate Scenarios

Table 1 provides an overview of the simulations and scenarios, including the acronyms used to refer to the different scenarios. For the simulation of extreme sea levels for the historical period (1979–2017), GTSMv3.0 is forced with 10 m wind speed and atmospheric pressure from the ERA5 climate reanalysis of ECMWF Copernicus Climate Change Service [C3S], 2017. ERA5 is the successor of the ERA-Interim climate reanalysis and has hourly fields with a spatial resolution of 0.25° × 0.25° (∼31 km). For the projections of extreme sea levels for climate change scenarios for the future period (2040–2100), we use meteorological fields from EC-Earth simulations

TABLE 1 | Overview of the different CoDEC simulations, including the epochs and scenarios simulated.

Simulation	Type	Period	Meteorological forcing	SLR scenarios
CoDEC-ERA5	Climate reanalysis	1979–2017	ERA5	–
CoDEC-HIST	Baseline climate scenario	1976–2005	EC-Earth CMIP5, DMI-HIRHAM5 for Europe	–
CoDEC-RCP8.5	Future climate scenario	2041–2070	EC-Earth CMIP5, DMI-HIRHAM5 for Europe	IPCC-AR5 ensemble mean RCP8.5
CoDEC-RCP4.5	Future climate scenario	2071–2100	EC-Earth CMIP5, DMI-HIRHAM5 for Europe	IPCC-AR5 ensemble mean RCP4.5

developed within the Climate Model Intercomparion Phase 5 (CMIP5) initiative (Taylor et al., 2012). The EC-Earth dataset has three hourly fields with a spatial resolution of 1.125° × 1.125° (∼125 km). For Europe, we use the downscaled projections developed within the World Climate Research Program Coordinated Regional Downscaling Experiment (EURO-CORDEX) initiative (Jacob et al., 2014). We use the DMI-HIRHAM5 regional climate simulations (Christensen et al., 2007), which were nested in the global EC-Earth simulations. The DMI-HIRHAM5 dataset had three hourly fields, with a spatial resolution of 0.11° × 0.11° (∼12.5 km).

For the future period, we appy two climate change scenarios, namely, Representative Concentration Pathways (R) 4.5 and 8.5, corresponding to a radiative forcing of 4.5 and 8.5 W/m^2 by the year 2100, respectively (Moss et al., 2010). The RCP8.5 pathway was developed in order to explore an unlikely high-risk future. While global carbon emissions have been tracking just above RCP8.5 (Peters et al., 2013), it is argued that recent climate policies, such as the Paris Agreement, have caused the RCP8.5 pathway to become increasingly implausible for the end of this century (Hausfather and Peters, 2020). Given computational constrains and the user requirements of the CoDEC project, it was decided to select the RCPs that we considered most plausible. Therefore, RCP8.5 is considered for the mid-century (i.e., 2041–2070), while RCP4.5 is considered for the end of the century (i.e., 2071–2100). In order to obtain a baseline simulation that would enable us to compute changes, we also simulate the historical period 1976–2005, using the same climate models.

For each scenario, we apply SLR projections that corresponded to the same RCPs. We use the mean ensemble from IPCC AR5 (Church et al., 2013), which is based on the CMIP5 models and distributed by the Integrated Climate Data Center of the University of Hamburg. The yearly SLR fields are referenced to the mean level over the period 1986–2005, with a spatial resolution of 1° × 1°.

The vertical reference of GTSMv3.0 is MSL. To make the definition of MSL consistent with the vertical reference used in the SLR fields, the mean sea-level pressure field (MSLP) over 1986–2005 is removed. The MSLP calculation is based on the ERA-Interim because ERA5 was not available at the time.

Simulations and Data Processing

We produce time series of the total water levels, surge levels, tides, and MSLs for each simulation. In order to be able to decompose the total water levels into the different sea level components, we run a tide-only simulation for each scenario. For the future climate scenarios, the tide-only simulation also includes SLR. Subsequently, the time series of surge level are computed by subtracting the tides from the total water level. The total number of simulated years is 230 years. Each year is simulated separately, using a spin-up time of 15 days. All the simulations are run on the Deltares computing cluster. Using a parallel setup with 4 cores, each 1-year simulation took 21 days to complete.

The time series are stored at a 10-min temporal resolution for 44,734 output locations. It is unfeasible to save the time series at all 5 million grid cells, as this would have generated huge amounts of data. In previous studies with GTSM (Muis et al., 2016, 2018), the output locations were based on the DIVA coastal segmentation, which included 16,611 locations (Vafeidis et al., 2008). For the CoDEC project, we develop a new set of output locations (**Figure 1**) based on the following procedure. First, we smooth the Natural Earth 1:10 m coastline at 5 km by applying a buffer and subsequently an inverse buffer in ArcGIS. This removes any estuaries and bays with an inlet less than 5 km wide. Second, we apply equidistant sampling along the coastline to generate points at every 50 km along the smoothed coastline. We use 10 km for Europe due to the higher resolution there. In addition, we add the locations of the tide gauge stations. In addition to the approximately 18,000 coastal output locations, we also include the output locations in the ocean that could be used as boundary conditions for regional hydrodynamic models. The output resolution is based on a regular grid that increases from the deep ocean toward the coast, that is, from 5.0 to 2.5 to 1.0° for, respectively, further than 500 km away from land, from 100 to 500 km from land, and closer than 100 km from land. The resolution is 1.0°, 0.5°, and 0.25°, respectively, for Europe. Output locations in high-latitude regions are excluded because the model performance is expected to be insufficient. This is because GTSM does not include sea ice physics and because the bathymetry in the Arctic areas is generally poor.

Post-processing and Extreme Value Statistics

All the output is stored in NetCDF4 file format. The processing and analysis is done with Python 3.0 using the xarray package (Hoyer and Hamman, 2017), which allows for label-based analysis of multi-dimensional arrays and supports parallel computations on datasets that do not fit into memory. In addition, we use the Climate Data Operators (CDOs) to compute the annual maxima (Schulzweida, 2019).

To obtain extreme sea levels for the various return periods, we fit a Gumbel distribution to the annual maxima using the maximum-likelihood method. We are aware of its limitations (see section "Future Research Directions"), but the annual maxima method is computationally less demanding than the peaks-over-threshold method. Moreover, the application of the annual

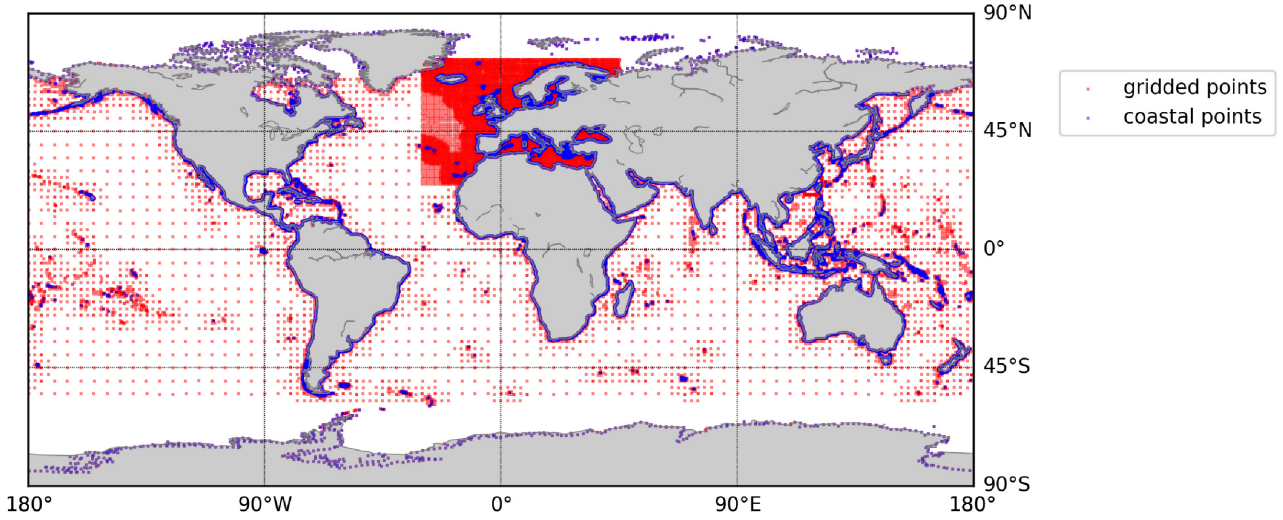

FIGURE 1 | Overview of the output locations used for the CoDEC dataset, including the coastal locations, tide gauge stations, and gridded points.

TABLE 2 | Overview of the main differences between the CoDEC-ERA5 dataset and the previous GTSR dataset.

Dataset	Hydrodynamic model	Meteorological forcing	Period	Vertical datum
GTSR	• Surge levels are simulated using GTSMv2.0 with a coastal resolution of 5 km • Tides are simulated using Finite Element Solution (FES2012) with a resolution of 1/16° • Total water levels are computed by superimposing surges and tides	ERA-Interim, 3 hourly fields with a spatial resolution of 0.75° × 0.75°	1979–2014	MSL as defined by the GEBCO bathymetry
CoDEC-ERA5	• Total water levels, composed of tides and surge levels, are simulated using GTSMv3.0 with a coastal resolution .5 km (1.25 km in Europe) • Dynamic interactions between tides, surges, and mean sea level are included	ERA5, hourly fields with a spatial resolution of 0.25° × 0.25°	1979–2017	MSL as defined by the bathymetry but corrected for MSLP and computed as the average sea level over 1986–2005 based on ERA-Interim

maxima method allows for easy comparison with the previous Global Tide and Surge Reanalysis (GTSR) dataset (see section "Evaluation of the CoDEC Dataset"). While this study focuses on the annual maxima and return periods, the CoDEC dataset also includes several other indicators, such as tidal water levels and annual percentiles for total water levels and surge levels.

Evaluation of the CoDEC Dataset

To validate CoDEC-ERA5, we compare the modeled sea levels with observed sea levels from the tide gauge stations in the Global Extreme Sea Level Analysis (GESLA) dataset (Woodworth et al., 2016). The GESLA dataset has an hourly resolution, but we use annual maxima obtained from Wahl et al. (2017). The water levels are referenced to the present-day MSL by removing the annual average sea level for each year, and subsequently also by subtracting the mean over the last 19 years from the (de-trended) time series. This dataset contains 591 tide gauge stations. Over the period 1979–2005, 327 stations have more than 20 years of data and 476 stations have more than 10 years of data. In a similar way to the modeled sea levels, we fit a Gumbel distribution to the annual maxima in order to estimate return periods. We use the tide gauge stations with more than 10 years of data and only used overlapping years.

The accuracy of the CoDEC-ERA5 sea levels is evaluated using various indicators, including Pearson's correlation coefficient r, the root-mean-squared error (RMSE), the mean absolute error (MAE) in meters, and the mean absolute percentage error (MAPE) in percentages. The modeled and observed 1 in 10-year water levels (RP10) are validated using the mean bias (MB) in meters, the MAE in meters, and the MAPE in percentages. We show the average values across all the tide gauge stations, together with the standard deviations (SDs).

In addition to evaluating against observed sea levels, we also evaluated CoDEC-ERA5 against the previous GTSR dataset (Muis et al., 2016). CoDEC-ERA5 is the successor of GTSR and is based on the next generation climate and hydrodynamic models. **Table 2** summarizes the main improvements.

CoDEC-HIST is validated by comparing the 1 in 10-year water levels against both the observations and CoDEC-ERA5. While the performance of CoDEC-HIST in comparison to the observations is influenced by the model performance of the GTSMv3.0, the comparison of CoDEC-HIST against CODEC-ERA5 exposes any bias between the baseline climate simulation and the observed

historical climate. A good performance provides confidence that the model setup can be used to assess changes in water levels under future climate scenarios.

RESULTS AND DISCUSSION

Evaluation of CoDEC-ERA5 on the Basis of Annual Maxima

The comparison between the observed annual maxima from GESLA and the modeled annual maxima from CoDEC-ERA5 indicates that the average value for Pearson's *r* was 0.54 (SD 0.28) across all the tide gauge stations, while the MB was -0.04 m (SD 0.32 m) (**Table 3**). The absolute bias is smaller than 0.2 m for 75% of the tide gauge stations. The MAPE indicates a relative error of 14.0% (SD 13.4%) across all the tide gauge stations. As the relatively high SDs indicate, the model performance varies spatially. **Figures 2A,B** show that CoDEC-ERA5 generally performs best in mid-latitude regions, such as northwestern Europe, southern Africa, and southern Australia. Along the coasts of islands in the Pacific Ocean, the Mediterranean Sea, and Indonesia, the correlation coefficients are generally lower than 0.5. At the same time, the absolute biases are also less than 0.1 m. This indicates a low variability in extremes in some regions, which may be due to few storms and a small tidal range, which make it difficult to capture the variability correctly. Moreover, in some regions steric processes, which are not included in the GTSM, may add to the sea level variability (Muis et al., 2018).

There is a clear improvement when comparing the performance of CoDEC-ERA5 against GTSR (see **Figures 2B,D**). The correlation coefficients increase for 90% of the tide gauge stations (yellow to green dots in **Figure 2E**), while the absolute biases reduce for 95% of the tide gauge stations (yellow to green dots in **Figure 2F**). With an MB of -0.04 m for CoDEC-ERA5 and -0.08 m for GTSR, the errors across all the tide gauge stations are reduced by 50% (**Table 3**). At the same time, there are also regions where the model performance worsens. It appears that biases increase in regions with a high tidal range, such as the North Sea, northern Australia, and the northwest of the United States and Canada, which could indicate that GTSM is outperformed by the FES2012 model that was used to develop the GTSR dataset. There was no clear spatial pattern for the correlation coefficients, although they appear to mainly decrease in tropical regions. **Figure 3** presents scatter density plots for the modeled and observed annual maxima for all the GESLA tide gauge stations combined. For water levels larger than 6 m, CoDEC-ERA5 tends to overestimate the water levels, while GTSR shows an underestimation. This is probably caused by the higher resolution of the meteorological forcing, which resolves extreme storms better. Overall, the comparison of the performance of CoDEC-ERA5 and GTSR demonstrates a significant improvement due to model development and improved forcing.

TABLE 3 | Model performance of the annual maxima (Amax) of the CoDEC-ERA5 dataset and the GTSR dataset.

Amax	CoDEC-ERA5	GTSR
Pearson's ρ	0.54 SD 0.28	0.46 SD 0.25
RMSE (m)	0.26 SD 0.73	0.30 SD 0.73
MB (m)	–0.04 SD 0.32	–0.08 SD 0.32
MAE (m)	0.21 SD 0.26	0.23 SD 0.25
MAPE (%)	14.0 SD 13.4	17.3 SD 16.4

The modeled Amax were compared against the observed Amax of the GESLA dataset (n = 485). The model performance was assessed in terms of Pearson's correlation coefficient, mean bias (MB), mean absolute error (MAE), and the mean absolute percentage error (MAPE).

Evaluation of CoDEC-ERA5 on the Basis of Return Periods

Figure 4A maps the 1 in 10-year water levels. When averaged across all the tide gauge stations, the modeled 1 in 10-year water levels for CoDEC-ERA5 are underestimated by -0.10 m (SD is 0.32), while the MAPE was 12.1% (SD 12.8) (**Table 4**). Overall, the absolute biases were lower than 0.3 m for 75% of the tide gauge stations. The relative errors were within -30% and + 15% for 75% of the tide gauge stations. Due to the poor global coverage of the tide gauge stations, it is difficult to identify a spatial pattern in the model performance (**Figure 4B**). But in general, there is a slight overestimation along the European coastline and an underestimation elsewhere. The difference in model performance in Europe could be linked to the fact that the GTSM resolution is more refined there, as well as the use of high-resolution bathymetry. In some regions, such as northern Australia and the northeastern United States, the biases are relatively large. These regions typically experience large sea level extremes due to a large tidal range and the occurrence of tropical cyclones.

There is a clear improvement in performance of the 1 in 10-year water levels from CoDEC-ERA5 to GTSR. **Table 4** indicates that the average MAE drops by 25%, from 0.25 m for GTSR to 0.19 m for CoDEC-ERA5, while the MAPE is reduced by 29%. For CoDEC-ERA5, 60% of the tide gauge stations have an MAE smaller than 0.2 m for CoDEC-ERA5, in comparison to 40% for GTSR. **Figure 4C** indicates that the largest changes between the two datasets are up to 1 m. This is rather high, and could be partly caused by the correction of the vertical datum by the MSLP, which has a magnitude up to 0.2 m. Moreover, the use of another tidal model could explain the large differences. In general, the 1 in 10-year water levels for CoDEC-ERA5 are higher than those for GTSR (blue points in **Figure 4C**). This could be linked to the higher resolution of CoDEC-ERA5 (i.e., model resolution as well as the resolution of the meteorological forcing), which leads to an improved accuracy of the most extreme water levels. However, there are also regions where the 1 in 10-year water levels in GTSR are higher those in CoDEC-ERA5 (red points in **Figure 4C**). For 66% of the tide gauge stations, the MAE was reduced when comparing CoDEC-ERA5 against GTSR (**Figure 4D**).

To illustrate the performance of the individual locations, **Figure 5** shows the ranked annual maxima and the fitted Gumbel distributions for four selected tide gauge stations. It shows a general good fit of the Gumbel distribution to the annual maxima. The plots also illustrate that for some locations, such as Aberdeen,

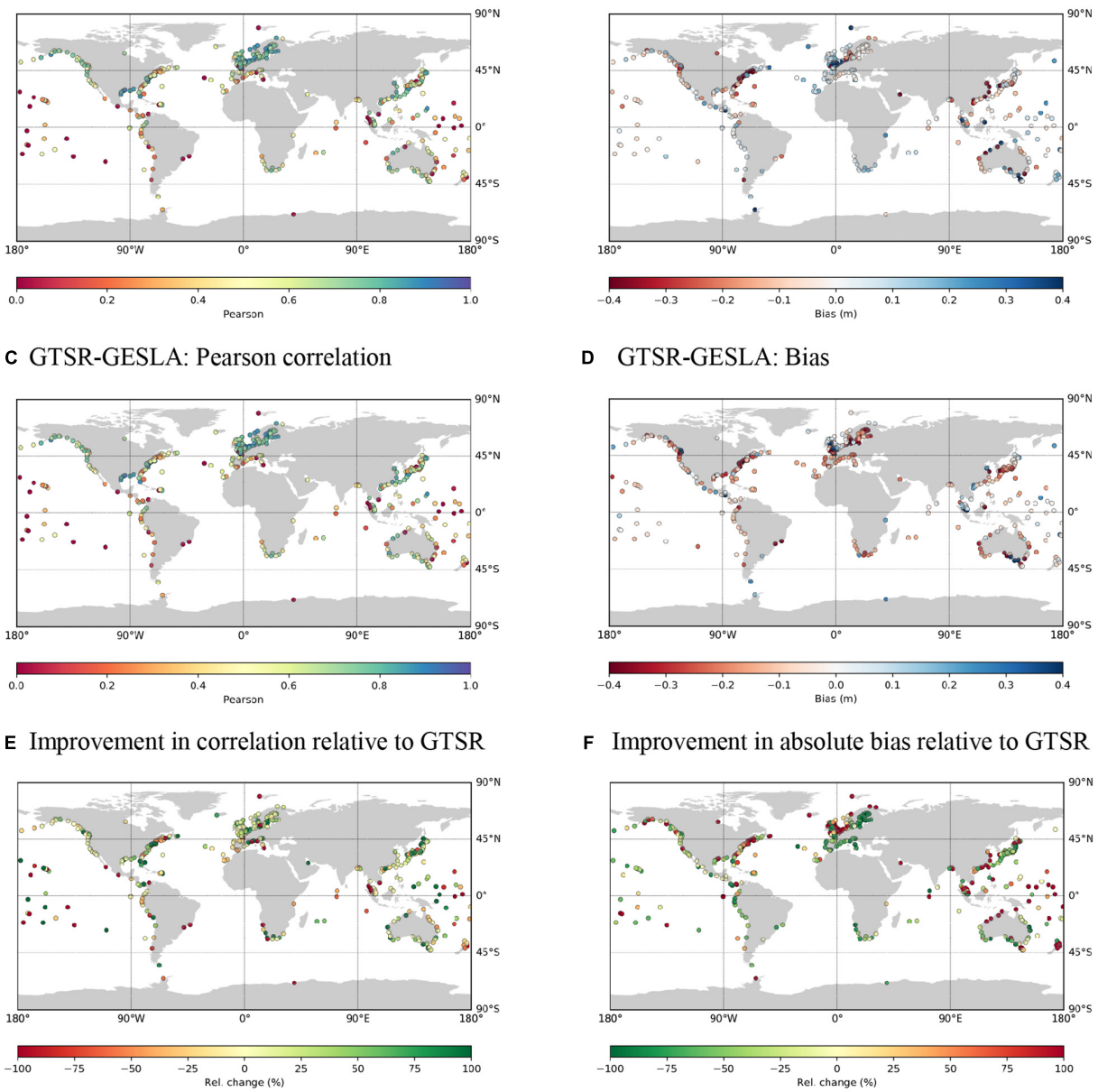

FIGURE 2 | Model performance of the modeled annual maxima evaluated against observed annual maxima from the GESLA dataset. We show Pearson's correlation coefficient of the annual maxima for **(A)** CoDEC-ERA5 and **(C)** GTSR, as well as **(E)** the relative changes in correlation coefficients between the two datasets. In addition, we show the mean bias over the annual maxima for **(B)** CoDEC-ERA5 and **(D)** GTSR, as well as **(F)** the relative changes in the mean bias between the two datasets.

the difference in performance between GTSR and CoDEC-ERA5 is negligible, while for other locations, such as Brisbane, the improvement in model performance is relatively large.

Evaluation of CoDEC-HIST to Assess Spatial Bias of the Climate Model

Before analyzing how extreme sea levels may change under future climate change scenarios, we evaluate how the performance of CoDEC-HIST return periods. The validation of the 1 in 10-year water levels shows an MB of -0.13 m, a mean MAE of 0.30 m, and a MAPE of 17.5% across all the tide gauge stations (**Table 4**). Mapping the bias of the 1 in 10-year water levels shows that they are generally overestimated in Europe and underestimated elsewhere (**Figure 6A**). The poor global coverage of the tide gauge stations makes it difficult to assess such a spatial bias. However, comparison of the 1 in 10-year water levels against those derived from the CoDEC-ERA5 simulations confirms the spatial bias

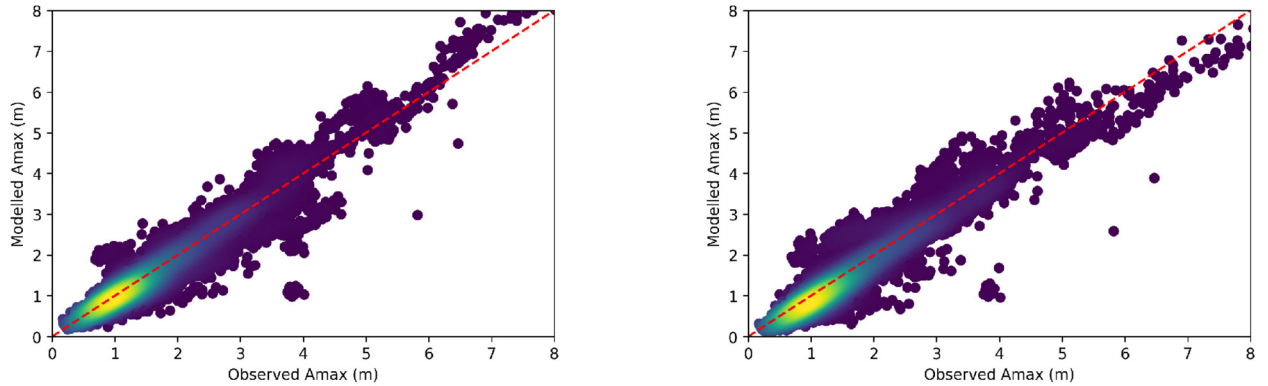

FIGURE 3 | Scatter density plots of the modeled and observed annual maxima (Amax) for the GESLA dataset for **(A)** the CoDEC-ERA5 dataset, and **(B)** the GTSR dataset. The data for all the tide gauge stations were combined. The red dotted line indicates the perfect fit line.

TABLE 4 | Model performance of the 1 in 10-year water levels (RP10) of the CoDEC-ERA, GTSR, and CoDEC-HIST dataset.

RP10	CoDEC-ERA5	GTSR	CoDEC-HIST
MB (m)	–0.10 SD 0.32	–0.14 SD 0.32	–0.13 SD 0.41
MAE (m)	0.19 SD 0.26	0.25 SD 0.25	0.30 SD 0.31
MAPE (%)	12.1 SD 12.8	17.4 SD 15.1	17.5 SD 15.1

The modelled RP10 values are compared against the observed RP10 values of the GESLA dataset (n = 485). The model performance is assessed in terms of the mean bias (MB), mean absolute error (MAE), and the mean absolute percentage error (MAPE).

(**Figure 6A**). While the bias compared to tide gauge stations is affected by the performance of GTSM, the bias between CoDEC-HIST and CoDEC-ERA5 is only affected by the difference in meteorological forcing. The bias between CoDEC-HIST and CoDEC-ERA5 is generally less than 0.2 m. Regions that are prone to tropical cyclones, such as Mozambique and the east coast of the United States, show a larger than average difference (>0.3 m). This appears to be an effect of the higher spatial resolution of the ERA5 forcing over the CMIP5 forcing (i.e., 0.5° × 0.5°, 3 hourly vs. 0.25° × 0.25°, hourly). In general, the 1 in 10-year water levels from CoDEC-HIST are lower than those from CoDEC-ERA5 (red points in **Figure 6B**). Some regions, including Europe (the Baltic Sea, the North Sea, and the Mediterranean Sea) and Alaska (Bering Sea), the 1 in 10-year water levels are higher in CoDEC-HIST (blue points in **Figure 6B**). The overestimation in Europe could be linked to the downscaling of EC-EARTH by the regional climate model DMI-HIRHAM that we applied for forcing for Europe. This regional model has a higher resolution than ERA5, and wind speeds will generally increase with a higher model resolution (Pryor et al., 2012). Moreover, the surface extreme wind fields in HIRHAM (25 and 50 km resolutions, downscaled from the reanalysis data) were evaluated by Donat et al. (2010), who concluded that HIRHAM simulated higher wind speed than the ERA-40 reanalysis data. The HIRHAM simulations (12 km resolution) used in this project have the same tendency (Yan et al., 2019). In general, the CMIP5 simulations are capable of capturing the spatial variability of the annual maximum wind speeds, while the historical temporal trends in annual maximum wind speeds are not well represented (Kumar et al., 2015). Since our focus is primarily on the average statistics over the entire period, this should not affect performance.

The overall performance of CoDEC-HIST is lower than the performance of CoDEC-ERA5. CoDEC-HIST tends to overestimate extreme sea levels in Europe. However, the differences in performance are rather small, and we conclude that CoDEC-HIST is sufficiently accurate to support large-scale assessments when used as baseline and for comparison against simulations for future climate scenarios with the same climate model.

Changes in 1 in 10-Year Water Levels in Response to Climate Change

Figure 7 maps the change in the 1 in 10-year water levels for the mid-century on the basis of CoDEC-RCP8.5 for the mid-century (2041–2070) and on the basis for CoDEC-RCP4.5 (2070–2100) for the end of the century, using CoDEC-HIST as a baseline. The average change across all output locations is 0.25 m (SD 0.15) and 0.34 m (SD 0.23) for CoDEC-RCP8.5 and CoDEC-RCP4.5, respectively. These relatively high SDs indicate a strong spatial heterogeneity. The most remarkable are the sea-level changes along the coastlines of the Baltic Sea and Hudson Bay, which experience sea-level fall rather than SLR due to the glacio-isostatic adjustment of land. When removing SLR, the average change across all output locations becomes negligible for both CoDEC-RCP8.5 and CoDEC-RCP4.5. It shows the change in 1 in 10-year water levels is largely driven by SLR. There are a few outliers that show large changes (the red dots in **Figures 7C,D**), which are probably due to spurious output when a grid cell falls dry (SLR may change when that occurs),

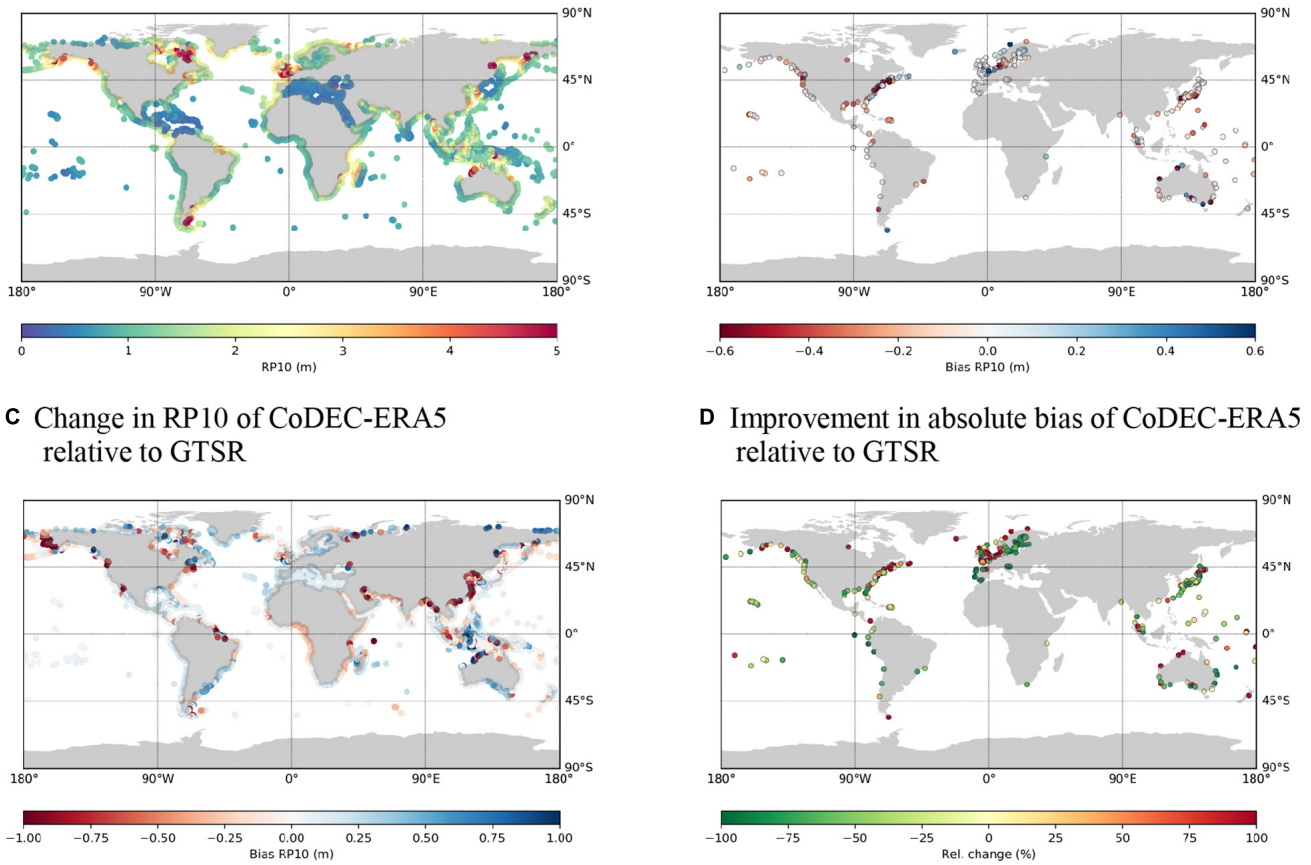

FIGURE 4 | Modeled water levels with **(A)** 1 in 10-year return periods (RP10) for **(A)** the CoDEC-ERA5 dataset, as well as **(B)** the bias of the 1 in 10-year water levels compared against observations from the GESLA dataset, **(C)** difference between the 1 in 10-year water levels derived from the CoDEC-ERA5 dataset and the GTSR dataset, and **(D)** Improvement in absolute bias of CoDEC-ERA5.

leading to large changes in comparison to the baseline. For both RCPs, only 5% of the output locations show a change larger than 0.1 m when the SLR signal is removed. **Figures 7C,D** show some spatial coherency regarding the projected change in the 1 in 10-year water levels. However, **Figure 8** indicates that aggregation of the changes at continental scales does not indicate significant changes in climate extremes. Europe shows the largest spread in changes (both negative and positive). For example, there are places along the Atlantic coasts of Spain, France, and Great Britain where the CoDEC projections indicate an increase in 1 in 10-year water levels of up to 0.2 m, in addition to SLR. This requires further analysis, but could possibly be linked to the northward movement of tropical cyclone tracks in the Atlantic (Haarsma et al., 2013). By contrast, the CoDEC projections indicate a decrease of the 1 in 10-year water levels near Denmark. It should be noted that changes in water level without SLR include both a change in storm surges and interaction effects in response to SLR. The tidal propagation and tide–surge interaction may respond to changes in water depth due to SLR (Arns et al., 2017; Haigh et al., 2019). This can also lead to changes in extreme sea levels, in addition to climatic changes.

On a global scale, our findings are largely in agreement with Vousdoukas et al. (2018b), who also concluded that changes in extreme sea levels are mainly driven by SLR. In contrast to our findings, they reported a very weak increasing trend for the projected global average of changes in storm surge in combination with wind-waves. While Vousdoukas et al. (2018b) did not differentiate between the contribution of wind-waves and storm surges to the water level change, wind-waves are probably more sensitive to climatic changes than storm surges. Similarly to our findings, Vousdoukas et al. (2018b) found strong spatial heterogeneity regarding the sign of water levels changes (increase vs. decrease) that tend to cancel each other when averaged over larger areas. When comparing our results to regional studies, the water level changes that exclude SLR appear to differ between studies. Like Colberg et al. (2019), who investigated extreme sea levels around Australia, we found an increase of near Tasmania and a decrease for most of the southern coastline, but our

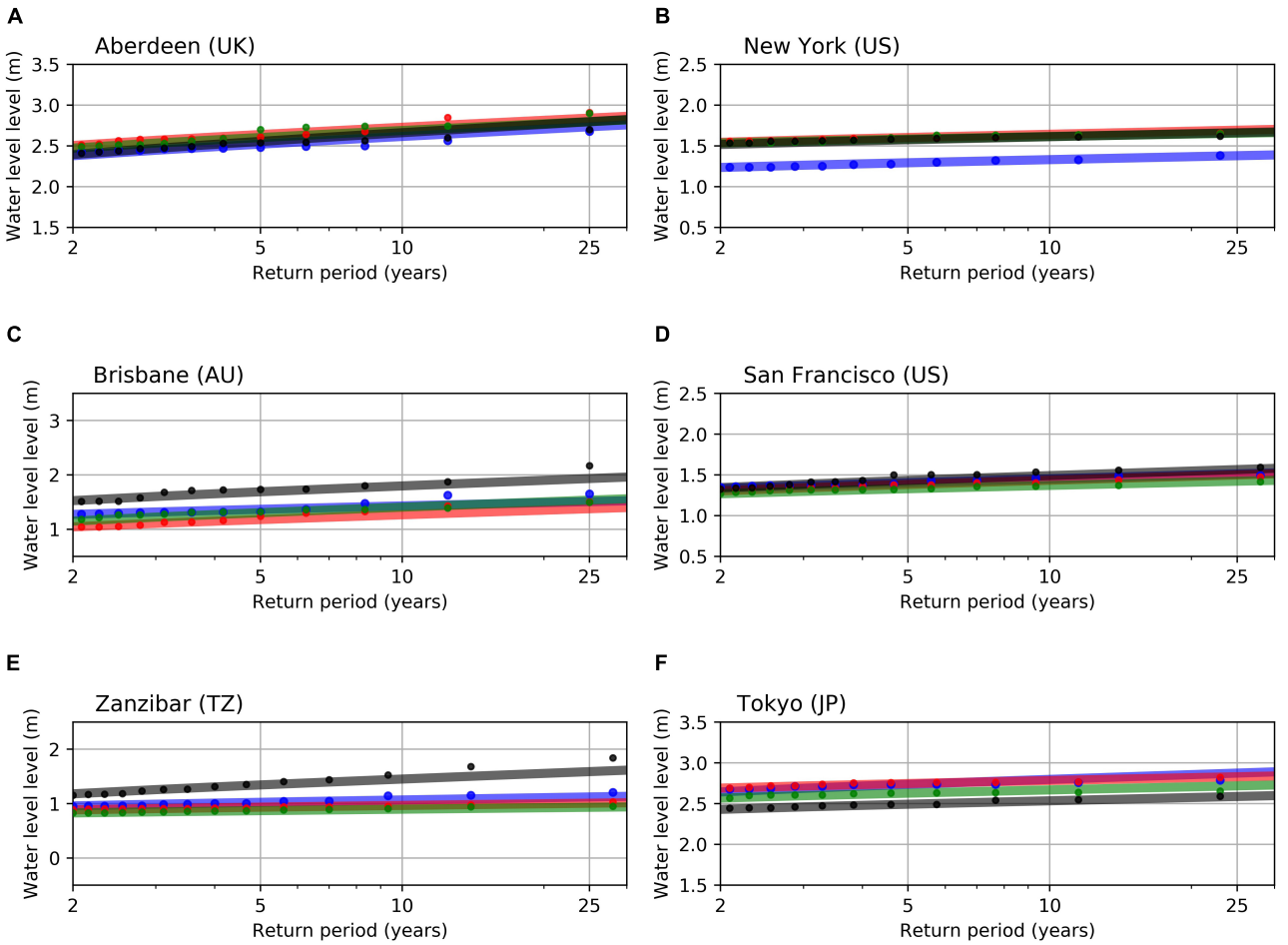

FIGURE 5 | Plots showing the Gumbel extreme value distribution fitted to the modeled and observed annual maxima at selected stations. The selected stations are **(A)** Aberdeen (UK), **(B)** New York, United States, **(C)** Brisbane, Australia, **(D)** San Fransisco, United States, **(E)** Zanzibar, Tanzania, and **(F)** Tokyo, Japan. The black line indicates the observed maxima, whereas GTSR, CoDEC-ERA5, and CoDEC-HIST are plotted as a blue, red, and green line, respectively. We also plot the empirical probabilities of the annual maxima (dots) based on the Weibull plotting positions.

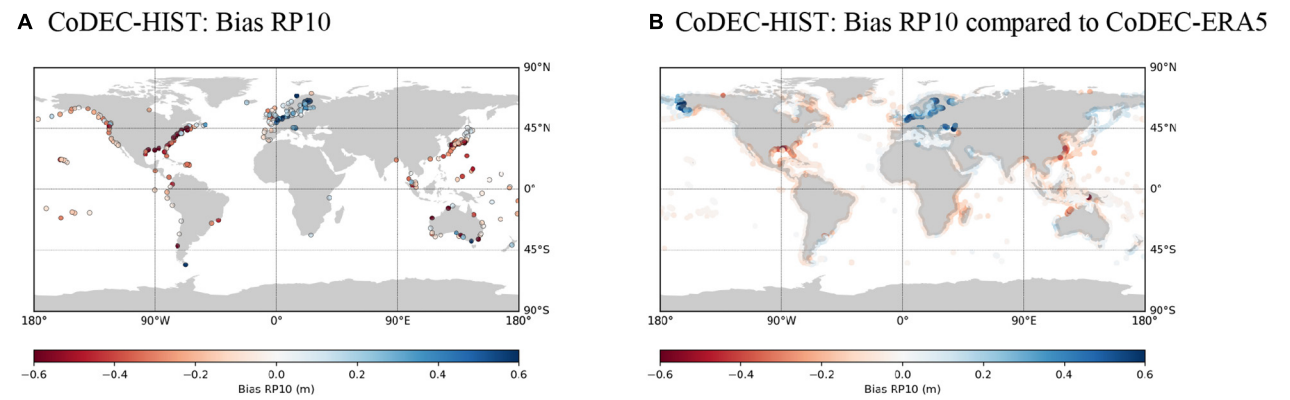

FIGURE 6 | Model performance of 1 in 10-year water levels for the CoDEC-HIST simulation shows as **(A)** the bias of the 1 in 10-year water levels compared against observations from the GESLA dataset and **(B)** the difference between the 1 in 10-year return periods derived from CoDEC-HIST and CoDEC-ERA5.

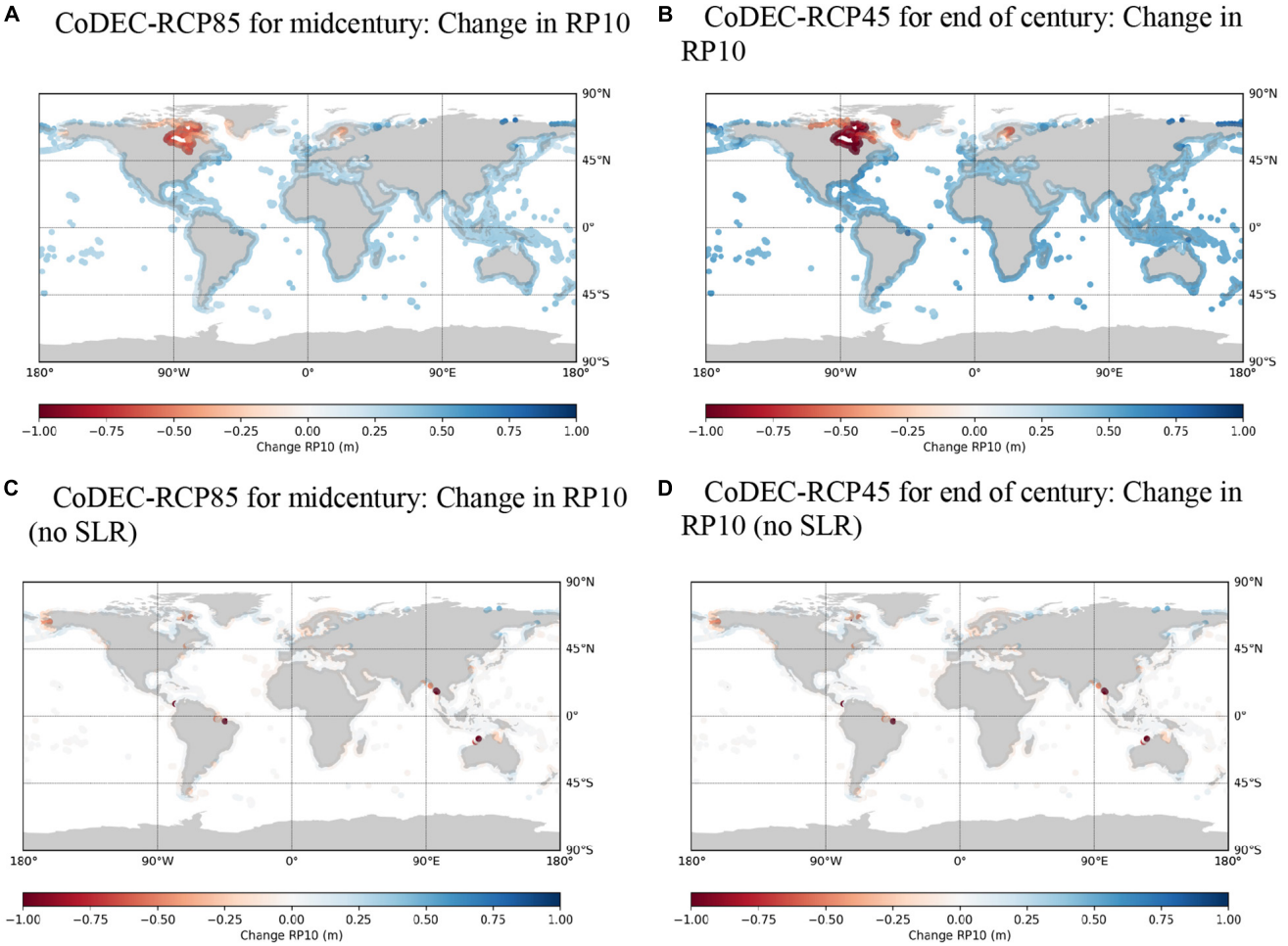

FIGURE 7 | Changes in the 1 in 10-year water levels (RP10) for **(A)** mid-century (2041–2070 with SLR of 2055) based on CoDEC-RCP8.5 compared to CoDEC-HIST and for **(B)** the end of the century (2071–2100 with SLR of 2085) based on CoDEC-RCP4.5 compared to CoDEC-HIST. We also show the change when SLR is not taken into account **(C,D)**. Note the different color scales.

results for the rest of the coastline are in contrast to theirs. Also in Europe there are many places where our results differ from Vousdoukas et al. (2016). The potential reasons for the discrepancies between different studies are wide-ranging. They could be due to the different climate models used, which show different climate signals. At the local scale, the differences could also be due to interaction effects, which are explicitly included in the CoDEC simulations (see section "Future Research Directions").

USE OF THE DATA FOR ASSESSING CLIMATE IMPACT AT LOCAL SCALE

As part of the project, the usability of the CoDEC dataset to assess climate impact for specific sectors was showcased by five use cases covering different parts of the European coastline. They considered a variety of coastal sectors and issues, such as flooding due to severe storm surge and wave overtopping, industrial sectors such as offshore wind, harbors, and ports, as well as coastal erosion and dune safety. One of these five use cases was on flood risk in Copenhagen, Denmark. Copenhagen is located on a connecting strait between the North Sea and the Baltic Sea in Northern Europe. While the strait is relatively sheltered during average weather conditions, the city has experienced storm surges. The historical city center is centered on the harbor, and the urban and industrial areas are located on the shoreline and include important infrastructure. The risk of flooding from the sea, especially due to storm surges, threatens economic assets, and this risk is projected to greatly increase with climate change (Hallegatte et al., 2011).

Therefore, climate adaptation is a focus point for the municipalities in the area, and a solid knowledge basis regarding coastal climate change is key to proper adaptation planning. European and global climate information services, such as the C3S portal, provide input for local use cases and national information regarding future climate change at the municipality

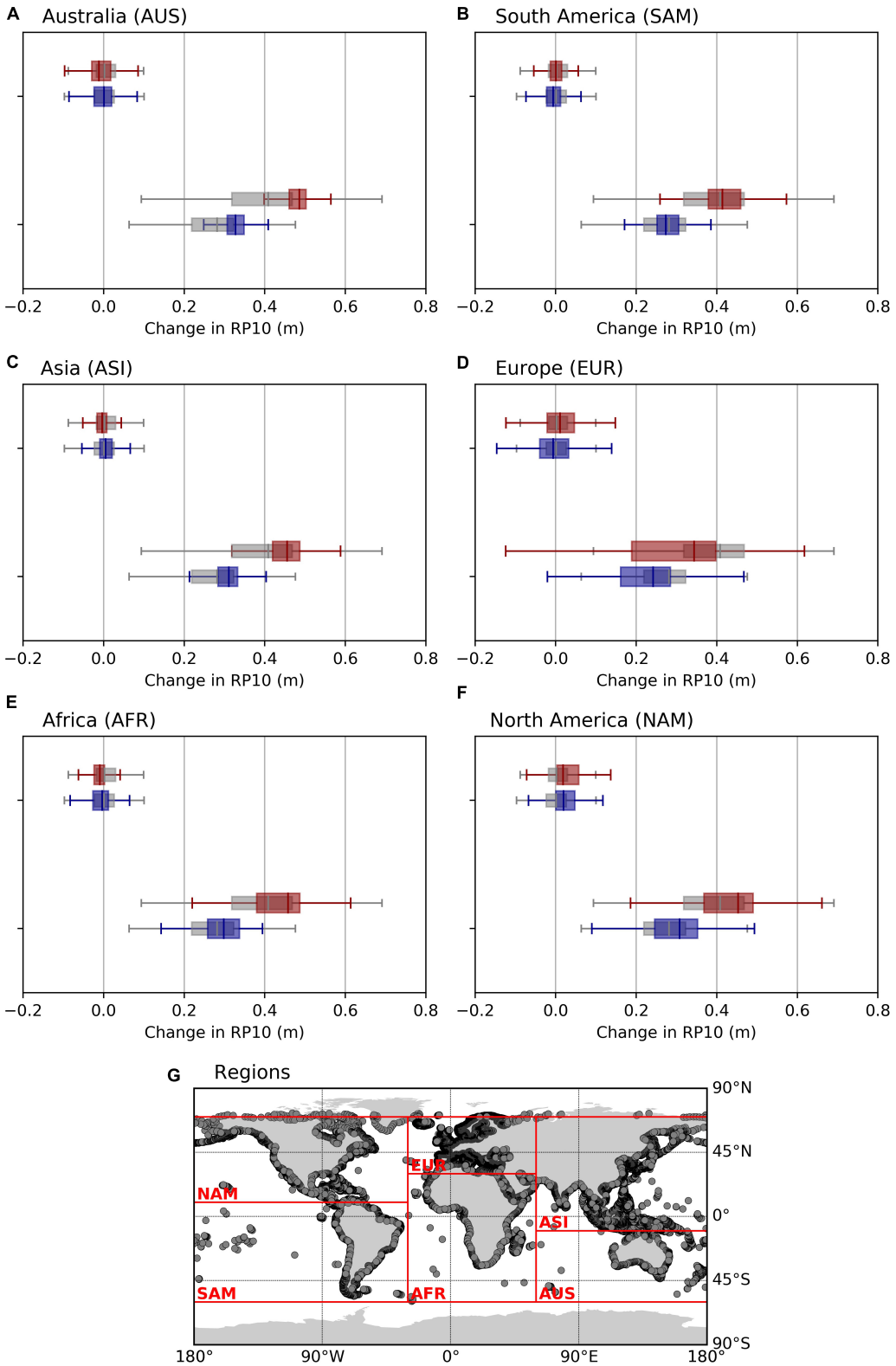

FIGURE 8 | Changes in the 1 in 10-year water levels (RP10) for different geographical regions, which are indicated in panel **G**. The regions shown are **(A)** Australia, **(B)** South America, **(C)** Asia, **(D)** Europe, **(E)** Africa, and **(F)** North America. We show the changes for the mid-century (2041–2070 with SLR of 2055) based on CoDEC-RCP8.5 compared to CoDEC-HIST (blue bars) and for the end of the century (2071–2100 with SLR of 2085) based on CoDEC-RCP4.5 compared to CoDEC-HIST (red bars). The gray bars indicate the global average. The box plots extend from the lower to upper quartile values of the data, with a line at the median. The whiskers indicate the 5th–95th percentiles.

TABLE 5 | Climate change indicators for the Copenhagen use case for the RCP8.5 mid-century (2041–2070) and RCP 4.5 end-century (2071–2100) periods relative to the present day (1977–2005).

Indicator		Unit	Present day	RCP8.5 mid century	RCP4.5 end century
Mean sea level		Meters change		0.22	0.26
Storm surge height (1 in 10-year event)		Percent change		19%	17%
Gate index (average no. of potential	Critical level 130 cm	Count	1	4	5
closures per year)	Critical level 150 cm	Count	0.2	1	1
	Critical level 170 cm	Count	0.1	0.4	0.4
Wave height (sea state)	Average	Percent change		–2%	*Not available*
	Storm surge conditions	Percent change		117%	*Not available*
Ocean current speed	Average	Percent change		–1%	–1%
	Storm surge conditions	Percent change		–9%	6%

Storm surge conditions are defined as the water level exceeding the 1 in 20-years return value.

level. Information has recently been collected into a Danish "Climate Atlas"[1], which contains information on temperature, precipitation, sea level, and storm surges.

To determine the needs for coastal climate change information, representatives of the expert technical staff of five municipalities in the Copenhagen area, together with the Danish Coastal Authority, were interviewed (Madsen et al., 2019). These experts identified information on changes in sea level, storm surges, and wave conditions as key needs. The idea of a "gate index" emerged during the interviews, which would provide information on the necessary number of closures of a potential new storm surge gate. Five indicators were formulated on the basis of the interviews (**Table 5**). The indicators were computed by downscaling the CoDEC simulations of MSL, together with regional simulations of waves and ocean current variability, using the WAM Cycle 4.5 wave model and the HBM-DKSS2013 3D ocean model, both of which are nested to have an approximately 1 km resolution in the study area (Günther et al., 1992; Berg and Poulsen, 2012). Wave simulations for the case study were only performed for the RCP8.5 scenario (**Table 5**).

Table 5 provides an overview of the results for the indicators. For MSL changes, the simulations show comparable values for the two RCPs. This indicates that, if the RCP8.5 scenario is followed, the study area will experience approximately the same sea level rise in the mid-century as it will for RCP4.5 at the end of the century. It should be noted that under RCP8.5, there is a continued acceleration of SLR, which will cause greater sea-level changes toward the end of the century and beyond. The changes in storm surge heights reflect the sea-level changes and indicate a risk of changes in the wind causing additional contributions to storm surges. However, further studies are needed, as changes in extreme wind in this region are rather uncertain. The gate index largely depends on the critical sea level to determine where the gate will be closed. Both RCPs show an increased number of closures with future SLR. Closures of potential gates will be required four to five times more frequently with a sea-level change in the range of 20–30 cm. The indicators on sea level and storm surge have been further detailed and derived for all the coastal stretches of Denmark in the Danish Climate Atlas.

[1] www.klimaatlas.dk

CONCLUSION

Aiming to contribute to the accurate global mapping of the impact of climate change on coastal regions, we have presented a novel global dataset of extreme sea levels, the CoDEC. This dataset is based on the next generation GTSMv3.0, which has a coastal resolution of 2.5 km (1.25 km in Europe). We have provided extreme sea levels for the period 1979–2017 that are based on the ERA5 climate reanalysis (CoDEC-ERA5), together with future climate projections from 2040 to 2100 (CoDEC-RCP4.5 and RCP8.5) and a baseline simulation (CoDEC-HIST). The validation of CoDEC-ERA5 against observed sea levels demonstrates a good performance. The annual maxima have a global MB of -0.04 m, which is 50% lower than the MB of the previous GTSR dataset. The validation of CoDEC-HIST shows a spatial bias, with higher sea levels in Europe and Alaska and lower sea levels elsewhere, but the overall performance is comparable, although slightly worse than CoDEC-ERA5. The average change in 1 in 10-year water levels across all the output locations was 0.25 and 0.34 m for CoDEC-RCP8.5 and CoDEC-RCP4.5, respectively. This change was largely driven by SLR, although at certain locations the change in water level was amplified by changes in climatic extremes, or by changes in the interaction effects in response to SLR.

The CoDEC dataset can be used for climate impact studies. CoDEC-ERA5 could, for example, be used to assess present-day flood damage, and to investigate the different aspects of coastal flooding, including climate variability and trends, or the cultural heritage and global infrastructure that is threatened by flooding (e.g., Muis et al., 2018; Reimann et al., 2018; Koks et al., 2019). The future projections can be used to assess how coastal flooding may change in response to climate change. In addition to the large-scale analysis of extreme sea levels, we have demonstrated how the CoDEC dataset can contribute to the understanding of climate impact on the local scale by presenting a use case for the city of Copenhagen. In comparison to the previous GTSR dataset, a promising innovation is that, in addition to the coastal points, the CoDEC dataset includes output on a regular grid in the ocean. We envisage that this way the CoDEC dataset can provide boundary conditions for regional models, which will facilitate dynamic downscaling from the global scale to the local scale.

FUTURE RESEARCH DIRECTIONS

In addition to the use of the CoDEC dataset for climate impact studies, there are various directions for future research. For example, it would be interesting to extend the evaluation of the model's performance. This could be done by also including a comparison with previous studies, both in Europe and worldwide (Cid et al., 2014; Vousdoukas et al., 2016; Paprotny and Terefenko, 2017; Fernández-Montblanc et al., 2019). Moreover, satellite altimetry could be used to evaluate the model's performance in areas where tide gauge data are unavailable (Cid et al., 2014). We have presented a first analysis of the sea-level changes in the CoDEC dataset based on the 1 in 10-year water levels, but this could be explored further. Decomposing the total water level to tides and storm surges would allow further investigation of the mechanisms driving the sea-level changes, and whether the interaction effects are important to include in large-scale assessments. Moreover, future research could quantify how the sea-level changes affect return periods (Vitousek et al., 2017; Frederikse et al., 2020). This could include an estimation of the uncertainty in the return periods due to fitting the extreme value distribution. In addition, recent studies have shown that fitting a Gumbel distribution to the annual maxima may lead to an overestimation of extreme sea levels, especially with lower probabilities (Buchanan et al., 2017; Wahl et al., 2017). Furthermore, the application of non-stationary approaches has several advantages in comparison to the stationary approaches used in this study (e.g., Menéndez and Woodworth, 2010; Mentaschi et al., 2016), which is worth exploring. A limitation of the current approach is that the return levels in regions prone to tropical cyclones may be underestimated. Tropical cyclones are relatively rare and generally affect a small stretch of coast. As a result, the length of the simulations is insufficient to estimate the return periods of the most extreme events. Studies have therefore relied on statistical methods to extend the historical period of several decades to thousands of years and to generate databases with synthetic tropical cyclones (Emanuel et al., 2006). Until now, studies that analyzed extreme sea levels based on synthetic tropical cyclones have been carried out on the continental to regional scale (Lin et al., 2012; Haigh et al., 2013; Marsooli et al., 2019). In the future, however, we aim to force GTSMv3.0 with a global dataset comprised of synthetic tropical cyclone tracks (Bloemendaal et al., 2020) and to develop reliable probabilities of storm surge generated by tropical cyclones. Users of the CoDEC dataset should be aware that the future projections are based on one climate model of the CMIP5 multi-model ensemble and on the CMIP5 ensemble MSL change. Previous studies have shown that future projections of extreme sea levels can have wide uncertainties, with a large spread between model ensemble members (Vousdoukas et al., 2018b; Colberg et al., 2019). The discrepancies between future projections from different studies highlight these uncertainties, and we cannot estimate the full uncertainties related to the future projections on the basis of one climate model. We have used a physically based approach to model the tides, surges, and changes in MSL, thereby dynamically including any interactions between them. Such a dynamic approach comes with large computational costs, and it was not feasible to run more than one model from the CMIP5 multi-model ensemble within the scope of the present study. However, having now developed the entire modeling framework, we see opportunities for addressing this limitation in the future.

DATA AVAILABILITY STATEMENT

The Gumbel parameters and the various return periods for the global coastline are available at the Zenodo repository with identifier 10.5281/zenodo.3660927. Time series, including storm surges, tides, and total water levels, together with the climate change indicators for Europe, will become available at the Climate Data Store (CDS) of the Copernicus Climate Change Service (C3S) at the following url: https://cds.climate.copernicus.eu/.

AUTHOR CONTRIBUTIONS

MA and SM were responsible for conducting the model runs and the post-processing. KY led the project and wrote the proposal together with MA and MV. SM wrote the manuscript, with contributions from KY and input from KM and JS for the Copenhagen case study. All the authors were involved in the writing of the manuscript, and discussed the results and the implications.

FUNDING

The research leading to these results was funded by Contract C3S-422-Lot2-Deltares European Services of the Copernicus Climate Change Service (11200665-003). Additional funding was received from the Deltares Strategic Research Program, Grant No. 11204672 and Grant No. l1000210-012). SM received additional funding from the MOSAIC research program (Grant No. ASDI.2018.036), which is financed by the Dutch Research Council (NWO). The Copernicus Climate Change Service (C3S) is funded by the European Union and aims to:

- Become an authoritative source of climate information for Europe.
- Build upon national investments and complement national climate service providers.
- Support the market for climate services in Europe.
- Provide free public access to climate change information.

ACKNOWLEDGMENTS

The authors would like to thank Thomas Wahl and Marta Marcos for providing the observed annual maxima from the GESLA dataset.

REFERENCES

Arns, A., Dangendorf, S., Jensen, J., Talke, S., Bender, J., and Pattiaratchi, C. (2017). Sea-level rise induced amplification of coastal protection design heights. *Sci. Rep.* 7:40171. doi: 10.1038/srep40171

Belmonte Rivas, M., and Stoffelen, A. (2019). Characterizing ERA-interim and ERA5 surface wind biases using ASCAT. *Ocean Sci. Discuss.* 15, 831–852. doi: 10.5194/os-2018-160

Berg, P., and Poulsen, W. J. (2012). *Implementation details for HBM*. DMI Technical Report No. 12-11. Copenhagen: Danish Meteorological Institute, 149.

Bloemendaal, N., Haigh, I. D., de Moel, H., Muis, S., Haarsma, R. J., and Aerts, J. C. J. H. (2020). Generation of a global synthetic tropical cyclone hazard dataset using STORM. *Sci. Data* 7:40. doi: 10.1038/s41597-020-0381-2

Bloemendaal, N., Muis, S., Haarsma, R. J., Verlaan, M., Apecechea, M. I., de Moel, H., et al. (2019). Global modeling of tropical cyclone storm surges using high-resolution forecasts. *Clim. Dyn.* 52, 5031–5044. doi: 10.1007/s00382-018-4430-x

Bloemendaal, N., Muis, S., Haarsma, R., Apechchea, M. I., Verlaan, M., Ward, P. J., et al. (2017). "Horizontal resolution effects on tropical cyclone storm surges," in *Proceedings of the 6th Summit on Hurricanes and Climate Change: from Hazard to Impact*, Heraklion.

Bouwer, L. M. (2018). Next-generation coastal risk models. *Nat. Clim. Chang.* 10:2010. doi: 10.1038/s41558-018-0262-2

Brown, S., Nicholls, R. J., Goodwin, P., Haigh, I. D., Lincke, D., Vafeidis, A. T., et al. (2018). Quantifying land and people exposed to sea-level rise with no mitigation and 1.5°C and 2.0°C rise in global temperatures to year 2300. *Earths Future* 6, 583–600. doi: 10.1002/2017EF000738

Buchanan, M. K., Oppenheimer, M., and Kopp, R. E. (2017). Amplification of flood frequencies with local sea level rise and emerging flood regimes. *Environ. Res. Lett.* 12:064009. doi: 10.1088/1748-9326/aa6cb3

Charnock, H. (1955). Wind stress on a water surface. *Q. J. R. Meteorol. Soc.* 81, 639–640. doi: 10.1002/qj.49708135027

Christensen, O. B., Drews, M., Christensen, J. H., Dethloff, K., Ketelsen, K., Hebestadt, I., et al. (2007). *The HIRHAM Regional Climate Model Version 5 (beta)*. Technical Report No. 06-17. Copenhagen: Danish Meteorological Institute.

Church, J. A., Clark, P. U., Cazenave, A., Gregory, J. M., Jevrejeva, S., Levermann, A., et al. (2013). "Sea level change," in *Climate Change 2013: The Physical Science Basis. Contribution of Working Group I to the Fifth Assessment Report of the Intergovernmental Panel on Climate Change*, eds T. F. Stocker, D. Qin, G.-K. Plattner, M. Tignor, S. K. Allen, J. Boschu, et al. (Cambridge: Cambridge University Press), doi: 10.1017/CB09781107415315.026

Cid, A., Castanedo, S., Abascal, A. J., Menéndez, M., and Medina, R. (2014). A high resolution hindcast of the meteorological sea level component for Southern Europe: the GOS dataset. *Clim. Dyn.* 43, 2167–2184. doi: 10.1007/s00382-013-2041-0

Colberg, F., McInnes, K. L., O'Grady, J., and Hoeke, R. (2019). Atmospheric circulation changes and their impact on extreme sea levels around Australia. *Nat. Hazards Earth Syst. Sci.* 19, 1067–1086. doi: 10.5194/nhess-19-1067-2019

Consortium EMODnet Bathymetry (2018). *EMODnet Digital Bathymetry (DTM)*. Available online at: https://sextant.ifremer.fr/record/18ff0d48-b203-4a65-94a9-5fd8b0ec35f6/ (accessed March, 2018).

Copernicus Climate Change Service [C3S] (2017). *ERA5: Fifth Generation of ECMWF Atmospheric Reanalyses of the Global Climate*. Available online at: https://cds.climate.copernicus.eu/cdsapp#!/home (accessed July, 2018).

de Lima Rego, J., and Li, C. (2010). Nonlinear terms in storm surge predictions: effect of tide and shelf geometry with case study from Hurricane Rita. *J. Geophys. Res.* 115:C06020. doi: 10.1029/2009JC005285

Donat, M. G., Leckebusch, G. C., Wild, S., and Ulbrich, U. (2010). Benefits and limitations of regional multi-model ensembles for storm loss estimations. *Clim. Res.* 44, 211–225. doi: 10.3354/cr00891

Dullaart, J. C. M., Muis, S., Bloemendaal, N., and Aerts, J. C. J. H. (2019). Advancing global storm surge modelling using the new ERA5 climate reanalysis. *Clim. Dyn.* 54, 1007–1021. doi: 10.1007/s00382-019-05044-0

Emanuel, K. A., Ravela, S., Vivant, E., and Risi, C. (2006). A statistical deterministic approach to hurricane risk assessment. *Bull. Am. Meteorol. Soc.* 87, 299–314. doi: 10.1175/BAMS-87-3-299

Fernández-Montblanc, T., Vousdoukas, M. I., Ciavola, P., Voukouvalas, E., Mentaschi, L., Breyiannis, G., et al. (2019). Towards robust pan-European storm surge forecasting. *Ocean Model.* 133, 129–144. doi: 10.1016/j.ocemod.2018.12.001

Frederikse, T., Buchanan, M. K., Lambert, E., Kopp, R. E., Oppenheimer, M., Rasmussen, D. J., et al. (2020). Antarctic Ice Sheet and emission scenario controls on 21st-century extreme sea-level changes. *Nat. Commun.* 11:390. doi: 10.1038/s41467-019-140496

Fretwell, P., Pritchard, H. D., Vaughan, D. G., Bamber, J. L., Barrand, N. E., Bell, R., et al. (2013). Bedmap2: improved ice bed, surface and thickness datasets for Antarctica. *Cryosphere* 7, 375–393. doi: 10.5194/tc-7-375-2013

GEBCO (2014). *General Bathymetric Chart of the Oceans (GEBCO) 2014 Grid*. Available online at: https://www.gebco.net/

Günther, H., Hasselmann, S., and Janssen, P. A. E. M. (1992). *The WAM Model Cycle 4.0*. Technical Report No. 4. Hamburg: Deutsches Klimarechenzentrum.

Haarsma, R. J., Hazeleger, W., Severijns, C., de Vries, H., Sterl, A., Bintanja, R., et al. (2013). More hurricanes to hit Western Europe due to global warming. *Geophys. Res. Lett.* 40, 1783–1788. doi: 10.1002/grl.50360

Haigh, I. D., Pickering, M. D., Green, J. A. M., Arbic, B. K., Arns, A., Dangendorf, S., et al. (2019). The Tides They Are a-Changin': a comprehensive review of past and future non-astronomical changes in tides, their driving mechanisms and future implications. *Rev. Geophys.* 58:e2018RG000636. doi: 10.1029/2018rg000636

Haigh, I. D., Wijeratne, E. M. S., MacPherson, L. R., Pattiaratchi, C. B., Mason, M. S., Crompton, R. P., et al. (2013). Estimating present day extreme water level exceedance probabilities around the coastline of Australia: tides, extra-tropical storm surges and mean sea level. *Clim. Dyn.* 42, 121–138. doi: 10.1007/s00382-012-1652-1

Hallegatte, S., Ranger, N., Mestre, O., Dumas, P., Corfee-Morlot, J., Herweijer, C., et al. (2011). Assessing climate change impacts, sea level rise and storm surge risk in port cities: A case study on Copenhagen. *Clim. Change* 104, 113–137. doi: 10.1007/s10584-010-9978-3

Hausfather, Z., and Peters, G. P. (2020). Emissions – the 'business as usual' story is misleading. *Nature* 577, 618–620. doi: 10.1038/d41586-020-001773

Hinkel, J., Lincke, D., Vafeidis, A. T., Perrette, M., Nicholls, R. J., Tol, R. S. J., et al. (2014). Coastal flood damage and adaptation costs under 21st century sea-level rise. *Proc. Natl. Acad. Sci. U.S.A.* 111, 3292–3297. doi: 10.1073/pnas.1222469111

Horsburgh, K. J., and Wilson, C. (2007). Tide-surge interaction and its role in the distribution of surge residuals in the North Sea. *J. Geophys. Res.* 112:C08003. doi: 10.1029/2006JC004033

Hoyer, S., and Hamman, J. J. (2017). xarray: N-D labeled Arrays and Datasets in Python. *J. Open Res. Softw.* 5:10. doi: 10.5334/jors.148

Irazoqui Apecechea, M., Verlaan, M., Zijl, F., Le Coz, C., and Kernkamp, H. W. J. (2017). Effects of self-attraction and loading at a regional scale: a test case for the Northwest European Shelf. *Ocean Dyn.* 67, 729–749. doi: 10.1007/s10236-017-1053-4

Jacob, D., Petersen, J., Eggert, B., Alias, A., Christensen, O. B., Bouwer, L. M., et al. (2014). EURO-CORDEX: New high-resolution climate change projections for European impact research. *Reg. Environ. Chang.* 14, 563–578. doi: 10.1007/s10113-013-0499-2

Jevrejeva, S., Jackson, L. P., Grinsted, A., Lincke, D., and Marzeion, B. (2018). Flood damage costs under the sea level rise with warming of 1.5∘C *and* 2∘C. *Environ. Res. Lett.* 13:074014. doi: 10.1088/1748-9326/aacc76

Kernkamp, H. W., Van Dam, A., Stelling, G. S., and de Goede, E. D. (2011). Efficient scheme for the shallow water equations on unstructured grids with application to the Continental Shelf. *Ocean Dyn.* 61, 1175–1188. doi: 10.1007/s10236-011-0423-6

Koks, E. E., Rozenberg, J., Zorn, C., Tariverdi, M., Vousdoukas, M., Fraser, S. A., et al. (2019). A global multi-hazard risk analysis of road and railway infrastructure assets. *Nat. Commun.* 10:2677. doi: 10.1038/s41467-019-10442-3

Kumar, D., Mishra, V., and Ganguly, A. R. (2015). Evaluating wind extremes in CMIP5 climate models. *Clim. Dyn.* 45, 411–453. doi: 10.1007/s00382-014-2306-2

Lin, N., Emanuel, K. A., Oppenheimer, M., and Vanmarcke, E. (2012). Physically based assessment of hurricane surge threat under climate change. *Nat. Clim. Chang.* 2, 462–467. doi: 10.1038/nclimate1389

Lincke, D., and Hinkel, J. (2018). Economically robust protection against 21st century sea-level rise. *Glob. Environ. Chang.* 51, 67–73. doi: 10.1016/j.gloenvcha.2018.05.003

Madsen, K. S., Murawski, J., Blokhina, M., and Su, J. (2019). Sea level change: mapping Danish municipality needs for climate information. *Front. Earth Sci.* 7:81. doi: 10.3389/feart.2019.00081

Marsooli, R., Lin, N., Emanuel, K., and Feng, K. (2019). Climate change exacerbates hurricane flood hazards along US Atlantic and Gulf Coasts in spatially varying patterns. *Nat. Commun.* 10:3785. doi: 10.1038/s41467-019-11755-z

Mawdsley, R. J., Haigh, I. D., and Wells, N. C. (2015). Global secular changes in different tidal high water, low water and range levels. *Earths Future* 3, 1–16. doi: 10.1002/2014EF000282

Menéndez, M., and Woodworth, P. L. (2010). Changes in extreme high water levels based on a quasi-global tide-gauge data set. *J. Geophys. Res* 115:C10011. doi: 10.1029/2009JC005997

Mentaschi, L., Vousdoukas, M., Voukouvalas, E., Sartini, L., Feyen, L., Besio, G., et al. (2016). The transformed-stationary approach: a generic and simplified methodology for non-stationary extreme value analysis. *Hydrol. Earth Syst. Sci.* 20, 3527–3547. doi: 10.5194/hess-20-3527-2016

Moss, R. H., Edmonds, J. A., Hibbard, K. A., Manning, M. R., Rose, S. K., Van Vuuren, D. P., et al. (2010). The next generation of scenarios for climate change research and assessment. *Nature* 463, 747–756. doi: 10.1038/nature08823

Muis, S., Haigh, I. D., Nobre, G. G., Aerts, J. C. J. H., and Ward, P. J. (2018). Influence of El Niño–Southern Oscillation on global coastal flooding. *Environ. Res. Lett.* 6, 1311–1322.

Muis, S., Lin, N., Verlaan, M., Winsemius, H. C., Ward, P. J., and Aerts, J. C. J. H. (2019). Spatiotemporal patterns of extreme sea levels along the western North-Atlantic coasts. *Sci. Rep.* 9:3391. doi: 10.1038/s41598-019-40157-w

Muis, S., Verlaan, M., Winsemius, H. C., Aerts, J. C. J. H. J. H., and Ward, P. J. (2016). A global reanalysis of storm surges and extreme sea levels. *Nat. Commun.* 7:11969. doi: 10.1038/ncomms11969

Nicholls, R. J., Brown, S., Goodwin, P., Wahl, T., Lowe, J., Solan, M., et al. (2018). Stabilization of global temperature at 1.5°C and 2.0°C: implications for coastal areas. *Philos. Trans. R. Soc. A Math. Phys. Eng. Sci.* 376:20160448. doi: 10.1098/rsta.2016.0448

Oppenheimer, M., Glavovic, B., Hinkel, J., van de Wal, R., Magnan, A. K., Abd-Elgawad, A., et al. (2019). "Sea level rise and implications for low lying islands, coasts and communities," in *PCC Special Report on the Ocean and Cryosphere in a Changing Climate*, eds H.-O. Pörtner, D. C. Roberts, V. Masson-Delmotte, P. Zhai, M. Tignor, E. Poloczanska, et al. (Cambridge: Cambridge University Press).

Paprotny, D., and Terefenko, P. (2017). New estimates of potential impacts of sea level rise and coastal floods in Poland. *Nat. Hazards* 85, 1249–1277. doi: 10.1007/s11069-016-2619-z

Peters, G. P., Andrew, R. M., Boden, T., Canadell, J. G., Ciais, P., Le Quéré, C., et al. (2013). The challenge to keep global warming below 2C. *Nat. Clim. Chang.* 3, 4–6. doi: 10.1038/nclimate1783

Pickering, M. D. D., Horsburgh, K. J. J., Blundell, J. R. R., Hirschi, J. J.-M. J. M., Nicholls, R. J. J., Verlaan, M., et al. (2017). The impact of future sea-level rise on the global tides. *Cont. Shelf Res.* 142, 50–68. doi: 10.1016/j.csr.2017.02.004

Pickering, M. D. D., Wells, N. C., Horsburgh, K. J., and Green, J. A. M. A. M. (2012). The impact of future sea-level rise on the European Shelf tides. *Cont. Shelf Res.* 35, 1–15. doi: 10.1016/j.csr.2011.11.011

Pryor, S. C., Nikulin, G., and Jones, C. (2012). Influence of spatial resolution on regional climate model derived wind climates. *J. Geophys. Res. Atmos.* 117:D03117. doi: 10.1029/2011JD016822

Reimann, L., Vafeidis, A. T., Brown, S., Hinkel, J., and Tol, R. S. J. (2018). Mediterranean UNESCO World Heritage at risk from coastal flooding and erosion due to sea-level rise. *Nat. Commun.* 9:4161. doi: 10.1038/s41467-018-06645-9

Schenkel, B. A., and Hart, R. E. (2012). An examination of tropical cyclone position, intensity, and intensity life cycle within atmospheric reanalysis datasets. *J. Clim.* 25, 3453–3475. doi: 10.1175/2011JCLI4208.1

Schulzweida, U. (2019). *CDO User Guide Version 1.9.6*. Available online at: https://doi.org/10.5281/zenodo.2558193 (accessed July, 2019).

Stammer, D., Ray, R. D., Andersen, O. B., Arbic, B. K., Bosch, W., Carrère, L., et al. (2014). Accuracy assessment of global barotropic ocean tide models. *Rev. Geophys.* 52, 243–282. doi: 10.1002/2014RG000450

Taylor, K. E., Stouffer, R. J., and Meehl, G. A. (2012). An overview of CMIP5 and the experiment design. *Bull. Am. Meteorol. Soc.* 93, 485–498. doi: 10.1175/BAMS-D-11-00094.1

Vafeidis, A. T., Nicholls, R. J., McFadden, L., Tol, R. S. J., Hinkel, J., Spencer, T., et al. (2008). A new global coastal database for impact and vulnerability analysis to sea-level rise. *J. Coast. Res.* 244, 917–924. doi: 10.2112/06-0725.1

Verlaan, M., De Kleermaeker, S., and Buckman, L. (2015). "GLOSSIS: global storm surge forecasting and information system," in *Proceedings of the 22nd Australasian Coastal and Ocean Engineering Conference and the 15th Australasian Port and Harbour Conference* (Auckland: Engineers Australia and IPENZ), 1–6.

Vitousek, S., Barnard, P. L., Fletcher, C. H., Frazer, N., Erikson, L., and Storlazzi, C. D. (2017). Doubling of coastal flooding frequency within decades due to sea-level rise. *Sci. Rep.* 7:1399. doi: 10.1038/s41598-017-01362-7

Vousdoukas, M. I., Mentaschi, L., Voukouvalas, E., Bianchi, A., Dottori, F., and Feyen, L. (2018a). Climatic and socioeconomic controls of future coastal flood risk in Europe. *Nat. Clim. Chang.* 8, 776–780. doi: 10.1038/s41558-018-0260-4

Vousdoukas, M. I., Mentaschi, L., Voukouvalas, E., Verlaan, M., and Feyen, L. (2017). Extreme sea levels on the rise along Europe's coasts. *Earths Future* 5, 304–323. doi: 10.1002/2016EF000505

Vousdoukas, M. I., Mentaschi, L., Voukouvalas, E., Verlaan, M., Jevrejeva, S., Jackson, L. P., et al. (2018b). Global probabilistic projections of extreme sea levels show intensification of coastal flood hazard. *Nat. Commun.* 9:2360. doi: 10.1038/s41467-018-04692-w

Vousdoukas, M. I., Voukouvalas, E., Annunziato, A., Giardino, A., and Feyen, L. (2016). Projections of extreme storm surge levels along Europe. *Clim. Dyn.* 47, 1–20. doi: 10.1007/s00382-016-3019-5

Wahl, T. (2017). Sea-level rise and storm surges, relationship status: complicated! *Environ. Res. Lett.* 12:111001. doi: 10.1088/1748-9326/aa8eba

Wahl, T., Haigh, I. D., Nicholls, R. J., Arns, A., Dangendorf, S., Hinkel, J., et al. (2017). Understanding extreme sea levels for broad-scale coastal impact and adaptation analysis. *Nat. Commun.* 8:16075. doi: 10.1038/ncomms16075

Ward, P. J., Jongman, B., Salamon, P., Simpson, A., Bates, P. D., De Groeve, T., et al. (2015). Usefulness and limitations of global flood risk models. *Nat. Clim. Chang.* 5, 712–715. doi: 10.1038/nclimate2742

Wilmes, S.-B., Green, J. A. M., Gomez, N., Rippeth, T. P., and Lau, H. (2017). Global tidal impacts of large-scale ice-sheet collapses. *J. Geophys. Res. Ocean* 122, 8354–8370. doi: 10.1002/2017JC013109

Woodworth, P. L., Hunter, J. R., Marcos, M., Caldwell, P., Menéndez, M., and Haigh, I. (2016). Towards a global higher-frequency sea level dataset. *Geosci. Data J.* 3, 50–59. doi: 10.1002/gdj3.42

Yan, K., Minns, T., Irazoqui Apecechea, M., and Muis, S. (2019). *C3S D422Lot2.DEL.3.3 User Guide*. Reading: ECMWF.

Conflict of Interest: The authors declare that the research was conducted in the absence of any commercial or financial relationships that could be construed as a potential conflict of interest.

The reviewer MV declared a past co-authorship with one of the authors MV to the handling Editor.

frontiers in Marine Science

ORIGINAL RESEARCH
published: 28 May 2020
doi: 10.3389/fmars.2020.00259

Coupling and Decoupling of High Biomass Phytoplankton Production and Hypoxia in a Highly Dynamic Coastal System: The Changjiang (Yangtze River) Estuary

Feng Zhou[1,2], Fei Chai[1,3]*, Daji Huang[1], Mark Wells[3,1], Xiao Ma[1], Qicheng Meng[1], Huijie Xue[3,4], Jiliang Xuan[1], Pengbin Wang[1,5], Xiaobo Ni[1], Qiang Zhao[6], Chenggang Liu[1,5], Jilan Su[5] and Hongliang Li[1]*

[1] State Key Laboratory of Satellite Ocean Environment Dynamics, Second Institute of Oceanography, Ministry of Natural Resources, Hangzhou, China, [2] School of Oceanography, Shanghai Jiao Tong University, Shanghai, China, [3] School of Marine Science, University of Maine, Orono, ME, United States, [4] State Key Laboratory of Tropical Oceanography, South China Sea Institute of Oceanology, Chinese Academy of Sciences, Guangzhou, China, [5] Key Laboratory of Marine Ecosystem Dynamics, Second Institute of Oceanography, Ministry of Natural Resources, Hangzhou, China, [6] Ningbo Marine Environment Monitoring Center Station, Ministry of Natural Resources, Ningbo, China

OPEN ACCESS

Edited by:
Marta Marcos,
University of the Balearic Islands, Spain

Reviewed by:
Sabine Schmidt,
Centre National de la Recherche Scientifique (CNRS), France
Antonio Olita,
Italian National Research Council (CNR), Italy

***Correspondence:**
Feng Zhou
zhoufeng@sio.org.cn
Fei Chai
fchai@maine.edu

Specialty section:
This article was submitted to Coastal Ocean Processes, a section of the journal Frontiers in Marine Science

Received: 31 October 2019
Accepted: 31 March 2020
Published: 28 May 2020

Citation:
Zhou F, Chai F, Huang D, Wells M, Ma X, Meng Q, Xue H, Xuan J, Wang P, Ni X, Zhao Q, Liu C, Su J and Li H (2020) Coupling and Decoupling of High Biomass Phytoplankton Production and Hypoxia in a Highly Dynamic Coastal System: The Changjiang (Yangtze River) Estuary. Front. Mar. Sci. 7:259. doi: 10.3389/fmars.2020.00259

The global increase in coastal hypoxia over the past decades has resulted from a considerable rise in anthropogenically-derived nutrient loading. The spatial relationship between surface phytoplankton production and subsurface hypoxic zones often can be explained by considering the oceanographic conditions associated with basin size, shape, or bathymetry, but that is not the case where nutrient-enriched estuarine waters merge into complex coastal circulation systems. We investigated the physical and biogeochemical processes that create high-biomass phytoplankton production and hypoxia off the Changjiang (Yangtze River) Estuary in the East China Sea (ECS). Extensive *in situ* datasets were linked with a coupled Regional Ocean Modeling Systems (ROMS) and carbon, silicate, and nitrogen ecosystem (CoSiNE) model to explain the temporary decoupling of phytoplankton production and hypoxia. The CoSiNE model contains two functional groupings of phytoplankton—diatoms and "other"—and the model results show that diatoms were the major contributors of carbon export and subsurface hypoxia. Both observations and simulations show that, although surface phytoplankton concentrations generally were much higher above hypoxic zones, high-biomass distributions during the summer–fall period did not closely align with that of the bottom hypoxic zones. Model results show that this decoupling was largely due to non-uniform offshore advection and detachment of subsurface segments of water underlying the Changjiang River plume. The near-bottom water carried organic-rich matter northeast and east of the major hypoxic region. The remineralization of this particle organic matter during transit created offshore patches of hypoxia spatially and temporally separated from the nearshore high-biomass phytoplankton production. The absence of high phytoplankton biomass offshore, and the 1–8 weeks' time lag between

the surface diatom production and bottom hypoxia, made it otherwise difficult to explain the expanded core hypoxic patch and detached offshore hypoxic patches. The findings here highlight the value of developing integrated physical and biogeochemical models to aid in forecasting coastal hypoxia under both contemporary and future coastal ocean conditions.

Keywords: hypoxia, diatom bloom, Changjiang Estuary, ROMS, CoSiNE, advection

INTRODUCTION

The flux of anthropogenically derived nutrients into estuaries and coastal oceans has been increasing worldwide over the past few decades (Anderson et al., 2002; Zhou et al., 2008; Conley et al., 2009; Liu et al., 2015). A fundamental effect of this increasing nutrient availability has been more frequent, intense, and widely distributed phytoplankton blooms (Smith, 2003; Anderson et al., 2008; Heisler et al., 2008) that often differ in species composition from earlier times (Glibert et al., 2001; Quay et al., 2013; Jiang et al., 2014). When these high-biomass blooms become nutrient-limited, the algae die and sink below the photic zone, where microbial respiration consumes dissolved oxygen (Officer et al., 1984; Cloern, 2001; Rabalais et al., 2002; Carrick et al., 2005). If bottom water replenishment rates are slow, the elevated decay rates below the pycnocline lead to hypoxia or even anoxia in severe cases (Anderson et al., 2002; Conley et al., 2002; Kasai et al., 2007).

There are numerous examples of increased hypoxia in nearshore waters over the past several decades, including the Baltic Sea (Conley et al., 2002; Carstensen et al., 2014; Neumann et al., 2017), the Chesapeake Bay (Newcombe and Horne, 1938; Hagy et al., 2004; Kemp et al., 2005), the Gulf of Mexico (Rabalais et al., 2002; Turner et al., 2008), as well as many other coastal waters (Legovi and Petricioli, 1991; Li et al., 2002; Dai et al., 2006; Conley et al., 2007; Nakayama et al., 2010; Tishchenko et al., 2011; Zhai et al., 2012; Ram et al., 2014; Zhang et al., 2015; Krogh et al., 2018), and inland waters (Zaitsev, 1992; Zhou et al., 2013). In most of these examples, the long-term increasing trend in hypoxia was shown to link with increased anthropogenic nutrient loading and the development of large-scale or frequent phytoplankton blooms. It is believed that the vast majority of anthropogenically enhanced inputs of nitrogen (N) and phosphorus (P) to the Changjiang (Yangtze River) watershed result from the tremendous use of fertilizers, leading to increased N:P and N:silicate (Si) ratios in estuarine waters (Glibert et al., 2006). Altered nutrient ratios ultimately can drive shifts in the dominant phytoplankton speciation away from Si-dependent diatoms that commonly support high fisheries productivities to less important primary producers or even toxic species (Quay et al., 2013; Jiang et al., 2015), although only after the Si concentrations decrease to growth rate-limiting levels. While the overall long-term trends in nutrient concentration and composition show enormous regional variations, strategies that control the input of both N and P are strongly suggested and found to be effective in lessening the negative impacts of cultural eutrophication (Conley et al., 2009; Paerl, 2009).

Waters beneath the highly productive surface layer become hypoxic when bacterial respiration associated with the decay of the sinking biomass reduces the dissolved oxygen concentration to <2–3 mg/L, and even anoxic when continued oxygen consumption results in dissolved oxygen <0.5 mg/L (Officer et al., 1984; Chan et al., 2008; Pitcher and Probyn, 2011). Most multicellular organisms cannot survive under hypoxic conditions, and in some areas mass mortalities of fish and benthos typically accompany the onset of hypoxia. However, hypoxia does not necessarily develop in regions with very high rates of natural or anthropogenically fueled primary production as long as the replenishment rates of the deep water are sufficiently strong to supply oxygen in excess of the demand for the decay of organic matter (Ishikawa et al., 2004; Fennel and Testa, 2018). These factors vary over time and often interact with estuary dynamics. The interactive complexity of these processes generates low dissolved oxygen conditions having different spatiotemporal features in coastal regions (Rabouille et al., 2008).

In many cases, the spatial relationship linking surface phytoplankton production and restricted subsurface water exchange can be reasonably predicted by considering the nutrient input rates, regional geomorphology, and oceanographic conditions (Justić et al., 1993; Scavia et al., 2003; Turner et al., 2006). More challenging are those estuarine systems that merge into open coastal or large embayment waters with dynamic circulation patterns. Here, a difference in surface and subsurface advection can lead to a temporal and spatial mismatch or decoupling of surface high-biomass regions and hypoxia zones in coastal waters.

The Changjiang Estuary (CJE) is subject to very high nutrient loading and high N:P and N:Si ratios (Tian et al., 1993; Zhang, 1996; Liu et al., 2003; Glibert et al., 2006; Jiang et al., 2014). Dissolved inorganic nitrogen (DIN) loading from the Changjiang has increased from 20 to 120 μM over the five decades between 1960 and 2010 (Li et al., 2007; Siswanto et al., 2008). In addition to this estuarine inflow, the coastal flow outside the CJE also brings oceanic nutrients to the estuarine region through a complex shelf-circulation system (**Figure 1**). Of particular importance is the subsurface injection of N and P from the strong western boundary current (the Kuroshio) (Liu et al., 1992; Chen, 1996; Zhang et al., 2007). The Kuroshio water mass that reaches the CJE originated from strong upwelling north of Taiwan (Su and Pan, 1987; Su, 1998; Wang et al., 2016; Ding et al., 2019) and contains nitrate concentrations that have increased by 25% over the same time frame (Guo et al., 2012). Once on shelf, the Kuroshio water joins the Taiwan Warm Current (TWC) (Su and Pan, 1987; Su, 1998; Zhu et al., 2004; Jan et al., 2006;

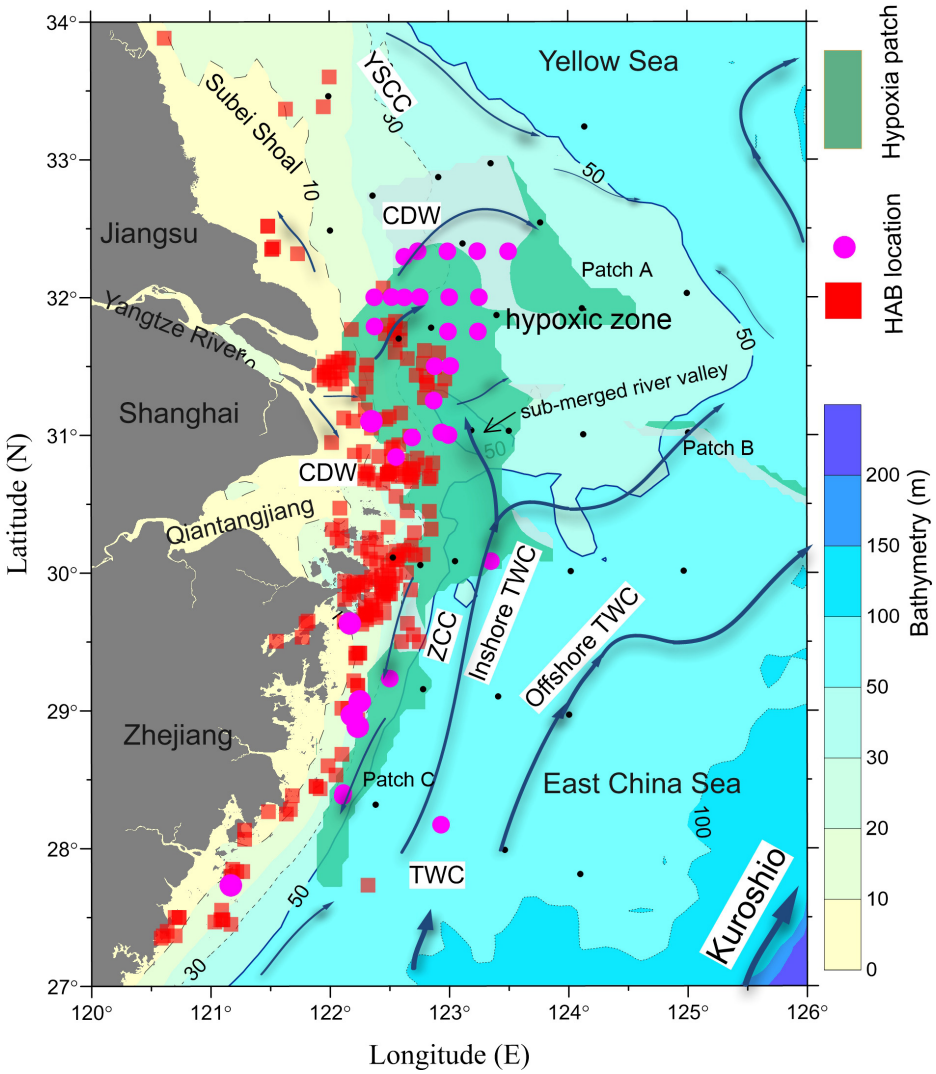

FIGURE 1 | The circulation pattern (*arrows*) in the coastal and shelf waters adjacent to the Changjiang Estuary. The expansion of the Changjiang Diluted Water (*CDW*) off the estuary depends on interplays among the Yellow Sea Coastal Current (*YSCC*) from the north, the Zhejiang Coastal Current (*ZCC*) from the south, the inshore and offshore Taiwan Warm Current (*TWC*) originated from the strong upwelling north of Taiwan and other forcing. The distributions of harmful algal blooms (HABs) during 1979–2009 (Liu et al., 2013) are shown by *red squares* and those for 2010–2016 by *pink circles* (Bulletin of China Marine Environment; **Supplementary Table S2**). The composite distribution of the hypoxic zones in this region since the early 1990s is depicted with *green shading* (**Supplementary Table S1**). *Black dots* represent the station locations for the three repeated surveys referred to in this study.

Wang et al., 2013; Wang and Oey, 2016; Xuan et al., 2017; **Figure 1**). In addition to the TWC, the shelf circulation systems in this area also include the CJE outflow (Zhu and Shen, 1997; Zhou et al., 2009, 2015; Wu et al., 2011), the Zhejiang Coastal Current (ZCC) (Yang et al., 2013), and the Yellow Sea Coastal Current (YSCC) (Zhu et al., 1998; **Figure 1**). Over the past five decades, these combined inflows have generated a fivefold increase (from 25 to 100) in the N:P and a 20-fold increase (from 0.2 to 5) in N:Si ratios off the CJE (Dai et al., 2010), making it one of the most severely impacted eutrophic regions in the coastal seas of China (Ning et al., 2004; Dai et al., 2013; Lu et al., 2014).

Beyond leading to higher phytoplankton standing stock (Zhou et al., 2008), this coastal eutrophication has resulted in a shift in the phytoplankton community composition in the East China Sea (ECS) (Zhou et al., 2001, 2008; Wang et al., 2016; Yu and Liu, 2016). In particular, there has been an increase in harmful algal blooms (HABs), including the toxic *Karenia mikimotoi* and *Alexandrium catenella* as well as the ecosystem-disruptive species *Prorocentrum donghaiense* and *Noctiluca scintillans* (**Figure 1**; Liu et al., 2013; Dai et al., 2014; Lu et al., 2014; Yu and Liu, 2016). Along with changes in plankton assemblages has come the annual development of large-scale hypoxia in the region (Li et al., 2002; Chen et al., 2007; Wei et al., 2007; Wang, 2009; Zhou et al., 2010; Ning et al., 2011; Zhu et al., 2011, 2016; Liu et al., 2012; Wang et al., 2012, 2016, 2017; Zhu et al., 2017; Luo et al., 2018; **Supplementary Figure S1**

and **Supplementary Table S1**). However, the quantitative linkages among these large-scale changes in the frequency and species composition of phytoplankton blooms, dissolved oxygen depletion, and the distribution and expansion of hypoxic areas are poorly understood, mainly due to the limitations of ship-based, discrete, and intermittent sampling of this highly dynamic coastal environment (**Figure 1**).

Like other anthropogenically affected coastal regions (Silva et al., 2016), marine environmental issues off the CJE demand an enhanced mechanistic understanding of the physical–biogeochemical processes to enable better forecasting of hypoxic conditions (Zhang et al., 2018). In this work, we use a coupled physical–biogeochemical model to explore the relationship between the spatial–temporal variability of high-biomass phytoplankton production and offshore hypoxia and to reveal the causal linkages among physical processes, nutrient cycling, phytoplankton production, and hypoxia at both seasonal and single-event timescales in the ECS. Although our understanding of this complex system is not yet complete, the findings here help to validate this coupled model approach and its predictive capacity. We hope that this approach can be adopted to support the design of ecosystem restoration strategies to mitigate hypoxia off the CJE.

MATERIALS AND METHODS

Field and Satellite Data

Three repeated multidisciplinary field surveys with coarsely spaced sampling stations were carried out off the CJE (122.0–125.0° E, 27.5–33.5° N) during June 2–11 (Jun cruise), August 19–30 (Aug cruise), and October 3–13 (Oct cruise) in 2006 (**Figure 1**, dots). Detailed information about these cruises are given in Zhou et al. (2010) and Zhu et al. (2011). A single intensive survey with high-resolution sampling stations into the Changjiang and in the adjacent coastal region was conducted during July 13–August 23, 2006 (Gao et al., 2011; Li et al., 2011). Additional cruise observational data were included from May (May 10–June 3) (Chen et al., 2008) and September (Zou et al., 2008; Wang et al., 2012) cruises in 2006 to facilitate our understanding of the seasonal development of hypoxia.

Vertical profiles of temperature and salinity were measured using a Sea-Bird conductivity, temperature, and depth (CTD). Discrete water samples were collected using a CTD rosette at near surface, 10 m, within the pycnocline, and near bottom. Chlorophyll *a* (Chl *a*) was measured by extraction into 90% acetone using the acidification method (Holm-Hansen et al., 1965). Remotely sensed Chl *a* data were used to resolve the high spatial–temporal variability of phytoplankton biomass. Daily level 3 surface Chl *a* data from the GlobColour[1] (hereafter, SAT Chl *a*), i.e., SeaWiFS, MERIS, and MODIS, were extracted for the study region and showed good agreement with *in situ* observations (**Supplementary Figure S2A**). A composite of these SAT Chl *a* datasets using the weighted averaging algorithm among different satellite sensors was used from the GlobColour. Chl *a* was overestimated by the satellite where *in situ* Chl *a* was <10 μg/L, but was underestimated where *in situ* Chl *a* was >10 μg/L (**Supplementary Figure S2A**). In spite of that, SAT Chl *a* showed overall good agreement ($r = 0.68$) with *in situ* Chl *a* data and the root mean squared difference (RMSD) of 0.39 μg/L (**Supplementary Figure S2A**).

Vertical profiles of dissolved oxygen were measured with a high-accuracy dissolved oxygen sensor (Sea-Bird SBE43), mounted on the CTD rosette. Dissolved oxygen was also measured from the sampled water by the titration method (Bryan et al., 1976) at discrete depths (surface, two or three depths spanning the pycnocline to improve the sampling resolution according to the pycnocline thickness, and near the seabed) to verify sensor accuracy (**Supplementary Figure S2B**). The sensor-measured dissolved oxygen data were validated with the titrated dissolved oxygen data and showed a high correlation coefficient of 0.97 with a low RMSD of 0.53 mg/L. Then, the high-vertical-resolution sensor-measured dissolved oxygen data were calibrated based on a linear regression $y = 0.9063x + 0.7265$. Here, y represents the calibrated sensor-measured dissolved oxygen (hereafter, DO) and x represents the titrated dissolved oxygen (**Supplementary Figure S2B**).

Physical–Biogeochemical Model

The physical processes were simulated by a customized Regional Ocean Modeling Systems (ROMS) (Shchepetkin and McWilliams, 2005; Haidvogel et al., 2008). The model covers the domain of 117.5–132.0° E and 23.5–41.0° N, with a curvilinear grid and an approximately homogeneous 4-km horizontal resolution and 30 vertical levels. The model was spun up for 3 years starting from a climatological January mean that was derived from multiyear observations between 1958 and 1987 (Chen, 1992) and driven by Comprehensive Ocean–Atmosphere Data Set (COADS) climatological monthly forcing (Da Silva et al., 1994). The last-year model output was used as the initialization for the realistic run of 2006, for which the surface heat and freshwater fluxes were obtained from the 3-hourly European Centre for Medium-Range Weather Forecasts (ECMWF) ERA-Interim (Dee et al., 2011). The wind stress was calculated from wind vector data as described by Large and Pond (1981), and the wind vector data were from the Blended Sea Winds (Zhang et al., 2006; Peng et al., 2013), which provide daily 0.25° gridded ocean surface vector wind based on multiple satellite observations. The same wind stress was also used for analyzing the wind mixing. Boundary conditions such as temperature, salinity, velocity, and sea surface elevation were extracted from Global Hybrid Coordinate Ocean Model (HYCOM) climatology averaged from 1979 to 2003 and HYCOM realistic run for 2006 (Kelly et al., 2007), respectively. Both the climatological run and the realistic run include the Changjiang runoff (**Table 1**). See Zhou et al. (2015) for more details on the circulation model setup and validation. The realistic run of 2006 was driven by the realistic forcing repeatedly for two cycles, and the last cycle output was analyzed in this article.

Observational evidence indicates that diatom blooms are the major source of organic matter export leading to hypoxia off the CJE (Wang et al., 2017). The 13-component carbon, silicate, and nitrogen ecosystem (CoSiNE) model was thus selected, which includes: silicate, nitrate, phosphate, ammonium, picophytoplankton, diatoms, microzooplankton,

[1]http://globcolour.info

TABLE 1 | Comparison of the monthly Changjiang runoff (unit: m^3/s).

	Jan	Feb	Mar	Apr	May	Jun	Jul	Aug	Sep	Oct	Nov	Dec
Climatology	10,099	12,639	15,300	23,209	34,947	40,641	49,266	44,572	41,568	35,547	24,515	14,809
2006	11,466	11,692	21,125	24,326	30,516	38,630	37,288	27,429	19,086	14,935	13,820	13,456
Change (%)	14	−8	38	5	−13	−5	−24	−39	−54	−58	−44	−9

mesozooplankton, small/suspended particles, large/sinking particles, oxygen, total CO_2, and total alkalinity. The detailed descriptions of the CoSiNE model are given in Chai et al. (2002) and Xiu and Chai (2014). For more details on the CoSiNE model setup and validation for the ECS and the CJE, see Zhou F. et al. (2017). All biological components were coupled online with physical processes, such as advection and diffusion. The simulated Chl *a* is referred to as modeled Chl *a* (MOD Chl *a*) to distinguish it from satellite-determined Chl *a* (SAT Chl *a*) and water column measurements (*in situ* Chl *a*).

RESULTS

Modeled Chl *a* and Currents

The spatial patterns of the bimonthly MOD Chl *a* (**Figures 2A–D**) were in reasonable agreement with the composite bimonthly SAT Chl *a* over the May through October study period, as was the magnitude of production in July and August. Both MOD Chl *a* and SAT Chl *a* showed a strong concentration gradient between the nearshore and offshore regions. The MOD Chl *a* showed high production mostly occurring off the CJE and adjacent nearshore regions. The simulations showed that phytoplankton production in the area had significant seasonality and peaked in July–August, which was similar to those of SAT Chl *a*. There were some mismatches between MOD Chl *a* and SAT Chl *a*. The spring phytoplankton production off the Zhejiang coast occurred later in the simulations than that of the satellite data (**Figure 2E**). The high-concentration Chl *a* tongue extending from the river mouth to beyond the 20-m isoline was underestimated in the simulations (**Figures 2F,G**). Meanwhile, the modeled Chl *a* levels were overestimated compared to SAT Chl *a* values during May–October, particularly in the nearshore regions such as the Subei Shoal and the Qiantangjiang Estuary (Hangzhou Bay) (**Figures 2F–H**).

The model-simulated current field suggested a prevailing monsoon-driven northeastward current at all layers from the surface to near bottom, namely, the TWC as suggested by Beardsley et al. (1985), Su and Pan (1987), and Su (1998), showing two branches in the southern ECS (**Figure 3**) similar to the current structure presented by Yuan et al. (1987), Ichikawa and Beardsley (2002), and Xuan et al. (2017). The nearshore branch was along the Zhejiang coast and separated from the offshore branch south of 28° N. The nearshore branch again bifurcated into two parts south of 30.5° N, with one part moving northward and pushing the Changjiang Diluted Water (CDW) to north of the river mouth until 33.5° N, and there the two parts turned together eastward and southeastward. The offshore part turned eastward at 30.5° N and finally joined the Cheju Warm Current, as suggested by Lie et al. (2000). The northeastward and later southeastward of the CDW tongue north of the river mouth was a well-recognized feature in previous *in situ* observations (Mao et al., 1963; Beardsley et al., 1985). The simulated current fields at different depths showed some similar patterns, but also significant differences off the CJE. For instance, the bottom layer suggested a notable northwestward onshore flow right outside of the river mouth, while the surface layer showed a bifurcation that extended northeastward and southeastward, respectively. The bottom layer also produced a band of convergence close to the 50-m isobath northeast of the river mouth, and at the convergent band place the CDW at the surface turned eastward and then southeastward. In addition, the 30-m and bottom layers seemed to have more trend of eastward movement in the offshore of the CJE.

Observed High Chl *a* Patch at the Surface and Hypoxia at the Seabed

Spatial distributions of the monthly mean SAT Chl *a* and DO in bottom waters are shown in **Figure 4**. SAT Chl *a* was elevated at the surface during May in a narrow band-like region along the coast from Zhejiang (34 μg/L) to the river mouth of the Changjiang (36 μg/L), centered long the 50-m isobath in the submerged ancient river valley (**Figure 4A**). The DO in the bottom water likely had not yet reached hypoxia (**Figure 4A**) based on a limited dataset showing the lowest DO concentration to be 4.96 mg/L (Chen et al., 2008).

A high concentration of SAT Chl *a* continued to occur in June at the surface over an *in situ* observed hypoxic patch of bottom waters along the Zhejiang coast south of the CJE. The SAT Chl *a* concentration along the Zhejiang coast (32 μg/L) was similar to that in May, as were the high *in situ* Chl *a* levels over the submerged river valley (see **Figure 1**) off the CJE (40 μg/L) (**Figure 4B**). The peak *in situ* Chl *a* measured during the cruise (10.5 μg/L) occurred on June 10, which was approximately 25% of the peak value estimated by the satellite on June 21. Episodic high Chl *a* levels were observed both *in situ* and from satellite primarily off the Zhejiang coast during both May and June with less variation than in the other regions, consistent with previous observations (Zhou et al., 2003; Zhao et al., 2004; Liu et al., 2013).

In contrast to June, high SAT Chl *a* (i.e., surface waters) during July coincided with low DO concentrations in bottom waters very close to the river mouth (**Figure 4C**). The high *in situ* Chl *a* was also observed by the cruise in July (not shown). These cruise data, benefitting from the greater sample station density in the CJE, clearly show the co-occurrence of high phytoplankton biomass and low DO, mainly between the 20- and 50-m depth east of the river mouth. Smaller patches of hypoxia were measured not only in this region but also to the east (126° E, 31° N and

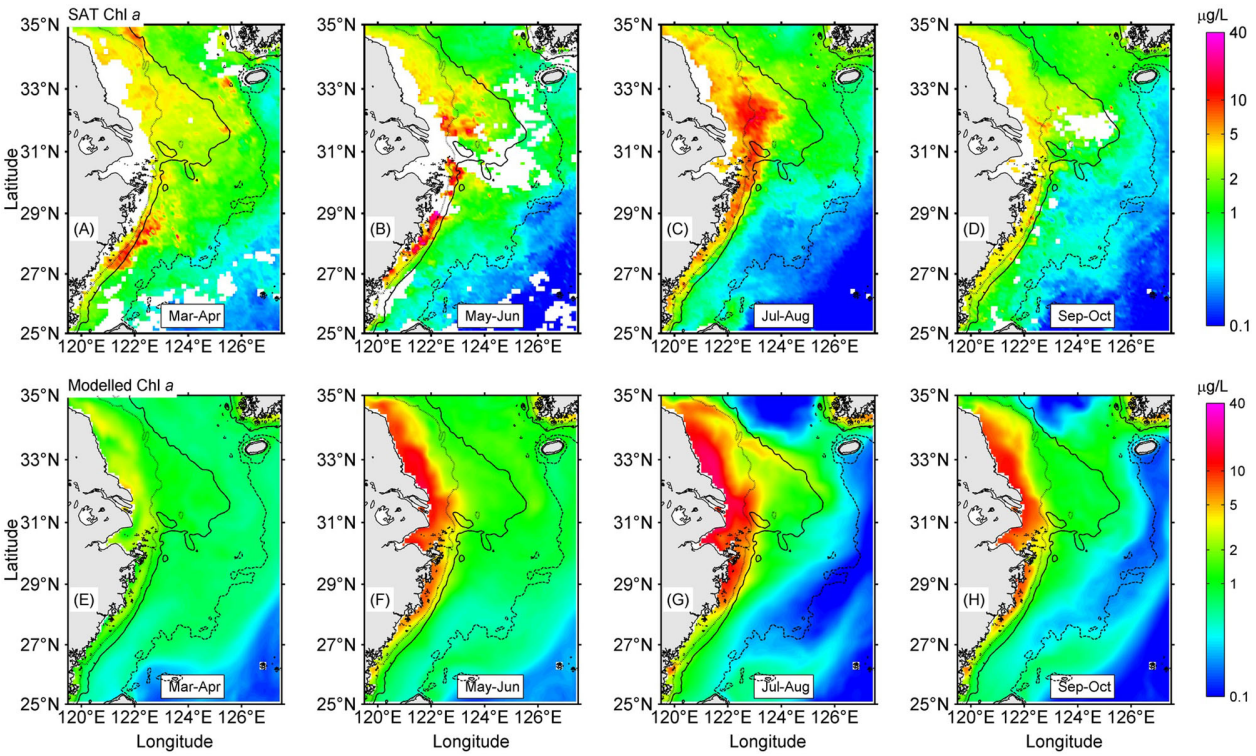

FIGURE 2 | The spatial distributions of bimonthly mean satellite (*SAT*) Chl *a* and modeled Chl *a* in the study region from March through October. The contours are isobaths of 20 m (*dotted*), 50 m (*solid*), and 100 m (*dashed*). Satelllite measured Chl *a* averaged between March to April **(A)**, May to June **(B)**, July to August **(C)** and September to October **(D)**. Modelled mean Chl *a* in March to April **(E)**, May to June **(F)**, July to August **(G)** and September to October **(H)**.

124° E, 31.5° N) in late July and early August. The highest *in situ* Chl *a* concentration measured in July was 21.3 μg/L, in close agreement with the SAT Chl *a* values (20 μg/L). The Changjiang and Qiantangjiang River estuaries had relatively low *in situ* Chl *a* near the river mouth in July (5 μg/L) compared to that occurring in May.

The high SAT Chl *a* concentration pattern (peak at 15 μg/L) in August was similar to that observed in July; in contrast, the low DO zone expanded significantly in both meridional and zonal directions (**Figure 4D**). DO concentrations were <3 mg/L across a spatial zone of 77,100 km^2, or about 10 times of the hypoxic area observed in July, and hypoxia was also more intense, with the minimum DO deceasing from 2.0 mg/L in July to 1.0 mg/L in August. Although the hypoxic region expanded and covered most of the study area, except close to the 100-m isobath, peak *in situ* Chl *a* concentrations decreased to 16.1 μg/L and were slightly lower than those in July. SAT Chl *a* showed a similar decreasing trend during August.

September brought a drastic decrease in SAT Chl *a* concentrations, and presumed ventilation of subsurface waters led to some relaxation in hypoxic intensity and contraction of the hypoxic zone. The minimum DO increased to 2.0 mg/L (Zou et al., 2008), and hypoxia north of the river mouth disappeared (Wang et al., 2012; **Figure 4E**). SAT Chl *a* in the study region showed a reduction by ∼30% relative to August, and the spatial extent of high biomass (Chl *a* > 10 μg/L) was less than 5% of that measured in August.

Moderately high SAT Chl *a* remained at the surface in the area north of the CJE during October, slightly lower than that in August but much higher than that in September (**Figure 4F**). The high Chl *a* patch along the Zhejiang coast that disappeared in September appeared again in October at more moderate levels. The peak *in situ* Chl *a* during the cruise (27.7 μg/L) was twice that of the SAT Chl *a* (14.0 μg/L) averaged over the larger area. The spatial extent of the hypoxic zone increased substantially, from 16,400 km^2 in September to 26,500 km^2 in October, and extended from the Zhejiang coast to the northern tip of the submerged river valley (**Figure 4F**).

As noted, the spatial distribution of high Chl *a* biomass did not match that of hypoxia during the summer–fall stratified period, illustrating a complex interaction between biological and physical processes. This variation is illustrated by the presence of minor hypoxic patches in regions with low Chl *a* (**Figures 4C,D**). In addition, the highest Chl *a* at the surface on the 31° N transect occurred along the outer edge of the upper front immediately outside of the river mouth, while the minimum DO occurred in the shore side of the front (**Figure 5**). Indeed, hypoxic bottom waters were overlain by low levels of Chl *a* biomass more often than that of high-biomass waters, according to the comparison of both SAT Chl *a* and *in situ* Chl *a* at the surface with DO measurements at the bottom layer (**Figure 6**). Given that advection would have contributed to the variable distribution of the high-biomass phytoplankton patches, the annual spatial dynamics of surface phytoplankton biomass was compared to the

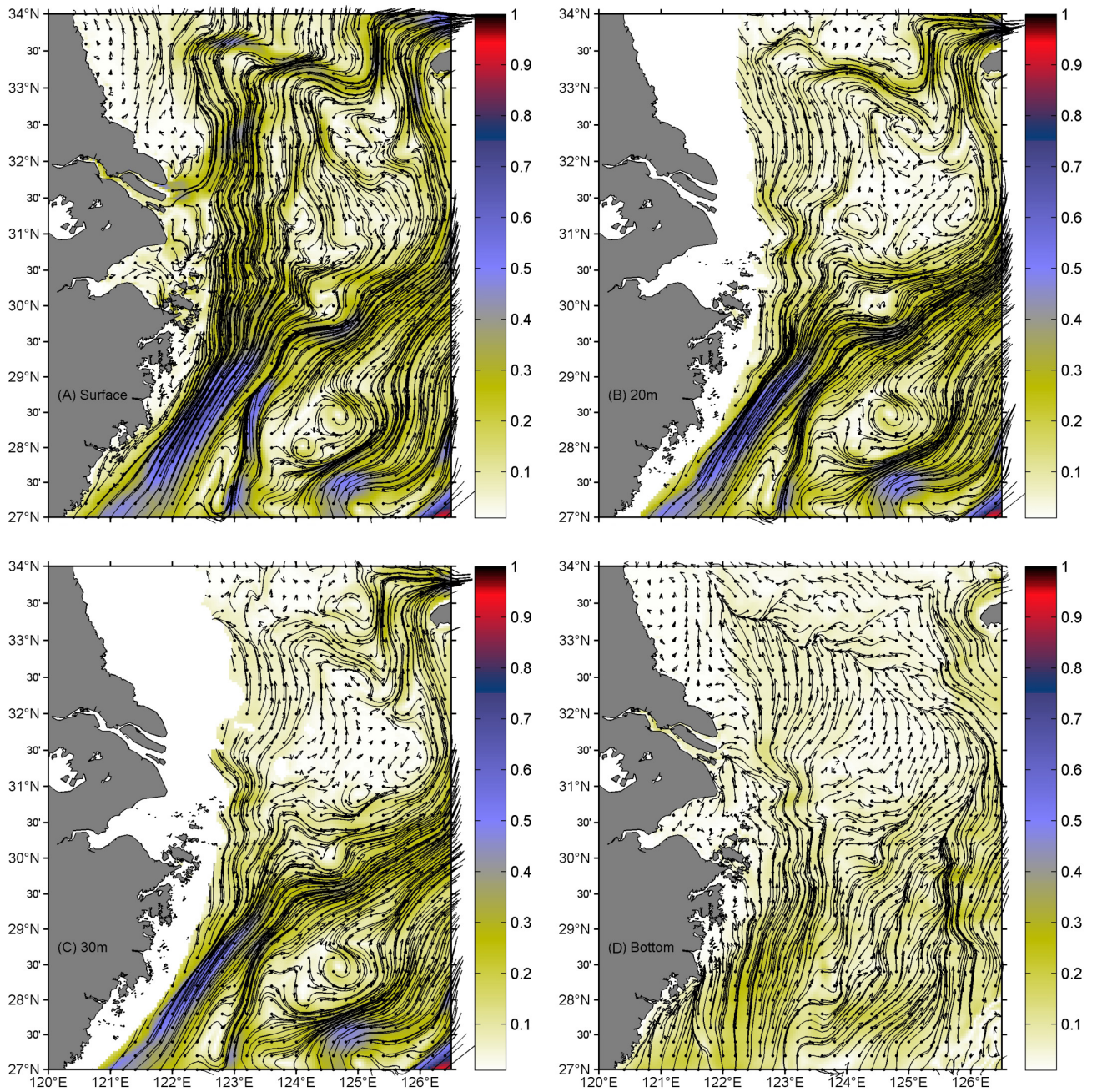

FIGURE 3 | Simulated current fields at different depths off Changjiang Estuary (CJE) in July 2006. Surface **(A)**, 20 m **(B)**, 30 m **(C)**, and near-bottom **(D)** layers. The current vectors drawn in this figure were selected in a search radius of ~20 km. *Shading* represents the current magnitude (in meters per second).

ROMS-determined spatial dynamics of bottom hypoxic waters in the study region.

Modeled Hypoxic Zone

As a first step, the low-level DO distribution during the year was extracted from the model to identify the most probable regions of oxygen depletion (**Figure 7A**). The modeled low DO concentration generally occurred below 20-m depth. To the north of the CJE, the model results suggested that oxygen depletion was distributed on both the western and eastern sides of the 30-m isobath, with the exception of an isolated low-DO patch further offshore at the 50-m isobath. To the south of the river mouth, the simulated oxygen depletion occurred along the coast between the 20- and 50-m isobaths and at the submerged river valley deeper than 50 m (**Figure 7A**).

The maximum hypoxic zone (modeled MHZ) during the year, defined as the assemblage of all grid points where hypoxia was detected in the model—see Zhou F. et al. (2017) for a detailed

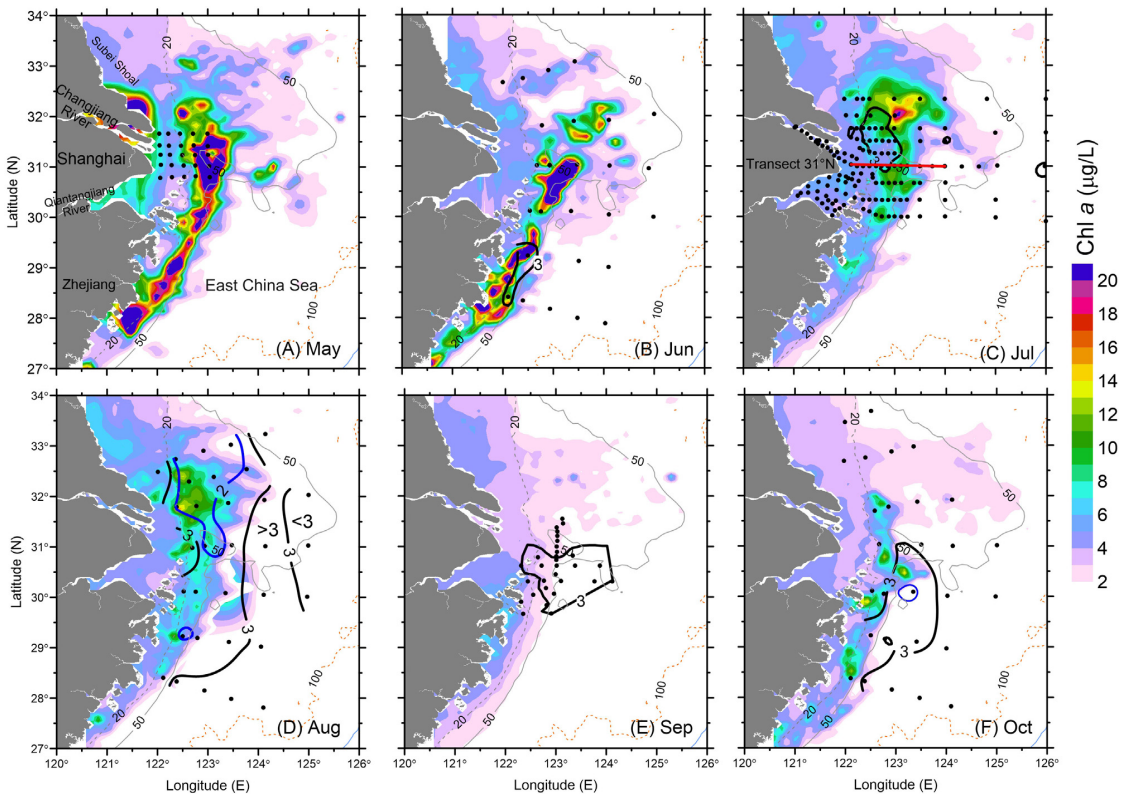

FIGURE 4 | Surface (*SAT*) Chl *a* and bottom water DO (*thick contour*) during May–October 2006: **(A)** May, **(B)** June, **(C)** July, **(D)** August, **(E)** September and **(F)** October. The hypoxic zone during September was digitized based on Wang et al. (2012). *Black contours* represent DO of 3 mg/L and *blue contours* are for DO of 2 mg/L. *Dots* represent sampling stations during the corresponding cruise.

discussion—was extracted to show the largest extent of hypoxic zone. The modeled MHZ existed as a narrow elongated band from the southern Jiangsu coast to the northern Zhejiang coast (**Figure 7B**). Three separate patches could be identified from the modeled MHZ, likely associated with the diversion of the CDW. Running north to south, the first hypoxic water patch, Patch A, lay approximately 300 km northeast of the river mouth near the 50-m isobath (**Figure 7B**). It had a long-duration core, reflecting the fact that the CDW passed through this region over most of the season. The second most intense patch, Patch B, lay meridionally distributed in the offshore vicinity of the CJE, while the third hypoxic patch, Patch C, occurred to the south along the Zhejiang coast (**Figure 7B**).

To better understand how organic matter production in the upper layers is linked to hypoxia, the modeled oxygen depletion under the pycnocline was compared with the time series of SAT Chl *a* inside and outside the modeled MHZ within the rectangular zone (120.5–128.5° E, 25.5–34.5° N) (**Supplementary Figure S3A**). The annual mean SAT Chl *a* within this MHZ was almost three times larger than that outside the region, consistent with hypoxia being attributable to the decay of nutrient-driven phytoplankton production in the overlying waters. There was a positive correlation (r = 0.52) between the fluctuations of the modeled Chl *a* and SAT Chl *a* within the MHZ. These SAT Chl *a* data show that phytoplankton biomass increased slowly from January through April and peaked with a bloom during May–June, followed by lower but still substantial chlorophyll levels in July–August. The modeled Chl *a* concentrations followed the measured SAT Chl *a* from January through April, did not capture the bloom in May–June, but reached maximum levels in late July that matched the SAT Chl *a* concentrations (**Supplementary Figure S3A**). Thereafter, there was generally good quantitative agreement between the SAT Chl *a* and modeled Chl *a*, with diminishing concentrations from August to mid-September, followed by a smaller phytoplankton bloom during October, and then decreasing to low winter values by December. Discrete measurements of the *in situ* Chl *a* >10 μg/L during the four cruises of this study (June through October) showed the same general pattern (**Supplementary Figure S3B**). Augmenting these data with the most current findings of the Bulletin of China Marine Environment (for 2006) also shows a vast bloom extent in May–June.

Modeled Physical–Biogeochemical Processes During Phytoplankton Blooms and Hypoxia

The time series of wind-induced mixing, stratification, nutrients, and phytoplankton succession were investigated in the model domain, using averaged values over the entire modeled MHZ,

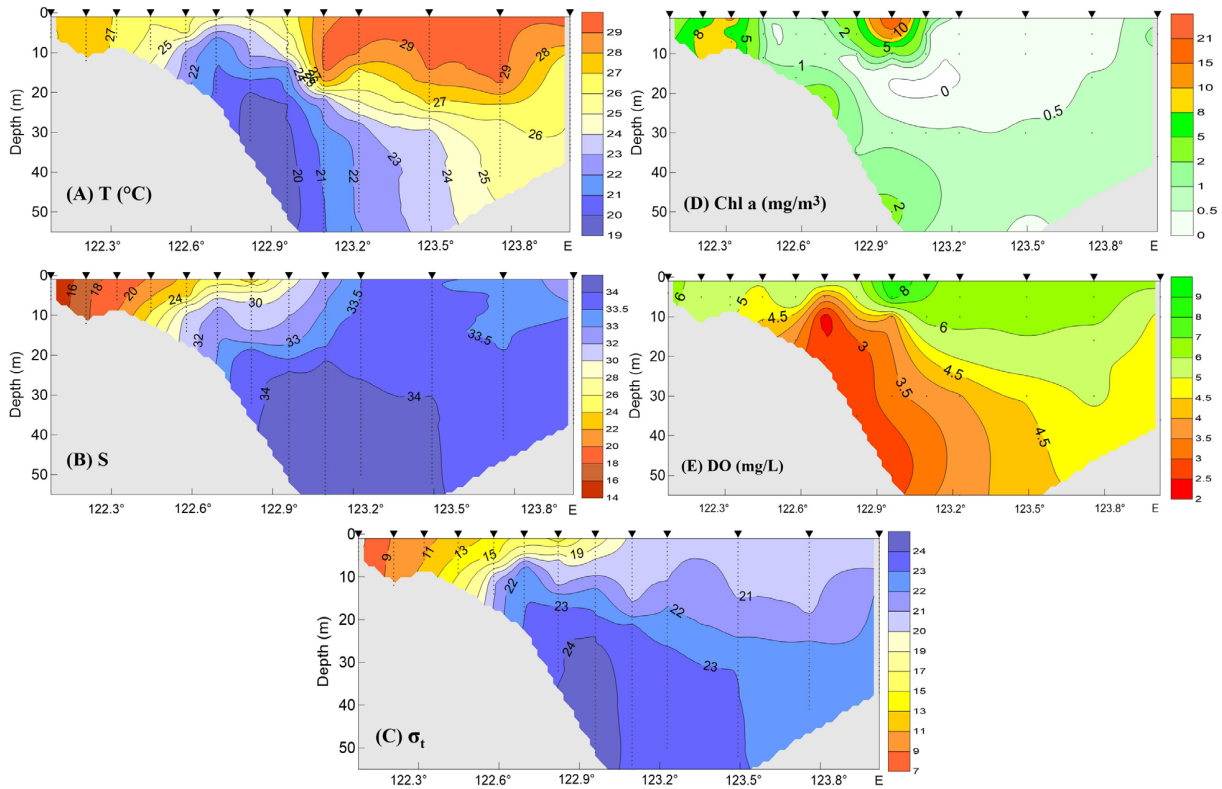

FIGURE 5 | Temperature **(A)**, salinity **(B)**, density anomaly by minusing 1000 kg/m^3 **(C)**, Chl *a* **(D)**, and DO **(E)** observations along the 31° N transect shown in **Figure 4C** during the intensive survey on August 12–15, 2006. *Triangles on the top* marked the sample stations.

to investigate the linkages of physical processes, nutrient cycling, phytoplankton blooms, and high Chl *a* with hypoxia (**Figure 8**).

The study area is dominated mostly by the monsoon wind patterns, with strong northerly wind occurring during the fall and winter, substantially weaker southerly winds during the summer, and more variable wind directions during the late spring and September–October transitional period (**Figure 8A**). The averaged wind speed usually was less than 7 m/s from late spring to summer, with the exception of sporadic tropical storm or typhoon events (depicted by the numbered circles in **Figure 8**), where wind speeds averaged up to ∼14 m/s within the study area.

The stratification intensity was approximately represented by the surface to bottom difference of density, temperature, and salinity. The weaker winds during the summer generally were not able to disrupt the density stratification of the water column, with only some slight reduction, e.g., in mid-August. The significant and rapid loss of stratification occurred only in early September, associated with the strong Tropical Storm Shanshan and subsequent strong northerly wind (**Figures 8A,B**). Both temperature and salinity difference contributed significantly to the stratification; however, their temporal patterns varied in complex ways, with salinity difference decreasing when the temperature difference increased during mid-June to early August (**Figure 8B**). The reduced contribution of salinity to stratification after mid-June was related to the reduction in riverine input (**Table 1**). The salinity difference above and below the pycnocline peaked in mid-June instead of August, in associated with the maximum Changjiang runoff in 2006 (**Table 1**), which was unusual compared to the climatological mean discharge. The increased runoff during late May to June coincided with an increase in the mean nitrate concentrations in surface waters (**Figure 8C**), but not in phosphate or silicate due to the phytoplankton uptake of these nutrients during the spring blooms. That is, a greater replenishment of N than P or Si in runoff waters led to more rapid depletion of the latter two as a consequence of phytoplankton growth.

The enhanced vertical mixing that accompanied the strong wind events in July, August, and September increased the modeled nutrient flux into surface waters (**Figures 8C,D**). The simulated diatom growth increased sharply immediately following these wind-induced mixing events, but reached maximum biomass ∼1–2 weeks after the wind events **Figure 8D**). These two largest diatom bloom events were followed by two large hypoxia events ∼2 weeks later, consistent with the model findings (**Figure 8E**).

The model also shows the succession of diatoms and non-diatoms, where increases in non-diatom biomass followed decreases in diatom biomass (**Figure 8D**). The onset of non-diatom blooms occurred rapidly on termination of the diatom blooms during mid-April and mid-May, mid-August, mid-September, late October, and in December. The model-derived time lag between the diatom and non-diatom blooms is

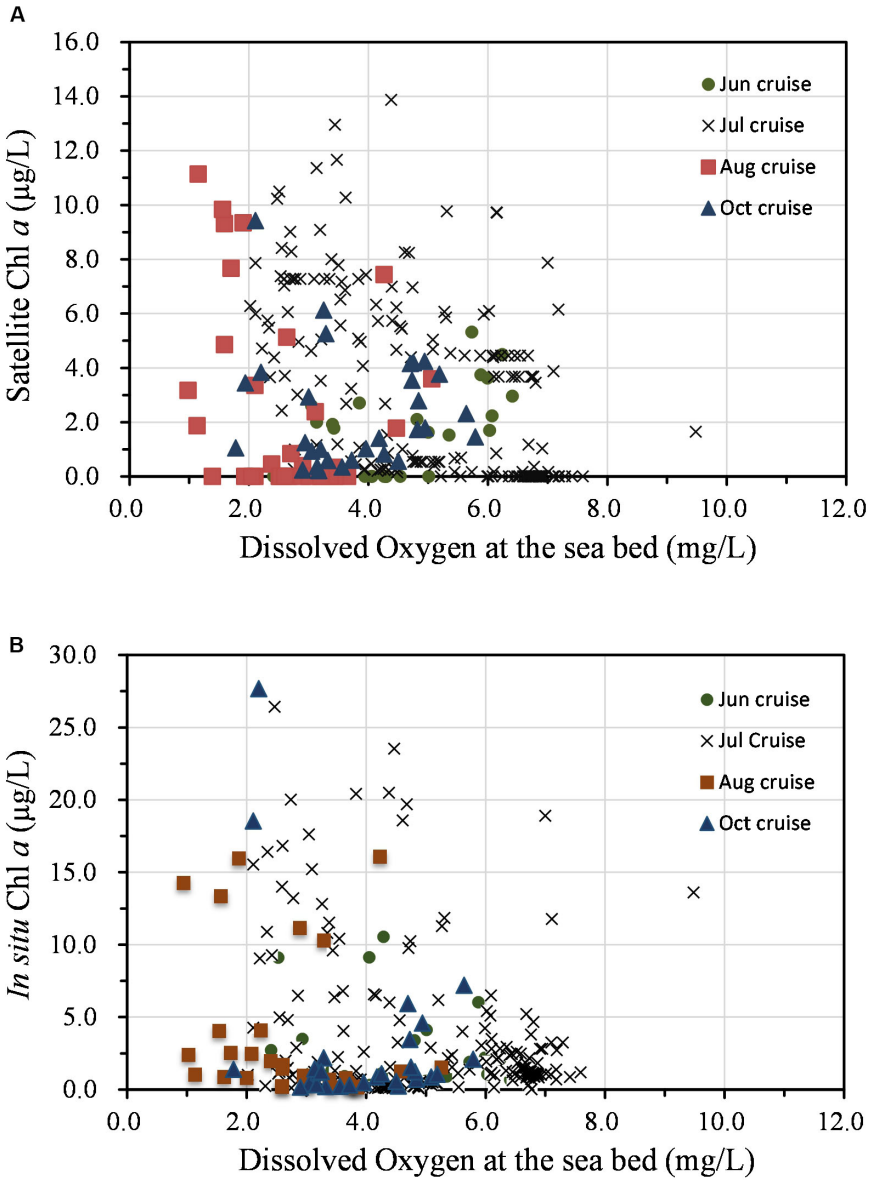

FIGURE 6 | Relationship between phytoplankton production (Chl *a*) at the surface and dissolved oxygen at the bottom layer based on field measurements in 2006. **(A)** Satellite Chl *a* and **(B)** *in situ* Chl *a*.

within a reasonable range of the field observations (data not shown). Diatom concentrations decreased to a very low level after October, and no blooms occurred during mid-November to late January.

A Hovmöller diagram (which displays time on one axis and distance on the other) along a more or less meridional transect was extracted from the simulation to examine the relationship between high-biomass phytoplankton production and oxygen depletion below the pycnocline (**Figure 9**). The transect cut through the middle of the long side of the modeled MHZ, with its origin set at the southern end. For simplicity, the vertically integrated diatom concentrations are shown, which illustrate a series of diatom blooms between March and November. Intensive blooms occurred on the along-shore transect at the end of June (**Figure 9A**). By mid-July, the vertically integrated phytoplankton production reached 2 mol C/m^2, assuming a C:N ratio of 9.88 (Harrison et al., 1977), and while oxygen began to be depleted in bottom waters at this time, the area and intensity of oxygen depletion did not enlarge substantially until the end of August/early September. The expansion of hypoxia was enhanced by the second and third high diatom biomass events in late August. The time lag was 1–18 days, but varied at different distances along the transect (**Figure 9**). The lag phase generally decreased south of the river mouth and increased north of the river mouth, except for the region where no significant diatom blooms occurred.

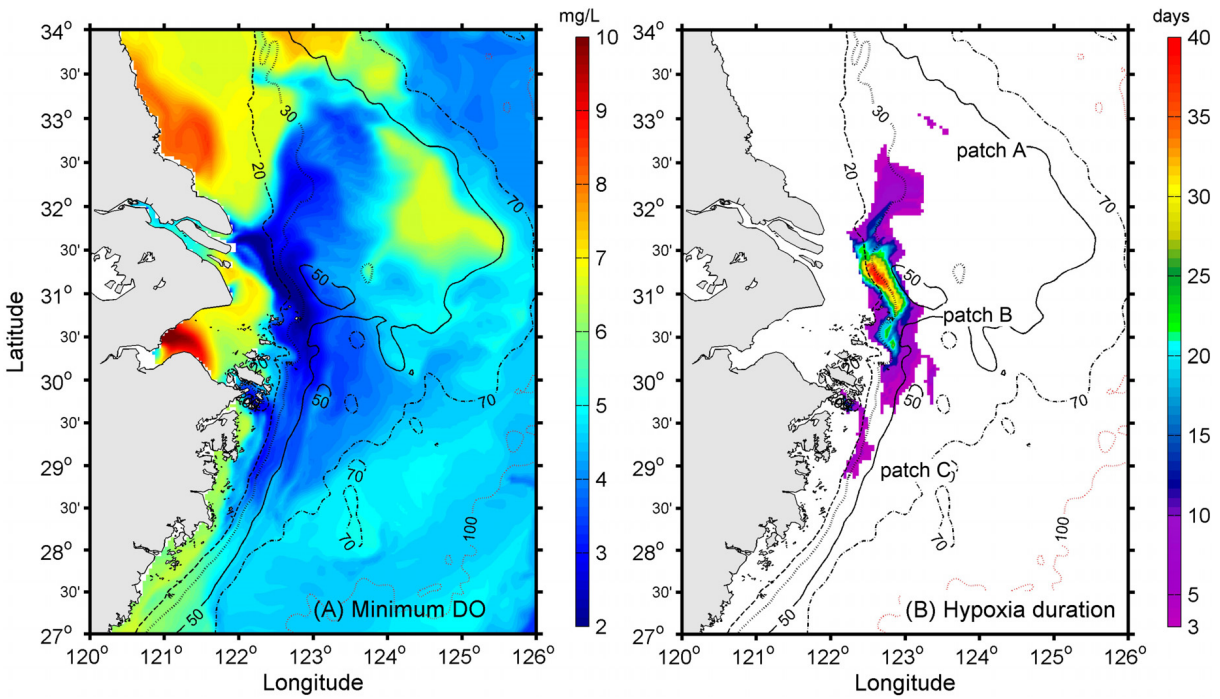

FIGURE 7 | (A) Simulated minimum DO concentrations during the hypoxic period and **(B)** simulated hypoxia duration in days, with the *colored regions* representing the maximum hypoxic zone (MHZ) with three spatially distinct patches.

Further correlation analysis showed that there was reasonable spatial agreement between diatom abundances and DO at the bottom layer in the model. The inverse correlation between vertically integrated diatom abundance and DO in bottom water is −0.60 for the whole transect (**Figure 9D**), while the coefficient is −0.58 between diatoms at the surface layer and DO at the near-bottom layer (**Supplementary Figure S4**). This inverse correlation was always greater than −0.5 along the transect where both hypoxia and diatoms showed significant concentrations, i.e., the distance from 50 to 150 km, and the strongest correlation was −0.73 at 15 km from the southern end of the transect (**Figure 9D**). The phase lag analysis showed that the oxygen depletion mostly occurred a week to 2 months later after the diatom blooms in this transect, where the correlation is >0.5 (**Figure 9E**). However, this was not always the case. The relationship between oxygen depletion and diatom abundance was significantly correlated at the distance around 50 km along the meridional transect shown in **Figure 9C**, but showed no remarkable time lag.

The model also shows the succession of diatoms and non-diatoms, where increases in non-diatom biomass followed decreases in diatom biomass (**Figure 8D**). The onset of non-diatom blooms occurred rapidly during mid-April and mid-May, respectively, at the termination of the diatom blooms. The non-diatom blooms occurred throughout most of the record, e.g., February, in mid-May, early August, and in late October. Decreases in the integrated concentrations of both diatoms and non-diatoms over the stratified period occurred after the strong northerly wind event, e.g., from August to October. Diatom blooms peaked approximately 1–2 weeks after the wind-mixing events, while non-diatom blooms generally appeared 1–2 weeks after the diatom blooms. The phase lag between these two blooms is within the reasonable range of field observations (Lu et al., 2000). A similar succession of microalgae blooms was also revealed in other modeling studies of this region (Zhou Z. et al., 2017). The simulated diatom concentrations decreased to very low levels after October, and no blooms occurred during mid-November to late January. Note that the two phytoplankton functional groups differed in their sinking rates, with the diatom detritus sinking velocity being ∼25 m each day (i.e., reaching the seabed within ∼1 day compared to the lower rate of 15 m each day for the non-diatoms).

DISCUSSION

Coupling and Decoupling Between Surface High-Biomass Diatom Blooms and Bottom Hypoxia

Forecasting the timing, position, spatial extent, and duration of hypoxic zones in the coastal and shelf regions surrounding the CJE is compounded by the dynamic linkages among the physical, chemical, and biological processes. The model results suggest that high-biomass phytoplankton production in this region is regulated by seasonal and intra-seasonal fluctuations in both the anthropogenic nutrient-rich Changjiang (Yangtze River) diluted water and the natural nutrient influx carried by several shelf

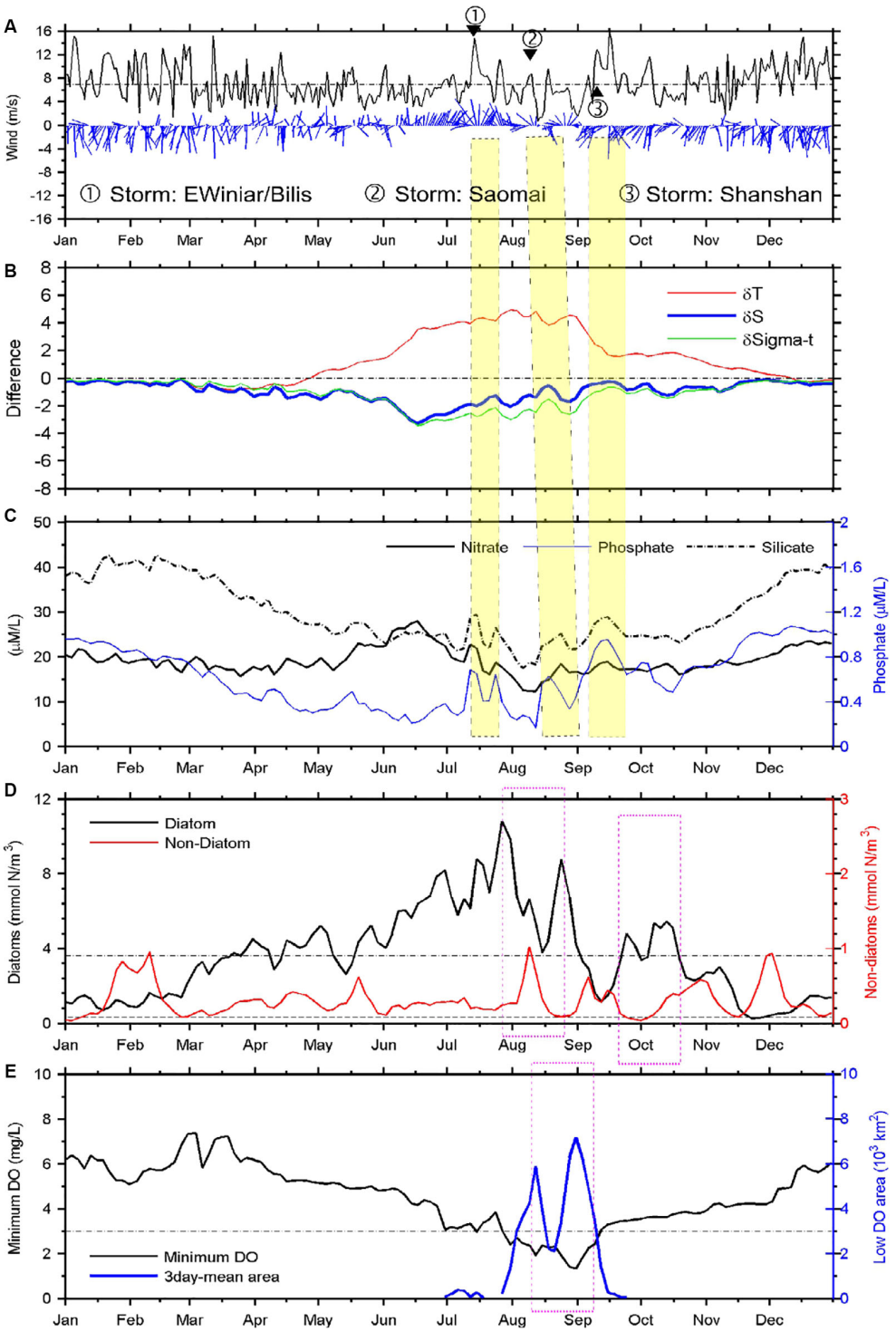

FIGURE 8 | Time series of satellite-observed wind and modeled variables. Wind vectors and speed **(A)**, stratification **(B)**, nutrients at the surface **(C)**, phytoplankton at the surface **(D)**, and hypoxia at the bottom **(E)**. Stratification, nutrients, phytoplankton concentrations, and minimum DO concentration represent the simulated averages within the study area. The simulated phytoplankton biomass concentrations of diatoms and non-diatoms are in nitrogen units (Chai et al., 2002).

currents. The model results also revealed that the event-scale variability in the resulting subsurface hypoxia is characterized by episodic disruption of the pycnocline associated with weather events, which enhances nutrient flux to surface waters and can trigger more severe hypoxia in the region. There exists a straightforward coupling between high-biomass diatom blooms

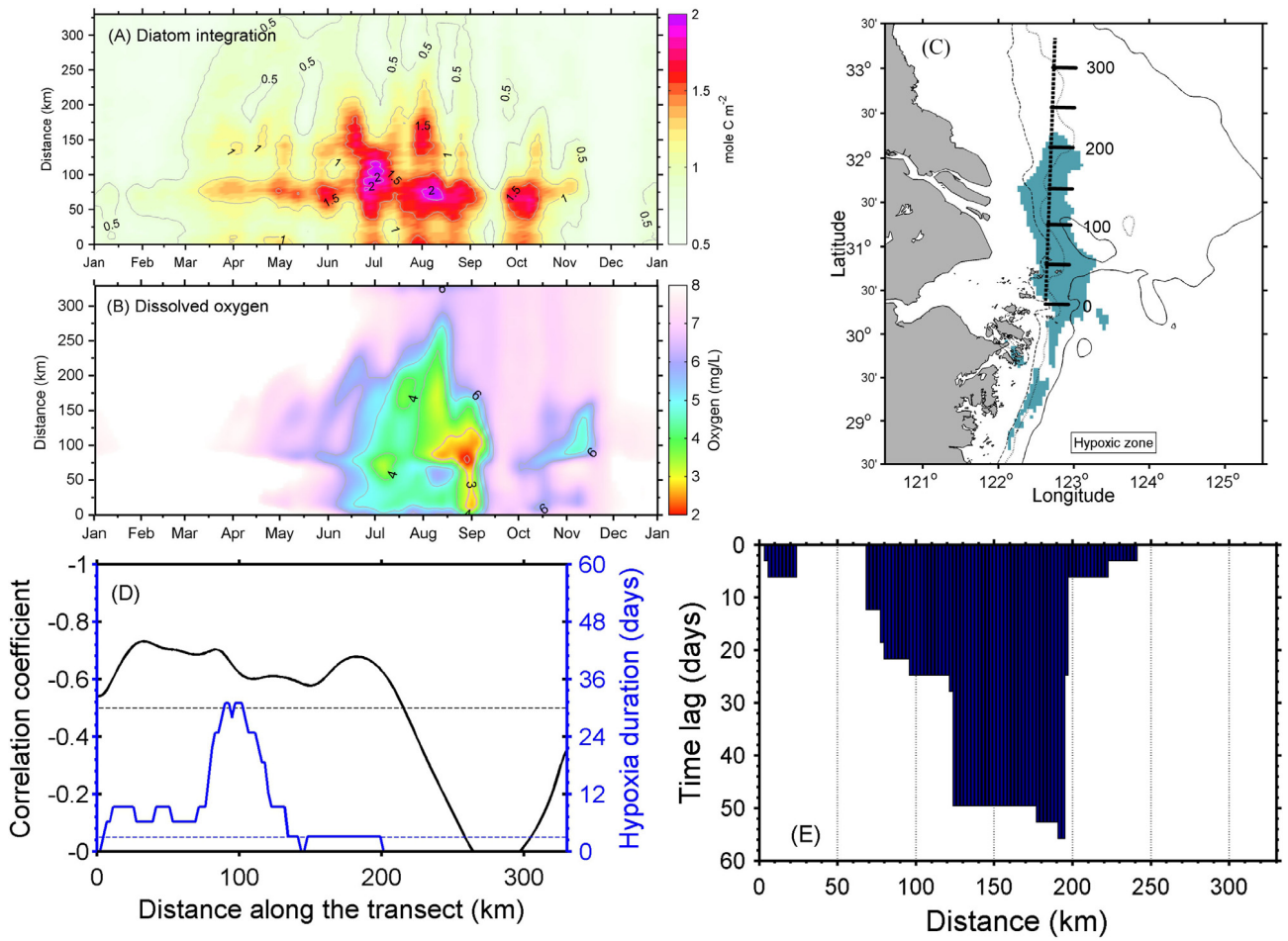

FIGURE 9 | (A) Hovmöller diagram of the vertically integrated diatom concentration and **(B)** dissolved oxygen at the seabed along the transect. **(C)** The transect location with its origin set at the southern end and distance labeled in kilometers. **(D)** Correlation coefficient between the vertically integrated diatom concentration and dissolved oxygen (DO) at the seabed (*black curve*), with hypoxia duration days (*blue curve*). **(E)** Lagged correlation analysis shows the days lagged between the vertically integrated diatom concentration and DO at the seabed.

and low DO in underlying waters near the core hypoxic region immediately adjacent to the mouth of the estuary; on average, the modeled phytoplankton Chl *a* biomass was approximately three times higher over the core hypoxic zone than in the surrounding regions (**Supplementary Figure S3**). However, there was also significant decoupling of production at the surface (or in the water column) and hypoxic zones during 2006, as seen from *in situ* observations (**Figures 5**, **6**) and simulations (**Figures 9A**, **10**). In general, subsurface hypoxia was not always correlated with Chl *a* biomass in the overlying waters across the broader region in the shelf sea outside of the CJE. Portions of the high-biomass blooms, or their underlying waters, often became detached from CJE and were advected along the coast and to the outer shelf (**Figures 3**, **10**). Such episodes were poorly captured by ship monitoring surveys, resulting in an underestimation of the spatial extent of hypoxia (**Supplementary Figure S3B**). Adequate mechanistic-based forecast of the development of these hypoxic events requires quantitative integration of the physical and biogeochemical processes.

Our model findings showed that diatoms accounted for a large portion of the high Chl *a* biomass, consistent with *in situ* observations (Wang et al., 2017), and were the major organic matter export that led to DO consumption below the pycnocline. Based on our simulations, the hypoxia tends to occur 1–8 weeks later than the diatom blooms. The findings here demonstrate how combining remote sensing, numerical simulations, and ship survey data can provide a more comprehensive assessment of the development and evolution of high diatom biomass and hypoxic conditions in this region.

Management Implications

Traditionally, the monitoring and research of "red tides" in Chinese coastal waters has been administratively restricted to toxic algae blooms. However, high-biomass productions that lead to hypoxia also are recognized as an important aspect of HABs having substantial ecological impacts to pelagic and benthic systems. Hypoxia off the CJE has become a seasonal phenomenon, and one where the intensity and spatial scale of

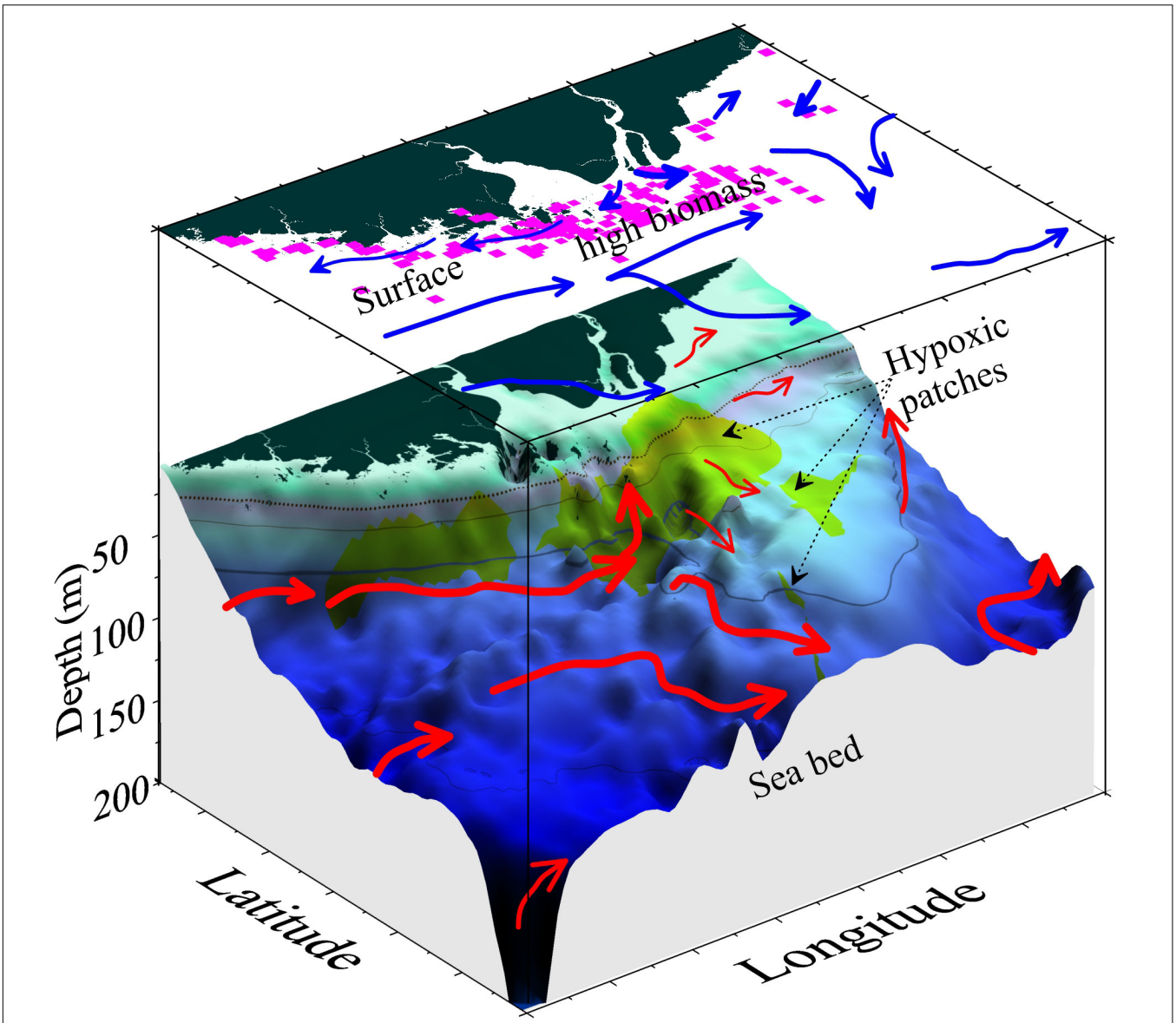

FIGURE 10 | Schematic diagram of the coupling and decoupling between high-biomass phytoplankton production (*pink squares*) and subsurface hypoxic patches (*green shading*). The decoupling is mostly associated with different current structures at the surface (*blue arrows*) and subsurface off the estuary (*red arrows*). Note that the current magnitude might not be represented proportionally by the *thickness of the arrow*.

hypoxia have been expanding. The definition of HABs in Chinese coastal waters should be broadened beyond only toxin-producing organisms to take into account the hypoxia generated by these massive algal blooms in the CJE and other coastal regions. This change would require expansion of the traditional HAB monitoring from not only nearshore regions but also further offshore where hypoxic events also develop.

CONCLUSION

Abundant supplies of nutrients facilitate a continued presence of high-biomass phytoplankton production and their eventual settling in the region and finally lead to multiple patches of hypoxia. Model results support that there is a time lag of a few weeks between bottom hypoxia and surface diatom blooms. Our findings show that, in most cases, hypoxia was spatially linked to primary production in the overlying waters; however, organic detritus in subsurface waters also were transported offshore with different rates and directions compared to the surface waters in this physically dynamic region, producing offshore patches of hypoxic waters. Advection significantly expands the hypoxic zone relative to the high-biomass phytoplankton zone, generating spatially decoupled relationships between bottom hypoxia and phytoplankton production in surface waters.

DATA AVAILABILITY STATEMENT

The datasets generated for this study are available on request to the corresponding author.

AUTHOR CONTRIBUTIONS

FZ, FC, and MW designed the original ideas presented in this manuscript and coordinated integration of the modeling results and observational data. DH conceived the hypoxia projects and the intensive cruise. FZ, JX, XN, CL, and HL collected the field measurements. FZ, XM, CL, and PW analyzed the field data. FZ, MW, HX, and JS wrote the original manuscript draft. FZ, FC, and HX prepared the physical–biological coupled modeling. FZ, QM, and QZ analyzed the results. All authors contributed to refining this manuscript.

FUNDING

This study was supported by the National Key Research & Development Program of China (grant 2016YFC1401603), NSFC-Zhejiang Joint Fund for the Integration of Industrialization and Informatization (grant U1609201), Scientific Research Fund of the Second Institute of Oceanography, MNR (grants JT1704 and 14283), the Zhejiang Provincial Natural Science Foundation (grant LR16D060001), and the National Natural Science Foundation of China (grants 41876026, 41576007, and NORC2013-03).

ACKNOWLEDGMENTS

Field data and model outputs used for the figures and tables are available *via* contacting the first author. We thank Dr. Zuoyi Zhu for providing DO titration data for calibrating sensors used in the three regular surveys and thank Dr. Jianfang Chen and his team for calibrating DO sensors in the intensive surveys. We also thank NOAA for providing gridded wind vector product *via* ftp://eclipse.ncdc.noaa.gov/pub/seawinds/.

SUPPLEMENTARY MATERIAL

The Supplementary Material for this article can be found online at: https://www.frontiersin.org/articles/10.3389/fmars.2020.00259/full#supplementary-material

REFERENCES

Anderson, D., Glibert, P., and Burkholder, J. (2002). Harmful algal blooms and eutrophication: nutrient sources, composition, and consequences. *Estuaries* 25, 704–726. doi: 10.1007/BF02804901

Anderson, D. M., Burkholder, J. M., Cochlan, W. P., Glibert, P. M., Gobler, C. J., Heil, C. A., et al. (2008). Harmful algal blooms and eutrophication: examining linkages from selected coastal regions of the United States. *Harmful Algae* 8, 39–53. doi: 10.1016/j.hal.2008.08.017

Beardsley, R. C., Limburner, R., Yu, H. S., and Cannon, G. A. (1985). Discharge of the Changjiang (Yangtze River) into the East China Sea. *Cont. Shelf Res.* 4, 57–76. doi: 10.1016/0278-4343(85)90022-6

Bryan, J. R., Rlley, J. P., and Williams, P. J. L. (1976). A winkler procedure for making precise measurements of oxygen concentration for productivity and related studies. *J. Exp. Mar. Biol. Ecol.* 21, 191–197. doi: 10.1016/0022-0981(76)90114-3

Carrick, H. J., Moon, J. B., and Gaylord, B. F. (2005). Phytoplankton dynamics and hypoxia in Lake Erie: a hypothesis concerning benthic-pelagic coupling in the central basin. *J. Great Lakes Res.* 31, 111–124. doi: 10.1016/s0380-1330(05)70308-7

Carstensen, J., Andersen, J. H., Gustafsson, B. G., and Conley, D. J. (2014). Deoxygenation of the Baltic Sea during the last century. *Proc. Natl. Acad. Sci. U.S.A.* 111, 5628–5633. doi: 10.1073/pnas.1323156111

Chai, F., Dugdale, R. C., Peng, T., Wilkerson, F. P., and Barber, R. T. (2002). One-dimensional ecosystem model of the equatorial Pacific upwelling system. Part I: model development and silicon and nitrogen cycle. *Deep Sea Res. Part II Top. Stud. Oceanogr.* 49, 2713–2745. doi: 10.1016/s0967-0645(02)00055-3

Chan, F., Barth, J. A., Lubchenco, J., Kirincich, A., Weeks, H., Peterson, W. T., et al. (2008). Emergence of anoxia in the California current large marine ecosystem. *Science* 319:920. doi: 10.1126/science.1149016

Chen, C. A. (1996). The Kuroshio intermediate water is the major source of nutrients on the East China Sea continental shelf. *Oceanol. Acta* 19, 523–527.

Chen, C. C., Gong, G. C., and Shiah, F. K. (2007). Hypoxia in the East China Sea: one of the largest coastal low-oxygen areas in the world. *Mar. Environ. Res.* 64, 399–408. doi: 10.1016/j.marenvres.2007.01.007

Chen, D., Zhang, L. X., Liu, H. Q., and Li, Z. E. (2008). Distribution characteristics and correlating factors analysis of dissolved oxygen in spring and summer in the Yangtze Estuary. *Mar. Environ. Sci.* 27(Suppl. 1), 49–53.

Chen, D. X. (ed.) (1992). *Marine Atlas of Bohai Sea, Yellow Sea and East China Sea, Hydrology*. Beijing: China Ocean Press, 13–96.

Cloern, J. E. (2001). Our evolving conceptual model of the coastal eutrophication problem. *Mar. Ecol. Prog. Ser.* 210, 223–253. doi: 10.3354/meps210223

Conley, D. J., Carstensen, J., Rtebjerg, G., Christensen, P. B., Dalsgaard, T., Hansen, J. L. S., et al. (2007). Long-term changes and impacts of hypoxia in Danish coastal waters. *Ecol. Appl.* 17, 165–184. doi: 10.1890/05-0766.1

Conley, D. J., Humborg, C., Rahm, L., Savchuk, O. P., and Wulff, F. (2002). Hypoxia in the Baltic Sea and basin-scale changes in phosphorus biogeochemistry. *Environ. Sci. Technol.* 36, 5315–5320. doi: 10.1021/es025763w

Conley, D. J., Paerl, H. W., Howarth, R. W., Boesch, D. F., Seitzinger, S. P., Havens, K. E., et al. (2009). Controlling eutrophication: nitrogen and phosphorus. *Science* 323, 1014–1015. doi: 10.1126/science.1167755

Da Silva, A., Young, A. C., and Levitus, S. (1994). *Atlas of Surface Marine Data 1994, volume 1: Algorithms and Procedures, NOAA Atlas NESDIS 6*. Washington, DC: U.S. Department of Commerce.

Dai, M., Guo, X., Zhai, W., Yuan, L., Wang, B., Wang, L., et al. (2006). Oxygen depletion in the upper reach of the Pearl River estuary during a winter drought. *Mar. Chem.* 102, 159–169. doi: 10.1016/j.marchem.2005.09.020

Dai, X., Lu, D., Guan, W., Wang, H., He, P., Xia, P., et al. (2014). Newly recorded Karlodinium veneficum dinoflagellate blooms in stratified water of the East China Sea. *Deep Sea Res. Part II Top. Stud. Oceanogr.* 101, 237–243. doi: 10.1016/j.dsr2.2013.01.015

Dai, X., Lu, D., Guan, W., Xia, P., Wang, H., He, P., et al. (2013). The Correlation between *Prorocentrum donghaiense* Blooms and the Taiwan Warm Current in the East China Sea-Evidence for the "Pelagic Seed Bank", Hypothesis. *PLoS One* 8:e64188. doi: 10.1371/journal.pone.0064188

Dai, Z., Du, J., Zhang, X., Su, N., and Li, J. (2010). Variation of Riverine Material Loads and Environmental Consequences on the Changjiang (Yangtze) Estuary in Recent Decades (1955-2008). *Environ. Sci. Technol.* 45, 223–227. doi: 10.1021/es103026a

Dee, D. P., Uppala, S. M., Simmons, A. J., Berrisford, P., Poli, P., Kobayashi, S., et al. (2011). The ERA-Interim reanalysis: configuration and performance of the data assimilation system. *Q. J. R. Meteorol. Soc.* 137, 553–597. doi: 10.1002/qj.828

Ding, R., Huang, D., Xuan, J., Zhou, F., and Pohlmann, T. (2019). Temporal and Spatial Variations of Cross-Shelf Nutrient Exchange in the East China Sea, as Estimated by Satellite Altimetry and In Situ Measurements. *J. Geophys. Res. Oceans* 124, 1331–1356. doi: 10.1029/2018JC014496

Fennel, K., and Testa, J. M. (2018). Biogeochemical controls on coastal hypoxia. *Annu. Rev. Mar. Sci.* 11, 105–130. doi: 10.1146/annurev-marine-010318-095138

Gao, S., Chen, J., Jin, H., Wang, K., Lu, Y., Li, H., et al. (2011). Characteristics of nutrients and eutrophication in the Hangzhou Bay and its adjacent waters. *J. Mar. Sci.* 29, 36–47.

Glibert, P. M., Harrison, J., Heil, C., and Seitzinger, S. (2006). Escalating worldwide use of urea–a global change contributing to coastal eutrophication. *Biogeochemistry* 77, 441–463. doi: 10.1007/s10533-005-3070-5

Glibert, P. M., Magnien, R., Lomas, M. W., Alexander, J., Tan, C., Haramoto, E., et al. (2001). Harmful algal blooms in the Chesapeake and coastal bays of Maryland, USA: comparison of 1997, 1998, and 1999 events. *Estuaries* 24, 875–883. doi: 10.2307/1353178

Guo, X. Y., Zhu, X. H., Wu, Q. S., and Huang, D. J. (2012). The Kuroshio nutrient stream and its temporal variation in the East China Sea. *J. Geophys. Res. Oceans* 117:C01026. doi: 10.1029/2011JC007292

Hagy, J. D., Boynton, W. R., Keefe, C. W., and Wood, K. V. (2004). Hypoxia in Chesapeake Bay, 1950–2001: long-term change in relation to nutrient loading and river flow. *Estuaries* 27, 634–658. doi: 10.1007/BF02907650

Haidvogel, D. B., Arango, H., Budgell, W. P., Cornuelle, B. D., Curchitser, E., Di Lorenzo, E., et al. (2008). Ocean forecasting in terrain-following coordinates: formulation and skill assessment of the Regional Ocean Modeling System. *J. Comput. Phys.* 227, 3595–3624. doi: 10.1016/j.jcp.2007.06.016

Harrison, P. J., Conway, H. L., Holmes, R. W., and Davis, C. O. (1977). Marine diatoms grown in chemostats under silicate or ammonium limitation. III. Cellular chemical composition and morphology of *Chaetoceros debilis*, *Skeletonema costatum*, and *Thalassiosira gravida*. *Mar. Biol.* 43, 19–31. doi: 10.1007/BF00392568

Heisler, J., Glibert, P. M., Burkholder, J. M., Anderson, D. M., Cochlan, W., Dennison, W. C., et al. (2008). Eutrophication and harmful algal blooms: a scientific consensus. *Harmful Algae* 8, 3–13. doi: 10.1016/j.hal.2008.08.006

Holm-Hansen, O., Lorenzen, C. J., Holmes, R. W., and Strickland, J. D. H. (1965). Fluorometric determination of chlorophyll. *ICES J. Mar. Sci.* 30, 3–15. doi: 10.1093/icesjms/30.1.3

Ichikawa, H., and Beardsley, R. C. (2002). The current system in the Yellow and East China Seas. *J. Oceanogr.* 58, 77–92. doi: 10.1023/A:1015876701363

Ishikawa, A. T., Suzuki, R. T., and Qian, X. (2004). Hydraulic study of the onset of hypoxia in the Tone River Estuary. *J. Environ. Eng.* 130, 551–561. doi: 10.1061/(asce)0733-9372(2004)130:5(551)

Jan, S., Sheu, D. D., and Kuo, H. M. (2006). Water mass and throughflow transport variability in the Taiwan Strait. *J. Geophys. Res.* 111:C12012. doi: 10.1029/2006JC003656

Jiang, Z., Chen, J., Zhou, F., Shou, L., Chen, Q., Tao, B., et al. (2015). Controlling factors of summer phytoplankton community in the Changjiang (Yangtze River) Estuary and adjacent East China Sea shelf. *Cont. Shelf Res.* 101, 71–84. doi: 10.1016/j.csr.2015.04.009

Jiang, Z. B., Liu, J. J., Chen, J. F., Chen, Q. Z., Yan, X. J., Xuan, J. L., et al. (2014). Responses of summer phytoplankton community to drastic environmental changes in the Changjiang (Yangtze River) estuary during the past 50 years. *Water Res.* 54, 1–11. doi: 10.1016/j.watres.2014.01.032

Justić, D., Rabalais, N. N., Eugene Turner, R., and Wiseman, W. J. Jr. (1993). Seasonal coupling between riverborne nutrients, net productivity and hypoxia. *Mar. Pollut. Bull.* 26, 184–189. doi: 10.1016/0025-326X(93)90620-Y

Kasai, A., Yamada, T., and Takeda, H. (2007). Flow structure and hypoxia in Hiuchi-nada, Seto Inland Sea, Japan. *Estuar. Coast. Shelf Sci.* 71, 210–217. doi: 10.1016/j.ecss.2006.08.001

Kelly, K. A., Thompson, L. A., Cheng, W., and Metzger, E. J. (2007). Evaluation of HYCOM in the Kuroshio extension region using new metrics. *J. Geophys. Res.* 112:C01004. doi: 10.1029/2006JC003614

Kemp, W. M., Boynton, W. R., Adolf, J. E., Boesch, D. F., Boicourt, W. C., Brush, G., et al. (2005). Eutrophication of Chesapeake Bay: historical trends and ecological interactions. *Mar. Ecol. Prog. Ser.* 303, 1–29. doi: 10.3354/meps303001

Krogh, J., Ianson, D., Hamme, R. C., and Lowe, C. J. (2018). Risks of hypoxia and acidification in the high energy coastal environment near Victoria, Canada's untreated municipal sewage outfalls. *Mar. Pollut. Bull.* 133, 517–531. doi: 10.1016/j.marpolbul.2018.05.018

Large, W. G., and Pond, S. (1981). Open ocean momentum flux measurements in moderate to strong winds. *J. Phys. Oceanogr.* 11, 324–336. doi: 10.1175/1520-0485(1981)011<0324:oomfmi>2.0.co;2

Legovi, T., and Petricioli, D. (1991). Hypoxia in a pristine stratified estuary (Krka, Adriatic Sea). *Mar. Chem.* 32, 347–359. doi: 10.1016/0304-4203(91)90048-2

Li, D. J., Zhang, J., Huang, D. J., Wu, Y., and Liang, J. (2002). Oxygen depletion off the Changjiang (Yangtze River) Estuary. *Sci. China Ser. D Earth Sci.* 45, 1137–1146. doi: 10.1360/02yd9110

Li, M., Xu, K., Watanabe, M., and Chen, Z. (2007). Long-term variations in dissolved silicate, nitrogen, and phosphorus flux from the Yangtze River into the East China Sea and impacts on estuarine ecosystem. *Estuar. Coast. Shelf Sci.* 71, 3–12. doi: 10.1016/j.ecss.2006.08.013

Li, X. A., Yu, Z. M., Song, X. X., Gao, X. H., and Yuan, Y. Q. (2011). The seasonal characteristics of dissolved oxygen distribution and hypoxia in the Changjiang Estuary. *J. Coast. Res.* 27, 52–62. doi: 10.2112/JCOASTRES-D-11-00013.1

Lie, H. J., Cho, C. H., Lee, J. H., Lee, S., and Tang, Y. (2000). Seasonal variation of the Cheju warm current in the northern East China Sea. *J. Oceanogr.* 56, 197–211. doi: 10.1023/A:1011139313988

Liu, H. X., Li, D. J., Gao, L., Wang, W. W., and Chen, W. Q. (2012). Study on main influencing factors of formation and deterioration of summer hypoxia off the Yangtze River Estuary. *Adv. Mar. Sci.* 30, 187–197.

Liu, K., Yan, W., Lee, H., Chao, S., Gong, G., and Yeh, T. (2015). Impacts of increasing dissolved inorganic nitrogen discharged from Changjiang on primary production and seafloor oxygen demand in the East China Sea from 1970 to 2002. *J. Mar. Syst.* 141, 200–217. doi: 10.1016/j.jmarsys.2014.07.022

Liu, K. K., Gong, G. C., Lin, S., Shyu, C. Z., Yang, C. Y., Wei, C. L., et al. (1992). The year-round upwelling at the shelf break near the northern tip of Taiwan as evidenced by chemical hydrography. *Terr. Atmos. Ocean. Sci.* 3, 234–276.

Liu, L., Zhou, J., Zheng, B., Cai, W., Lin, K., and Tang, J. (2013). Temporal and spatial distribution of red tide outbreaks in the Yangtze River Estuary and adjacent waters, China. *Mar. Pollut. Bull.* 72, 213–221. doi: 10.1016/j.marpolbul.2013.04.002

Liu, S. M., Zhang, J., Chen, H. T., Wu, Y., Xiong, H., and Zhang, Z. F. (2003). Nutrients in the Changjiang and its tributaries. *Biogeochemistry* 62, 1–18. doi: 10.1023/A:1021162214304

Lu, D. D., Gobel, J., Wang, C. S., and Liu, Z. S. (2000). Monitoring of harmful microalgae and nowcasting of red tides in Zhejiang coastal water. *Donghai Mar. Sci.* 18, 33–44.

Lu, D. D., Qi, Y. Z., Gu, H. F., Dai, X. F., Wang, H. X., Gao, Y. H., et al. (2014). Causative species of harmful algal blooms in Chinese coastal waters. *Algological Studies.* 14, 145–168. doi: 10.1127/1864-1318/2014/0161

Luo, X., Wei, H., Fan, R., Liu, Z., Zhao, L., and Lu, Y. (2018). On influencing factors of hypoxia in waters adjacent to the Changjiang estuary. *Cont. Shelf Res.* 152, 1–13. doi: 10.1016/j.csr.2017.10.004

Mao, H. L., Kan, Z. J., and Lan, S. F. (1963). A preliminary study of the Yangtze Diluted Water and its mixing processes. *Oceanol. Limnol. Sin.* 5, 183–206.

Nakayama, K., Sivapalan, M., Sato, C., and Furukawa, K. (2010). Stochastic characterization of the onset of and recovery from hypoxia in Tokyo Bay, Japan: derived distribution analysis based on "strong wind" events. *Water Resour. Res.* 46:W12532. doi: 10.1029/2009WR008900

Neumann, T., Radtke, H., and Seifert, T. (2017). On the importance of major Baltic inflows for oxygenation of the central Baltic Sea. *J. Geophys. Res. Oceans* 122, 1090–1101. doi: 10.1002/2016JC012525

Newcombe, C. L., and Horne, W. A. (1938). Oxygen-poor waters of the Chesapeake Bay. *Science* 88, 80–81. doi: 10.1126/science.88.2273.80

Ning, X. R., Lin, C. L., Su, J. L., Liu, C. G., Hao, Q., and Le, F. F. (2011). Long-term changes of dissolved oxygen, hypoxia, and the responses of the ecosystems in the East China Sea from 1975 to 1995. *J. Oceanogr.* 67, 59–75. doi: 10.1007/s10872-011-0006-7

Ning, X. R., Shi, J. X., Cai, Y. M., and Liu, C. G. (2004). Biological productivity front in the Changjiang Estuary and the Hangzhou Bay and its ecological effect. *Acta Oceanol. Sin.* 26, 96–106.

Officer, C. B., Biggs, R. B., Taft, J. L., Cronin, L. E., Tyler, M. A., and Boynton, W. R. (1984). Chesapeake Bay anoxia: origin, development, and significance. *Science* 223, 22–27. doi: 10.1126/science.223.4631.22

Paerl, H. W. (2009). Controlling Eutrophication along the Freshwater–Marine Continuum: dual Nutrient (N and P) Reductions are Essential. *Estuaries Coasts* 32, 593–601. doi: 10.1007/s12237-009-9158-8

Peng, G., Zhang, H., Frank, H. P., Bidlot, J., Higaki, M., Stevens, S., et al. (2013). Evaluation of various surface wind products with OceanSITES buoy measurements. *Weather Forecast.* 28, 1281–1303. doi: 10.1175/WAF-D-12-00086.1

Pitcher, G. C., and Probyn, T. A. (2011). Anoxia in southern Benguela during the autumn of 2009 and its linkage to a bloom of the dinoflagellate Ceratium balechii. *Harmful Algae* 11, 23–32. doi: 10.1016/j.hal.2011.07.001

Quay, D., Rabalais, N. N., Turner, E. R., and Qureshi, N. A. (2013). "Impacts of changing Si/N ratios and phytoplankton species composition," in *Coastal Hypoxia: Consequences for Living Resources and Ecosystems*, eds N. N. Rabalais and R. E. Turner (Washington, DC: American Geophysical Union (AGU)), 37–48. doi: 10.1029/CE058p0038

Rabalais, N. N., Turner, R. E., and Wiseman, W. J. Jr. (2002). Gulf of Mexico hypoxia, AKA" The dead zone". *Annu. Rev. Ecol. Syst.* 33, 235–263. doi: 10.1146/annurev.ecolsys.33.010802.15051

Rabouille, C., Conley, D. J., Dai, M. H., Cai, W. J., Chen, C. T. A., Lansard, B., et al. (2008). Comparison of hypoxia among four river-dominated ocean margins: the Changjiang (Yangtze), Mississippi, Pearl, and Rhone rivers. *Cont. Shelf Res.* 28, 1527–1537. doi: 10.1016/j.csr.2008.01.020

Ram, A., Jaiswar, J. R. M., Rokade, M. A., Bharti, S., Vishwasrao, C., and Majithiya, D. (2014). Nutrients, hypoxia and Mass Fishkill events in Tapi Estuary, India. *Estuar. Coast. Shelf Sci.* 148, 48–58. doi: 10.1016/j.ecss.2014.06.013

Scavia, D., Rabalais, N. N., Turner, R. E., Justic, D., and Wiseman, J. W. (2003). Predicting the response of Gulf of Mexico hypoxia to variations in Mississippi River nitrogen load. *Limnol. Oceanogr.* 48, 951–956. doi: 10.4319/lo.2003.48.3.0951

Shchepetkin, A. F., and McWilliams, J. C. (2005). The regional oceanic modeling system (ROMS): a split-explicit, free-surface, topography-following-coordinate oceanic model. *Ocean Model.* 9, 347–404. doi: 10.1016/j.ocemod.2004.08.002

Silva, A., Pinto, L., Rodrigues, S. M., de Pablo, H., Santos, M., Moita, T., et al. (2016). A HAB warning system for shellfish harvesting in Portugal. *Harmful Algae* 53(Suppl. C), 33–39. doi: 10.1016/j.hal.2015.11.017

Siswanto, E., Nakata, H., Matsuoka, Y., Tanaka, K., Kiyomoto, Y., Okamura, K., et al. (2008). The long-term freshening and nutrient increases in summer surface water in the northern East China Sea in relation to Changjiang discharge variation. *J. Geophys. Res.* 113:C10030. doi: 10.1029/2008JC004812

Smith, V. H. (2003). Eutrophication of freshwater and coastal marine ecosystems a global problem. *Environ. Sci. Pollut. Res.* 10, 126–139. doi: 10.1065/espr2002.12.142

Su, J. (1998). "Circulation dynamics of the China Seas north of 18°N," in *The Sea*, eds K. H. Brink and A. R. Robinson (New York, NY: Wiley), 483–505.

Su, J. L., and Pan, Y. Q. (1987). On the shelf circulation north of Taiwan. *Acta Oceanol. Sin.* 6(Suppl. 1), 1–20. doi: 10.1371/journal.pone.0137863

Tian, R. C., Hu, F. X., and Martin, J. M. (1993). Summer nutrient fronts in the Changjiang (Yantze River) Estuary. *Estuar. Coast. Shelf Sci.* 37, 27–41. doi: 10.1006/ecss.1993.1039

Tishchenko, P. P., Tishchenko, P. Y., Zvalinskii, V. I., and Sergeev, A. F. (2011). The carbonate system of Amur Bay (sea of Japan) under conditions of hypoxia. *Oceanology* 51, 235–257. doi: 10.1134/S0001437011020172

Turner, E., Rabalais, N., and Justic, D. (2008). Gulf of Mexico hypoxia: alternate states and a legacy. *Environ. Sci. Technol.* 42, 2323–2327. doi: 10.1021/es071617k

Turner, R. E., Rabalais, N. N., and Justic, D. (2006). Predicting summer hypoxia in the northern Gulf of Mexico: Riverine N. P, and Si loading. *Mar. Pollut. Bull.* 52, 139–148. doi: 10.1016/j.marpolbul.2005.08.012

Wang, B., Chen, J., Jin, H., Li, H., Huang, D., and Cai, W. (2017). Diatom bloom-derived bottom water hypoxia off the Changjiang estuary, with and without typhoon influence. *Limnol. Oceanogr.* 62, 1552–1569. doi: 10.1002/lno.10517

Wang, B. D. (2009). Hydromorphological mechanisms leading to hypoxia off the Changjiang estuary. *Mar. Environ. Res.* 67, 53–58. doi: 10.1016/j.marenvres.2008.11.001

Wang, B. D., Wei, Q. S., Chen, J. F., and Xie, L. P. (2012). Annual cycle of hypoxia off the Changjiang (Yangtze River) Estuary. *Mar. Environ. Res.* 77, 1–5. doi: 10.1016/j.marenvres.2011.12.007

Wang, H. J., Dai, M. H., Liu, J. W., Kao, S., Zhang, C., Cai, W. J., et al. (2016). Eutrophication-Driven Hypoxia in the East China Sea off the Changjiang Estuary. *Environ. Sci. Technol.* 50, 2255–2263. doi: 10.1021/acs.est.5b06211

Wang, J., Hong, H., Jiang, Y., Chai, F., and Yan, X. (2013). Summer nitrogenous nutrient transport and its fate in the Taiwan Strait: a coupled physical-biological modeling approach. *J. Geophys. Res. Oceans* 118, 4184–4200. doi: 10.1002/jgrc.20300

Wang, J., and Oey, L. Y. (2016). Seasonal exchanges of the Kuroshio and shelf waters and their impacts on the shelf currents of the East China Sea. *J. Phys. Oceanogr.* 46, 1615–1632. doi: 10.1175/JPO-D-15-0183.1

Wei, H., He, Y., Lia, Q., Liu, Z., and Wang, H. (2007). Summer hypoxia adjacent to the Changjiang Estuary. *J. Mar. Syst.* 67, 292–303. doi: 10.1016/j.jmarsys.2006.04.014

Wu, H., Zhu, J., Shen, J., and Wang, H. (2011). Tidal modulation on the Changjiang River plume in summer. *J. Geophys. Res.* 116:C08018. doi: 10.1029/2011JC007209

Xiu, P., and Chai, F. (2014). Connections between physical, optical and biogeochemical processes in the Pacific Ocean. *Prog. Oceanogr.* 122, 30–53. doi: 10.1016/j.pocean.2013.11.008

Xuan, J., Huang, D., Pohlmann, T., Su, J., Mayer, B., Ding, R., et al. (2017). Synoptic fluctuation of the Taiwan Warm Current in winter on the East China Sea shelf. *Ocean Sci.* 13, 105–122.

Yang, D., Yin, B., Sun, J., and Zhang, Y. (2013). Numerical study on the origins and the forcing mechanism of the phosphate in upwelling areas off the coast of Zhejiang province, China in summer. *J. Mar. Syst.* 123–124, 1–18. doi: 10.1016/j.jmarsys.2013.04.002

Yu, R. C., and Liu, D. Y. (2016). Harmful Algal Blooms in the Coastal Waters of China: current situation, long-term changes and prevention strategies. *Bull. Chin. Acad. Sci.* 31, 1167–1174. doi: 10.16418/j.issn.1000-3045.2016.10.005

Yuan, Y. C., Su, J. L., and Xia, S. Y. (1987). Three dimensional diagnostic calculation of circulation over the East China Sea shelf. *Acta Oceanol. Sin.* 6, 36–50.

Zaitsev, Y. P. (1992). Recent changes in the trophic structure of the Black Sea. *Fish. Oceanogr.* 1, 180–189. doi: 10.1111/j.1365-2419.1992.tb00036.x

Zhai, W., Zhao, H., Zheng, N., and Xu, Y. (2012). Coastal acidification in summer bottom oxygen-depleted waters in northwestern-northern Bohai Sea from June to August in 2011. *Chin. Sci. Bull.* 57, 1062–1068.

Zhang, H. M., Bates, J. J., and Reynolds, R. W. (2006). Assessment of composite global sampling: Sea surface wind speed. *Geophys. Res. Lett.* 33:L17714. doi: 10.1029/2006GL027086.

Zhang, J. (1996). Nutrient element in large Chinese estuaries. *Cont. Shelf Res.* 16, 1023–1045.

Zhang, J., Liu, S. M., Ren, J. L., Wu, Y., and Zhang, G. L. (2007). Nutrient gradients from the eutrophic Changjiang (Yangtze River) Estuary to the oligotrophic Kuroshio waters and re-evaluation of budgets for the East China Sea Shelf. *Prog. Oceanogr.* 74, 449–478. doi: 10.1016/j.pocean.2007.04.019

Zhang, P., Pang, Y., Pan, H., Shi, C., Huang, Y., and Wang, J. (2015). Factors contributing to hypoxia in the Minjiang River Estuary, Southeast China. *Int. J. Environ. Res. Public Health* 12, 9357–9374. doi: 10.3390/ijerph120809357

Zhang, W., Wu, H., and Zhu, Z. (2018). Transient hypoxia extent off Changjiang River Estuary due to Mobile Changjiang River Plume. *J. Geophys. Res. Oceans* 123, 9196–9211. doi: 10.1029/2018JC014596

Zhao, D., Zhao, L., Zhang, F., and Zhang, X. (2004). temporal occurrence and spatial distribution of red tide events in China's coastal waters. *Hum. Ecol. Risk Assess. Int. J.* 10, 945–957. doi: 10.1080/10807030490889030

Zhou, F., Chai, F., Huang, D., Xue, H., Chen, J., Xiu, P., et al. (2017). Investigation of hypoxia off the Changjiang Estuary using a coupled model of ROMS-CoSiNE. *Prog. Oceanogr.* 159, 237–254. doi: 10.1016/j.pocean.2017.10.008

Zhou, F., Huang, D. J., Ni, X. B., Xuan, J. L., Zhang, J., and Zhu, K. X. (2010). Hydrographic analysis on the multi-time scale variability of hypoxia adjacent to the Changjiang Estuary. *Acta Ecol. Sin.* 30, 4728–4740.

Zhou, F., Xuan, J. L., Ni, X. B., and Huang, D. J. (2009). A preliminary study on variations of the Changjiang Diluted Water between August 1999 and 2006. *Acta Oceanol. Sin.* 28, 1–11. doi: 10.3969/j.issn.0253-505X.2009.06.001

Zhou, F., Xue, H. J., Huang, D. J., Xuan, J. L., Ni, X. B., Xiu, P., et al. (2015). Cross-shelf exchange in the shelf of the East China Sea. *J. Geophys. Res. Oceans* 120, 1545–1572. doi: 10.1002/2014JC010567

Zhou, M. J., Shen, Z. L., and Yu, R. C. (2008). Responses of a coastal phytoplankton community to increased nutrient input from the Changjiang (Yangtze) River. *Cont. Shelf Res.* 28, 1483–1489. doi: 10.1016/j.csr.2007.02.009

Zhou, M. J., Yan, T., and Zou, J. Z. (2003). Preliminary analysis of the characteristics of red tide areas in Changjiang River estuary and its adjacent sea. *Chin. J. Appl. Ecol.* 14, 1031–1038.

Zhou, M. J., Zhu, M. Y., and Zhang, J. (2001). Status of harmful algal blooms and related research activities in China. *Chin. Bull. Life Sci.* 13, 53–59.

Zhou, Y., Obenour, D. R., Scavia, D., Johengen, T. H., and Michalak, A. M. (2013). Spatial and Temporal Trends in Lake Erie Hypoxia, 1987–2007. *Environ. Sci. Technol.* 47, 899–905. doi: 10.1021/es303401b

Zhou, Z., Yu, R., and Zhou, M. (2017). Seasonal succession of microalgal blooms from diatoms to dinoflagellates in the East China Sea: a numerical simulation study. *Ecol. Model.* 360, 150–162. doi:10.1016/j.ecolmodel.2017.06.027

Zhu, J. R., Chen, C. S., Ding, P. X., Li, C. Y., and Lin, H. C. (2004). Does the Taiwan warm current exist in winter? *Geophys. Res. Lett.* 31:L12302. doi: 10.1029/2004GL019997

Zhu, J. R., and Shen, H. T. (1997). *The Mechanism of the Expansion of the Changjiang Diluted Water*. Shanghai: East China Normal University Press, 50–80.

Zhu, J. R., Xiao, C. Y., Shen, H. T., and Zhu, S. X. (1998). The impact of the Yellow Sea Cold Water Mass on the expansion of the Changjiang Diluted Water. *Oceanol. Limnol. Sin.* 29, 389–394.

Zhu, Z., Wu, H., Liu, S., Wu, Y., Huang, D., Zhang, J., et al. (2017). Hypoxia off the Changjiang (Yangtze River) estuary and in the adjacent East China Sea: quantitative approaches to estimating the tidal impact and nutrient regeneration. *Mar. Pollut. Bull.* 125, 103–114. doi: 10.1016/j.marpolbul.2017.07.029

Zhu, Z. Y., Hu, J., Song, G. D., Wu, Y., Zhang, J., and Liu, S. M. (2016). Phytoplankton-driven dark plankton respiration in the hypoxic zone off the Changjiang Estuary, revealed by in vitro incubations. *J. Mar. Syst.* 154(Part A), 50–56. doi: 10.1016/j.jmarsys.2015.04.009

Zhu, Z. Y., Zhang, J., Wu, Y., Zhang, Y. Y., Lin, J., and Liu, S. M. (2011). Hypoxia off the Changjiang (Yangtze River) Estuary: oxygen depletion and organic matter decomposition. *Mar. Chem.* 125, 108–116. doi: 10.1016/j.marchem.2011.03.005

Zou, J. J., Yang, G., Liu, J. H., Shi, X. F., and Fang, X. S. (2008). Distribution characteristics of dissolved oxygen in the sea area adjacent to the Changjiang River Estuary in September. *Adv. Mar. Sci.* 26, 65–73.

Conflict of Interest: The authors declare that the research was conducted in the absence of any commercial or financial relationships that could be construed as a potential conflict of interest.

frontiers in Marine Science

ORIGINAL RESEARCH
published: 03 July 2020
doi: 10.3389/fmars.2020.00535

Efficient Modeling of Complex Sandy Coastal Evolution at Monthly to Century Time Scales

Dano Roelvink[1,2,3], Bas Huisman[2,3], Ahmed Elghandour[1,4], Mohamed Ghonim[1] and Johan Reyns[1,2]*

[1] IHE Institute for Water Education, Delft, Netherlands, [2] Deltares, Delft, Netherlands, [3] Delft University of Technology, Delft, Netherlands, [4] Department of Civil Engineering, Faculty of Engineering, Port Said University, Port Said, Egypt

With large-scale human interventions and climate change unfolding as they are now, coastal changes at decadal timescales are not limited to incremental modifications of systems that are fixed in their general geometry, but often show significant changes in layout that may be catastrophic for populations living in previously safe areas. This poses severe challenges that are difficult to meet for existing models. A new free-form coastline model, ShorelineS, is presented that is able to describe large coastal transformations based on relatively simple principles of alongshore transport gradient driven changes as a result of coastline curvature, including under highly obliquely incident waves, and consideration of splitting and merging of coastlines, and longshore transport disturbance by hard structures. An arbitrary number of coast sections is supported, which can be open or closed and can interact with each other through relatively straightforward merging and splitting mechanisms. Rocky parts or structures may block wave energy and/or longshore sediment transport. These features allow for a rich behavior including shoreline undulations and formation of spits, migrating islands, merging of coastal shapes, salients and tombolos. The main formulations of the (open-source) model, which is freely available at www.shorelines.nl, are presented. Test cases show the capabilities of the flexible, vector-based model approach, while field validation cases for a large-scale sand nourishment (the Sand Engine; 21 million m3) and an accreting groin scheme at Al-Gamil (Egypt) show the model's capability of computing realistic rates of coastline change as well as a good representation of the shoreline shape for real situations.

Keywords: coastal evolution, coastline model, spit, barrier, salient, tombolo

OPEN ACCESS

Edited by:
Rafael Almar, Institut de Recherche Pour le Développement (IRD), France

Reviewed by:
Andrés Payo, British Geological Survey (BGS), United Kingdom
Bruno Castelle, Centre National de la Recherche Scientifique (CNRS), France

****Correspondence:***
Dano Roelvink
d.roelvink@un-ihe.org

Specialty section:
This article was submitted to Coastal Ocean Processes, a section of the journal Frontiers in Marine Science

Received: *20 March 2020*
Accepted: *12 June 2020*
Published: *03 July 2020*

Citation:
Roelvink D, Huisman B, Elghandour A, Ghonim M and Reyns J (2020) Efficient Modeling of Complex Sandy Coastal Evolution at Monthly to Century Time Scales. Front. Mar. Sci. 7:535. doi: 10.3389/fmars.2020.00535

INTRODUCTION

Sandy beaches are extremely valuable natural resources, providing the first line of defense against coastal storm impacts, as well as other ecosystem services (Barbier et al., 2011) such as ecological habitats and recreation areas. These beaches often are an essential part of a nation's heritage. However, many of the world's coastlines suffer erosion, due to interruption of sand flows from upstream (Syvitski et al., 2005) and alongshore, sand mining and sea-level rise effects, which is especially the case in the vicinity of tidal inlets (Ranasinghe et al., 2013). Science-based strategies for

managing complex sandy coasts are, therefore, of the utmost importance, requiring stable, robust and rapid evaluation methods.

Coastline changes along sandy beaches at timescales beyond events and seasons often are dominated by gradients in wave-driven longshore transport. The first practical concept for predicting coastline change due to interruption of this wave-driven longshore transport was developed by Pelnard-Considère (1956), who derived a diffusion-type equation based on the assumptions of a small angle of incidence and a constant cross-shore profile shape. The first very limiting assumption of a small wave angle was relaxed to some extent by numerical, one-dimensional (1D) model approaches, such as GENESIS (Hanson, 1989), LITPACK (Kristensen et al., 2016), and UNIBEST (Tonnon et al., 2018). These models, which we will refer to as 'standard 1D models' also applied increasingly powerful and more advanced physics-based approaches using newer transport formulations (e.g., Bijker, 1967; Kamphuis, 1991; van Rijn, 2014), to estimate the transport rate as a function of incident wave conditions, sediment parameters and profile shape. However, the main characteristic of the transport curve as a function of the wave angle remained a sine curve, with a maximum at roughly 45°. For relative angles beyond this critical angle, longshore transport decreases for increasing angles and the morphological behavior of the coastline becomes fundamentally unstable.

While the existing coastline models had no real solution for this instability, the Coastal Evolution Model (CEM) proposed by Ashton et al. (2001) addressed this point using a grid-based, upwind approach, which they showed to be able to explain a variety of coastal forms found in nature. The high angle wave instability mechanism (HAWI) has been studied extensively through linear and non-linear stability analysis (Falqués and Calvete, 2005; e.g., Ashton and Murray, 2006; van den Berg et al., 2011; Falqués et al., 2017) the latter included both this and the low angle instability mechanism (LAWI) proposed by Idier et al. (2011). These analyses pointed out the importance of the refraction on the foreshore of shoreline undulations, which generally stabilize the coastline relative to the original HAWI mechanism proposed by Ashton et al. (2001). Recently, Robinet et al. (2018, 2020), starting from the same grid-based one-line approach, extended the concept by coupling it with a 2D wave refraction model and including cross-shore transport. Such models are quite powerful in describing complex coastal shapes but at the cost of requiring complex and relatively time-consuming codes.

The standard 1D models approaches so far address either a single, possibly curving, coastline or disparate sections of coastline represented by separate models. However, there are many cases where islands, shoals and spits shield other parts of the coast from waves. In other situations, spits weld onto the coast to form lagoons that in turn may break up into different parts, or islands migrate toward the coast and weld onto it. Even though some gradual reshaping from a straight beach to a bay shape was achieved with numerical models (e.g., Hanson, 1989), still the grid definition in existing models only allows for a small re-curvature of the coast, generally much less than 90°. As a result, research often focuses on a final stage of the morphological development (e.g., a static bay shape; Hsu et al., 2010). The flexible generation of the grid at each time step is a requisite to deal with complex shoreline shapes which may change substantially over time, such as spits, salients and tombolos.

A vector-based approach to represent the coastline was first used by Kaergaard and Fredsoe (2013a), as part of a system that coupled a one-line coastline approach with a two-dimensional description of the wave and sediment transport, on an unstructured mesh. They applied a quite complicated approach to ensure the volume balance, using triangular and trapezoidal elements. The original coastline representation proposed by Kaergaard and Fredsoe (2013a) was adopted by Hurst et al. (2015) which followed a similar approach to the one presented in this manuscript but for a single coastline (i.e., no splitting or merging was included). Kaergaard and Fredsoe (2013a) and Hurst et al. (2015) implicitly assumed sediment rich environments. Payo et al. (2017) extended the use of vector-based coastline models to sediment-starved environments and applied it to a field study case to simulate the coastal change after defense removal (Payo et al., 2018). In all these vector-based models the coastline followed is at the top of the active profile. This choice implies a strong need to correct the volume balance for strongly curved coasts. As we will explain in detail, our approach follows a more representative coastline, situated approximately at Mean Sea Level (MSL). This recognizes the fact that typically, over longer periods aimed at by this model, the active profile extends from a closure depth to the crest of foredunes; these are at approximately equal vertical distances from the MSL contour. The approach has two advantages: the contour usually extracted from satellite imagery is the MSL contour, and as we will show, complex curvature corrections to the sediment balance are not needed, which makes our method much simpler.

It is noted that computations can be made with complex two-dimensional horizontal (2DH) process-based models, as was shown for the recent case of the 'Sand Engine' in Holland (Luijendijk et al., 2017) as well as for other complex coastal forms. However, this comes at great computational expense and requires considerable expertise. Even though an effort was made to increase the robustness and efficiency of the process-based morphological models (Kaergaard and Fredsoe, 2013a), still these detailed field models are appropriate for the investigation of specific processes (i.e., science), but are often less suited to apply in engineering (design phase) for data poor environments where quick scenario evaluations are needed. So, engineers are rather stuck with one approach which does not capture the complexity of coastal evolution and another which is too expensive.

Consequently, a new approach is needed to robustly follow coastal features through complete lifecycles at reasonable computational cost. The main objective of the current paper is to demonstrate the capabilities that arise when a model with a flexible, coastline-following grid is used: namely, straightforward definition of a complex planform, freedom to allow coastal evolution in any direction, and the possibility to merge and split coastline sections where needed. The characteristic features of the model are presented for a selection of analytical and principle test cases. In addition, the practical simulation of coastline evolution

is validated for a large-scale, manmade land reclamation and a case of a groin field filling in. In this paper we do not yet consider event-scale and seasonal variations, which are mostly due to cross-shore transport. Methods for including this as recently described by e.g., Vitousek et al. (2017), Robinet et al. (2018), Antolínez et al. (2019), Palalane and Larson (2020), and Tran and Barthélemy (2020) are currently under consideration.

MODEL DESCRIPTION

Introduction

To overcome the severe limitations of existing coastline models with a fixed reference line, while avoiding the complexities of grid-based approaches and geometrically complex volume reconstructions, a new Shoreline Simulation model (ShorelineS) was developed, which is aimed at predicting coastline evolution over periods of years to centuries. Its description of coastlines is of strings of grid points (see **Figure 1**) that can move around, expand and shrink freely. The coastline points are assumed to be representative of the movement of the active coastal profile, and hence are situated at the MSL contour. The model can have multiple sections which may be closed (islands, lagoons). Sections can develop spits and other features and they may break up or merge as the simulation continues.

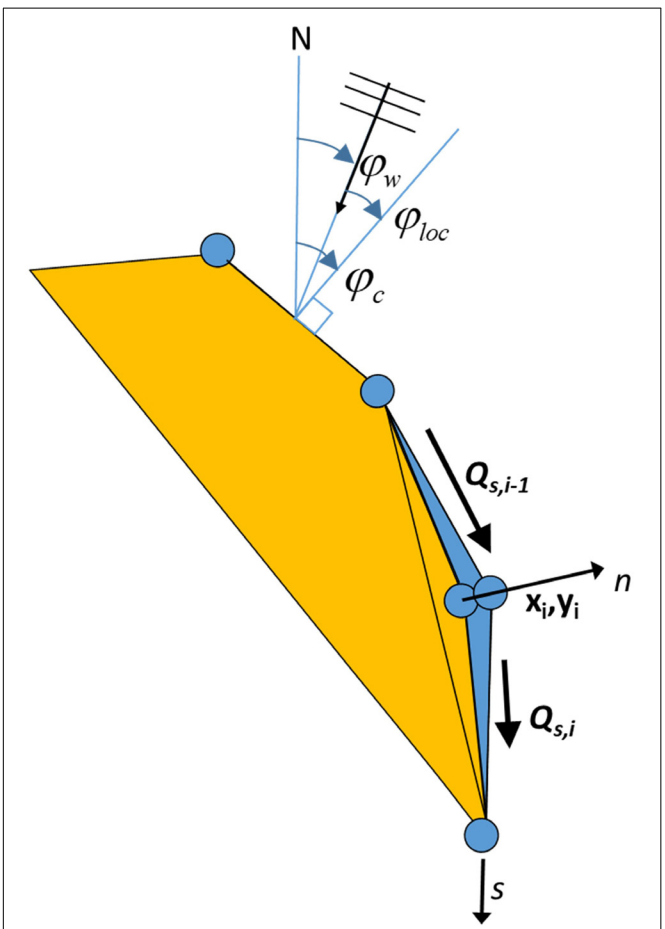

FIGURE 1 | Coastline-following coordinate system and definition of wave and coast angles. φ_c is the orientation of the shore normal with respect to North; φ_w is the angle of incidence of the waves with respect to North and φ_{loc} the local angle between waves and coast, defined as $\varphi_c - \varphi_w$.

Basic Equation

The basic equation for the updating of the coastline position is based on the conservation of sediment:

$$\frac{\partial n}{\partial t} = -\frac{1}{D_c}\frac{\partial Q_s}{\partial s} - \frac{RSLR}{\tan\beta} + \frac{1}{D_c}\sum q_i \qquad (1)$$

where n is the cross-shore coordinate, s the longshore coordinate, t is time, D_c is the active profile height, Q_s is the longshore transport (m^3/yr), tan β is the average profile slope between the dune or barrier crest and the depth of closure, *RSLR* is the relative sea-level rise (m/yr) and q_i is the source/sink term (m^3/m/yr) due to cross-shore transport, overwashing, nourishments, sand mining and exchanges with rivers and tidal inlets. In the Volume Balance section in the Supplementary Information we explain why equation (1) correctly represents the balance of both dry land area and the sediment volume, even for curved coasts.

Transport Formulations

The coastline changes are driven by wave-driven longshore transport, which is computed using a choice of formulations, which can be calibrated to match the local transport rates. The formulations listed in **Table 1** have been implemented. The definitions of the angles are as in **Figure 1**.

CERC1 and CERC2 are defined in terms of the offshore wave angle, and CERC3 and KAMP are defined in terms of the breaking wave angle. However, in all cases the transport follows a shape rather similar to CERC1 when plotted against the deep water wave angle, with a maximum occurring at an offshore angle of 40° to 45° from wave incidence.

CERC1 is the simplest formula and is mainly meant for illustrating the principles of the behavior of the coastline model. CERC2 is derived from the official CERC formula to formally include the effect of refraction and shoaling. Though its behavior is quite similar to CERC1, it allows for a direct comparison with the Coastal Evolution model that utilizes it. The CERC3 and KAMP formulas are widely used in models worldwide such as GENESIS or UNIBEST and again can be useful for intercomparison with such models. CERC1, CERC2 and CERC3 have a single calibration coefficient, whereas the KAMP formula requires, usually uncertain, extra inputs such as beach slope and grain size but has the ambition to be a more accurate, predictive formula.

In **Table 1**, H_{S0} and H_{sb} are the significant wave height at the offshore location and point of breaking respectively (m), T is the peak wave period (s), D_{50} is the median grain diameter (m), m_b is the mean bed slope (beach slope in the breaking zone), Φ_{loc} is the relative angle of wave incidence for waves offshore and Φ_{locb} is the relative angle of waves at the breaking point; b and K_2 are the calibration coefficients of CERC1 and CERC2 formulations

TABLE 1 | Implemented longshore transport formulations.

Author	Notation	Formula
USACE (1984) (simplified)	CERC1	$Q_s = bH_{S0}^{5/2} \sin 2(\phi_{loc})$
Ashton and Murray (2006)	CERC2	$Q_s = K_2 H_{S0}^{\frac{12}{5}} T^{\frac{1}{5}} \cos^{\frac{6}{5}}(\phi_{loc}) \sin(\phi_{loc})$
USACE (1984)	CERC3	$Q_s = bH_{sb}^{5/2} \sin 2(\phi_{locb})$
Kamphuis (1991)	KAMP	$Q_s = 2.33 H_{sb}^2 T^{1.5} m_b^{0.75} D_{50}^{-0.25} \sin^{0.6}(2\phi_{locb})$

respectively, which are computed as:.

$$b = \frac{k\rho\sqrt{g/k}}{16(\rho_s - \rho)(1-p)} \tag{2}$$

$$K_2 = (\frac{\sqrt{g\gamma}}{2\pi})^{\frac{1}{5}} K_1, \qquad K_1 \sim 0.4\, m^{1/2}/s \tag{3}$$

where k is the default calibration coefficient according to the Shore Protection Manual USACE (1984), ρ the density of the water (kg/m^3), ρ_s the density of the sediment (kg/m^3), g the acceleration of gravity (m/s^2) and γ the breaker criterion.

Numerical Implementation

The ShorelineS model is implemented in Matlab. The flow diagram of the model is depicted in **Figure 2**. In the following we will describe the procedure point by point.

The coastline positions are given in two column vectors x_{mc} and y_{mc}, where the different coast sections are separated by NaN's. The sea is defined to the left when following the coastline positions. If a section ends at the same coordinates as where it starts, it is treated as a cyclic section and may represent either an island or a closed lagoon. The coordinates may be in any Cartesian (metric) system. Structures are defined in a similar way, as two column vectors where different structures may be defined, separated by NaN's.

The offshore wave climate can be specified in three ways:

- By means of wave direction and a spreading sector, where a uniform distribution is assumed between the mean wave direction and plus or minus half the spreading sector. For each time step a random wave direction will be chosen from this sector.
- By a wave climate consisting of a number of wave conditions characterized by significant wave height, peak period and mean wave direction, each with equal probability of occurrence. A condition will be chosen randomly for each time step.
- By a time series of these wave conditions, from which the model will interpolate in time.

Various lateral boundary conditions were implemented in the model to represent a variety of coastal situations. For the non-cyclic sections the lateral boundary conditions are specified by controlling the sediment transport rate at the start and end of the boundary, thereby specifying a constant coastline position, a constant coastline orientation or a periodic boundary condition. One type of boundary condition is applied at all open-ended sections, whether existing or newly created. The model detects when a section end point is near the section start point and then always applies cyclic boundary conditions.

Nourishments can be prescribed through a number of polygons within which each nourishment takes place, start and end times, and the total volume of each nourishment. This information is then internally converted into a shoreline accretion rate by dividing the total volume by the time period, the length of coastline within the polygon and the profile height, D_c. By the same mechanism sediment discharged by a river can be distributed over a coastline section within a specified polygon. Shoreline recession as a result of relative sea level rise can be specified, e.g., resulting from the Bruun rule (Bruun, 1962), as given by eq. (1).

All inputs are collected in a single structure S that is passed on to the main function ShorelineS. Preparation of the input can be done in a tailor-made script, but ShorelineS and its sub-functions normally do not have to be altered for a specific application. The main function ShorelineS contains default values for all inputs that are not application-dependent.

The cumulative distance s along each coast section is computed, and this is then distributed over equidistant longshore grid cells based on a given initial grid size. The x and y positions of the coastline then are interpolated along s to obtain the x and y positions of the grid points.

In cases where the grid sizes expand (e.g., at the tip of an expanding spit), new grid points are inserted where the grid size exceeds twice the initial prescribed grid size. Where the grid distances shrink (e.g., at an infilling bay or a shrinking spit) grid points are removed when the grid distance becomes less than half the original grid size.

To avoid strong variations in grid size after inserting or extracting grid cells in expanding or shrinking sections, some smoothing of the s-grid is applied. The smoothing factor has to be chosen carefully as too much smoothing may lead to a loss of planform area and will tend to straighten out sections that should not move at all. The smoothing formulation applied is a simple 3-point smoothing according to:

$$s_{i,smooth} = fs_{i-1} + (1-2f)s_i + fs_{i+1} \tag{4}$$

where f is a smoothing factor, with default value of 0.1. Smoothing can lead to losses in the sediment balance and in situations where this is critical a value closer to zero is advised.

The local wave angle is estimated through the wave transformation from deep water to the nearshore using Snell's law of refraction and from the nearshore to the breaking line using the equations of van Rijn (2014). The refraction from deep water to the toe of the dynamic profile can be done based on the assumption of parallel offshore depth contours, or using a 2D refraction model to provide alongshore-varying wave conditions.

Some parts of the coastline might be sheltered by structures or other parts (sections) of the coast. Hard structures or rocky shores are represented by an arbitrary number of polylines, which shield waves and block longshore transport where they cross a coastline. Thus, sea walls, hard rocks and headlands can represent supply limited situations where the transport is determined by

FIGURE 2 | Flow diagram of the ShorelineS model.

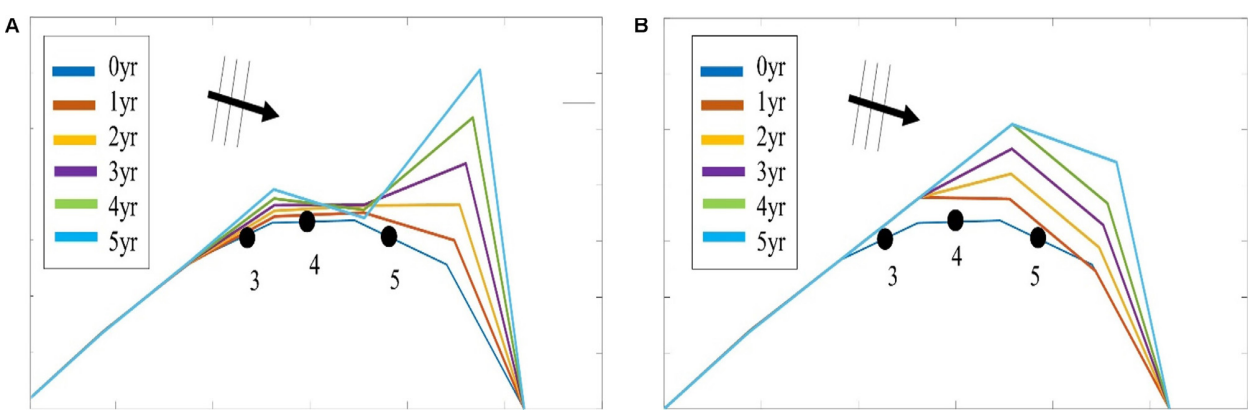

FIGURE 3 | Example of high-angle instability with standard central scheme **(A)** and upwind scheme **(B)**.

the updrift sand supply and 'plugs' of sand are bypassed. The waves at any location can be shielded by other coast sections or hard structures, see **Supplementary Figure SI01**. This approach is valid when the scale of the structures is much larger than the wave length; if this is not the case, diffraction can be activated using different approximations (Elghandour, 2018).

Given the local wave angle with respect to the coast normal and the refracted wave conditions (or deep water wave directions in the case of the CERC1 and CERC2 formulas) the longshore transport can be computed at each transport point between two adjacent coastline points. At present, a choice of formulations as listed in **Table 1** is available to be used.

Coastline Evolution

At each point the local direction of the coast is determined from the two adjacent points (as a reference line), then the longshore transport is calculated for each segment. The difference leads the points to build out or to shrink. The mass conservation equation is solved using a staggered forward time–central space explicit scheme (see **Figure 1**):

$$\Delta n_i^j = -\frac{1}{D_c}\frac{2(Q_{s,i}^j - Q_{s,i-1}^j)}{L_i}\Delta t \tag{5}$$

where j is the time step index, $\Delta t$is the time step (yr), i is the point/node index and L_i is the length of the considered grid element computed from $L_i = \sqrt{(x_{i+1} - x_{i-1})^2 + (y_{i+1} - y_{i-1})^2}$and x_i and y_i are the Cartesian coordinates of point i. From the normal displacement it follows that the change in position of point i then becomes:

$$\begin{aligned} \Delta x_i^j &= -\Delta n_i^j \left(y_{i+1} - y_{i-1}\right)/L_i \\ \Delta y_i^j &= \quad \Delta n_i^j \left(x_{i+1} - x_{i-1}\right)/L_i \\ x_i^{j+1} &= x_i^j + \Delta x_i^j \\ y_i^{j+1} &= y_i^j + \Delta y_i^j \end{aligned} \tag{6}$$

The scheme can be shown to be conserving the land area. Since an explicit scheme is applied, the time step is limited by the following criterion (Vitousek and Barnard, 2015):

$$\frac{\varepsilon\,\Delta t}{\Delta s^2} < \frac{1}{2} \tag{7}$$

where the diffusivity ε is related to the maximum gradient of the sediment transport with respect to the wave angle relative to the coast, which can be approximated by:

$$\varepsilon_{\max} = 2Q_{\max}/D_c \tag{8}$$

where Q_{max} is the maximum transport rate in the model.

Therefore the following is obtained:

$$\Delta t < \frac{D_c \Delta s^2}{4Q_{\max}} \tag{9}$$

This criterion can be restrictive for small grid sizes (e.g., less than 100 m). Stability is, however, guaranteed through this adaptive timestep.

High-Angle Instability

A special treatment takes care of so-called high-angle instability (Ashton et al., 2001), which allows spits to develop. In cases where the local angle exceeds the critical angle on one side and is less than the critical angle at the updrift side, the transport at the downdrift point is set to the maximum transport (or the angle is set to the critical angle). **Figure 3** illustrates the effect of this treatment, where a central scheme would lead to unstable behavior, the local upwind treatment ensures a smooth development into a spit. The physics in the model is the same as in Ashton et al. (2001, 2016), and Ashton and Murray (2006), and therefore it inherits most of the behavior of their Coastal Evolution Model. The novelty in ShorelineS is that it achieves the same behavior with a vector-based rather than a grid-based approach. This is more elegant and more efficient, especially when large areas need to be covered.

Barrier or Spit Overwash

For simulating barriers that already exist or that are in the form of developed spits due to high wave angle instability, it was necessary to represent the overwash process as it maintains the width of the barrier to a certain limit (Leatherman, 1979).

(Ashton and Murray, 2006) introduced the physical process of overwash by assuming a minimum barrier width such that sediment eroded from the seaward side is deposited on the landward side. By simultaneously retreating the seaward and landward sides of a section narrower than the specified critical width, the retreating section creates a longshore transport gradient that tends to fill it up; thus, the retreating helps maintain the width.

A similar concept was implemented in ShorelineS in a simple approach for treating the barrier width. At each time step, the model checks the local barrier width at each point/node, measured in the incident wave direction. If the barrier is narrower than the critical width, then overwash occurs. The overwash process moves the landward point a distance equal to the difference between the actual width and the critical width. Such a distance is not allowed to exceed a given percentage (e.g., 10%) of the local spatial discretization distance of the grid per time step to avoid discretization artifacts. Then the model looks for the closest node on the seaward side to erode it by the same amount (**Supplementary Figure SI02**). A possible refinement is, as in Ashton and Murray (2006), to assume different profile depths on the seaward and landward sides, as is logical in some settings, e.g., for the case of an eroding barrier island. In this case the landward extension would be larger than the erosion on the seaward side.

Merging and Splitting

One of the advantages of the ShorelineS model is that it can simulate multiple coastal sections at the same time, and these sections can affect each other by shielding the waves. Small parts of the coast are allowed to split and migrate as the spits are growing and in some cases break up and migrate as a small island. An example of the splitting procedure is shown in **Supplementary Figure SI03**. Such splitting typically happens when the seaward side of a section erodes by more than the

overwashing process allows for or when the latter is not activated. The numbering is indicated to show how the grid cell connections change after the splitting procedure: from one continuous coastline section to two separately numbered sections.

If two sections intersect, they may merge into one section as the simulation continues, as is illustrated in **Supplementary Figure SI04**. Such merging typically happens due to shoreward migration or extension of a spit toward the mainland coast. Again, the numbering is included to indicate how the separate spit and mainland coast sections are now joined at the seaward side as a continuous coastline numbered 12-20 and a lagoon numbered 1-10.

Treatment of Groins

Groins can be treated simply as any structure crossing the coastline, where the transport at the transport point closest to the intersection between the structure polyline and the coastline is set to zero. However, such a treatment does not give a very accurate representation of the groin position and local coastline evolution, and does not account for bypassing in a smooth way. Therefore, a more eleborate treatment was presented in Ghonim (2019), which is summarized as follows. First, additional grid points exactly on either side of each groin are introduced. Second, the local coastline position at either side of the groin is forced to move along the groin. Third, bypassing and transmission are accounted for, according to the following mechanisms.

Bypassing can be simulated in two ways, either as starting only when the updrift accretion has reached the tip of the groin, or gradually increasing if the depth at the tip of the groin is less than the depth of active transport. The first approach follows the considerations of, assuming a fully impermeable structure, such as a groin with complete blockage of the longshore transport. Sand bypassing takes place only when the groin is filled with sand. Based on that, the longshore sediment transport is set to zero at the structure and the sand bypassing factor (*BPF*) also is set to zero from the start of the simulation until the moment when the sediment reaches the tip of the groin. Then, the bypassing factor is set to its maximum value (*BPF* = 1), which means that all sediment bypasses the groin's tip and moves towards its downdrift side. In that case the lateral boundary condition at grid point *i* (see **Supplementary Figure SI05**), which is located at the groin representing the bypassed volume can be expressed as:

$$QS_i = BPF\, QS_{i-1} \tag{10}$$

where QS_i is the longshore transport at grid point *i*. There were many options for how the bypassed sediment should be distributed downdrift of the groin. The most appropriate distribution of the bypassed sediment, in line with the expected flow pattern around the groin, which attaches roughly at the end of the sheltered area, is to pass all the bypassed sediment at the last sheltered grid point *ilast* and to leave the sheltered area untouched. To do so numerically, the lateral boundary conditions at the downdrift side of the groin are set as follows:

$$QS_{i+1} = QS_{i+2} \ldots = QS_{ilast} = QS_i \tag{11}$$

Eq. (11) ensures that only the last sheltered grid point obtains all the bypassed sediment and equal signs indicate that there is no sediment transport gradient from the grid point *i* to the last sheltered grid point *ilast*. This approach keeps the sheltered grid points fixed in their positions except for the last one, which gives a transport gradient to its following grid point.

That this treatment is more realistic than the classical Pelnard-Considère solution where an erosion peak at the downdrift end of the groin is assumed follows from many examples worldwide, where the erosion peak is rarely found right next to the groin but always some distance downdrift, due to the wave sheltering and recirculation in this area. An example is shown in **Supplementary Figure SI06**, for a groin field at Eastbourne, United Kingdom.

The second approach (Larson et al., 1987) assumes that sand bypassing does not take place only when the groin is totally filled with sand, but it may take place just after the construction of the groin. While sand moves along the coastline, it is influenced by the presence of the shore-normal structures, such as groins and the response of the coastline to those structures varies for different locations and different types of structures. The main parameters that influence the response of the shoreline at the structure are the structure permeability and the bypassing ratio, which is the ratio between the water depth at the head of the structure D_s and the water depth of the active longshore transport D_{LT}. The bypassing ratio varies between 0 and 1 (Hanson and Kraus, 2011).

Sand bypassing occurs at the seaward end of the groin as long as D_s is less than D_{LT}. The depth of the active longshore transport is similar to the depth of the highest 1/10 waves at the updrift side of the structure (Hanson, 1989), and represents the time-dependent depth for longshore sediment transport, which is often less than closure depth D_c, and can be estimated as:

$$D_{LT} = \frac{A_w}{\gamma} \left(H_{1/3}\right)_b \tag{12}$$

where A_w = 1.27, a factor that converts the 1/10 highest wave height to significant wave height [-]; γ is the breaker index, the ratio between wave height to wave depth at breaking line [-] and $(H_{1/3})_b$ is the significant wave height at the line of breaking [m].

Based on the assumption of equilibrium profile shape (Dean, 1991), the water depth at the structure's head D_s can be determined as:

$$D_s = A_p y_{str}^{2/3} \tag{13}$$

where A_p is the sediment scale parameter [$m^{1/3}$] and y_{str} is the distance from the structure's head to the nearest point of the coastline [m]. In that case, the bypassing factor (*BPF*) is estimated based on the following equation:

$$BPF = 1 - \frac{D_s}{D_{LT}} \tag{14}$$

and the bypassing volume increases until reaching its maximum value when the groin is filled with sediment [*BPF* = 1]. The lateral boundary conditions at the groin are otherwise equal to those for the first approach, as given by Eqs. (6) and (7).

ANALYTICAL TESTS

A number of analytical tests were done to verify the correct implementation of the governing equations and the numerical scheme. They are described extensively in Elghandour (2018). Here, for brevity, the results are summarized for only two of these tests.

Linear Diffusion Test

The first test is the verification test used by Vitousek and Barnard (2015) to validate the CoSMoS model. The shoreline starts with the configuration $y = a\cos(kx)$, where $k = 4\pi/L$ and the analytical solution of the shoreline evolution is $y = a\exp\left(-\nu k^2 t\right)\cos\left(kx\right)$ where $\nu = 2Q_o/D_c$. The model was run with an adaptive time step based on the criterion $\Delta t < \Delta x^2/2\nu$. The amplitude of the shoreline perturbation was 100 m, the domain length 5 km, the wave angle 0°. Q_o was taken at 10^5 m^3/yr, the space step was 50 m and the total simulation time 30 yr. The resulting evolution is stable and accurate, see **Figure 4**.

Pelnard-Considère Groin Test

This test reproduces the well-known analytical solution for the accretion and erosion on either side of a groin on a uniform coast, according to Pelnard-Considère (1956). However, the validity of that solution ends when the updrift side of the groin is completely filled with sand or when the incident wave angle is too high. Both bypassing approaches were tested with different incident wave angles. As expected, the first approach has produced a perfect agreement with the analytical solution for a wave angle of 10° (see **Figure 5A**), while a slight difference in the shoreline position is observed for a wave angle of 25°, at which the analytical solution loses its validity and overestimates the rate of change in the shoreline position (see **Figure 5B**). That difference increases when applying the second approach, due to the partial bypassing which slows down the shoreline movement; moreover, the difference downdrift of the groin is due to the effect of the wave shadowing which is not taken into account in the analytical solution (see **Figure 5C**).

Overall it may be concluded that the comparison with analytical test cases is satisfactory, both for the diffusion test and the groin case, and that the basic equations and numerical scheme have been implemented correctly.

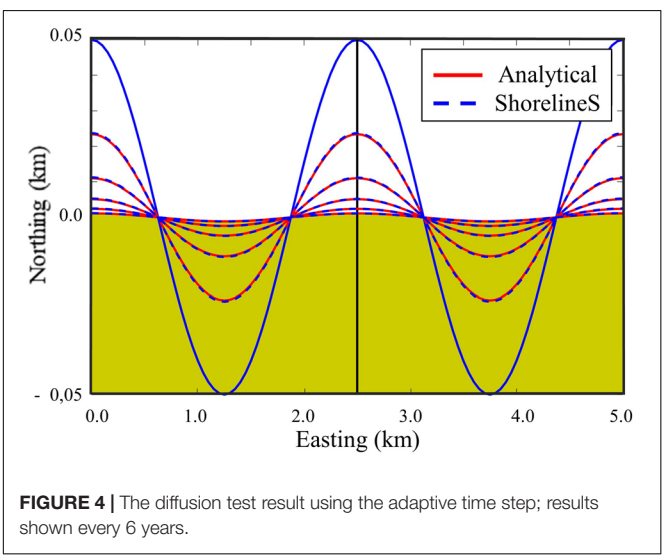

FIGURE 4 | The diffusion test result using the adaptive time step; results shown every 6 years.

PRINCIPLE TESTS OF COMPLEX BEHAVIOR

Island Deformation

This test was designed to investigate the behavior of a deforming island under different wave spreading and spit overwashing scenarios. The initial coastline is a perfect circle with a radius of 500 m. The mean wave direction is from the West, 270° N. A wave height of 1 m and a transport coefficient of the *CERC1* formula was applied, leading to a maximum transport of 1 Mm^3/year. The simulation ran for 4 years in all cases. The wave spreading varied between 0°, 90°, and 180° and the grid resolution was 50 m.

For the case without wave spreading two long and narrow spits extend from the island, under the theoretical (Ashton et al., 2016) angle of 45° relative to the wave propagation direction. In the case where no spit overwashing is allowed the section of the spits nearest to the island becomes thinner and at some point breaches; this process repeats itself. The overwashing process paradoxically ensures the survival of the spit as the landward migration attracts sediment due to the longshore transport gradient that is created

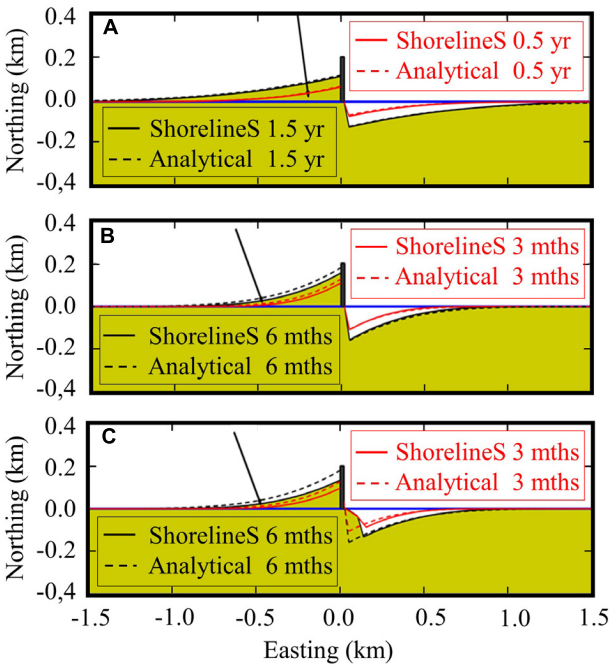

FIGURE 5 | Shoreline response for both the analytical solution and ShorelineS with different wave angles and bypassing approaches. Panel **A:** incident angle 10°, no shadowing; panel **B:** incident angle 25°, no shadowing; panel **C:** incident angle 25°, with partial bypassing and shadowing.

by the local retreat due to overwashing. In **Figure 6** the effect of the critical spit width is illustrated. In the left panel, without the overwash mechanism, the spit breaks apart; the overwashing with spit width of 100 m (middle panel) or 200 m (right panel) clearly leads to more robust spit behavior. For the case with 90° spreading the coastline is more curved and the spit wider because (a) waves can initially reach further around the island and (b) the transport can get around the tip of the spits more easily during the conditions most perpendicular to the spit. For the case of 180° spreading the spits cannot fully develop and are wrapped around the island, which turns into a retreating, jellyfish-like shape. For the cases with larger spreading the spit overwashing has a much less dominant effect.

Island Merging

This test has been designed to examine the model stability and behavior under the merging and splitting of different coastal sections. The initial island configuration and the wave conditions and other settings are the same as in the previous test case, but now the island is located 800 m from a straight beach facing West. The duration of the simulation is 10 years in this case. In **Figure 7** the process of island deformation, migration to the coast and welding with the coast is illustrated for the case of a critical spit width of 100 m. In the top panels, the case of no directional spreading shows the formation of a lagoon after 2 years. The barrier overwash procedure allows for the rollover of the barrier enclosing the lagoon, leading to a rapid landward migration and welding of the barrier with the original coastline, after which the island has interestingly left two distinct humps and two small lagoons on the original coastline. A similar process, though slower and with less longshore extent, takes place with the higher spreading of 90°. In this case one extended lagoon remains. Finally, for a large directional spreading of 180° the island as a whole migrates onshore and welds to the beach, leaving only a small lagoon. Since the island is shielding northerly wave directions in the South and southerly directions in the North, it also acts like an offshore breakwater, attracting sand behind the island at the cost of erosion at some distance. For this case the final coastal shape is quite stable, as the southern part is oriented toward waves from the South and shielded from those from the North and vice versa.

These developments appear to be realistic and demonstrate the capability of the model to evolve coastal shapes through significant changes. Welding of a spit to the coast is frequently observed, as in, for instance, the case of the Sandmotor, shown in Section "FIELD VALIDATION." Configurations such as the final one for a spreading of 180° are commonly seen when the wave climate has a large spreading, as for instance for the island heads in Zeeland, in the south of the Netherlands. A jellyfish-like shape migrating in the wave propagation direction as seen in the bottom panels of **Figure 7** and the right-hand shapes of **Figure 6** are clearly visible in, e.g., the Noorderhaaks, a sandy island between the coasts of North Holland and Texel in the Netherlands.

Flying Spits

In order to test the model performance under a high angle of wave incidence, and to verify the model ability to grow spits through the instability mechanism according to Ashton et al. (2001), the test conditions follow the numerical test introduced by Kaergaard and Fredsoe (2013b). For this test the initial grid size = 250 m, spit width = 250 m, closure depth = 15 m and the CERC2 formula was applied; the total simulation time was 250 years. The total shoreline length was 100 km, the initial undulation length was set to 5 km and the initial amplitude of the undulation was 50 m. The wave conditions were kept constant at a wave height of 1 m, a peak wave period of 5 s and a mean wave direction of 300°.

Periodic boundary conditions were used to the left and Neumann boundary conditions were used on the right boundary. **Figure 8** shows a section of 50 km in the middle of the test coastline at different stages. We clearly see the initial disturbances grow into wave-like patterns, which grow and merge into larger length scales, and finally reach the stage of flying spits, from which even small islands can be detached.

The single high angle wave direction leads to small protuberances, which accrete forming larger bumps (around

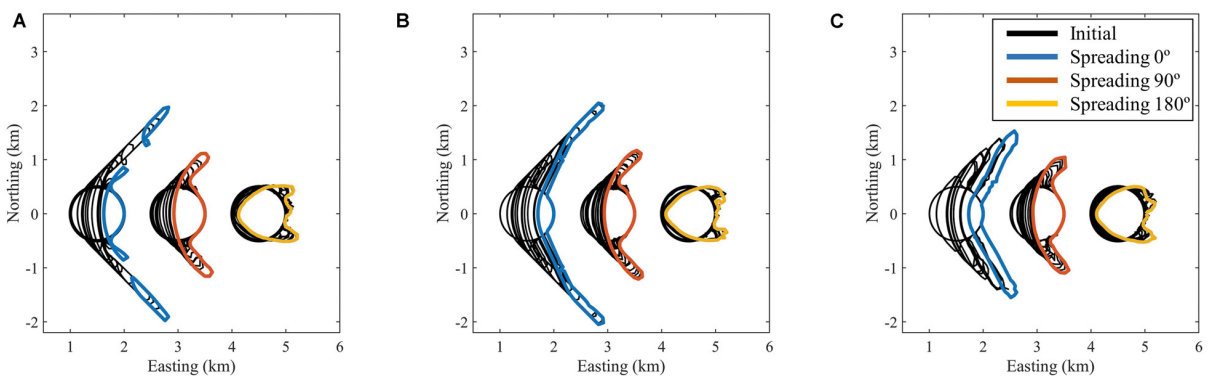

FIGURE 6 | Deformation of an island due to waves with mean direction from the West; wave spreading uniform 0°, 90°, and 180°, respectively. Left panel **(A)**: no overwash. Middle panel **(B)**: critical spit width 100 m. Right panel **(C)**: critical spit width 200 m.

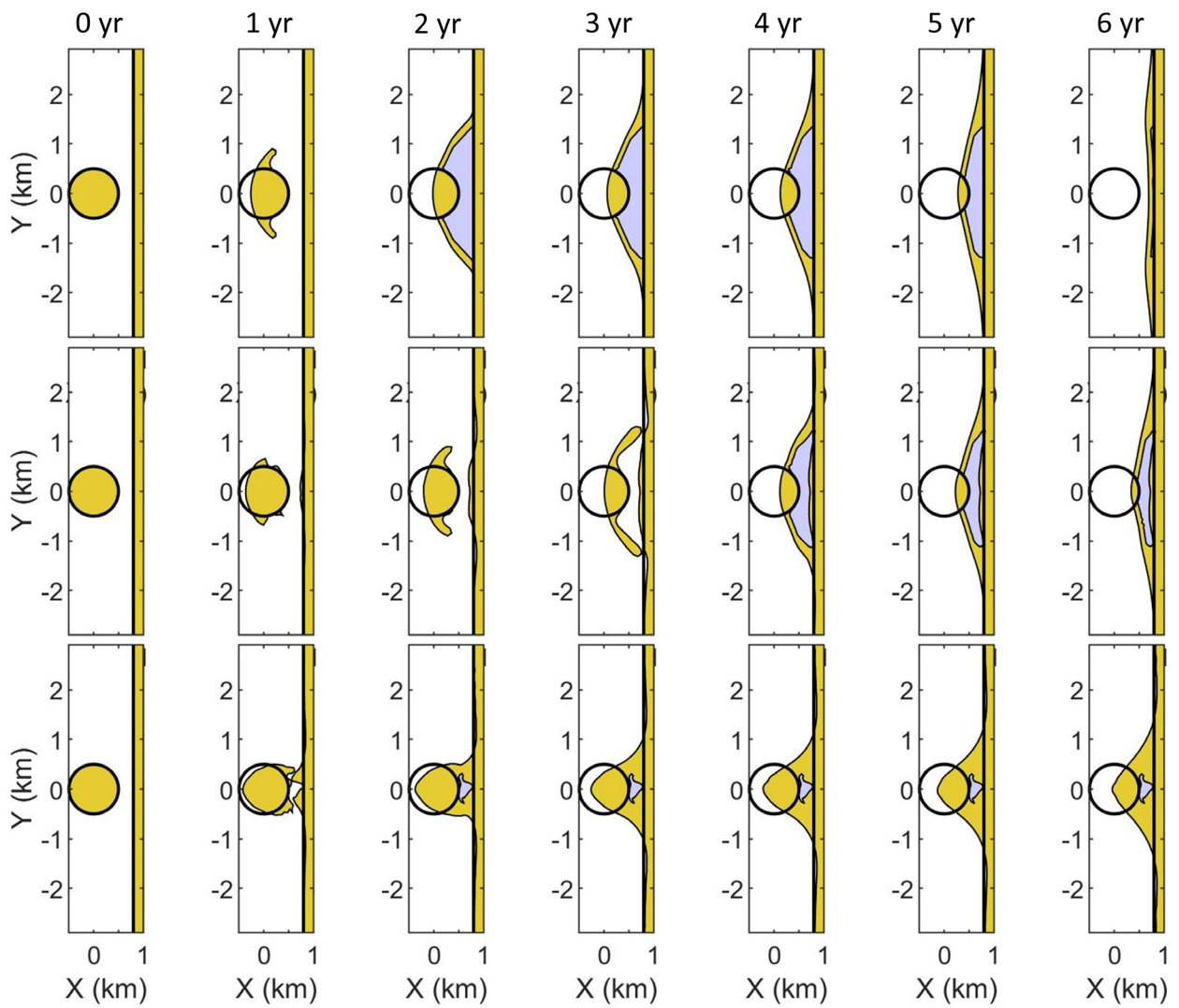

FIGURE 7 | Evolution of an island merging with the coast, for a critical spit width of 100 m. **Top row:** directional spreading 0°; **middle row**: 90° and **bottom row:** 180°. Time between subsequent figures approximately 1 year.

100 years) and the bumps' crests evolve while the flanks retreat. This continues until they reach the point when the shoreline angle is equal to the maximum transport angle, when the upwind correction applies so that a spit forms. The shoreline angle at the up drift side increases but cannot exceed the maximum transport angle. The spit evolves to the down drift direction. As shown in **Figure 8**, after a while sometimes breaching might occur at the spit neck so small islands can be detached. Part of the shoreline at the down drift side of the spit is shadowed from the approaching waves; that feature does not change after spit formation. This is not always the case in reality as it might be filled up by aeolian transport, due to overwashing or due to wave approach from the down drift direction.

As the spit extends offshore, the spit tip migrates toward the down drift direction and repeatedly a new spit tip forms, taking over the old tip. The spit migration speed is 28 m/yr on average. The growth rate of the spit was approximately estimated to be 15 m/yr at Walvis Bay, Namibia according to Elfrink et al. (2003).

Though different in details from the results of Kaergaard and Fredsoe (2013a) we also see the development of the spits with a wave length in the order of 5 km after approx. 120 years; their model includes nearshore wave refraction over the evolving bathymetry and thereby suppresses smaller-scale disturbances apparent in our model.

Overall the growth rate is slower than estimated by the model presented by Ashton and Murray (2006); the reason for the slower growth rate is mainly that the transport coefficient they applied leads to sediment transport in the tens of millions of m^3/yr, which is not realistic.

In natural conditions, the entire coast is affected by multiple wave approach angles and also the alongshore boundary

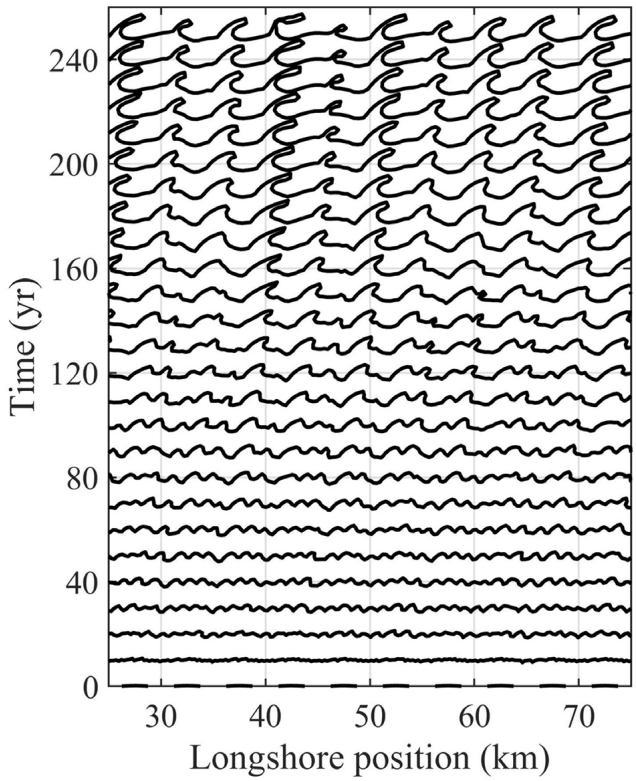

FIGURE 8 | Shoreline undulations under test conditions of Kaergaard and Fredsoe (2013a).

condition impacts the evolution behavior. More complicated conditions and real cases will be the subject of further studies. The current case, however, shows that the new numerical approach is capable of reproducing similar flying spit features as in both Ashton and Murray (2006) and Kaergaard and Fredsoe (2013a).

Van Rijn's Compendium of Coastal Forms

The following case is inspired by the picture in van Rijn (1998), see **Figure 9**. It describes a compendium of coastal features, based on the author's experience, and the authors' ambition was to re-create most of them in a single simulation, highlighting that any coastal shape predominantly created by wave-driven longshore transport can be produced by the proposed model.

The initial setup is shown in the top panel of **Figure 10**. It contains a coast with sharp variations in orientation with a sandy island and two hard offshore breakwaters or rocky obstacles. The wave climate is from the South with a constant offshore significant wave height of 1m and a random spreading of 120°. The CERC1 formula was used, with a coefficient b of 1 $Mm^{1/2}$/yr. The grid resolution was 200 m and a fixed time step of 1/50 yr was applied. The profile height was taken as 6 m and the critical spit width was taken as 100 m. We see a number of spits developing, on the sides of the island and on all protruding parts of the coast 'bay-mouth spits' can be seen (**Figure 10**). After 20 years the island spits weld to the coast creating a lagoon. The western breakwater captures the westward longshore transport, creating a tombolo. After 50 years the central spits merge together and start extending seaward, while the island has fully disappeared, its sand distributed along the eroding coast. On the western coast the headland spit has welded to the coast, creating a curved embayment with an enclosed lagoon.

These developments seem quite realistic and intermediate shapes bear substantial resemblance to the sketches in **Figure 9**. They form an illustration of the capability of ShorelineS to represent not just incremental coastal changes, but radical transformations of the coast over long timescales.

The coloring of **Figure 10** is done through post-processing on a fine grid, where for each pixel a record is kept of when it has become land or sea. This representation facilitates a comparison with observed horizontal stratigraphic features such as beach ridges.

In order to test the sensitivity of the model, in this case involving drastic transformations, to the grid resolution an additional test was done with half the grid size, e.g., 100 m instead of 200 m. The resulting evolution over the first 50 years is shown in **Supplementary Figure SI07**. Qualitatively, the same features are generated and on several elongated coastal stretches the differences are quite small. Because of the random variation of wave conditions, the differences are relatively larger in the beginning than at the end of the

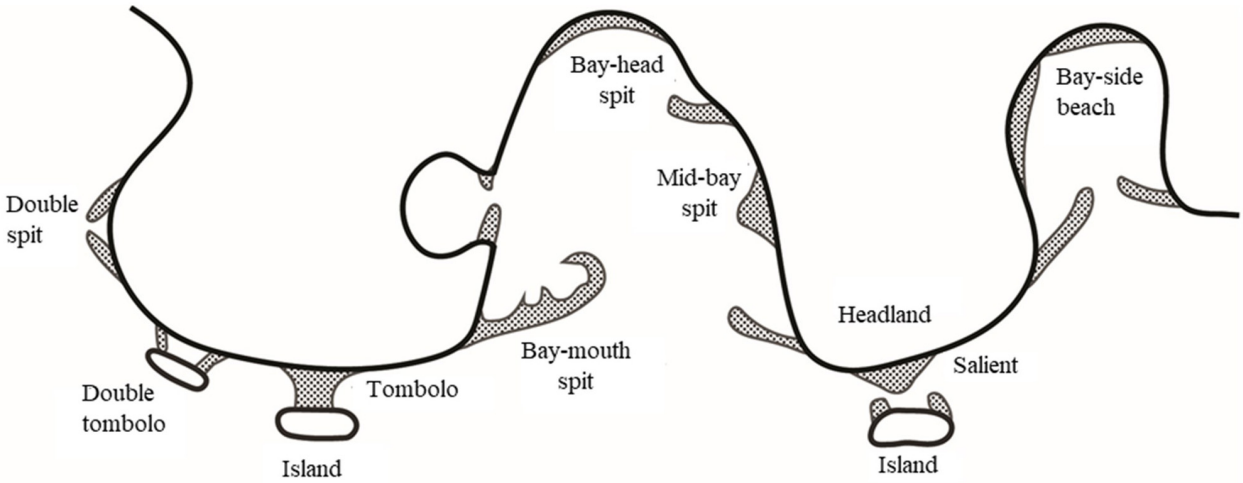

FIGURE 9 | Overview of sandy coastal shapes, from van Rijn (1998).

simulation; largest differences occur near the tips of spits, as would be expected.

It may be concluded from this test case that ShorelineS is capable of producing a range of observed coastal features, just based on an initial coastal configuration. Whether ShorelineS also predicts the properties of these features and the rate of change of their evolution correctly will be the subject of further study. In the following, two field case studies are given that show a (still limited) validation of this capability to quantitatively predict coastal evolution for complex cases.

FIELD VALIDATION

The capability of ShorelineS to represent real-world coastal evolution is illustrated through the example of the Sand Engine (Stive et al., 2013; de Schipper et al., 2016), as well as for a groin scheme at Al-Gamil Beach, Egypt. Especially, the appropriate representation of rates of change (i.e., transport rates and subsequent gradients) and the shape of the coastline are considered essential properties of a shoreline model.

Sand Engine, Ter Heijde, the Netherlands

The Sand Engine is a large-scale sand nourishment (21 million m^3 of sand) which can also be seen as a temporary land reclamation. The hydrodynamics and morphology at the Sand Engine have been the subject of intensive modeling efforts with 2DH process-based models (Luijendijk et al., 2017; Huisman et al., 2018), 1D line models (Tonnon et al., 2018) and hybrid approaches (Arriaga et al., 2017), all of which take considerable time to set up, calibrate and run (run times of up to months), and require a high level of expertise. The results are reasonable after considerable tuning, but only the most expensive process-based approach leaves behind a lagoon after the spit has merged with the mainland. Furthermore, typical coastline models represent either the shape (e.g., Ashton et al., 2001) or transport rates (Tonnon et al., 2018) well, but seldom perform well for both.

The ShorelineS model, on the other hand, requires only the initial, complex coastline and a nearby deep water wave climate. The latter is given as a probability distribution of (50) wave direction bins, each with equal total energy flux, with one wave height class per direction, as depicted in **Supplementary Figure SI08**, since an accurate representation of the directional wave climate is the most important aspect in the schematization. The shape of the distribution is constant in time. Dots indicate offshore measurements over a 10-year period. Each bin (contained in the red boxes) contains the same total energy flux and the representative wave height for each bin is denoted by the red dots. Each time step a wave condition is selected randomly from these 50 conditions.

The initial model resolution was set at 100 m. After this the only tuning needed was of the transport magnitude (formula CERC1, b = 500,000 $m^{1/2}$/yr/rad), and the profile height (10 m). These parameters only influence the speed of developments, not the shape.

The results of the Sand Engine forecast (**Figure 11**) qualitatively reproduce well the shoreline reshaping over time and quantitatively reproduce the observed behavior, at minimal runtime (approximately 15 min). Even the shape of the spit is reproduced well in the model showing a smooth elongated connection to the mainland in September 2016 similar to the field observations. The temporal development of the erosion (middle panel in **Figure 11**) obviously misses the seasonal component (with sudden steps of erosion due to storm events) which is due to the use of an average climate, but the use of a temporally varying nearshore wave climate would also allow for the computation of the steps over time.

To quantitatively assess the performance of the model the distances $dist_{mess(t)-initial}$ between two observed coastlines and between the observed and computed coastlines at a given time, $dist_{comp(t)-meas(t)}$ are computed. These distances are assigned a

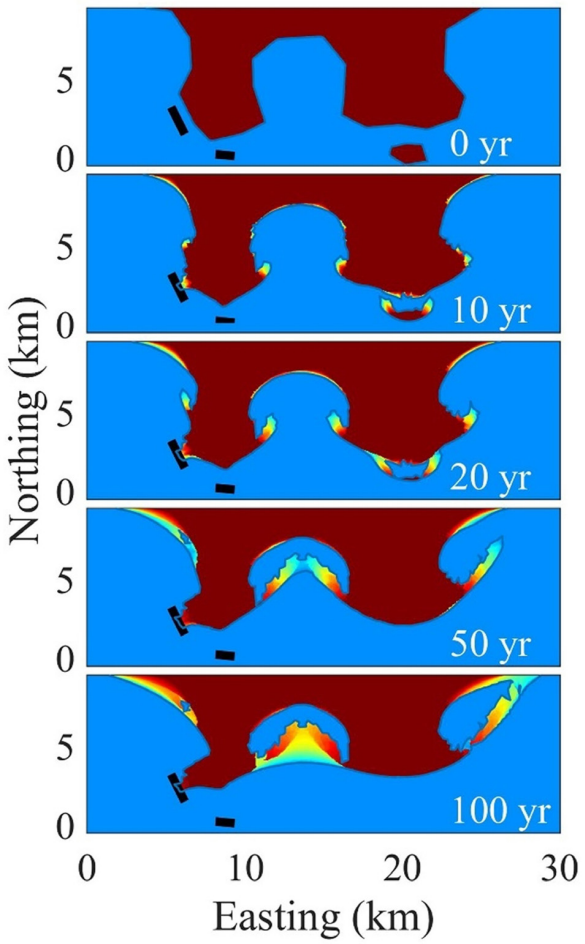

FIGURE 10 | Evolution of coastal features in a geometry resembling van Rijn's overview of coastal shapes. Colors indicate age of deposition, with green the most recent deposition to dark red for the oldest deposition.

positive sign when the coastline moves seaward and negative when it moves landward. The following parameters:

$$\begin{aligned} biasm\,(t) &= \tfrac{1}{L}\int_0^L dist_{meas(t)-initial}\,ds \\ rmsm\,(t) &= \sqrt{\tfrac{1}{L}\int_0^L dist^2_{meas(t)-initial}\,ds} \\ biascm\,(t) &= \tfrac{1}{L}\int_0^L dist_{comp(t)-meas(t)}\,ds \\ rmscm\,(t) &= \sqrt{\tfrac{1}{L}\int_0^L dist^2_{comp(t)-meas(t)}\,ds} \\ BSS(t) &= 1-\tfrac{rmscm(t)}{rmsm(t)} \end{aligned} \tag{15}$$

In these parameters, *biasm* denotes the net measured shift of the coastline (positive seaward), *rmsm* the root-mean- square deviation of the measured coastline, *biascm* is the net shift between measured and computed coastline positions, *rmscm* is the root-mean-square difference between measured and computed coastline and *BSS* is the Brier Skill Score, a measure of the model skill frequently used in morphodynamic modeling, e.g., **Figure 12** shows an example of this computation, with the observed and computed coastlines in the left panel, along with their error parameters, and the distances as a function of the alongshore distance in the right panel. Region A shows accretion in measurements and computations, Region B has a huge erosion. Region C is the area where the spit welds to the coast and then spreads North. In region D the lagoon that is formed by this welding is seen. Region E includes the original lake that does not move much. The rms error between measured and computed coastlines at this time is 42 m, whereas the rms difference between the initial and measured profiles at the same time is 144 m. In **Figure 13** the development of the errors in time is visualized, showing that the error between observations and computation increases slowly in time, whereas the observed change keeps increasing; hence, the skill, as represented by the Brier Skill Score (BSS) commonly used to assess morphological model results, increases from 0.22 in the first half year to 0.65–0.7 and remains relatively constant. The relatively low skill in the beginning is due to a combination of the occurrence of a very stormy season and a low signal to noise ratio. According to the classification given by Sutherland et al. (2004) the skill develops from *good* (0.2–0.5) to *excellent* (0.5–1.0).

Application at Al-Gamil Beach, Port Said, Egypt

The main aim of this application is to validate the model in simulating shoreline response within a groin field where sand nourishment with different nourishment rates has been placed along the groin field. Moreover, it is aimed to evaluate the effect of the sand bypassing introduced through the new treatment of the groins, as discussed in Section "Treatment of Groins" and (Ghonim, 2019) in obtaining more realistic results. Data for this case were obtained from the Egyptian Shore Protection Authority through personal communication.

Background

Port Said is a coastal city located in the North-East of Egypt and stretches about 30 km along the Mediterranean Sea. **Supplementary Figure SI09** shows the study area which is located west of the city and lies between (31°16′52.6″N, 32°14′48.43″E) and (31°16′33.31″N, 32°17′05.96″E). The existence of a tidal inlet in the west of the area causes imbalances in the longshore sediment distribution as it works as a sink, where the longshore drift tends to be deposited inside the inlet. This has caused erosion problems in the study area which is located downdrift of the tidal inlet, given that waves are dominantly approaching the coast from the North-west direction. A groin field that consists of 14 groins with different lengths varying from 80 to 50 m, and constant spacing of 170 m was constructed from 2010 to 2011 to minimize the erosion in that area. Moreover, a sand nourishment of around 125,000 m^3 was placed in the spaces in between the western 6 groins, while approximately 75,000 [m3] of sand was nourished in the areas in between the remaining groins since they are shorter, so as to accelerate the effectiveness of the groin field in countering erosion. In addition, 800 m along the downdrift side of the groin field were nourished with around 280,000 m^3 of sand to compensate for the shortage of sediment there and to let the sand move naturally along the coastline. The

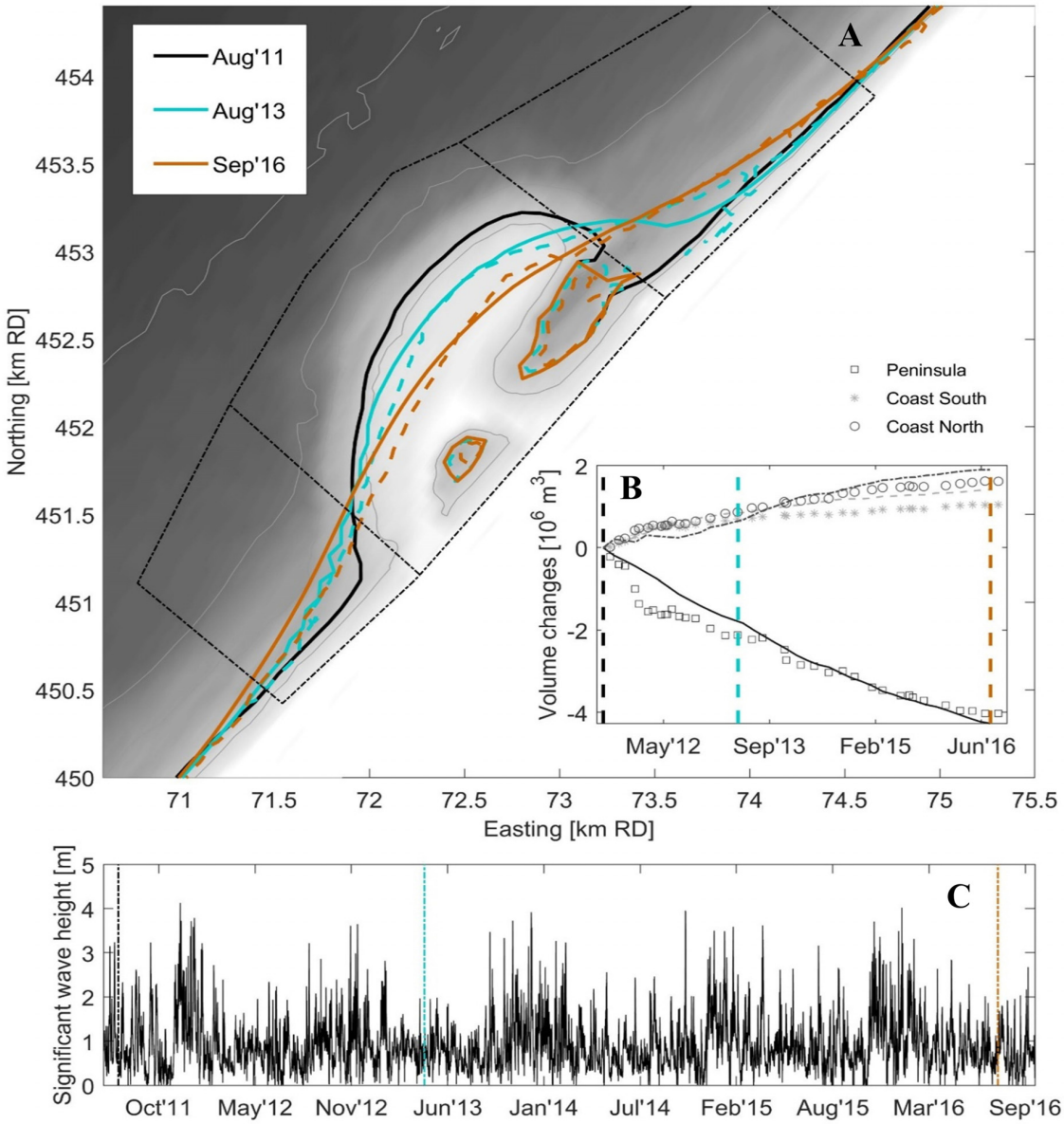

FIGURE 11 | (A) Observed and simulated evolution of the Sand Engine using ShorelineS; Color-coded lines are coastlines extracted from repeat topo-bathymetry surveys (drawn lines) and from calculations (dashed lines) for 2011 (initial), 2013 and 2016. **(B)** Observed and computed volume change for the areas indicated by the black dash-dot lines. **(C)** Time series of actual significant wave height.

nourishment work started just after the construction of the groin field and took six months to be completed.

Wave Climate and Historical Shoreline

The historical satellite images in Google Earth Engine were used to manually extract the groin field location and shoreline locations in 2011 and 2018 in World Geodetic System (WGS) 84; then, all coordinates were converted to Universal Transverse Mercator (UTM) coordinates. The wave climate of the ERA5 reanalysis with 0.25° × 0.25° resolution, produced by the European Centre for Medium-Range Weather Forecasts (ECMWF) was used to extract wave climate during the simulation period at a location 1 km offshore of the study area. The wave climate was schematized to 50 wave directions and their representative heights using the same method as for the Sand Engine case; the resulting distribution is shown in **Supplementary Figure SI10**, showing a dominance of wave directions from the North-west.

Model Setup

The initial coastline in 2012 and the groin field were introduced as land boundaries in UTM coordinates. The partial bypassing approach according to Larson et al. (1997) was used in this application as it gives a better representation of the real bypassing

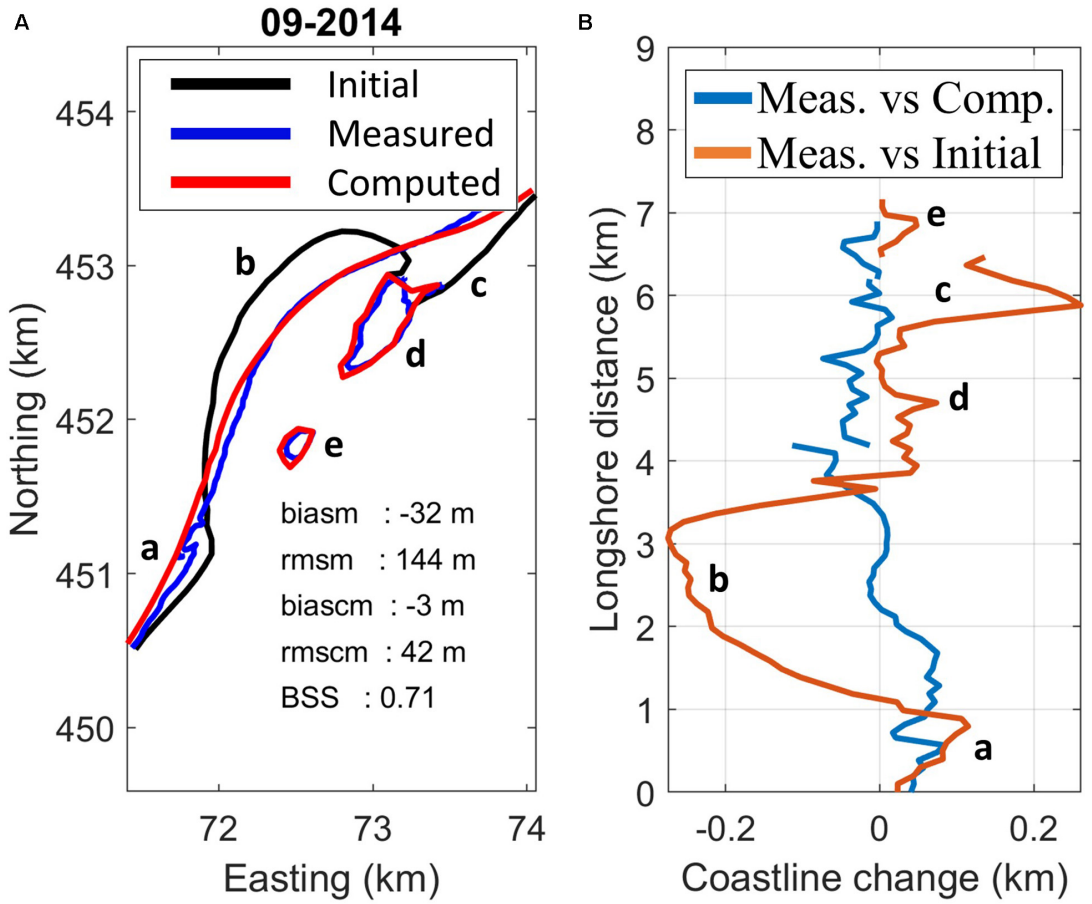

FIGURE 12 | Initial (2011), measured (meas.) and computed (comp.) coast lines after 3 years **(A)**; coastline change vs alongshore distance: measured vs computed, and measured vs. initial **(B)** Letters in both panels indicate the corresponding areas.

around groins. The model estimates the bypassing factor, *BPF*, based on the water depth at the tip of each groin D_s (Eq. 13) and the depth of the active longshore transport D_{LT} (Eq. 12). The median grain size D_{50} is 0.20 mm as the Port Said coast is characterized by fine sand. The sand nourishment was introduced in the model as nourishment rates with start and finish dates, based on the applied nourishment volumes and the active profile height. An initial grid size of 25 m was chosen. Since the sand nourishment was introduced in the model within the first six months of the simulation, the nourishment rates were set to zero from the first of July 2012 until the end of the simulation. The nourishment volumes were 125,000 m^3, 75,000 m^3, and 280,000 m^3 in between the western six groins, in between the remaining groins and along the area downdrift of the groin field, respectively. The width of the nourishment area in between the groins was set to 170 m representing the constant spacing between the groins, and 800 m for the area downdrift the groin field. The active profile height is the beach berm height plus the closure depth, D_c, which is equal to approximately $9H_s$ where H_s is the mean annual significant wave height (m). The period of the nourishment process was set to six months. The wave climate is discretized based on a probability distribution of 50 wave direction bins, each with equal total energy flux and one wave height class per direction as seen in **Supplementary Figure SI10**, At each time step, a wave condition was selected randomly from this distribution and the transport was estimated using the CERC1 formulation. The beach profile was estimated using a Dean (1991) profile, and the depth of active longshore transport is estimated every time step according to the wave height (Eq. 12). The partial bypassing method was chosen since the depth of active longshore transport frequently exceeded the estimated depth at the tip of the groins.

Model Results

The model results at the end of the simulation (2018) are shown in **Figure 14**. The figure also indicates the shoreline location extracted from the historical satellite images in Google Earth Engine in 2011 and 2018.

Figure 14 indicates that the model has produced satisfactory results compared to reality, although the diffraction phenomena behind the structures were not taken into account, leading to local errors just in the lee of each groin. The advancement of the coastline and the increase of the bypassing factor, *BPF*, were high during the first six months due to the high nourishment

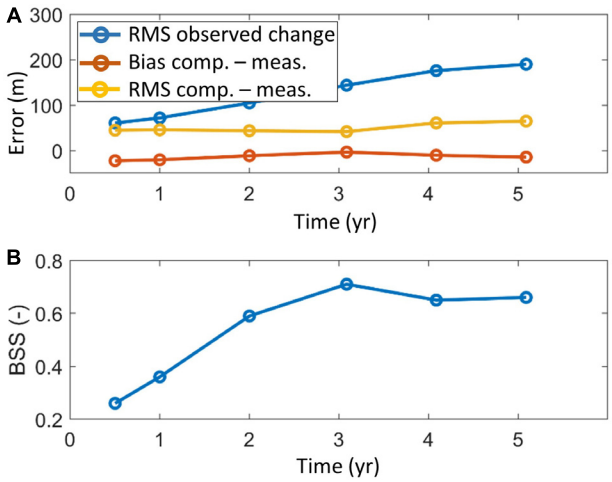

FIGURE 13 | Bias between computed and measured coastlines, rms observed change and rms error vs time **(A)**; Brier Skill Score (BSS) vs. time **(B)**.

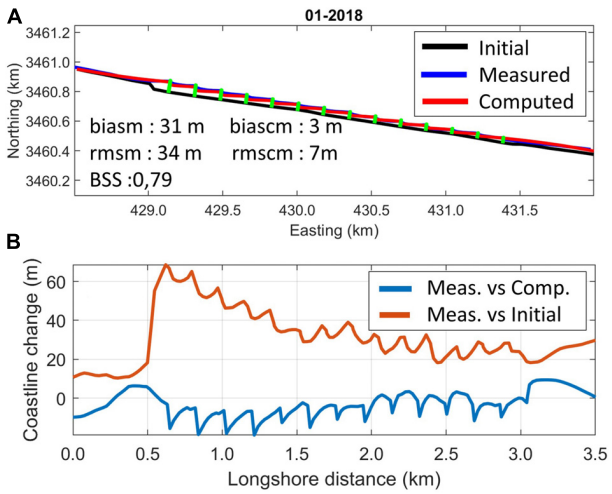

FIGURE 14 | Measured (meas.) and computed (comp.) coastline evolution 2011-2018, Al-Gamil **(A)**; observed change and difference between measurements and model results **(B)**.

rates. Then, the nourishment was stopped and the coastline kept advancing due to the longshore transport and the bypassed sediment. Furthermore, the coastline reached a stable state at the tips of the groins where the maximum bypassing factor, *BPF*, was achieved, proving the validity of the model in representing the effect of bypassing in stabilizing the coastline.

Similar error statistics as for the Sand Engine case were computed, with a small bias and rms error of 3 m and 7 m, respectively, between measured values and model results, compared to rms of measured changes of 34 m. The model performed in the category *excellent*, with a BSS of 0.79.

DISCUSSION

The flexible grid in the ShorelineS model allows for the evaluation of coastline changes for a wide range of applications that are not covered in most existing models, such as complex spit development and merging islands. At the same time, the standard cases with mildly curved coastlines are dealt with successfully. The model is extremely easy to run, as it merely requires initial coastline polylines, polylines of hard structures, offshore wave data and some parameter settings. These data are generally readily available through satellite imagery and global or regional wave hindcasts, or local wave data.

A first validation with a complex real-world case (the Sand Engine; de Schipper et al., 2016) shows that the methodology has the potential to be used as an efficient engineering tool, accurately reproducing the average erosion of the peninsula over time. The initial deformation of the spit and welding to the coast is impossible to simulate with standard coastline models, and the detailed 2DH morphodynamic models that can, in principle, describe this take several orders of magnitude more computation time (months vs. tens of minutes). Also the accretion on both sides of the harbor of IJmuiden, as described in Roelvink and Reniers (2011), is readily reproduced. Apparently, the shielding of waves at the structures is already sufficient to reproduce the local coastline orientation. The case of Al Gamil, Egypt also shows that the effect of local structures such as the groin scheme implemented there, in combination with nourishments, can be simulated with excellent skill, when a realistic bypassing function is applied.

The active profile depth is typically fixed in coastline models such as ShorelineS, but may, in practice, vary spatially and temporally depending on the wave conditions and the pre-existing bathymetry. The current approach is considered suitable for coastlines with rather uniform profiles (with similar orientation toward the sea), which is often the case for a shelf sea coast (e.g., in the Netherlands or Gulf countries). The Sand Engine case could, for example, be modeled well with just a single active height despite being a complex landform with slightly different conditions acting at the seaward extending head and lateral sides. However, the antecedent bathymetry may play a large role for landward propagating coastal barriers or spits over low-lying marshes or lagoons, where the seaward side is much more exposed to waves than the landward side, which is much shallower. Consequently, the landward retreat of spits due to overwash may be less than computed by the model, taking into account that less sand is needed on the landward side to build the profile. A more precise definition of the active heights based on global and local resources would, therefore, be very desirable for such situations to precisely assess these changes at landward propagating coastal barriers or spits over low-lying marshes or lagoons.

In sediment-starved nearshore regions, the actual alongshore sediment transport is smaller than the potential transport, which eventually affects the alongshore gradient and corresponding morphological change, as shown by Payo et al. (2018). In our model such processes are not yet represented.

An easy step to take into account variations in wave height and direction due to refraction over uneven offshore bathymetry is to create a transformation table from offshore to nearshore wave conditions along a depth contour or on a large-scale grid, from which ShorelineS can interpolate the alongshore-varying wave direction and height. Such applications are already applied in practice and ShorelineS supports this through the use of a fast 2D wave refraction solver. Steps further are to feed back the shoreline changes into the bathymetry used in the wave model, as e.g., in Robinet et al. (2018), or to even consider emerged, un-erodible layers due to geological formations, which may potentially be buried by sand but may have a significant influence on shoreline evolution, as in Robinet et al. (2020).

The flexible grid is essential for unconstrained modeling of strongly curved local coastline features such as salients and tombolos at offshore breakwater schemes. Many methods are available to estimate the effect of diffraction and refraction behind offshore breakwaters and other hard structures or headlands (Wiegel, 1962; Goda et al., 1978; Dabees, 2000), which can, in combination with the flexible grid of ShorelineS, be used to quickly and accurately evaluate the morphological development of salients or tombolos behind structures. This will be a great step forward since the existing reduced complexity coastline models on the other hand suffer from the requirement that a reference position of the grid should be provided (Hsu et al., 2010; Ruggiero and Buijsman, 2010) which cannot follow the considerable changes in coastline curvature that may take place when a tombolo develops. Even the complex field models solving these features on a map often need very dense grids or require rather elaborate wave modeling, such as Boussinesq wave modeling (Karambas and Samaras, 2014), thus slowing down simulations considerably. These models often have difficulties in assessing the precise position of the waterline as a natural profile shape is difficult to maintain (Grunnet et al., 2004; van Duin et al., 2004). First steps to include diffraction in ShorelineS were taken in Elghandour (2018) and full implementation and validation will be described in an upcoming paper.

The current approach used in the ShorelineS model assumes a static profile which can move in the cross-shore direction depending on incoming sand supply and the defined active height. In practice this works well for most engineering problems, which are dominated by the alongshore wave-driven transport and act at a yearly time scale. Over longer time-frames the smaller but consistently present cross-shore losses play an increasingly important role as was shown by Vitousek et al. (2017) for the erosion at the Pacific Coast of California. In their study they estimated that sea level rise will contribute 69% of the losses over the period 2010 to 2100, while it contributes only 1% over the hindcast period from 1995 to 2010. Approaches to account for sea-level rise (e.g., effect, barrier rollover and basin infilling) will be needed to further enhance the capabilities of ShorelineS on longer time horizons. In addition, it is considered relevant to also include seasonal changes due to wave energy variations (Yates et al., 2009) to keep track of a set of cross-shore profile positions (Larson et al., 2016). It will then be possible to also assess seasonal variations in beach position and potential retreat rates for extreme situations (Ranasinghe et al., 2012). Ensemble forecasts can then be made with the relatively swift ShorelineS model to assess a number of realizations of the future coastline position accounting for variations in initial and boundary conditions as well as uncertainty in model parameters. The potential for such approaches was recently shown by Montaño et al. (2020) in a unique comparison of a number of mostly equilibrium-type cross-shore models and data-driven models against a 15-year calibration dataset followed by a blind 3-year 'shorecast.'

The relatively straightforward model input of the ShorelineS model provides a unique opportunity to automatically process large data sets of remotely sensed coastal information, as the precise definition of the coastal reference lines does not affect the forecasts. Satellite derived time-series of shoreline positions (Luijendijk et al., 2018) may be derived at intervals of days to a few months (depending on the number of cloudy days) with sub-pixel accuracy. This provides a basis for calibration and validation of coastline models, which continuously improve the predictions through data-assimilation.

Coastline models are typically not suitable for the details of the rather complex three-dimensional (3D) bathymetries in the vicinity of tidal inlets, but as an outlook to the future it is envisioned that 2DH bathymetry can be coupled to the ShorelineS model for which computations of tide and waves can be performed with a numerical model. A two-way coupling between the coastline and a relatively coarse hydraulic 2DH model such as Delft3D (Lesser et al., 2004), can already provide very accurate morphological computations solving the tidal currents, without the need of placing very detailed grid cells in the 2DH model as the transport processes close to the coast are solved within ShorelineS. Changes in coastline position feed back into the 2DH model bathymetry by assuming a cross-shore profile shape. Such developments are also considered essential for long-term computations of coastline development to assess the effects of climate change or geological reconstructions of coasts and deltas, since the computational power of present-day computers is hardly sufficient to solve the effects of longshore currents at large coastal sections ($>$ 100 km) over yearly time scales. As such, the potential of ShorelineS to be easily coupled to more complex field models with relatively coarse grids is a necessity for answering future questions related to sea level rise at century time scales.

Another, much less cumbersome method to treat the behavior of river mouths and tidal inlets through simple algorithms that keep a mouth open at a specified width depending on the discharge, redistribute sediment locally or add the sediment discharge of the river to the adjacent coastal areas. Such approaches have recently been tested and will be the subject of upcoming papers.

CONCLUSION

The development of a new coastline model is described and the model was applied to a number of theoretical and field cases, showing the value of the application of a flexible grid. The test cases show that the model can represent the physics of both low and high-angle wave incidence coasts with simple

structures. Quantitatively the model can accurately hindcast the erosion of a large-scale temporary land reclamation (Sand Engine), providing confidence that not only the patterns but also the spatial distribution of changes can be predicted, with only a single transport coefficient as a calibration parameter. The Brier Skill Score (BSS) increases with time from 0.22 shortly after construction to around 0.7 after a few years. A second validation case describing a groin scheme in Egypt show similar skill when an appropriate groin bypassing function is applied. As such the model is very capable of resolving coastline changes at intermediate time scales (years) for rather alongshore uniform coasts or coasts with spit features. Still, a number of relevant aspects could be improved that are likely to affect performance of the model at short (days to months) and long (decades to centuries) timescales, such as the inclusion of small but consistent losses due to sea level rise (e.g., profile adaptation and ingress of sediment in tidal basins) and a potential retreat due to storms for statistical analyses of coastal safety.

In general, a large number of coastal issues can be solved with the ShorelineS model thanks to the flexible grid, which will allow its application to coasts with large changes in shape such as present at local salient and tombolo developments. Even the migration of barrier islands and tidal inlets is expected to be possible in the near future when ShorelineS is coupled with relatively simple 2DH models (e.g., Delft3D, XBeach) that provide nearshore source/sink terms while ShorelineS updates the 2D bathymetric changes. Development is continuing on a number of issues as previously outlined.

DATA AVAILABILITY STATEMENT

Publicly available datasets were analyzed in this study. This data can be found here: https://data.4tu.nl/repository/collection: zandmotor. Matlab source code for the ShorelineS model is available at www.shorelines.nl.

AUTHOR CONTRIBUTIONS

DR developed the original code, carried out the principle tests, supervised AE and MG and is lead author. BH improved the code structure, implemented different transport formulations, developed the Sand Engine test case and contributed to the manuscript. AE carried out validation tests, solved a number of issues with the code and contributed to the manuscript writing. MG improved the treatment of groins and carried out the Al Gamil field test. JR co-supervised AE and MG and contributed to the model code and manuscript. All authors contributed to the article and approved the submitted version.

FUNDING

AE was funded by Portuguese Science Foundation (FCT) through project: ALG-01-0145-FEDER913 28949 "ENLACE". BH contributed in the framework of Deltares Strategic Research.

SUPPLEMENTARY MATERIAL

The Supplementary Material for this article can be found online at: https://www.frontiersin.org/articles/10.3389/fmars.2020.00535/full#supplementary-material

REFERENCES

Antolínez, J. A. A., Méndez, F. J., Anderson, D., Ruggiero, P., and Kaminsky, G. M. (2019). Predicting climate-driven coastlines with a simple and efficient multiscale model. *J. Geophys. Res.* 124, 1596–1624. doi: 10.1029/2018JF004790

Arriaga, J., Rutten, J., Ribas, F., Falqués, A., and Ruessink, G. (2017). Modeling the long-term diffusion and feeding capability of a mega-nourishment. *Coast. Eng.* 121, 1–13. doi: 10.1016/J.COASTALENG.2016.11.011

Ashton, A. D., and Murray, A. B. (2006). High-angle wave instability and emergent shoreline shapes: 1. Modeling of sand waves, flying spits, and capes. *J. Geophys. Res. Earth Surf.* 111, 1–19. doi: 10.1029/2005JF000422

Ashton, A. D., Murray, A. B., and Arnoult, O. (2001). Formation of coastline features by large-scale instabilities induced by high-angle waves. *Nature* 414, 296–300. doi: 10.1038/415666a

Ashton, A. D., Nienhuis, J., and Ells, K. (2016). On a neck, on a spit: controls on the shape of free spits. *Earth Surf. Dyn.* 4, 193–210. doi: 10.5194/esurf-4-193-2016

Barbier, E. B., Hacker, S. D., Kennedy, C., Koch, E. W., Stier, A. C., and Silliman, B. R. (2011). The value of estuarine and coastal ecosystem services. *Ecol. Monogr.* 81, 169–193. doi: 10.1890/10-1510.1

Bijker, E. W. (1967). *Some Considerations About Scales for Coastal Models with Movable Bed. Publication No. 50*. Delft: Delft Hydraulics Laboratory.

Bruun, P. (1962). Sea level rise as a cause of shore erosion. *J. Waterways Harb. Divis.* 88, 117–132.

Dabees, M. (2000). *Efficient Modeling of Beach Evolution*. Ph.D. Thesis, Queen's University, Kingston.

de Schipper, M. A., de Vries, S., Ruessink, G., de Zeeuw, R. C., Rutten, J., van Gelder-Maas, C., et al. (2016). Initial spreading of a mega feeder nourishment: observations of the Sand Engine pilot project. *Coast. Eng.* 111, 23–38. doi: 10.1016/J.COASTALENG.2015.10.011

Dean, R. G. (1991). Equilibrium beach profiles: characteristics and applications. *J. Coast. Res.* 7, 53–84.

Elfrink, B., Prestedge, G., Rocha, C. B. M., and Juhl, J. (2003). "Shoreline evolution due to highly oblique incident waves at Walvis Bay, Namibia," in *Proceeding International Conference on Coastal Sediments 2003*, (Clearwater Beach, FL: U. S. World Scientific).

Elghandour, A. M. (2018). *Efficient Modelling of coastal evolution Development, verification and validation of ShorelineS Model*. Delft: IHE Delft Insitute for Water Education.

Falqués, A., and Calvete, D. (2005). Large-scale dynamics of sandy coastlines: diffusivity and instability. *J. Geophys. Res. Oceans* 110, 1–15. doi: 10.1029/2004JC002587

Falqués, A., Ribas, F., Idier, D., and Arriaga, J. (2017). Formation mechanisms for self-organized kilometer-scale shoreline sand waves. *J. Geophys. Res. Earth Surf.* 122, 1121–1138. doi: 10.1002/2016JF003964

Ghonim, M. E. (2019). *Recent Developments in Numerical Modelling of Coastline Evolution Advanced Development and Evaluation of ShorelineS Coastline Model*. Delft: IHE Delft Institute for Water Education.

Goda, Y., Takayama, T., and Suzuki, Y. (1978). "Diffraction diagrams for directional random waves," in *Proceedings of the Coastal Engineering 1978* (New York, NY: American Society of Civil Engineers), 628–650.

Grunnet, N. M., Walstra, D.-J. R., and Ruessink, B. G. (2004). Process-based modelling of a shoreface nourishment. *Coast. Eng.* 51, 581–607. doi: 10.1016/J.COASTALENG.2004.07.016

Hanson, H. (1989). Genesis: a generalized shoreline change numerical model. *J. Coast. Res.* 5, 1–27.

Hanson, H., and Kraus, N. C. (2011). Long-term evolution of a long-term evolution model. *J. Coast. Res.* 59, 118–129. doi: 10.2112/SI59-012.1

Hsu, J. R.-C., Yu, M.-J., Lee, F.-C., and Benedet, L. (2010). Static bay beach concept for scientists and engineers: a review. *Coast. Eng.* 57, 76–91. doi: 10.1016/J.COASTALENG.2009.09.004

Huisman, B. J. A., Ruessink, B. G., de Schipper, M. A., Luijendijk, A. P., and Stive, M. J. F. (2018). Modelling of bed sediment composition changes at the lower shoreface of the Sand Motor. *Coast. Eng.* 132, 33–49. doi: 10.1016/J.COASTALENG.2017.11.007

Hurst, M. D., Barkwith, A., Ellis, M. A., Thomas, C. W., and Murray, A. B. (2015). Exploring the sensitivities of crenulate bay shorelines to wave climates using a new vector-based one-line model. *J. Geophys. Res. F Earth Surf.* 120, 2586–2608. doi: 10.1002/2015JF003704

Idier, D., Falqués, A., Ruessink, B. G., and Garnier, R. (2011). Shoreline instability under low-angle wave incidence. *J. Geophys. Res. Earth Surf.* 116:F04031. doi: 10.1029/2010JF001894

Kaergaard, K., and Fredsoe, J. (2013a). A numerical shoreline model for shorelines with large curvature. *Coast. Eng.* 74, 19–32. doi: 10.1016/j.coastaleng.2012.11.011

Kaergaard, K., and Fredsoe, J. (2013b). Numerical modeling of shoreline undulations part 2: varying wave climate and comparison with observations. *Coast. Eng.* 75, 77–90. doi: 10.1016/j.coastaleng.2012.11.003

Kamphuis, J. W. (1991). Alongshore sediment transport rate. *J. Waterway PortCoast. Ocean Eng.* 117, 624–640. doi: 10.1061/(asce)0733-950x(1991)117:6(624)

Karambas, T. V., and Samaras, A. G. (2014). Soft shore protection methods: the use of advanced numerical models in the evaluation of beach nourishment. *Ocean Eng.* 92, 129–136. doi: 10.1016/J.OCEANENG.2014.09.043

Kristensen, S. E., Drønen, N., Deigaard, R., and Fredsoe, J. (2016). Impact of groyne fields on the littoral drift: a hybrid morphological modelling study. *Coast. Eng.* 111, 13–22. doi: 10.1016/j.coastaleng.2016.01.009

Larson, M., Hanson, H., and Kraus, N. C. (1987). *Analytical Solutions of the On-line Model of Shoreline Change*. Reston: ASCE.

Larson, M., Hanson, H., and Kraus, N. C. (1997). Analytical solutions of one-line model for shoreline change near coastal structures. *J. Waterway Port Coast. Ocean Eng.* 123, 180–191. doi: 10.1061/(asce)0733-950x(1997)123:4(180)

Larson, M., Palalane, J., Fredriksson, C., and Hanson, H. (2016). Simulating cross-shore material exchange at decadal scale. Theory and model component validation. *Coast. Eng.* 116, 57–66. doi: 10.1016/J.COASTALENG.2016.05.009

Leatherman, S. P. (1979). Migration of Assateague Island, Maryland, by inlet and overwash processes. *Geology* 7, 104–107.

Lesser, G. R., Roelvink, J. A., van Kester, J. A. T. M., and Stelling, G. S. (2004). Development and validation of a three-dimensional morphological model. *Coast. Eng.* 51, 883–915. doi: 10.1016/j.coastaleng.2004.07.014

Luijendijk, A. P., Hagenaars, G., Ranasinghe, R., Baart, F., Donchyts, G., and Aarninkhof, S. (2018). The state of the world's beaches. *Sci. Rep.* 8:6641. doi: 10.1038/s41598-018-24630-6

Luijendijk, A. P., Ranasinghe, R., de Schipper, M. A., Huisman, B. A., Swinkels, C. M., Walstra, D. J. R., et al. (2017). The initial morphological response of the Sand Engine: a process-based modelling study. *Coast. Eng.* 119, 1–14. doi: 10.1016/J.COASTALENG.2016.09.005

Montaño, J., Coco, G., Antolínez, J. A. A., Beuzen, T., Bryan, K. R., Cagigal, L., et al. (2020). Blind testing of shoreline evolution models. *Sci. Rep.* 10, 1–10. doi: 10.1038/s41598-020-59018-y

Palalane, J., and Larson, M. (2020). A long-term coastal evolution model with longshore and cross-shore transport. *J. Coast. Res.* 36, 411–423. doi: 10.2112/JCOASTRES-D-17-00020.1

Payo, A., Favis-Mortlock, D., Dickson, M., Hall, J. W., Hurst, M. D., Walkden, M. J. A., et al. (2017). Coastal Modelling Environment version 1.0: a framework for integrating landform-specific component models in order to simulate decadal to centennial morphological changes on complex coasts. *Geosci. Model Dev.* 10, 2715–2740. doi: 10.5194/gmd-10-2715-2017

Payo, A., Walkden, M., Ellis, M. A., Barkwith, A., Favis-Mortlock, D., Kessler, H., et al. (2018). A quantitative assessment of the annual contribution of platform downwearing to beach sediment budget: Happisburgh, England, UK. *J. Mar. Sci. Eng.* 6:113. doi: 10.3390/jmse6040113

Pelnard-Considère, R. (1956). Essai de theorie de l'evolution des formes de rivage en plages de sable et de galets. *Les Energies de La Mer* 1, 13–15.

Ranasinghe, R., Callaghan, D., and Stive, M. J. F. (2012). Estimating coastal recession due to sea level rise: beyond the Bruun rule. *Clim. Change* 110, 561–574. doi: 10.1007/s10584-011-0107-8

Ranasinghe, R., Duong, T. M., Uhlenbrook, S., Roelvink, D., and Stive, M. (2013). Climate-change impact assessment for inlet-interrupted coastlines. *Nat. Clim. Change* 3, 83–87. doi: 10.1038/nclimate1664

Robinet, A., Castelle, B., Idier, D., Harley, M. D., and Splinter, K. D. (2020). Controls of local geology and cross-shore/longshore processes on embayed beach shoreline variability. *Mar. Geol.* 422:106118. doi: 10.1016/j.margeo.2020.106118

Robinet, A., Idier, D., Castelle, B., and Marieu, V. (2018). A reduced-complexity shoreline change model combining longshore and cross-shore processes: the LX-Shore model. *Environ. Model. Softw.* 109, 1–16. doi: 10.1016/j.envsoft.2018.08.010

Roelvink, D., and Reniers, A. (2011). *A Guide to Modeling Coastal Morphology*. Singapore: World Scientific.

Ruggiero, P., and Buijsman, M. (2010). Modeling the effects of wave climate and sediment supply variability on large-scale shoreline change. *Mar. Geol.* 273, 127–140. doi: 10.1016/J.MARGEO.2010.02.008

Stive, M. J. F., de Schipper, F., Matthieu, A., Luijendijk, A. P., Aarninkhof, S. G. J., van Gelder-Maas, C., et al. (2013). A new alternative to saving our beaches from sea-level rise: the sand engine. *J. Coast. Res.* 29, 1001–1008. doi: 10.2112/JCOASTRES-D-13-00070.1

Sutherland, J., Peet, A. H., and Soulsby, R. L. (2004). Evaluating the performance of morphological models. *Coast. Eng.* 51, 917–939. doi: 10.1016/j.coastaleng.2004.07.015

Syvitski, J. P. M., Vörösmarty, C. J., Kettner, A. J., and Green, P. (2005). Impact of humans on the flux of terrestrial sediment to the global coastal ocean. *Science* 308, 376–380. doi: 10.1126/science.1109454

Tonnon, P. K., Huisman, B. J. A., Stam, G. N., and van Rijn, L. C. (2018). Numerical modelling of erosion rates, life span and maintenance volumes of mega nourishments. *Coast. Eng.* 131, 51–69. doi: 10.1016/J.COASTALENG.2017.10.001

Tran, Y. H., and Barthélemy, E. (2020). Combined longshore and cross-shore shoreline model for closed embayed beaches. *Coast. Eng.* 158:103692. doi: 10.1016/j.coastaleng.2020.103692

USACE (1984). *Shore Protection Manual. Coastal Engineering Research Center (Vol. 1)*. Washington, DC: US Army Corps of Engineers.

van den Berg, N., Falqués, A., and Ribas, F. (2011). Long-term evolution of nourished beaches under high angle wave conditions. *J. Mar. Syst.* 88, 102–112. doi: 10.1016/J.JMARSYS.2011.02.018

van Duin, M. J. P., Wiersma, N. R., Walstra, D. J. R., van Rijn, L. C., and Stive, M. J. F. (2004). Nourishing the shoreface: observations and hindcasting of the Egmond case, The Netherlands. *Coast. Eng.* 51, 813–837. doi: 10.1016/J.COASTALENG.2004.07.011

van Rijn, L. C. (1998). *Principles of Coastal Morphology*. Amsterdam: Aqua Publications.

van Rijn, L. C. (2014). A simple general expression for longshore transport of sand, gravel and shingle. *Coast. Eng.* 90, 23–39. doi: 10.1016/j.coastaleng.2014.04.008

Vitousek, S., and Barnard, P. L. (2015). "A nonlinear, implicit one-line model to predict long-term shoreline change," in *Proceedings of the Coastal Sediments 2015*, (Singapore: World Scientific).

Vitousek, S., Barnard, P. L., Limber, P., Erikson, L., and Cole, B. (2017). A model integrating longshore and cross-shore processes for predicting long-term shoreline response to climate change. *J. Geophys. Res. Earth Surf.* 122, 782–806. doi: 10.1002/2016JF004065

Wiegel, R. L. (1962). Diffraction of waves by semi-infinite breakwater. *J. Hydraulics Divis. ASCE* 88, 27–44.

Yates, M. L., Guza, R. T., and O'Reilly, W. C. (2009). Equilibrium shoreline response: observations and modeling. *J. Geophys. Res. Oceans* 114:C09014. doi: 10.1029/2009JC005359

Conflict of Interest: The authors declare that the research was conducted in the absence of any commercial or financial relationships that could be construed as a potential conflict of interest.

frontiers in Marine Science

ORIGINAL RESEARCH
published: 10 July 2020
doi: 10.3389/fmars.2020.00542

A Holistic Modeling Approach to Project the Evolution of Inlet-Interrupted Coastlines Over the 21st Century

Janaka Bamunawala[1,2], Ali Dastgheib[2], Roshanka Ranasinghe[1,2,3], Ad van der Spek[4,5], Shreedhar Maskey[2], A. Brad Murray[6], Trang Minh Duong[1,2,3], Patrick L. Barnard[7] and T. A. J. G. Sirisena[1,2]*

[1] Department of Water Engineering and Management, University of Twente, Enschede, Netherlands, [2] IHE Delft Institute for Water Education, Delft, Netherlands, [3] Harbour, Coastal and Offshore Engineering, Deltares, Delft, Netherlands, [4] Applied Morphodynamics, Deltares, Delft, Netherlands, [5] Department of Physical Geography, Faculty of Geosciences, Utrecht University, Utrecht, Netherlands, [6] Division of Earth and Ocean Sciences, Nicholas School of the Environment, Center for Non-linear and Complex Systems, Duke University, Durham, NC, United States, [7] United States Geological Survey, Pacific Coastal and Marine Science Center, Santa Cruz, CA, United States

OPEN ACCESS

Edited by:
Zeng Zhou,
College of Harbour, Coastal and Offshore Engineering, Hohai University, China

Reviewed by:
Ian Townend,
University of Southampton, United Kingdom
Maitane Olabarrieta,
University of Florida, United States

***Correspondence:**
Janaka Bamunawala
j.bamunawala@un-ihe.org

Specialty section:
This article was submitted to Coastal Ocean Processes, a section of the journal Frontiers in Marine Science

Received: 02 April 2020
Accepted: 15 June 2020
Published: 10 July 2020

Citation:
Bamunawala J, Dastgheib A, Ranasinghe R, van der Spek A, Maskey S, Murray AB, Duong TM, Barnard PL and Sirisena TAJG (2020) A Holistic Modeling Approach to Project the Evolution of Inlet-Interrupted Coastlines Over the 21st Century. Front. Mar. Sci. 7:542. doi: 10.3389/fmars.2020.00542

Approximately one-quarter of the World's sandy beaches, most of which are interrupted by tidal inlets, are eroding. Understanding the long-term (50–100 year) evolution of inlet-interrupted coasts in a changing climate is, therefore of great importance for coastal zone planners and managers. This study, therefore, focuses on the development and piloting of an innovative model that can simulate the climate-change driven evolution of inlet-interrupted coasts at 50–100 year time scales, while taking into account the contributions from catchment-estuary-coastal systems in a holistic manner. In this new model, the evolution of inlet-interrupted coasts is determined by: (1) computing the variation of total sediment volume exchange between the inlet-estuary system and its adjacent coast, and (2) distributing the computed sediment volume along the inlet-interrupted coast as a spatially and temporally varying quantity. The exchange volume, as computed here, consists of three major components: variation in fluvial sediment supply, basin (or estuarine) infilling due to the sea-level rise-induced increase in accommodation space, and estuarine sediment volume change due to variations in river discharge. To pilot the model, it is here applied to three different catchment-estuary-coastal systems: the Alsea estuary (Oregon, United States), Dyfi estuary (Wales, United Kigdom), and Kalutara inlet (Sri Lanka). Results indicate that all three systems will experience sediment deficits by 2100 (i.e., sediment importing estuaries). However, processes and system characteristics governing the total sediment exchange volume, and thus coastline change, vary markedly among the systems due to differences in geomorphic settings and projected climatic conditions. These results underline the importance of accounting for the different governing processes when assessing the future evolution of inlet-interrupted coastlines.

Keywords: anthropogenic activities, climate change, coastline change, numerical modeling, tidal inlets

INTRODUCTION

Open sandy coasts are complex coastal systems that are continually changing under the influence of both natural and anthropogenic drivers (Stive, 2004; Ranasinghe et al., 2013; Ranasinghe, 2016; Anthony et al., 2015; Besset et al., 2019). The majority of the world's sandy coasts are interrupted by inlets (Aubrey and Weishar, 1988; Davis and Fitzgerald, 2003; Woodroffe, 2003; FitzGerald et al., 2015; Duong et al., 2016; McSweeney et al., 2017). Both oceanic and terrestrial processes contribute to the long term (50–100 year) evolution of these inlet-interrupted coasts (Stive et al., 1998; Stive and Wang, 2003; Ranasinghe et al., 2013). Moreover, future changes in temperature and precipitation due to climate change, and anthropogenic activities at catchment scale can alter the fluvial sediment supply to the coast, which in turn will affect the evolution of inlet-adjacent coastlines. While being spatio-temporally dynamic due to their sensitivity to both oceanic and terrestrial processes, inlet-interrupted coasts are also highly utilized, often containing public and private property, roads, bridges, and ports and marinas (McGranahan et al., 2007; Wong et al., 2014; Neumann et al., 2015). Significant changes in coastline position at these systems are therefore likely to lead to severe socio-economic impacts. To avoid such impacts and associated losses, a good understanding, and the ability to reliably predict the long-term evolution of inlet-interrupted coasts is of great importance for coastal zone planners and managers.

The key oceanic processes that may affect inlet-interrupted coasts include mean sea-level change, tides and waves, and longshore sediment transport (Hayes, 1980; Davis and Fox, 1981; Davis and Hayes, 1984; Davis, 1989; Davis and Barnard, 2000, 2003), while the key terrestrial processes that may affect these coasts include river flow, fluvial sediment supply, land use/agricultural patterns, and land management (Cowell et al., 2003; Syvitski et al., 2009; Green, 2013). While the influence of oceanic processes on the evolution of inlet-interrupted coasts is well known and well accepted, the effect that terrestrial processes may have on coastal evolution is less well studied. Nevertheless, there are a number of studies that have investigated the evolution of delta systems while taking into account the changes in fluvial sediment supply (e.g., Ericson et al., 2006; Yang et al., 2006, 2018; Syvitski and Saito, 2007; Syvitski, 2008; Overeem and Syvitski, 2009; Syvitski et al., 2009; Barnard et al., 2012, 2013a,b; Anthony et al., 2013, 2015, 2019; Tessler et al., 2015; Szabo et al., 2016; Dunn et al., 2018, 2019).

Essentially, there are three major components to be considered in the source to sink sediment pathway from the catchment to the coast (**Figure 1**): (1) catchment-scale sediment production fed by weathering and soil erosion, (2) the transition zone characterized by fluvial sedimentation and reworking, and (3) the deposition and redistribution zone dominated by sediment exchange between the estuary and its adjacent coast. The long-term evolution of most inlet-interrupted coastlines is affected by processes that govern the behavior of all these zones making up the complete sediment pathway. However, it should also be noted that some inlet-interrupted coasts (e.g., estuary-inlet systems in the Southeast of the United States) are not affected by the fluvial sediment supply. Such systems are characterized by low fluvial sediment supply and contain small deltas at the heads of estuaries that sequester the coarse sediment delivered by rivers. In such systems, it is not necessary to consider the fluvial sediment delivery aspects to determine the long-term evolution of inlet-interrupted coasts.

Globally, rivers contribute about 95% of the sediment received by the oceans (Syvitski et al., 2003). Generation of this sediment starts in the mountains, where rocks weather into sediment through mechanical, chemical and biological processes (Syvitski and Milliman, 2007). Climate change is expected to result in increased temperatures (Stocker et al., 2013b), which will affect both chemical and mechanical weathering, thus increasing the rate of soil erosion at the catchment scale (Syvitski et al., 2003; Syvitski and Milliman, 2007). Future changes in precipitation will also affect the amount of soil eroded at catchment scale. The rate of sediment generation at catchment scale also depends on anthropogenic activities, such as land clearance for agriculture, urbanization, road construction and de-and re-forestation (Syvitski and Milliman, 2007; Syvitski et al., 2009; Overeem et al., 2013). All these climate-change impacts and anthropogenic activities will alter the magnitude of sediment production at catchment scale, which, in turn, will affect the sediment volume received by the coast.

Sediment generated in the catchment is transported to the coast by rivers. Climate-change driven variations in future precipitation will alter the river discharge, thus affecting the throughput of eroded soil material at catchment scale (Syvitski et al., 2003; Kettner et al., 2005; Shrestha et al., 2013). Anthropogenic activities, however, will exert significant influences on the ultimate fluvial sediment supply to the coast. Activities that reduce the fluvial sediment supply capacity include anthropogenic sediment retention by dams, river sand mining, reduction in sedimentation area due to levee/dyke construction, and reduction in river flow due to water withdrawal for irrigation/drinking water supply. On the other hand, activities such as increased surface runoff due to urbanization and deforestation would increase the fluvial sediment loads (Verstraeten and Poesen, 2001; Vörösmarty et al., 2003; Syvitski, 2005; Syvitski and Milliman, 2007; Syvitski and Saito, 2007; Slagel and Griggs, 2008; Syvitski et al., 2009; Walling, 2009; Overeem et al., 2013; Chu, 2014; Ranasinghe et al., 2019). In combination, these anthropogenic activities and climate-change driven impacts can change the total fluvial sediment throughput from the catchment to the coast.

The final segment of the sediment pathway from catchment to the coast is the deposition and redistribution of sediment within the estuary and the adjacent inlet-interrupted coast. The estuarine accommodation volume is affected by both the sediment input from the river and anthropogenic influences within the estuary, such as sand mining, construction of causeways, bridges, and finger canals (Davis and Barnard, 2000; Barnard and Kvitek, 2010; Dallas and Barnard, 2011). Climate-change induced sea-level rise will increase the accommodation space within the estuary. The net sediment volume imported or exported by the estuary is, therefore, a direct function of the relative magnitudes of the sediment demand from the

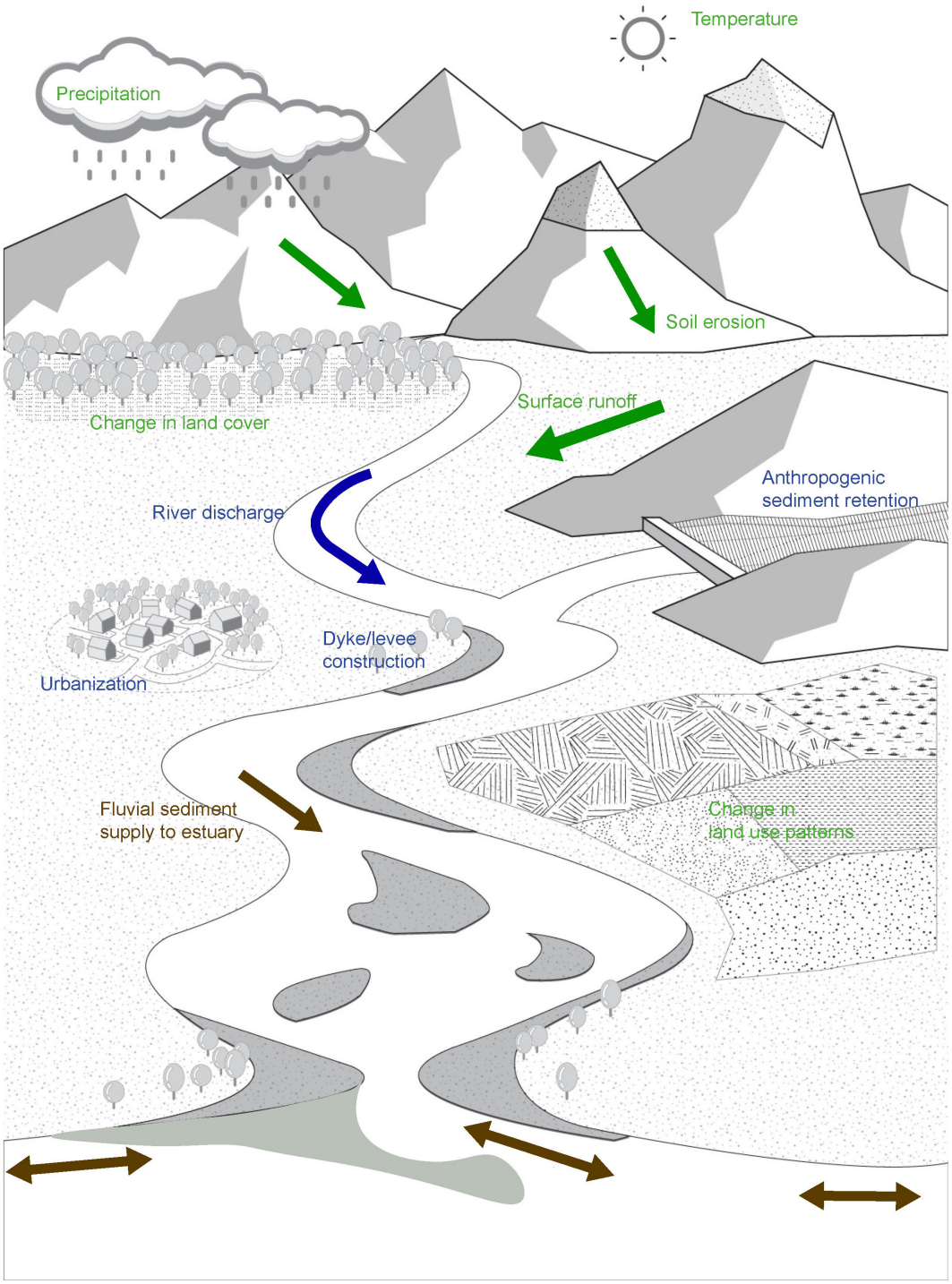

FIGURE 1 | Schematic representation of the sediment pathway from source to the coast. The three colors used in the figure denote the major components (i.e., zones) related to this sediment pathway: (1) catchment-scale sediment production zone fed by soil erosion (in green), (2) transition zone of sediment throughput (in blue), and (3) deposition and redistribution zone dominated by sediment exchange between the estuary and its adjacent coast (in brown). Two-way arrows in brown denote sediment exchange between the estuary and its adjacent inlet-interrupted coast.

increased accommodation space, fluvial sediment supply, and the anthropogenic activities within the estuary. Depending on whether the estuary is a sediment importing or exporting system, the inlet-interrupted coast may, respectively, recede or prograde (Ranasinghe et al., 2013; Ranasinghe, 2016). The spatio-temporal alongshore variation of the coastline recession/progradation is

a function of the relationship between the sediment volume exchange between the estuary and the adjacent coast and wave driven longshore sediment transport capacity in the vicinity of the inlet (Dalrymple, 1992; Dalrymple and Choi, 2003, 2007).

Due to the complex interplay and dependencies between coastline change and catchment, estuarine and coastal processes, any modeling technique that attempts to simulate long-term evolution of inlet interrupted coasts would benefit by considering the holistic behavior of Catchment-Estuary-Coastal (CEC) systems. However, only a limited number of studies to date have considered these systems in a holistic way (e.g., Shennan et al., 2003; Samaras and Koutitas, 2012; Ranasinghe et al., 2013). To investigate the interactions between the subsystems (catchment/fluvial, estuarine, and coastal), a range of modeling approaches are theoretically possible. In one end member, for each subsystem, models representing the relevant processes in as much detail as possible, resolving time and space scales as finely as possible, could be coupled together. Highly detailed models are available for some of the processes in some of the subsystems. For example, models representing flow and sediment transport on time and space scales that allow explicit simulation of hydrodynamics (based directly on approximations to the Navier Stokes equations) could theoretically be employed to represent fluvial, estuarine and coastal morphodynamics. Although the term "process-based" has often been used to describe such highly detailed models currently being used in practice (e.g., Delft3D, Mike21). Since a wide range of modeling approaches are in fact used to simulate physical processes, whether represented on the finest scales practical or on larger scales, here we avoid using the term "process based" and use the more generic term "highly detailed" instead.

There are three obstacles to coupling together an array of highly detailed models in the context of this study. First, processes in the subsystems involve physical, ecological, and human dynamics-and their couplings, but highly detailed models are not available for all of the relevant dynamics and couplings. Second, even when based on state-of-the-art representations of small-scale processes and parameterizations for sub-grid processes, highly detailed models, like all models, are imperfect. Model imperfections can cascade up through the scales when explicitly representing dynamics on scales much smaller than those of interest, especially where long-term simulations are concerned, limiting the quantitative reliability of model results on the scales of interest (Murray, 2007). Finally, limits on computational power make the use of a highly detailed modeling approach to simulate holistic behavior of CEC systems at 50–100 year time scales a daunting task. Therefore, presently available highly detailed modeling approaches are not capable of providing the probabilistic estimates of coastline change via multiple model realizations, which are needed by coastal zone planners/managers for risk-informed decision making (Ranasinghe, 2016, 2020).

To holistically model CEC systems, here we use an approach which represents the aggregated effects that processes occurring on much smaller scales have on the scales of interest, rather than explicitly resolving the interactions between myriad degrees of freedom that can be identified on much smaller scales. This approach embraces the way modeling (conceptual, analytical and numerical) has most often been done in Earth-surface science (Murray, 2013). For example, when simulating interactions on a macroscopic scale, e.g., hydrodynamics, we use parameterizations representing the collective effects at macroscopic scales of interactions between the many degrees of freedom that appear at microscales. For example, the Navier Stokes equations are in a sense parameterizations describing the interactions between macroscopic variables (e.g., pressure, density) that emerge from the collective dynamics at microscales (e.g., molecular dynamics). Thus, the modeling approach adopted here might best be termed "Appropriate Complexity" (French et al., 2016), since it embraces the philosophy of representing processes and interactions at scales commensurate with those of the phenomena of interest to effectively address dynamics at that scale. In this sense, models resolving hydrodynamic and sediment dynamics on fine time and space scales have an appropriate level of complexity for addressing questions across a range of scales, but models that aggregate the effects of those detailed processes to address questions on much larger scales are also appropriate. Compared to more highly detailed models, models in Earth-surface science using a more synthesized (Paola, 2000) or scale-aggregated approach have often been called "Reduced Complexity" models. We recognize that this term has its drawbacks (French et al., 2016), including the fact that all models are "reduced complexity" compared to the natural (or anthropogenic) systems they are representing.

The Scale-aggregated Model for Inlet-interrupted Coasts (SMIC) presented by Ranasinghe et al. (2013) is the first of its kind that treats CEC systems holistically while giving due consideration to the description of physics governing the behavior of the integrated system. Although SMIC provides a platform to probe into CEC systems holistically, its utility to address the long-term evolution of inlet-interrupted coasts under climate change impacts and anthropogenic activities is limited by (a) its applicability to only small tidal inlets, (b) its simplistic method of quantifying the fluvial sediment supply, and (c) the omission of alongshore spatio-temporal variation in coastline change. The present study attempts to address these shortcomings by developing a more generally applicable modeling tool that can simulate the climate-change driven evolution of inlet-interrupted coasts at macro (50–100 year) time scales.

It should be noted that the model developed here is partly data driven, using empirically-based parameterizations representing the behaviors of some component subsystems (e.g., terrestrial sediment yield). Representing the emergent effects of much smaller scale processes with empirically-based parameterizations can potentially be more quantitatively reliable than basing a model explicitly on the smaller scale dynamics (even if computational power were not a limitation), avoiding the possible cascade of model imperfections (Murray, 2007).

It is important to note that inlet-interrupted coasts include both mainland and barrier island coasts. For inlet-interrupted coasts along the mainland, sediment deposition and redistribution processes are closely linked with the type of estuary they are attached to (Ranasinghe et al., 2013; FitzGerald et al., 2014). The scope of this study is restricted to the

long-term evolution of inlet-interrupted coastlines attached to bar-built (barrier) estuaries, which are commonly found along mainland sandy coasts located in wave-dominated, micro-tidal environments. Examples of bar-built estuaries can be seen along the eastern coast of the United States (near mid-latitudes), the Gulf of Mexico, Australia, Brazil, India, and in the regions of Amazon and Nile River (Ranasinghe et al., 1999; Davis and Fitzgerald, 2003; Woodroffe, 2003).

This study concentrates on coastlines interrupted by (a) estuaries with low-lying margins, and (b) small tidal inlets. Estuaries with low-lying margins contain tidal flats and salt marshes along their margins as well as banks with mild slopes. In these systems, increased sea level would lead to a significant increase in surface area of the estuary surrounded by mildly sloping banks, leading to an increase in the tidal prism, and consequently affecting the inlet cross-section area (O'Brien, 1969). On the other hand, small tidal inlets can be considered as a unique subset of barrier estuaries that (generally) have little or no intertidal flats, tidal marshes or ebb-tidal deltas (Duong et al., 2016, 2017, 2018).

MATERIALS AND METHODS

Part of the future coastline change at tidal inlets will arise from changes in the net volume of sediment exchanged between inlet-estuary systems and their adjacent coast (Stive et al., 1998; Stive and Wang, 2003), driven by climate change and anthropogenic activities. This exchange sediment volume can be discretized into three main components: (1) basin (or estuary) infilling volume due to the sea level rise-induced increase in accommodation space, (2) basin (or estuary) volume change due to variation in river discharge, and (3) change in net annual fluvial sediment supply (Ranasinghe et al., 2013). Depending on whether the estuary is in sediment importing or exporting mode (relative to the ocean side of the estuary), and the magnitude of the aforementioned three sediment budget components, an inlet-affected coastline will experience a certain amount of coastline recession or progradation. In addition, the entire coastal profile is expected to respond to sea-level rise by moving landward and upward (Bruun, 1962); a process now commonly referred to as the Bruun effect. The model developed in this study mainly revolves around the physics-based representation of these processes and the way they interact with each other in driving coastline change.

Change in Total Sediment Volume Exchange Between a Barrier-Estuary System and Its Inlet-Interrupted Coast

Assuming the system is presently in dynamic equilibrium, the first step in determining the evolution of an inlet-interrupted coastline is to compute the change in the net annual volume of sediment exchanged between the inlet-estuary system and its adjacent coast. This calculation presumes that any given inlet-estuary system would tend toward and eventually reach its natural equilibrium. Hence, any excess amount of sediment would be exported to its adjacent coast. If there is a deficit in sediment (from the equilibrium value), an inlet-estuary system will import sand from its adjacent coast. This sediment volume can be computed by the summation of the three different processes mentioned above, and given by the following equation (Ranasinghe et al., 2013):

$$\Delta V_{\mathrm{T}} = \Delta V_{\mathrm{BI}} + \Delta V_{\mathrm{BV}} + \Delta V_{\mathrm{FS}} \tag{1}$$

where ΔV_{T} is the cumulative change in the total sediment-volume exchange between the estuary and its adjacent coast, ΔV_{BI} is the sediment demand of the basin due to sea-level rise-driven change in basin volume (i.e., basin infilling volume), ΔV_{BV} is the change in basin infill sediment volume due to variation in river discharge, and ΔV_{FS} is the change in fluvial sediment supply due to combined effects of climate change and anthropogenic activities (all volumes in m^3).

Sea-level rise may affect the tides as well. However, possible changes in tides due to rising sea level are projected to be marginal. For example, Pickering et al. (2017) have shown that for 2.0 m of sea-level rise, the possible changes in the mean high water level of tides are less than 0.1 m. Therefore, this aspect was not considered in this study. Further, the nodal tidal elevation changes (e.g., Baart et al., 2012; Peng et al., 2019) are also not taken into account in the present model.

The schematic diagram presented below (**Figure 2**) shows the connectivity among these processes and the sediment-volume components comprising ΔV_{T}.

Basin Infilling Volume Due to Sea-Level Rise-Induced Increase in Accommodation Space

Accommodation space is the additional volume created within the basin (or estuary) due to an increase relative mean sea level [ΔRSL (m)]. This increase in volume, given by $A_{\mathrm{b}}.\Delta RSL$; where, A_{b} is the basin surface area (m^2), results in an extra sediment demand by the estuary [ΔV_{BI} (m^3); Factor 1 in **Figure 2**]. Taking into account also the time lag between sea-level rise (hydrodynamic forcing) and the associated basin infilling (morphological response), ΔV_{BI} can be expressed by the following equation, where the negative sign indicates sediment imported into the inlet-estuary system.

$$\Delta V_{\mathrm{BI}} = -\mathrm{fac}\,(A_{\mathrm{b}}\,\Delta RSL) \tag{2}$$

where "fac" ($0 < \mathrm{fac} < 1$) accounts for the morphological response lag. In this study, it is taken as 0.5 (following the argumentation and formulations in Ranasinghe et al. (2013) for the original SMIC model) in all model simulations.

Basin Volume Change Due to Variations in River Flow

Changes in river discharge [ΔQ_{R} (m^3)] will affect the infill volume of the estuary. Such changes in river discharge would alter the tidal flow volume during the ebbing phase of the tide, and subsequently, the estuarine and inlet velocities. Due to the tendency of velocities in a basin-inlet system (averaged over the net cross section) to approach an equilibrium value, the basin-inlet system will change its cross-section by either scouring or accretion, until the equilibrium cross section is reached. Depending on the sign of change in future river discharge [i.e.,

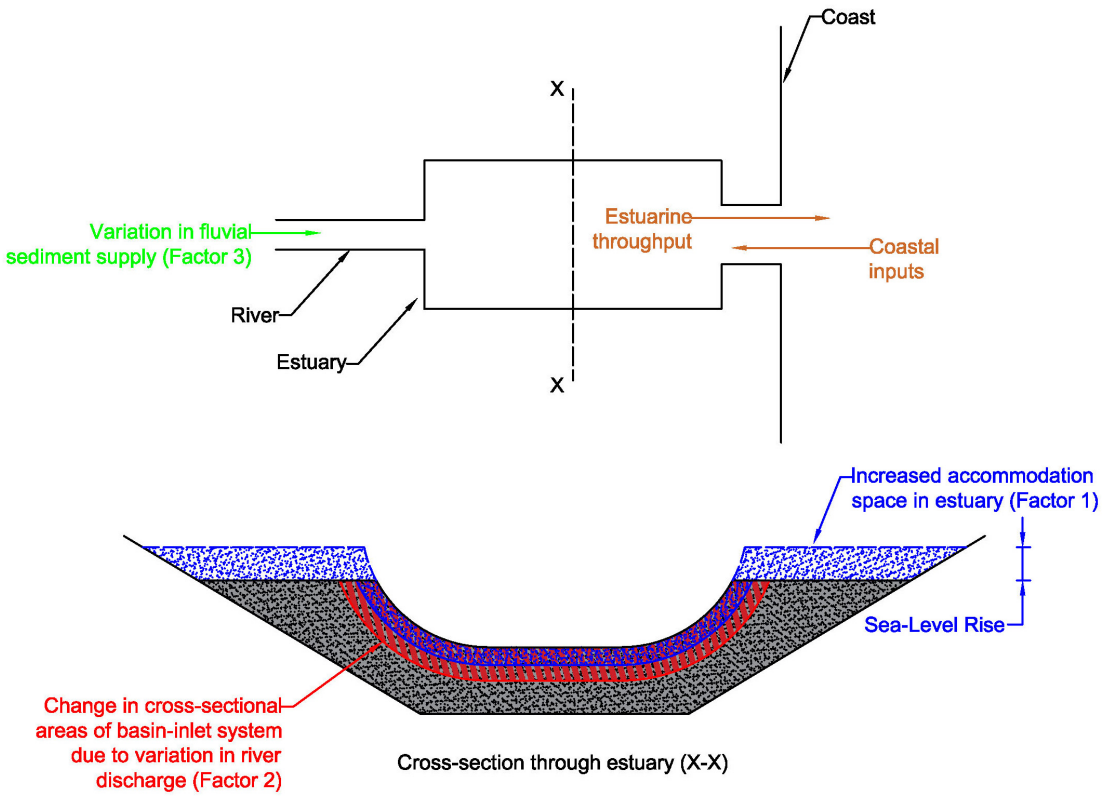

FIGURE 2 | Schematic illustration of the connections between sediment volume components associated with the change in total sediment-volume exchange (ΔV_T) between inlet-estuary system and its adjacent coast.

increase (+)/decrease (−)], a particular volume of sediment [ΔV_{BV}(m^3); Factor 2 in **Figure 2**] would be exchanged between the inlet-basin system and its adjacent coast to accommodate this basin-inlet cross-sectional change. This sediment volume (ΔV_{BV}) can be computed as follows (Ranasinghe et al., 2013):

$$\Delta V_{BV} = \frac{\Delta Q_R V_B}{(P + Q_R)} \tag{3}$$

where Q_R is the present river flow into the basin during ebb (m^3), ΔQ_R is the climate change-driven variation in river flow during ebb (m^3), V_B is the present basin volume (m^3), and P is the mean equilibrium ebb-tidal prism (m^3).

Determining equilibrium tidal prism for estuaries with low-lying margins

The above sediment volume ΔV_{BV} depends on the equilibrium tidal prism. This equilibrium tidal prism in estuaries with low-lying margins is linked with the concurrent sea level and cross-sectional area of the tidal inlet and channels in the basin. When the sea level is gradually increasing, as it is doing now (Stocker et al., 2013b), it is necessary to determine the equilibrium tidal prism at these inlet-estuary systems for the increased mean sea level, so that the corresponding basin volume change and subsequent amount of sediment exchange can be correctly computed. **Figure 3** illustrates the non-linear, iterative calculation procedure adopted here to represent this phenomenon, followed by a description of the associated physical processes.

The total ebb-tidal prism (P) consists of two components: (1) the volume of water flowing out of the estuary system due to tidal forcing alone (P_T), and (2) the volume of water supplied by the river flow during the ebbing phase of the tide (P_R).

$$P = P_T + P_R \tag{4}$$

Owing to the low-lying margins of these systems, the basin surface area of the estuary (A_b) will change with sea-level rise. Therefore, a look-up table for the basin surface area was developed with the aid of a Digital Elevation Model (DEM), to determine the basin surface area (A_b) associated with different sea levels.

Assuming there is no phase lag in tidal elevations within the systems, which is a reasonable assumption for not-very-long estuaries (Dronkers, 1964) the ebb-tidal prism (P_T) corresponding to this new basin surface area can be calculated according to the relationship presented by Keulegan (1951).

$$P_T = A_b(2a_b) \tag{5}$$

where A_b is the surface area of the estuary and a_b is the mean tidal amplitude within the estuary.

Tidal inlets throughout the world exhibit several consistent relationships that have allowed coastal engineers and

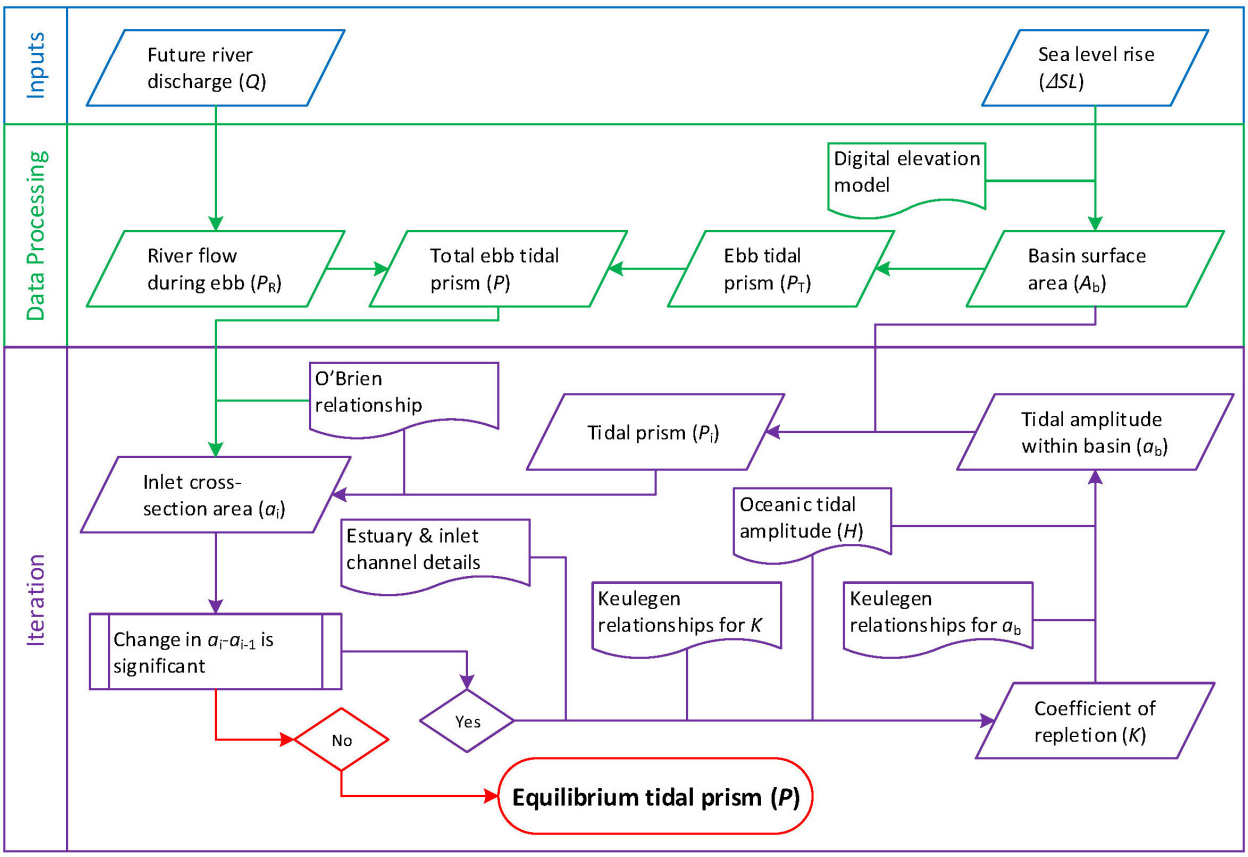

FIGURE 3 | Flowchart of the iteration procedure to determine equilibrium tidal prism at estuaries with low-lying margins (modified from Bamunawala et al., 2018b).

marine geologists to formulate predictive models. One such widely-known relationship is O'Brien's relationship between inlet channel cross-sectional area (a) and tidal prism (P) (O'Brien, 1969).

$$a = c_1 P^{c_2} \tag{6}$$

where c_1 and c_2 are empirical coefficients.

It should be noted that there can be instances where the estuary systems deviate from the above a-P relationship (e.g., Hume and Herdendorf, 1993; Gao and Collins, 1994). Townend (2005) suggested that the deviation from the a-P relationship can be attributed to the state of the respective estuary system's response to contemporary processes over the Holocene. Besides, there are some other systems, of which the geological constraints do not accommodate the eroding of the inlet channel. In such cases, the tidal prism has to change to maintain the equilibrium conditions.

Thus, when P changes, the inlet cross-sectional area a will also need to change. According to Keulegan (1951), such changes in the inlet cross-sectional area could also affect tidal attenuation characteristics in the inlet channel as attenuation is a function of the inlet-channel geometry. Table 2 of Keulegan (1951) provides a look-up table for an expression (left-hand side of the equation below), which includes the coefficient of repletion (K), basin surface area (A_b), inlet channel cross-sectional area (a) and oceanic tidal amplitude (H) for a given inlet-channel length (L_c), inlet-channel hydraulic radius (r) and Manning's roughness (n).

$$\frac{A_b K \sqrt{H}}{a} \times 10^{-4} = \mathrm{f}(n, r, L_c) \tag{7}$$

This relationship allows determining the coefficient of repletion (K). The resulting tidal amplitude within the basin (a_b) can then be computed using:

$$\frac{a_b}{H} = \sin(\tau) \tag{8}$$

where $\sin(\tau)$ is a function of the coefficient of repletion (K), and can be determined through another look-up table (Table 4) provided in Keulegan (1951).

It should be noted that Eqs 7 and 8 inherently assume that the presence of a narrow and relatively straight inlet channel which connects the ocean to an estuary/lagoon that is significantly wide compared to the inlet channel.

Use of the above computed tidal amplitude in Eq. (5) provides the new tidal prism (for the considered mean sea level), which will consequently result in a new inlet cross-sectional area as per Eq. (6). A new inlet cross-sectional area will have a different coefficient of repletion (K) and, thus a new tidal amplitude within the basin. Therefore, Eqs (5–8) are here used iteratively, until

the difference between two subsequent computed inlet cross-sectional areas (for a given mean sea level) is less than 1% of the former value (**Figure 3**).

Change in Fluvial Sediment Supply

Climate change and anthropogenic activities could result in significant changes in the annual fluvial sediment volume [ΔQ_S (m^3)] supplied to the coast (Vörösmarty et al., 2003; Syvitski, 2005; Palmer et al., 2008; Ranasinghe et al., 2019). Consequently, these changes will affect the total volume of sediment exchanged between the inlet-estuary system and its neighboring coast [ΔV_{FS} (m^3); Factor 3 in **Figure 2**] over the period considered [t (in years)]. The changes in fluvial sediment volume are here calculated as (Ranasinghe et al., 2013):

$$\Delta V_{FS} = \int_0^t \Delta Q_S(t)\, dt \tag{9}$$

Assessment of fluvial sediment supply to coasts

Sediment generation and fluvial sediment throughput at catchment scale are affected by both climate change-driven impacts and anthropogenic activities (Syvitski et al., 2003, 2009; Syvitski and Milliman, 2007; Shrestha et al., 2013). Bamunawala et al. (2018a) illustrated that the empirical BQART model presented by Syvitski and Milliman (2007) can be used effectively to assess the annual fluvial sediment supply to the coast while considering both climate change-driven impacts and human activities. This empirical model is based on 488 globally-distributed datasets. For catchments with a mean annual temperature greater than or equal to 2°C, the BQART model estimates the annual sediment volume (Q_S) transported downstream to the coast by the following equation:

$$Q_S = \omega B Q^{0.31} A^{0.5} R T \tag{10}$$

where ω is 0.02 or 0.0006 for the sediment volume (Q_S), expressed in kg/s or MT/year, respectively, Q is the annual river discharge from the catchment considered (km^3/yr), A is the catchment area (km^2), R is the relief of the catchment (km), and T is the catchment-wide mean annual temperature (°C).

Term "B" in the above equation represents the catchment sediment production and comprises glacial erosion (I), catchment lithology (L) that accounts for its soil type and erodibility, a reservoir trapping-efficiency factor (T_E), and human-induced erosion factor (E_h), which is expressed as the following equation:

$$B = IL(1 - T_E)E_h \tag{11}$$

Glacial erosion (I) in the above equation is expressed as follows:

$$I = 1 + (0.09A_g) \tag{12}$$

where A_g is the percentage of ice cover of the catchment area.

Syvitski and Milliman (2007) stated that the human-induced erosion factor (E_h; anthropogenic factor) depends on land-use practices, socio-economic conditions and population density. In their study, E_h values were determined based on the Gross National Product (per capita) and population density. Based on the global dataset used, the optimum range of E_h was suggested to be 0.3–2.0.

In this study, however, instead of using coarse countrywide estimates of Gross National Product (GNP)/capita and population density to estimate the human-induced soil erosion factor (E_h), the human footprint index (HFPI), which is based on high-resolution spatial information published by the Wildlife Conservation Society [WCS] and Columbia University Center for International Earth Science Information Network [CIESIN] (2005) is used to achieve a better representation of anthropogenic influences on sedimentation (Balthazar et al., 2013; Bamunawala et al., 2018a). The HFPI is developed by using several global datasets such as population distribution, urban areas, roads, navigable rivers, electrical infrastructures and agricultural land use (Sanderson et al., 2002).

Reference Conditions for Baseline Simulations

The modeling approach presented above is used here to compute the total sediment exchange volume between the inlet-estuary system and its adjacent coastline for the 2020–2100 period. In order to compute these future changes, first, baseline conditions need to be established. Here, CEC system conditions at 2019 were used as the reference condition in all sediment-volume computations. However, as both mean annual temperature (T) and cumulative river discharge (Q) show significant inter-annual variability, using T and Q values specifically for the year 2019 as the reference condition would not be accurate. Therefore, the mean values of T and Q over the last decade (2010–2019) were used as the reference conditions for these two variables. As there is no significant inter-annual variability in mean sea level, all future changes in sea level over the 2020–2100 period were computed relative to the 2019 mean sea level.

Modeling the Spatio-Temporal Evolution of Inlet-Interrupted Coastlines

Changes in the total sediment exchange between barrier estuaries and their adjacent coasts (ΔV_T) will act as sediment source/sink at the coast, which, in turn, will contribute to the evolution of the inlet-interrupted coast. The extent and magnitude of such coastline variations are also related to the wave-driven longshore sediment transport capacity in the vicinity of the inlet. Many studies have indicated that potential climate-change impacts during the 21st century may result in changing mean wave conditions across the world's oceans (Mori et al., 2010; Hemer et al., 2013; Semedo et al., 2013; Casas-Prat et al., 2018; Morim et al., 2019). Such changes in wave conditions could result in variations in longshore sediment transport rates and gradients therein (e.g., Hemer et al., 2012; Casas-Prat and Sierra, 2013; Erikson et al., 2015; Grabemann et al., 2015; Wolf et al., 2015; Dastgheib et al., 2016; Shimura et al., 2016). However, all available wave projections only provide averaged changes of wave conditions [i.e., not for individual Representative Concentration Pathways (RCPs)] over the last two/three decades of the 21st century (i.e., not for the entire 21st century). Furthermore, projected changes in offshore wave conditions are rather small for most of the global coastline, especially where sandy coasts are concerned, implying that associated changes in nearshore waves

would also be small. Therefore, in this study, which considers all RCPs over the entire 21st century, it is assumed that the ambient rates of longshore sediment transport remain invariant throughout the 21st century, and thus, the projected changes in coastlines are computed based on the present-day longshore sediment transport rates. With this assumption, the conceptual framework used to compute the spatio-temporal variations of inlet-interrupted coastlines is described below.

Following the overarching objective of this study, a simplified framework of a generically applicable coastline model that provides first-order estimates of coastline variations at macro time scales was developed. It represents the general changes of the inlet-interrupted coastline by considering the total change in sediment volume exchange between the inlet-estuary system and the adjacent coast (ΔV_T), while assuming uniform shoreline orientations along up- and down-drift coasts and the lack of any coastal structures.

The maximum extent of inlet-affected coastline in both up-drift and down-drift directions from an inlet is constrained by the existence of headlands, rock outcrops, inlets or by other prominent changes in mean shoreline orientation. Following the method adopted in the SMIC applications by Ranasinghe et al. (2013), the maximum extent of this inlet-affected coastline distance was considered to be ∼25 km. If there is no known gradient in the net annual alongshore sediment transport rate along the coastline (i.e., both up- and down-drift coasts), it can be assumed that the coastal cell concerned is presently in equilibrium at annual time scales.

Within the development of this simplified coastline change model, it is assumed that the longshore sediment transport (LST) occurs uniformly over the cross-shore profile. **Figure 4** illustrates the hypothetical equilibrium cross-shore profile. Given that the change in total sediment volume exchange (ΔV_T) is computed annually (Eqs 1–12), ΔV_T is first divided into a number of equal fragments (n_v). This volume fragment (V_{fr}), which is calculated using Eq. [13] was then distributed along the coastline.

$$V_{fr} = \frac{\Delta V_T}{n_v} \tag{13}$$

Depending on the equivalent longshore transport capacity (ΔQ_{LST}; calculated using Eq. 14), all or part of this volume fragment is transported along the coast.

$$\Delta Q_{LST} = \frac{Q_{LST}}{n_v} \tag{14}$$

Following the assumption of a balanced sediment budget within the coastal cell, any volume of sediment that gets transported in the down-drift direction will result in coastal progradation at the farthermost section of the down-drift coast. If the volume fragment is larger than the equivalent longshore transport capacity (ΔQ_{LST}), the surplus volume (ΔV; computed using Eq. 15) will result in a seaward translation of the coastline position (Δy) within the considered alongshore distance (Δx) (**Figure 4**). This also holds when $V_{fr} < \Delta Q_{LST}$, which will lead to coastline recession.

$$\Delta V = V_{fr} - \Delta Q_{LST} \tag{15}$$

Assuming that the shoreline moves cross-shore parallel to itself while maintaining its equilibrium profile, the following relationship can be derived to determine the resulting change in coastline position (Δy).

$$\min(\Delta V, V_{fr}) = \Delta x(D\Delta y)$$

where D is the depth of closure.

The above procedure is repeated n_V times, so that the total change in sediment volume exchange between the estuary and adjacent coast (ΔV_T) is fully distributed along the coastal cell. These computations are closely connected to an expression for the longshore sediment transport rate (Q_{LST}), which, in turn, is related to the longshore current generated by oblique incident breaking waves. Q_{LST} is thus presented as:

$$Q_{LST} = Q_0 \sin(2\alpha_b) \tag{16}$$

where Q_0 is the amplitude of the longshore sediment transport rate (m^3/yr), and α_b is the breaking wave angle between wave crest line and coastline, which can be expressed as follows, assuming small-angles:

$$\alpha_b = \alpha_0 - \frac{\Delta y}{\Delta x} \tag{17}$$

where α_0 (rad) is the angle of breaking wave crests (relative to the coastline).

Since the local coastline position (Δy) would be updated with the alongshore distribution of each volume fragment, breaking wave angle (α_b) and longshore sediment transport rate (Q_{LST}) are also updated after completion of the distribution of each volume fragment. If the present-day longshore sediment transport rate and the corresponding angle of breaking wave crest (α_0) are known, the above-described procedure can be implemented to distribute the sediment volume along the inlet-interrupted coast. If such information is not available, the amplitude of the longshore sediment transport rate (Q_0) can be reasonably estimated by using a bulk longshore sediment transport equation such as the CERC formula (CERC, 1984), the Kamphuis formula (Kamphuis, 1991), and the Bayram formula (Bayram et al., 2007). An example of such formulation of Q_0 [from the US Army corps, Coastal Engineering Research Centre (CERC), published in the Shore Protection Manual (CERC, 1984)] is shown in Eq. (18).

$$Q_0 = \frac{0.77\sqrt{g}}{32(1-p)\left(\frac{\rho_s}{\rho} - 1\right)\sqrt{\gamma_b}} \times H_{sb}^{2.5} \tag{18}$$

where H_{sb} is the significant wave height at breaker line (m), γ_b is the breaking parameter for irregular waves (0.55), ρ_s is the density of sand ($2,650$ kg/m^3), ρ is the density of seawater ($1,030$ kg/m^3), p is the porosity of sand (0.4), and g is the gravitational acceleration (9.81 m/s^2).

In addition to the above-described coastline change, regional relative sea-level rise (ΔRSL) will shift the active cross-shore profile upward and landward, which, in the absence of sediment sources supplying sand to the coast, will result in additional coastline recession (Bruun, 1962). The magnitude of this

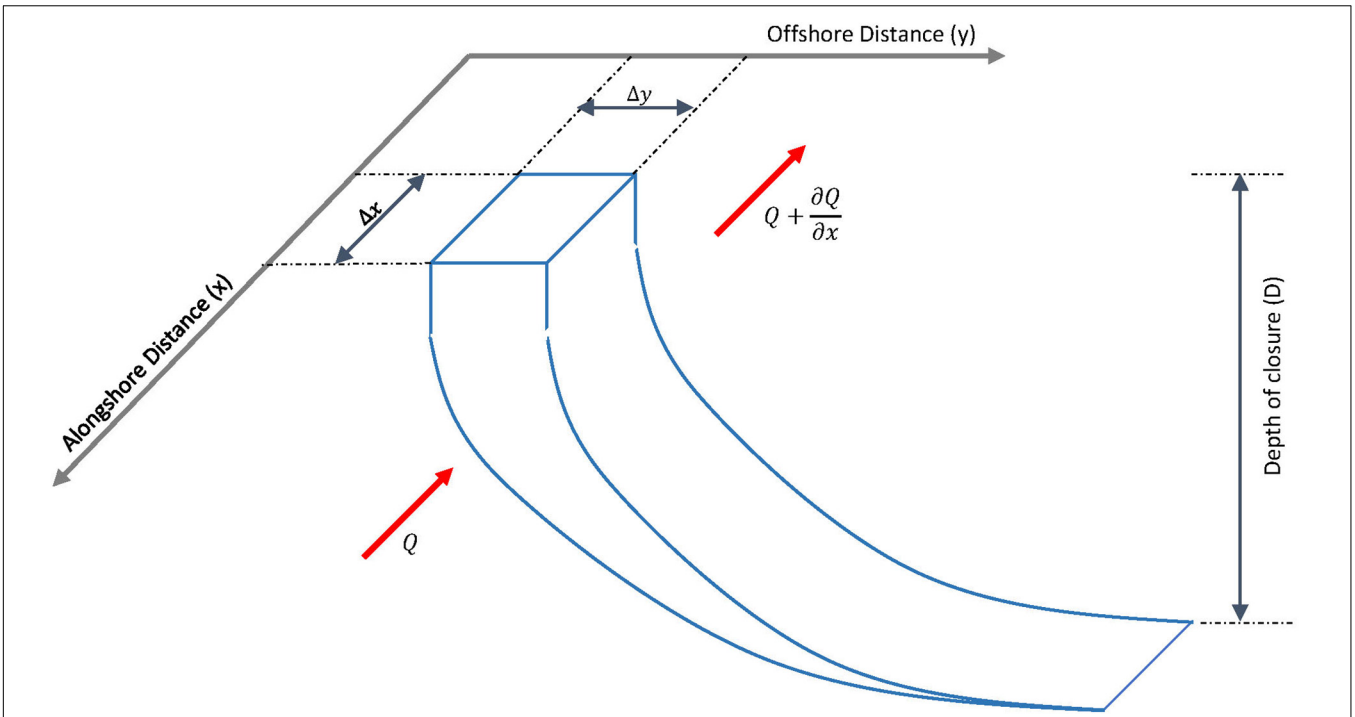

FIGURE 4 | Schematic illustration of a hypothetical equilibrium cross-shore profile and the variables used in developing the one-line coastline change model.

so-called Bruun effect driven coastline recession is expressed according to the following equation:

$$\Delta C_{BE} = \frac{\Delta RSL}{\tan(\beta)} \tag{19}$$

where ΔC_{BE} is the coastline recession (m), ΔRSL is the sea-level rise (m), and β is the average slope of the active beach profile from the shoreline to the depth of closure (D; **Figure 4**). It is important to note the the coastline change computed in this way will represent only the change that would be due to climate change impacts and will not be inclusive of any ambient coastline change that would occur even without any future variations in system forcing (e.g., due to alongshore gradients in LST, cross-shore feeding of sediment, fluvial sediment supply).

Input Data Sources

The reduced-complexity model presented in sections "Change in Total Sediment Volume Exchange Between a Barrier-Estuary System and Its Inlet-Interrupted Coast" and "Modeling the Spatio-Temporal Evolution of Inlet-Interrupted Coastlines," requires four main drivers to project the long-term evolution of inlet-interrupted coasts: annual mean temperature (T), annual cumulative river discharge (Q), change in regional relative sea-level (ΔRSL), and anthropogenic activities in the catchment, as represented by the human-induced erosion factor (E_h).

Temperature and runoff projections were obtained from General Circulation Models (GCMs) of the Coupled Model Intercomparison Project Phase 5 [CMIP5 data portal; Earth System Grid-Centre for Enabling Technologies (ESG-CET); available on the webpage http://pcmdi9.llnl.gov/]. Projected daily/monthly values of temperature and surface runoff were obtained for all four Representative Concentration Pathways (RCPs). Initially, the GCMs with both temperature and surface runoff projections for all RCPs over the 2010–2100 period were considered as data sources. Of these, GCMs with spatial resolution finer than 2.5° were selected to obtain the necessary climate inputs (T and Q). Where possible, the suitability of the above-selected data sources was assessed regionally, by considering the guidelines published on the appropriateness of GCMs in respective areas (e.g., CSIRO and Bureau of Meteorology, 2015, for Australia).

According to Nicholls et al. (2014), the regional relative sea-level changes (ΔRSL) can be calculated according to the following equation:

$$\Delta RSL = \Delta SL_G + \Delta SL_{RM} + \Delta SL_{RG} + \Delta SL_{VLM} \tag{20}$$

where ΔRSL is the change in relative sea level, ΔSL_G is the change in global mean sea level, ΔSL_{RM} is the regional variation in sea level from the global mean due to meteo-oceanographic factors, ΔSL_{RG} is the regional variation in sea level due to changes in the earth's gravitational field, and ΔSL_{VLM} is the change in sea level due to vertical land movement (all values in meters).

The regional relative sea-level change projections by 2100 (ΔRSL) were obtained from Figure TS.23 of Stocker et al. (2013a), while the corresponding global mean sea level change (ΔSL_G) was obtained from Table SPM. 2 of Stocker et al. (2013b). The difference between those two sets of values provide the cumulative contribution of ΔSL_{RM}, ΔSL_{RG}, and partly

ΔSL_{VLM} (excluding any local subsidence/rebound) for 2100. Those differences were linearly distributed from the year 2000 to obtain the yearly cumulative contribution of ΔSL_{RM}, ΔSL_{RG}, and ΔSL_{VLM}. Those linearly distributed values were then added to the yearly changes in global mean sea level (ΔSL_G), following the method presented by Mehvar et al. (2016), to obtain yearly projections of regional relative sea-level changes. The yearly changes in global mean sea level (ΔSL_G) are calculated following Nicholls et al. (2014) as:

$$\Delta SL_G = a_1 t + a_2 t^2 \quad (21)$$

where; ΔSL_G is the change in global sea level (m) since 2000, "t" is the number of years since 2000, a_1 is the trend in sea level change (m/yr), and a_2 is the change in the rate of sea-level change trend (m/yr^2). The relevant coefficients were obtained from Mehvar et al. (2016).

The HFPI data were obtained from the WCS-CIESN database, which is available at a spatial resolution of 30 arc-seconds and is regionally normalized to account for the interaction between the natural environment and human influences (Sanderson et al., 2002). Global and continental-scale raster files of HFPI data are available at https://doi.org/10.7927/H4M61H5F.

Case Study Sites and Input Data

The above-introduced reduced-complexity model was applied at three selected systems representing (a) barrier estuaries with low-lying margins (Alsea estuary, Oregon, United States, and Dyfi estuary, Wales, United Kingdom) and (b) small tidal inlets (Kalutara inlet, Sri Lanka). **Table 1** summarizes the key properties of these systems and **Figure 5** shows the locations of the selected case study sites, their respective watershed areas and HFPI.

TABLE 1 | Properties of the selected barrier estuary systems (reference conditions).

Parameter	Alsea	Dyfi	Kalutara
Mean ebb-tidal prism (P in 10^6 m^3)	9.0	71.1	6.2
Basin surface area (A_b in 10^6 km^2)	9.1	17.3	1.75
Basin volume (V_B in 10^6 m^3)	20.0	44.98	5.25
Catchment area (A in km^2)	1,225	670	2,778
Catchment relief (R in km)	1.25	0.66	2.25
Lithology factor (L)	1.0	0.75	0.5
Anthropogenic factor (E_h)	0.67	0.93	0.93
Beach profile slope ($\tan\beta$)	0.02	0.02	0.02
Depth of closure (h_{DoC} in m)	15	15	15

Values of mean ebb-tidal prism, basin surface area and basin volume for Alsea, Dyfi, and Kalutara CEC systems were obtained from O'Neil (1987), National Rivers Authority Welsh Region (1995), and Duong (2015), respectively. Catchment area values were determined by the respective watershed shapefiles. Catchment relief values were determined by the use of one arc-second resolution digital elevation models obtained from the USGS Earth Explorer tool (Farr et al., 2007). Catchment-averaged lithological factors for the selected systems were obtained from Syvitski and Milliman (2007). Catchment wide anthropogenic factors (E_h) were obtained by rescaling the Human FootPrint Index (HFPI), given in Wildlife Conservation Society [WCS] and Columbia University Center for International Earth Science Information Network [CIESIN] (2005). The active coastal-profile slope values and depths of closure values were obtained from Athanasiou et al. (2019).

Present-day HFPI values within the catchment were rescaled linearly to fit the optimum scale of E_h suggested by Syvitski and Milliman (2007). These rescaled HFPI values were then averaged over the catchment to determine a representative factor for human-induced erosion (E_h). Given the contemporary rate of population growth and urbanization, it is safe to assume that E_h will increase by 2100. Owing to numerous uncertainties associated with such projections (e.g., Veerbeek, 2017), the value of E_h by 2100 was assumed to increase by 15% of its present-day value.

The T and Q values were obtained by an ensemble of four selected GCMs (viz., GFDL-CM3, GFDL-ESM2G, and GFDL-ESM2M from NOAA, United States, and IPSL-CM5A-MR from IPSL in France). **Table 2** presents the averaged T and Q projections for the reference (2010–2019), mid-century (2046–2065), and end-century (2081–2100) periods, indicating the variation of the respective model inputs across the 21st century for different RCPs.

Figure 6 shows the projected variations of regional relative sea-level (ΔRSL) at the selected study locations for the four RCPs.

RESULTS

Model hindcasted coastline changes are presented in section "Model Hindcasts for the 1986–2005 Period." Results of model applications at the three case study locations are presented in sections "Projected Variation of Total Sediment Volume Exchange (ΔV_T): 2020–2100" and "Projected Coastline Change at the Case Study Locations: 2020–2100." Section " Projected Variation of Total Sediment Volume Exchange (ΔV_T): 2020–2100" presents, for each system, the projected variations in the total sediment volume exchange between the estuary and the adjacent coast (ΔV_T), together with an assessment of the predominant sediment volume component at each case study location. Section "Projected Coastline Change at the Case Study Locations: 2020–2100" presents the projected changes in coastline position at each location by 2060 and 2100.

Model Hindcasts for the 1986–2005 Period

As a model validation exercise, the above-presented modeling technique was applied to a historical period (1986–2005) to compare the model hindcasts with observed shoreline change at the studied mainland barrier estuary systems. To achieve this objective, the following simplifications were made when obtaining the model inputs/reference conditions.

For the historical period (1986–2005), the ensemble of GCMs described in section "Case Study Sites and Input Data" was used to obtain the yearly values of T and Q. The reference conditions for the T and Q for this hindcast period were taken as the mean value of the GCM ensemble over the 1976–1985 period. The rate of global mean sea-level rise was taken as 2.1 mm/yr for the 1986–2005 period, following the projections presented in Chapter 4 of the IPCC Special Report on the Ocean and Cryosphere in a Changing Climate (i.e., Oppenheimer et al., 2019). The present value of HFPI was considered as a constant

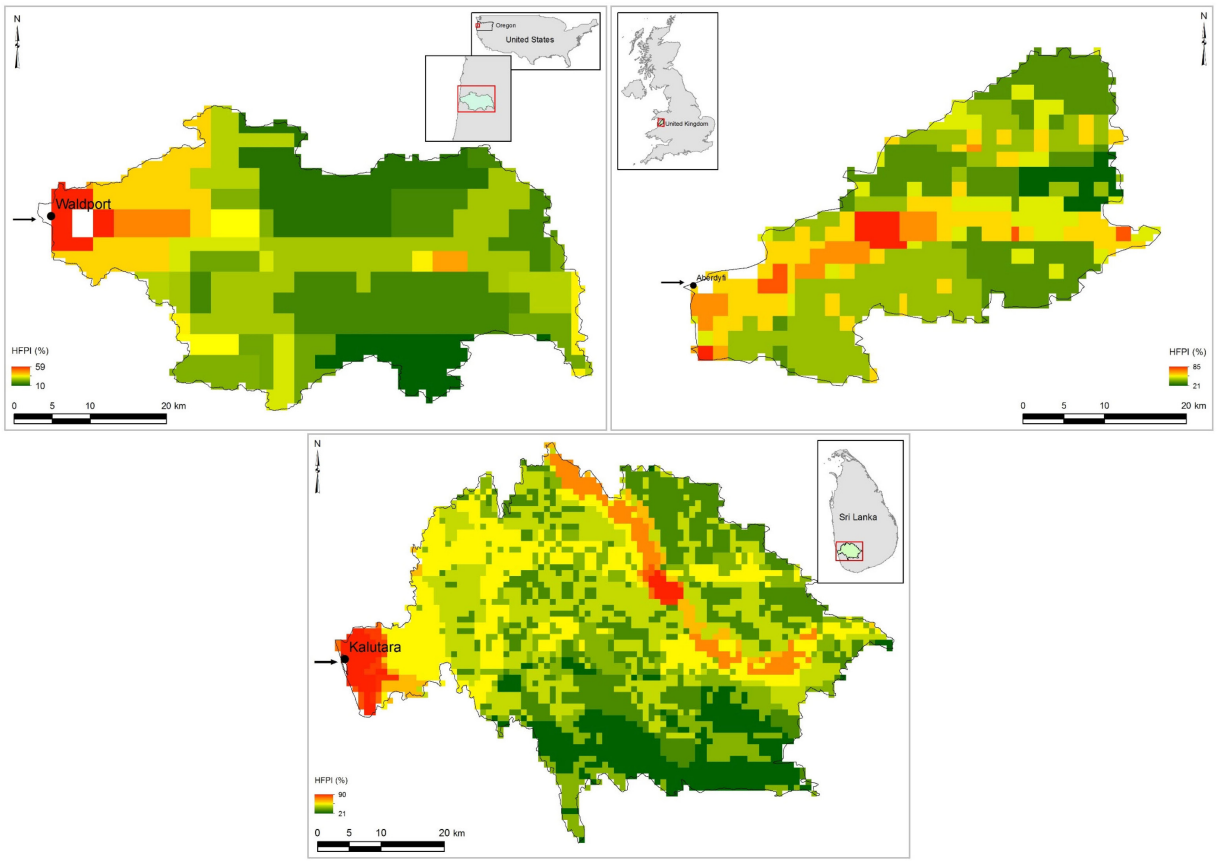

FIGURE 5 | Human FootPrint Index (HFPI), location and watershed areas of the selected CEC systems (Alsea estuary: **top-left**, Dyfi estuary: **top-right**, and Kalutara estuary: **bottom**). HFPI data were obtained from https://doi.org/10.7927/H4M61H5F.

throughout the historical period. The model hindcasted coastline change rates at the three case study locations were compared with satellite-image derived ambient shoreline change rates presented by Luijendijk et al. (2018).

The results of the comparison are shown in **Table 3**. This comparison indicates that the modeled coastline change at all three systems for the validation period compare well with ambient shoreline change rates presented by Luijendijk et al. (2018) over the same period, providing confidence in the model.

Projected Variation of Total Sediment Volume Exchange (ΔV_T): 2020–2100

Figures 7–9 show the projected change in total sediment volume exchange (ΔV_T) between each case study estuary and the adjacent coast over the 21st century (left) and the individual contributions of the three main sediment volume components [i.e., basin infilling (ΔV_{BI}), basin volume change (ΔV_{BV}), and fluvial sedimentation (ΔV_{FS})].

The model projections indicate that the Alsea estuary system will import sediment from its adjacent coast throughout the 21st century. The maximum and minimum projected volumes of sediment imports by 2100 are −1.25 million cubic meters (MCM) (RCP 8.5) and −1.0 MCM (RCP 2.6). The results also indicate that ΔV_T at the Alsea estuary system is predominantly governed by the process of basin infilling (ΔV_{BI}) and that the projected variations of ΔV_{BV} have trivial impacts on ΔV_T for all RCPs. The increased supply of fluvial sediment toward the end-century period slightly reduce sediment demand due to basin infilling for all RCPs. These increases in fluvial sediment supply toward the end-of-the-century are governed by the projected increments in temperature (**Table 2**) and the increase in human-induced erosion factor.

The model projections indicate that the Dyfi estuary system will also import sediment from the adjacent coast throughout the 21st century. The maximum and minimum projected volumes of sediment imports by 2100 are −5.0 MCM (RCP 8.5) and −2.5 MCM (RCP 2.6). The results here too indicate that ΔV_T at the Dyfi estuary system is governed by the basin sediment demand (ΔV_{BI}), while projected variations of ΔV_{BV} and ΔV_{FS} have trivial impacts on ΔV_T for all RCPs. The river catchment area of this CEC system is relatively small compared with the estuary surface area. Hence, despite the projected increments in temperature (**Table 2**) and the increase in human-induced erosion, fluvial sediment supply by the Dyfi River catchment contributes little to the sediment volume demand due to basin infilling for all RCPs.

TABLE 2 | Average annual mean temperature and cumulative runoff at the selected case study locations over the present, mid-21st century and end 21st century time slices.

System	Period	Mean annual temperature (°C)				Annual cumulative runoff (km^3)			
		RCP 2.6	RCP 4.5	RCP 6.0	RCP 8.5	RCP 2.6	RCP 4.5	RCP 6.0	RCP 8.5
Alsea, United States	2010–2019	11.11	11.07	10.86	10.91	0.437	0.449	0.467	0.431
	2046–2065	11.66	12.01	11.72	12.56	0.459	0.431	0.438	0.446
	2081–2100	11.69	12.51	12.86	14.12	0.458	0.458	0.459	0.421
Dyfi, United Kingdom	2010–2019	10.30	10.16	10.37	10.29	0.134	0.130	0.126	0.131
	2046–2065	10.71	11.24	10.83	11.55	0.128	0.127	0.130	0.133
	2081–2100	10.57	11.42	11.75	13.06	0.133	0.127	0.126	0.128
Kalutara inlet, SL	2010–2019	26.85	26.92	26.89	26.83	0.799	0.685	0.707	0.812
	2046–2065	27.32	27.79	27.47	28.17	0.805	0.837	0.935	0.999
	2081–2100	27.36	28.01	28.40	29.61	0.793	0.878	0.897	1.054

The temperature and runoff values in the table were obtained by averaging the annual ensembles of the four selected GCMs over the respective time slices.

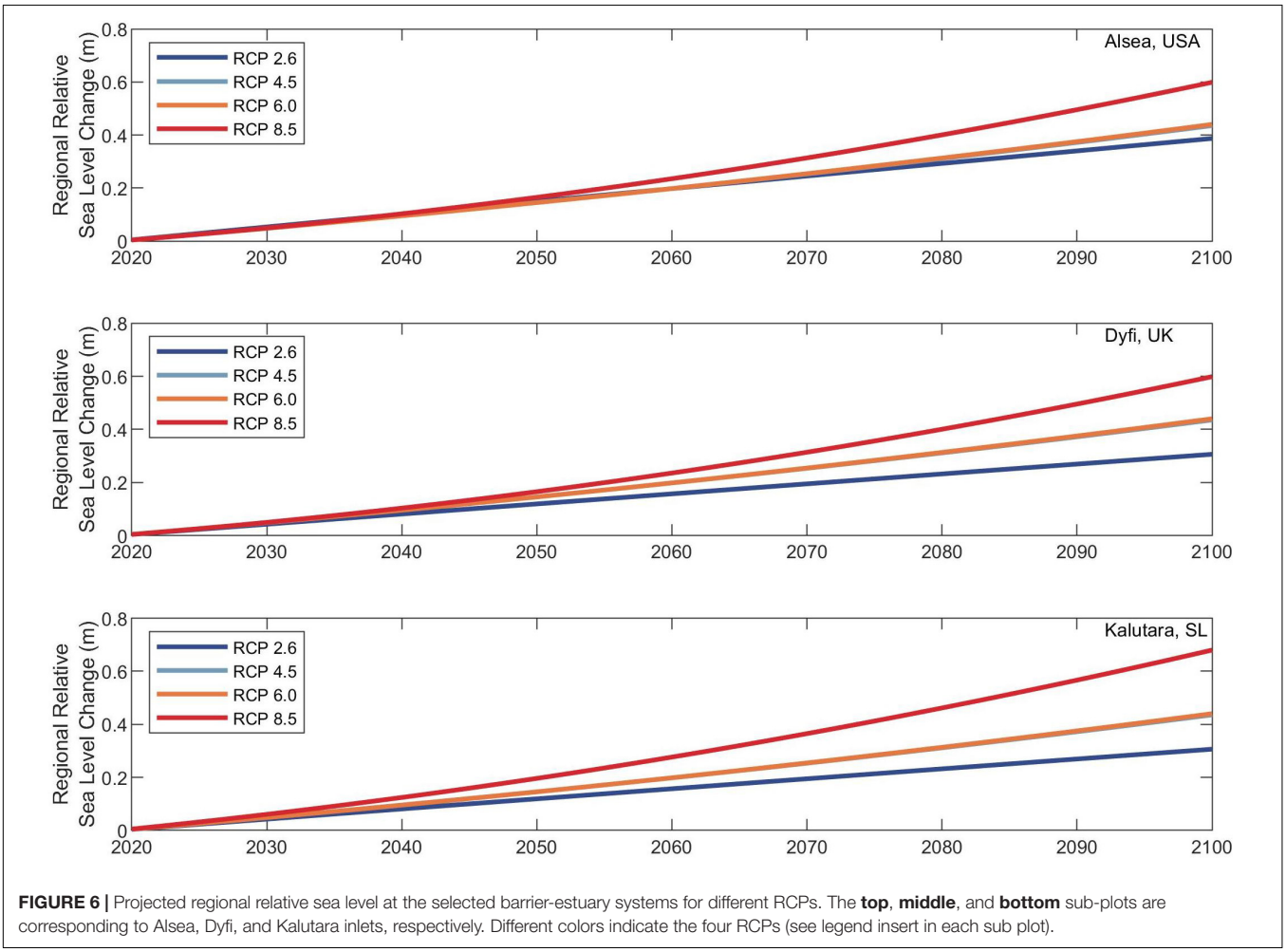

FIGURE 6 | Projected regional relative sea level at the selected barrier-estuary systems for different RCPs. The **top**, **middle**, and **bottom** sub-plots are corresponding to Alsea, Dyfi, and Kalutara inlets, respectively. Different colors indicate the four RCPs (see legend insert in each sub plot).

The model projections indicate that the Kalutara estuary system will also import sediment from the adjacent coast throughout the 21st century. The maximum and minimum projected volumes of sediment imports by 2100 are −7.0 MCM (RCP 2.6) and -3.0 MCM (RCP 8.5). The results here indicate that ΔV_T at the Kalutara estuary system is governed by the fluvial sediment supply (ΔV_{FS}), while projected variations of ΔV_{BV} and ΔV_{BI} have trivial impacts on ΔV_T for all RCPs. However, it should be noted that the fluvial sediment supply from the Kalu River catchment is significantly affected by river sand mining (Bamunawala et al., 2018b), which is taken into account in these simulations (423,000 m^3/yr). Model projections show that,

TABLE 3 | Comparison of the model hindcasted rates of coastline change over 1986–2005 with the ambient shoreline change rates presented by Luijendijk et al. (2018) over the same period.

CEC system	Rate of coastline change over 1986–2005 (m/yr)	
	Luijendijk et al. (2018)	RC model hindcast
Alsea estuary (United States)	−0.7	−0.5
Dyfi estuary (United Kingdom)	−1.0	−0.8
Kalutara estuary (Sri Lanka)	−1.0	−0.7

Negative rates of coastline change indicate coastline recession.

despite river sand mining, Kalutara estuary will export sediment to the adjacent coast during the end-century period for RCP 8.5. This is due to the significant increments of the projected T and Q (**Table 2**) over 2091–2100 (relative to the reference period), which substantially increases ΔV_{FS}, and to a lesser degree ΔV_{BV}.

Projected Coastline Change at the Case Study Locations: 2020–2100

The ΔV_T values computed in section "Projected Variation of Total Sediment Volume Exchange (ΔV_T): 2020–2100" were used to determine the changes in the position of the coastlines adjacent to the three case studies (**Figure 10**). All the coastline change projections presented here exclude ambient coastline changes. Therefore, the actual (resultant) coastline changes by 2060 and 2100 might be different to what is computed and presented in **Figure 10**.

At the Alsea estuary, the sediment volume demand of the basin (i.e., ΔV_T) acts as a sink at the inlet. However, the magnitude of ΔV_T is smaller than the existing LST capacity at the inlet. Therefore, the down-drift coast will be subjected to additional coastline recession driven by the ΔV_T, over and above that due to the Bruun effect. The total recession along the down-drift coast may vary between 71 m (RCP 2.6) and 75 m (RCP 8.5) by 2100. The up-drift coast is only affected by the coastline recession due to the Bruun effect, which is projected to vary between 50 m (RCP 2.6) and 70 m (RCP 8.5) by 2100.

At the Dyfi estuary too, ΔV_T causes the inlet to act as a sediment sink. As the magnitude of ΔV_T here is greater than the existing LST capacity at the inlet, both the up- and down-drift coast should provide sediment to the basin. Thus, both the up- and down-drift coasts will be subjected to additional coastline recession driven by the ΔV_T, over and above that of Bruun effect. The extent of additional coastline recession along the down-drift coastline is constrained by the longshore sediment transport capacity while that along the up-drift coast corresponds to the deficit in sediment volume (i.e., the difference between the estuarine sediment demand and longshore sediment transport capacity). The model projections indicate that the down-drift coast at the Dyfi estuary may erode by 78 m (RCP 2.6) to 96 m (RCP 8.5) by 2100. However, the up-drift coast is projected to erode between 85 m (RCP 2.6) and 140 m (RCP 8.5) by 2100.

The Kalutara estuary is also projected to act as a sediment sink during all but the end-century period for RCP 8.5. Since these projected magnitudes of ΔV_T values are less than the existing LST capacity at the inlet, the down-drift coast will be subjected to additional coastline recession driven by ΔV_T, over and above the Bruun effect. Under RCP 8.5, the inlet acts as a sediment source during the end-century period, thus reducing recession due to Bruun effect along the down-drift coast. The projected coastline recession along the down-drift coast vary between 82 m (RCP 2.6) and 110 m (RCP 8.5) by 2100. The up-drift coast is only affected by the coastline recession due to the Bruun effect, which varies between 50 m (RCP 2.6) and 70 m (RCP 8.5) by 2100.

DISCUSSION

Application of the newly developed model to the three barrier estuary case-studies indicates that macro-time-scale evolution of

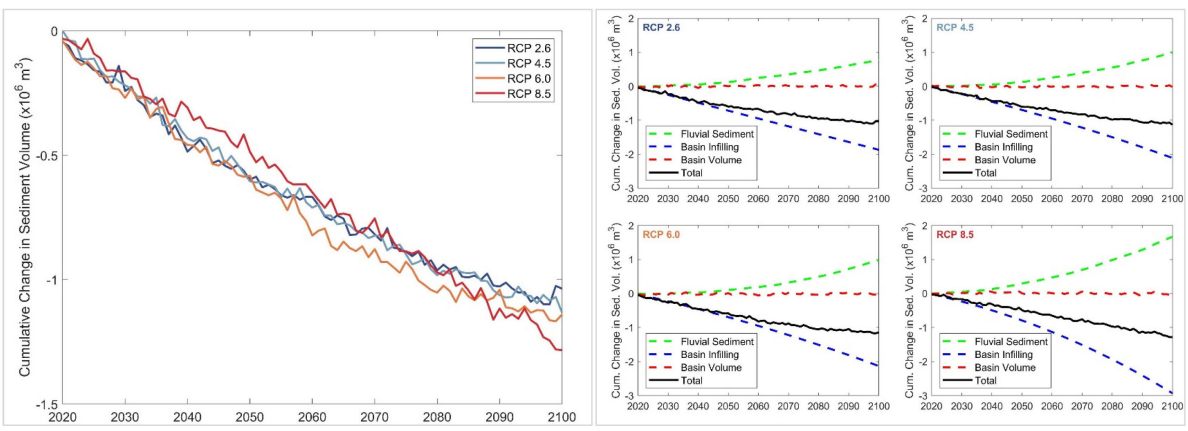

FIGURE 7 | Projected change in total sediment volume exchange (ΔV_T) between the Alsea estuary and the adjacent coast **(left)**, and the relative contributions of the three different sediment volume components **(right)** over the 21st century for RCP 2.6, 4.5, 6.0, and 8.5. Negative and positive values of ΔV_T indicate sediment imported to the estuary from the adjacent coast and sediment exported from the estuary to the adjacent coast, respectively.

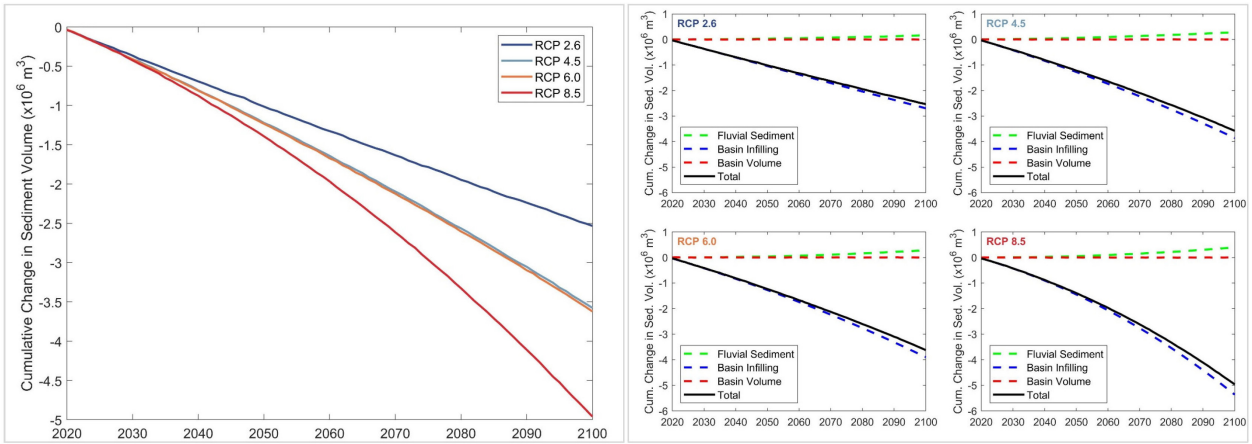

FIGURE 8 | Projected change in total sediment volume exchange (ΔV_T) between the Dyfi estuary and the adjacent coast **(left)**, and the relative contributions of the three different sediment volume components **(right)** over the 21st century for RCP 2.6, 4.5, 6.0, and 8.5. Negative and positive values of ΔV_T indicate sediment imported to the estuary from the adjacent coast and sediment exported from the estuary to the adjacent coast, respectively.

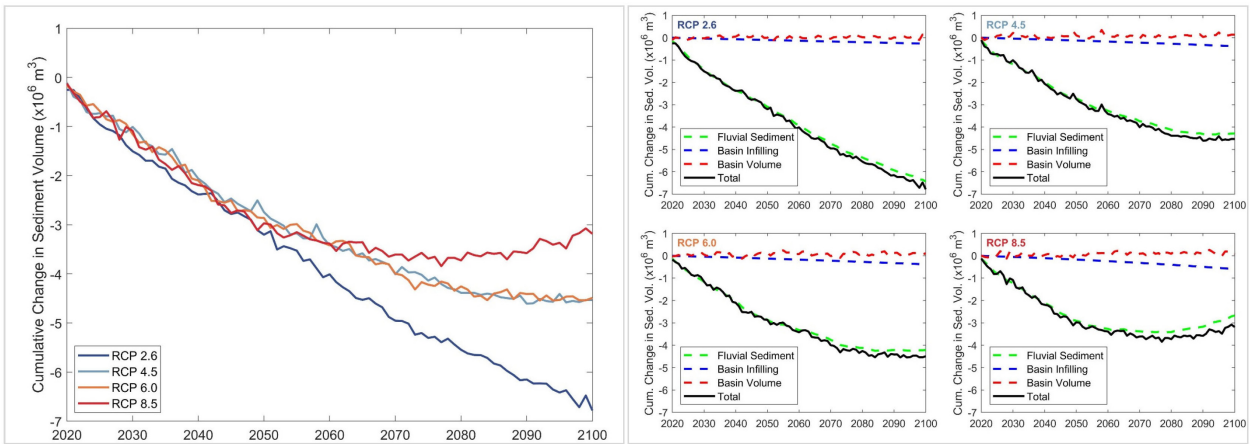

FIGURE 9 | Projected change in total sediment volume exchange (ΔV_T) between the Kalutara estuary and the adjacent coast **(left)**, and the relative contributions of the three different sediment volume components **(right)** over the 21st century for RCP 2.6, 4.5, 6.0, and 8.5. Negative and positive values of ΔV_T indicate sediment imported to the estuary from the adjacent coast and sediment exported from the estuary to the adjacent coast, respectively.

inlet-interrupted coasts under the influences of climate change-driven impacts and anthropogenic activities would vary markedly from system to system. Although the coastlines at these case study sites are projected to erode by the end of this century, the physical processes governing the erosion are different among the three systems.

Model projections show that the future sediment exchange between the estuary and the coast at both the Alsea and Dyfi estuary systems will be governed by the sediment demand due to basin infilling, although, the Alsea inlet system will also be partially influenced by fluvial sediment supply, especially toward the latter part of the 21st century. Due to the small projected changes in annual cumulative river discharges and the size of the basin volumes, both these systems are not affected by the sediment demand due to variations in basin volume size.

The projected future sediment exchange behavior at the Kalutara estuary system is rather different and is governed by the fluvial sediment supply. Due to the combined effects of the projected increments in temperature and river discharge, and anthropogenic activities, the Kalutara river catchment may generate a surplus of sediment throughout the 21st century. However, if the present practice of river sand mining continues, the catchment generated sediment surplus will be significantly reduced, resulting in eroding the adjacent coast. Due to the relatively small basin size (both volume and surface area), effects of sediment demand due to variations in basin volume size and basin infilling are negligible at the Kalutara CEC system.

The coastline change projections presented by Vousdoukas et al. (2020) indicate 50 m of erosion along both up-and down-drift coast of the Alsea estuary by 2100 for RCP 8.5. The same

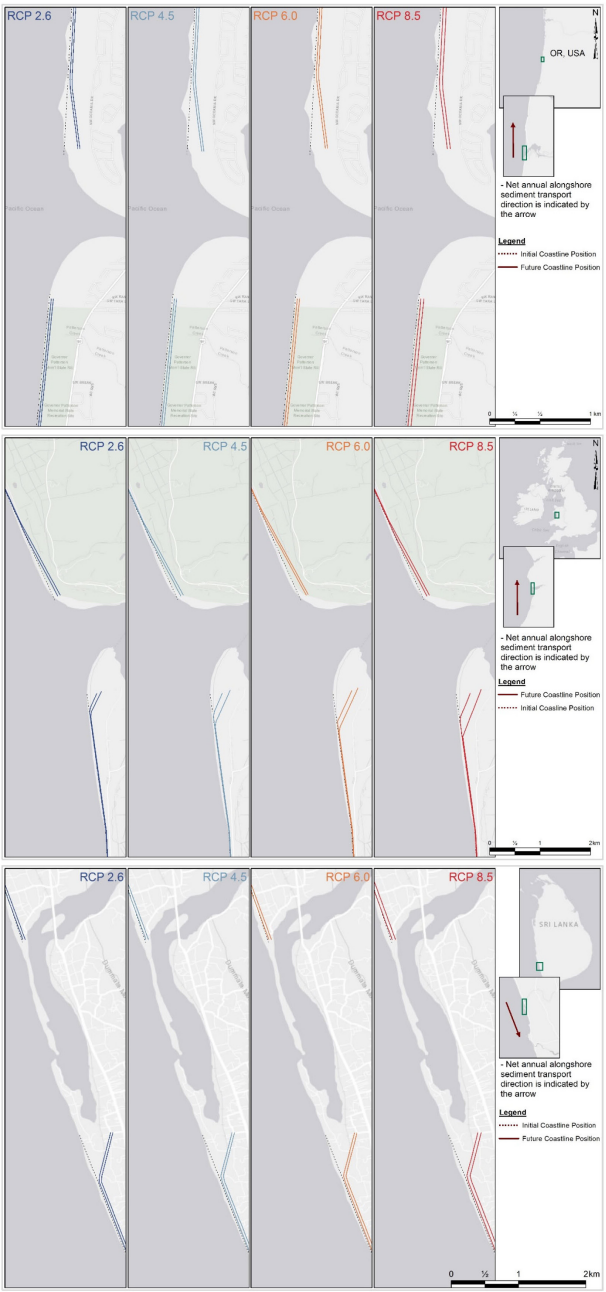

FIGURE 10 | Projected changes of the coastline adjacent to Alsea estuary **(top)**, Dyfi estuary **(middle)**, and Kalutara estuary **(bottom)** (excluding ambient coastline change). The two solid lines in each subplot represent the coastline position by 2060 and 2100 (in the same order, moving landward from the most seaward line). The dotted line in each subplot represents the initial (reference) coastline position considered.

study indicates 100 and 150 m erosion along both up-and down-drift coast of the Dyfi estuary and Kalutara inlet, respectively for RCP 8.5 by 2100. It should, however, be noted that the global assessment of sandy coastline variation presented by Vousdoukas et al. (2020) does not consider any estuarine effects and also incorporates a correction factor for Bruun effect-driven coastline recession. As a result, the model projections of the present study will, by necessity, differ from the coastline variation presented by Vousdoukas et al. (2020) at the study locations.

In the model presented here, everything seaward of the shoreline is considered as the "outside world," in order to avoid making this model over-complicated by bringing in complex ebb delta dynamics. Moreover, there are no significant ebb deltas in the three selected CEC systems. In general terms, the presence of ebb deltas would not affect the computation of sediment exchange volumes. However, if there is a significant ebb delta, in which the sand is mobile, part of the sediment demand of the inlet-estuary system (for an importing estuary) could be met by sand supply from the ebb delta. This will affect the coastline change projections by reducing the volume of sediment eroded from the coast. In such situations, the projections given by this model can be considered as pessimistic estimates of coastline recession. At sediment exporting inlet-estuary systems, part of the sediment supplied to the coast may contribute to the development of the ebb delta. Therefore, coastline changes projected by the model under these circumstances will over-predict coastline accretions (i.e., optimistic estimates).

It should also be noted that the simplified one-line coastline change model presented in this study only provides preliminary (i.e., first-order) estimates of variations along the inlet-interrupted coasts. This simplified modeling framework uses a relatively shallow profile (up to the depth of closure) and does not account for any local changes in coastline orientation (i.e., straight shoreline segments are assumed) or the presence of any coastal structures. Since the model projections are based on the total change in exchange volume between the inlet-estuary system and the adjacent coast, results presented here are the changes in coastline the would occur in addition to the ambient coastline change. Thus, the actual coastline changes by 2060 and 2100 might be different to that presented in this manuscript. In addition, for computational efficiency, the coastline change modeling used here treats the coastline up-drift and down-drift of the inlet separately, and as sequences of linear shoreline segments. This treatment results in a rather coarse representation of coastline change and does not resolve subtle coastline curvatures that are coupled with gradients in net alongshore sediment transport and shoreline change rates, which has implications for the way in which erosion or progradation might propagate along the coast. Coupling the terrestrial and estuarine model components with a coastline change model that is able to simulate more realistic changes in coastline shape and orientation [e.g., Coastline Evolution Model (CEM); Ashton and Murray, 2006; the Coastal One-line Vector Evolution Model (COVE); Hurst et al., 2015, or ShorelineS, Roelvink et al., 2020], will improve model predictions significantly. Usage of such a coastline change model will enable more realistic forecasts of changes in coastline shape and orientation, which equate to the capacity to predict shoreline-change hot spots, in response to future changes in wave climate (Slott et al., 2006; Hurst et al., 2015; Anderson et al., 2018; Antolínez et al., 2018). Besides, future changes in wave climate may also alter the in longshore sediment transport rates and gradients therein. Such variations in LST may affect the evolution

of inlet-interrupted coasts and thus need to be considered via detailed site-specific assessments of coastline change.

Results of this study show that fundamental CEC system properties such as basin volume and surface area, river catchment area and projected climatic conditions over the river catchment are closely related to the long-term evolution of inlet-interrupted coasts. The existence of any generally applicable relationships/dependencies between these properties/forcing and coastline change could be investigated by applying the model presented here at a larger number of CEC systems with diverse environmental and geographical settings.

There are significant uncertainties in future climate change and anthropogenic activities that need to be borne in mind when considering the projections of coastline change provided here, especially at small tidal-inlet systems, which are highly sensitive to changes in forcing conditions. As a result [in addition to the uncertainties associated with the modeling technique(s) adopted], projections of inlet-interrupted coastline changes will inherit the variabilities in climate change forcing and anthropogenic activities (i.e., input uncertainties) considered. In some situations, for example, to inform catchment/coastal zone management decisions, it may be desirable to have a quantitative understanding of the separate contribution of climate change and anthropogenic activities to the total uncertainty of the coastline change projections. This may be achieved via a Variance Based Sensitivity Analysis (VBSA) using Sobol indices (Sobol', 2001) as done by Le Cozannet et al. (2019).

CONCLUSION

A new model that can rapidly simulate the climate-change driven evolution of inlet-interrupted coasts at 50–100 year time scales, while taking into account the contributions from catchment-estuary-coastal systems in a holistic manner has been developed and piloted at three different case study locations. The spatio-temporal evolution of inlet-interrupted coasts is simulated by (1) computing the variation of total sediment volume exchange between the inlet-estuary system and its adjacent coast (ΔV_T), and (2) distributing the computed ΔV_T along the inlet-interrupted coast as a spatially and temporally varying quantity. The exchange volume ΔV_T is calculated as a function of variations in fluvial sediment supply (ΔV_{FS}), basin (or estuarine) infilling due to the sea-level rise-induced increase in accommodation space (ΔV_{BI}), and estuarine sediment volume change due to variations in river discharge (ΔV_{BV}).

The three case study locations considered in this study are: the Alsea estuary (Oregon, United States), Dyfi estuary (Wales, United Kingdom), and Kalutara inlet (Sri Lanka), which broadly represent some of the barrier estuary systems and geomorphic settings found across the world. The model was first validated at the three case study locations against the satellite image derived ambient shoreline change rates presented by Luijendijk et al. (2018) over 1986–2005. Subsequently, the model was applied in forecast mode at the case study sites, with the aim of investigating system behavior under projected climate-change impacts and anthropogenic activities.

Results indicated that all three systems will experience sediment deficits by 2100 (i.e., sediment importing estuaries) leading to coastline recession along the inlet-adjacent coasts. However, the processes and system characteristics governing the total sediment exchange volume, and thus coastline change, vary among the systems due to differences in geomorphic settings and projected climatic conditions. Therefore, the results of this study demonstrate the importance of carefully considering catchment and estuarine processes (i.e., fluvial sediment supply, basin infilling and basin volume change) in obtaining projections of coastline change at inlet-interrupted coasts at macro time scales.

DATA AVAILABILITY STATEMENT

The raw data supporting the conclusions of this article will be made available by the authors, without undue reservation, to any qualified researcher.

AUTHOR CONTRIBUTIONS

JB, AD, AS, and RR conceived and designed the study. JB developed the model, carried out all model applications, and wrote the first draft of the manuscript. SM provided specific guidance on the catchment hydrology aspects of the study. TD provided specific guidance on the SMIC model adaptation, and QA'd the new code. TS assisted with GCM data collection and catchment delineation. All authors provided feedback on the manuscript and contributed text.

FUNDING

This study was part of JB's Ph.D. research which was supported by the Deltares research program "Understanding System Dynamics; from River Basin to Coastal Zone" and the AXA Research Fund.

ACKNOWLEDGMENTS

JB was supported by the Deltares research program "Understanding System Dynamics; from River Basin to Coastal Zone" and the AXA Research Fund. RR is supported by the AXA Research Fund and the Deltares Strategic Research Programme "Coastal and Offshore Engineering." Last of the Wild Project, Global Human Footprint, Version 2 data were developed by the Wildlife Conservation Society – WCS and the Columbia University Center for International Earth Science Information Network (CIESIN), Columbia University and were obtained from the NASA Socioeconomic Data and Applications Center (SEDAC) at http://dx.doi.org/10.7927/H4M61H5F, accessed 1 October 2015. Any use of trade, firm, or product names is for descriptive purposes only and does not imply endorsement by the U.S. Government.

REFERENCES

Anderson, D., Ruggiero, P., Antolínez, J. A. A., Méndez, F. J., and Allan, J. (2018). A climate index optimized for longshore sediment transport reveals interannual and multidecadal littoral cell rotations. *J. Geophys. Res. Earth Surf.* 123, 1958–1981. doi: 10.1029/2018JF004689

Anthony, E. J., Besset, M., Dussouillez, P., Goichot, M., and Loisel, H. (2019). Overview of the Monsoon-influenced Ayeyarwady River delta, and delta shoreline mobility in response to changing fluvial sediment supply. *Mar. Geol.* 417:106038. doi: 10.1016/j.margeo.2019.106038

Anthony, E. J., Brunier, G., Besset, M., Goichot, M., Dussouillez, P., and Nguyen, V. L. (2015). Linking rapid erosion of the Mekong River delta to human activities. *Sci. Rep.* 5:14745. doi: 10.1038/srep14745

Anthony, E. J., Gardel, A., Proisy, C., Fromard, F., Gensac, E., Peron, C., et al. (2013). The role of fluvial sediment supply and river-mouth hydrology in the dynamics of the muddy, Amazon-dominated Amapá–Guianas coast, South America: a three-point research agenda. *J. South Am. Earth Sci.* 44, 18–24. doi: 10.1016/j.jsames.2012.06.005

Antolínez, J. A. A., Murray, A. B., Méndez, F. J., Moore, L. J., Farley, G., and Wood, J. (2018). Downscaling changing coastlines in a changing climate: the hybrid approach. *J. Geophys. Res. Earth Surf.* 123, 229–251. doi: 10.1002/2017JF004367

Ashton, A. D., and Murray, A. B. (2006). High-angle wave instability and emergent shoreline shapes: 1. Modeling of sand waves, flying spits, and capes. *J. Geophys. Res. Earth Surf.* 111:F04012. doi: 10.1029/2005JF000422

Athanasiou, P., van Dongeren, A., Giardino, A., Vousdoukas, M., Gaytan-Aguilar, S., and Ranasinghe, R. (2019). Global distribution of nearshore slopes with implications for coastal retreat. *Earth Syst. Sci. Data Discuss.* 2019, 1–29. doi: 10.5194/essd-2019-71

Aubrey, D. G., and Weishar, L. (eds) (1988). *Hydrodynamics and Sediment Dynamics of Tidal Inlets*. New York, NY: Springer.

Baart, F., Gelder, P. H. A. J. M., van Ronde, J., de Koningsveld, M., and van Wouters, B. (2012). The effect of the 18.6-year lunar nodal cycle on regional sea-level rise estimates. *J. Coast. Res.* 28, 511–516. doi: 10.2112/JCOASTRES-D-11-00169.1

Balthazar, V., Vanacker, V., Girma, A., Poesen, J., and Golla, S. (2013). Human impact on sediment fluxes within the Blue Nile and Atbara River basins. *Geomorphology* 180–181, 231–241. doi: 10.1016/j.geomorph.2012.10.013

Bamunawala, J., Maskey, S., Duong, T., and van der Spek, A. (2018a). Significance of fluvial sediment supply in coastline modelling at tidal inlets. *J. Mar. Sci. Eng.* 6:79. doi: 10.3390/jmse6030079

Bamunawala, J., Ranasinghe, R., van der Spek, A., Maskey, S., and Udo, K. (2018b). Assessing future coastline change in the vicinity of tidal inlets via reduced complexity modelling. *J. Coast. Res.* 85, 636–640. doi: 10.2112/SI85-128.1

Barnard, P. L., Foxgrover, A. C., Elias, E. P. L., Erikson, L. H., Hein, J. R., McGann, M., et al. (2013a). Integration of bed characteristics, geochemical tracers, current measurements, and numerical modeling for assessing the provenance of beach sand in the San Francisco Bay Coastal System. *Mar. Geol.* 336, 120–145. doi: 10.1016/j.margeo.2012.11.008

Barnard, P. L., Hansen, J. E., and Erikson, L. H. (2012). Synthesis study of an erosion hot spot, ocean beach, California. *J. Coast. Res.* 28, 903–922. doi: 10.2112/JCOASTRES-D-11-00212.1

Barnard, P. L., and Kvitek, R. G. (2010). Anthropogenic influence on recent bathymetric change in West-Central San Francisco Bay. *San Fr. Estuary Watershed Sci.* 8:13. doi: 10.15447/sfews.2010v8iss3art2

Barnard, P. L., Schoellhamer, D. H., Jaffe, B. E., and McKee, L. J. (2013b). Sediment transport in the San Francisco Bay coastal system: an overview. *Mar. Geol.* 345, 3–17. doi: 10.1016/j.margeo.2013.04.005

Bayram, A., Larson, M., and Hanson, H. (2007). A new formula for the total longshore sediment transport rate. *Coast. Eng.* 54, 700–710. doi: 10.1016/j.coastaleng.2007.04.001

Besset, M., Anthony, E. J., and Bouchette, F. (2019). Multi-decadal variations in delta shorelines and their relationship to river sediment supply: an assessment and review. *Earth Sci. Rev.* 193, 199–219. doi: 10.1016/j.earscirev.2019.04.018

Bruun, P. M. (1962). Sea-level rise as a cause of shore erosion. *Am. Soc. Civ. Eng. Proc. J. Waterw. Harb. Div.* 88, 117–132.

Casas-Prat, M., and Sierra, J. P. (2013). Projected future wave climate in the NW Mediterranean Sea. *J. Geophys. Res. Ocean.* 118, 3548–3568. doi: 10.1002/jgrc.20233

Casas-Prat, M., Wang, X. L., and Swart, N. (2018). CMIP5-based global wave climate projections including the entire Arctic Ocean. *Ocean Model.* 123, 66–85. doi: 10.1016/j.ocemod.2017.12.003

CERC (1984). *Shore Protection Manual*. Washington, DC: CERC.

Chu, Z. (2014). The dramatic changes and anthropogenic causes of erosion and deposition in the lower Yellow (Huanghe) River since 1952. *Geomorphology* 216, 171–179. doi: 10.1016/j.geomorph.2014.04.009

Cowell, P. J., Stive, M. J. F., Niedoroda, A. W., De-Vriend, H. J., Swift, D. J. P., Kaminsky, G. M., et al. (2003). The coastal-tract (Part 1): a conceptual approach to aggregated modeling of low-order coastal change. *J. Coast. Res.* 19, 812–827.

CSIRO, and Bureau of Meteorology (2015). *Climate Change in Australia Information for Australia's Natural Resource Management Regions: Technical Report*. Australia: CSIRO and Bureau of Meteorology.

Dallas, K. L., and Barnard, P. L. (2011). Anthropogenic influences on shoreline and nearshore evolution in the San Francisco Bay coastal system. *Estuar. Coast. Shelf Sci.* 92, 195–204. doi: 10.1016/j.ecss.2010.12.031

Dalrymple, R. W. (1992). "'Tidal depositional systems'," in *Facies Models: Response to Sea Level Change*, eds R. G. Walker and N. P. James (St John's: Geological Association of Canada), 195–218.

Dalrymple, R. W., and Choi, K. (2007). Morphologic and facies trends through the fluvial–marine transition in tide-dominated depositional systems: a schematic framework for environmental and sequence-stratigraphic interpretation. *Earth Sci. Rev.* 81, 135–174. doi: 10.1016/j.earscirev.2006.10.002

Dalrymple, R. W., and Choi, K. S. (2003). "'Sediment transport by tides'," in *Encyclopedia of Sediments and Sedimentary Rocks*, ed. G. V. Middleton (Dordrecht: Springer), 606–609.

Dastgheib, A., Reyns, J., Thammasittirong, S., Weesakul, S., Thatcher, M., and Ranasinghe, R. (2016). Variations in the wave climate and sediment transport due to climate change along the coast of vietnam. *J. Mar. Sci. Eng.* 4:86. doi: 10.3390/jmse4040086

Davis, R. A. Jr., and Fitzgerald, D. M. (2003). *Beaches and Coasts*. Hoboken, NJ: Wiley-Blackwell.

Davis, R. A. (1989). "Morphodynamics of the West-Central Florida barrier system: the delicate balance between wave- and tide-domination," in *Coastal Lowlands: Geology and Geotechnology*, eds W. J. M. van der Linden, S. A. P. L. Cloetingh, J. P. K. Kaasschieter, W. J. E. van de Graaff, J. Vandenberghe, and J. A. M. van der Gun (Dordrecht: Springer), 225–235. doi: 10.1007/978-94-017-1064-0_15

Davis, R. A., and Barnard, P. (2003). Morphodynamics of the barrier-inlet system, west-central Florida. *Mar. Geol.* 200, 77–101. doi: 10.1016/S0025-3227(03)00178-6

Davis, R. A., and Barnard, P. L. (2000). How anthropogenic factors in the back-barrier area influence tidal inlet stability: examples from the Gulf Coast of Florida, USA. *Geol. Soc. Lond. Spec. Publ.* 175, 293–303. doi: 10.1144/GSL.SP.2000.175.01.21

Davis, R. A., and Fox, W. T. (1981). Interaction between wave- and tide-generated processes at the mouth of a microtidal estuary: matanzas River, Florida (U.S.A.). *Mar. Geol.* 40, 49–68. doi: 10.1016/0025-3227(81)90042-6

Davis, R. A., and Hayes, M. O. (1984). What is a wave-dominated coast? *Mar. Geol.* 60, 313–329. doi: 10.1016/0025-3227(84)90155-5

Dronkers, J. J. (1964). *Tidal Computations in Rivers and Coastal Waters*. New York, NY: North-Holland Pub. Co.

Dunn, F. E., Darby, S. E., Nicholls, R. J., Cohen, S., Zarfl, C., and Fekete, B. M. (2019). Projections of declining fluvial sediment delivery to major deltas worldwide in response to climate change and anthropogenic stress. *Environ. Res. Lett.* 14:84034. doi: 10.1088/1748-9326/ab304e

Dunn, F. E., Nicholls, R. J., Darby, S. E., Cohen, S., Zarfl, C., and Fekete, B. M. (2018). Projections of historical and 21st century fluvial sediment delivery to the Ganges-Brahmaputra-Meghna, Mahanadi, and Volta deltas. *Sci. Total Environ.* 642, 105–116. doi: 10.1016/j.scitotenv.2018.06.006

Duong, T. M. (2015). *Climate Change Impacts on the Stability of Small Tidal Inlets*. Delft: Delft University of Technology.

Duong, T. M., Ranasinghe, R., Luijendijk, A., Walstra, D., and Roelvink, D. (2017). Assessing climate change impacts on the stability of small tidal inlets: part 1 - Data poor environments. *Mar. Geol.* 390, 331–346. doi: 10.1016/j.margeo.2017.05.008

Duong, T. M., Ranasinghe, R., Thatcher, M., Mahanama, S., Wang, Z. B., Dissanayake, P. K., et al. (2018). Assessing climate change impacts on the

stability of small tidal inlets: part 2 - Data rich environments. *Mar. Geol.* 395, 65–81. doi: 10.1016/j.margeo.2017.09.007

Duong, T. M., Ranasinghe, R., Walstra, D., and Roelvink, D. (2016). Assessing climate change impacts on the stability of small tidal inlet systems: why and how? *Earth Sci. Rev.* 154, 369–380. doi: 10.1016/j.earscirev.2015.12.001

Ericson, J. P., Vörösmarty, C. J., Dingman, S. L., Ward, L. G., and Meybeck, M. (2006). Effective sea-level rise and deltas: causes of change and human dimension implications. *Glob. Planet. Change* 50, 63–82. doi: 10.1016/j.gloplacha.2005.07.004

Erikson, L. H., Hegermiller, C. A., Barnard, P. L., Ruggiero, P., and van Ormondt, M. (2015). Projected wave conditions in the Eastern North Pacific under the influence of two CMIP5 climate scenarios. *Ocean Model.* 96, 171–185. doi: 10.1016/j.ocemod.2015.07.004

Farr, T. G., Rosen, P. A., Caro, E., Crippen, R., Duren, R., Hensley, S., et al. (2007). The shuttle radar topography mission. *Rev. Geophys.* 45:RG2004. doi: 10.1029/2005RG000183

FitzGerald, D., Georgiou, I., and Miner, M. (2015). "Estuaries and tidal inlets," in *Coastal Environments and Global Change Wiley Online Books*, eds G. Masselink and R. Gehrels (Chichester, UK: John Wiley & Sons, Ltd), 268–298. doi: 10.1002/9781119117261.ch12

FitzGerald, D. M., Georgiou, I., and Miner, M. (2014). "Estuaries and tidal inlets," in *Coastal Environments and Global Change*, eds G. Masselink and R. Gehrels (Sussex: John Wiley & Sons, Ltd and American Geophysical Union), 268–298. doi: 10.1002/9781119117261.ch12

French, J., Payo, A., Murray, B., Orford, J., Eliot, M., and Cowell, P. (2016). Appropriate complexity for the prediction of coastal and estuarine geomorphic behaviour at decadal to centennial scales. *Geomorphology* 256, 3–16. doi: 10.1016/j.geomorph.2015.10.005

Gao, S., and Collins, M. (1994). Tidal inlet equilibrium, in relation to cross-sectional area and sediment transport patterns. *Estuar. Coast. Shelf Sci.* 38, 157–172. doi: 10.1006/ecss.1994.1010

Grabemann, I., Groll, N., Möller, J., and Weisse, R. (2015). Climate change impact on North Sea wave conditions: a consistent analysis of ten projections. *Ocean Dyn.* 65, 255–267. doi: 10.1007/s10236-014-0800-z

Green, M. O. (2013). Catchment sediment load limits to achieve estuary sedimentation targets. *New Zeal. J. Mar. Freshw. Res.* 47, 153–180. doi: 10.1080/00288330.2012.757241

Hayes, M. O. (1980). General morphology and sediment patterns in tidal inlets. *Sediment. Geol.* 26, 139–156. doi: 10.1016/0037-0738(80)90009-3

Hemer, M. A., Fan, Y., Mori, N., Semedo, A., and Wang, X. L. (2013). Projected changes in wave climate from a multi-model ensemble. *Nat. Clim. Chang.* 3, 471–476. doi: 10.1038/nclimate1791

Hemer, M. A., McInnes, K. L., and Ranasinghe, R. (2012). Climate and variability bias adjustment of climate model-derived winds for a southeast Australian dynamical wave model. *Ocean Dyn.* 62, 87–104. doi: 10.1007/s10236-011-0486-4

Hume, T. M., and Herdendorf, C. E. (1993). On the use of empirical stability relationships for characterising estuaries. *J. Coast. Res.* 9, 413–422.

Hurst, M. D., Barkwith, A., Ellis, M. A., Thomas, C. W., and Murray, A. B. (2015). Exploring the sensitivities of crenulate bay shorelines to wave climates using a new vector-based one-line model. *J. Geophys. Res. Earth Surf.* 120, 2586–2608. doi: 10.1002/2015JF003704

Kamphuis, J. W. (1991). Alongshore sediment transport rate. *J. Waterw. Port Coast. Ocean Eng.* 117, 624–640. doi: 10.1061/(ASCE)0733-950X1991117:6(624)

Kettner, A. J., Syvitski, J. P., and Gomez, B. (2005). "Simulating the effects of natural events and anthropogenic activity on sediment discharge to the poverty shelf, new zealand during the late holocene," in *Proceedings of the Eos Trans. AGU, 86(52), Fall Meet. Suppl., Abstract H51C-0388* (Washington, DC: IEEE).

Keulegan, G. H. (1951). *Third Progress Report on Tidal Flow in Entrances, Water Level Fluctuations of Basins in Communication with Seas*. Report No. 1146. Washington D.C: National Bureau of Standards.

Le Cozannet, G., Bulteau, T., Castelle, B., Ranasinghe, R., Wöppelmann, G., Rohmer, J., et al. (2019). Quantifying uncertainties of sandy shoreline change projections as sea level rises. *Sci. Rep.* 9:42. doi: 10.1038/s41598-018-37017-4

Luijendijk, A., Hagenaars, G., Ranasinghe, R., Baart, F., Donchyts, G., and Aarninkhof, S. (2018). The State of the World's beaches. *Sci. Rep.* 8:6641. doi: 10.1038/s41598-018-24630-6

McGranahan, G., Balk, D., and Anderson, B. (2007). The rising tide: assessing the risks of climate change and human settlements in low elevation coastal zones. *Environ. Urban* 19, 17–37. doi: 10.1177/0956247807076960

McSweeney, S. L., Kennedy, D. M., Rutherfurd, I. D., and Stout, J. C. (2017). Intermittently Closed/Open Lakes and Lagoons: their global distribution and boundary conditions. *Geomorphology* 292, 142–152. doi: 10.1016/j.geomorph.2017.04.022

Mehvar, A., Dastgheib, A., and Ranasinghe, R. (2016). *Relative Sea Level Rise Scenarios: Central Coast of Bangladesh*. Delft: Delft University of Technology.

Mori, N., Yasuda, T., Mase, H., Tom, T., and Oku, Y. (2010). Projection of extreme wave climate change under global warming. *Hydrol. Res. Lett.* 4, 15–19. doi: 10.3178/hrl.4.15

Morim, J., Hemer, M., Wang, X. L., Cartwright, N., Trenham, C., Semedo, A., et al. (2019). Robustness and uncertainties in global multivariate wind-wave climate projections. *Nat. Clim. Chang.* 9, 711–718. doi: 10.1038/s41558-019-0542-5

Murray, A. B. (2007). Reducing model complexity for explanation and prediction. *Geomorphology* 90, 178–191. doi: 10.1016/j.geomorph.2006.10.020

Murray, A. B. (2013). "'Which models are good (enough), and when?'," in *Treatise on Geomorphology*, ed. J. F. Shroder (Oxford: Elsevier-Academic Press), 50–58. doi: 10.1016/b978-0-12-374739-6.00027-0

National Rivers Authority Welsh Region (1995). *Dyfi and Leri Catchment Management Plan Consultation Report*. Bristol: National Rivers Authority Welsh Region.

Neumann, B., Vafeidis, A. T., Zimmermann, J., and Nicholls, R. J. (2015). Future coastal population growth and exposure to sea-level rise and coastal flooding - a global assessment. *PLoS One* 10:e0118571. doi: 10.1371/journal.pone.0118571

Nicholls, R. J., Hanson, S. E., Lowe, J. A., Warrick, R. A., Lu, X., and Long, A. J. (2014). Sea-level scenarios for evaluating coastal impacts. *Wiley Interdiscip. Rev. Clim. Chang.* 5, 129–150. doi: 10.1002/wcc.253

O'Brien, M. P. (1969). Equilibrium flow areas of tidal inlets on sandy coasts. *J. Waterw. Harb. Div.* 95, 43–52.

O'Neil, D. J. (1987). Variations in Alsea River Flow; Implications for Alsea Spit & Inlet Stability. Department of Geography, Oregon State University, Oregon.

Oppenheimer, M., Glavovic, B. C., Hinkel, J., Van-de-Wal, R., Magnan, A. K., Abd-Elgawad, A., et al. (2019). "Sea level rise and implications for low-lying islands, coasts and communities," in *IPCC Special Report on the Ocean and Cryosphere in a Changing Climate*, eds H.-O. Pörtner, D. C. Roberts, V. Masson-Delmotte, P. Zhai, M. Tignor, and E. Poloczanska (Geneva: IPCC).

Overeem, I., Kettner, A. J., and Syvitski, J. P. M. (2013). "Impacts of humans on river fluxes and morphology," in *Treatise on Geomorphology*, eds J. F. Shroder, and E. Wohl (Amsterdam: Elsevier), 828–842. doi: 10.1016/b978-0-12-374739-6.00267-0

Overeem, I., and Syvitski, J. P. M. (2009). *Dynamics and Vulnerability of Delta Systems*. Geesthacht: GKSS Research Center. LOICZ Reports & Studies No. 35.

Palmer, M. A., Liermann, C. A. R., Nilsson, C., Flörke, M., Alcamo, J., Lake, P. S., et al. (2008). Climate change and the world's river basins: anticipating management options. *Front. Ecol. Environ.* 6, 81–89. doi: 10.1890/060148

Paola, C. (2000). Quantitative models of sedimentary basin filling. *Sedimentology* 47, 121–178. doi: 10.1046/j.1365-3091.2000.00006.x

Peng, D., Hill, E. M., Meltzner, A. J., and Switzer, A. D. (2019). Tide Gauge Records Show That the 18.61-Year Nodal Tidal Cycle Can Change High Water Levels by up to 30 cm. *J. Geophys. Res. Ocean.* 124, 736–749. doi: 10.1029/2018JC014695

Pickering, M. D., Horsburgh, K. J., Blundell, J. R., Hirschi, J. J.-M., Nicholls, R. J., Verlaan, M., et al. (2017). The impact of future sea-level rise on the global tides. *Cont. Shelf Res.* 142, 50–68. doi: 10.1016/j.csr.2017.02.004

Ranasinghe, R. (2016). Assessing climate change impacts on open sandy coasts: a review. *Earth Sci. Rev.* 160, 320–332. doi: 10.1016/j.earscirev.2016.07.011

Ranasinghe, R. (2020). On the need for a new generation of coastal change models for the 21st century. *Sci. Rep.* 10:2010. doi: 10.1038/s41598-020-58376-x

Ranasinghe, R., Duong, T. M., Uhlenbrook, S., Roelvink, D., and Stive, M. (2013). Climate-change impact assessment for inlet-interrupted coastlines. *Nat. Clim. Chang.* 3, 83–87. doi: 10.1038/nclimate1664

Ranasinghe, R., Pattiaratchi, C., and Masselink, G. (1999). A morphodynamic model to simulate the seasonal closure of tidal inlets. *Coast. Eng.* 37, 1–36. doi: 10.1016/S0378-3839(99)00008-3

Ranasinghe, R., Wu, C. S., Conallin, J., Duong, T. M., and Anthony, E. J. (2019). Disentangling the relative impacts of climate change and human activities on

fluvial sediment supply to the coast by the world's large rivers: pearl River Basin, China. *Sci. Rep.* 9:9236. doi: 10.1038/s41598-019-45442-2

Roelvink, D., Huisman, B., Elghandour, A., Ghonim, M., and Reyns, J. (2020). Efficient modeling of complex sandy coastal evolution at monthly to century time scales. *Front. Mar. Sci.* doi: 10.3389/fmars.2020.00535

Samaras, A. G., and Koutitas, C. G. (2012). An integrated approach to quantify the impact of watershed management on coastal morphology. *Ocean Coast. Manag.* 69, 68–77. doi: 10.1016/j.ocecoaman.2012.08.010

Sanderson, E. W., Jaiteh, M., Levy, M., Redford, K. H., Wannebo, A. V., and Woolmer, G. (2002). The Human Footprint and the Last of the Wild. *Bioscience* 52, 891–904.

Semedo, A., Weisse, R., Behrens, A., Sterl, A., Bengtsson, L., and Günther, H. (2013). Projection of global wave climate change toward the end of the Twenty-First Century. *J. Clim.* 26, 8269–8288. doi: 10.1175/JCLI-D-12-00658.1

Shennan, I., Coulthard, T., Flather, R., Horton, B., Macklin, M., Rees, J., et al. (2003). Integration of shelf evolution and river basin models to simulate Holocene sediment dynamics of the Humber Estuary during periods of sea-level change and variations in catchment sediment supply. *Sci. Total Environ.* 31, 737–754. doi: 10.1016/S0048-9697(03)00081-0

Shimura, T., Mori, N., and Hemer, M. A. (2016). Variability and future decreases in winter wave heights in the Western North Pacific. *Geophys. Res. Lett.* 43, 2716–2722. doi: 10.1002/2016GL067924

Shrestha, B., Babel, M. S., Maskey, S., van Griensven, A., Uhlenbrook, S., Green, A., et al. (2013). Impact of climate change on sediment yield in the Mekong River basin: a case study of the Nam Ou basin, Lao PDR. *Hydrol. Earth Syst. Sci.* 17, 1–20. doi: 10.5194/hess-17-1-2013

Slagel, M. J., and Griggs, G. B. (2008). Cumulative Losses of Sand to the California Coast by Dam Impoundment. *J. Coast. Res.* 243, 571–584. doi: 10.2112/06-0640.1

Slott, J. M., Murray, A. B., Ashton, A. D., and Crowley, T. J. (2006). Coastline responses to changing storm patterns. *Geophys. Res. Lett.* 33:L18404. doi: 10.1029/2006GL027445

Sobol, I. M. (2001). Global sensitivity indices for nonlinear mathematical models and their Monte Carlo estimates. *Math. Comput. Simul.* 55, 271–280. doi: 10.1016/S0378-4754(00)00270-6

Stive, M. J. F. (2004). How important is global warming for coastal erosion? *Clim. Change* 64, 27–39. doi: 10.1023/B:CLIM.0000024785.91858.1d

Stive, M. J. F., Capobianco, M., Wang, Z. B., Ruol, P., and Buijsman, M. C. (1998). "'Morphodynamics of a tidal lagoon and the adjacent coast'," in *Physics of Estuaries and Coastal Seas*, eds J. Dronkers and M. Scheffers (Rotterdam: A. A. Balkema), 397–407.

Stive, M. J. F., and Wang, Z. B. (2003). "'Morphodynamic modeling of tidal basins and coastal inlets'," in *Advances in Coastal Modeling*, ed. V. C. B. T.-E. O. S. Lakhan (Oxford: Elsevier), 367–392. doi: 10.1016/s0422-9894(03)80130-7

Stocker, T. F., Qin, D., Plattner, G.-K., Alexander, L. V., Allen, S. K., Bindoff, N. L., et al. (2013a). "Technical summary," in *Climate Change 2013: The Physical Science Basis. Contribution of Working Group I to the Fifth Assessment Report of the Intergovernmental Panel on Climate Change*, eds T. F. Stocker, D. Qin, G.-K. Plattner, M. Tignor, S. K. Allen, J. Boschung, et al. (Cambridge, MA: Cambridge University Press).

Stocker, T. F., Qin, D., Plattner, G.-K., Tignor, M., Allen, S. K., Boschung, J., et al. (eds) (2013b). "IPCC, 2013: summary for policymakers," in *Climate Change 2013: The Physical Science Basis. Contribution of Working Group I to the Fifth Assessment Report of the Intergovernmental Panel on Climate Change* (Cambridge: Cambridge University Press).

Syvitski, J. P. M. (2005). Impact of humans on the flux of terrestrial sediment to the Global Coastal Ocean. *Science* 308, 376–380. doi: 10.1126/science.1109454

Syvitski, J. P. M. (2008). Deltas at risk. *Sustain. Sci.* 3, 23–32. doi: 10.1007/s11625-008-0043-3

Syvitski, J. P. M., Kettner, A. J., Overeem, I., Hutton, E. W. H., Hannon, M. T., Brakenridge, G. R., et al. (2009). Sinking deltas due to human activities. *Nat. Geosci.* 2, 681–686. doi: 10.1038/ngeo629

Syvitski, J. P. M., and Milliman, J. D. (2007). Geology, geography, and humans battle for dominance over the delivery of fluvial sediment to the Coastal Ocean. *J. Geol.* 115, 1–19. doi: 10.1086/509246

Syvitski, J. P. M., Peckham, S. D., Hilberman, R., and Mulder, T. (2003). Predicting the terrestrial flux of sediment to the global ocean: a planetary perspective. *Sediment. Geol.* 162, 5–24. doi: 10.1016/S0037-0738(03)00232-X

Syvitski, J. P. M., and Saito, Y. (2007). Morphodynamics of deltas under the influence of humans. *Glob. Planet. Change* 57, 261–282. doi: 10.1016/j.gloplacha.2006.12.001

Szabo, S., Brondizio, E., Renaud, F. G., Hetrick, S., Nicholls, R. J., Matthews, Z., et al. (2016). Population dynamics, delta vulnerability and environmental change: comparison of the Mekong, Ganges–Brahmaputra and Amazon delta regions. *Sustain. Sci.* 11, 539–554. doi: 10.1007/s11625-016-0372-6

Tessler, Z. D., Vorosmarty, C. J., Grossberg, M., Gladkova, I., Aizenman, H., Syvitski, J. P. M., et al. (2015). Profiling risk and sustainability in coastal deltas of the world. *Science* 349, 638–643. doi: 10.1126/science.aab3574

Townend, I. (2005). An examination of empirical stability relationships for UK estuaries. *J. Coast. Res.* 2005, 1042–1053. doi: 10.2112/03-0066R.1

Veerbeek, W. (2017). *Estimating the Impacts of Urban Growth on Future Flood Risk: A Comparative Study*. Delft: Delft University of Technology.

Verstraeten, G., and Poesen, J. (2001). Factors controlling sediment yield from small intensively cultivated catchments in a temperate humid climate. *Geomorphology* 40, 123–144. doi: 10.1016/S0169-555X(01)00040-X

Vörösmarty, C. J., Meybeck, M., Fekete, B., Sharma, K., Green, P., and Syvitski, J. P. M. (2003). Anthropogenic sediment retention: major global impact from registered river impoundments. *Glob. Planet. Change* 39, 169–190. doi: 10.1016/S0921-8181(03)00023-7

Vousdoukas, M. I., Ranasinghe, R., Mentaschi, L., Plomaritis, T. A., Athanasiou, P., Luijendijk, A., et al. (2020). Sandy coastlines under threat of erosion. *Nat. Clim. Chang.* 10, 260–263. doi: 10.1038/s41558-020-0697-0

Walling, D. E. (2009). *The Impact of Global Change on Erosion and Sediment Transport by Rivers: Current Progress and Future Challenges*. The United Nations World Water Development Report 3 Water in a Changing World. Paris: UNESCO-IHP.

Wildlife Conservation Society [WCS], and Columbia University Center for International Earth Science Information Network [CIESIN] (2005). *Last of the Wild Project, Version 2, 2005 (LWP-2): Global Human Footprint Dataset (Geographic)*. Palisades, NY: CIESIN.

Wolf, J., Lowe, J., and Howard, T. (2015). "Climate downscaling: local mean sea level, surge and wave modelling," in *Broad Scale Coastal Simulation. Advances in Global Change Research*, eds R. J. Nicholls, R. Dawson, and S. Day (Dordrecht: Springer), 79–102. doi: 10.1007/978-94-007-5258-0_2

Wong, P. P., Losada, I. J., Gattuso, J.-P., Hinkel, J., Khattabi, A., McInnes, K. L., et al. (2014). "'Coastal systems and low-lying areas'," in *Climate Change 2014: Impacts, Adaptation, and Vulnerability. Part A: Global and Sectoral Aspects. Contribution of Working Group II to the Fifth Assessment Report of the Intergovernmental Panel on Climate Change*, eds C. B. Field, V. R. Barros, D. J. Dokken, K. J. Mach, M. D. Mastrandrea, T. E. Bilir, et al. (Cambridge: Cambridge University Press), 361–409.

Woodroffe, C. D. (2003). *Coasts: Form, Process and Evolution*. Cambridge, MA: Cambridge University Press.

Yang, H. F., Yang, S. L., Xu, K. H., Milliman, J. D., Wang, H., Yang, Z., et al. (2018). Human impacts on sediment in the Yangtze River: a review and new perspectives. *Glob. Planet. Change* 162, 8–17. doi: 10.1016/j.gloplacha.2018.01.001

Yang, S. L., Li, M., Dai, S. B., Liu, Z., Zhang, J., and Ding, P. X. (2006). Drastic decrease in sediment supply from the Yangtze River and its challenge to coastal wetland management. *Geophys. Res. Lett.* 33:L06408. doi: 10.1029/2005GL025507

Conflict of Interest: The authors declare that the research was conducted in the absence of any commercial or financial relationships that could be construed as a potential conflict of interest.

frontiers in Marine Science

ORIGINAL RESEARCH
published: 16 December 2020
doi: 10.3389/fmars.2020.579203

Probabilistic Application of an Integrated Catchment-Estuary-Coastal System Model to Assess the Evolution of Inlet-Interrupted Coasts Over the 21st Century

Janaka Bamunawala[1,2], Ali Dastgheib[2], Roshanka Ranasinghe[1,2,3], Ad van der Spek[4,5], Shreedhar Maskey[2], A. Brad Murray[6], Patrick L. Barnard[7], Trang Minh Duong[1,2,3] and T. A. J. G. Sirisena[1,2]*

[1] Department of Water Engineering & Management, University of Twente, Enschede, Netherlands, [2] IHE Delft Institute for Water Education, Delft, Netherlands, [3] Harbour, Coastal and Offshore Engineering, Deltares, Delft, Netherlands, [4] Applied Morphodynamics, Deltares, Delft, Netherlands, [5] Department of Physical Geography, Faculty of Geosciences, Utrecht University, Utrecht, Netherlands, [6] Division of Earth and Ocean Sciences, Nicholas School of the Environment, Center for Nonlinear and Complex Systems, Duke University, Durham, NC, United States, [7] United States Geological Survey, Pacific Coastal and Marine Science Center, Santa Cruz, CA, United States

OPEN ACCESS

Edited by:
Zeng Zhou,
Hohai University, China

Reviewed by:
Pushpa Dissanayake,
University of Kiel, Germany
Andrea D'Alpaos,
University of Padua, Italy

***Correspondence:**
Janaka Bamunawala
j.bamunawala@gmail.com

Specialty section:
This article was submitted to Coastal Ocean Processes, a section of the journal Frontiers in Marine Science

Received: 01 July 2020
Accepted: 23 November 2020
Published: 16 December 2020

Citation:
Bamunawala J, Dastgheib A, Ranasinghe R, van der Spek A, Maskey S, Murray AB, Barnard PL, Duong TM and Sirisena TAJG (2020) Probabilistic Application of an Integrated Catchment-Estuary-Coastal System Model to Assess the Evolution of Inlet-Interrupted Coasts Over the 21st Century. Front. Mar. Sci. 7:579203. doi: 10.3389/fmars.2020.579203

Inlet-interrupted sandy coasts are dynamic and complex coastal systems with continuously evolving geomorphological behaviors under the influences of both climate change and human activities. These coastal systems are of great importance to society (e.g., providing habitats, navigation, and recreational activities) and are affected by both oceanic and terrestrial processes. Therefore, the evolution of these inlet-interrupted coasts is better assessed by considering the entirety of the Catchment-Estuary-Coastal (CEC) systems, under plausible future scenarios for climate change and increasing pressures due to population growth and human activities. Such a holistic assessment of the long-term evolution of CEC systems can be achieved via reduced-complexity modeling techniques, which are also ably quantifying the uncertainties associated with the projections due to their lower simulation times. Here, we develop a novel probabilistic modeling framework to quantify the input-driven uncertainties associated with the evolution of CEC systems over the 21st century. In this new approach, probabilistic assessment of the evolution of inlet-interrupted coasts is achieved by (1) probabilistically computing the exchange sediment volume between the inlet-estuary system and its adjacent coast, and (2) distributing the computed sediment volumes along the inlet-interrupted coast. The model is applied at three case study sites: Alsea estuary (United States), Dyfi estuary (United Kingdom), and Kalutara inlet (Sri Lanka). Model results indicate that there are significant uncertainties in projected volume exchange at all the CEC systems (min-max range of 2.0 million cubic meters in 2100 for RCP 8.5), and the uncertainties in these projected volumes illustrate the need for probabilistic modeling approaches to evaluate the long-term evolution of CEC systems.

A comparison of 50th percentile probabilistic projections with deterministic estimates shows that the deterministic approach overestimates the sediment volume exchange in 2100 by 15–30% at Alsea and Kalutara estuary systems. Projections of coastline change obtained for the case study sites show that accounting for all key processes governing coastline change along inlet-interrupted coasts in computing coastline change results in projections that are between 20 and 134% greater than the projections that would be obtained if only the Bruun effect were taken into account, underlining the inaccuracies associated with using the Bruun rule at inlet-interrupted coasts.

Keywords: catchment-estuary-coastal systems, climate change, inlet-interrupted coasts, input uncertainties, probabilistic model

INTRODUCTION

The coastal zone is the dynamic link that connects the land and oceans and has always attracted human settlement because of its multiple uses, rich bio-diversity and resources. Due to the many activities that are of great importance to society [e.g., navigation and access, defense and military, tourism, use of various marine/ecosystem resources and services, waste disposal, development of various coastal infrastructures, research, art, and recreational activities (McGranahan et al., 2007; Wong et al., 2014; Neumann et al., 2015)], the Low Elevation Coastal Zone (LECZ) is heavily urbanized and comprises approximately 10% of the world's population (Vafeidis et al., 2011). Due to predicted population growth, economic development and urbanization, human pressures on coasts and coastal ecosystems will very likely increase significantly over the 21st century, with over 1 billion people expected to live in the coastal zone by 2050 (Hugo, 2011; Wong et al., 2014; Merkens et al., 2016). Apart from human-induced pressures, physical (environmental) forcing also places stresses on this environment, where projected climate-change driven variations in mean sea level, wave conditions, intensity and frequency of storm surges, and river flow will affect the coastal zone in many ways (FitzGerald et al., 2008; Syvitski and Kettner, 2008; Ranasinghe and Stive, 2009; Syvitski et al., 2009; Woodruff et al., 2013; Brown et al., 2014; Wong et al., 2014; Ranasinghe, 2016; Spencer et al., 2016). Rising sea level is likely to inundate many low-lying communities (Neumann et al., 2015; Ranasinghe, 2016). In conjunction with rising sea level, regional changes in wave and storm conditions and increased river flows will likely result in more frequent and intense episodic coastal flooding (Ranasinghe, 2016). Future changes in river flow will also directly control the amount of sediment received by coasts and subsequently transported onto beaches. Changes in fluvial sediment supply to the coast will affect flooding and erosion of low-lying coastal areas as beaches are the first line of defense for coastal hazards (Syvitski et al., 2009; Dunn et al., 2018, 2019; Besset et al., 2019). The potential socio-economic impacts of climate-driven flooding and beach losses are likely to be enormous. For example, forced migration due to sea-level rise driven coastline recession over this century is expected to cost about 1 trillion USD (Hinkel et al., 2013) while the potential economic losses in coastal cities due to flooding are expected cost more than 1 trillion USD by 2050 (Hallegatte et al., 2013) if the appropriate adaptation strategies are not implemented. Some other studies have shown that, under extreme emission and sea-level rise scenarios, average annual damage due to coastal flooding in Europe may also cost about 1.5 billion euros while affecting millions of people by the end of the 21st century if no new adaptation measures are taken in future (Bosello et al., 2012; Prahl et al., 2018; Vousdoukas et al., 2018, 2020a; Kirezci et al., 2020).

Coasts are highly varied and complex systems, and although the variety of coastal classifications is large, there is a societal need to focus on increasing our understanding of systems with pronounced anthropogenic influences and hazard risk. Here, we focus on sandy coasts, which comprise about one-third of the world's coastlines (Luijendijk et al., 2018). Sandy coasts are considered to be one of the most complex coastal systems because the physical forcing acting on them and their geomorphic response are continually changing due to the influences of both natural and anthropogenic drivers (Ranasinghe, 2016; Toimil et al., 2017). The majority of these sandy coasts is interrupted by inlets (Aubrey and Weishar, 1988; Davis and Fitzgerald, 2003; Woodruff et al., 2013; FitzGerald et al., 2015; Duong et al., 2016; McSweeney et al., 2017). It should be noted that all the inlet-interrupted coasts are not necessarily connected with estuaries. Here, we focus on inlet-interrupted mainland coasts that are attached to estuaries receiving non-trivial river flows. These inlet-interrupted coasts are highly dynamic due to being governed by the interplay of oceanic and terrestrial processes (Stive, 2004; Ranasinghe et al., 2013; Anthony et al., 2015; Ranasinghe, 2016; Besset et al., 2019). Furthermore, as discussed above, climate change and anthropogenic activities in the coastal zone are likely to exert substantial changes to the complex and dynamic behavior of inlet-interrupted coasts. Such changes along inlet-interrupted coasts could lead even direr socio-economic impacts on this type of coasts compared to uninterrupted coasts, making a bad situation worse. Therefore, it is important to understand the physical responses of inlet-interrupted coasts under the plausible range of future variations in environmental forcing and anthropogenic activities.

Potential climate-change impacts on inlet-interrupted coasts can vary widely both on spatial and temporal scales. Climate-change impacts on sandy coasts are generally classified as short-term (hours to days), medium-term (years to decadal), and long-term (decades to century) with changes in sea level,

wave conditions and storm surges, and river flow patterns being the primary climate-related impact drivers (Ranasinghe, 2016). Owing to the slow nature of rising sea level, coastal responses driven by sea-level rise will also be relatively slow. Under the Bruun effect, the coast will retreat as sediment shifts in the cross-shore direction across the nearshore seabed (Bruun, 1962) and potentially across subaerial portions of the coastal landscape [e.g., Wolinsky and Murray (2009), Dean and Houston (2016), Murray and Moore (2018)]. Additionally, inlet-interrupted coasts will undergo further coastal recession due to sea-level rise driven basin infilling as well (Stive et al., 1990, 1998; Stive, 2004; Ranasinghe et al., 2013). Along with these influences, future changes in temperature, precipitation and anthropogenic activities at catchment scale will alter the fluvial sediment supply received by the coasts (Syvitski and Milliman, 2007; Overeem and Syvitski, 2009; Syvitski et al., 2009; Ranasinghe et al., 2019), which in turn would affect sedimentation patterns, including beach behavior on inlet-interrupted coasts (Bamunawala et al., 2018a, 2020).

There are significant uncertainties in future climate change and anthropogenic driven impacts that could affect shoreline changes along sandy coasts (Ranasinghe, 2016, 2020; Le Cozannet et al., 2017). As a result, in addition to the uncertainties associated with the modeling techniques (i.e., model uncertainties), model-derived projections of future changes along inlet-interrupted coastlines will inherit the uncertainties related to the climate-related impact drivers and anthropogenic activities (i.e., input uncertainties) considered. Therefore, it is necessary to quantify the uncertainties associated with the shoreline change projections to better inform adaptation measures to manage the impacts of future climate change and anthropogenic activities, including potential socio-economic losses. Such measures will avoid unnecessary restrictions that are usually associated with conventional deterministic estimates of future coastline changes, thus enabling optimum utilization of the highly valuable land areas along coasts (Jongejan et al., 2016; Dastgheib et al., 2018). The added value of risk-informed coastal zone planning and management strategies (e.g., economically optimal setback lines) is amply illustrated by Jongejan et al. (2016) and Dastgheib et al. (2018), where the Probabilistic Coastal Recession (PCR) model (Ranasinghe et al., 2012) was applied to determine economically optimal coastal setback lines at the Narrabeen Beach, Sydney, Australia, and along the eastern coast of Sri Lanka, respectively.

Here, we develop a probabilistic modeling framework that can quantify the input uncertainties in the long-term evolution of CEC systems. Probabilistic estimates of coastline change along inlet-interrupted coasts under climate-change impacts and anthropogenic activities require multiple realizations using stochastic model inputs (i.e., Monte Carlo simulations). Hypothetically, if unlimited computational resources were available, such probabilistic modeling applications could be undertaken with coupled, highly detailed (i.e., hydrodynamics resolving) coastal and catchment models for the entire period considered so that the episodic (e.g., storms, surges, extreme river flows), medium-term (e.g., changes in river flow/mean wave conditions) and long-term impacts (e.g., sea-level rise, changes in fluvial sediment supply and longshore sediment transport capacity) due to climate change are deterministically accounted for in assessing the changes along inlet-interrupted coasts. However, the use of such highly detailed modeling techniques for ∼100-year simulations is impractical due to computational restrictions, or necessarily accurate, due to the potential cascade of model imperfections through temporal and spatial upscaling (Murray, 2007), as well as the accumulation of numerical errors within the computational domain during long-term simulations, which in turn may lead to morphological instabilities (Duong et al., 2016; Ranasinghe, 2016, 2020). Even if such a multi-scale highly detailed modeling technique were developed, the computational demand and the simulation time per each model realization would likely to make it impractical to be used in a probabilistic framework to estimate the coastline changes along inlet-interrupted coasts (Ranasinghe, 2016, 2020). These drawbacks can be overcome via the use of reduced-complexity models, which have proven to be very useful in obtaining insights into long-term coastal zone evolution at regional scales at low computational cost (Ranasinghe, 2016, 2020; van Maanen et al., 2016; Bamunawala et al., 2020). Due to their computational efficiency (compared to highly detailed models), reduced complexity models can be easily applied within a probabilistic framework to quantify the uncertainties in future changes along inlet-interrupted coastlines.

Here, a novel probabilistic modeling framework is presented to quantify the input uncertainties associated with projections derived from the reduced complexity model developed and demonstrated (albeit in deterministic mode) by Bamunawala et al. (2020). To enable a direct comparison of the two modeling approaches (i.e., deterministic vs. probabilistic), the probabilistic approach presented here is applied to the same coastal systems used by Bamunawala et al. (2020).

MATERIALS AND METHODS

The reduced complexity model used here is described in detail by Bamunawala et al. (2020), and therefore, only a summary is presented below. In this model (G-SMIC), which is based on the SMIC model originally presented by Ranasinghe et al. (2013), the long-term evolution of inlet-interrupted coasts is represented by combining two major components: (1) coastline change due to the variation in total sediment volume exchanged (ΔV_T) between the estuary and the adjacent inlet-interrupted coast, (2) sea-level rise-driven landward movement of the coastline (i.e., the Bruun effect).

Determining Changes in Total Sediment Volume Exchange Between an Estuary and the Adjacent Inlet-Interrupted Coast

Assuming that the coastal-estuary system is in dynamic equilibrium, the variation in total sediment volume exchanged (ΔV_T) between the estuary system and its adjacent inlet-interrupted coast is calculated as a summation of three processes (Ranasinghe et al., 2013), given by the following equation.

$$\Delta V_T = \Delta V_{BI} + \Delta V_{BV} + \Delta V_{FS} \quad (1)$$

where ΔV_T is the cumulative change in the total sediment volume exchange between the estuary and its adjacent coast, ΔV_{BI} is the sediment demand of the basin due to sea-level rise-driven change in basin volume (i.e., basin infilling volume), ΔV_{BV} is the change in basin volume due to variation in river discharge, and ΔV_{FS} is the change in fluvial sediment supply due to combined effects of climate change and anthropogenic activities, with all volumes in m^3. A brief description of the three sediment volume components of equation [1] is given below [for detailed derivations, please see Ranasinghe et al. (2013) and Bamunawala et al. (2020)].

Basin Infilling Volume Due to Sea-Level Rise-Induced Increase in Accommodation Space

Rising sea level creates an additional volume within the basin. This additional volume (i.e., accommodation space) results in an extra sediment volume demand by the basin (ΔV_{BI}), which can be computed as:

$$\Delta V_{BI} = -\text{fac}\,(A_b \Delta RSL) \tag{2}$$

where A_b is the basin surface area (m^2), "fac" ($0 < \text{fac} < 1$) accounts for the morphological response lag that exists between the hydrodynamic forcing (i.e., sea-level rise) and resulting morphological response of the basin [i.e., basin infilling volume (ΔV_{BI})]. In this study, the value of "fac" is set as 0.5 for all the simulations [adopted from Ranasinghe et al. (2013)].

Basin Volume Change Due to Variation in River Flow

The ebb-tidal flow volume of estuaries may change due to variations in future river flow. Such a change in the ebb-flow volume induces variations in estuarine and inlet flow velocities. In the process of striving to achieve its initial equilibrium flow velocity, an inlet-estuary system will therefore undergo changes in its channel cross-section and bed level. Such variations in the inlet-estuary system are associated with a specific volume of sediment (ΔV_{BV}) exchanged between the inlet-estuary system and the adjacent inlet-interrupted coast, which can be calculated as:

$$\Delta V_{BV} = \frac{\Delta Q_R V_B}{(P + Q_R)} \tag{3}$$

where Q_R is the present river flow into the basin during ebb, ΔQ_R is the climate change-driven variation in river flow during ebb, V_B is the present basin volume, and P is the mean equilibrium ebb-tidal prism, all volumes in m^3.

Change in Fluvial Sediment Supply

Future changes in climate and anthropogenic activities at the catchment scale will result in changing the annual fluvial sediment supply received by an inlet-estuary system (Vörösmarty et al., 2003; Syvitski, 2005; Palmer et al., 2008; Ranasinghe et al., 2019). This change in fluvial sediment supply [ΔV_{FS} (m^3)] over the t (years) period considered can be calculated as:

$$\Delta V_{FS} = \int_0^t \Delta Q_S\,(t)\,dt \tag{4}$$

where ΔQ_S is the change in annual fluvial sediment supply (m^3).

Bamunawala et al. (2018a) and Bamunawala et al. (2020) have demonstrated that the empirical model presented by Syvitski and Milliman (2007) can be used to calculate the annual fluvial sediment throughput at the catchment scale.

$$Q_S = \omega B Q^{0.31} A^{0.5} R T \tag{5}$$

where ω is a coefficient equal to 0.02 or 0.0006 for the annual fluvial sediment supply (Q_S) expressed in kg/s or MT/year at catchments, in which mean annual temperature is greater than 2°C, Q is the annual cumulative river discharge (km^3), A is the river catchment area (km^2), R is the catchment relief (km), and T is the catchment-wide mean annual temperature (°C). Note that equation [5] does not automatically account for any limitation in catchment-wide sediment volume generation. Therefore, in catchments with known limits to sediment generation, an appropriate threshold should be considered to limit the catchment-wide sediment production.

The catchment sediment production capacity is represented by the term "B" of the above equation, which is expressed as the following equation.

$$B = IL\,(1 - T_E)\,E_h \tag{6}$$

where L is the lithology factor that represents the catchment's soil type and erodibility, ΔV_T is the catchment-wide reservoir trapping efficiency factor, and E_h is catchment's human-induced erosion factor.

The term I of the above equation [6] is the glacial erosion factor, which can be calculated according to the following equation.

$$I = 1 + \left(0.09 A_g\right) \tag{7}$$

where A_g is the ice cover percentage within the catchment area.

Syvitski and Milliman (2007) have suggested a range of factors for the human-induced erosion factor ($0.2 \leq E_h \leq 2.0$) by considering the population density of the country and its Gross National Production (per capita). However, this human-induced erosion factor (E_h) can be better approximated by the use of high-resolution Human FootPrint Index (HFPI) spatial data (Balthazar et al., 2013; Bamunawala et al., 2018a, 2020).

G-SMIC utilizes four main drivers to compute the change in total sediment volume exchange (ΔV_T) between the estuary and the adjacent inlet-interrupted coast: annual mean temperature (T), annual cumulative river discharge (Q), change in regional relative sea-level (ΔRSL), and human-induced erosion factor (E_h). The climatic inputs (i.e., T and Q) are obtained from the Coupled Model Intercomparison Project Phase 5 (i.e., CMIP5) General Circulation Models (i.e., GCMs) (Taylor et al., 2011). There are unavoidable uncertainties associated with GCM projections. Similarly, the values obtained from different GCMs for the same Representative Concentration Pathway (RCP) also vary. Despite the inherent uncertainties among different GCM projections, many climate-change impact assessment studies use GCM outputs to drive future impact models. Projections of sea-level change also contain uncertainties. Human activities that may exert changes to the natural environment also vary along various dimensions (e.g., population growth, urbanization, and

economic development). The probabilistic approach developed in this study quantifies the uncertainty in ΔV_T arising from these input-uncertainties through stochastic treatment of the input variables.

In this study, the modeling period is defined as 2020–2100. Similar to the method adopted in Bamunawala et al. (2020), catchment-estuary-coastal (CEC) system conditions in 2019 were used as the reference condition in all the simulations. The climatic conditions over the last decade (i.e., 2010–2019) were used to determine the baseline values of T and Q (from CMIP5 GCMs) in all the model applications, to avoid the potentially biased representation of reference climatic conditions that would arise if only 2019 T and Q values were used.

Probabilistic Assessment of Change in Total Sediment Volume Exchange at an Estuary-Inlet System

The logical sequence of the probabilistic modeling approach adopted here is presented in **Figure 1**, followed by a description of the different computational steps involved.

Input Data

Temperature and runoff data for the 2009–2100 period (including the 2010–2019 reference period) were obtained from the General Circulation Models (GCMs) from the Coupled Model Intercomparison Project Phase 5 (CMIP5 data portal; Earth System Grid-Centre for Enabling Technologies (ESG-CET); available at http://pcmdi9.llnl.gov/). Projected values of temperature and surface runoff were obtained for all four RCPs of selected GCMs based on parameter output availability. Initially, GCMs with both temperature and surface runoff projections for four RCPs over the 2020–2100 period were considered as data sources. Out of these, GCMs with spatial resolution finer than 2.5° were selected to obtain the necessary climate inputs (T and Q). Further, where possible, the suitability of the above-selected data sources was assessed regionally, by considering published regional guidelines on model selection [e.g., CSIRO, and Bureau of Meteorology (2015) for Australia]. Based on these criteria, four GCMs (i.e., GFDL-CM3, GFDL-ESM2G, and GFDL-ESM2M from NOAA, United States, IPSL-CM5A-MR from IPSL) were selected to obtain the required T and Q values. These four GCMs were also the source of T and Q values used for deterministic G-SMIC projections presented in Bamunawala et al. (2020).

The regional relative sea-level change (ΔRSL) values at the respective case study locations were calculated according to the following equation (Nicholls et al., 2011):

$$\Delta RSL = \Delta SL_G + \Delta SL_{RM} + \Delta SL_{RG} + \Delta SL_{VLM} \quad (8)$$

where ΔRSL is the change in relative sea level, ΔSL_G is the change in global mean sea level, ΔSL_{RM} is the regional variation in sea level from the global mean due to meteo-oceanographic factors, ΔSL_{RG} is the regional variation in sea level due to changes in the earth's gravitational field, and ΔSL_{VLM} is the change in sea level due to vertical land movement, all values are in m.

IPCC projections of ΔRSL at a given location by 2100 can be determined from Figure TS. 23 of Stocker et al. (2013a) and the corresponding ΔSL_G values were obtained from Table SPM. 2 of Stocker et al. (2013b). The difference between these two sets of values provides the cumulative contribution of ΔSL_{RM}, ΔSL_{RG}, and ΔSL_{VLM} for 2100. The temporal variation of the above three components was assumed to vary linearly from 2000 to 2100 (Mehvar et al., 2016) to enable the computation of these SLR components at yearly time steps as required by G-SMIC.

Yearly minimum, mean, and maximum values of global sea-level change (ΔSL_G) were calculated according to the following equation (Nicholls et al., 2011).

$$\Delta SL_G = a_1 t + a_2 t^2 \quad (9)$$

where ΔSL_G is the change in global sea level (m) since 2000, "t" is the number of years since 2000, a_1 is the trend in sea level change (m/yr), and a_2 is the change in the rate of sea-level change trend (m/yr^2). The a_1 and a_2 coefficient values were obtained from published literature (Mehvar et al., 2016).

The human-induced erosion factor (E_h), which contributes to catchment scale sediment generation is here represented via the Human FootPrint Index (HFPI). HFPI values within the catchment were rescaled linearly to fit the optimum scale of E_h suggested in the literature (Syvitski and Milliman, 2007). These rescaled HFPI values were then averaged over the catchment to determine a representative factor for human-induced erosion (E_h). Given the contemporary rate of population growth and urbanization, it is safe to assume that E_h will have increased by 2100. Owing to numerous uncertainties associated in such projections [e.g., Veerbeek (2017)], the increment of E_h by 2100 was assumed to follow a triangular distribution with a mean, minimum and maximum of respectively 15, 10, and 20 percent of its present-day value.

Data Processing

The next step of the proposed modeling framework involves data preparation (green box in **Figure 1**). Here, annual cumulative distribution functions (CDFs) of the four model input parameters [viz., mean annual temperature (T), annual cumulative river discharge (Q), regional relative sea-level change (ΔRSL), and human-induced erosion factor (E_h)] were developed, so that the required stochastic model inputs could be generated.

Precipitation, evapotranspiration, runoff, and groundwater flow are the main components of the total water budget at catchment scales, with temperature, evapotranspiration, and precipitation being closely correlated parameters (Trenberth et al., 2007; Hegerl et al., 2015). Since T and Q values are inter-related, it is necessary to consider their dependencies when generating the stochastic model inputs. In order to capture the correlation between T and Q, joint probability distributions were generated for every year between 2020 and 2100 to determine the annual mean temperature and cumulative river discharge values at the catchment scale. Joint probability distributions for the 2020–2100 period were created by using ensembles of T and Q values obtained from the selected GCMs. A joint probability distribution of T and Q for the reference conditions was also generated by the use of annual mean temperature and cumulative river discharge values for the 2010–2019 period, using the output of the selected GCMs for this period.

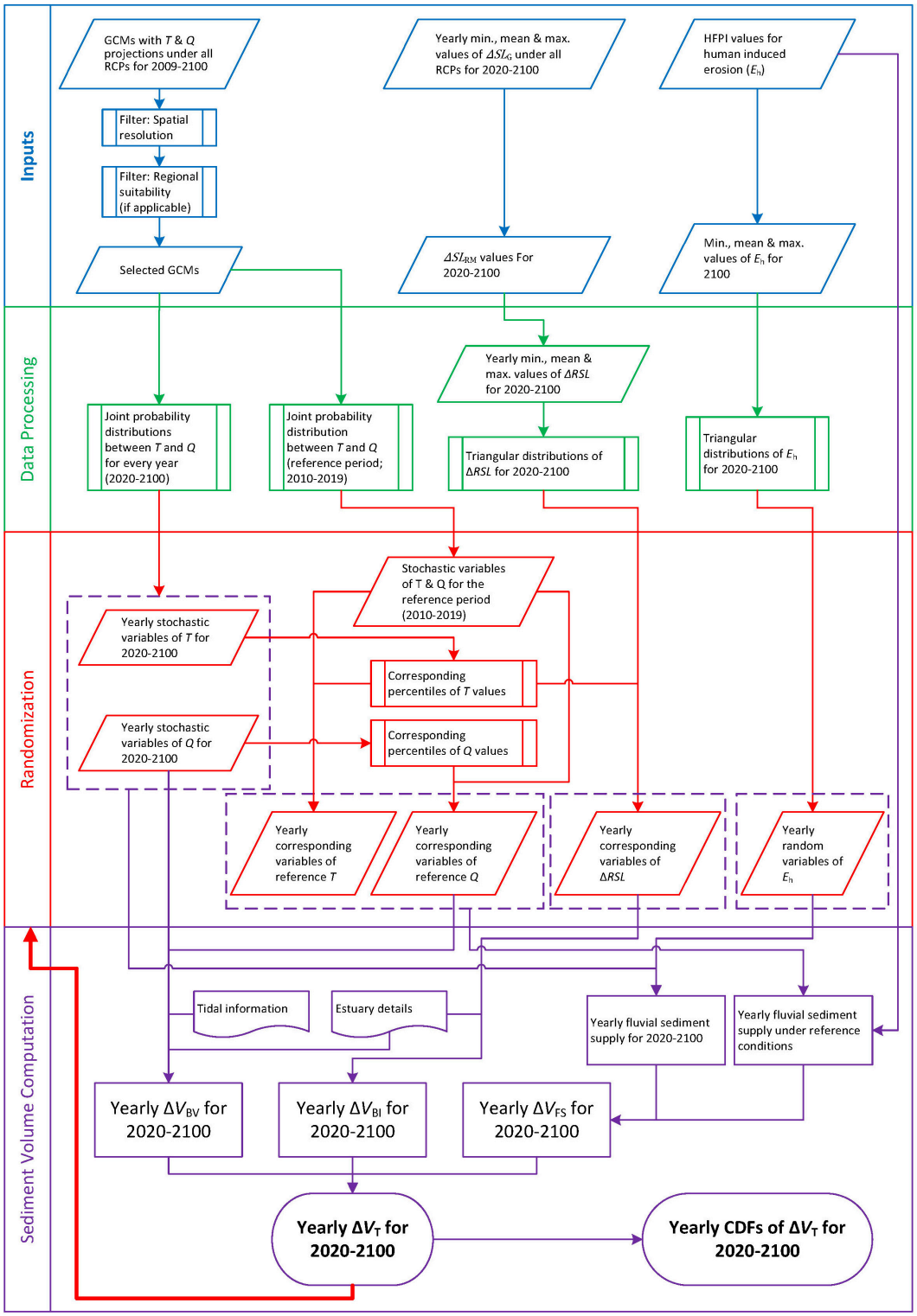

FIGURE 1 | Flowchart of the modeling approach adopted to probabilistically determine the change in total sediment volume exchange between an estuary system and its adjacent inlet-interrupted coast.

The yearly values of ΔRSL (obtained as described above) were used to fit triangular distributions to represent ΔRSL for each year (2020–2100). For the human-induced erosion factor (E_h), the above-adopted minimum, mean, and maximum increments by 2100 were assumed to be reached via a linear increase from 2020, and triangular distributions were fitted to represent yearly E_h values for the 2020–2100 period.

Generating Stochastic Model Inputs

The third stage of the proposed probabilistic modeling framework is devoted to generating the stochastic model input for temperature, river discharge, regional relative sea-level change, and the human-induced erosion factor (i.e., randomization; red box in **Figure 1**). The fitted joint probability distributions for temperature and river discharge were here used to generate stochastic model inputs for T and Q for each year (100,000 randomly pairs of T and Q per year) for the future period (2020–2100) and the reference period (2010–2019). For all the future T and Q between 2020 and 2100, reference values with the same probability of occurrences were selected (i.e., reference T and Q with the same percentiles as the future values).

The two main causes of global sea-level rise are thermal expansion (i.e., steric effect) caused by warming of the oceans and increased melting of land-based ice, such as glaciers and ice sheets (Stocker et al., 2013b). Both of these factors are directly related to increasing temperature. Therefore, in all the model applications, a direct relationship was assumed between annual mean temperatures (T) and change in regional relative sea-level (ΔRSL) (Rahmstorf, 2007). In order to achieve this direct relationship, percentiles of each annual mean temperature (T) value obtained through the fitted joint probability models (as described above) were calculated. The ΔRSL values with the same percentiles as T were selected from the fitted triangular distributions that represent the regional relative sea-level change (ΔRSL) for each year between 2020 and 2100 (100,000 values per year).

Fitted triangular distributions that represent the human-induced erosion factor (E_h) were used to generate stochastic variables of E_h for 2020–2100 (100,000 random values per each year).

Computing Sediment Exchange Volumes

All the above computed stochastic model inputs were then used in the final phase of the probabilistic modeling framework to determine the change in total sediment volume exchange (ΔV_T) between a given estuary system and the adjacent inlet-interrupted coast (i.e., sediment volume computation; purple box in **Figure 1**). The above-computed Q values were used together with estuarine and tidal information to calculate the variations in sediment volume due to changes in basin volume (ΔV_{BV}) during 2020–2100. Generated ΔRSL values were used together with estuarine information to determine the sediment volume demands due to basin infilling (ΔV_{BI}) for 2020–2100. Changes in fluvial sediment supply (ΔV_{FS}) were computed using the stochastically generated future and reference T and Q values, human-induced erosion factor values, and other required river catchment information. These three sediment volume components were then used to compute the total change in sediment volume exchange (ΔV_T) (100,000 values per year), and empirical cumulative distributions of ΔV_T were developed for each year over the 2020–2100 projection period.

Simplified One-Line Coastline Change Model

The simplified one-line coastline change model used here is also described in detail by Bamunawala et al. (2020), and hence only a summary of that modeling approach is presented below. This simplified approach assumes uniform coastline orientation and lack of any coastal structures along up- and down-drift coasts. It also adopts time-invariant longshore sediment transport rate and depth of closure value for all future coastline change projections. The maximum extent of inlet-affected coastline length is considered to be ∼25 km from an inlet. Otherwise, this distance from an inlet is constrained by the presence of rock outcrops, headlands, noticeable change in mean shoreline orientation or inlets. If there are no gradients in annual longshore sediment transport rates along up- and down-drift coasts, the coastal cell considered is assumed to be in equilibrium at annual time scales.

A selected percentile value of the above computed ΔV_T can be used to determine the subsequent changes along the adjacent inlet-interrupted coast. Here, the 50th percentile values of ΔV_T were used to determine the changes along the inlet-interrupted coasts. Since the ΔV_T is computed annually, it is first divided into a number of equal fragments (n_v). This volume fragment (V_{fr}) is then distributed along the adjacent coastline. Volume fragment (V_{fr}) is calculated using the following equation.

$$V_{fr} = \frac{\Delta V_T}{n_v} \tag{10}$$

All or a part of this sediment volume fragment will be transported along the coast. This is closely related to the equivalent longshore sediment transport capacity at the vicinity ($\Delta Q_{LST} = \frac{Q_{LST}}{n_v}$). Based on the assumption of a balanced sediment budget within the coastal cell, sediment volume that gets transported to the farthermost section of the down-drift coast will contribute to progradate that coastline. For eroding coastlines, computation is started from the section nearest to the inlet. If V_{fr} is larger than ΔQ_{LST}, the surplus sediment volume ($\Delta V = V_{fr} - \Delta Q_{LST}$) will result in prograding the shoreline (Δy) within the longshore distance considered (Δx) (Please refer to **Supplementary Figure 1** for a schematic illustration of a hypothetical equilibrium cross-shore profile).

The magnitude of seaward translation (Δy) of the longshore distance (Δx) can be computed using the following equation when the shoreline is assumed to move cross-shore parallel to itself while maintaining the initial equilibrium profile.

$$\min(\Delta V, V_{fr}) = \Delta x(D\Delta y) \tag{11}$$

where D is the depth of closure.

The above procedure is repeated within subsequent longshore distances (Δx) until a sediment volume fragment (V_{fr}) is

distributed. Then the procedure is repeated n_v times, so that the ΔV_T is fully distributed within the coastal cell. These computations are closely related with an expression for longshore sediment transport rate (Q_{LST}), which can be expressed as the following equation.

$$Q_{\mathrm{LST}} = Q_0 \sin(2\alpha \mathrm{b}) \tag{12}$$

where Q_0 is the amplitude of the longshore sediment transport rate (m^3/yr), and αb is the breaking wave angle, measured between the wave crest lines and coastline. This angle can be calculated using the following equation.

$$\alpha_b = \alpha_0 - \frac{\Delta y}{\Delta x} \tag{13}$$

where α_0 is the angle of breaking wave crests, measured relative to the coastline.

The coastline position (Δy) would be updated locally with the longshore distribution of every volume fragment (V_{fr}). Hence, the breaking wave angle (αb) and longshore sediment transport rate (Q_{LST}) are also update accordingly after the distribution of V_{fr}. Once the ΔV_T is fully distributed, the final coastline position can be obtained by superimposing the coastline recession due to the Bruun effect (Bruun, 1962).

Case Study Sites and Stochastic Model Inputs

The above-presented modeling technique was applied to the case study locations considered in Bamunawala et al. (2020) (i.e., Alsea estuary, Oregon, United States, Dyfi estuary, Wales, United Kingdom, and Kalutara inlet, Sri Lanka; **Supplementary Figure 2**). **Table 1** summarizes the key properties of the selected three systems [for more details, please see Bamunawala et al. (2020)].

Figures 2–4 show the GCM derived projected variations of annual mean temperature (T) and the annual cumulative river discharge (Q) of the Alsea, Dyfi, and Kalu River catchments, respectively over the three decadal periods considered (2021–2030, 2056–2065, and 2091–2100). **Figure 5** shows the projected variations in the mean, minimum, and maximum regional relative sea-level changes (ΔV_T) in the vicinity of the Alsea, Dyfi, and Kalutara inlets over the 21st century.

Similar to the globally averaged temperature variation published by Stocker et al. (2013b), the 50th percentile T values in Alsea river catchment show hardly any change during mid- and end-century periods for RCP 2.6 [**Figure 2**, Panel I, subplot (a)]. The projected maximum and minimum increments of the 50th percentile T values by 2100 are 3.0°C and 0.5°C for RCP 8.5 and 2.6, respectively. The projected variations in Q values of the Alsea River catchment indicate only minor variations over the 21st century for all RCPs (**Figure 2**, Panel II). Except for RCP 8.5, projected Q values are slightly increased by 2100 [relative to the early-century (2021–2030) period], where the maximum and minimum increments in the 50th percentile magnitudes are 0.2 km^3/yr and <0.1 km^3/yr for RCP 2.6 and 4.5, respectively. The projected 50th percentile Q value by 2100 is marginally decreased (<0.1 km^3/yr) for RCP 8.5.

Unlike the globally averaged temperature variation published by Stocker et al. (2013b), the 50th percentile T values in the Dyfi River catchment show differences during mid- and end-century periods for RCP 2.6, in which the projections for the latter period (i.e., 2091–2100) are approximately 0.5°C warmer than the former duration [**Figure 3**, Panel I, subplot (a)]. The projected maximum and minimum increments of the 50th percentile T values by 2100 are 2.5°C and 0.5°C for RCP 8.5 and 2.6, respectively. The projected variations in Q values of the Dyfi River catchment indicate minor variations over the 21st century for all RCPs (**Figure 3**, Panel II). Except for RCP 6.0, the projected Q values are slightly increased by 2100 (relative to the early-century period). However, all these projected variations (i.e., both reductions and increments) are quite trivial, and thus only result in minor variations of Q (<0.05 km^3/yr) in the Dyfi River catchment over the 21st century.

The 50th percentile T values in the Kalu River catchment also show differences during mid- and end-century periods for RCP 2.6, in which the latter period (i.e., 2091–2100) projection is approximately 0.25°C warmer than the former [**Figure 4**, Panel I, subplot (a)]. The projected maximum and minimum increments of the 50th percentile T values by 2100 are 2.5°C and <0.5°C for RCP 8.5 and 2.6, respectively. The projected variations in Q values in the Kalu River catchment indicate increased river discharge over the 21st century for all RCPs (**Figure 4**, Panel II). Except for RCP 2.6, the projected Q values are increased by 2050 as well (relative to early-century period). The projected maximum and minimum increments in the 50th percentile Q values by 2100 are 0.75 km^3/yr and 0.25 km^3/yr for RCP 8.5 and 2.6, respectively. The projections for RCP 8.5 indicated a small likelihood (~1% probability of exceedance) of extreme discharges (about 3.0 km^3/yr) over the latter part of the 21st century [**Figure 4**, Panel II, subplot (d)], which is about twice the magnitude of the 50th percentile Q values over the same period.

Figure 5 indicates that the projected mean change of ΔRSL by 2100 is largest in the vicinity of the Kalutara inlet system (Sri Lanka), whereas the minimum change by 2100 is projected for the Alsea estuary (Oregon, United States). However, the

TABLE 1 | Properties of the selected case study CEC systems [after Bamunawala et al. (2020)].

Parameter	Alsea	Dyfi	Kalutara
Mean ebb-tidal prism (P in 10^6 m^3)	9.0	71.1	6.2
Basin surface area (A_b in 10^6 km^2)	9.1	17.3	1.75
Basin volume (V_B in 10^6 m^3)	20.0	44.98	5.25
Catchment area (A in km^2)	1,225	670	2,778
Catchment relief (R in km)	1.25	0.66	2.25
Lithology factor (L)	1.0	0.75	0.5
Anthropogenic factor (E_h)	0.67	0.93	0.93
Beach profile slope (tan β)	0.02	0.02	0.02
Depth of closure D in m	15	15	15
Reservoir trapping efficiency (T_E)	0	0	0

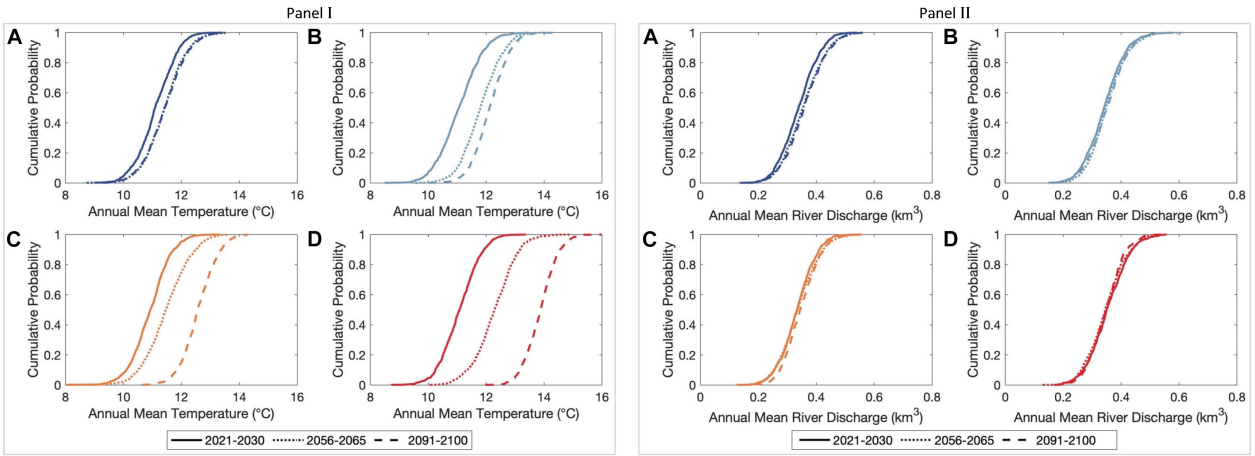

FIGURE 2 | Empirical cumulative distributions of averaged annual mean temperature **(Panel I)** and the annual cumulative river discharge **(Panel II)** in the Alsea River catchment, Oregon, the United States over the three decadal periods considered. Subplots **(A)**, **(B)**, **(C)**, and **(D)** are for the RCPs 2.6, 4.5, 6.0, and 8.5, respectively.

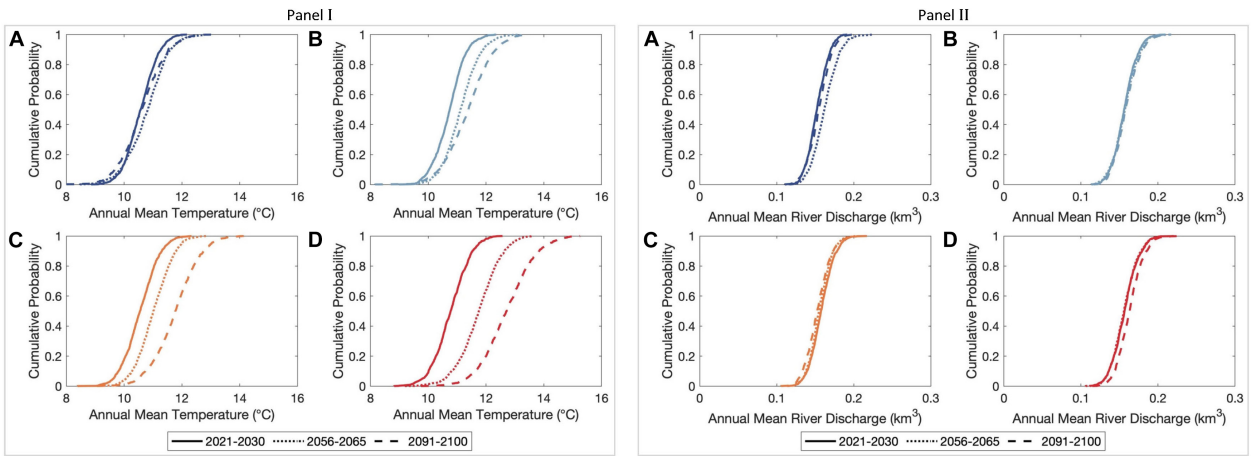

FIGURE 3 | Empirical cumulative distributions of averaged annual mean temperature **(Panel I)** and the annual cumulative river discharge **(Panel II)** in the Dyfi River catchment, Wales, the United Kingdom over the three decadal periods considered. Subplots **(A)**, **(B)**, **(C)**, and **(D)** are for the RCPs 2.6, 4.5, 6.0, and 8.5, respectively.

largest range (min-max) of projected ΔV_{BV} by 2100 is projected in the vicinity of the Dyfi estuary (Wales, United Kingdom).

It should be noted that river sand mining activities are carried out along the Kalu River (Bamunawala et al., 2018b). The annual volume of this sand extraction is about 423,060 m^3/yr, which is assumed to be linearly increased by 20% over the 2020–2100 simulation period.

RESULTS

The results obtained by applying the above-described modeling approach to the three case study sites are presented in two steps: (1) probabilistic estimates of projected variations in the total sediment volume exchange (ΔV_T) between the inlet-estuary systems and their adjacent coasts and (2) projected evolution of the inlet-interrupted coasts at the study sites.

Projected Variations of Total Sediment Volume Exchange (ΔV_T) (2020–2100)

Alsea Estuary System

Figure 6 shows that, at Alsea estuary, both RCP 2.6 and 8.5 result in similar ranges of uncertainty and 50th percentile values of ΔV_T during 2020–2050 [−0.5 Million Cubic Meters (MCM) by 2050]. From that point onward, the projected uncertainty ranges and the 50th percentile values of ΔV_T under RCP 8.5 tend to deviate from those under RCP 2.6 and result in a much greater 50th percentile value by 2100 (−1.7 MCM). The projected uncertainties of ΔV_T in 2100 are quite similar for all but RCP 8.5. The results also highlight that the deterministic projections of ΔV_T for RCP 8.5 presented in Bamunawala et al. (2020) are consistently greater than the 50th percentile values of the probabilistic projections, by as much as 0.5 MCM (∼30%) by 2100.

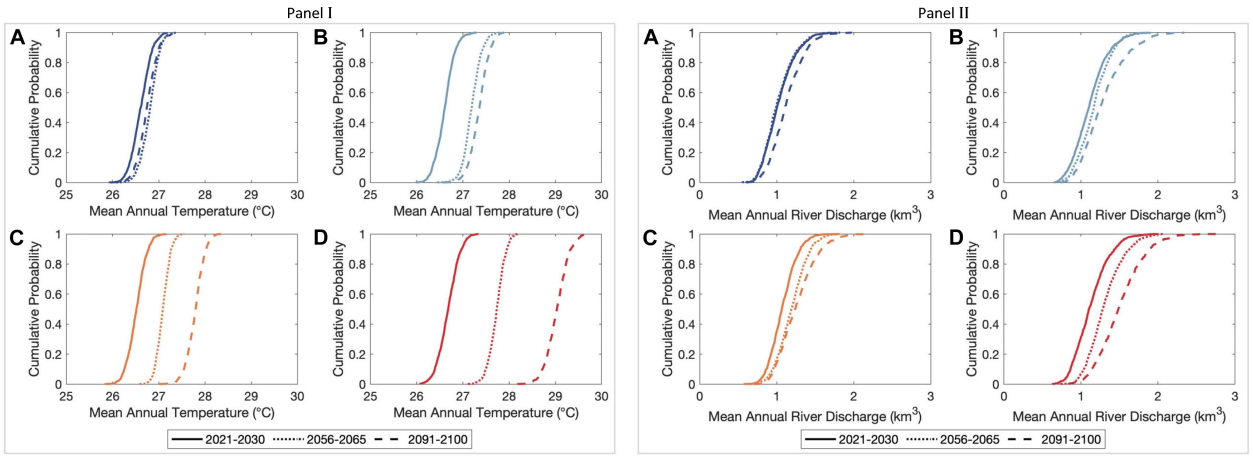

FIGURE 4 | Empirical cumulative distributions of averaged annual mean temperature **(Panel I)** and the annual cumulative river discharge **(Panel II)** in the Kalu River catchment, Sri Lanka over the three decadal periods considered. Subplots **(A)**, **(B)**, **(C)**, and **(D)** are for the RCPs 2.6, 4.5, 6.0, and 8.5, respectively.

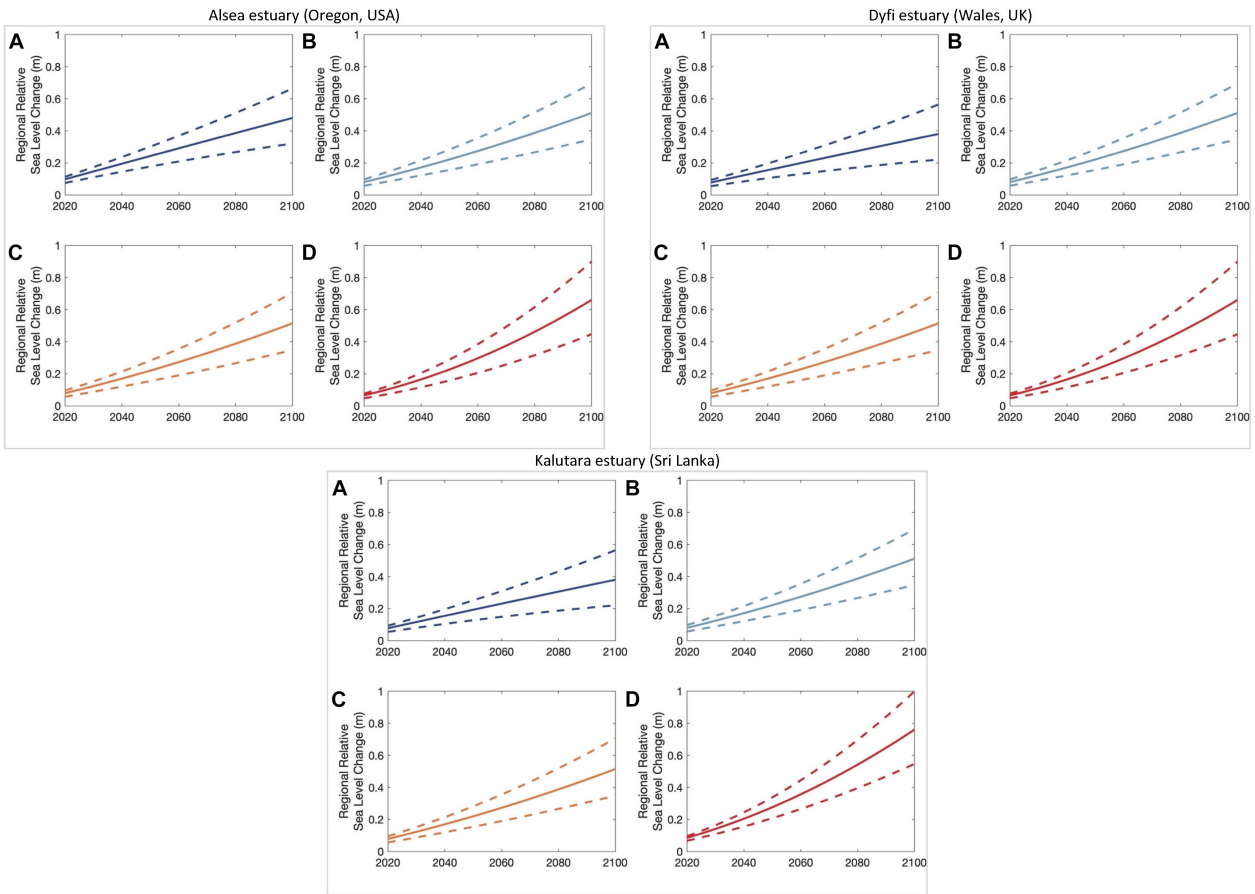

FIGURE 5 | Projected changes in regional relative sea level in the vicinities of the three case study CEC systems. The solid line indicates the mean change, while the two dashed lines indicate the computed maximum and minimum values of ΔRSL. Subplots **(A)**, **(B)**, **(C)**, and **(D)** are for the RCPs 2.6, 4.5, 6.0, and 8.5, respectively.

The empirical CDF plots in **Figure 7**-Panel I indicate the total uncertainties associated with the projected ΔV_T at the Alsea estuary system (in contrast to the selected range between 10th and 90th percentiles presented in **Figure 6**). During the first decadal period, there is very little uncertainty in the ΔV_T projections under all four RCPs, as evidenced by almost

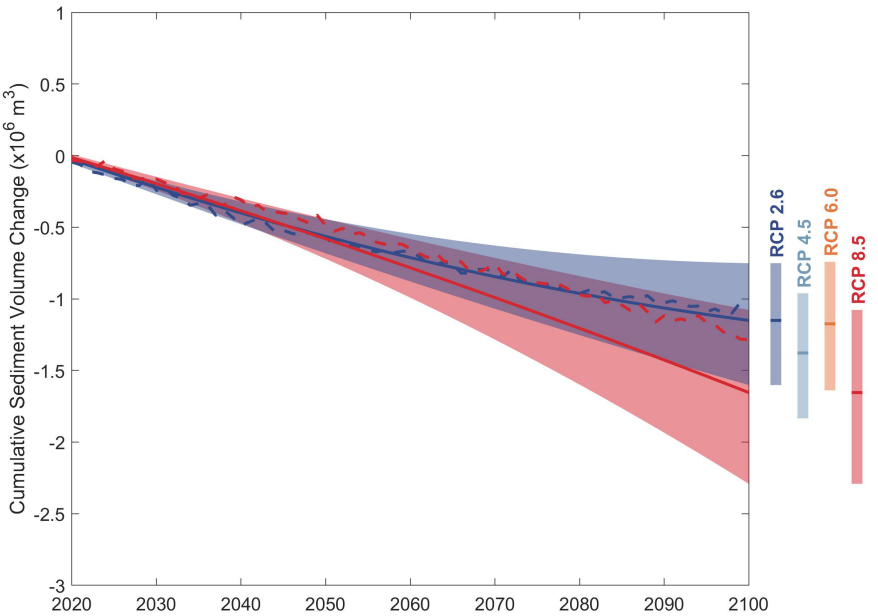

FIGURE 6 | Projected variation of change in total sediment volume exchange (ΔV_T) between the Alsea estuary and the adjacent coast over the 21st century. The projected ranges between 10th and 90th percentile are shown as shaded bands with the variation of the 50th percentile values indicated by the solid lines for RCP 2.6 (blue) and RCP 8.5 (red). The negative volumes indicate that the estuary traps more sediment at the expense of the open coast. Deterministic projections of ΔV_T presented in Bamunawala et al. (2020) for RCP 2.6 (blue) and RCP 8.5 (red) are indicated by the dashed lines. Vertical bars indicate the projected ranges between the 10th and 90th percentiles in 2100 for all RCPs with the 50th percentile values indicated as horizontal lines.

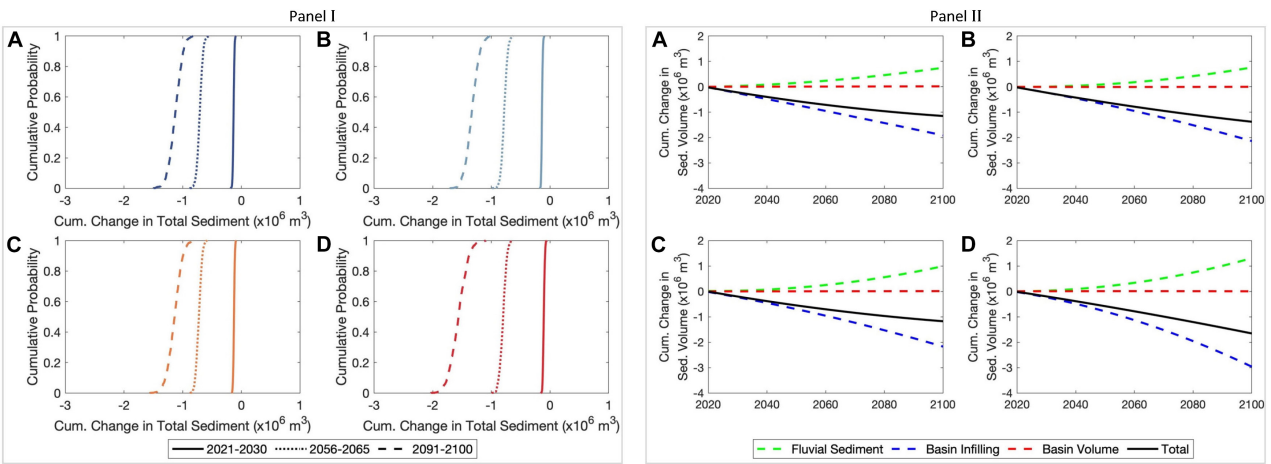

FIGURE 7 | Empirical cumulative distributions of the projected change in total sediment volume exchange (ΔV_T) between the Alsea estuary and the adjacent coast over the three decadal periods considered **(Panel I)**. The empirical cumulative distributions were developed by averaging the projected ΔV_T values over the three decadal periods considered. **(Panel II)** shows the computed variations of the projected 50th percentile values of change in total sediment volume exchange (ΔV_T) and contributions from different processes to ΔV_T at the Alsea estuary over the 21st century. Negative volumes indicate that the estuary traps more sediment at the expense of the open coast (i.e., sediment importing estuary). Subplots **(A)**, **(B)**, **(C)**, and **(D)** are for the RCPs 2.6, 4.5, 6.0, and 8.5, respectively.

vertical CDFs. These uncertainties increase slightly over the mid-century period for all RCPs (<0.25 MCM), increasing to considerable uncertainties by the end-century period, in which the least (0.75 MCM) and the most (1.0 MCM) variations by 2100 are projected for RCP 4.5 and 8.5, respectively. The results presented in **Figure 7**-Panel II indicate that the future evolution of ΔV_T at Alsea estuary system will be governed by the basin infilling volume (ΔV_{BI}). The results also indicate that the projected variations of ΔV_{BV} have negligible impacts on ΔV_T for all RCPs, because of the trivial changes in the projected annual cumulative river discharge values of this river catchment (**Figure 2**-Panel II).

The sediment demand due to basin infilling (ΔV_{BI}) is projected to increase rapidly during the late 21st century

under RCP 8.5 [due to projected acceleration in ΔRSL under this scenario as shown in **Figure 5**-Alsea estuary (Oregon, United States)], thus resulting in the largest 50th percentile cumulative estuary sediment volume demand by 2100 (3.0 MCM). Projected changes in mean annual temperature (**Figure 2**-Panel I), and the human-induced erosion factor (E_h) contribute positively to the sediment balance by leading to increases in fluvial sediment supply (ΔV_{FS}) toward the latter part of 2100 (i.e., after 2080) for all RCPs. The increase in fluvial sediment supply offsets the sea-level-rise-driven basin infilling volume demand. Therefore, the largest projected 50th percentile value of ΔV_T in the Alsea estuary system by 2100 is −1.5 MCM under RCP 8.5.

Dyfi Estuary System

Figure 8 shows that, both RCP 2.6 and 8.5 result in similar ranges of uncertainties of ΔV_T at the Dyfi estuary system during the 2020–2050 period. However, the magnitude of the 50th percentile value of ΔV_T for RCP 8.5 (−1.5 MCM) is 50% larger than that for RCP 2.6 (−1.0 MCM) by 2050. From that point onward, projected uncertainty ranges and the 50th percentile values of ΔV_T under RCP 8.5 tend to deviate from those under RCP 2.6 and result in 100% larger median value by 2100 (−5.0 MCM under RCP 8.5 compared to −2.5 MCM under RCP 2.6). The deterministic model results presented in Bamunawala et al. (2020) are similar to the 50th percentile values of ΔV_T of the probabilistic projections.

The empirical CDFs presented in **Figure 9**-Panel I indicate that the projections of ΔV_T at the Dyfi estuary system show very little uncertainty under all four RCPs during the first decadal period (i.e., 2021–2030). These uncertainties increase slightly over the mid-century period (i.e., 2056–2065) for all RCPs (0.5 MCM), increasing to considerable uncertainties by the end-century period (i.e., 2091–2100), in which the largest (1.5 MCM) variations by 2100 are projected for RCP 8.5. The results presented in **Figure 9**-Panel II indicate that ΔV_T at Dyfi estuary system is governed by basin infilling volume (ΔV_{BI}) for all RCPs, and ΔV_{BV} and ΔV_{FS} have trivial impacts on projected ΔV_T regardless of the RCP.

The relative contribution from ΔV_{BV} is negligible because the projected changes in the annual cumulative river discharge values of the river catchment are trivial (**Figure 3**-Panel II). Despite the projected increments in mean annual temperature (**Figure 3**-Panel I) and the human-induced erosion (E_h), the projected increases in fluvial sediment throughput of the small Dyfi River catchment is not sufficient to noticeably offset the estuarine sediment demand due to the basin infilling process. The sediment demand due to basin infilling (ΔV_{BI}) is projected to increase rapidly under RCP 8.5, especially during the late 21st century [due to the projected acceleration in ΔRSL under RCP 8.5; **Figure 5**-Dyfi estuary (Wales, United Kingdom)], thus resulting in the largest 50th percentile cumulative sediment volume demand by the estuary (5.5 MCM by 2100). The projected maximum and minimum 50th percentile values of ΔV_T at Dyfi estuary system by 2100 are −2.5 MCM and −5.0 MCM for RCP 2.6 and 8.5, respectively.

Kalutara Inlet System

Figure 10 indicates that the 50th percentile value and the uncertainty in projected ΔV_T at the Kalutara estuary system will increase gradually over the 21st century. Interestingly, however, the 50th percentile ΔV_T under RCP 8.5 decreases until the mid-century and then increases toward the end-century period. The largest and the smallest magnitudes of the projected 50th percentile value of ΔV_T by 2100 are 7.5 MCM and 3.5 MCM for RCP 2.6 and 8.5, respectively. The deterministic projections of ΔV_T for RCP 2.6 presented in Bamunawala et al. (2020) is about 15% larger than the 50th percentile values of the probabilistic projections by the end of the 21st century.

During the first decadal period (i.e., 2021–2030), ΔV_T at the Kalutara inlet-estuary system shows very little uncertainty under all four RCPs (**Figure 11**-Panel I). These uncertainties increase slightly over the mid-century period (i.e., 2056–2065) for all RCPs (1.0 MCM), increasing to considerable uncertainties by the end-century period (i.e., 2091–2100), with the largest (5.0 MCM) uncertainty under RCP 8.5. **Figure 11**-Panel II indicate that ΔV_T at the Kalutara estuary system is governed by the fluvial sediment supply (ΔV_{FS}) under all RCPs and the projected variations of ΔV_{BV} and ΔV_{BI} have trivial impact on ΔV_T regardless of the RCP.

The largest projected 50th percentile cumulative sediment volume demand by the Kalutara estuary in 2100 is 7.0 MCM for RCP 2.6. This is due to the reduction in fluvial sediment supply as a result of river sand mining in this system. In this case, the projected increases in fluvial sediment supply due to increased T (**Figure 4**, Panel I), and Q (**Figure 4**, Panel II) under RCP 2.6 are unable to compensate for river sand mining at any time in the 21st century. Despite the same reduction in fluvial sediment due to river sand mining, fluvial sediment supply under RCP 8.5 is projected to increase rapidly toward the end of this century, resulting in a ΔV_T of −3.5 MCM by 2100 (relative to 2020), which is about 12% less than the largest estuarine sediment demand of 4.0 MCM reached in 2075.

Projections of Coastline Change

The above-computed variation in total sediment volume exchange (ΔV_T) were used to determine the future evolution of inlet-interrupted coasts at the case study sites. Here, the simplified one-line coastline change model (see section "Simplified One-Line Coastline Change Model") presented in Bamunawala et al. (2020) is used to obtain first-order approximations of the evolution of the selected inlet-interrupted coasts. In this study, the 50th percentile values of the above projected ΔV_T values were used to obtain projections of coastline change. The coastline recession due to the Bruun effect was calculated for the same percentile of ΔRSL at the respective locations. **Figure 12** shows thus obtained projected variations of the inlet-interrupted coasts at the three case study CEC systems.

At the Alsea estuary system, the sediment demand of the basin (ΔV_T) acts as a sediment sink. Therefore, the estuary imports sediment from the adjacent coast. The magnitude of the sediment demand of the estuary (ΔV_T) is smaller than that of the ambient longshore sediment transport capacity at

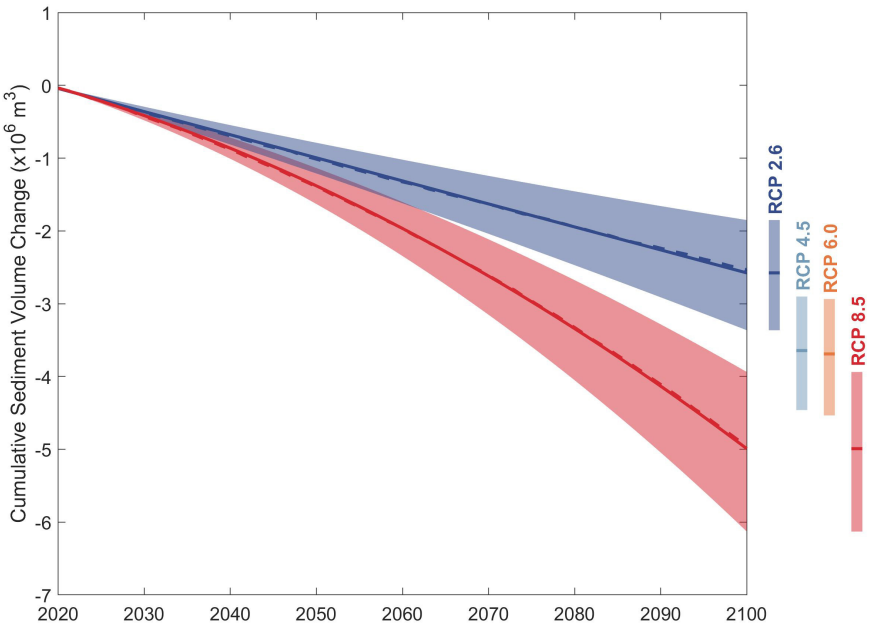

FIGURE 8 | Projected variation of change in total sediment volume exchange (ΔV_T) between the Dyfi estuary and the adjacent coast over the 21st century. The projected ranges between 10th and 90th percentile are shown as shaded bands with the variation of the 50th percentile values indicated by the solid lines for RCP 2.6 (blue) and RCP 8.5 (red). The negative volumes indicate that the estuary traps more sediment at the expense of the open coast. Deterministic projections of ΔV_T presented in Bamunawala et al. (2020) for RCP 2.6 (blue) and RCP 8.5 (red) are indicated by the dashed lines. Vertical bars indicate the projected ranges between the 10th and 90th percentiles in 2100 for all RCPs with the 50th percentile values indicated as horizontal lines.

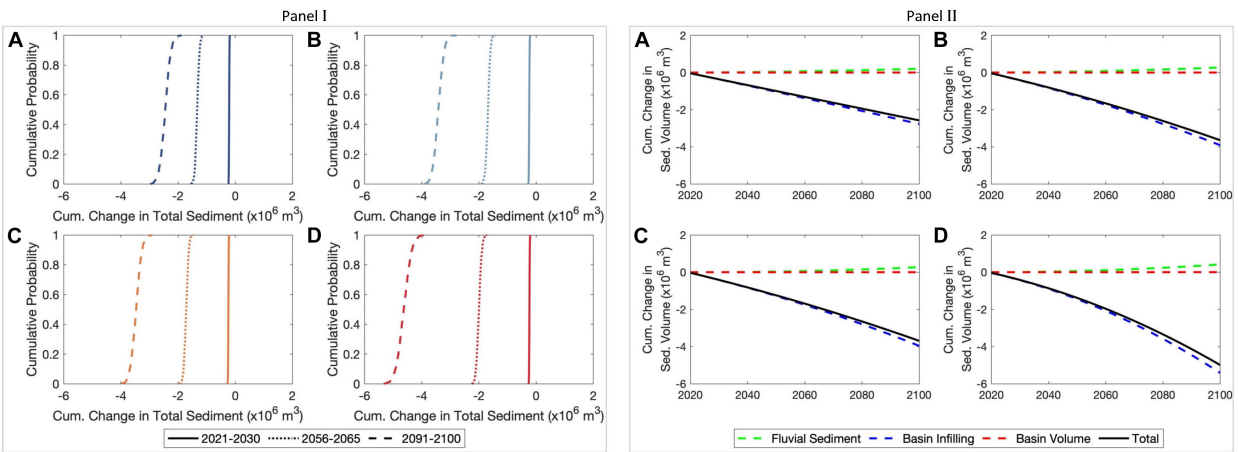

FIGURE 9 | Empirical cumulative distributions of the projected change in total sediment volume exchange (ΔV_T) between the Dyfi estuary and the adjacent coast over the three decadal periods considered **(Panel I)**. The empirical cumulative distributions were developed by averaging the projected ΔV_T values over the three decadal periods considered. **(Panel II)** shows the computed variations of the projected 50th percentile values of change in total sediment volume exchange (ΔV_T) and contributions from different processes to ΔV_T at the Dyfi estuary over the 21st century. Negative volumes indicate that the estuary traps more sediment at the expense of the open coast (i.e., sediment importing estuary). Subplots **(A)**, **(B)**, **(C)**, and **(D)** are for the RCPs 2.6, 4.5, 6.0, and 8.5, respectively.

the Alsea estuary system. Therefore, the down-drift coast at the Alsea estuary system will be subjected to an additional coastline recession due to the variation in ΔV_T, on top of recession due to the Bruun effect. **Figure 12** (top) shows that the coastal recession along the down-drift coast of the Alsea estuary may vary between 67 m (RCP 2.6) and 86 m (RCP 8.5) by 2100. The up-drift coast is only affected by the coastal recession due to Bruun effect and hence projected to be move landward by between 54 m (RCP 2.6) and 72 m (RCP 8.5) by 2100.

At the Dyfi estuary system also, ΔV_T acts as a sediment sink, and hence sediment will be imported into the estuary from the adjacent coast. The magnitude of the sediment demand of the estuary (ΔV_T) is larger than that of the ambient longshore sediment transport capacity at the Dyfi estuary system. Therefore,

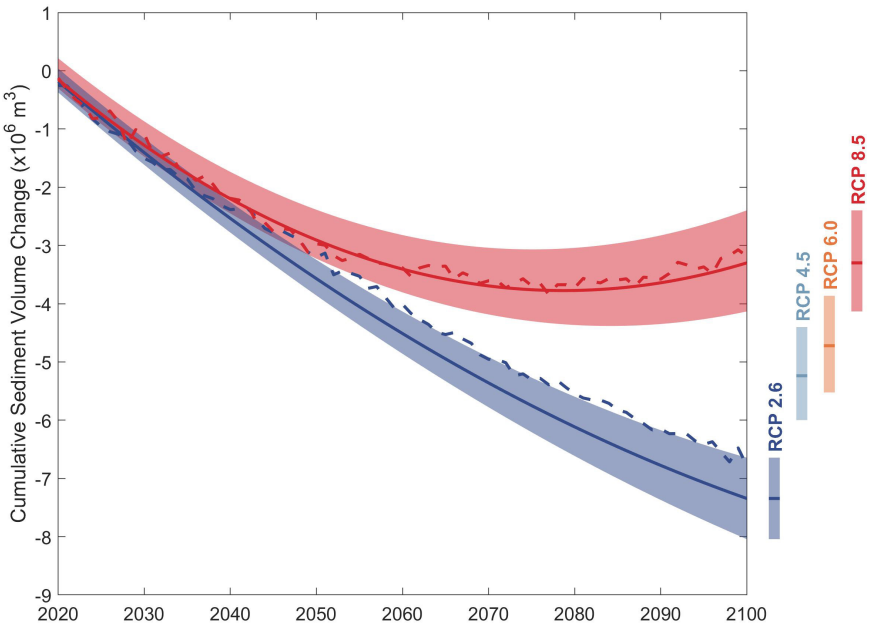

FIGURE 10 | Projected variation of change in total sediment volume exchange (ΔV_T) between the Kalutara estuary and the adjacent coast over the 21st century. The projected ranges between 10th and 90th percentile are shown as shaded bands with the variation of the 50th percentile values indicated by the solid lines for RCP 2.6 (blue) and RCP 8.5 (red). The negative volumes indicate that the estuary traps more sediment at the expense of the open coast. Deterministic projections of ΔV_T presented in Bamunawala et al. (2020) for RCP 2.6 (blue) and RCP 8.5 (red) are indicated by the dashed lines. Vertical bars indicate the projected ranges between the 10th and 90th percentiles in 2100 for all RCPs with the 50th percentile values indicated as horizontal lines.

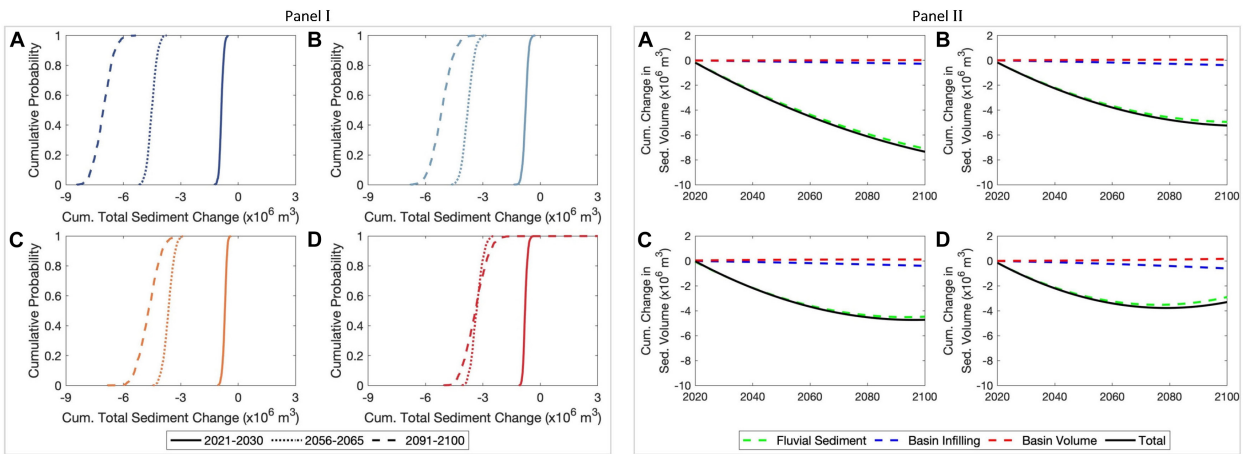

FIGURE 11 | Empirical cumulative distributions of the projected change in total sediment volume exchange (ΔV_T) between the Kalutara estuary and the adjacent coast over the three decadal periods considered **(Panel I)**. The empirical cumulative distributions were developed by averaging the projected ΔV_T values over the three decadal periods considered. **(Panel II)** shows the computed variations of the projected 50th percentile values of change in total sediment volume exchange (ΔV_T) and contributions from different processes to ΔV_T at the Kalutara estuary over the 21st century. Negative volumes indicate that the estuary traps more sediment at the expense of the open coast (i.e., sediment importing estuary). Subplots **(A)**, **(B)**, **(C)**, and **(D)** are for the RCPs 2.6, 4.5, 6.0, and 8.5, respectively.

both the up- and down-drift coasts at the Dyfi estuary system will be subjected to additional coastline recessions (on top of that due to the Bruun effect) to satisfy the estuarine sediment demand. The extent of the additional down-drift coastal recession is constrained by the magnitude of LST. The additional up-drift coastal recession is equivalent to the magnitudinal difference between the estuarine sediment demand (i.e., ΔV_T) and the LST capacity. The model results shown in **Figure 12** (middle) indicate that the down-drift coast at the Dyfi estuary may move landward by between 75 m (RCP 2.6) and 92 m (RCP 8.5) by 2100. The recession along the up-drift coast is larger and projected to be between 95 m (RCP 2.6) and 152 m (RCP 8.5) by 2100.

The Kalutara estuary system is also projected to import sediment from its adjacent coast and hence acts as a sediment

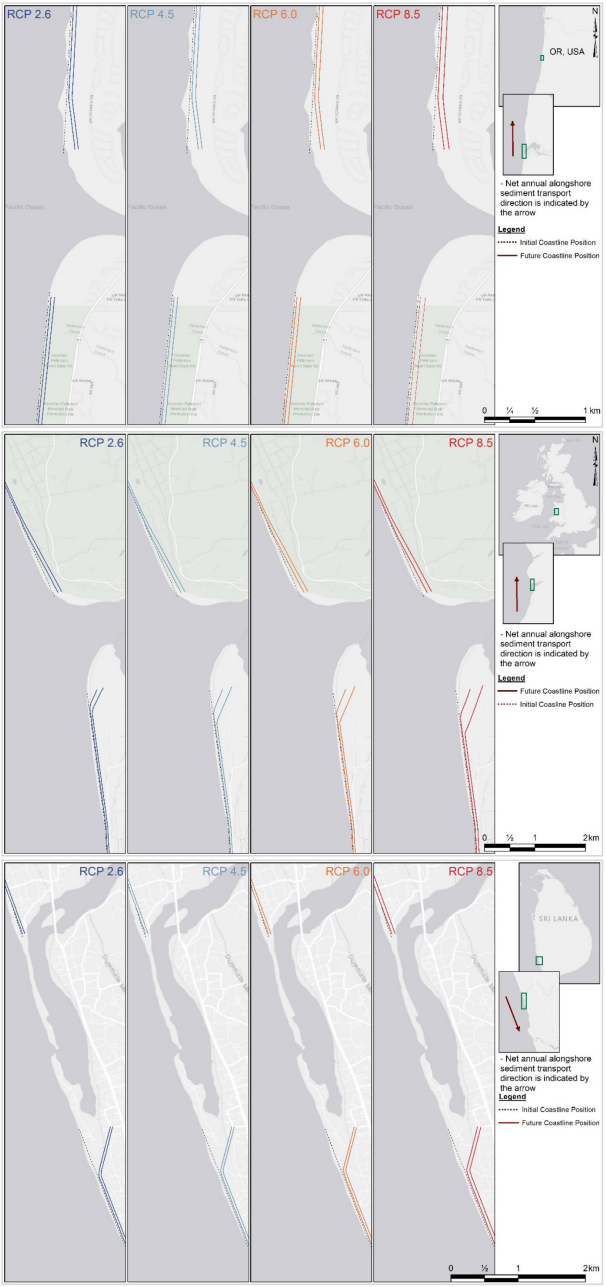

FIGURE 12 | Projected changes of the inlet-affected coastline at the Alsea estuary **(top)**, Dyfi estuary **(middle)**, and Kalutara estuary **(bottom)**. The two solid lines in each subplot represent the final coastline position by 2060 and 2100 (in the same order, moving landward from the most seaward line). The dotted line in each subplot represents the initial (reference) coastline position.

sink for all but the end-century period under RCP 8.5. The magnitude of the sediment demand from the estuary is less than the current longshore sediment transport capacity at the inlet. Therefore, the down-drift coast will experience additional coastal recession driven by ΔV_T, on top of that due to the Bruun effect. Under RCP 8.5, the fluvial sediment supply to the estuary increases during the 2080–2100 period, which results in a net positive ΔV_T during this period. Thus, the Kalutara estuary system acts as a sediment source during this period under RCP 8.5. Therefore, the down-drift coast at Kalutara estuary is projected to prograde after 2080 under RCP 8.5 as sediment is exported by the estuary to the coast. However, this coastline progradation is less than the projected coastline recession due to the Bruun effect over the same period. Consequently, the cumulative effect of these two opposing contributions results in a net coastline recession along the down-drift coast. The up-drift coast is only affected by the coastline recession due to the Bruun effect. The model results [**Figure 12** (bottom)] indicate that the down-drift coast at the Kalutara inlet may erode by between 92 m (RCP 2.6) to 105 m (RCP 8.5) by 2100. The up-drift coast is projected to erode by between 50 m (RCP 2.6) to 67 m (RCP 8.5) by 2100.

To scrutinize the contribution of river catchments and estuarine processes to the projected coastline changes along the inlet-interrupted coasts, the maximum and minimum shoreline change projections obtained from G-SMIC is compared with the coastline recessions due to the Bruun rule only. This comparison (**Table 2**) illustrates that the Bruun rule only is always underestimating the potential shoreline recessions at the three case study locations. The minimum projections of G-SMIC at Alsea estuary system is about 24% larger than projections obtained from the Bruun rule only. The same comparison at Dyfi and Kalutara estuary shows that G-SMIC projections area 84% larger than coastal recession due to the Bruun rule only. The maximum shoreline change projections obtained by G-SMIC at the Alsea and Kalutara estuary systems are respectively 20 and 57% larger than the Bruun rule only projections. The maximum shoreline change projection obtained by G-SMIC at the Dyfi estuary systems is 134% larger than the Bruun rule only projections of shoreline change. These numbers illustrates the significance of incorporating catchment and estuarine processes when simulating the evolution of inlet-interrupted coasts.

TABLE 2 | Comparison of maximum and minimum coastline changes by 2100, obtained from G-SMIC applications and the Bruun rule only.

CEC system	Projected coastline change (m) by 2100			
	Minimum value (RCP 2.6)		Maximum value (RCP 8.5)	
	G-SIMC application	The Bruun rule only	G-SIMC application	The Bruun rule only
Alsea estuary	−67	−54	−86	−72
Dyfi estuary	−92	−50	−152	−65
Kalutara estuary	−92	−50	−105	−67

Minimum and maximum coastline change projections of G-SMIC applications are related to RCP 2.6 and 8.5, respectively (across both up-and down-drift coasts). G-SMIC projections were obtained for the 50th percentile total sediment volume exchange between inlet-estuary systems and the adjacent coast (ΔV_T). Coastline changes due to the Bruun effect were also computed for the 50th percentile regional relative sea-level changes (ΔRSL). Negative values of coastline change indicate coast recession.

DISCUSSION

The results of this study indicate that the variability in model inputs result in substantial uncertainties of the projected ΔV_T by 2100. Results also show that future variation in total sediment volume exchange at tidal inlets (i.e., ΔV_T) would be governed by one or two of its contributing components [i.e., basin infilling (ΔV_{BI}), basin volume (ΔV_{BV}), and fluvial sediment supply (ΔV_{FS})]. In this study, the focus was limited to quantifying the uncertainties associated with model inputs (i.e., only input uncertainties not model uncertainties). Specifically, this study takes into account the uncertainties in projections of temperature (T), river discharge (Q), regional relative sea-level change (ΔRSL), and human-induced erosion factor (E_h). Given that all GCM projections of T, Q and SLR are based on the Representative Concentration Pathways (RCPs) adopted by the IPCC, this study quantifies the differences in model projections obtained for the four IPCC RCPs.

However, it should be noted that the uncertainties quantified here are those associated with the single reduced-complexity model used. To quantify "model uncertainty" it would be necessary to derive projections from several different coastline change models (i.e., a multi-model ensemble). The result of such a multi-model ensemble is required to determine the likelihood ranges as adopted by the IPCC, which, as a precursor needs a high level of confidence (Cubasch et al., 2013). Therefore, the 10–90% ranges presented in the results only correspond to the output variability due to the model input uncertainties, and cannot be taken as an indication of likelihoods of the projections. As the results of the model are probabilistic, another interesting analysis that would be possible is the evaluation of the contribution of each input variable to the total variance of the projected coastline change. This could be achieved via the global sensitivity analysis approach (Sobol', 2001). One application of this method with respect to coastline projection is presented by Le Cozannet et al. (2019).

Scrutinizing the projected model inputs indicate that annual mean temperature and cumulative river discharge have more significant uncertainties that the regional relative sea-level change projections. Therefore, variabilities associated with projections of T and Q are the major sources of model input uncertainties in this application. These are reflected in the projected uncertainties of ΔV_T at the case study systems, as discussed in more detail below.

Projected sea-level rise has substantial implications on the behavior of all but the Kalutara inlet system, which has a relatively small estuary surface area. The overall variation of ΔV_T at Kalutara estuary is governed by the change in fluvial sediment supply. Due to the uncertainties in key climatic model inputs (i.e., T and Q), the projected ΔV_T at the Kalutara estuary system shows substantial variations, especially for RCP 8.5 during the end-century period. The deterministic projections of ΔV_T for RCP 2.6 presented in Bamunawala et al. (2020) deviates (by about 15%) from the 50th percentile values of ΔV_T of the probabilistic projections presented here. This deviation is due to the uncertainties associated with the model inputs (i.e., T and Q). The averaged ensemble values of T and Q used in the deterministic application of G-SMIC presented in Bamunawala et al. (2020) do not adequately account for the uncertainties associated with the GCM projections.

In addition to the estuarine sediment demand due to basin infilling, the Alsea estuary system is also significantly affected by the fluvial sediment supply. As a result, the projected ΔV_T values at the Alsea estuary show considerable uncertainties for all RCPs, especially toward the end-century period (min-max range of 1.0 MCM for RCP 8.5). These uncertainties also arise from the variations associated with the model inputs (i.e., T and Q projections). However, due to the dominance of sea-level rise driven basin infilling in this case, these uncertainties are not as prominent as at the Kalutara estuary system. The deterministic projections of ΔV_T for RCP 8.5 presented in Bamunawala et al. (2020) deviates (by about 30%) from the 50th percentile values of ΔV_T of the probabilistic projections presented here. This deviation is due to the uncertainties associated with the model inputs (i.e., T and Q).

The Dyfi estuary system is dominated by the sea-level rise driven basin infilling. Therefore, the projected 50th percentile values of ΔV_T at the Dyfi estuary system shows the best agreement with the deterministic model results presented by Bamunawala et al. (2020). This agreement illustrates the impact of the uncertainties associated with the climatic model inputs (i.e., T and Q) have on the projected ΔV_T at CEC systems. The uncertainties of the projected ΔV_T values at the Dyfi estuary

TABLE 3 | Comparison of projected coastline change by 2100 with the results presented in Vousdoukas et al. (2020b) (for RCP 8.5).

CEC system	Projected coastline change (m) by 2100 under RCP 8.5				Remarks
	Vousdoukas et al. (2020b)		G-SMIC application		
	Up-drift	Down-drift	Up-drift	Down-drift	
Alsea estuary	−50	−50	−72	−86	Up-drift projections do not vary by more than 50%, but the down-drift projections are varied by ∼70%
Dyfi estuary	−100	−100	−152	−92	Down-drift projections are within 10% of each other, and the up-drift projections do not vary by more than ∼50%
Kalutara estuary	−150	−150	−67	−105	Projections do not vary by more than ∼50%

Negative values of coastline change indicate coastal recessions. The 50th percentile values of coast recessions presented in Vousdoukas et al. (2020b) at the vicinity of the three selected CEC systems are used in this comparison.

follow the variability of ΔRSL and hence increases rapidly toward the end-century period for RCP 8.5.

The projected coastline changes at the case study sites by 2100 are compared with the model results presented in a global assessment of coastline change by Vousdoukas et al. (2020b) (**Table 3**). Here, only the projections made under RCP 8.5 are considered in this comparison. It should, however, be noted that the global assessment of sandy coastline variation presented by Vousdoukas et al. (2020b) does not consider the estuarine and watershed effects and incorporates a correction factor for Bruun effect-driven coastline recession. Therefore, the coastline change projections presented in this study will, by necessity, differ from the results presented in the global assessment of sandy shorelines by Vousdoukas et al. (2020b).

It should be noted that because the shoreline changes presented here and by Bamunawala et al. (2020) are based on deviations from present (reference) river discharge and sediment input rates (and on SLR rates that are greater than present). These shoreline change rates are best interpreted as representing future deviations from present (reference) rates of shoreline change. For CEC systems with present rates of shoreline change that have a magnitude similar to the projected rates of shoreline change, based on the analysis presented here, final shoreline positions over the future time slices should be derived by superimposing the projected and reference rates of coastline change. For CEC systems in which projected rates of change based on this analysis are much larger than those under reference conditions, final shoreline positions will result mainly from the deviations from the present rates. The model hindcasts presented by Bamunawala et al. (2020) indicate that, for all the case study sites considered in this study, rates of projected coastline changes are of the same order of magnitude as the hindcast values. Therefore, in this study, all future coastline positions should be obtained by superimposing the hindcast rates of coastline changes presented by Bamunawala et al. (2020) with projected coastline changes shown in section "Projections of Coastline Change" and **Figure 12**.

It should also be noted that the coastline change projections presented here were obtained using the simplified one-line model presented in Bamunawala et al. (2020). This simplified coastline change model does not account for possible changes in longshore sediment transport rates and gradients therein due to future changes in wave conditions, local variations in coastline orientation (i.e., straight shoreline segments are assumed) or the presence of any coastal structures. The model also does not contain a built-in facility to apply any known limits to eroding sand from up- and down-drift coasts to fulfill estuarine sediment demand. Therefore, when applied along coasts with known limits for sand erodibility, an appropriate threshold should be considered. The model also does not consider the role that the deltas (when present) could play in distributing the exchange sediment volume (ΔV_T). In general, in an inlet-estuary system containing significant ebb deltas with sediment that can be mobilized, part of the sediment demand from the estuary will be supplied from the ebb delta [e.g., Dissanayake et al. (2009, 2012)]. In such cases, these simplified model projections will overestimate coastline recession (i.e., pessimistic estimates). For a sediment exporting estuary system, a part of sediment received by the coast will contribute to the development of ebb delta. In such circumstances, model projections made by this simplified approach can be considered as optimistic projections (i.e., over-projection of coastline progradation). Therefore, these coastline change projections only provide first-order approximations of the long-term evolution of the coastline at the case study sites. Coupling the projected sediment volumes with a coastline change model that provides a more realistic representation of the shape and orientation of coastlines, such as the Coastline Evolution Model (CEM) (Ashton and Murray, 2006), the Coastal One-line Vector Evolution Model (COVE) (Hurst et al., 2015), or ShorelineS (Roelvink et al., 2020) will significantly enhance the quality of coastline change projections.

CONCLUSION

This manuscript presents the development and application of a reduced-complexity modeling technique that can probabilistically assess climate change-driven evolution of inlet-interrupted coasts at time scales of 50 to 100 years while taking into account the contributions from CEC systems in a holistic manner. The model represents the main physical processes that govern the variations of total sediment volume exchange between the estuary system (ΔV_T) and the adjacent coast under the influence of climate change and anthropogenic activities. The probabilistic framework within which the model is applied here enabled the quantification of the uncertainties associated with the projected change in sediment volume exchange between the inlet-estuary systems and the adjacent coast and consequent coastline changes, arising from model input uncertainties. The model was applied to three case-study: the Alsea estuary (Oregon, United States), Dyfi estuary (Wales, United Kingdom), and Kalutara inlet (Sri Lanka) over the period 2020–2100.

Results obtained for the three case study sites showed that future variation in total sediment volume exchange at tidal inlets (i.e., ΔV_T) could be governed by any of the contributing components [i.e., basin infilling (ΔV_{BI}), basin volume (ΔV_{BV}), and fluvial sediment supply (ΔV_{FS})] or combinations thereof. As such, the results of this study underlines the importance of taking into account all these processes when investigating future variations in the sediment budget at CEC systems.

Model projections showed that there are significant uncertainties associated with the sediment volume exchange between the estuary system (ΔV_T) and inlet-interrupted coasts, especially for RCP 8.5 and toward the end-century period (2091–2100). These uncertainties arise mainly due to the intra-annual variabilities in projections of climatic variables (i.e., T and Q), and variations among the General Circulation Model (GCM) projections. Compared to the uncertainties in projections of T and Q, projections of regional relative sea-level change (ΔRSL) contain less variability over the 21st century. Inter-site differences between the projected 50th percentile values and the deterministic estimates of ΔV_T illustrate the importance of adopting probabilistic modeling techniques to evaluate the long-term evolution of CEC systems.

Projections of coastline change at the three case study sites obtained with the 50th percentile projections of total sediment exchange volume (ΔV_T) showed that accounting for basin infilling (ΔV_{BI}), basin volume (ΔV_{BV}), and fluvial sediment supply (ΔV_{FS}) in computing coastline change at these inlet-interrupted coasts results in projections that are between 20% - 134% greater than the projections that would be obtained if only the Bruun effect were taken into account. This further emphasizes the need to consider the CEC systems in a holistic fashion when investigating coastline change along inlet-interrupted coasts.

DATA AVAILABILITY STATEMENT

The raw data supporting the conclusions of this article will be made available by the authors, without undue reservation.

AUTHOR CONTRIBUTIONS

JB, AD, AS, and RR conceived and designed the study. JB developed the model, carried out all model applications, and wrote the first draft of the manuscript. SM provided specific guidance on the catchment hydrology aspects of the study. TD provided specific guidance on the SMIC model adaptation and QA'd the new code. TS assisted with GCM data collection and catchment delineation. All authors provided feedback on the manuscript and contributed text.

FUNDING

This study is part of JB's Ph.D. research which is supported by the Deltares Research Programme 'Understanding System Dynamics; from River Basin to Coastal Zone' and the AXA Research Fund. RR was supported by the AXA Research Fund and the Deltares Strategic Research Programme 'Coastal and Offshore Engineering'.

ACKNOWLEDGMENTS

Last of the Wild Project, Global Human Footprint, Version 2 data were developed by the Wildlife Conservation Society – WCS and the Center for International Earth Science Information Network (CIESIN), Columbia University and were obtained from the NASA Socioeconomic Data and Applications Center (SEDAC) at http://dx.doi.org/10.7927/H4M61H5F. Accessed 1 October 2015. Any use of trade, firm, or product names is for descriptive purposes only and does not imply endorsement by the United States Government.

SUPPLEMENTARY MATERIAL

The Supplementary Material for this article can be found online at: https://www.frontiersin.org/articles/10.3389/fmars.2020.579203/full#supplementary-material

REFERENCES

Anthony, E. J., Brunier, G., Besset, M., Goichot, M., Dussouillez, P., and Nguyen, V. L. (2015). Linking rapid erosion of the Mekong River delta to human activities. *Sci. Rep.* 5:14745. doi: 10.1038/srep14745

Ashton, A. D., and Murray, A. B. (2006). High-angle wave instability and emergent shoreline shapes: 1. Modeling of sand waves, flying spits, and capes. *J. Geophys. Res. Earth Surf.* 111:F04011. doi: 10.1029/2005JF000422

Aubrey, D. G., and Weishar, L. (eds) (1988). *Hydrodynamics and Sediment Dynamics of Tidal Inlets*. New York, NY: Springer, doi: 10.1007/978-1-4757-4057-8

Balthazar, V., Vanacker, V., Girma, A., Poesen, J., and Golla, S. (2013). Human impact on sediment fluxes within the blue nile and atbara river basins. *Geomorphology* 180–181, 231–241. doi: 10.1016/j.geomorph.2012.10.013

Bamunawala, J., Dastgheib, A., Ranasinghe, R., van der Spek, A., Maskey, S., Murray, A. B., et al. (2020). A holistic modeling approach to project the evolution of inlet-interrupted coastlines over the 21st century. *Front. Mar. Sci.* 7:542. doi: 10.3389/fmars.2020.00542

Bamunawala, J., Maskey, S., Duong, T., and van der Spek, A. (2018a). Significance of fluvial sediment supply in coastline modelling at tidal inlets. *J. Mar. Sci. Eng.* 6:79. doi: 10.3390/jmse6030079

Bamunawala, J., Ranasinghe, R., van der Spek, A., Maskey, S., and Udo, K. (2018b). Assessing future coastline change in the vicinity of tidal inlets via reduced complexity modelling. *J. Coast. Res.* 85, 636–640. doi: 10.2112/SI85-128.1

Besset, M., Anthony, E. J., and Bouchette, F. (2019). Multi-decadal variations in delta shorelines and their relationship to river sediment supply: an assessment and review. *Earth Sci. Rev.* 193, 199–219. doi: 10.1016/j.earscirev.2019.04.018

Bosello, F., Nicholls, R. J., Richards, J., Roson, R., and Tol, R. S. J. (2012). Economic impacts of climate change in Europe: sea-level rise. *Clim. Change* 112, 63–81. doi: 10.1007/s10584-011-0340-1

Brown, S., Nicholls, R. J., Hanson, S., Brundrit, G., Dearing, J. A., Dickson, M. E., et al. (2014). Shifting perspectives on coastal impacts and adaptation. *Nat. Clim. Chang.* 4, 752–755. doi: 10.1038/nclimate2344

Bruun, P. M. (1962). Sea-level rise as a cause of shore erosion. *J. Waterw. Harb. Div.* 88, 117–132.

CSIRO, and Bureau of Meteorology (2015). *Climate Change in Australia Information for Australia's Natural Resource Management Regions: Technical Report*. Australia: CSIRO and Bureau of Meteorology.

Cubasch, U., Wuebbles, D., Chen, D., Facchini, M. C., Frame, D., Mahowald, N., et al. (2013). "'Introduction'," in *Climate Change 2013: The Physical Science Basis. Contribution of Working Group I to the Fifth Assessment Report of the Intergovernmental Panel on Climate Change*, eds T. F. Stocker, D. Qin, G.-K. Plattner, M. Tignor, S. K. Allen, J. Boschung, et al. (Cambridge: Cambridge University Press).

Dastgheib, A., Jongejan, R., Wickramanayake, M., and Ranasinghe, R. (2018). Regional scale risk-informed land-use planning using probabilistic coastline recession modelling and economical optimisation: east coast of Sri Lanka. *J. Mar. Sci. Eng.* 6:120. doi: 10.3390/jmse6040120

Davis, R. A. Jr., and Fitzgerald, D. M. (2003). *Beaches and Coasts*. Hoboken, NJ: Wiley-Blackwell.

Dean, R. G. G., and Houston, J. R. R. (2016). Determining shoreline response to sea level rise. *Coast. Eng.* 114, 1–8. doi: 10.1016/j.coastaleng.2016.03.009

Dissanayake, D. M. P. K., Ranasinghe, R., and Roelvink, J. A. (2012). The morphological response of large tidal inlet/basin systems to relative sea level rise. *Clim. Change* 113, 253–276. doi: 10.1007/s10584-012-0402-z

Dissanayake, D. M. P. K., Roelvink, J. A., and van der Wegen, M. (2009). Modelled channel patterns in a schematized tidal inlet. *Coast. Eng.* 56, 1069–1083. doi: 10.1016/j.coastaleng.2009.08.008

Dunn, F. E., Darby, S. E., Nicholls, R. J., Cohen, S., Zarfl, C., and Fekete, B. M. (2019). Projections of declining fluvial sediment delivery to major deltas worldwide in response to climate change and anthropogenic stress. *Environ. Res. Lett.* 14:84034. doi: 10.1088/1748-9326/ab304e

Dunn, F. E., Nicholls, R. J., Darby, S. E., Cohen, S., Zarfl, C., and Fekete, B. M. (2018). Projections of historical and 21st century fluvial sediment delivery to the Ganges-Brahmaputra-Meghna, Mahanadi, and Volta deltas. *Sci. Total Environ.* 642, 105–116. doi: 10.1016/j.scitotenv.2018.06.006

Duong, T. M., Ranasinghe, R., Walstra, D., and Roelvink, D. (2016). Assessing climate change impacts on the stability of small tidal inlet systems: why and how? *Earth Sci. Rev.* 154, 369–380. doi: 10.1016/j.earscirev.2015.12.001

FitzGerald, D. M., Fenster, M. S., Argow, B. A., and Buynevich, I. V. (2008). Coastal impacts due to sea-level rise. *Annu. Rev. Earth Planet. Sci.* 36, 601–647. doi: 10.1146/annurev.earth.35.031306.140139

FitzGerald, D. M., Georgiou, I., and Miner, M. (2015). "'Estuaries and tidal inlets," in *Coastal Environments and Global Change*, eds G. Masselink and R. Gehrels (Chichester: John Wiley & Sons Ltd), 268–298. doi: 10.1002/9781119117261.ch12

Hallegatte, S., Green, C., Nicholls, R. J., and Corfee-Morlot, J. (2013). Future flood losses in major coastal cities. *Nat. Clim. Chang.* 3:802. doi: 10.1038/nclimate1979

Hegerl, G. C., Black, E., Allan, R. P., Ingram, W. J., Polson, D., Trenberth, K. E., et al. (2015). Challenges in quantifying changes in the global water cycle. *Bull. Am. Meteorol. Soc.* 96, 1097–1115. doi: 10.1175/BAMS-D-13-00212.1

Hinkel, J., Nicholls, R. J., Tol, R. S. J., Wang, Z. B., Hamilton, J. M., Boot, G., et al. (2013). A global analysis of erosion of sandy beaches and sea-level rise: an application of DIVA. *Glob. Planet. Change* 111, 150–158. doi: 10.1016/j.gloplacha.2013.09.002

Hugo, G. (2011). Future demographic change and its interactions with migration and climate change. *Glob. Environ. Chang.* 21, S21–S33. doi: 10.1016/j.gloenvcha.2011.09.008

Hurst, M. D., Barkwith, A., Ellis, M. A., Thomas, C. W., and Murray, A. B. (2015). Exploring the sensitivities of crenulate bay shorelines to wave climates using a new vector-based one-line model. *J. Geophys. Res. Earth Surf.* 120, 2586–2608. doi: 10.1002/2015JF003704

Jongejan, R., Ranasinghe, R., Wainwright, D., Callaghan, D. P., and Reyns, J. (2016). Drawing the line on coastline recession risk. *Ocean Coast. Manag.* 122, 87–94. doi: 10.1016/j.ocecoaman.2016.01.006

Kirezci, E., Young, I. R., Ranasinghe, R., Muis, S., Nicholls, R. J., Lincke, D., et al. (2020). Projections of global-scale extreme sea levels and resulting episodic coastal flooding over the 21st Century. *Sci. Rep.* 10:11629.

Le Cozannet, G., Bulteau, T., Castelle, B., Ranasinghe, R., Wöppelmann, G., Rohmer, J., et al. (2019). Quantifying uncertainties of sandy shoreline change projections as sea level rises. *Sci. Rep.* 9:42. doi: 10.1038/s41598-018-37017-4

Le Cozannet, G., Nicholls, J. R., Hinkel, J., Sweet, V. W., McInnes, L. K., Van de Wal, S. W. R., et al. (2017). Sea level change and coastal climate services: the way forward. *J. Mar. Sci. Eng.* 5:49. doi: 10.3390/jmse5040049

Luijendijk, A., Hagenaars, G., Ranasinghe, R., Baart, F., Donchyts, G., and Aarninkhof, S. (2018). The State of the World's Beaches. *Sci. Rep.* 8:6641. doi: 10.1038/s41598-018-24630-6

McGranahan, G., Balk, D., and Anderson, B. (2007). The rising tide: assessing the risks of climate change and human settlements in low elevation coastal zones. *Environ. Urban.* 19, 17–37. doi: 10.1177/0956247807076960

McSweeney, S. L., Kennedy, D. M., Rutherfurd, I. D., and Stout, J. C. (2017). Intermittently Closed/Open lakes and lagoons: their global distribution and boundary conditions. *Geomorphology* 292, 142–152. doi: 10.1016/j.geomorph.2017.04.022

Mehvar, A., Dastgheib, A., and Ranasinghe, R. (2016). *Relative Sea Level Rise Scenarios: Central Coast of Bangladesh*. Delft: Delft University of Technology.

Merkens, J.-L., Reimann, L., Hinkel, J., and Vafeidis, A. T. (2016). Gridded population projections for the coastal zone under the shared socioeconomic pathways. *Glob. Planet. Change* 145, 57–66. doi: 10.1016/j.gloplacha.2016.08.009

Murray, A. B. (2007). Reducing model complexity for explanation and prediction. *Geomorphology* 90, 178–191. doi: 10.1016/j.geomorph.2006.10.020

Murray, A. B., and Moore, L. J. (2018). "'Geometric constraints on long-term barrier migration: from simple to surprising BT'," in *Barrier Dynamics and Response to Changing Climate*, eds L. J. Moore and A. B. Murray (Cham: Springer International Publishing), 211–241. doi: 10.1007/978-3-319-68086-6_7

Neumann, B., Vafeidis, A. T., Zimmermann, J., and Nicholls, R. J. (2015). Future coastal population growth and exposure to sea-level rise and coastal flooding - a global assessment. *PLoS One* 10:e0118571. doi: 10.1371/journal.pone.0118571

Nicholls, R. J., Hanson, S. E., Lowe, J. A., Warrick, R. A., Lu, X., Long, A. J., et al. (2011). *Constructing Sea-Level Scenarios for Impact and Adaptation Assessment of Coastal Area: A Guidance Document. Supporting Material, Intergovernmental Panel on Climate Change Task Group on Data and Scenario Support for Impact and Climate Analysis*. Geneva: IPCC.

Overeem, I., and Syvitski, J. P. M. (2009). *Dynamics and Vulnerability of Delta Systems*. LOICZ Reports & Studies No. 35. Geesthacht: GKSS Research Center.

Palmer, M. A., Liermann, C. A. R., Nilsson, C., Flörke, M., Alcamo, J., Lake, P. S., et al. (2008). Climate change and the world's river basins: anticipating management Options. *Front. Ecol. Environ.* 6:81–89. doi: 10.1890/060148

Prahl, B. F., Boettle, M., Costa, L., Kropp, J. P., and Rybski, D. (2018). Damage and protection cost curves for coastal floods within the 600 largest European cities. *Sci. Data* 5:180034. doi: 10.1038/sdata.2018.34

Rahmstorf, S. (2007). A semi-empirical approach to projecting future sea-level rise. *Science* 315, 368–370. doi: 10.1126/science.1135456

Ranasinghe, R. (2016). Assessing climate change impacts on open sandy coasts: a review. *Earth-Science Rev.* 160, 320–332. doi: 10.1016/j.earscirev.2016.07.011

Ranasinghe, R. (2020). On the need for a new generation of coastal change models for the 21st century. *Sci. Rep.* 10:2010. doi: 10.1038/s41598-020-58376-x

Ranasinghe, R., Callaghan, D., and Stive, M. J. F. (2012). Estimating coastal recession due to sea level rise: beyond the Bruun rule. *Clim. Change* 110, 561–574. doi: 10.1007/s10584-011-0107-8

Ranasinghe, R., Duong, T. M., Uhlenbrook, S., Roelvink, D., and Stive, M. (2013). Climate-change impact assessment for inlet-interrupted coastlines. *Nat. Clim. Chang.* 3, 83–87. doi: 10.1038/nclimate1664

Ranasinghe, R., and Stive, M. J. F. (2009). Rising seas and retreating coastlines. *Clim. Change* 97:465. doi: 10.1007/s10584-009-9593-3

Ranasinghe, R., Wu, C. S., Conallin, J., Duong, T. M., and Anthony, E. J. (2019). Disentangling the relative impacts of climate change and human activities on fluvial sediment supply to the coast by the world's large rivers: Pearl River Basin. *China. Sci. Rep.* 9:9236. doi: 10.1038/s41598-019-45442-2

Roelvink, D., Huisman, B., Elghandour, A., Ghonim, M., and Reyns, J. (2020). Efficient modeling of complex sandy coastal evolution at monthly to century time scales. *Front. Mar. Sci.* 7:535. doi: 10.3389/fmars.2020.00535

Sobol', I. M. (2001). Global sensitivity indices for nonlinear mathematical models and their Monte Carlo estimates. *Math. Comput. Simul.* 55, 271–280. doi: 10.1016/S0378-4754(00)00270-6

Spencer, T., Schuerch, M., Nicholls, R. J., Hinkel, J., Lincke, D., Vafeidis, A. T., et al. (2016). Global coastal wetland change under sea-level rise and related stresses: the DIVA wetland change model. *Glob. Planet. Change* 139, 15–30. doi: 10.1016/j.gloplacha.2015.12.018

Stive, M. J. F. (2004). How important is global warming for coastal erosion? *Clim. Change* 64, 27–39. doi: 10.1023/B:CLIM.0000024785.91858.1d

Stive, M. J. F., Capobianco, M., Wang, Z. B., Ruol, P., and Buijsman, M. C. (1998). "'Morphodynamics of a tidal lagoon and the adjacent Coast," in *Physics of Estuaries and Coastal Seas*, eds J. Dronkers and M. Scheffers (Rotterdam: A. A. Balkema), 397–407.

Stive, M. J. F., Roelvink, J. A., and de Vriend, H. J. (1990). "Large-scale coastal evolution concept," in *Proceedings of the 22nd International Conference on Coastal Engineering*, (Delft: Delft University), 1962–1974. doi: 10.1061/9780872627765.150

Stocker, T. F., Qin, D., Plattner, G.-K., Alexander, L. V., Allen, S. K., Bindoff, N. L., et al. (2013a). "'Technical summary'," in *Climate Change 2013: The Physical Science Basis. Contribution of Working Group I to the Fifth Assessment Report of the Intergovernmental Panel on Climate Change*, eds T. F. Stocker, D. Qin, G.-K. Plattner, M. Tignor, S. K. Allen, J. Boschung, et al. (Cambridge: Cambridge University Press).

Stocker, T. F., Qin, D., Plattner, G.-K., Tignor, M., Allen, S. K., Boschung, J., et al. (eds) (2013b). "IPCC, 2013: summary for policymakers," in *Climate Change 2013: The Physical Science Basis. Contribution of Working Group I to the 5th Assessment Report of the Intergovernmental Panel on Climate Change*, (Cambridge: Cambridge University Press).

Syvitski, J. P. M. (2005). Impact of humans on the flux of terrestrial sediment to the global coastal Ocean. *Science* 308, 376–380. doi: 10.1126/science.1109454

Syvitski, J. P. M., and Kettner, A. J. (2008). "Scaling sediment flux across landscapes," in *Sediment Dynamics in Changing Environments*, eds J. Schmidt, T. Cochrane, C. Phillips, S. Elliot, T. Davies, and L. Basher (Christchurch: IAHS Publications), 149–156.

Syvitski, J. P. M., Kettner, A. J., Overeem, I., Hutton, E. W. H., Hannon, M. T., Brakenridge, G. R., et al. (2009). Sinking deltas due to human activities. *Nat. Geosci.* 2, 681–686. doi: 10.1038/ngeo629

Syvitski, J. P. M., and Milliman, J. D. (2007). Geology, geography, and humans battle for dominance over the delivery of fluvial sediment to the Coastal Ocean. *J. Geol.* 115, 1–19. doi: 10.1086/509246

Taylor, K., Ronald, S., and Meehl, G. (2011). An overview of CMIP5 and the experiment design. *Bull. Am. Meteorol. Soc.* 93, 485–498. doi: 10.1175/BAMS-D-11-00094.1

Toimil, A., Losada, I. J., Camus, P., and Díaz-Simal, P. (2017). Managing coastal erosion under climate change at the regional scale. *Coast. Eng.* 128, 106–122. doi: 10.1016/j.coastaleng.2017.08.004

Trenberth, K. E., Smith, L., Qian, T., Dai, A., and Fasullo, J. (2007). Estimates of the global water budget and its annual cycle using observational and model Data. *J. Hydrometeorol.* 8, 758–769. doi: 10.1175/JHM600.1

Vafeidis, A., Neumann, B., Zimmermann, J., and Nicholls, R. J. (2011). *MR9: Analysis of Land Area and Population in the Low-Elevation Coastal Zone (LECZ)*. London: The Government Office for Science, 172.

van Maanen, B., Nicholls, R. J., French, J. R., Barkwith, A., Bonaldo, D., Burningham, H., et al. (2016). Simulating mesoscale coastal evolution for decadal coastal management: a new framework integrating multiple, complementary modelling approaches. *Geomorphology* 256, 68–80. doi: 10.1016/j.geomorph.2015.10.026

Veerbeek, W. (2017). Estimating the Impacts of Urban Growth on Future Flood Risk: A Comparative Study. Leiden: CRC Press/Balkema – Taylor & Francis Group. doi: 10.1016/j.geomorph.2015.10.026

Vörösmarty, C. J., Meybeck, M., Fekete, B., Sharma, K., Green, P., and Syvitski, J. P. M. (2003). Anthropogenic sediment retention: major global impact from registered river impoundments. *Glob. Planet. Change* 39, 169–190. doi: 10.1016/S0921-8181(03)00023-27

Vousdoukas, M. I., Mentaschi, L., Hinkel, J., Ward, P. J., Mongelli, I., Ciscar, J.-C., et al. (2020a). Economic motivation for raising coastal flood defenses in Europe. *Nat. Commun.* 11:2119. doi: 10.1038/s41467-020-15665-3

Vousdoukas, M. I., Ranasinghe, R., Mentaschi, L., Plomaritis, T. A., Athanasiou, P., Luijendijk, A., et al. (2020b). Sandy coastlines under threat of erosion. *Nat. Clim. Chang.* 10, 260–263. doi: 10.1038/s41558-020-0697-0

Vousdoukas, M. I., Mentaschi, L., Voukouvalas, E., Bianchi, A., Dottori, F., and Feyen, L. (2018). Climatic and socioeconomic controls of future coastal flood risk in Europe. *Nat. Clim. Chang.* 8, 776–780. doi: 10.1038/s41558-018-0260-4

Wolinsky, M. A., and Murray, A. B. (2009). A unifying framework for shoreline migration: 2. Application to wave-dominated coasts. *J. Geophys. Res. Earth Surf.* 114:F01009. doi: 10.1029/2007JF000856

Wong, P. P., Losada, I. J., Gattuso, J.-P., Hinkel, J., Khattabi, A., McInnes, K. L., et al. (2014). "'Coastal systems and low-lying areas," in *Climate Change 2014: Impacts, Adaptation, and Vulnerability. Part A: Global and Sectoral Aspects. Contribution of Working Group II to the Fifth Assessment Report of the Intergovernmental Panel on Climate Change*, eds C. B. Field, V. R. Barros, D. J. Dokken, K. J. Mach, M. D. Mastrandrea, T. E. Bilir, et al. (Cambridge: Cambridge University Press), 361–409.

Woodruff, J. D., Irish, J. L., and Camargo, S. J. (2013). Coastal flooding by tropical cyclones and sea-level rise. *Nature* 504, 44–52. doi: 10.1038/nature12855

Conflict of Interest: The authors declare that the research was conducted in the absence of any commercial or financial relationships that could be construed as a potential conflict of interest.

The reviewer AD'A declared a past co-authorship with one of the authors AM to the handling editor.

frontiers in Marine Science

ORIGINAL RESEARCH
published: 13 January 2021
doi: 10.3389/fmars.2020.566277

Dynamical Downscaling of Coastal Dynamics for Two Extreme Storm Surge Events in Japan

Joško Trošelj[1,2], Junichi Ninomiya[3], Satoshi Takewaka[4] and Nobuhito Mori[2]*

[1] Transdisciplinary Science and Engineering Program, Graduate School of Advanced Science and Engineering, Hiroshima University, Hiroshima, Japan, [2] Disaster Prevention Research Institute, Kyoto University, Kyoto, Japan, [3] Institute of Science and Engineering, Kanazawa University, Kanazawa, Japan, [4] Department of Engineering Mechanics and Energy, University of Tsukuba, Tsukuba, Japan

Hindcasts of the downscaled fine resolution scale coastal dynamics are important to quantitatively analyze variations in storm surge heights, water temperature, salinity and high velocities which induce shoreline changes. This study quantifies the impact of two extreme storm surge events in October 2006 on the Ibaraki Coast in Japan to the coastal Sea Surface Height (SSH), vertically averaged velocity (V_{bar}), Sea Surface Temperature (SST), and Sea Surface Salinity (SSS) by reproducing hindcasts of the dynamically downscaled coastal dynamics from a 10 km resolution parent dataset (Four-dimensional Variational Ocean ReAnalysis for the Western North Pacific over 30 years, FORA-WNP30) to related 2 km, 667 and 222 m resolution datasets using three domain nesting Coupled-Ocean-Atmosphere-Wave-Sediment-Transport Modeling System (COAWST). Validation was made by comparing the SSH, V_{bar}, SST, and SSS modeled results with observed data and discussing differences in their values in the downscaled and the parent datasets. This study concludes that the low-pressure system event on October 7 had much bigger impact to the SSH and V_{bar} than the one on October 24, which had similar peak of southward surface wind but lower Sea Level Pressure drop, whereas the impact to the SST and SSS was similar. These findings are helpful in understanding and assessing shoreline changes and damages on the well-developed local fishery and seashell industry. Finally, these findings and modeling approach are useful for climate change impact assessment and can ultimately serve as guidelines for developing adaptation policies.

Keywords: hindcasts, extreme storm surges, ocean model application, COAWST, dynamical downscaling, 3 domain nesting, climate change

OPEN ACCESS

Edited by:
Goneri Le Cozannet, Bureau de Recherches Géologiques et Minières, France

Reviewed by:
Pushpa Dissanayake, University of Kiel, Germany
Begoña Pérez-Gómez, Independent Researcher, Madrid, Spain

****Correspondence:***
Joško Trošelj
josko@hiroshima-u.ac.jp; josko.troselj@gmail.com

Specialty section:
This article was submitted to Coastal Ocean Processes, a section of the journal Frontiers in Marine Science

Received: *27 May 2020*
Accepted: *09 December 2020*
Published: *13 January 2021*

Citation:
Trošelj J, Ninomiya J, Takewaka S and Mori N (2021) Dynamical Downscaling of Coastal Dynamics for Two Extreme Storm Surge Events in Japan. Front. Mar. Sci. 7:566277. doi: 10.3389/fmars.2020.566277

INTRODUCTION

Storm surge is a coastal phenomenon which has been occurring recently with increasing frequency due to the impact of climate change. Consequently, an increase is projected in the global mean sea level and other oceanic and atmospheric parameters (Intergovernmental Panel on Climate Change (IPCC), 2014). Coastal zones are particularly susceptible to the effects of climate change because of shallow water environment where, as opposed to deeper oceanic waters, a little change in any oceanic parameter [e.g., Sea Surface Height (SSH), vertically averaged velocity (V_{bar}), Sea Surface Temperature (SST), and Sea Surface Salinity (SSS)]; in any atmospheric parameter, [e.g., Sea Level Pressure (SLP) or surface wind]; or in any fluvial parameter (e.g., river discharge), can cause a

Modelling approach of this study is useful for climate change impact assessment and can ultimately serve as a guideline for developing adaptation policies and also to assess shoreline changes and damages to the local fishery and seashell industry

(1) This study quantifies the impact of the two extreme storm surge events from October 2006 on the Ibaraki Coast in Japan to the coastal Sea Surface Height (SSH), Vertically averaged velocity (V_{bar}), Sea Surface Temperature (SST) and Sea Surface Salinity (SSS) by reproducing hindcasts of 3 domain nesting dynamically downscaled coastal dynamics from 10 km to 222 m resolution.

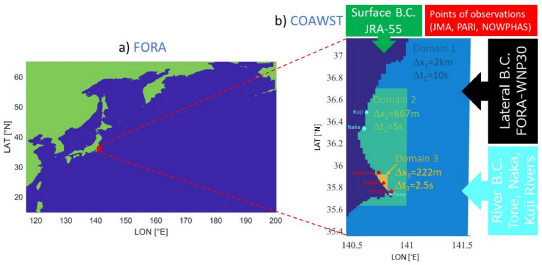

(a) Geographic position of FORA domain and COAWST domain 1 (red dot) on the Ibaraki Coast
(b) Schematic representation of COAWST model setup (resolutions at domain 1: 2 km; domain 2: 667 m; domain 3: 222 m), and marked locations of river mouths (cyan dots) and observation points (red dots).

(2) The downscaled COAWST model results of SSH, V_{bar}, SST and SSS from domain 2 (667 m resolution) were validated with observed data. The SSH validation showed that the downscaled model shows better performance than parent dataset FORA-WNP30 in reproducing variabilities of extreme SSH from the two storm surge events. However, FORA-WNP30 showed better performance in reproducing mean model state.

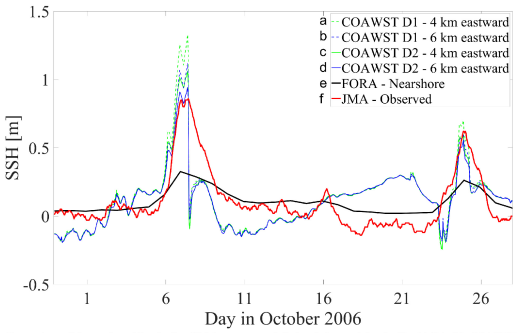

Comparison of time series of Sea Surface Height among modelled and observed data in Choshi ((a), (b): COAWST model 4 and 6 km eastward (2nd and 3rd grids) offshore, respectively, for domain 1; (c), (d): COAWST model 4 and 6 km eastward (6th and 9th grids) offshore, respectively, for domain 2; (e) FORA model nearshore; (f): JMA observed data).

(3) Modelled SSS values close to river mouths lower than 30 PSU showed good agreement with observed Chlorophyll-a (Chl-a) concentrations higher than 5 mg/m^3 for the same considered locations. This is an expected mechanism during an extreme storm surge event because high river discharge causes reduced SSS whereas increased concentrations of Chl-a indicate enhanced supply of organic material and phytoplankton transported from the river to the ocean.

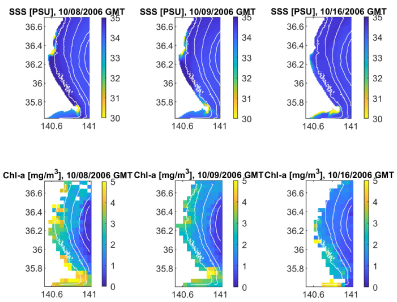

Comparison of modelled Sea Surface Salinity (upper) and observed Chlorophyll-a concentrations (lower) in domain 2 for 8th (left), 9th (middle) and 16th (right) of October, GMT time zone. Bathymetry contours represent depths of 25, 50, 100 and 200 m.

(4) Finally, differences of the two storm surge events in terms of SSH, Sea Level Pressure (SLP), Sea surface wind (W10), V_{bar}, SST and SSS in Hasaki observation point were discussed. This study concludes that the extreme low-pressure system event on the 1st storm showed much bigger impact to the coastal SSH and V_{bar} than on the 2nd storm, which had similar values of W10 but lower SLP drop. This mechanism might be due to meteorological tsunami.

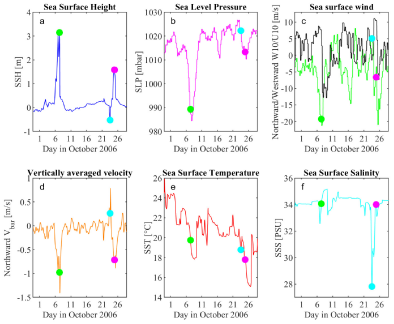

COAWST modelled results of (a) SSH, (b) SLP, (c) W10; U10 (green: N-S; black: W-E direction), (d) V_{bar} (N-S direction), (e) SST and (f) SSS in Hasaki (green dot: 7th of October at 9 a.m.; cyan dot: 23rd of October at 1 p.m.; magenta dot: 24th of October at 9 p.m.).

GRAPHICAL ABSTRACT | Study domains and model setup **(up-left)**, Sea Surface Height results validation **(up-right)**, Sea Surface Salinity results validation **(down-left)** and impact of the two storm surge events to the associated coastal dynamics variables **(down-right)**.

much bigger impact on the coastal environment or local fishery and seashell industry. The mutual interplays of all of these coastal parameters are important in reproducing hindcasts of storm surge events. Since coarse resolution scale global climate models cannot precisely reproduce hindcasts of these coastal parameters, the downscaling of coastal dynamics to finer spatiotemporal resolution scales is needed. In the following paragraphs, past related studies with common topic of extreme surge events are discussed according to the spatial scale of relevance for this study: first, similar recent studies outside of Japan are discussed on the example of Typhoon Haiyan in Philippines, then past related studies occurred in Japan are discussed, and afterwards past related studies on the Ibaraki Coast of Japan are discussed. Finally, it is pointed out the literature gap which is missing in all those related studies, which is therefore the objective of this study.

Many recent studies about extreme storm surge events focus, for example, on the extreme super Typhoon Haiyan which struck the Philippines in 2013. Mori et al. (2014) found that the Haiyan storm surge was about 5–6 m high and wind-induced surge and bay oscillation caused extreme surge height. Lagmay et al. (2015) documented the storm surge simulations which were used as basis for the warnings provided to the public 2 days prior to the howler's landfall. Takayabu et al. (2015) indicated that the worst case scenario of a storm surge in the Gulf of Leyte may be worse by 20% due to the already occurred global warming since 1870. Lee and Kim (2015) parametrized the wave-induced dissipation stress from breaking waves, whitecapping and depth-induced wave breaking. Kim et al. (2015) found that determination of the radius of the Typhoon is important to simulate the Haiyan surge and wave heights inside of the Leyte Gulf. Soria et al. (2016) compared Haiyan storm surge heights with its predecessor from 1897, which had similar heights on the open Pacific Coast but the heights were twice lower than in San Pedro bay. Takagi et al. (2016) evaluated the impact of flood waters caused by the storm surge on evacuation in urban areas, and recommended that evacuation of pedestrians during a storm peak is usually more hazardous than allowing them to stay in their homes. Kumagai et al. (2016) estimated the return periods of storm surge levels to be 240 to 360 years. Tajima et al. (2016) carried numerical experiments to investigate dynamic behavior of storm surge and

storm waves on San Pedro bay and found that the bay seiche may be one of the dominant factors that amplify the surge height at the inner part of the bay. Al Mohit et al. (2018) showed that the maximum water level of the storm surge was reduced by up to 20% near the river mouth due to the penetration of piled up water inside the Meghna River if the impact of freshwater inflow was considered in the coastal ocean model, thus, making it important to include rivers when conducting storm surge simulations. Khanal et al. (2019) analyzed near-simultaneous occurrence of high river discharge and storm-surge peak and found that the hazard of their co-occurrence cannot be neglected in a robust risk assessment. Ye et al. (2020) united traditional hydrologic and ocean models in a single modeling platform to show that the baroclinicity was a major driving force in adjustment phase of rebounding water level and the sustained high water-level during the ensuing river flooding for the Hurricane Irene event in 2011. Höffken et al. (2020) emphasized the high importance of uncertainty related to temporal variability of storm surge events on flood characteristics in coastal zones. Tadesse et al. (2020) simulated storm surges at the global scale using data-driven models and showed that mean sea-level pressure is the most important predictor to model daily maximum surge. The most recently, Muis et al. (2020) projected a high resolution global dataset of extreme sea levels, tides and storm surges for the period 1979–2017 as well as future climate projections from 2040 to 2100.

In Japan, there have been many studies of hindcasts, forecasts and future projections of extreme storm surges that are mainly induced by extreme typhoons or low-pressure events. Higaki et al. (2009) developed a numerical storm surge model to provide the basis for warnings to mitigate the effects of such disasters. Kim et al. (2010) showed that wave-induced set-up is important for determining storm surge water levels during Typhoon Anita. Lee et al. (2010) developed a new method for wave–current interaction in terms of momentum transfer due to whitecapping in deep water and depth-induced wave breaking in shallow water for storm surge events in Seto Inland Sea for Typhoons Yancy and Chaba. Kim et al. (2014) found that the characteristic of the after-runner storm surge from Typhoon Songda comes from the Ekman setup which is impacted by the Coriolis force over the Tottori Coasts. Ninomiya et al. (2017) conducted dynamical downscaling to study present and future climate conditions and storm surge simulation for Typhoon Vera. Troselj et al. (2017) found that the impact of freshwater outflow on sea surface salinity during and after Typhoons Roke and Chataan was significant. Mori et al. (2019a) presented the maximum storm surge of 3.29 m at the Osaka Tide Station and analyzed the relation between maximum water level and the resulting damage from Typhoon Jebi of 2018. Mori et al. (2019b) projected that extreme storm surge will be accelerated by global warming with the similar magnitude to sea-level rise in + 4K condition, which represents future climate experiments of 2051–2110 years × 90 members.

On the Ibaraki Coast of Japan, several past studies have focused on the longshore current driving forces and hindcasts of extreme storm surge events. Goda (2006) showed that various current driving forces other than waves are important for generating longshore currents. Nobuoka et al. (2007) specifically analyzed the driving force of storm surge in the October 2006 event and the maximum water level recorded along the coast. They reported that the Ekman transport was the main physical force that generated this high tide level and that unusual time and spatial distribution of winds around the low-pressure system considerably affected the force. Makino and Nobuoka (2016) probabilistically estimated storm surge and showed that it was possible to minimize local variations by regional frequency analysis and to predict average storm surge inundation. Endo et al. (2017) found that the low salinity waters from Tone River sometimes flow into the coastal zone of Kujukuri due to southward current flow and that warm waters sometimes flow toward Kashima-Nada. More recently, Troselj et al. (2018) and Troselj et al. (2019) conducted dynamical downscaling of coastal dynamics emphasizing freshwater impact from three major rivers and seasonal variabilities of SST and SSS, respectively. Furthermore, several past studies focused on shoreline variabilities along the Ibaraki Coast (Takewaka and Galal, 2007, 2015; Suzuki and Kuriyama, 2014; An, 2016; Banno et al., 2016; Takewaka and Wen, 2017), with some of them dealing with impacts due to the October 2006 storms. Galal and Takewaka (2011) conducted erosion analyzes along the Kashima Coast in Ibaraki for the extreme October 2006 storm from the viewpoint of wave energy flux distribution. The M2 tidal constituent dominates on the Ibaraki Coast with the approximate astronomical tidal range from 0.6 m until 1.5 m. Furthermore, Takewaka and Galal (2007) and Galal and Takewaka (2011) showed that the maximum astronomical tidal range were 1.5 and 1.2 m, maximum significant wave heights were 7 and 6 m and maximum wave periods were 14 and 12 s in the considered study domains during the two extreme October 2006 storms, respectively. The stronger of the two extreme storm surge events from October 7 is referred as S1, while the weaker one from October 24 is referred as S2 hereafter.

While the simulation of SSH during extreme storm surge events have been the focus of most of the above-mentioned studies, other oceanic parameters occurring simultaneously with the extreme events (e.g., V_{bar}, SST, or SSS) have not yet been accurately quantified. Such quantification of parameters on fine resolution spatial and temporal scales is essential for accurate assessment of an extreme storm surge event. Furthermore, the coastal erosion processes on the Ibaraki Coast are numerous and are mostly induced by the coastal current as a result of strong winds, which is why most previous studies focused on shoreline variabilities along the Ibaraki Coast. These studies, however, did not take into consideration accurate hindcasts of coastal ocean currents on fine resolution spatial and temporal scales to enhance the analysis of their results. Reproducing hindcasts of the downscaled fine resolution scale coastal ocean current is important to quantitatively improve analysis of the surge heights and high velocities which can induce shoreline change. Moreover, quantification of variations in water temperature and salinity for extreme storm surge events is important to properly understand and assess the significant impacts on the well-developed local fishery and seashell industry on the Ibaraki Coast, so that improved countermeasures can be implemented in future.

Furthermore, the comprehensive results of this study and its modeling approach can also be useful for climate change impact assessment and ultimately serve as guidelines for developing adaptation policies.

The objective of this study is to quantify the impact of the two extreme storm surge events in October 2006 on the Ibaraki Coast in Japan to the coastal SSH, V_{bar}, SST, and SSS by reproducing hindcasts of downscaled coastal dynamics from coarse resolution (10 km) of global scale to 222 m resolution in local scale. Changes in values of the identified parameters in the downscaled and parent datasets are compared and discussed in this study.

DYNAMICAL DOWNSCALING METHODOLOGY

Model Setup

In this study, Coupled-Ocean-Atmosphere-Wave-Sediment-Transport Modeling System (COAWST), as described in Warner et al. (2010), was used for dynamical downscaling computations. COAWST is a terrain-following 3D primitive Euler equation ocean circulation model for curvilinear coordinate with the hydrostatic and Boussinesq approximations. The 1-year COAWST model run, with detailed methodology described in Troselj et al. (2019), started with an initial ocean state condition on January 1, 2006 and ended on December 31, 2006. The analyzed model run between the two studies is the same, but this study provides a more detailed and comprehensive validation of the model parameters by separately validating four coastal dynamics parameters. Furthermore, this current study also analyses time series data of each S1 and S2 with focus on more comprehensively analyzed impact of the storm surge events to multiple coastal dynamics parameters, while the previous study analyzed seasonal and inter-annual variabilities of SSS and SST.

Methods for dynamical downscaling from the ocean reanalysis dataset Four-dimensional Variational Ocean ReAnalysis for the Western North Pacific over 30 years, FORA-WNP30, with 10 km resolution and daily output values (FORA, Usui et al. (2017)) were developed using COAWST model with 2 km resolution and hourly output values. **Figure 1A** shows the geographic position of FORA domain and COAWST domain 1 on the Ibaraki Coast. The COAWST model used 3 domain nesting with 2 km (domain 1), 667 m (domain 2) and 222 m (domain 3) resolution and 10, 5, and 2.5 s baroclinic time steps, respectively, in the horizontal and 30 sigma layers in the vertical. Although choice of the largest domain for downscaling is arbitrary, the size of domain 1 was determined based on target area for downscaling, water depth and grid coverage in parent domain by FORA. The sensitivity of estimated optimal model spatial resolutions from 2 km, 667 m and to 222 m was checked for SSH and V_{bar} (not shown in the manuscript). The sensitivity of estimated optimal model temporal resolutions from 10, 5, and 2.5 s was checked in terms of running stability and total duration of the simulation (not shown in the manuscript). When estimating model domains extent, consideration was given so that the offshore boundaries should not be too close to shoreline ($< \Delta x$ of forcing) but also not so far for downscaling. The finest domain resolution covered Hasaki observation point and was set to 222 m for assessing coastal current in the shallow water environment. The COAWST model does not include astronomical tides directly by itself, but tides can be included from the parent dataset FORA on all four lateral boundaries numerically. This study focus on storm surge height excluding astronomical tide. **Figure 1B** schematically shows the setup of the COAWST model, extent of the domains and locations of marked river mouth and observation points, which were used for validation.

Lateral boundary conditions of three dimensional velocity, temperature and salinity as well as two dimensional SSH were given by FORA with open boundary conditions Chapman-implicit (free surface, from Chapman, 1985), Flather (2D momentum, from Flather, 1976) and Gradient (3D momentum, mixing turbulent kinetic energy, temperature and salinity). The sea surface initial and boundary conditions were given by the atmospheric reanalysis JRA-55 (Ebita et al., 2011; Kobayashi et al., 2015) with 55 km spatial resolution averaged to the COAWST model domain sizes, and three hourly data resolution averaged to six hourly input data to the COAWST model. The applied atmospheric forcing were wind speed, sea level pressure, air temperature, relative humidity, precipitation, shortwave radiation flux, and cloud fraction. The same methodology for the sea surface initial and boundary conditions was used in FORA.

The bathymetry M7000 Digital Bathymetric Chart obtained by Japan Hydrographic Association (JHA) (2019) submarine topography digital data was used for making grid data. The resolution of the bathymetry input to the model was 10–50 m, depending on the water depth. Observed hourly river water temperature and discharge data were obtained from Japan's Ministry of Land, Infrastructure, Transport and Tourism (MLIT) (2017). River forcing boundary conditions were used as an assumed constant salinity of 0.5 PSU for Tone, Naka, and Kuji Rivers. As an example of Tone River, the observed river water temperature and discharge data were obtained from the closest observation station to the river mouth which was not affected by tides, and then (for discharge only) multiplied by the ratio between the river mouth's and the station's basin areas, with goal to realistically represent freshwater budget flowing into the ocean on the river mouth location, rather than on the upstream observation station location. Hourly river discharge data were obtained from Fukawa station, located 76.47 km upstream from the river mouth and with the station's basin area of 12,458 km^2. However, Tone River has total basin area of 15,872 km^2, so all the obtained discharge data were multiplied by factor 15,872/12,458, as described above. River discharge data were available for the majority of the periods and eventual missing data were obtained by discharge-stage (Q-H) curve relationship. River water temperature data were obtained from Sawara station, located 40.8 km upstream from the river mouth in irregular intervals during daytime, approximately once per month, and data for missing periods were obtained by linear interpolation of two consecutive measurements. The same principal methodology for obtaining river water temperature and discharge data was used for Naka and Kuji Rivers.

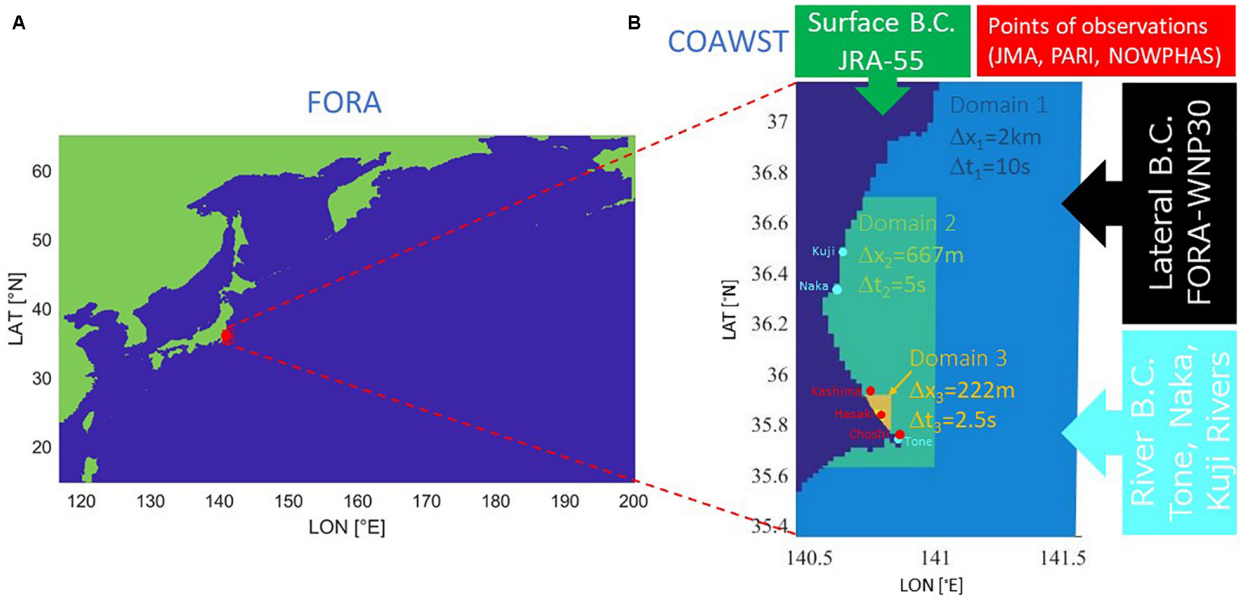

FIGURE 1 | (A) Geographic position of FORA domain and COAWST domain 1 (red dot) on the Ibaraki Coast; **(B)** Schematic representation of COAWST model setup (resolutions at domain 1: 2 km; domain 2: 667 m; domain 3: 222 m), and marked locations of river mouths (cyan dots) and observation points (red dots).

Model Validation

The COAWST downscaled results of SSH, V_{bar}, SST and SSS from domain 2 (667 m resolution) in October 2006 were validated against observed measurements.

Time series of modeled SSH, V_{bar}, and SST were validated against observed coastal data obtained as filtered values of hourly deviation from astronomic tide from the Japan Meteorological Agency (JMA) (2020) in Choshi (SSH), hourly variations of mean current from The Nationwide Ocean Wave information network for Ports and HArbourS (NOWPHAS) (2019) in Kashima (V_{bar}) and hourly ocean water temperature from Port and Airport Research Institute (PARI) (2018) in Hasaki (SST). These modeled results were also compared with the parent dataset FORA from September 28 to October 27 in order to highlight the importance of downscaling and the necessity of including river forcing boundary conditions, since river forcing was not considered in FORA.

The modeled results of SSS were validated with observed remote-sensing Version 4.0 of European Space Agency Ocean Color Climate Change Initiative Level 3 mapped Chlorophyll-a concentration (hereafter: Chl-a) data [Sathyendranath et al., 2012; Troselj et al., 2017; European Space Agency Ocean Colour Climate Change Initiative (ESA-OC-CCI), 2019], that comprises globally merged MERIS, Aqua-MODIS, SeaWiFS and VIIRS data with associated per-pixel uncertainty information obtained at 4 km and 1-day resolution. The observed Chl-a data were obtained for October 8, 9 and 16 because for other dates were the data coverage was not sufficient.

Before analysis, model bias correction was applied for SSH and SSS data of COAWST and SSH data of FORA modeled results, with added +0.49 m SSH and +3 PSU to SSS to the entire COAWST dataset as well as +0.33 m SSH to the entire FORA dataset. The SSH bias has occurred since the beginning of simulation due to numerical computational error at the start of modeling (model spin-up) and has remained constant during the simulation. The SSS bias has occurred instantly during extreme rainfall events in the typhoon season when salinity has suddenly been decreased for about 3 PSU over entire modeled domains and has remained low afterward during the simulation.

RESULTS AND DISCUSSION

In this section, the validation of SSH, V_{bar}, SST, and SSS are separately presented. After multiple validation of the modeled results, an analysis was made of the impact of the event to SSH, SLP, Sea Surface northward Wind (W10), V_{bar}, SST, and SSS in Hasaki point as well as to Tone and Naka River discharges, from September 28 to October 27.

Sea Surface Height

Validations of the COAWST downscaled SSH results from various aspects are presented in this section.

Figure 2A shows peak SSH horizontal distribution from onshore to 6 km eastward offshore at Choshi. The results are shown for COAWST domain 1 and domain 2 for S1 and S2 and compared with surge data observed by JMA at Choshi Tidal Station at location N 35°45′ and E 140°52′. The modeled results in domain 2 show maximum of 1.6 and 0.75 m nearshore for the two considered storms, respectively, which is due to the sudden increase of SSH during the extreme storm surge events in shallow water environments. These results are overestimating observed data because the effect of amplified nearshore SSH increases the modeled results in shallower waters. The exact JMA observation

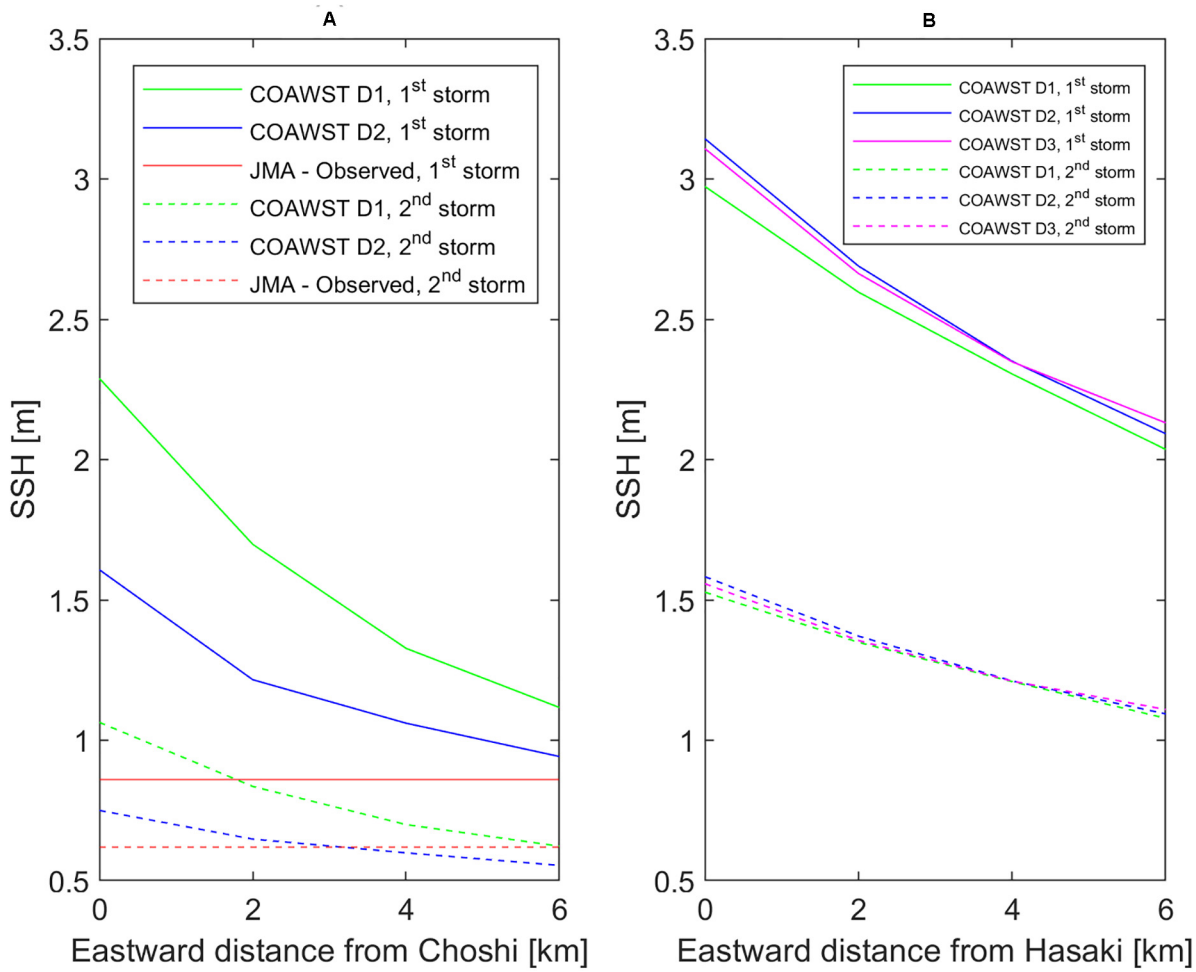

FIGURE 2 | Peak Sea Surface Height horizontal distribution from onshore to 6 km eastward offshore at **(A)** Choshi and **(B)** Hasaki for COAWST domain 1 (green), domain 2 (blue) and domain 3 (magenta, only in Hasaki) for S1 (full line) and S2 (dashed line) compared with surge data observed by JMA at Choshi Tidal Station (red, only in Choshi).

location is located within the Choshi Fishing Port which is semi-enclosed to open ocean and, therefore, the full effect of amplified nearshore SSH is not recorded in the observed data. Furthermore, the modeled results show clear resolution dependence of storm surge height, as maximum SSH in domain 1 are 2.3 and 1.05 m nearshore for the two considered storms, respectively. Therefore, modelled SSH domain 2 results from 4 to 6 km eastward offshore from Choshi are validated with the tide data observed by JMA at Choshi Tidal Station. **Figure 2B** shows peak SSH horizontal distribution from onshore to 6 km eastward offshore at Hasaki. The results are shown for COAWST domain 1, domain 2 and domain 3 for S1 and S2. Observed SSH data for Hasaki are not available. Maximum nearshore SSH values in Hasaki are up to 3.2 m and 1.6 m for S1 and S2, respectively, which is bigger than in Choshi because Hasaki is located at a longshore uniform section, while Choshi is at the tip point of a cape where the direction of coastline changes sharply. Furthermore, the results in Hasaki do not show noticeable resolution dependence of storm surge height which might be due to smaller variabilities of magnitudes and directions of ocean currents in the Hasaki longshore uniform section than in the Choshi tip point of a cape.

Figure 3 shows comparison of time series of SSH among (a) FORA results nearshore and the modeled results, (b) 4 km and (c) 6 km eastward offshore from Choshi for domain 1, and (d) 4 km and (e) 6 km for domain 2, and (f) tide data observed by JMA at Choshi Tidal Station. Results at various distances from the shoreline are shown because it was observed that sensitivity of location from offshore to onshore in terms of SSH is significant, being inversely proportional to water depth. The modeled results show good agreement with peaks of observed data from both S1 and S2 (0.8 and 0.6 m, respectively) at a few grids locations, 4–6 km (2nd and 3rd grids in domain 1, 6th and 9th grids in domain 2) eastward offshore from Choshi, while peaks of FORA for the same events are not well reproduced (about 0.25 and 0.2 m, respectively). As the wind-induced surge monotonically increases from offshore to onshore and spatial scale of storm surge is small, spatial resolution is sensitive to simulate maximum storm surge heights along the coast. Besides the spatial resolution,

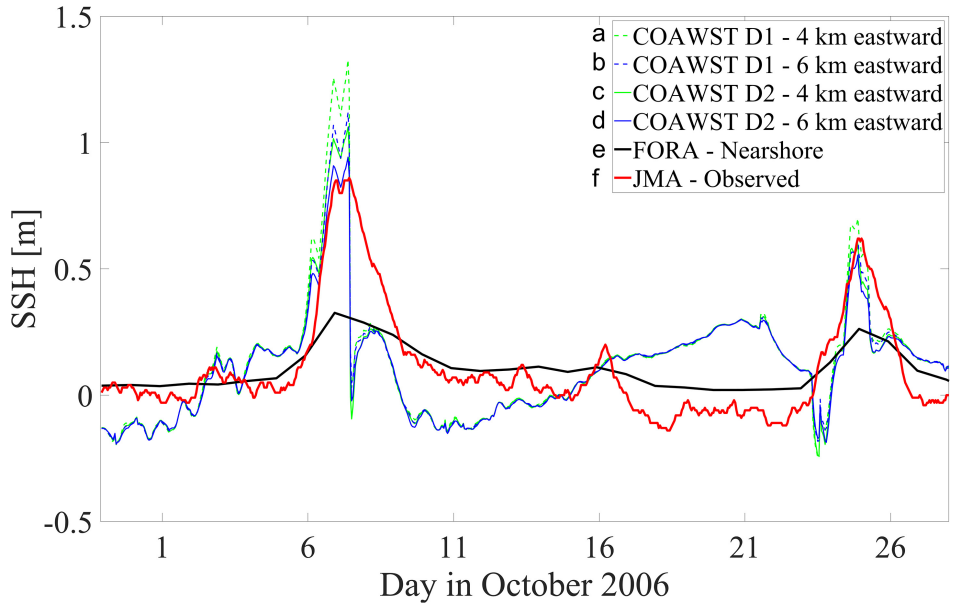

FIGURE 3 | Comparison of time series of Sea Surface Height among modeled and observed data in Choshi [(a,b): COAWST model 4 and 6 km eastward (2nd and 3rd grids) offshore, respectively, for domain 1; (c,d): COAWST model 4 and 6 km eastward (6th and 9th grids) offshore, respectively, for domain 2; (e) FORA model nearshore; (f): JMA observed data].

TABLE 1 | Correlation coefficient, RMSE and bias of **(a)** FORA nearshore and COAWST (domain 2) modeled runs at **(b)** 4 and **(c)** 6 km eastward offshore from Choshi for the total analyzed period, S1 and S2.

SSH	(a) FORA - nearshore			(b) COAWST - 4 km			(c) COAWST - 6 km		
Indicator	**Corcoff**	**RMSE**	**Bias**	**Corcoff**	**RMSE**	**Bias**	**Corcoff**	**RMSE**	**Bias**
Total	0.81	0.16	0.00	0.54	0.21	0.01	0.52	0.20	0.00
S1	0.68	0.33	−0.25	0.55	0.30	−0.09	0.58	0.28	−0.12
S2	0.48	0.21	−0.12	0.71	0.18	−0.09	0.70	0.18	−0.10

another factor causing the huge difference between COAWST and FORA results is temporal output resolution, which is hourly in COAWST but daily in FORA. Therefore, physical processes which are mainly occurring on hourly time scales such as the considered S1 and S2 cannot be realistically reproduced by FORA and because of that finer spatiotemporal modeling scales are needed for their reproducibility. Additionally, the JMA sea level observation data are filtered values but COAWST modeled output data are just one data output per every hour and FORA modeled data are also just one data output but per every day. Therefore, we did not compare the same data obtaining processes which additionally reduced accuracy of the validation process.

Table 1 shows correlation coefficient, RMSE and bias of above-mentioned three records from modeled runs (FORA – nearshore, COAWST domain 2 – 4 km and 6 km offshore) for the total analyzed period, S1 on October 7 and S2 on October 24. In **Table 1**, the modeled results from 4 to 6 km offshore show the best fit with observed data (correlation coefficient 0.54 for total period, 0.55 for S1 and 0.71 for S2, respectively, for 4 km offshore; and 0.52 for total period, 0.58 for the S1 and 0.70 for the S2, respectively, for 6 km offshore). As such, these distances should be used for the best validation of the modeled results, whereas in shallower waters, the effect of amplified nearshore SSH increases the modeled results. FORA results nearshore have higher correlation coefficient of 0.81 for total period but lower correlation coefficients than COAWST of 0.68 for the S1 and 0.48 for the S2, respectively. The correlation coefficient for the S1 is comparable to that of COAWST and FORA, but this is because COAWST underestimates observed data after the peak of S1. However, COAWST results up to the maximal SSH for the S1 is much closer to observed data than FORA. Furthermore, COAWST RMSE is higher than FORA for the total period but lower for S1 and S2. Therefore, the model shows better performance than FORA in reproducing variabilities of ocean state such as the two events' extreme SSH, while FORA shows better performance in reproducing mean state of the model. The most important feature of downscaling is that it is used for reproducibility of extreme coastal variabilities of the ocean rather than its mean values, because the parent dataset with coarser resolution is already good enough to accurately reproduce its mean values. Bias in COAWST results is smaller

by about 13–16 cm than in FORA for S1; and by about 2–3 cm for S2 because FORA does not reproduce hindcasts of S1's and S2's peaks well. SSH validation showed that the downscaled model shows better performance than FORA in reproducing peaks and variabilities of extreme SSH from the two events, while FORA shows better performance in reproducing mean state of the model.

Finally, we discuss spatiotemporal variation of SSH alongside the Ibaraki Coast. **Figure 4** compares time series of modeled SSH from COAWST domains 1 and 2 and FORA on four locations alongside the Ibaraki Coast. The results suggest that magnitude of the SSH was increased from south to north reaching up to 3.8 m for S1 and 2.3 m for S2, respectively. These modeled values of S1 SSH are in range of the most extreme storm surges that have been recorded on the Ibaraki Coast. However, these extreme SSH values for S1 and S2 are not well reproduced in FORA alongside the entire Ibaraki Coast. **Figure 4** additionally suggest that differences between domain 1 and domain 2 are minor alongside the Ibaraki Coast but are significant on to most southern point Choshi which was used for the SSH validation. In Choshi, domain 2 SSH results greatly underestimate domain 1 SSH results. These findings suggest that nesting approach is important to reproduce SSH along open coasts.

Vertically Averaged Velocity

The validation of the COAWST downscaled V_{bar} results is presented in this section. **Figure 5** shows comparison of time series of V_{bar} (North-South direction) among the modeled results, FORA results and NOWPHAS observed velocity data in Kashima at location N 35°53′55″ and E 140°45′14″ at depth 24 m by Ultra Sonic Wavemeter (USW). The observed data has no coverage during S1 at October 7 because the USW velocimeter failed to collect data.

The modeled results have correlation coefficient 0.68, RMSE 0.27 and bias −0.03, while FORA has values of 0.63, 0.19, and 0.07, respectively, for total time period when there was available observed data. For the S2, the modeled results show a correlation coefficient 0.68, RMSE 0.44, and bias −0.02, while FORA has

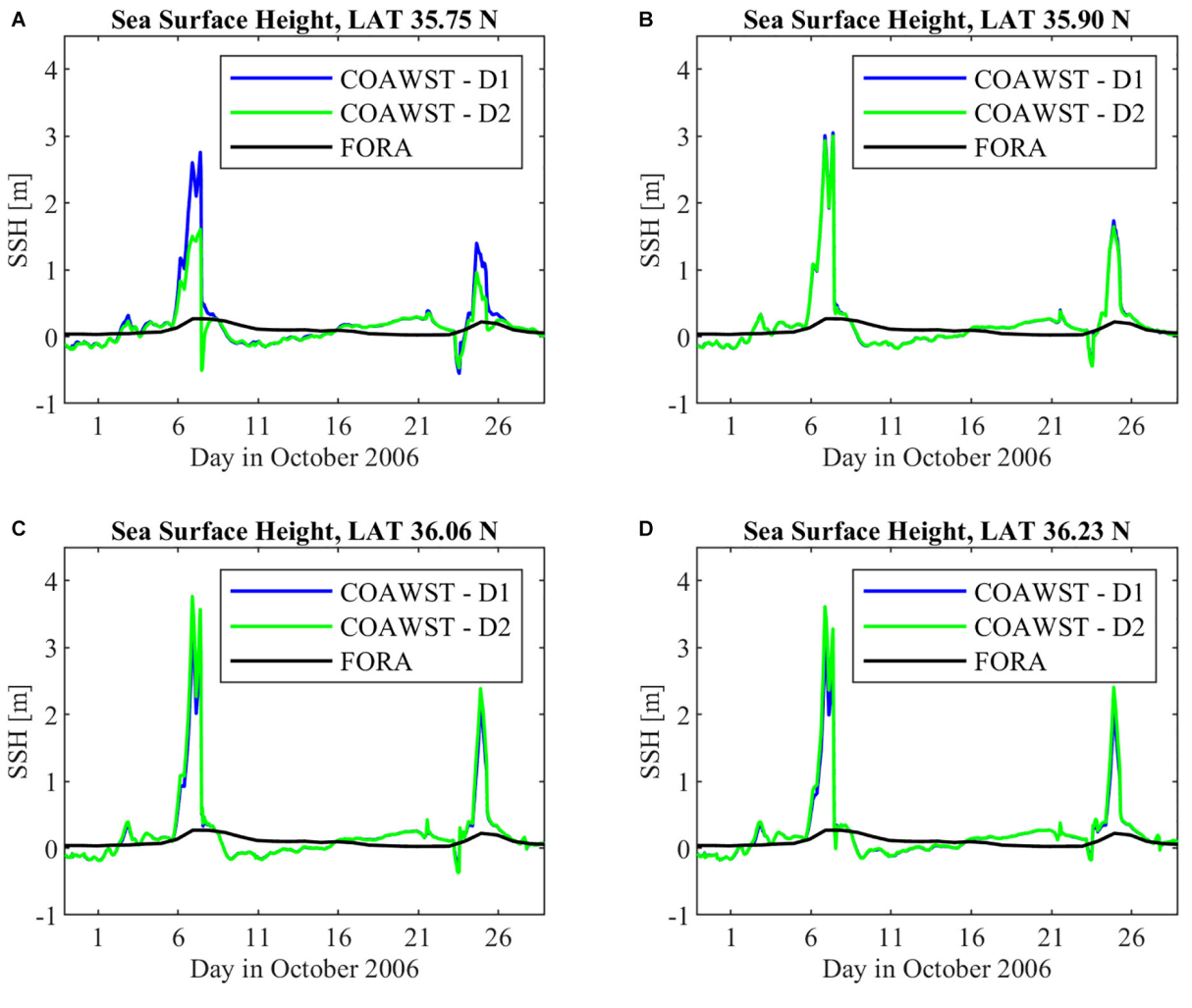

FIGURE 4 | Comparison of time series of modeled Sea Surface Height (blue – COAWST domain 1, green – COAWST domain 2, black – FORA) alongside the Ibaraki Coast on four locations corresponding to LON **(A)** 35.75 N, **(B)** 35.90 N, **(C)** 36.06 N, **(D)** 36.23 N.

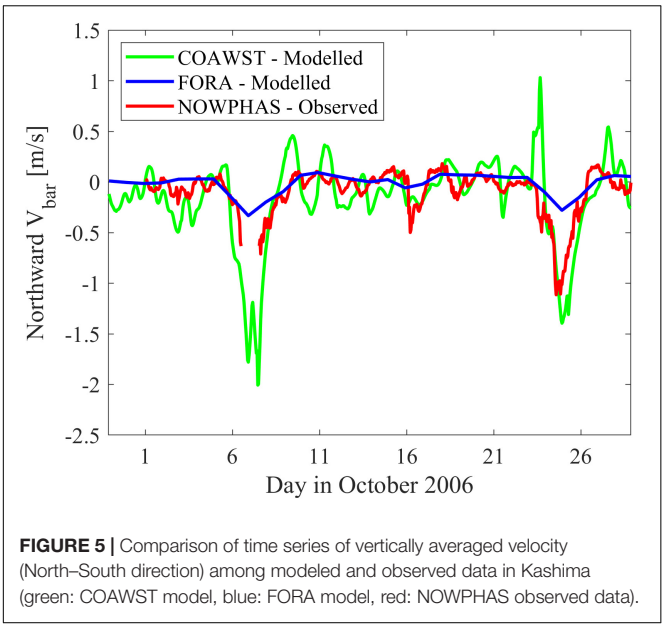

FIGURE 5 | Comparison of time series of vertically averaged velocity (North–South direction) among modeled and observed data in Kashima (green: COAWST model, blue: FORA model, red: NOWPHAS observed data).

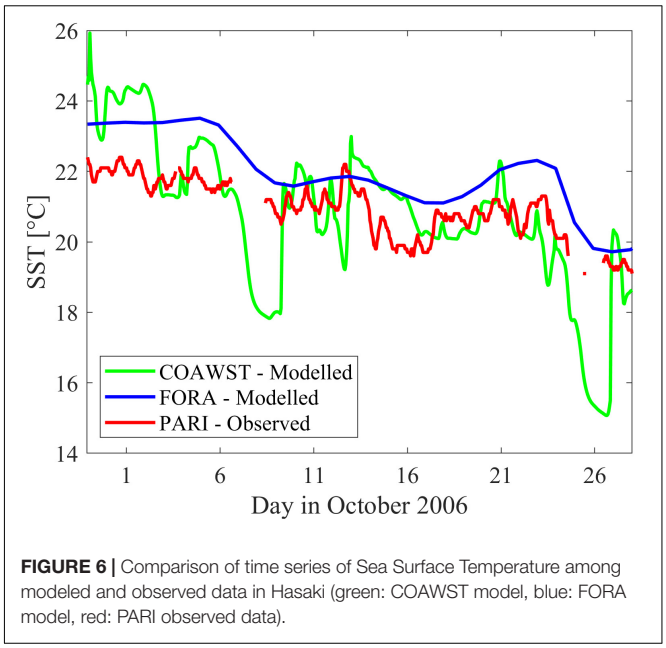

FIGURE 6 | Comparison of time series of Sea Surface Temperature among modeled and observed data in Hasaki (green: COAWST model, blue: FORA model, red: PARI observed data).

values of 0.28, 0.43, and 0.27, respectively. The modeled results show good agreement with the peak of the S2 reproducing hindcasts of extreme velocity of about 1.4 m/s southwards, while FORA hindcasts peak for the same event are not well reproduced, not even exceeding 0.3 m/s. For S1, the modeled results were reaching peak of up to 2 m/s while FORA results peak did not exceed 0.4 m/s. V_{bar} validation showed similar hindcasts of mean state of the model between COAWST and FORA for total time period, but much better hindcasts of strong southward V_{bar} for energetic periods by using COAWST.

Sea Surface Temperature

The validation of the COAWST downscaled SST results is presented in this section. **Figure 6** shows comparison of time series of SST among the modeled results, FORA results and PARI observed ocean water temperature data in Hasaki located 2–3 m below sea level at location N 35°50′27″ and E 140°45′42″. The observed data has no coverage during both extreme events but show good agreement with the modeled results in other periods, while FORA results slightly overestimate them.

The modeled results have correlation coefficient 0.67, RMSE 1.43, and bias 0.19, while FORA has their values at 0.77, 1.30, and 1.14, respectively, for total time period when there was available observed data. This shows that in terms of SST, both the model and FORA show similar hindcasts for normal conditions but the quality of the hindcasts for S1 and S2 is still uncertain due to missing observation data. The modeled results show a decrease in SST of about 4°C during S1 and S2 on October 7 and 24 while FORA shows a smaller decrease of about 2°C for both events. SST validation showed similar hindcasts in both the model and FORA at normal conditions but the quality of the hindcasts for S1 and S2 is still uncertain due to missing observation data. Therefore, it is noted that accurate validation of modeled SST results for S1 and S2 could not be fully conducted.

Sea Surface Salinity

The validation of the COAWST downscaled SSS results is presented in this section. **Figure 7** shows the comparison of the modeled SSS results (upper) and ESA-OC-CCI Version 4.0 observed remote-sensing Chl-a concentration data (lower) in domain 2 for October 8 (left), 9 (middle), and 16 (right) GMT time zone, respectively. Only the **Figure 7** is shown in GMT time zone, which is +9 h compared to JST time zone used elsewhere in this study, because the observed ESA-OC-CCI data are provided using daily values in the GMT time zone. These three days are used for validation because there are no available observed data on other days due to extensive cloud coverage in the targeted domain. FORA did not include river forcing, so no comparison of SSS results was made between the two models. Modeled SSS values nearshore close to river mouths are below 30 PSU and this shows good agreement with observed Chl-a concentrations higher than 5 mg/m^3 for the same locations. This is an expected mechanism during an extreme storm surge event because high river discharge causes reduced SSS whereas increased concentrations of Chl-a indicate enhanced supply of organic material and phytoplankton transported from the river to the ocean. Therefore, there was no expectation for a strong correlation between SSS and Chl-a concentrations in the offshore zone, where freshwater from the river plume could not reach. SSS validation showed that impact of freshwater discharge to lowering SSS and increasing Chl-a concentration values nearshore was greatest just after the extreme storm surge event but diminishes afterward due to lower supply of freshwater, organic material and phytoplankton from rivers.

Furthermore, an evaluation of the impact of freshwater discharge from rivers to SST and SSS values was made. **Figure 8** shows observed time series of Tone and Naka River mouth discharge from September 28 to October 27. Kuji River was excluded from this analysis because of its smaller discharge

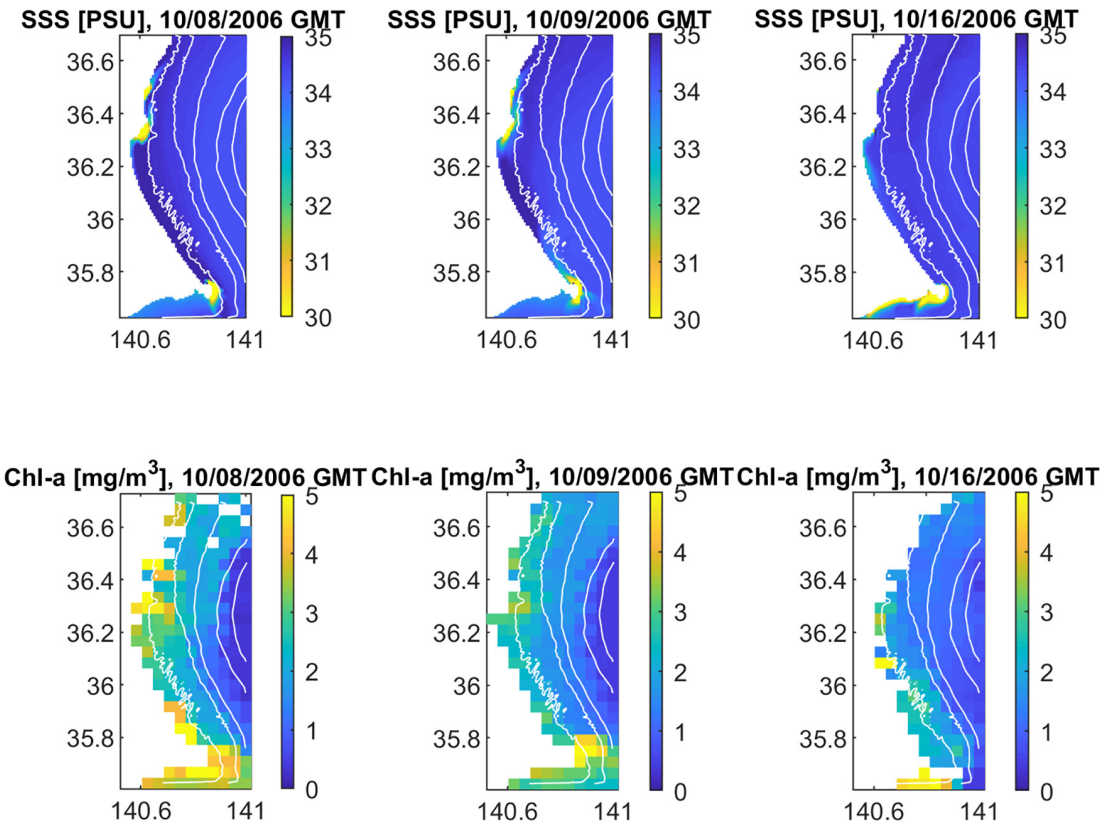

FIGURE 7 | Comparison of modeled Sea Surface Salinity **(upper)** and observed Chlorophyll-a concentrations **(lower)** in domain 2 for October 8 **(left)**, 9 **(middle)**, and 16 **(right)**, GMT time zone. Bathymetry contours represent depths of 25, 50, 100, and 200 m.

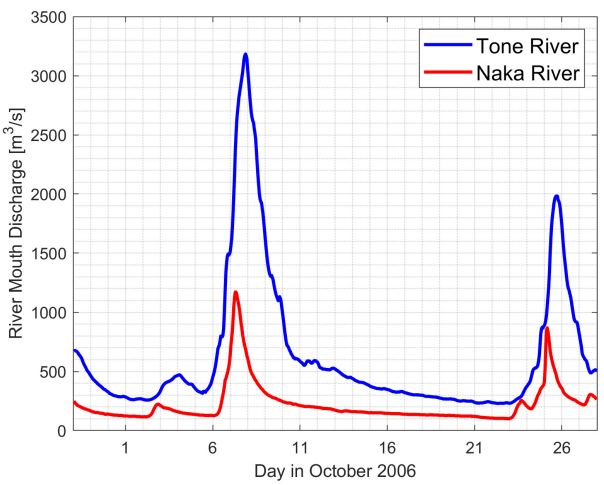

FIGURE 8 | Observed time series of Tone and Naka River mouth discharge from September 28 to October 27 (blue: Tone River, red: Naka River).

and its location further northward from the considered coastal zone. The peaks of both river discharges occurred during S1 and S2 were reaching 3,200 and 2,000 m^3/s for Tone and 1,200 and 800 m^3/s for Naka River, respectively. For the considered study domains, these amounts of freshwater discharges are not significant during extreme events when considering hydrological flood disasters, but are large enough to produce significant impact to decreasing SSS and increasing Chl-a concentrations nearshore at aftermaths of extreme storm surge events. By combining **Figures 6**, **8**, it can be concluded that the freshwater impact to SST is minor because river water temperature has similar range of values to ocean water temperatures. By combining **Figures 7**, **8**, on the other hand, it can be concluded that the impact of freshwater discharge to decreasing SSS and increasing Chl-a concentrations nearshore was highest just after S1, on October 8, but decreased on October 9 and further decreased on October 16. It was because freshwater from the river plume changed its location from near river mouths to the southern part of Choshi aftermaths the extreme storm surge event due to influence from southwards coastal currents. It can be concluded that the freshwater impact to SST is negligible but it can have significant impact to reducing SSS, as was likewise concluded in Troselj et al. (2018).

Impact of the Storm Surge Events

The impact of the storm surge events in terms of SSH, depth averaged velocity (Overbar{UV}), SST and SSS in domain 2 is discussed in this section.

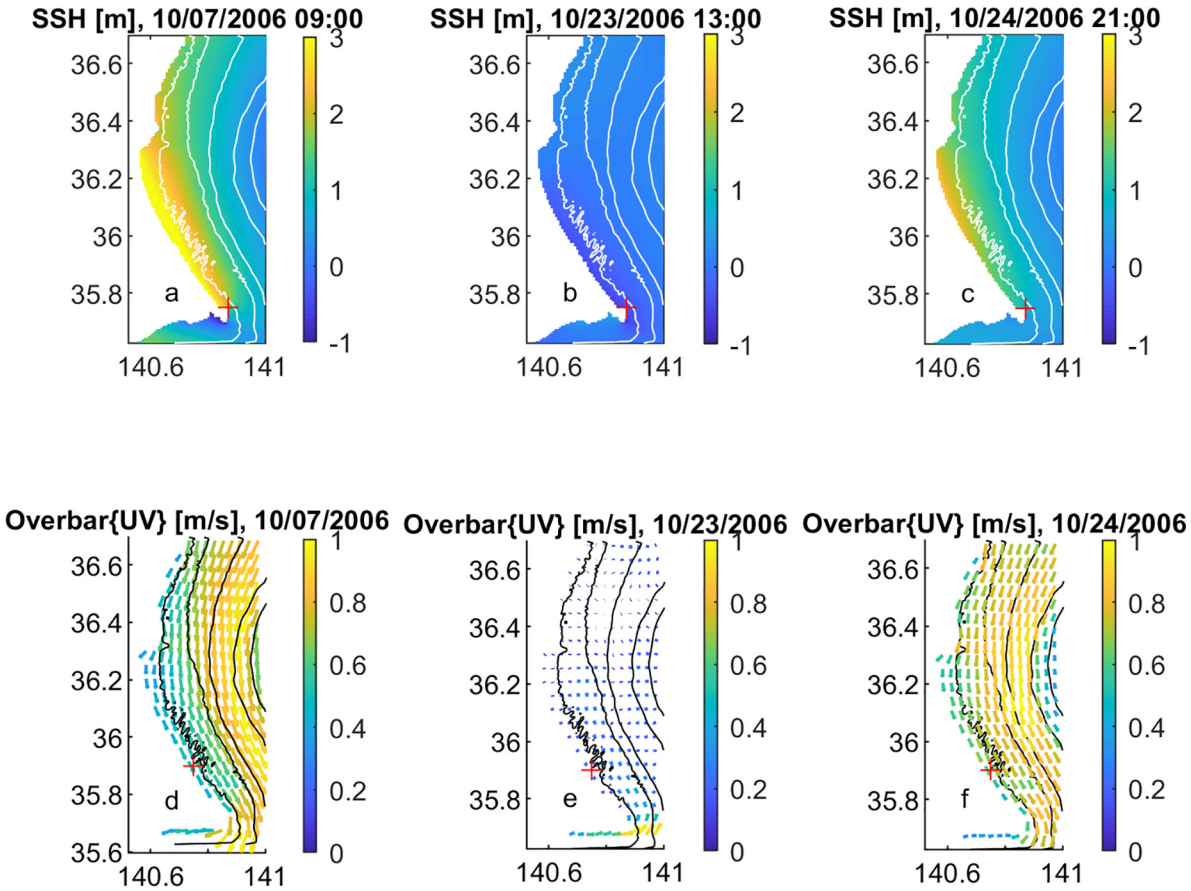

FIGURE 9 | Sea Surface Height **(upper)** and depth averaged velocity **(lower)** for October 7 at 9 am **(left)**, October 23 at 1 pm **(middle)** and of October 24 at 9 pm **(right)**. Bathymetry contours represent depths of 25, 50, 100, and 200 m. Red cross indicates the location of the corresponding observed data.

Figure 9 shows the modeled SSH and Overbar{UV} for October 7 at 9 am, October 23 at 1 pm and October 24 at 9 pm. These particular moments represent three peaks of SSH variation (extreme S1 and S2 on October 7 and 24, and sudden drop of SSH on October 23 with negative SSH peak, when the modeled results show the counter–current flow to the northward direction preceding the following S2). **Figure 9A** shows that magnitude of SSH for October 7 event exceeded 3 m in the coastal zone of Ibaraki with higher values at the northern part. A similar occurrence mechanism but with lower SSH magnitudes of up to 2.2 m was found for October 24 event (**Figure 9C**). On the October 23, values lower than zero mean sea level were distributed uniformly across the whole domain with negative peaks nearshore (**Figure 9B**). **Figures 9D,F** show that magnitude of Overbar{UV} for October 7 and 24 had similar occurrence mechanism, and both exceeded values of 1 m/s in southward direction from northern part of Choshi toward its coastal zone, with slightly lower values at nearshore. On October 23, the northward velocity approached its maximum of about 0.8 m/s near Choshi and gradually decreased toward the north (**Figure 9E**). The impact of the extreme storm surge events S1 and S2 was significant especially in terms of SSH and Overbar{UV}, which is important in assessment of erosion analyses and shoreline variabilities along the Ibaraki Coast.

Similarly, **Figure 10** shows the same modeled outputs as **Figure 9** but for SST and SSS. There was a dominant impact of strong southward current on October 7 and 24 to coastal transport of colder northern waters of about 16–18°C (**Figure 10A**), while warmer waters of more than 22°C were trapped on the offshore zone by the strong southward Overbar{UV}. On October 24 (**Figure 10C**), an SST pattern was observed similar to October 7 but with about 2°C lower average values due to later seasonal period. On October 23 (**Figure 10B**), the ocean water was warmer by about 1°C than on the October 24 especially in the coastal zone due to the impact of northward currents which transported warmer waters from Kuroshio. There was also an interesting mechanism of SSS coastal transport, which shows that SSS values between 34 and 35 PSU were transported by the southward current on October 7 (**Figure 10D**, south from LON 35.75), but on October 24, there was a coastal backflow of reduced SSS near Tone River mouth (**Figure 10F**, around LON 35.75) that had been previously transported alongshore with northward current as a freshwater lens on October 23

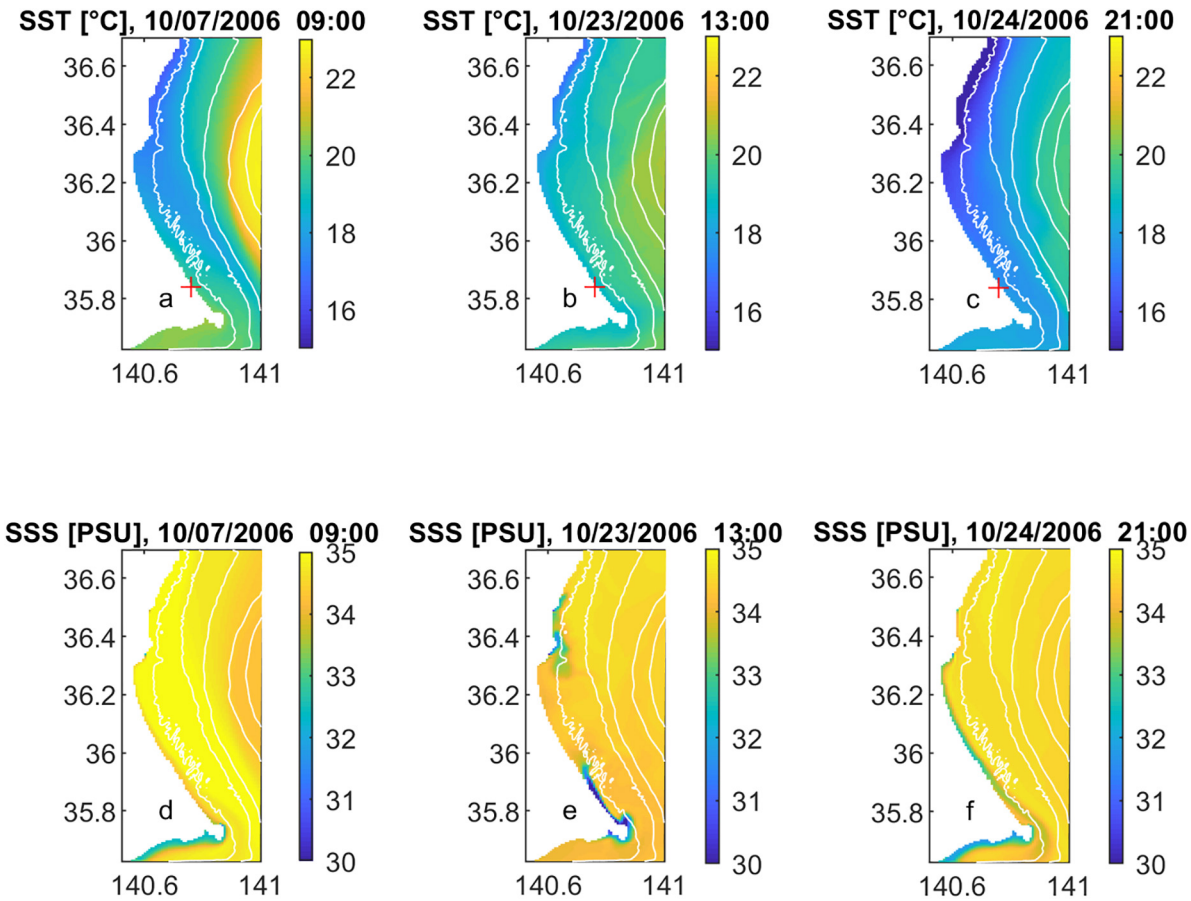

FIGURE 10 | Sea Surface Temperature **(upper)** and Sea Surface Salinity **(lower)** for October 7 at 9 am **(left)**, October 23 at 1 pm **(middle)** and October 24 at 9 pm **(right)**. Bathymetry contours represent depths of 25, 50, 100, and 200 m. Red cross indicates the location of the corresponding observed data.

(**Figure 10E**, from LON 35.75 to 35.95). Therefore, the impact of S1 and S2 in terms of SST and SSS might be considerable in possibly causing non-negligible damage to the well-developed local fishery and seashell industry on the Ibaraki Coast.

Finally, differences of S1 and S2 are discussed in terms of the COAWST downscaled results of SSH, SLP, W10, V_{bar}, SST, and SSS in Hasaki on the same location where SST was validated. **Figure 11** shows the results with significantly marked occurrence times at the above-mentioned three extreme SSH events. The SLP (**Figure 11B**) and W10 results (**Figure 11C** – green line) show that on October 7, there were both extreme SLP (down to 985 mbar) and strong southward surface wind (up to 20 m/s) occurring simultaneously. However, on October 24, only the southward surface wind (up to 20 m/s) was extreme and its peak was just after the peak of SSH while SLP was in higher range of about 1,010 mbar. Simultaneously, the Sea Surface westward Wind (U10) results (**Figure 11C** – black line) showed interesting mechanisms during S1 and S2. Peak U10 of up to 13 m/s occurred just after W10 peak of S1 in eastward direction. However, peak U10 of up to 11 m/s occurred just before W10 peak of S2 in westward direction. Additionally, on October 23, SLP was about 1,025 mbar and northward surface wind was about 5 m/s, which generated the reduced SSH with northward alongshore current. These magnitudes and directions of extreme coastal southward surface wind correspond well with the findings from Nobuoka et al. (2007). Therefore, the results under this study might support their conclusion that Ekman transport was the main physical force that generated the high tide level on October 7 and possibly also on October 24.

The SSH results (**Figure 11A**) show that Hasaki was more exposed to extreme storm surge levels than Choshi Tidal Station, because peaks of the SSH in Hasaki reached up to 3 m on October 7 and about 1.8 m on October 24; while in Choshi, they reached up to 1.6 m on October 7 and about 1 m on October 24. On October 23, there were values of about −0.5 m occurring instantly. The V_{bar} results (**Figure 11D**) were up to 1.5 and 1 m/s southwards on October the 7 and 24, respectively, and about 0.8 m/s northwards on October 23, which correlates well with the dynamics of coastal SSH occurrence and with coastal transport of SST and SSS. The SST results (**Figure 11E**) show delayed response to the extreme events. There was an initial decrease of about 2°C occurring about 1 day before the peak of SSH, and further decrease of about 2°C occurring 2 days

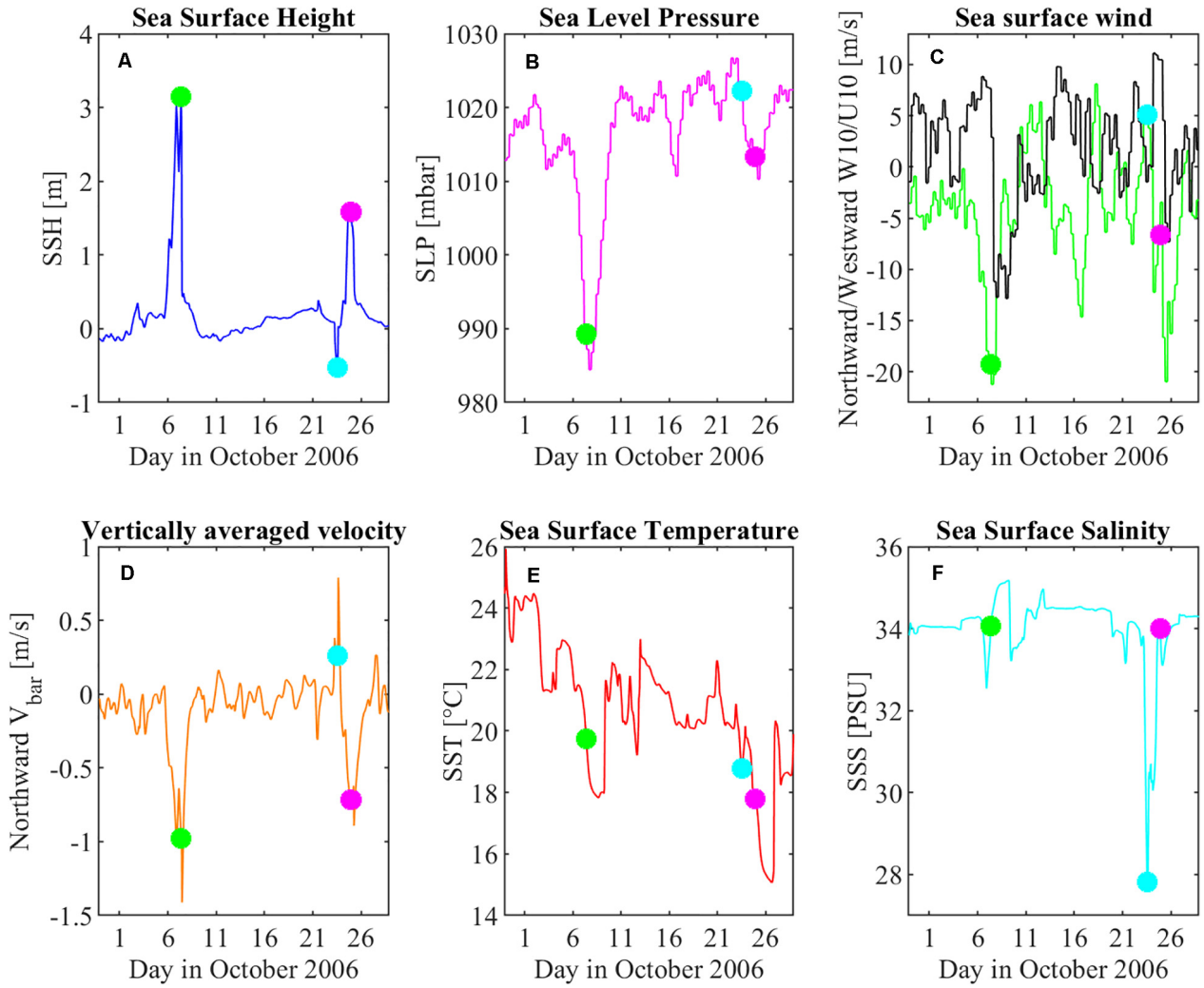

FIGURE 11 | COAWST modeled results of **(A)** Sea Surface Height, **(B)** Sea Level Pressure, **(C)** Sea surface wind (green: North–South direction; black: West–East direction), **(D)** Vertically averaged velocity (North–South direction), **(E)** Sea Surface Temperature, and **(F)** Sea Surface Salinity in Hasaki (green dot: October 7 at 9 am; cyan dot: October 23 at 1 pm; magenta dot: October 24 at 9 pm).

after the peak of SSH on both October 7 and 24. On October 23, there was no significant change in SST. The SSS results (**Figure 11F**) show an increase of up to 35 PSU after October 7 event, a decrease up to 28 PSU during the peak northward current on October 23 due to alongshore transport of freshwater lens from Tone River and reverting back to about 34 PSU on October 24 due to coastal backflow of reduced SSS near Tone River mouth.

The extreme low-pressure system event of the S1 showed much bigger impact to the coastal SSH and V_{bar} than on the S2, which had similar peak values of W10 but a lower SLP drop, while the impact to the coastal SST and SSS was similar. This indicates that the SLP drop itself has an important role in assessing extreme SSH levels, in addition to W10 which directly influences V_{bar} values. This mechanism of increasing SSH levels might be due to meteorological tsunami, which also occurs when rapid changes in SLP cause the displacement of a body of water as manifested by the rapid increase in SSH levels. However, additional analyses which are not in scope of this study should be conducted to further evaluate this indication.

CONCLUSION

In this study, dynamical downscaling with reproduced hindcasts of coastal dynamics on the Ibaraki Coast was conducted using COAWST model including SSH, V_{bar}, SST, and SSS. Particularly highlighted was the importance of downscaling to hindcasts of the two extreme storm surge events in October 2006 on the Ibaraki Coast. The impact of the events to associated values of coastal parameters in the downscaled and the parent datasets was also considered.

Validation of COAWST downscaled results of SSH, V_{bar}, SST, and SSS from domain 2 (667 m resolution) in October 2006

was made with observed data and a comparison was conducted with FORA to highlight the importance of downscaling. SSH validation showed that the downscaled model shows better performance than FORA in reproducing hindcasts of extreme values of SSH from the two events. As the downscaling model is focused on accurate reproducibility of the coastal variabilities, then its results sometimes differ from mean values due to hourly variabilities in the surface forcing data as well as their uncertainty. However, the downscaling model can be accurately used for objectives that it is designed for, which are reproducibility of hourly extreme variability values of the coastal dynamics parameters. V_{bar} validation showed better hindcasts of strong southward V_{bar} for S2, while observed data for October 7 are missing. SST validation showed similar hindcasts in both the model and FORA for normal conditions although the quality of the hindcasts for S1 and S2 is still uncertain due to missing observation data. However, the estimated 2°C bigger decrease of SST in this study's model than in FORA indicates that the model can better reproduce hindcasts of the local southward alongshore transport of SST during extreme events. SSS validation showed that impact of freshwater discharge to decreased SSS lower than 30 PSU and increased Chl-a concentrations bigger than 5 mg/m^3 nearshore is the greatest just after S1, on October 8, but decreases afterward. These validations with existing observed data satisfactorily showed goodness of fit for the two events for all considered coastal dynamics parameters.

Turning to the modeled SSH, Overbar{UV}, SST and SSS results in domain 2, magnitude of SSH was about 3 and 2.2 m for the two events, respectively, with larger values at northern part of the Ibaraki Coast. Magnitude of Overbar{UV} for the two events had similar occurrence mechanism and both exceeded values of 1 m/s in southward direction in position from northwards of Choshi toward its coastal zone. The dominant impact of strong southward current to coastal SST transport of colder northern waters of about 16–18°C occurred during both extreme events. SSS transport of the freshwater lens from rivers was dependent on directions of extreme currents before and during the two events. It was shown that the impact of S1 and S2 was significant particularly in terms of SSH and Overbar{UV}, which is important for assessment of erosion analyses and shoreline variabilities along the Ibaraki Coast. The impact of S1 and S2 in terms of SST and SSS might be considerable for the local fishery and seashell industry on the Ibaraki Coast.

Moreover, the impact of the two events in Hasaki was quantified. It was found that that the main difference in atmospheric forcing between the two events was in SLP, with peak down to 985 mbar on October 7 but about 1,010 mbar on October 24, while strong W10 occurred in both cases with peaks up to 20 m/s. The SSH results show that Hasaki (3 and 1.6 m, respectively) was more exposed to extreme storm surge levels than Choshi (1.8 and 1 m, respectively) during both S1 and S2. The V_{bar} results show up to 1.5 and 1 m/s southward currents for the two events. The SST results show 2 days delayed response to the extreme event of up to −4°C during both events. The SSS results show a decrease of down to 28 PSU during the peak northward current on October 23, due to alongshore transport of freshwater lens from Tone River. This study concludes that the extreme low-pressure system event on October 7 had much bigger impact to the coastal SSH and V_{bar} than that on October 24, which had similar peak values of W10 but a lower SLP drop, whereas the impact to the coastal SST and SSS was similar.

Limitations of the modeled results are the COAWST modeled SSH (−0.49 m) and SSS (−3 PSU) biases, which did not significantly affect results after applying bias corrections. However, it is important to account for the SSH and SSS biases in future studies by using improved methodology in order to reduce them, when possible. Another considerable limitation is that the validation of SSH results was conducted by comparing daily modeled outputs from FORA with hourly modeled outputs from COAWST and validating them with filtered JMA hourly observed values. Therefore, different temporal resolutions of validated results and different way of the data obtaining processes decreased reliability of intended considering the impact of increasing spatial resolution because the temporal resolution effect is also important in consideration of explaining the observed differences. Additional limitation to note is that the COAWST downscaled results have too coarse resolution to sufficiently represent physical processes within the Choshi Fishing Port, which is semi-enclosed to open ocean. Therefore we believe that the physical processes within the Port are in range of less than 100 m of spatial resolution whereas in this study the same location was downscaled of down to 667 m. Because of this limitation, we used indirect validation of modeled SSH results on locations from 4 to 6 km offshore versus observed data in the Port.

In future studies, an assessment of erosion analyses and shoreline variabilities along the Ibaraki Coast, as well as future projection analysis of the coastal dynamics using the COAWST model, which was validated in this study, will be conducted. The modeling approach used in this study, with differently applied lateral and surface boundary forcing conditions, can be useful for similar modeling of climate change impact assessment and can ultimately serve as guidelines for developing adaptation policies.

DATA AVAILABILITY STATEMENT

The raw data supporting the conclusions of this article will be made available by the authors, upon a reasonable request to the corresponding author.

AUTHOR CONTRIBUTIONS

JT compiled, pre-processed and ran the COAWST model, conducted post-processing data analysis as well as wrote and edited the whole manuscript. JN assisted to compile, pre-process and run the COAWST model. ST obtained NOWPHAS mean current data and assisted in post-processing data analysis. NM coordinated the work among all co-authors by conceptually leading the study, provided the working environment for JT and assisted to compile, pre-process and run the COAWST model. All authors reviewed,

discussed and suggested revisions for the submitted and revised versions of the manuscript.

FUNDING

The study was conducted under the Social Implementation Program on Climate Change Adaptation Technology (SI-CAT), Integrated Research Program for Advancing Climate Models (TOUGOU) Grant Number JPMXD0717935498 and Japan Society for the Promotion of Science (JSPS) Grants-in-Aid for Scientific Research (KAKENHI), all supported by the Ministry of Education, Culture, Sports, Science and Technology, Japan (MEXT).

ACKNOWLEDGMENTS

The authors are grateful to Yoichi Ishikawa and Shiro Nishikawa from Japan Agency for Marine-Earth Science and Technology for providing modeled data from the parent dataset FORA-WNP30 and to Masayuki Banno from Port and Airport Research Institute for providing observed water temperature data in Hasaki. We appreciate NOWPHAS wave data provided by Ministry of Land, Infrastructure, Transport and Tourism, Japan. Finally, we thank to the Associate Editor Goneri Le Cozannet and two Reviewers, Pushpa Dissanayake and Begoña Pérez-Gómez, for their useful comments which greatly improved quality of the manuscript.

REFERENCES

Al Mohit, M. A., Yamashiro, M., Hashimoto, N., Mia, M. B., Ide, Y., and Kodama, M. (2018). Impact assessment of a major River basin in Bangladesh on storm surge simulation. *J. Mar. Sci. Eng.* 6:99. doi: 10.3390/jmse6030099

An, S. (2016). A Study on the morphological characteristics around artificial headlands in Kashima coast. Japan. *J. Coast. Res.* 32, 508–518. doi: 10.2112/jcoastres-d-15-00122.1

Banno, M., Kuriyama, Y., and Takewaka, S. (2016). Large scale shoreline advancement on the Hasaki coast in the past 50 years. *J. Japan Soc. Civ. Eng. Ser. B2 (Coast. Eng.)* 72, 661–666. doi: 10.2208/kaigan.72.i_661

Chapman, D. C. (1985). Numerical treatment of cross-shelf open boundaries in a Barotropic coastal ocean model. *J. Phys. Oceanogr.* 15, 1060–1075.

Ebita, A., Kobayashi, S., Ota, Y., Moriya, M., Kumabe, R., Onogi, K., et al. (2011). The Japanese 55-year reanalysis 'JRA-55': an interim report. *Sci. Online Lett. Atmos.* 7, 149–152. doi: 10.2151/sola.2011-038

Endo, J., Sugimatsu, K., Yagi, H., Udagawa, T., Oguchi, S., Ohmura, Y., et al. (2017). Study on numerical ocean model in coastal regions of Kashima-Nada and Kujukuri. *J. Japan Soc. Civ. Eng. Ser. B2 (Coast. Eng.)* 73, 1171–1176. doi: 10.2208/kaigan.73.i_1171

European Space Agency Ocean Colour Climate Change Initiative (ESA-OC-CCI) (2019). Available online at: https://esa-oceancolour-cci.org/ (accessed August 23, 2019).

Flather, R. A. (1976). A tidal model of the North-West European continental shelf. *Mém. Soc. R. Sci. Liège* 6, 141–164.

Galal, E. M., and Takewaka, S. (2011). The influence of alongshore and cross-shore wave energy flux on large- and small-scale coastal erosion patterns. *Earth Surf. Process. Landf.* 36, 953–966. doi: 10.1002/esp.2125

Goda, Y. (2006). Examination of the influence of several factors on longshore current computation with random waves. *Coast. Eng.* 53, 157–170. doi: 10.1016/j.coastaleng.2005.10.006

Higaki, M., Hayashibara, H., and Nozaki, F. (2009). *Outline of the Storm Surge Prediction Model at the Japan Meteorological Agency*. Tokyo: Japan Meteorolological Agency.

Höffken, J., Vafeidis, A. T., MacPherson, L. R., and Dangendorf, S. (2020). Effects of the temporal variability of storm surges on coastal flooding. *Front. Mar. Sci.* 7:98. doi: 10.3389/fmars.2020.00098

Intergovernmental Panel on Climate Change (IPCC) (2014). *Climate Change 2014: Synthesis Report. Contribution of Working Groups I, II and III to the Fifth Assessment Report of the Intergovernmental Panel on Climate Change*. Geneva: IPCC.

Japan Hydrographic Association (JHA) (2019). Available online at: https://www.jha.or.jp/en/jha (accessed June 26, 2019).

Japan Meteorological Agency (JMA) (2020). Available online at: https://www.data.jma.go.jp/gmd/kaiyou/db/tide/genbo/genbo.php?stn=CS (accessed March 19, 2020).

Khanal, S., Ridder, N., de Vries, H., Terink, W., and van den Hurk, B. (2019). Storm surge and extreme river discharge: a compound event analysis using ensemble impact modeling. *Front. Earth Sci.* 7:224. doi: 10.3389/feart.2019.00224

Kim, S., Matsumi, Y., Yasuda, T., and Mase, H. (2014). Storm surges along the Tottori coasts following a typhoon. *Ocean Eng.* 91, 133–145. doi: 10.1016/j.oceaneng.2014.09.005

Kim, S., Mori, N., Mase, H., and Yasuda, T. (2015). The role of sea surface drag in a coupled surge and wave model for Typhoon Haiyan 2013. *Ocean Model.* 96, 65–84. doi: 10.1016/j.ocemod.2015.06.004

Kim, S. Y., Yasuda, T., and Mase, H. (2010). Wave set-up in the storm surge along open coasts during Typhoon Anita. *Coast. Eng.* 57, 631–642. doi: 10.1016/j.coastaleng.2010.02.004

Kobayashi, S., Ota, Y., Harada, Y., Ebita, A., Moriya, M., Onoda, H., et al. (2015). The JRA-55 reanalysis: general specifications and basic characteristics. *J. Meteorol. Soc Japan* 93, 5–48. doi: 10.2151/jmsj.2015-001

Kumagai, K., Mori, N., and Nakajo, S. (2016). Storm surge Hindcast and return period of a Haiyan-like super Typhoon. *Coast. Eng. J.* 58:1640001. doi: 10.1142/S0578563416400015

Lagmay, A. M. F., Agaton, R. P., Bahala, M. A. C., Briones, J. B. L. T., Cabacaba, K. M. C., Caro, C. V. C., et al. (2015). Devastating storm surges of Typhoon Haiyan. *Int. J. Disaster Risk Reduct.* 11, 1–12. doi: 10.1016/j.ijdrr.2014.10.006

Lee, H. S., and Kim, K. O. (2015). Storm surge and storm waves modelling due to Typhoon Haiyan in november 2013 with improved dynamic meteorological conditions. *Procedia Eng.* 116, 699–706. doi: 10.1016/j.proeng.2015.08.353

Lee, H. S., Yamashita, T., Komaguchi, T., and Mishima, T. (2010). "Storm surge in Seto Inland Sea with consideration of the impacts of wave breaking on surface currents," in *Proceedings of the Coastal Engineering Conference*, Shanghai. doi: 10.9753/icce.v32.currents.17.

Makino, K., and Nobuoka, H. (2016). Probabilistic storm surge inundation estimation along Ibaraki Prefecture coast by using regional frequency analysis method. *J. Japan Soc. Civ. Eng. Ser. B2 (Coast. Eng.)* 72, 193–198. doi: 10.2208/kaigan.72.i_193

Ministry of Land, Infrastructure, Transport and Tourism (MLIT) (2017). Available online at: http://www1.river.go.jp/ (accessed June 13, 2017).

Mori, N., Kato, M., Kim, S., Mase, H., Shibutani, Y., Takemi, T., et al. (2014). Local amplification of storm surge by super Typhoon Haiyan in Leyte Gulf. *Geophys. Res. Lett.* 41, 5106–5113. doi: 10.1002/2014GL060689

Mori, N., Shimura, T., Yoshida, K., Mizuta, R., Okada, Y., Fujita, M., et al. (2019b). Future changes in extreme storm surges based on mega-ensemble projection using 60-km resolution atmospheric global circulation model. *Coast. Eng. J.* 61, 295–307. doi: 10.1080/21664250.2019.1586290

Mori, N., Yasuda, T., Arikawa, T., Kataoka, T., Nakajo, S., Suzuki, K., et al. (2019a). 2018 Typhoon Jebi post-event survey of coastal damage in the Kansai region, Japan. *Coast. Eng. J.* 61, 278–294. doi: 10.1080/21664250.2019.1619253

Muis, S., Apecechea, M. I., Dullaart, J., de Lima Rego, J., Madsen, K. S., Su, J., et al. (2020). A high-resolution global dataset of extreme sea levels, tides, and storm

surges, including future projections. *Front. Mar. Sci.* 7:263. doi: 10.3389/fmars.2020.00263

Ninomiya, J., Mori, N., Takemi, T., and Arakawa, O. (2017). SST ensemble experiment-based impact assessment of climate change on storm surge caused by pseudo-global warming: case study of Typhoon vera in 1959. *Coast. Eng. J.* 59:1740002. doi: 10.1142/S0578563417400022

Nobuoka, H., Kato, F., Takewaka, S., and Matsuura, T. (2007). Driving force of storm surge along Ibaraki coast of Japan in october 2006. *Proc. Coast. Eng. JSCE* 54, 306–310. doi: 10.2208/proce1989.54.306

Port and Airport Research Institute (PARI) (2018). Available online at: https://www.pari.go.jp/ (accessed July 4, 2018).

Sathyendranath, S., Brewin, B., Mueller, D., Doerffer, R., Krasemann, H., Melin, F., et al. (2012). "Ocean colour climate change initiative – approach and initial results," in *Proceedings of the2012 IEEE International Geoscience and Remote Sensing Symposium (IGARSS)*, Munich, 2024–2027. doi: 10.1109/IGARSS.2012.6350979

Soria, J. L. A., Switzer, A. D., Villanoy, C. L., Fritz, H. M., Bilgera, P. H. T., Cabrera, O. C., et al. (2016). Repeat storm surge disasters of Typhoon Haiyan and its 1897 predecessor in the Philippines. *Bull. Am. Meteorol. Soc.* 97, 31–48. doi: 10.1175/BAMS-D-14-00245.1

Suzuki, T., and Kuriyama, Y. (2014). The effects of offshore wave energy flux and longshore current velocity on medium-term shoreline change at Hasaki, Japan. *Coast. Eng. J.* 56:1450007. doi: 10.1142/S0578563414500077

Tadesse, M., Wahl, T., and Cid, A. (2020). Data-driven modeling of global storm surges. *Front. Mar. Sci.* 7:260. doi: 10.3389/fmars.2020.00260

Tajima, Y., Gunasekara, K. H., Shimozono, T., and Cruz, E. C. (2016). Study on locally varying inundation characteristics induced by super Typhoon Haiyan. Part 1: dynamic behavior of storm surge and waves around San Pedro Bay. *Coast. Eng. J.* 58:1640002. doi: 10.1142/S0578563416400027

Takagi, H., Li, S., de Leon, M., Esteban, M., Mikami, T., Matsumaru, R., et al. (2016). Storm surge and evacuation in urban areas during the peak of a storm. *Coast. Eng.* 108, 1–9. doi: 10.1016/j.coastaleng.2015.11.002

Takayabu, I., Hibino, K., Sasaki, H., Shiogama, H., Mori, N., Shibutani, Y., et al. (2015). Climate change effects on the worst-case storm surge: a case study of Typhoon Haiyan. *Environ. Res. Lett.* 10:064011. doi: 10.1088/1748-9326/10/6/064011

Takewaka, S., and Galal, E. M. (2007). Analyses on erosion of Kashima coast due to 2006 autumn storm event. *Proc. Coast. Eng. JSCE* 54, 581–585. doi: 10.2208/proce1989.54.581

Takewaka, S., and Galal, E. M. (2015). 10 years cross-shore and alongshore shoreline variabilities observed at Hasaki coast. Japan. *J. Japan Soc. Civ. Eng. Ser. B2 (Coast. Eng.)* 71, 673–678. doi: 10.2208/kaigan.71.i_673

Takewaka, S., and Wen, T. (2017). Study on shoreline variabilities observed at the southern end of Kashimanada coast. *J. Japan Soc. Civ. Eng. Ser. B2 (Coast. Eng.)* 73, 679–684. doi: 10.2208/kaigan.73.i_679

The Nationwide Ocean Wave information network for Ports and HArbourS (NOWPHAS) (2019). Available online at: https://www.mlit.go.jp/kowan/nowphas/ (accessed July 15, 2019).

Troselj, J., Imai, Y., Ninomiya, J., and Mori, N. (2018). Coastal current downscaling emphasizing freshwater impact on Ibaraki coast. *J. Japan Soc. Civ. Eng. Ser. B2 (Coast. Eng.)* 74, 1357–1362. doi: 10.2208/kaigan.74.i_1357

Troselj, J., Imai, Y., Ninomiya, J., and Mori, N. (2019). Seasonal variabilities of sea surface temperature and salinity on Ibaraki coast. *J. Japan Soc. Civ. Eng. Ser. B2 (Coast. Eng.)* 75, 1213–1218. doi: 10.2208/kaigan.75.I_1213

Troselj, J., Sayama, T., Varlamov, S. M., Sasaki, T., Racault, M.-F., Takara, K., et al. (2017). Modeling of extreme freshwater outflow from the north-eastern Japanese river Basins to western Pacific ocean. *J. Hydrol.* 555, 956–970. doi: 10.1016/j.jhydrol.2017.10.042

Usui, N., Wakamatsu, T., Tanaka, Y., Hirose, N., Toyoda, T., Nishikawa, S., et al. (2017). Four-dimensional variational ocean reanalysis: a 30-year high-resolution dataset in the western north Pacific (FORA-WNP30). *J. Oceanogr.* 73, 205–233. doi: 10.1007/s10872-016-0398-5

Warner, J. C., Armstrong, B., He, R., and Zambon, J. B. (2010). Development of a coupled ocean-atmosphere-wave-sediment transport (COAWST) modeling system. *Ocean Model.* 35, 230–244. doi: 10.1016/j.ocemod.2010.07.010

Ye, F., Zhang, Y. J., Yu, H., Sun, W., Moghimi, S., Myers, E., et al. (2020). Simulating storm surge and compound flooding events with a creek-to-ocean model: importance of baroclinic effects. *Ocean Model.* 145:101526. doi: 10.1016/j.ocemod.2019.101526

Conflict of Interest: The authors declare that the research was conducted in the absence of any commercial or financial relationships that could be construed as a potential conflict of interest.

frontiers in Marine Science

ORIGINAL RESEARCH
published: 28 May 2021
doi: 10.3389/fmars.2021.569992

High-End Scenarios of Sea-Level Rise for Coastal Risk-Averse Stakeholders

Hugo Dayan[1], Goneri Le Cozannet[2], Sabrina Speich[1] and Rémi Thiéblemont[2]*

[1] Laboratoire de Météorologie Dynamique/IPSL, Ecole Normale Supérieure, PSL Research University, École Polytechnique, IP Paris, CNRS, Sorbonne Université, Paris, France, [2] Bureau de Recherches Géologiques et Minières, Orléans, France

Sea-level rise (SLR) will be one of the major climate change-induced risks of the 21st century for coastal areas. The large uncertainties of ice sheet melting processes bring in a range of unlikely – but not impossible – high-end sea-level scenarios (HESs). Here, we provide global to regional HESs exploring the tails of the distribution estimates of the different components of sea level. We base our scenarios on high-end physical-based model projections for glaciers, ocean sterodynamic effects, glacial isostatic adjustment and contributions from land-water, and we rely on a recent expert elicitation assessment for Greenland and Antarctic ice-sheets. We consider two future emissions scenarios and three time horizons that are critical for risk-averse stakeholders (2050, 2100, and 2200). We present our results from global to regional scales and highlight HESs spatial divergence and their departure from global HESs through twelve coastal city and island examples. For HESs-A, the global mean-sea level (GMSL) is projected to reach 1.06(1.91) in the *low*(*high*) emission scenario by 2100. For HESs-B, GMSL may be higher than 1.69(3.22) m by 2100. As far as 2050, while in most regions SLR may be of the same order of magnitude as GMSL, at local scale where ice-sheets existed during the Last Glacial Maximum, SLR can be far lower than GMSL, as in the Gulf of Finland. Beyond 2050, as sea-level continue to rise under the HESs, in most regions increasing rates of minimum(maximum) HESs are projected at high(low-to-mid) latitudes, close to (far from) ice-sheets, resulting in regional HESs substantially lower(higher) than GMSL. In regions where HESs may be extremely high, some cities in South East Asia such as Manila are even more immediately affected by coastal subsidence, which causes relative sea-level changes that exceed our HESs by one order of magnitude in some sectors.

Keywords: sea-level rise, high-end scenario, projections, climate change, coastal areas, risk-averse stakeholders

OPEN ACCESS

Edited by:
Juan Jose Munoz-Perez, University of Cádiz, Spain

Reviewed by:
Thomas Wahl, University of South Florida, United States
Dewi Le Bars, Royal Netherlands Meteorological Institute, Netherlands

****Correspondence:***
Hugo Dayan
Hugo.dayan@lmd.ens.fr
orcid.org/0000-0002-8705-8154

Specialty section:
This article was submitted to Coastal Ocean Processes, a section of the journal Frontiers in Marine Science

Received: *05 June 2020*
Accepted: *15 April 2021*
Published: *28 May 2021*

Citation:
Dayan H, Le Cozannet G, Speich S and Thiéblemont R (2021) High-End Scenarios of Sea-Level Rise for Coastal Risk-Averse Stakeholders. Front. Mar. Sci. 8:569992. doi: 10.3389/fmars.2021.569992

INTRODUCTION

Since the late 19th century, global mean sea-level (GMSL) has increased due to the effects of anthropogenic warming (Slangen et al., 2016; Dangendorf et al., 2019). GMSL accelerated from 1.4 mm/year over the 1901–2009 to 3.6 mm/year over 2006–2015 (Oppenheimer et al., 2019). It now reaches a rate of 4.6 mm/year according to the latest altimetric measurements[1].

[1]https://www.aviso.altimetry.fr/en/data/products/ocean-indicators-products/mean-sea-level/products-and-images-selection-without-saral-old.html

Regardless of future emissions, GMSL will continue to rise and further accelerate over the next decades (Church et al., 2013), making sea-level rise (SLR) potentially one of the major climate change-induced risks of the 21th century for coastal areas (Nicholls and Cazenave, 2010).

In absence of well-defined adaptation plans and even with the Paris agreement being implemented to maintain global warming below the 2°C threshold, coastal societies will experience profound consequences (IPCC, Intergovernmental Panel on Climate Change [IPCC], 2018). SLR will threaten settlements and ecosystems of low-lying land and islands, where 10% of the world's population lives (Intergovernmental Panel on Climate Change [IPCC], 2014, 2019). Densely populated coastal areas will be in particular affected by permanent inundation due to long-term SLR, superimposed on coastal flooding caused by storm surges (Intergovernmental Panel on Climate Change [IPCC], 2019). To address this threat, coastal decision-makers such as coastal engineers for infrastructure design and land use or coastal policy-makers, and planners, have a strong need for regional to local sea-level changes information to assess risk and plan context-specific adaptation measures (Nicholls et al., 2014; Hinkel et al., 2015, 2019; Le Cozannet et al., 2017b).

At regional and local scale, SLR rate and magnitude may substantially differ from GMSL because of multiple mechanisms driving the spatial variability: atmosphere/ocean dynamics, the changes in Earth gravity, Earth rotation and viscoelastic solid-Earth deformation (GRD, Gregory et al., 2019) induced by the mass redistribution on the height of the geoid and the Earth's surface and the glacial isostatic adjustment (GIA). All the physical processes inducing global through regional to local SLR include considerable uncertainties, especially beyond 2050 (Church et al., 2013). The lack of detailed knowledge about future greenhouse gas (GHG) emissions and our limited understanding of physical processes controlling future mass loss from the Greenland ice-sheet (GrIS) and the Antarctic ice-sheet (AIS) embody the largest uncertainties, in particular for long-term projections of SLR (Ritz et al., 2015; Intergovernmental Panel on Climate Change [IPCC], 2019).

At local scales, subsidence induced by sediment compaction following anthropogenic groundwater and hydrocarbon withdrawal, for example, constitutes another uncertainty source as future demographic pressure on water and hydrocarbon remains uncertain (Church et al., 2013). In addition, apart from raising uncertainties, the climate driven SLR has sometimes lower impact where local subsidence is larger and more studied, such as for deltas, sedimentary lowlands (Tessler et al., 2018), or some coastal cities practicing groundwater withdrawal such as Jakarta (Nicholls et al., 2021).

Over the 20th century, GMSL was driven by the ocean thermal expansion due to warming water and ice mass loss caused by melting of glaciers (Marzeion et al., 2012) and ice-sheets (Shepherd et al., 2012). Sea-level change due to dam construction and groundwater withdrawal had a less important impact, but potentially not as minor as previously thought (Frederikse et al., 2020). During the 21th century, it is expected that the total contribution of ice-sheet and glaciers melting will be the main contribution to GMSL, while the thermal expansion will continue to increase (Intergovernmental Panel on Climate Change [IPCC], 2019). Since the publication of the Fifth Assessment Report of the Intergovernmental Panel on Climate Change (Intergovernmental Panel on Climate Change [IPCC], 2013, hereafter IPCC AR5), the observations of GMSL and the understanding of physical processes that control SLR have progressed substantially. This is true in particular, for ice-sheets modeling (Nowicki et al., 2016; Nowicki and Seroussi, 2018) and observations of mass loss in Antarctica in recent decades (Shepherd et al., 2018; Rignot et al., 2019).

By 2100, IPCC AR5 has projected a *likely range* – defined as a probability exceeding 66%, (Mastrandrea et al., 2011) – of GMSL ranging from 0.28/0.52 to 0.61/0.98 m under Representative Concentration Pathways (RCP)2.6/8.5 (Church et al., 2013). The *likely range* is defined differently in the sea-level chapter of the IPCC Special Report on Ocean and Cryosphere in a Changing Climate (Intergovernmental Panel on Climate Change [IPCC], 2019, hereafter SROCC), as the 17-83% probability range (Oppenheimer et al., 2019). Both definitions recognize the possibility for future sea-levels to exceed the projected *likely range*, the associated probability being up to 33% according to IPCC AR5, and 17% for SROCC.

Lastly, several publications are now considering the high-end tails of the probability of future SLR (Kopp et al., 2014; Grinsted et al., 2015; Carson et al., 2016; Jackson and Jevrejeva, 2016; Slangen et al., 2016; Le Bars et al., 2017; Le Cozannet et al., 2017a; Stammer et al., 2019; Thiéblemont et al., 2019). The upper tail of the distribution is considered useful information for stakeholders interested in the high-end sea-level scenarios (HESs), that is decision-makers with low-uncertainty tolerance (hereafter, risk-averse stakeholders), such as managers of critical infrastructures like coastal cities, ports, coastal cultural heritage, chemical industries, or nuclear plants (Reimann et al., 2018; Hinkel et al., 2019). This brief review shows that the concept of HESs is now well defined and established, and that high-end scenarios for SLR are now accessible for components contributing to sea-level changes such as AIS (e.g., Bamber et al., 2019, B19 hereafter). However, regional maps of HESs are not yet available, or, those already published remain limited to specific geographical regions (e.g., Thiéblemont et al., 2019). This prevents the stakeholders mentioned above from accessing science-based high-end scenarios in their regions.

The present work contributes to filling this gap by assessing the regional implications of the recent study of B19 assessing ice-sheet melting scenarios based on expert elicitation together with physical-based model projections for glaciers, ocean sterodynamic effects, glacial isostatic adjustment and contributions from land-water. We estimate global to regional HESs for two future emissions scenarios as defined in B19 and three critical time horizons (2050, 2100, and 2200) in order to address risk-averse stakeholders information needs for periods ranging from next decades (e.g., urban planners, city engineers, coastal managers) to 100 years or more (e.g., cultural heritage, coastal nuclear power decision-makers). We put a particular emphasis in highlighting regional HESs discrepancies and their divergence from global HESs through 12 coastal city and island examples (**Figure 1**) that differ from their distance to ice-sheets,

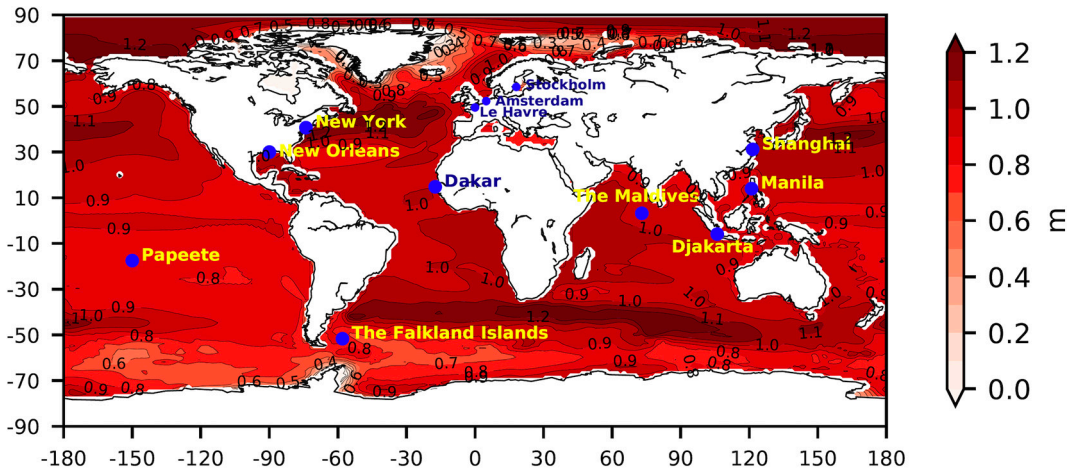

FIGURE 1 | Regional sea-level change (m) in 2100 relative to 1986–2005 in RCP8.5. The selected sites for discussing regional scenarios are represented by the blue circles. Each value for each grid cell corresponds to the upper-end of the *likely range* obtained from sea-level projections provided by the Integrated Climate Data Center (Carson et al., 2016).

which is one of the most uncertain control on the regional distribution of sea-level change. We then discuss our results in general terms and provide confidence in our global to regional HESs for the benefit of local risk-averse stakeholders.

METHOD: APPROACH FOR ASSESSING HESs CHANGE

General Approach

High-end sea-level scenarios are defined as unlikely (low probability), but possible, scenarios for future sea-level changes (Jevrejeva et al., 2014). Approaches to estimate HESs use various lines of evidence (Stammer et al., 2019). The most common approach is a probabilistic framework combining emission scenarios from the IPCC (RCPs) and estimates from simulation of the individual components of sea-level change based on a model selection and assumptions on ice-sheets contributions (Jevrejeva et al., 2019). However, relying on the highest quantiles of probabilistic sea-level projections is not always an appropriate method to estimate HESs, especially when the upper quantiles do not necessarily match the outcomes of processes not taken into account in the physical modeling of future sea-level changes. For example, relying on the upper quantiles of a distribution of the future Antarctic contribution to SLR assuming the marine ice-sheet instability (MISI) cannot quantitatively reflect the possibility of the marine ice-cliffs instabilities (MICI) (DeConto and Pollard, 2016; Kopp et al., 2017; Jevrejeva et al., 2019). In such cases of recognized ignorance, expert elicitation has been proposed as a way to overcome this difficulty (Bamber and Aspinall, 2013; B19).

Here, we use a combination of physical-based models and expert elicitation evidence, as illustrated in **Figure 2**. Our major goal is the regionalization of future sea-level changes as well as highlighting departure from GMSL for two emission scenarios and for three critical time horizons. We combine the projections for sterodynamic, glaciers, GIA and land water storage (LWS) from physical-based models with the future GrIS and AIS contributions from the last updated expert elicitation estimates of B19. Our projections are high-end because we consider the upper quantiles of these physical-based models or expert elicitations. Hence, the selection of expert-elicitation or physical models is guided by our motivation to select high-end scenario. Specifically, we distinguish two cases:

- if is no specific reason to consider a high-end well above the projected contribution (e.g., sterodynamic or glacier components), we rely on the high quantiles of the distribution (83rd and 95th percentiles).
- if some experts consider that high ends well above the projected contribution can be possible (e.g., Antarctica and Greenland ice melting), we consider the higher quantiles of an authoritative structured expert-elicitation of future ice-sheets melting to SLR.

The structured expert judgment estimate of B19 has the advantage to introduce non-Gaussian uncertainty into the tails of GrIS and AIS contributions, taking into account physical processes that are not necessarily represented by all ice-sheet models. We construct HESs for the two emissions scenarios from B19, the *low* emission scenario slightly warmer than RCP2.6 from IPCC AR5 and the *high* emission scenario almost as warm as RCP8.5 from IPCC AR5. We assume the *low* and *high* emission scenarios to be the same as RCP2.6 and RCP8.5 scenarios with regard to glaciers and sterodynamic contributions to global sea-level change. B19 do not account for the large temperature uncertainty from each RCP, and they assume temperature stabilization at 5°C for their high scenario, which can be considered optimistic in terms of climate forcing (Collins et al., 2013). Yet, their ice-sheets melting projections

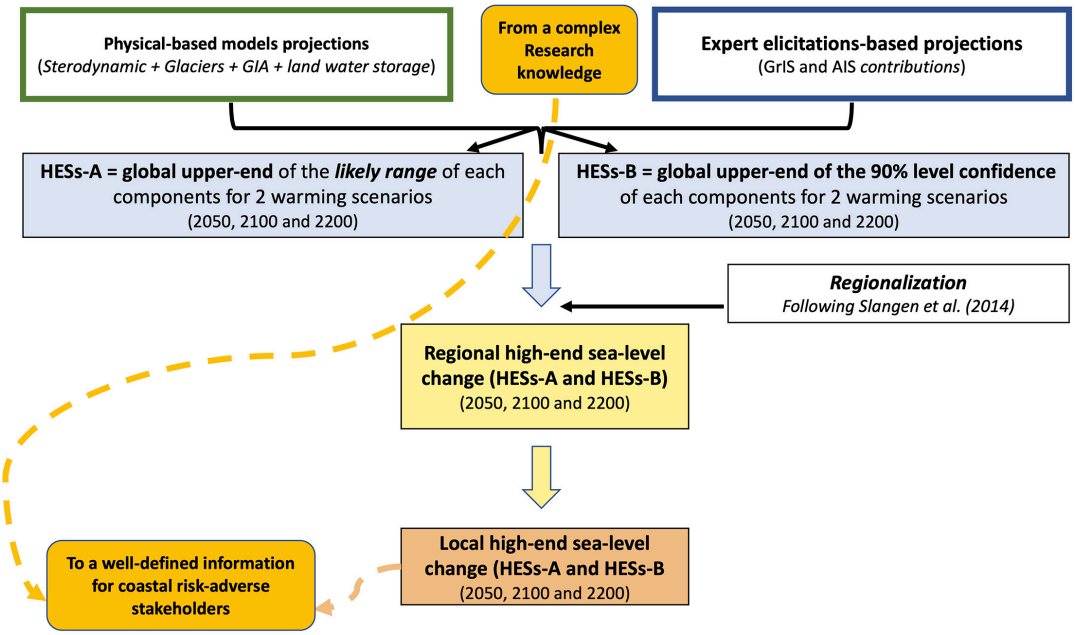

FIGURE 2 | Scheme of our general approach for assessing global to regional and local HESs. Blue boxes display high-end design choices that can be adjusted depending on user's preferences.

belong to the highest in the published literature, and can therefore be considered high-end.

We first build two HESs for GMSL combining each sea-level change contribution: HESs-A based on the upper-end of the *likely range* (83rd percentile) and HESs-B based on the upper-end of the 90% confidence level (95th percentile) of the distribution estimates of the different components of sea-level change. We do not pretend that summing 95th(83rd) percentiles for each component results in 95th(83rd) percentile projection: this would be true only for fully correlated components. We just take these percentiles to derive a HESs scenario, without providing a probability associated to it, as in Jevrejeva et al. (2014). The probability of these scenarios is low, but it cannot be quantified because we do not know the dependencies between contributions (Le Bars, 2018).

We then regionalize HESs following the method of Slangen et al. (2014): we sum the regional sterodynamic term, the regional sea-level equivalent (SLE) change from barystatic-GRD using fingerprint, a constant geographical pattern which generates the spatial sea-level variability induced by the mass redistribution on the Earth (see **Supplementary Material** for more details), and the regional GIA-induced sea-level change. While fingerprints will evolve over time or for varying temperature, and also depending on the exact source of melting (Meyssignac et al., 2017), we assume that they do not change over time as a first approximate, following previous studies (Slangen et al., 2014).

Sterodynamic Component

We use the thermal expansion projections of Kopp et al. (2014). These projections are based on a subset of 29 CMIP5 GCMs and result in a larger thermal expansion than that provided by the 21 CMIP5 GCMs used for the IPCC AR5 (Church et al., 2013). Note that the 29 CMIP5 GCMs of Kopp et al. (2014) comprise all the 21 CMIP5 GCMs of the IPCC AR5. The thermal expansion projections of Kopp et al. (2014) have the advantage to extend until 2200. Yet, the number of sterodynamic CMIP5 model outcomes drops from 29 to 6 models between 2100 and 2200 for the RCP8.5 scenario and from 20 to 6 models for the RCP2.6 scenario (see details in Kopp et al., 2014). The substantial difference in the number of models leads to a small discontinuity and a variance reduction at the start of the 22nd century. We select two high-end scenarios: HESs-A corresponds to the upper-end of the multi-model *likely range* (83rd percentile) from Kopp et al. (2014), while HESs-B corresponds to the 95th percentile (see values in **Table 1**). Our estimates for the sterodynamic component are slightly higher than the 83rd percentile of SROCC projections (Oppenheimer et al., 2019), and therefore can be considered high-end.

To produce the regional SLR of the sterodynamic contribution, we use the spatial patterns of ocean dynamic sea-level changes of the IPCC AR5 models. This relies on the assumption that the regional variability of sea-level sterodynamic projections is driven by the same mechanisms in Kopp et al. (2014) and for the IPCC AR5, as suggested by Couldrey et al. (2021).

Only a subset of climate models deliver information in semi-enclosed seas, which leads to significant differences on both sides of the strait of Gibraltar (West-Atlantic and Mediterranean seas) and Danish Straits (North and Baltic seas), for example. Hence, to eliminate these potential sources of errors in HESs, we constrain the sterodynamic component within each semi-enclosed basin with that of the oceanic area, where all models are available,

TABLE 1 | (A) Global mean sea-level changes (m) in the *low* emission scenario by 2100 relative to the end of the 20th century of each sea-level contribution for (left) the IPCC AR5/SROCC upper-end of the *likely range* (83th percentile), (middle) HESs-A and (right) HESs-B.

(A) Low emission scenario ~ RCP2.6	IPCC AR5/SROCC (m) (83rd percentile in RCP2.6)*[1]			HESs-A (m) (83rd percentile)			HESs-B (m) (95th percentile)		
Year Component	**2050**	**2100**	**2200**	**2050**	**2100**	**2200**	**2050**	**2100**	**2200**
Thermal expansion	0.14[1]	0.20[2]	–	0.14[4]	0.26[4]	0.40[4]	0.16[5]	0.31[5]	0.40[5]
Glaciers	0.09[1]	0.16[2]	–	0.08[4]	0.15[4]	0.20[4]	0.09[5]	0.17[5]	0.30[5]
Greenland	0.05[1]	0.14[2]	–	0.11[6]	0.31[6]	0.79[6]	0.18[7]	0.57[7]	1.49[7]
Antarctic (WAIS + EAIS)	0.06[1]	0.18[3]	–	0.08[8]	0.27[8]	0.86[8]	0.27[9]	0.56[9]	1.52[9]
Land water storage	0.03[1]	0.11[2]	–	0.03[10]	0.07[10]	0.16[10]	0.03[11]	0.08[11]	0.17[11]
GMSL	0.37[12]	0.80[12]	–	0.44[12]	1.06[12]	2.41[12]	0.73[12]	1.69[12]	3.98[12]

(B) High emission scenario ~ RCP8.5	IPCC AR5/SROCC (m) (83rd percentile in RCP8.5)*[2]			HESs-A (m) (83rd percentile)			HESs-B (m) (95th percentile)		
Year Component	**2050**	**2100**	**2200**	**2050**	**2100**	**2200**	**2050**	**2100**	**2200**
Thermal expansion	0.16[1]	0.39[2]	–	0.16[4]	0.46[4]	1.10[4]	0.19[5]	0.52[5]	1.20[5]
Glaciers	0.10[1]	0.26[2]	–	0.09[4]	0.21[4]	0.40[4]	0.10[5]	0.24[5]	0.40[5]
Greenland	0.07[1]	0.31[2]	–	0.14[6]	0.60[6]	1.22[6]	0.27[7]	0.99[7]	2.16[7]
Antarctic (WAIS + EAIS)	0.06[1]	0.35[2]	–	0.12[8]	0.57[8]	1.57[8]	0.25[9]	1.39[9]	7.22[9]
Land water storage	0.04[1]	0.11[2]	–	0.03[10]	0.07[10]	0.16[10]	0.03[11]	0.08[11]	0.17[11]
GMSL	0.43[12]	1.42[12]	–	0.54[12]	1.91[12]	4.45[12]	0.84[12]	3.22[12]	11.15[12]

(B) *The same than* ***(A)*** *but in the high emission scenario. All values are rounded at two significant digits beyond the decimal point. See text for details.*
*[*1] Roughly equivalent to the low emission scenario in B19.*
*[*2] Roughly equivalent to the high emission scenario in B19.*
[1] [ICDC] http://icdc.cen.uni-hamburg.de/1/daten/ocean/ar5-slr.html.
[2] IPCC AR5.
[3] SROCC.
[4] Based on the upper-end of the 17–83% probability range (defined as the likely range in IPCC AR5) in Kopp et al. (2014).
[5] Based on the upper-end of the 5-95% probability range in Kopp et al. (2014).
[6] Based on the upper-end of the 17-83% probability range in B19.
[7] Based on the upper-end of the 5-95% probability range in B19.
[8] Based on the AIS sum (WAIS + EAIS) of the upper-end of the 17–83% probability range in B19.
[9] Based on the AIS sum (WAIS + EAIS) of the upper-end of the 5–95% probability range in B19.
[10] Based on the upper-end of the 17–83% probability range in Nauels et al. (2017).
[11] Based on the upper-end of the 5–95% probability range in Nauels et al. (2017).
[12] Sum of the percentile values for each of the different terms.

as in Thiéblemont et al. (2019). This approach is supported by studies analyzing the processes governing multi-decadal sea-level changes e.g., in the Baltic Sea (Weisse et al., 2019).

Barystatic-GRD Components

Glaciers

The glaciers projections are obtained combining process-based glacier models and output (precipitation and temperature) projections from CMIP5's AOGCMs (Slangen and van de Wal, 2011). By 2100(2050), IPCC AR5 estimated an upper-end of the *likely range* of 0.16(0.1) m for RCP2.6 and 0.26(0.11) m for RCP8.5. Lower upper-end of the *likely range* projections were estimated by Marzeion et al. (2012) with 0.15 m from non-Antarctic glaciers by 2100 for RCP2.6 and 0.21 cm for RCP8.5. More recent modeling estimates by Huss and Hock (2015), also project slightly lower glacier mass losses than IPCC AR5 (Slangen et al., 2017). Given these slight differences in glacier mass loss projections between IPCC AR5 and updated studies, we opt for the Marzeion et al. (2012) projections by 2100, also used in Kopp et al. (2014) who provide in addition the projections of glaciers and GMSL for 2050 and 2200. Similarly to oceanographic process, GCM-based model projections of glacier contribution rely on a significantly reduced number of models after 2100 (Kopp et al., 2014). Here again, this limitation is considered by rounding 22nd century projections to the nearest decimeter. HESs-A for the glaciers contribution is defined using the upper-end of the multi-model *likely range* (83rd percentile) of Kopp et al. (2014), while HESs-B is defined as the upper-end of the 90% confidence level under normality hypothesis (95th percentile). Our glacier's SLE estimates for each emission scenario, each HESs and each time horizon retained, are listed in **Table 1**. Because our estimates of the Glacier contribution to SLR are close to the 83rd percentile of SROCC projections (Oppenheimer et al., 2019), they can be considered as a realistic high-end. The regional SLR of the glaciers contribution is obtained from the fingerprint of glaciers sea-level changes used in IPCC AR5, and provided by the

Integrated Climate Data Center (ICDC) of Hamburg University (Carson et al., 2016).

Ice-Sheets

GrIS and AIS are the planet's ice-sheets and contain more than 65% of the Earth's freshwater (Church et al., 2013). AIS is larger than GrIS and contains about eight times more ice than the latter, corresponding to 58.2 against 7.3 m SLE (Church et al., 2013). Considering a complete melting of both ice-sheets, GMSL would rise by roughly 65 m relative to present-day (Alley et al., 2005). While such a dramatic global SLR is excluded within the coming centuries (Pfeffer et al., 2008), both ice-sheets are losing mass, increasingly faster (Rignot et al., 2011; Shepherd et al., 2018). By 2100 and beyond, ice-sheets will continue to melt, even with strong mitigation measures to maintain global warming under 2°C relative to preindustrial global temperatures. Sea-level change driven by mass transfer from ice-sheets melting to the ocean can be explained through two physical processes which are the surface mass balance (SMB) and the dynamic effect (DYN). The former corresponds to the sum of accumulation and ablation driven by atmospheric processes and is quite well understood, while the latter is driven by changes in the dynamical discharge of glaciers and marine ice-sheets.

IPCC AR5 estimated that by 2100 the upper-end of the *likely range* of GrIS's melting would be 0.28(0.01) m under RCP8.5(2.6) scenario, controlled by SMB by roughly two thirds. Since IPCC AR5, GrIS contribution to sea-level change has been slightly reevaluated (Fürst et al., 2015; Vizcaino et al., 2015), generally suggesting future Greenland ice dynamic losses are self-limited, although potentially substantial in marine terminating glaciers of west Greenland (Choi et al., 2021). SROCC estimates of GrIS's contribution to future sea-level are the same as those reported in IPCC AR5.

The AIS contribution to sea-level change is broadly and vigorously debated in the literature (SROCC). The associated uncertainties are the largest and strongly depend on the understanding of DYN processes which trigger ice-sheet mass loss and their evolution under global warming. The two mechanisms involved are MISI, probably underway in West-Antarctica (Joughin et al., 2014; Rignot et al., 2014), and MICI, which has not been observed in Antarctica in the modern era, and whose contribution to past sea-level changes during previous interglacial is debated. It is unsure that MICI can be initiated during the 21st century (DeConto et al., 2019). Recently, SROCC reassessed upward the upper-end of the *likely range* of AIS contribution to GMSL: 0.37 m by 2100 under RCP8.5, against the 0.19 m provided by IPCC AR5, but this does not include a potential onset of MICI. Yet, if MICI is initiated during the 21st century, the ice-sheet of Antarctica may contribute by 0.8 (Edwards et al., 2019) or 1 m (DeConto and Pollard, 2016) in 2100, well above the projections of SROCC.

Here, we use the most recent elicitations-based projections of B19 on ice-sheet contributions, which give an upper-end of the *likely range* at 0.31(0.60) m by 2100 for the *low*(*high*) emission scenario. B19 report that their results have probably been influenced by expert reflecting the following research results: (1) paleo-evidences showing the sensitivity of the Antarctic ice-sheet to CO_2 changes during past interglacial; (2) recent results of MICI (3) the warming trends in arctic and increasing contribution of Greenland to SLR since two decades, which experts have assumed being a consequence of external forcing in the B19 study. As a consequence, the uncertainties of B19 projections are revised upwards compared to Bamber and Aspinall (2013). HESs-A for the ice-sheets melting contribution is defined using the upper-end of the *likely range* (83rd percentile) from B19, while HESs-B is defined as the upper-end of the 90% confidence level under normality hypothesis (95th percentile) (**Table 1**). As noted in section "General approach," the temperature assumptions in B19 are optimistic in the sense that they assume a stabilization at 5°C after 2100. Yet, **Table 1** shows that their 95th percentile reaches 1.39 m for 2100, which is comparable to the results of DeConto and Pollard (2016) for RCP8.5 (1.14 ± 0.36 m). Hence, the B19 scenarios can be considered high-end.

B19 provided the total GIS contribution and separated the West Antarctic ice-sheet (WAIS) contribution from that of the East Antarctic ice-sheet. In IPCC AR5, the regional SLR of the ice-sheet contributions is obtained using the fingerprint of ice-sheet sea-level changes, using a separate fingerprint for the DYN effects and for the SMB effects. Here, we compute SLR of the ice-sheet contributions using both fingerprints used in IPCC AR5 for both ice sheets, thus assuming that melting is not uniform on the ice-sheet but that melting will be more prominent in West Antarctica and West Greenland. Specifically, we assign a weight of 0.33 to the fingerprint centered on West-Greenland and above 0.75 to the fingerprint centered on West-Antarctica (precise value for West-Antarctica, as in B19). Different assumptions on the precise location of melting would result in large differences in sea-level change scenarios close to the ice-sheet, but small differences far from it, where most people live.

Land Water Storage (LWS)

This contribution to SLR is driven by two major processes: the water impoundment, which contributes to mitigate SLR, and groundwater depletion which increases SLR. Projected anthropogenic LWS contribution to SLR and associated uncertainties are under debate due to incomplete process understanding (Konikow, 2011; Pokhrel et al., 2012; Wada et al., 2012, 2016; Church et al., 2013; Frederikse et al., 2020). Since the late 20th century, water storage contribution has decreased (Gregory et al., 2013), embodying groundwater depletion as the main anthropogenic LWS contribution to SLR over the 21st century and beyond. Since the IPCC AR5 projections which considered a 0.11 m SLR due to groundwater overuse, Wada et al. (2016) revised estimates assessing that previous studies overestimated groundwater depletion contribution to SLR without considering that only ∼80% of annually depleted groundwater ends up in the oceans, reducing the Wada et al. (2012) SLR contribution estimates from groundwater depletion by 20%.

We use the LWS projections of Nauels et al. (2017). These projections are based on the approach used by Wada et al. (2012), corrected by the 20% fraction of depleted groundwater that does not end up in the global ocean (Wada et al., 2016), adding extended projections up to 2200 considering the 30-year average

annual depletion rate for the period 2071–2100. To do so, Nauels et al. (2017) assumed that human water use and groundwater extraction will carry on beyond 2100.

As in previous studies, we assume that LWS contribution to SLR is climate emission scenario-independent as differences are insignificant by the end of the 21st century, uncertainties are large together and processes at play beyond 2100 are underdetermined (Church et al., 2013). Our LWS' SLE estimates for each HESs and time horizon are listed in **Table 1**. They are comparable to the 83rd percentile in SROCC projections, and can therefore be considered high-end. The regional SLR of the LWS contribution is obtained from the fingerprint of LWS sea-level changes used in IPCC AR5, and provided by ICDC.

Glacial Isostatic Adjustment (GIA)

Within IPCC AR5, GIA uncertainties are taken into account using two different GIA models (Church et al., 2013), whereby the best estimate is the mean of the two models and "one standard error of the GIA uncertainty is evaluated as the departures of the two different GIA estimates (from ICE-5G and ANU/SELEN models) from their mean value" (Church et al., 2013). Here, the GIA-induced regional sea-level change is defined for the HESs-A as the 1*standard deviation around the mean, and for the HESs-B as 1.7*regional standard deviation around the mean (i.e., upper-end of the 90% confidence level under normality hypothesis). GIA projections for the 22nd century are obtained by linearly extrapolating the 21st century values.

RESULTS

This section presents our resulting HESs as a function of emission scenarios and time horizons (**Tables 2**, **3** and **Figure 3**). **Supplementary Figure 3** allow to illustrate more precisely global patterns relative to GMSL.

Global HESs

Under the *low* and *high* emission scenarios, both global HESs-A and HESs-B are larger than most of the values discussed in recent publications providing global HESs, regardless of the time horizon (**Table 2**). Although our global HESs estimates are built upon the same evidence as B19, they are substantially larger. This is because these authors assume dependencies between the various processes, so that the total ice-sheet contribution is not simply the sum of each ice-sheet contribution. Here, in contrast to the approach of B19, we explore global HESs that are not associated with any precise probability.

In 2050, HESs-A provides a GMSL roughly the same as B19 for both, *low* and *high,* emission scenarios, while HESs-B projects a 0.73(0.84) GMSL in the *low*(*high*) emission scenario, that is approximately 25% larger than B19. In 2100, for HESs-A, in the *low*(*high*) emission scenario, we found HESs values for GMSL that reach 1.06(1.91) m that is approximately 10% larger than in B19, while for HESs-B GMSL may increase up to 1.69(3.22) m that is approximately 25% larger than in B19. However, in the *high* emission scenario Kopp et al. (2017) and Le Bars et al. (2017) found a higher global HESs than our HESs-A. In fact, these two studies both included MICI from DeConto and Pollard (2016), that is, the largest GrIS and AIS melting projected so far by means of ice-sheet melting modeling. Hence, while the 1.69 m GMSL suggests that HESs could be relevant even for *low* emission scenarios, the 3.22 m GMSL is consistent with studies assuming possible rapid melting processes induced by MICI (DeConto and Pollard, 2016) that could cause a GMSL rise exceeding 1 m by 2100 (SROCC). Our results are slightly higher than those of Jevrejeva et al. (2014), who used a similar method: this is because we use different assumptions for the thermal expansion and glacier contributions, and also because their study relied on the previous expert elicitation from Bamber and Aspinall (2013). In 2200, GMSL may increase up to 2.41(4.45) m for HESs-A and 3.98(11.15) m for HESs-B in the *low(high*) emission scenario. These values are far larger than SROCC projections by the end of the 22nd century. They are also substantially larger than the SLR projections of Kopp et al. (2014), whose highest quantiles were constrained by the previous expert elicitation conducted by Bamber and Aspinall (2013). However, in the *high* emission scenario Le Bars et al. (2017) found a higher global HESs than our HESs-A, as they include MICI from DeConto and Pollard (2016).

From Global to Regional HESs

In this sub-section, we describe the spatial divergence of HESs and the regional contributions to HESs for two large areas (the northern Atlantic, **Figure 4**, and the south-eastern Pacific, **Figure 5**), as they show both important sea-level change gradients and host highly inhabited coastal cities, lands and islands (e.g., Amsterdam, Dakar, Le Havre, New Orleans, New York, Papeete, and Stockholm). While the coastal areas around the Indian Ocean, the north-eastern Pacific and the western Pacific also host inhabited coasts and islands, we choose not to describe them as they show a more homogeneous sea-level change pattern (see **Figure 3** which displays sea-level spatial distribution at global scale). As the patterns for both emission scenarios are fairly similar (with lower values in the *low* emission scenario, see **Figure 3A**), we only discuss HESs spatial distribution in the *high* emission scenario. **Supplementary Figures 1**, **2** allow to illustrate more precisely regional patterns relative to GMSL.

As time goes by and as HESs get worse, the northern Atlantic(south-eastern Pacific) displays an increasingly important southwest-northeast(south-north) sea-level change gradient (**Figures 4**, **5**). Both regions show increasing rates of minimum(maximum) SLR at high(low-to-mid) latitudes, close to (far from) ice-sheets, resulting from the redistribution of ice mass from land to ocean. As a consequence, HESs values are substantially lower than GMSL in the vicinity of ice-sheets, regardless of time horizon. This is an obvious consequence of the gravitational effects associated to ice-sheet mass losses (Spada et al., 2013), which are larger here than in previous studies due to the more substantial amount of mass losses in ice-sheets involved by high-end scenarios. Hence, HESs display spatial variability mostly due to the sterodynamic contribution, ice-sheets melting and the GIA effects (Slangen et al., 2014). Here, we detail the role of each sea-level contribution.

High-end sea-level scenarios patterns in the northern Atlantic result from several main processes (**Figure 4**). First, the

TABLE 2 | Global HESs (m) as provided in selected recent publications and in the present work.

Emission scenario	**Low ~ RCP2.6**						**High ~ RCP8.5**					
Global HESs (m)	**HESs-A (83rd percentile)**			**HESs-B (95th percentile)**			**HESs-A (83rd percentile)**			**HESs-B (95th percentile)**		
Year Authors	**2050**	**2100**	**2200**	**2050**	**2100**	**2200**	**2050**	**2100**	**2200**	**2050**	**2100**	**2200**
Present work	0.44	1.06	2.41	0.73	1.69	3.98	0.54	1.91	4.45	0.84	3.22	11.15
Bamber et al., 2019	0.40	0.98	–	0.49	1.26	–	0.47	1.74	–	0.61	2.38	–
Kopp et al., 2017	0.33	0.78	1.61	0.41	0.98	2.06	0.40	2.09	8.96	0.48	2.43	9.62
Le Bars et al., 2017	–	–	–	–	–	–	–	2.38*	–	–	2.92	–
Jackson and Jevrejeva, 2016	–	–	–	–	–	–	–	0.98	–	–	1.18	–
Grinsted et al., 2015	–	–	–	–	–	–	–	1.20	–	–	1.83	–
Kopp et al., 2014	0.29	0.65	1.60	0.33	0.82	2.40	0.34	1.00	2.80	0.38	1.21	3.70

*No value is given when it has not been directly provided in the publications. Red boxes display the highest GMSL values, while orange boxes indicate when the GMSL value is higher than ours.*Actually, Le Bars et al. (2017) only provide the 80th percentile of the probability density function.*

TABLE 3 | Regional HESs (m) for the selected sites given by HESs-A and HESs-B for each emission scenario and for each time horizons (2050, 2100, and 2200).

Emission scenario	**Low~ RCP2.6**						**High ~ RCP8.5**					
Regional HESs (m)	**HESs-A**			**HESs-B**			**HESs-A**			**HESs-B**		
Year Site	**2050**	**2100**	**2200**	**2050**	**2100**	**2200**	**2050**	**2100**	**2200**	**2050**	**2100**	**2200**
Global	0.44	1.06	2.41	0.73	1.69	3.98	0.54	1.91	4.45	0.84	3.22	11.15
Amsterdam	0.41	0.90	1.94	0.73	1.48	3.22	0.50	1.57	3.79	0.77	2.77	10.45
Dakar	0.48	1.09	2.48	0.81	1.77	4.16	0.58	1.95	4.56	0.90	3.37	12.01
Djakarta	0.45	1.12	2.62	0.87	1.85	4.45	0.56	2.07	4.89	0.91	3.59	12.57
The Falkland Islands	0.43	0.91	1.78	0.57	1.36	2.96	0.50	1.52	3.04	0.73	2.35	7.04
Le Havre	0.41	0.85	1.86	0.66	1.31	2.96	0.48	1.48	3.55	0.70	2.57	10.04
The Maldives	0.51	1.16	2.61	0.85	1.88	4.43	0.62	2.09	4.77	0.97	3.59	12.50
Manila	0.49	1.13	2.58	0.82	1.85	4.40	0.60	2.03	4.63	0.94	3.54	12.39
New Orleans	0.48	1.12	2.61	0.86	1.87	4.41	0.58	1.94	4.62	0.94	3.43	12.24
New York	0.45	1.11	2.59	0.83	1.84	4.22	0.55	1.99	5.05	0.91	3.42	12.49
Papeete	0.49	1.15	2.63	0.83	1.89	4.51	0.60	2.05	4.68	0.95	3.58	12.47
Shanghai	0.53	1.08	2.36	0.85	1.78	4.12	0.62	1.89	4.14	0.95	3.32	11.50
Stockholm	0.17	0.48	1.10	0.52	1.14	2.52	0.25	1.20	3.14	0.57	2.46	9.85

Colored boxes display when regional HESs are appreciably below GMSL (blue boxes), roughly as large as GMSL (yellow boxes), and appreciably above GMSL (red boxes). Given the uncertainties in the face of HESs and to highlight local discrepancies from GMSL, we arbitrarily consider a (not) appreciably local SLR value when (not) differing from GMSL from more than 10 cm. Note that SLR appreciably lower than GMSL can be qualitatively explained when sites are close to ice-sheets, thus less affected by the changes in Earth Gravity, Earth Rotation, and crustal deformation induced by ice-sheet melting.

sterodynamic component through the combination of the northward shift of the North Atlantic Current (Landerer et al., 2007) and a weakening of the meridional overturning circulation (Yin et al., 2009), increasing SLR particularly on the northeast coast of the United States. Second, the ice-sheets contributions, decreasing(increasing) SLR close to (far from) ice-sheets, and the GIA contribution acting on vertical ground motions in regions where large ice-sheets existed during the LGM. While in Scandinavia GIA induces high rates of uplift, the region of the Chesapeake Bay in the East-US coast undergoes substantial subsidence. As a consequence, as time passes by and HESs worsen, SLR in the northeast coast of the United States might be not only larger than GMSL, but also higher than SLR along other northern Atlantic coasts, such as the European and east African coasts. SLR in northern Europe (e.g., around the Gulf of Finland) is lower due to the effects of GIA (**Figure 4**). Over the Arctic, HESs show higher SLR values (**Figure 4**).

As to the south-eastern Pacific, Slangen et al. (2014) described the south-north sea-level change gradient – a meridional gradient across the Antarctic Circumpolar Current – as the result of several main processes. First, the combination of low thermal expansion coefficients regarding colder temperatures in the extreme south and a strengthening and southward shift of the Antarctic Circumpolar Current in response to increasing CO2 emissions. Second, the West AIS dynamic, which leads to drastic SLR gradients from south to north in the South America continent (**Figure 5**). As a consequence, in 2100 and for HESs-B, for example, at the southern tip of Chili SLR might be lower by more than 1 m than the 3.22 GMSL, whereas in northern Chili SLR might equal GMSL (**Figure 5**). Yet, the actual values in this

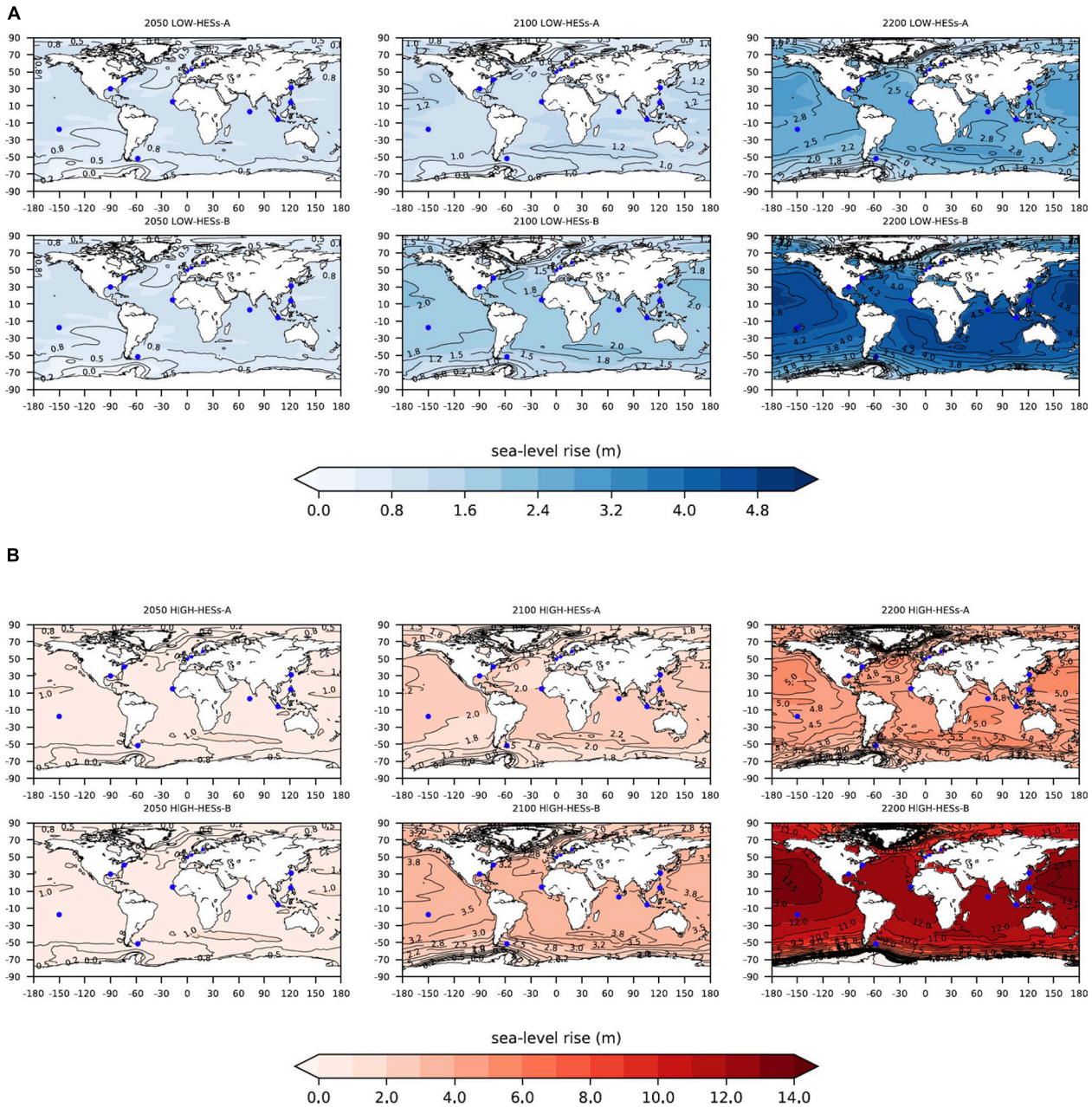

FIGURE 3 | HESs at global scale for (first row) HESs-A and (second row) HESs-B in **(A)** the *low* emission scenario and **(B)** the *high* emission scenario. Colors and contours display SLR (m) by (left) 2050, (middle) 2100, and (right) 2200 relative to 1986–2005. Blue circles represent the selected sites (refer to **Figure 1** for the names) discussing from regional to local HESs.

region are dependent on the location of melting in the Antarctic ice-sheet, an uncertainty which is not accounted for in this study.

From Regional to Coastal City and Island Scale HESs

For each coastal city and island scale HESs, time horizon and emission scenario, the reader can refer to both **Figure 3** displaying sea-level spatial distribution at global scale and **Table 3**. Given the uncertainties in HESs and to highlight local departure from GMSL, we arbitrarily consider that the difference between local SLR and GMSL is *not appreciable* when it differs by less than ±10 cm. For example, SLR is *appreciably* lower than GMSL close to ice-sheets.

2050

In 2050, for HESs-A in the *low/high* emission scenario, SLR does *not appreciably* differ from GMSL (low emission

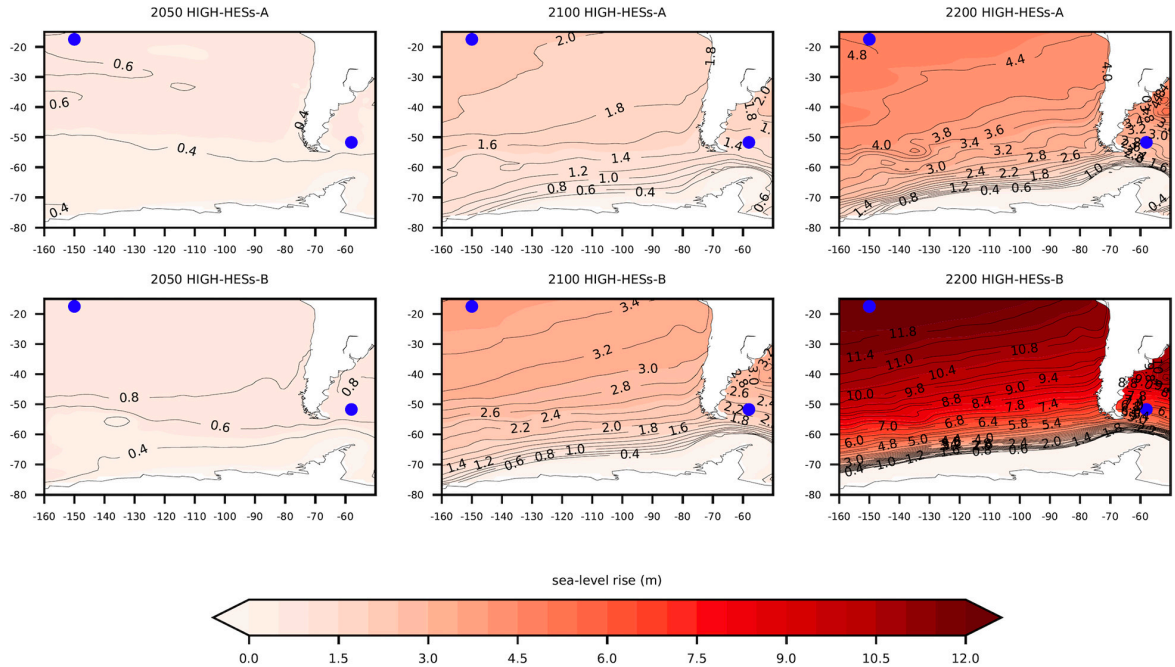

FIGURE 4 | Regional HESs for (first row) HESs-A and (second row) HESs-B in the northern Atlantic. Colors and contours display SLR (m) by **(left)** 2050, **(middle)** 2100, and **(right)** 2200 relative to 1986–2005. Blue circles represent the selected sites (refer to **Figure 1** for the names) discussing from regional to local HESs.

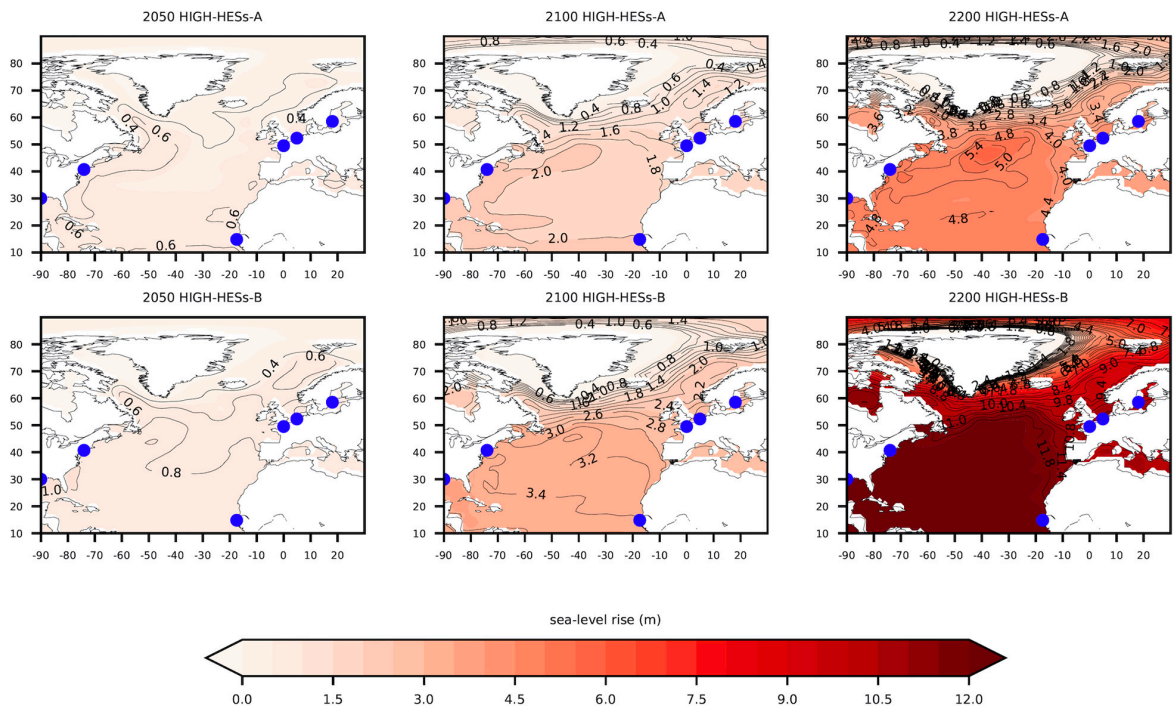

FIGURE 5 | The same as **Figure 4**, but in the south-eastern Pacific.

scenario: 0.44/high emission scenario: 0.54 m) in Amsterdam (0.41/0.50 m), Dakar (0.48/0.58 m), Djakarta (0.45/0.56 m), the Falkland Islands (0.43/0.50 m), Le Havre (0.41/0.48 m), the Maldives (0.51/0.62 m), Manila (0.49/0.60 m), New Orleans (0.48/0.58 m), New York (0.45/0.55 m), Papeete (0.49/0.60 m), and Shanghai (0.53/0.62 m), while it may be *appreciably* lower

than GMSL for both emission scenarios in Stockholm due to GIA (0.17/0.25 m). For HESs-B in the *low* emission scenario, SLR *appreciably* differ from GMSL (0.73 m) in the Falkland Islands (0.57 m) and Stockholm (0.52 m) where it is *appreciably* below GMSL. In Djakarta (0.87), the Maldives (0.85 m), New Orleans (0.86 m), New York (0.83 m), Papeete (0.83 m), and Shanghai (0.85 m) it *appreciably* exceeds GMSL. For HESs-B in the *high* emission scenario, SLR does *not appreciably* differ from GMSL (0.84 m) in Amsterdam (0.77 m), Dakar (0.90 m), Djakarta (0.91 m), and New York (0.91 m), whereas it may be *appreciably* higher than GMSL in the Maldives (0.97 m), Manila (0.94 m), New Orleans (0.94 m), Papeete (0.95 m), and Shanghai (0.95 m) and lower than GMSL in the Falkland Islands (0.73 m), Le Havre (0.70 m), and Stockholm (0.57 m). This result illustrates that provided there is no additional vertical ground motion besides GIA, 2050 is a relevant time horizon for local coastal stakeholders to start considering regional sea-level projections in their adaptation plans.

2100

For HESs-A in the *low* emission scenario, SLR may *appreciably* differ from GMSL (1.06 m) in Amsterdam (0.90 m), the Falkland Islands (0.91), Le Havre (0.85 m), and Stockholm (0.48 m). It may *appreciably* differ from GMSL (1.91 m) in the *high* scenario not only in the latter four sites but also in Djakarta (2.07 m), the Maldives (2.09 m), Manila (2.03 m), and Papeete (2.05 m).

For HESs-B in the *low* emission scenario and relative to HESs-A, discrepancies increase with SLR *appreciably* differing from GMSL (1.69 m). These discrepancies include Djakarta (1.85 m), the Maldives (1.88 m), Manila (1.85 m), New Orleans (1.87 m), New York (1.84 m), and Papeete (1.89 m). For HESs-B in the *high* emission scenario, all the sites may *appreciably* exceed (Dakar, Djakarta, The Maldives, Manila, New Orleans, New York, Papeete, and Shanghai) or be lower (Amsterdam, The Falkland Islands, Le Havre, and Stockholm) than GMSL (3.22 m).

2200

For HESs-A in the *low/high* emission scenario, while SLR remains *appreciably* lower than the GMSL (2.41/4.45 m) in Amsterdam (1.94/3.79 m), the Falkland Islands (1.78/3.04 m), Le Havre (1.86/3.55 m), and Stockholm (1.10/3.14 m), it may *appreciably* exceed GMSL in Dakar (only in the *high* emission scenario, 4.56 m), Djakarta (2.62/4.89 m), the Maldives (2.61/4.77 m), Manila (2.58/4.63 m), New Orleans (2.61/4.62 m), New York (2.59/5.05 m), and Papeete (2.63/4.68 m). Regarding Shanghai, scenarios are *not appreciably* lower than GMSL in the *low* emission scenario and *appreciably* lower than GMSL in the high emission scenario.

For HESs-B in the *low/high* emission scenario, GMSL may reach 3.98/11.15 m and SLR may *appreciably* differ in all locations. Values are higher than GMSL in Dakar (4.16/12.01 m), Djakarta (4.45/12.57 m), the Maldives (4.43/12.50 m), Manila (4.40/12.39 m), New Orleans (4.41/12.24 m), New York (4.22/12.49 m), Papeete (4.51/12.47 m), and Shanghai (4.14/11.50 m). They are lower in Amsterdam (3.22/10.45 m), in the Falkland Islands (2.96/7.04 m), Le Havre (2.96/10.04 m), and Stockholm (2.52/9.85 m).

Regional Contributions to Coastal City and Island HESs

Figures 6A,B illustrate the different contributions to HESs for each site by 2050, 2100, and 2200 relative to 1986–2005.

In 2100, for HESs-A and in the *low* emission scenario the largest contribution to sea-level changes are caused by sterodynamic oceanic processes in Amsterdam, Le Havre, New York, and Stockholm and are dominated by ice-sheets processes in the others cities. In the *high* emission scenario, ice-sheets processes seem to step up and dominate sea-level changes everywhere except in New York and Stockholm. In the *high* emissions scenario, the relative contribution of glaciers to SLR is more substantial than in the *low* emission scenario in all sites. Land water storage and GIA contribute to a lesser extent to SLR in all sites, except in Stockholm where GIA influences sea-level change almost at the same rate as oceanic or ice-sheets processes.

In 2200, for HESs-A in both emission scenarios, sea-level change would be driven mostly by ice-sheets, and then by sterodynamic oceanic processes in most of the twelve sites, except in Stockholm where GIA tends to dominate oceanic processes and substantially decrease SLR. Glaciers are the fourth contribution to SLR, except in New Orleans and New-York where GIA increases sea-level at least equally as important as Glaciers.

DISCUSSION

Limitations

A number of limitations need to be remembered: first, the whole discussion on HESs comes from limited understanding of ice-sheet melting processes (Stammer et al., 2019). However, there is not a consensus in the community of ice-sheet glaciologists that such large contributions to SLR are physically plausible, as illustrated by the discussion around the MICI (DeConto and Pollard, 2016; Edwards et al., 2019). Another difficulty lies in the projections beyond 2100, which have less confidence than those applicable during the 21st century due to the lack of knowledge about GHG emissions.

Some of the choices made for designing our high-end scenarios can be revised to fit user preference. In particular, we selected two quantile levels (83th and 95th) to reflect different degrees of risk aversion (Hinkel et al., 2019; Thiéblemont et al., 2019), but others may be more relevant. As a caveat, the selection of a particular quantile level should be made with attention to the number of samples used to fit the probability distribution (Wilks, 1941). In other words, there is generally not enough information in probabilistic projections of sea-level contributions to realistically evaluate the 99th percentile level. Finally, even if we have updated the ice sheet-related sea level projections from B19, we note that we rely on a single probabilistic projection, which is not sufficient (Jevrejeva et al., 2019). One way forward to go beyond the limits of this study would be to "*involve users with sea level information providers to co-design appropriate projections,*" as promoted in projects aiming at developing climate services such as the ERA4CS.

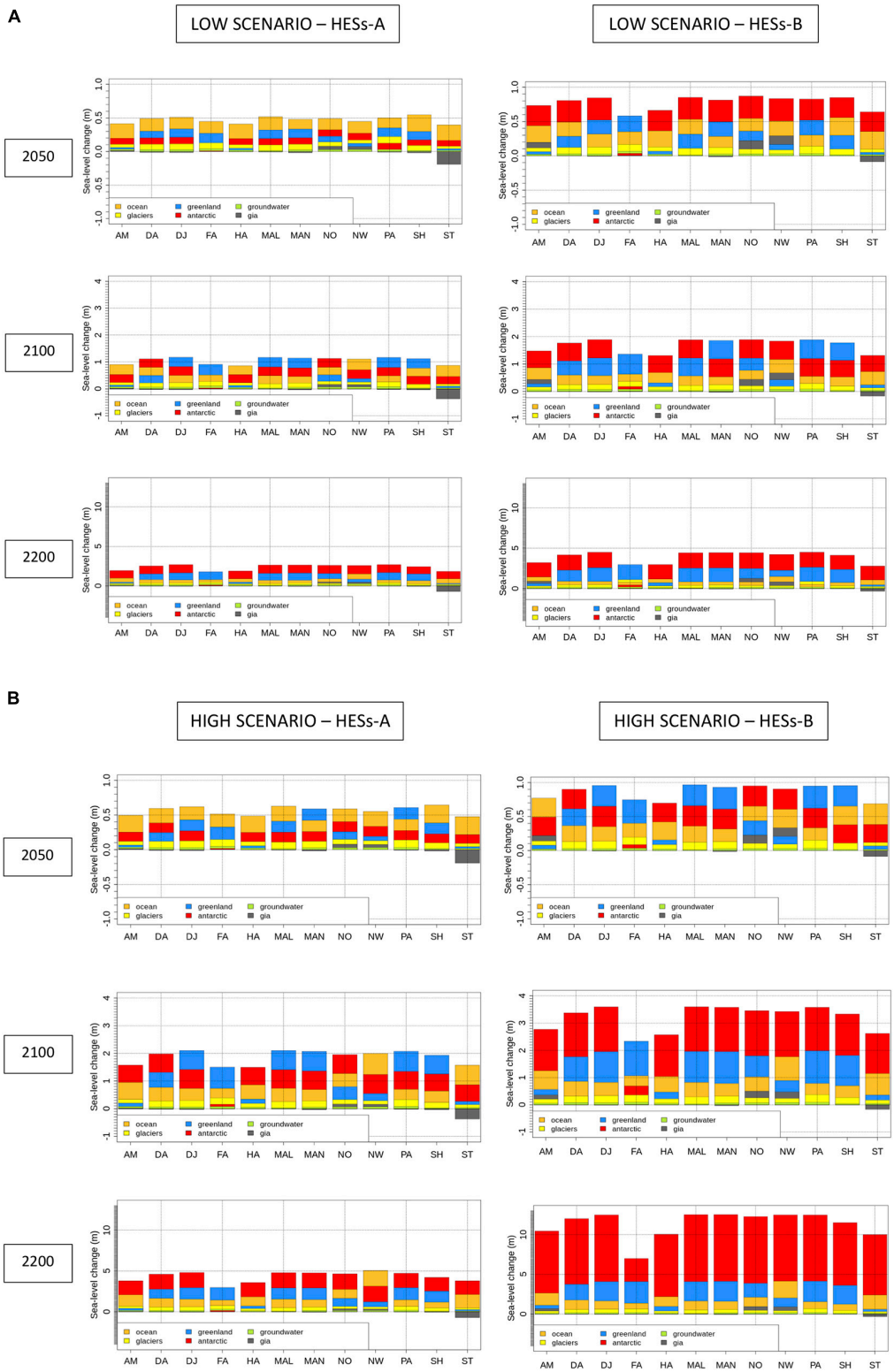

FIGURE 6 | Contributions to sea-level change (m) by 2050, 2100, and 2200 relative to 1986–2005 for both HESs in **(A)** the *low* emission scenario at left(right) and **(B)** the *high* emission scenario. The *X*-axis indicates the twelve selected sites: AM (AMsterdam), DA (DAkar), DJ (DJakarta), FA (The FAlkland Islands), HA (Le HAvre), MAL (The MALdives), MAN (MANila), NO (New Orleans), NW (New York), PA (PApeete), SH (SHanghai), and ST (STockholm). The top of each bar of the histogram indicates the regional SLR for each site including all the contributions (see **Table 3** for detailed values), while each color bar indicates the relative contribution to sea-level change for each component and are sorted in ascending order. Note that the boundaries of the *Y*-axis are different for each time horizon.

Other Drivers of Change

A number of bio-physical and human processes have been overlooked in this study. For example, coastal hydrodynamic processes may alter our HESs by up to a few percent (e.g., Zhang et al., 2004, 2017). This can be considered negligible given the uncertainties surrounding HESs. More importantly, vertical ground motions such as subsidence or uplift (Nicholls et al., 2021), coastal sediment losses and accumulation (Toimil et al., 2020), potential changes in extreme water levels due to potential storminess, bathymetry or river flow changes, or human adaptation actions (Oppenheimer et al., 2019), may locally cause changes in flooding and erosion risks that are larger than the impacts of the HESs presented above. For example, while these HESs appear extremely high, especially by 2050 for high emissions, we recall that subsidence can generate similar relative sea-level changes: in some coastal areas of Manilla, groundwater extractions are causing subsidence in the order of 5 cm/year in the north-western coast of the city and 1 cm/year at the tide gauge close to the city center (Raucoules et al., 2013). While these processes are highly non-linear in time, they mean that locally, relative sea-level changes comparable to those found here in our worst case HESs can happen within 10 years. Similar issues are known to already happening in other rapidly developing cities, especially in Southeast Asia, such as Djakarta. However, the example of Shanghai (Wang et al., 2012) shows that reducing groundwater extractions or refilling aquifers can mitigate the phenomenon.

Relevance to Coastal Adaptation

This study can be considered as a step forward compared to the previous approach consisting in defining high-end scenarios based on global SLR projections (Purvis et al., 2008; Nicholls et al., 2014; Le Cozannet et al., 2015; Rohmer et al., 2019). In fact, we explicitly account for the regional implications of the high-end ice-sheets melting scenarios that might cause SLR exceeding the IPPC *likely range*. Neglecting this effect leads to underestimating high-end sea-level changes in a number of places: for example, **Figure 3** shows that SLR in 2100 for the *high* emission scenario and HESs-B exceeds the global mean sea-level (GMSL, 3.22 m) in Dakar, Djakarta, the Maldives, Manila, New Orleans, New York, Papeete, and Shanghai (see **Table 3** for detailed values). While this phenomena can be qualitatively anticipated based on the fingerprints associated with ice-sheets melting, in particular, this study provides quantitative insight.

Recent works suggest that such HESs are particularly relevant for decision makers and risk-averse stakeholders to implement informed adaptation measures (Haasnoot et al., 2013; Ranger et al., 2013; Nicholls et al., 2014). In particular, risk-averse stakeholders are looking forward to information on high-end SLR tails of the distribution outside the specified IPPC *likely range* (Hinkel et al., 2015, 2019; Le Cozannet et al., 2017a). Hence, his study potentially brings relevant and context-specific SLR information to these risk-averse stakeholders (Hinkel et al., 2015, 2019; Stammer et al., 2019), but also to decision makers and any coastal end-users. One of the major results of our work is that the rate of SLR can differ substantially in different locations (see **Figure 3** and **Table 3**). For example, in the *high* emission HESs-B scenario, the Maldives may experience a rise of sea-level that is comparable to the global mean until 2050. Then, SLR would accelerate substantially, so that sea-level may exceed GMSL by about 30 cm in 2100 due to GRD effects associated with mass losses in Antarctica and Greenland. This type of result can be relevant for adaptation practitioners considering the timing of adaptation (Haasnoot et al., 2020). Another important result of this study is the 1.69 m GMSL in 2100 for the HESs-B and in the *low* emission scenario (largely above the 0.59 m GMSL given by the upper-end of the *likely range* in SROCC), suggesting that HESs could be relevant even for low emission scenarios (see also **Figure 3A**).

Future research in this area may lead to excluding a number of scenarios that cannot be ruled out today. Meanwhile, risk-averse users concerned with long term decisions still need guidance (Hinkel et al., 2019), and may refer to the values presented in this paper and others (Nicholls et al., 2014; Thiéblemont et al., 2019). While these HESs are highly uncertain, they correspond to very high risk of economic, environmental and very likely human losses, and they deserve some attention in adaptation planning, as it has already made in several domains such as nuclear safety (Destercke and Chojnacki, 2008), food engineering (Baudrit et al., 2009), environmental risk (Baudrit et al., 2007), or CO2 geological storage-related risk (Loschetter et al., 2016).

CONCLUSION

This study delivers global and regional HESs. Such scenarios have a major societal relevance, because they induce either large adaptation needs, or they imply retreat of coastlines in highly vulnerable low-elevated lands and islands during the second half of the 21st century. Several studies delivered HESs using a probabilistic framework combining greenhouse gas emission scenarios and estimates from simulation of the individual components of sea-level change based on a model selection and assumptions on ice-sheets contributions. However, this is not always an appropriate method to estimate HESs, especially because the physical models of future sea-level changes do not take into account some non-linear dynamical ice-sheet processes. We have used published expert elicitation for ice-sheet contributions, combining physical-based model projections for glaciers, ocean sterodynamic effects and glacial isostatic adjustment, updated contributions from land-water. We highlight that provided there is no additional vertical ground motion besides GIA, the likely projected SLR might be significantly exceeded as soon as 2050. Today, planning and implementing coastal relocation, accommodation or protection typically takes several decades. Hence, our result means that for risk-averse coastal managers, adaptation decision horizons might be much closer than previously thought. Our results also suggest that HESs should be taken into account even for low emission scenarios.

The regional HESs presented in this paper can be used by risk-averse coastal stakeholders to determine adaptation pathways over the 21st century and beyond. However, local subsidence effects can still represent a substantial contribution to future relative sea-level changes in some areas such as Manila or Djakarta, and they need to be characterized where needed. By construction, HESs have a low probability to occur, but as their effects may be dramatic they cannot be excluded given the present state of knowledge. In the coming years, research on SLR and the ice-sheets evolution will precise the confidence that can be assigned to the different sets of HESs that are being considered today. This will allow coastal adaptation to progressively adjust their adaptation pathways to the level of effort that is required.

DATA AVAILABILITY STATEMENT

The datasets presented in this study can be found in online repositories. The names of the repository/repositories and accession number(s) can be found below: https://vesg.ipsl.upmc.fr/thredds/catalog/IPSLFS/hdayan/Data_HESs/catalog.html.

AUTHOR CONTRIBUTIONS

HD and GL conceived of the presented idea. HD performed the computations and carried out the analyses. All authors discussed the results and contributed to the final manuscript.

FUNDING

This study benefited from the IPSL Prodiguer-Ciclad facility is supported by CNRS, UPMC, Labex L-IPSL (Grant #ANR-10-LABX-0018), and the European FP7 IS-ENES2 project (Grant #312979). This study was supported by a grant from the French Ministry for an Ecological and Solidary Transition as part of the Convention on financial support for climate services and the ANR Storisk project (ANR-15-CE03-0003).

ACKNOWLEDGMENTS

We acknowledge the World Climate Research Programme's Working Group on Coupled Modeling, which is in charge of the fifth Coupled Model Intercomparison Project, and we thank the climate modeling groups for producing and making available their model output. We acknowledge the Integrated Climate Data Center (ICDC, icdc.cen.uni-hamburg.de) University of Hamburg, Hamburg, Germany, for distributing the regional sea level data from IPCC AR5 as well as Kopp et al. (2014), Nauels et al. (2017), and Bamber et al. (2019) for making their data available.

SUPPLEMENTARY MATERIAL

The Supplementary Material for this article can be found online at: https://www.frontiersin.org/articles/10.3389/fmars.2021.569992/full#supplementary-material

REFERENCES

Alley, R. B., Clark, P. U., Huybrechts, P., and Joughin, I. (2005). Ice-sheet and sea-level changes. *Science* 310, 456–460. doi: 10.1126/science.1114613

Bamber, J. L., and Aspinall, W. P. (2013). An expert judgement assessment of future sea level rise from the ice sheets. *Nat. Clim. Chang* 3, 424–427. doi: 10.1038/nclimate1778

Bamber, J. L., Oppenheimer, M., Kopp, R. E., Aspinall, W. P., and Cooke, R. M. (2019). Ice sheet contributions to future sea-level rise from structured expert judgment. *Proc. Natl. Acad. Sci. U. S. A.* 116, 11195–11200. doi: 10.1073/pnas.1817205116

Baudrit, C., Guyonnet, D., and Dubois, D. (2007). Joint propagation of variability and imprecision in assessing the risk of groundwater contamination. *J. Contam. Hydrol.* 93, 72–84. doi: 10.1016/j.jconhyd.2007.01.015

Baudrit, C., Hélias, A., and Perrot, N. (2009). Joint treatment of imprecision and variability in food engineering: application to cheese mass loss during ripening. *J. Food Eng.* 93, 284–292. doi: 10.1016/j.jfoodeng.2009.01.031

Carson, M., Köhl, A., Stammer, D., Slangen, A. B. A., Katsman, C. A., van de Wal, R. S. W., et al. (2016). Coastal sea level changes, observed and projected during the 20th and 21st century. *Clim. Change* 134, 269–281. doi: 10.1007/s10584-015-1520-1521

Choi, Y., Morlighem, M., Rignot, E., and Wood, M. (2021). Ice dynamics will remain a primary driver of greenland ice sheet mass loss over the next century. *Commun. Earth Environ.* 2:26. doi: 10.1038/s43247-021-00092-z

Church, J. A., Clark, P. U., Cazenave, A., Gregory, J. M., Jevrejeva, S., Levermann, A., et al. (2013). "Chapter 13: sea level change," in *Climate Change 2013: The Physical Science Basis. Contribution of Working Group I to the Fifth Assessment Report of the Intergovernmental Panel on Climate Change*, eds T. F. Stocker, D. Qin, G.-K. Plattner, M. Tignor, S. K. Allen, and J. Boschung (Cambridge, NY: Cambridge University Press), doi: 10.1017/CB09781107415315.026

Collins, M., Knutti, R., Arblaster, J., Dufresne, J.-L., Fichefet, T., Friedlingstein, P., et al. (2013). "Long-term climate change: projections, commitments and irreversibility," in *Climate Change 2013 - The Physical Science Basis: Contribution of Working Group I to the Fifth Assessment Report of the Intergovernmental Panel on Climate Change*, eds T. F. Stocker, D. Qin, G.-K. Plattner, M. M. B. Tignor, S. K. Allen, J. Boschung, et al. (Cambridge: Cambridge University Press).

Couldrey, M. P., Gregory, J. M., Oluwayemi, G., Griffies, S. M., Haak, H., Hu, A., et al. (2021). What causes the spread of model projections of ocean dynamic sea-level change in response to greenhouse gas forcing? *Climate Dynam.* 56, 155–187. doi: 10.1007/s00382-020-05471-4

Dangendorf, S., Hay, C., Calafat, F. M., Marcos, M., Piecuch, C. G., Berk, K., et al. (2019). Persistent acceleration in global sea-level rise since the 1960s. *Nat. Clim. Chang* 9, 705–710. doi: 10.1038/s41558-019-0531-538

DeConto, R. M., Ekaykin, A., Mackintosh, A., Van de Wal, R., Bassis, J., Cross-Chapter Box 8 | Future Sea Level Changes and Marine Ice Sheet Instability in Meredith, M., et al. (2019). "Polar regions," in *IPCC Special Report on the Ocean and Cryosphere in a Changing Climate*, eds H.-O. Pörtner, D. C. Roberts, V. Masson-Delmotte, P. Zhai, M. Tignor, and E. Poloczanska (Geneva: IPCC).

DeConto, R. M., and Pollard, D. (2016). Contribution of Antarctica to past and future sea-level rise. *Nature* 531, 591–597. doi: 10.1038/nature17145

Destercke, S., and Chojnacki, E. (2008). Methods for the evaluation and synthesis of multiple sources of information applied to nuclear computer codes. *Nucl. Eng. Des.* 238, 2484–2493. doi: 10.1016/j.nucengdes.2008.02.003

Edwards, T. L., Brandon, M. A., Durand, G., Edwards, N. R., Golledge, N. R., Holden, P. B., et al. (2019). Revisiting Antarctic ice loss due to marine ice-cliff instability. *Nature* 566, 58–64. doi: 10.1038/s41586-019-0901-904

Frederikse, T., Landerer, F., Caron, L., Adhikari, S., Parkes, D., Humphrey, V. W., et al. (2020). The causes of sea-level rise since 1900. *Nature* 584, 393–397. doi: 10.1038/s41586-020-2591-2593

Fürst, J. J., Goelzer, H., and Huybrechts, P. (2015). Ice-dynamic projections of the Greenland ice sheet in response to atmospheric and oceanic warming. *Cryosphere* 9, 1039–1062. doi: 10.5194/tc-9-1039-2015

Gregory, J. M., Griffies, S. M., Hughes, C. W., Lowe, J. A., Church, J. A., Fukimori, I., et al. (2019). Concepts and terminology for sea level: mean, variability and change, both local and global. *Surv. Geophys.* 40, 1251–1289. doi: 10.1007/s10712-019-09525-z

Gregory, J. M., White, N. J., Church, J. A., Bierkens, M. F. P., Box, J. E., Van Den Broeke, M. R., et al. (2013). Twentieth-century global-mean sea level rise: is the whole greater than the sum of the parts? *J. Clim.* 26, 4476–4499. doi: 10.1175/JCLI-D-12-00319.1

Grinsted, A., Jevrejeva, S., Riva, R. E. M., and Dahl-Jensen, D. (2015). Sea level rise projections for Northern Europe under RCP8.5. *Clim. Res.* 64, 15–23. doi: 10.3354/cr01309

Haasnoot, M., Kwadijk, J., Van Alphen, J., Le Bars, D., Van Den Hurk, B., Diermanse, F., et al. (2020). Adaptation to uncertain sea-level rise; how uncertainty in Antarctic mass-loss impacts the coastal adaptation strategy of the Netherlands. *Environ. Res. Lett.* 15:034007. doi: 10.1088/1748-9326/ab666c

Haasnoot, M., Kwakkel, J. H., Walker, W. E., and ter Maat, J. (2013). Dynamic adaptive policy pathways: a method for crafting robust decisions for a deeply uncertain world. *Glob. Environ. Chang* 23, 485–498. doi: 10.1016/j.gloenvcha.2012.12.006

Hinkel, J., Church, J. A., Gregory, J. M., Lambert, E., Le Cozannet, G., Lowe, J., et al. (2019). Meeting user needs for sea level rise information: a decision analysis perspective. *Earth's Futur.* 7, 320–337. doi: 10.1029/2018EF001071

Hinkel, J., Jaeger, C., Nicholls, R. J., Lowe, J., Renn, O., and Peijun, S. (2015). Sea-level rise scenarios and coastal risk management. *Nat. Clim. Chang* 5, 188–190. doi: 10.1038/nclimate2505

Huss, M., and Hock, R. (2015). A new model for global glacier change and sea-level rise. *Front. Earth Sci.* 3:54. doi: 10.3389/feart.2015.00054

Intergovernmental Panel on Climate Change [IPCC] (2013). "Climate change 2013 the physical science basis," in *Contribution of Working Group I to the Fifth Assessment Report of the Intergovernmental Panel on Climate Change*, eds T. F. Stocker, D. Qin, G.-K. Plattner, M. Tignor, S. K. Allen, and J. Boschung (Cambridge NY: Cambridge University Press).

Intergovernmental Panel on Climate Change [IPCC] (2014). *Climate Change 2014 Mitigation of Climate Change*. Geneva: IPCC, doi: 10.1017/cbo9781107415416

Intergovernmental Panel on Climate Change [IPCC] (2019). *Special Report: The Ocean and Cryosphere in a Changing Climate*. Geneva: IPCC.

Intergovernmental Panel on Climate Change [IPCC] (2018). An IPCC Special Report on the impacts of global warming of 1.5°C. *Intergov. Panel Clim. Chang*

Jackson, L. P., and Jevrejeva, S. (2016). A probabilistic approach to 21st century regional sea-level projections using RCP and High-end scenarios. *Glob. Planet. Change* 146, 179–189. doi: 10.1016/j.gloplacha.2016.10.006

Jevrejeva, S., Frederikse, T., Kopp, R. E., Le Cozannet, G., Jackson, L. P., and van de Wal, R. S. W. (2019). Probabilistic Sea level projections at the coast by 2100. *Surv. Geophys.* 40, 1673–1696. doi: 10.1007/s10712-019-09550-y

Jevrejeva, S., Grinsted, A., and Moore, J. C. (2014). Upper limit for sea level projections by 2100. *Environ. Res. Lett.* 9:104008. doi: 10.1088/1748-9326/9/10/104008

Joughin, I., Smith, B. E., and Medley, B. (2014). Marine ice sheet collapse potentially under way for the thwaites glacier basin. *West Antarctica. Sci.* 344, 735–738. doi: 10.1126/science.1249055

Konikow, L. F. (2011). Contribution of global groundwater depletion since 1900 to sea-level rise. *Geophys. Res. Lett.* 38:L18601. doi: 10.1029/2011GL048604

Kopp, R. E., DeConto, R. M., Bader, D. A., Hay, C. C., Horton, R. M., Kulp, S., et al. (2017). Evolving understanding of antarctic ice-sheet physics and ambiguity in probabilistic sea-level projections. *Earth's Futur.* 5, 1217–1233. doi: 10.1002/2017EF000663

Kopp, R. E., Horton, R. M., Little, C. M., Mitrovica, J. X., Oppenheimer, M., Rasmussen, D. J., et al. (2014). Probabilistic 21st and 22nd century sea-level projections at a global network of tide-gauge sites. *Earth's Futur.* 2, 383–406. doi: 10.1002/2014ef000239

Landerer, F. W., Jungclaus, J. H., and Marotzke, J. (2007). Regional dynamic and steric sea level change in response to the IPCC-A1B scenario. *J. Phys. Oceanogr.* 37, 296–312. doi: 10.1175/JPO3013.1

Le Bars, D. (2018). Uncertainty in sea level rise projections due to the dependence between contributors. *Earth's Futur.* 6, 1275–1291. doi: 10.1029/2018EF000849

Le Bars, D., Drijfhout, S., and De Vries, H. (2017). A high-end sea level rise probabilistic projection including rapid Antarctic ice sheet mass loss. *Environ. Res. Lett.* 12:044013. doi: 10.1088/1748-9326/aa6512

Le Cozannet, G., Manceau, J. C., and Rohmer, J. (2017a). Bounding probabilistic sea-level projections within the framework of the possibility theory. *Environ. Res. Lett.* 12:014012. doi: 10.1088/1748-9326/aa5528

Le Cozannet, G., Nicholls, R., Hinkel, J., Sweet, W., McInnes, K., Van de Wal, R., et al. (2017b). Sea level change and coastal climate services: the way forward. *J. Mar. Sci. Eng.* 5:49. doi: 10.3390/jmse5040049

Le Cozannet, G., Rohmer, J., Cazenave, A., Idier, D., van de Wal, R., de Winter, R., et al. (2015). Evaluating uncertainties of future marine flooding occurrence as sea-level rises. *Environ. Model. Softw.* 73, 44–56. doi: 10.1016/j.envsoft.2015.07.021

Loschetter, A., Rohmer, J., de Lary, L., and Manceau, J. C. (2016). Dealing with uncertainty in risk assessments in early stages of a CO2 geological storage project: comparison of pure-probabilistic and fuzzy-probabilistic frameworks. *Stoch. Environ. Res. Risk Assess.* 30, 813–829. doi: 10.1007/s00477-015-1035-1033

Marzeion, B., Jarosch, A. H., and Hofer, M. (2012). Past and future sea-level change from the surface mass balance of glaciers. *Cryosphere* 6, 1295–1322. doi: 10.5194/tc-6-1295-2012

Mastrandrea, M. D., Mach, K. J., Plattner, G. K., Edenhofer, O., Stocker, T. F., Field, C. B., et al. (2011). The IPCC AR5 guidance note on consistent treatment of uncertainties: a common approach across the working groups. *Clim. Change* 108:675. doi: 10.1007/s10584-011-0178-176

Meyssignac, B., Fettweis, W., Chevrier, R., and Spada, G. (2017). Regional Sea level changes for the twentieth and the twenty-first centuries induced by the regional variability in greenland ice sheet surface mass loss. *J. Climate* 30, 2011–2028. doi: 10.1175/JCLI-D-16-0337.1

Nauels, A., Meinshausen, M., Mengel, M., Lorbacher, K., and Wigley, T. M. L. (2017). Synthesizing long-Term sea level rise projections-the MAGICC sea level model v2.0. *Geosci. Model. Dev.* 10, 2495–2524. doi: 10.5194/gmd-10-2495-2017

Nicholls, R. J., Lincke, D., Hinkel, J., Brown, S., Vafeidis, A. T., Meyssignac, B., et al. (2021). A global analysis of subsidence, relative sea-level change and coastal flood exposure. *Nat. Claim. Chang* 11, 338–342.

Nicholls, R. J., and Cazenave, A. (2010). Sea-level rise and its impact on coastal zones. *Science* 328, 1517–1520. doi: 10.1126/science.1185782

Nicholls, R. J., Hanson, S. E., Lowe, J. A., Warrick, R. A., Lu, X., and Long, A. J. (2014). Sea-level scenarios for evaluating coastal impacts. *Wiley Interdiscip. Rev. Clim. Chang* 5, 129–150. doi: 10.1002/wcc.253

Nowicki, S., and Seroussi, H. (2018). Projections of future sea level contributions from the greenland and antarctic ice sheets: challenges beyond dynamical ice sheet modeling. *Oceanography* 31, 109–117. doi: 10.5670/oceanog.2018.216

Nowicki, S. M. J., Payne, A., Larour, E., Seroussi, H., Goelzer, H., Lipscomb, W., et al. (2016). Ice Sheet Model Intercomparison Project (ISMIP6) contribution to CMIP6. *Geosci. Model Dev.* 9, 4521–4545. doi: 10.5194/gmd-9-4521-2016

Oppenheimer, M., Glavovic, B., Hinkel, J., van de Wal, R., Magnan, A. K., Abd-Elgawad, A., et al. (eds) (2019). "Sea level rise and implications for low lying islands, coasts and communities," in *IPCC Special Report on the Ocean and Cryosphere in a Changing Climate*, eds H.-O. Pörtner, et al. (Cambridge: Cambridge University Press).

Pfeffer, W. T., Harper, J. T., and O'Neel, S. (2008). Kinematic constraints on glacier contributions to 21st-century sea-level rise. *Science* 321, 1340–1343. doi: 10.1126/science.1159099

Pokhrel, Y., Hanasaki, N., Koirala, S., Cho, J., Yeh, P. J. F., Kim, H., et al. (2012). Incorporating anthropogenic water regulation modules into a land surface model. *J. Hydrometeorol.* 13, 255–269. doi: 10.1175/JHM-D-11-013.1

Purvis, M. J., Bates, P. D., and Hayes, C. M. (2008). A probabilistic methodology to estimate future coastal flood risk due to sea level rise. *Coast. Eng.* 55, 1062–1073. doi: 10.1016/j.coastaleng.2008.04.008

Ranger, N., Reeder, T., and Lowe, J. (2013). Addressing 'deep' uncertainty over long-term climate in major infrastructure projects: four innovations of the Thames Estuary 2100 Project. *EURO J. Decis. Process.* 1, 233–262. doi: 10.1007/s40070-013-0014-15

Raucoules, D., Le Cozannet, G., Wöppelmann, G., de Michele, M., Gravelle, M., Daag, A., et al. (2013). High nonlinear urban ground motion in Manila (Philippines) from 1993 to 2010 observed by DInSAR: implications for sea-level measurement. *Remote Sens. Environ.* 139, 386–397. doi: 10.1016/j.rse.2013.08.021

Reimann, L., Vafeidis, A. T., Brown, S., Hinkel, J., and Tol, R. S. J. (2018). Mediterranean UNESCO world heritage at risk from coastal flooding and erosion due to sea-level rise. *Nat. Commun.* 9:4161. doi: 10.1038/s41467-018-06645-6649

Rignot, E., Mouginot, J., Morlighem, M., Seroussi, H., and Scheuchl, B. (2014). Widespread, rapid grounding line retreat of Pine Island, Thwaites, Smith, and Kohler glaciers, West Antarctica, from 1992 to 2011. *Geophys. Res. Lett.* 41, 3502–3509. doi: 10.1002/2014GL060140

Rignot, E., Mouginot, J., Scheuchl, B., Van Den Broeke, M., Van Wessem, M. J., and Morlighem, M. (2019). Four decades of Antarctic ice sheet mass balance from 1979–2017. *Proc. Natl. Acad. Sci. U S A.* 116, 1095–1103. doi: 10.1073/pnas.1812883116

Rignot, E., Velicogna, I., Van Den Broeke, M. R., Monaghan, A., and Lenaerts, J. (2011). Acceleration of the contribution of the Greenland and Antarctic ice sheets to sea level rise. *Geophys. Res. Lett.* 38:L05503. doi: 10.1029/2011GL046583

Ritz, C., Edwards, T. L., Durand, G., Payne, A. J., Peyaud, V., and Hindmarsh, R. C. A. (2015). Potential sea-level rise from Antarctic ice-sheet instability constrained by observations. *Nature* 528, 115–118. doi: 10.1038/nature16147

Rohmer, J., Le Cozannet, G., and Manceau, J. C. (2019). Addressing ambiguity in probabilistic assessments of future coastal flooding using possibility distributions. *Clim. Chang.* 155, 95–109. doi: 10.1007/s10584-019-02443-4

Spada, G., Bamber, J. L., and Hurkmans, R. T. W. L. (2013). The gravitationally consistent sea-level fingerprint of future terrestrial ice loss. *Geophys. Res. Lett.* 40, 482–486. doi: 10.1029/2012GL053000

Shepherd, A., Ivins, E., Rignot, E., Smith, B., Van Den Broeke, M., Velicogna, I., et al. (2018). Mass balance of the Antarctic Ice Sheet from 1992 to 2017. *Nature* 558, 219–222. doi: 10.1038/s41586-018-0179-y

Shepherd, A., Ivins, E. R., Geruo, A., Barletta, V. R., Bentley, M. J., Bettadpur, S., et al. (2012). A reconciled estimate of ice-sheet mass balance. *Science* 338, 1183–1189. doi: 10.1126/science.1228102

Slangen, A. B. A., Adloff, F., Jevrejeva, S., Leclercq, P. W., Marzeion, B., Wada, Y., et al. (2017). A review of recent updates of sea-level projections at global and regional scales. *Surv. Geophys.* 38, 385–406. doi: 10.1007/s10712-016-9374-9372

Slangen, A. B. A., Carson, M., Katsman, C. A., van de Wal, R. S. W., Köhl, A., Vermeersen, L. L. A., et al. (2014). Projecting twenty-first century regional sea-level changes. *Clim. Change* 124, 317–332. doi: 10.1007/s10584-014-1080-1089

Slangen, A. B. A., Church, J. A., Agosta, C., Fettweis, X., Marzeion, B., and Richter, K. (2016). Anthropogenic forcing dominates global mean sea-level rise since 1970. *Nat. Clim. Chang* 6, 701–705. doi: 10.1038/nclimate2991

Slangen, A. B. A., and van de Wal, R. S. W. (2011). An assessment of uncertainties in using volume-area modelling for computing the twenty-first century glacier contribution to sea-level change. *Cryosph* 5, 673–686. doi: 10.5194/tc-5-673-2011

Stammer, D., van de Wal, R. S. W., Nicholls, R. J., Church, J. A., Le Cozannet, G., Lowe, J. A., et al. (2019). Framework for high-end estimates of sea level rise for stakeholder applications. *Earth's Futur.* 7, 923–938. doi: 10.1029/2019EF001163

Tessler, Z. D., Vörösmarty, C. J., Overeem, I., and Syvitski, J. P. M. (2018). A model of water and sediment balance as determinants of relative sea level rise in contemporary and future deltas. *Geomorphology* 305, 209–220. doi: 10.1016/j.geomorph.2017.09.040

Thiéblemont, R., Le Cozannet, G., Toimil, A., Meyssignac, B., and Losada, I. J. (2019). Likely and high-end impacts of regional sea-level rise on the shoreline change of European sandy coasts under a high greenhouse gas emissions scenario. *Water* 11:2607. doi: 10.3390/w11122607

Toimil, A., Camus, P., Losada, I. J., Le Cozannet, G., Nicholls, R. J., Idier, D., et al. (2020). Climate change-driven coastal erosion modelling in temperate sandy beaches: methods and uncertainty treatment. *Earth-Science Rev.* 202:103110. doi: 10.1016/j.earscirev.2020.103110

Vizcaino, M., Mikolajewicz, U., Ziemen, F., Rodehacke, C. B., Greve, R., and Van Den Broeke, M. R. (2015). Coupled simulations of greenland ice sheet and climate change up to A.D. 2300. *Geophys. Res. Lett.* 42, 3927–3935. doi: 10.1002/2014GL061142

Wada, Y., Lo, M. H., Yeh, P. J. F., Reager, J. T., Famiglietti, J. S., Wu, R. J., et al. (2016). Fate of water pumped from underground and contributions to sea-level rise. *Nat. Clim. Chang* 7, 777–780. doi: 10.1038/nclimate3001

Wada, Y., Van Beek, L. P. H., Sperna Weiland, F. C., Chao, B. F., Wu, Y. H., and Bierkens, M. F. P. (2012). Past and future contribution of global groundwater depletion to sea-level rise. *Geophys. Res. Lett.* 39:L09402. doi: 10.1029/2012GL051230

Wang, J., Gao, W., Xu, S., and Yu, L. (2012). Evaluation of the combined risk of sea level rise, land subsidence, and storm surges on the coastal areas of Shanghai. China. *Clim. Change* 115, 537–558. doi: 10.1007/s10584-012-0468-467

Weisse, R., and Hünicke, B. (2019). Baltic sea level: past, present, and future. *Oxford Res. Encycl. Clim. Sci.* doi: 10.1093/acrefore/9780190228620.013.693

Wilks, S. S. (1941). Determination of sample sizes for setting tolerance limits. *Ann. Math. Stat.* 12, 91–96. doi: 10.1214/aoms/1177731788

Yin, J., Schlesinger, M. E., and Stouffer, R. J. (2009). Model projections of rapid sea-level rise on the northeast coast of the United States. *Nat. Geosci.* 2, 262–266. doi: 10.1038/ngeo462

Zhang, K., Douglas, B. C., and Leatherman, S. P. (2004). Global warming and coastal erosion. *Clim. Change* 64:41. doi: 10.1023/B:CLIM.0000024690.32682.48

Zhang, X., Church, J. A., Monselesan, D., and McInnes, K. L. (2017). Sea level projections for the Australian region in the 21st century. *Geophys. Res. Lett.* 44, 8481–8491. doi: 10.1002/2017GL074176

Conflict of Interest: The authors declare that the research was conducted in the absence of any commercial or financial relationships that could be construed as a potential conflict of interest.

Advantages of publishing in Frontiers

OPEN ACCESS
Articles are free to read for greatest visibility and readership

FAST PUBLICATION
Around 90 days from submission to decision

HIGH QUALITY PEER-REVIEW
Rigorous, collaborative, and constructive peer-review

TRANSPARENT PEER-REVIEW
Editors and reviewers acknowledged by name on published articles

Frontiers
Avenue du Tribunal-Fédéral 34
1005 Lausanne | Switzerland

Visit us: www.frontiersin.org
Contact us: frontiersin.org/about/contact

REPRODUCIBILITY OF RESEARCH
Support open data and methods to enhance research reproducibility

DIGITAL PUBLISHING
Articles designed for optimal readership across devices

FOLLOW US
@frontiersin

IMPACT METRICS
Advanced article metrics track visibility across digital media

EXTENSIVE PROMOTION
Marketing and promotion of impactful research

LOOP RESEARCH NETWORK
Our network increases your article's readership